IAEA-TECDOC-1626

Advanced Reactor Technology Options for Utilization and Transmutation of Actinides in Spent Nuclear Fuel

IAEA
International Atomic Energy Agency

IAEA-TECDOC-1626

Advanced Reactor Technology Options for Utilization and Transmutation of Actinides in Spent Nuclear Fuel

IAEA
International Atomic Energy Agency

The following States are Members of the International Atomic Energy Agency:

AFGHANISTAN
ALBANIA
ALGERIA
ANGOLA
ARGENTINA
ARMENIA
AUSTRALIA
AUSTRIA
AZERBAIJAN
BAHRAIN
BANGLADESH
BELARUS
BELGIUM
BELIZE
BENIN
BOLIVIA
BOSNIA AND HERZEGOVINA
BOTSWANA
BRAZIL
BULGARIA
BURKINA FASO
BURUNDI
CAMEROON
CANADA
CENTRAL AFRICAN REPUBLIC
CHAD
CHILE
CHINA
COLOMBIA
CONGO
COSTA RICA
CÔTE D'IVOIRE
CROATIA
CUBA
CYPRUS
CZECH REPUBLIC
DEMOCRATIC REPUBLIC OF THE CONGO
DENMARK
DOMINICAN REPUBLIC
ECUADOR
EGYPT
EL SALVADOR
ERITREA
ESTONIA
ETHIOPIA
FINLAND
FRANCE
GABON
GEORGIA
GERMANY
GHANA
GREECE
GUATEMALA
HAITI
HOLY SEE
HONDURAS
HUNGARY
ICELAND
INDIA
INDONESIA
IRAN, ISLAMIC REPUBLIC OF
IRAQ
IRELAND
ISRAEL
ITALY
JAMAICA
JAPAN
JORDAN
KAZAKHSTAN
KENYA
KOREA, REPUBLIC OF
KUWAIT
KYRGYZSTAN
LATVIA
LEBANON
LESOTHO
LIBERIA
LIBYAN ARAB JAMAHIRIYA
LIECHTENSTEIN
LITHUANIA
LUXEMBOURG
MADAGASCAR
MALAWI
MALAYSIA
MALI
MALTA
MARSHALL ISLANDS
MAURITANIA
MAURITIUS
MEXICO
MONACO
MONGOLIA
MONTENEGRO
MOROCCO
MOZAMBIQUE
MYANMAR
NAMIBIA
NEPAL
NETHERLANDS
NEW ZEALAND
NICARAGUA
NIGER
NIGERIA
NORWAY
OMAN
PAKISTAN
PALAU
PANAMA
PARAGUAY
PERU
PHILIPPINES
POLAND
PORTUGAL
QATAR
REPUBLIC OF MOLDOVA
ROMANIA
RUSSIAN FEDERATION
SAUDI ARABIA
SENEGAL
SERBIA
SEYCHELLES
SIERRA LEONE
SINGAPORE
SLOVAKIA
SLOVENIA
SOUTH AFRICA
SPAIN
SRI LANKA
SUDAN
SWEDEN
SWITZERLAND
SYRIAN ARAB REPUBLIC
TAJIKISTAN
THAILAND
THE FORMER YUGOSLAV REPUBLIC OF MACEDONIA
TUNISIA
TURKEY
UGANDA
UKRAINE
UNITED ARAB EMIRATES
UNITED KINGDOM OF GREAT BRITAIN AND NORTHERN IRELAND
UNITED REPUBLIC OF TANZANIA
UNITED STATES OF AMERICA
URUGUAY
UZBEKISTAN
VENEZUELA
VIETNAM
YEMEN
ZAMBIA
ZIMBABWE

The Agency's Statute was approved on 23 October 1956 by the Conference on the Statute of the IAEA held at United Nations Headquarters, New York; it entered into force on 29 July 1957. The Headquarters of the Agency are situated in Vienna. Its principal objective is "to accelerate and enlarge the contribution of atomic energy to peace, health and prosperity throughout the world".

FOREWORD

Renewed interest in the potential of nuclear energy to contribute to a sustainable worldwide energy mix is strengthening the IAEA's statutory role in fostering the peaceful uses of nuclear energy, in particular the need for effective exchanges of information and collaborative research and technology development among Member States on advanced nuclear power technologies (Articles III-A.1 and III-A.3).

The major challenges facing the long term development of nuclear energy as a part of the world's energy mix are improvement of the economic competitiveness, meeting increasingly stringent safety requirements, adhering to the criteria of sustainable development, and public acceptability. The concern linked to the long life of many of the radioisotopes generated from fission has led to increased R&D efforts to develop a technology aimed at reducing the amount of long lived radioactive waste through transmutation in fission reactors or accelerator driven hybrids. In recent years, in various countries and at an international level, more and more studies have been carried out on advanced and innovative waste management strategies (i.e. actinide separation and elimination). Within the framework of the Project on Technology Advances in Fast Reactors and Accelerator Driven Systems (http://www.iaea.org/inisnkm/nkm/aws/fnss/index.html), the IAEA initiated a number of activities on utilization of plutonium and transmutation of long lived radioactive waste, accelerator driven systems, thorium fuel options, innovative nuclear reactors and fuel cycles, non-conventional nuclear energy systems, and fusion/fission hybrids. These activities are implemented under the guidance and with the support of the IAEA Nuclear Energy Department's Technical Working Group on Fast Reactors (TWG-FR).

This publication compiles the analyses and findings of the Coordinated Research Project (CRP) on Studies of Advanced Reactor Technology Options for Effective Incineration of Radioactive Waste (2002–2007). The overall objective of the CRP, performed within the framework of the TWG-FR) was to increase the capability of interested Member States in developing and applying advanced technologies in the area of long lived radioactive waste utilization and transmutation. The final goal of the CRP was to deepen the understanding of the dynamics of transmutation systems, to qualify the available methods, specify their range of validity, and formulate requirements for future theoretical developments. Twenty institutions from 15 Member States and three international organizations have actively participated in this CRP. The comparative investigations cover burner reactors and transmuters both containing fertile and fertile-free fuels. The systems are designed either as neutronically critical or sub-critical (hybrid) driven by an external neutron source. The neutron spectra of the reactors extend from low thermal to fusion neutron energy levels. Further, systems with solid fuels and with molten salt fuels are compared. The solid fuel systems investigated also cover the impact of various coolants from sodium to heavy liquid metals and gas.

The main scientific driving force behind the CRP was W. Maschek from the Kernforschungszentrum Karlsruhe, Germany. The IAEA would like to express its appreciation to him and to the contributors listed at the end of the publication. The IAEA officer responsible for this publication was A. Stanculescu of the Division of Nuclear Power.

The originating Section of this publication in the IAEA was:

Nuclear Power Technology Development Section
International Atomic Energy Agency
Vienna International Centre
PO Box 100
1400 Vienna, Austria

ADVANCED REACTOR TECHNOLOGY OPTIONS FOR UTILIZATION AND TRANSMUTATION OF ACTINIDES IN SPENT NUCLEAR FUEL
IAEA, VIENNA, 2009

IAEA-TECDOC-1626

ISBN 978–92–0–109309–7
ISSN 1011-4289

Printed by the IAEA in Austria
September 2009

EDITORIAL NOTE

The use of particular designations of countries or territories does not imply any judgement by the publisher, the IAEA, as to the legal status of such countries or territories, of their authorities and institutions or of the delimitation of their boundaries.

The mention of names of specific companies or products (whether or not indicated as registered) does not imply any intention to infringe proprietary rights, nor should it be construed as an endorsement or recommendation on the part of the IAEA.

CONTENTS

INTRODUCTION

A Coordinated Research Project (CRP) on Studies of Advanced Reactor Technology Options for Effective Incineration of Radioactive Waste has been performed within the framework of IAEA's Technical Working Group on Fast Reactors (TWG-FR). The overall objective of the CRP was to increase the capability of interested Member States in developing and applying advanced technologies in the area of long lived radioactive waste utilization and transmutation. The final goal of the CRP was to deepen the understanding of the dynamics of transmutation systems (e.g. the accelerator driven system), in particular of systems with deteriorated safety parameters, to qualify the available methods, specify the range of validity of these methods, and formulate requirements for future theoretical developments. Based on the results, the CRP concluded on the potential need of transient experiments and makes some proposals for experimental programs. Twenty institutions from 15 Member States and three international organizations have actively participated in this CRP:

The CRP concentrated on the assessment of the transient behavior of various transmutation systems. For a sound assessment of the transient and accident behavior, neutron kinetics and dynamics methods and codes had to be qualified, even more so as the margins for the safety relevant neutronics parameters are becoming small in transmutation systems, especially in transmuters with fertile-free fuels. Hence, the availability of adequate and qualified methods for the analysis of the various systems was an important point of the exercise. A benchmarking effort between the codes and nuclear data used for the analyses was performed, which eventually substantiated the methodology, the validity range of assumptions, and also identified the requirements for future theoretical and experimental research. The inter-comparisons performed within the framework of the CRP were not merely a comparison exercise between codes, but should reflect the overall status of methods and data-bases used by the individual participants. Therefore, individual responsibility was given to the participants to use their methods and data-bases. However an extensive benchmarking effort has been performed to guarantee the validity of results.

The main thrust of the benchmarking work was on 'long timescale' effects of transients in the ms to s range, initiated by strong perturbations of the core and/or the external neutron source. This means that changes of the flux-shape and power caused, e.g. by a strong reactivity perturbation were in the centre of interest.

The comparative investigations covered burner reactors and transmuters both containing fertile and fertile-free, so-called 'dedicated' fuels. These reactors are loaded with differing amounts of minor actinides (MAs). The systems are designed either as neutronically critical or sub-critical (hybrid) driven by an external neutron source. The neutron spectra of the reactors extend from low thermal to fusion neutron energy levels. Further, both systems with solid fuels and molten salt fuels are compared. The solid fuel systems investigated range from ordinary MOX to advanced dedicated fuels and cover also the impact of various coolants from sodium to heavy liquid metals and gas.

Specifically, the systems investigated are allocated to eight different domains, which comprise in detail:

DOMAIN-I:	Critical fast reactor with transmutation capability and with fertile fuel
DOMAIN-II:	Critical fast reactor with transmutation capability and with fertile-free fuel
DOMAIN-III:	Hybrid system (ADS) with fertile fuel
DOMAIN-IV:	Hybrid system (ADS) with fertile-free fuel
DOMAIN-V:	Molten salt reactor with fertile fuel
DOMAIN-VI:	Molten salt reactor with fertile-free fuels
DOMAIN-VII:	Gas cooled hybride (ADS) systems with fertile-free fuels
DOMAIN-VIII:	Fission-fusion hybride system

The focus of Domain-I is on the fast reactor option for incineration of radioactive waste. The fast reactors dedicated to burn minor actinides use solid fuel and fertile breeder material in the core/blanket. A common characteristic of the reactors is the preference of Th to ^{238}U as fertile to

reduce production of MA. The CRP participants have independently designed fast reactor models under this domain and studied their static and transient safety related neutronic behavior. The models and contributions of IGCAR and IPPE are based on an existing power reactor design, with variations accommodated for the specific need of MA incineration. The model of JRC finally considers the design of a lead-cooled fast reactor (LFR) and a sodium-cooled fast reactor (SFR), of the 600 MW(e) power class.

The Domain-II analyzed critical reactors with solid non-fertile fuel provided by JRC. A comparison of a sodium cooled fast reactor (SFR) versus a lead cooled fast reactor (LFR), both as Pu and MA burners has been performed. Both systems are fuelled with CERMET fuel based on a fertile-free ^{92}Mo matrix, and are rated at 600 MW(e).

The Domain III benchmark exercises are based on the MYRRHA concept, as originally developed by SCK•CEN within EURATOM's 5th Framework Program. MYRRHA is a lead-bismuth eutectic cooled 50 MW(th) sub-critical reactors driven by a spallation source. Two configurations were analyzed: a reference sub-critical core configuration consisting of 45 MOX fuel assemblies (30 wt% Pu enrichment), and a core with 24 uranium-free assemblies containing MAs embedded in an MgO matrix plus 48 MOX assemblies.

In Domain-IV, FZK and Kyushu University contributed two benchmark cases. Two fertile-free ADS systems (both of 580 MW(th) power) with three core zones and varying fuel/matrix and Pu/MA ratios have been developed and investigated. The fuels are based on a ZrO_2 and MgO inert matrices respectively. Both the static and transient calculations were performed with the help of the SIMMER-III code. Fertile-free cores with a large amount of Minor Actinides are characterized by the lack of the prompt stabilizing Doppler temperature feedback, very small β_{eff}, and considerable fuel, coolant, and cladding material density reactivity effects. In ADS, sub-criticality offers a means to design cores that would cope with such fuels.

The Domain-V analyzed a critical molten salt reactor with fertile fuel of the 2 250 MW(th) power class. The benchmark is based on the Li/Be/Th-F AMSTER (Actinides Molten Salt TransmutER) incinerator concept, originally proposed by EdF as part of EURATOM's 5th Framework Program MOST Project. AMSTER is based on ORNL's Molten Salt Breeder Reactor (MSBR) design (proposed in the 1970s to optimize breeding in a thorium cycle), and comprises a 'burner' concept utilizing the actinides originating from PWRs and a 'breeder' concept having a conversion factor close to 1.0 designed to reduce the amount of long lived waste.

The benchmark case investigated in Domain-VI, provided by RRC-KI, is based on the Na/Be/Li-F MOlten Salt Advanced Reactor Transmuter (MOSART) concept that was investigated within the framework of the ISTC project #1606. The benchmark considers the MOSART concept as incinerator of actinides from LWR spent fuel. Hence, actinide (An) composition of the MOSART start-up and feed fuel correspond to the composition of the unloaded commercial PWR UOX fuel. MOSART is a 2400 MW(th) system with a cylindrical core, and has an intermediate to fast neutron spectrum.

In Domain-VII 400 MW(th) helium cooled ADS was proposed by CEA. The actinides (Pu, Np, Am and Cm) bearing CERCER fuel has an MgO matrix. For the gas cooled system only static neutronic analyses and benchmarking has been performed.

The fusion/fission system benchmarks are based on ASIPP and AGH University of Science and Technology proposals (FDS-I and Tandem Mirror Concept, respectively). The Tandem Mirror Concept is of the 500 MW(th) class with a subcritical k_{eff} of 0.84 with MA loaded blankets. FDS-I is a sub-critical system (k_{eff}=0.946) in which 14.1 MeV neutrons produced by a 150 MW(th) DT-plasma are driving a blanket loaded with actinides and fission products. The actinide fuel is carbide particle fuel cooled by lithium-tritium eutectic.

For a general assessment and comparison, the safety coefficients (prompt feedback effects like the Doppler effect, thermal fuel expansion, the delayed feedback from clad, coolant and other core constituents, and finally the kinetics parameters) were determined for the individual systems. In a

second step, transient analyses were performed which should reflect the generic behaviour of the reactor types and should allow a comparative assessment of, e.g. fertile versus fertile-free cores, critical versus sub-critical source driven systems, and solid fuel versus molten salt fuels. Besides the safety and transients related work the transmutation capability of the various systems was confirmed and questions of the fuel cycle were dealt with. Finally a material data base has been developed within this CRP providing valuable input for other projects.

In the report the individual DOMAINS are described in complete and self-contained chapters. The general conclusions from the benchmark exercise and key features of the individual systems are provided in a separate chapter, highlightening also the differences in the dynamic behaviour.

CHAPTER 1. DOMAIN-I: CRITICAL FAST REACTORS WITH TRANSMUTATION CAPABILITY AND WITH FERTILE FUELS

1.1. Introduction

India's nuclear energy programme consists of three stages of using its limited uranium and abundant thorium resources with closed fuel cycle. The natural uranium fuelled heavy water moderated pressurized heavy water reactors (PHWR) of the first stage presently dominate our nuclear energy programme. Experience with the operating fast breeder test reactor (FBTR), and the design of a mixed oxide fueled 500 MW(e) prototype fast breeder reactor (PFBR) under construction at Kalpakkam mark the beginning of the second stage, wherein the plutonium and the depleted uranium obtained from the PHWR spent fuel are used as the fuel. The world's only operating ^{233}U fueled small thermal reactor at Kalpakkam, KAMINI, and the innovative design of an advanced heavy water reactor (AHWR), both utilizing fuel of the thorium cycle, prepare us to take on the third stage in future.

The IAEA Coordinated Research Programme (CRP) on Studies of Advanced Reactor Technology Options for Effective Incineration of Radioactive Waste [1] has an overall objective of carrying out R&D towards demonstrating the transmutation and incineration of the long lived minor actinides (MA) using accelerator driven systems (ADS) and fast reactors. The majority of actinide waste production in India, at present, is from PHWRs, some of which could be incinerated in a fast reactor spectrum. With this motivation behind our participation in the CRP, an FBR model has been designed, with the PFBR core features [2] almost maintained, and with modifications done as necessitated by deliberate inclusion of 5% MA in the fresh fuel. The radial blanket is made of ThO_2, and not depleted UO_2 as in PFBR, in order to reduce production of some long lived higher actinides. The initial composition of MA taken for the study correspond to that of the Indian PHWR discharged fuel (uncooled). This FBR model, designed at the Indira Gandhi Centre for Atomic Research (IGCAR), Kalpakkam, shows a potential to incinerate nearly 10% of the MA, during one equilibrium cycle, with satisfactory safety parameters. For ease of reference, this FBR model is called 'FBR-MA' in this report. Salient results of the following studies made on FBR-MA are presented:

— Static analysis: The results were presented in the Second CRP meeting in Hefei, China, during November 2004 [3];
— Transient analysis: The results were presented in the CRP consultancy meeting at the IAEA Headquarters in Vienna, Austria, during November 2005 [4];
— MA data from different evaluations: This study has been done during this year, to see the spread in the results due to the spread in the nuclear data of minor actinides in different evaluations. The results were presented in the Third CRP meeting held in India during January 2007;
— Thorium in axial blankets: This study has been done during this year. While the original design has UO_2 in the axial blankets with ThO_2 in radial blanket, this study considers ThO_2 for the axial blankets as well. The results were also presented in the third CRP Meeting held in India during January 2007.

1.2. Neutronic codes and nuclear data

The computer codes, as well as the nuclear data, employed are basically the popular imported ones, but significantly augmented, updated, and interfaced with indigenous ones. In IGCAR, most of the FBR core-physics calculations are done using a modified 25-group Cadarache Version 2 cross-section set (called CV2M set). However, as the CV2M set does not give data for many of the actinide nuclides needed in this study, a 26-group set, called XSET-98 that contains data for all the actinides involved, including MA has been used for the present study. The codes, ALCIALMI (2-D diffusion theory) [5], ALEX (for breeding ratio, power distribution, reaction rates, etc.) [6] and NEWPERT (perturbation code for Doppler/material worths) [7] are used. As these codes are initially customized for the 25-group Cadarache set, modifications needed to handle higher actinides data and the 26-group structure of XSET-98 set have been made in these codes. Further, the code CONSYST [8] was used to obtain the effective mixture cross-sections for each reactor zone under study, supported with EFCONSY for ensuring compatibility with ALCIALMI. Data for delayed neutrons were used for U and Pu isotopes [9].

For the estimation of buildup/depletion of nuclides due to irradiation/decay, the well-known code ORIGEN2 (of the Oak Ridge National Laboratory) [10] has been employed. The database associated with ORIGEN2 has been updated using JNDC-FP-2000 (Japanese) data for the fission product decay [11], and ENDF/B6-FPY (American) data for the fission product yields [12]. The preprocessed point cross sections, POINT2000 (American) [13], were averaged to 26 groups using REX1-99 [14] code. The region-dependent effective one group cross sections were calculated using program ONE-G [14], with the appropriate flux-weighting, corresponding to Beginning of Life (BOL) fluxes and were plugged into the ORIGEN2 database. All the basic (evaluated) nuclear data libraries were received from the IAEA Nuclear Data Section.

1.3. The composition of FBR-MA

The FBR-MA uses mixed oxide fuel. Its inner and outer cores respectively have 85 and 102 subassemblies (SA) with enrichments 19.5 and 27.1%, respectively. The axial blankets are depleted UO_2. There are 180 ThO_2 radial blanket SA in 3 rows, and 72 SA of steel reflector in one row beyond the radial blanket. There are 9 Control and Safety Rods (CSR) for the usual controls, and 3 Diverse Safety Rods (DSR) only to SCRAM the reactor. B_4C pellets, 65% enriched in ^{10}B, are used both for CSR and DSR. The fuel consists of 5% MA (by weight) in the inner and the outer cores. The percentage MA composition, typical of those in the uncooled fuel discharged from PHWRs, is:

^{237}Np	^{241}Am	^{242m}Am	^{243}Am	^{242}Cm	^{243}Cm
88.6	5.4	0.045	5.131	0.674	0.004

The BOL fuel inventories of various zones of FBR-MA are given in Table 1. Figure 1 gives the cross sectional view of the system at the core mid-plane. The R-Z model used for this study is given in Fig. 2. The total power of FBR-MA is 1150 MWt.

TABLE 1. FUEL COMPOSITION (GRAMS) OF FBR-MA AT BOL

Nuclides	Core		Blanket			Total
	Inner	Outer	Lower Axial	Upper Axial	Radial	
Th-232	0.0	0.0	0.0	0.0	1.862E+07	1.8615E+07
U-235	6.850E+03	7.415E+03	6.594E+03	6.594E+03	0.0	2.7453E+04
U-238	2.770E+06	2.997E+06	2.665E+06	2.665E+06	0.0	1.1097E+07
Np-237	1.620E+05	1.955E+05	0.0	0.0	0.0	3.5750E+05
Pu-239	4.920E+05	8.239E+05	0.0	0.0	0.0	1.3159E+06
Pu-240	1.770E+05	2.959E+05	0.0	0.0	0.0	4.7290E+05
Pu-241	3.800E+04	6.354E+04	0.0	0.0	0.0	1.0154E+05
Pu-242	9.780E+03	1.637E+04	0.0	0.0	0.0	2.6150E+04
Am-241	1.010E+04	1.212E+04	0.0	0.0	0.0	2.2220E+04
Am-242m	8.420E+01	1.014E+02	0.0	0.0	0.0	1.8560E+02
Am-243	9.640E+03	1.161E+04	0.0	0.0	0.0	2.1250E+04
Cm-242	1.260E+03	1.518E+03	0.0	0.0	0.0	2.7780E+03
Cm-243	7.530E+00	9.027E+00	0.0	0.0	0.0	1.6557E+01
Cm-244	2.750E+02	3.316E+02	0.0	0.0	0.0	6.0660E+02
Fuel Total	3.6770E+06	4.4253E+06	2.6716E+06	2.6716E+06	1.862E+07	3.2066E+07
MA Total	1.8337E+05	2.2119E+05	0.0	0.0	0.0	4.0456E+05
MA/Fuel	5 %	5 %				

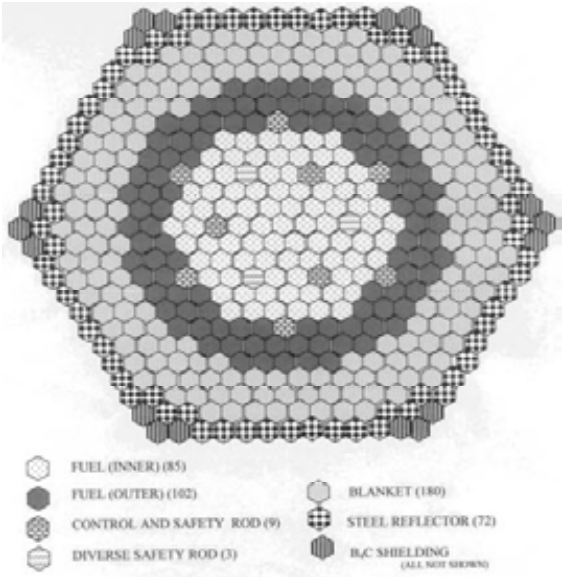

FIG. 1. Cross-sectional view of the FBR-MA at core mid-plane.

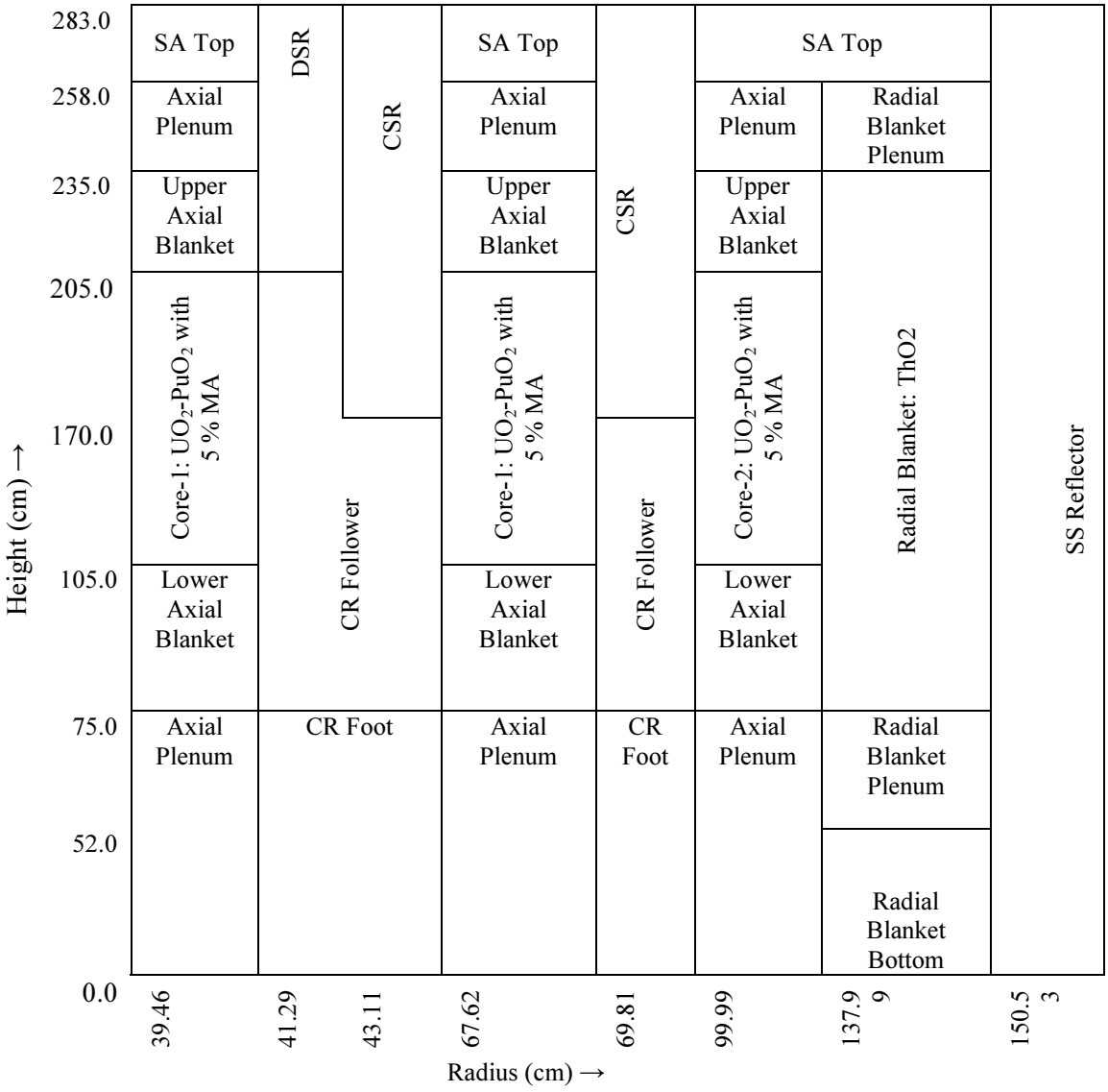

FIG. 2. R-Z Model of FBR-MA.

1.4. Static calculations

1.4.1. *Parameters calculated*

The core physics parameters of FBR-MA, viz. k_{eff}, breeding ratio, Doppler and material worths for fuel, sodium and steel, corresponding to the fresh core (BOL) are computed. The changes in the fuel composition due to burnup are estimated, from which the net production/depletion of the minor actinides within each cycle-length of operation is obtained. The material and Doppler worths are estimated both by first order perturbation theory and '2k' methods. The changes in these parameters and those in the total delayed neutron fraction at BOL, BOEC and EOEC are observed.

1.4.2. *Burnup details*

The specific power (MW/t) of each zone, the irradiation time (days) and the corresponding burnups are given in Table 2.

TABLE 2. BURNUP SCHEMES

Region	Specific Power (MW/t)	Burnup Cycles*					
		Cycle-1		Cycle-2		Cycle-3	
		(GWd/t)	Days	(GWd/t)	Days	(GWd/t)	Days
Inner Core	125.177	25	200	49	392	72	575
Outer Core	110.290	22	200	43	390	64	580
Lower Axial	7.187	1.5	209	2.9	406	4.2	584
Upper Axial	3.600	0.8	222	1.5	417	2.1	583

* Correspond to continuous irradiation; the days given reckoned from BOL.

The radial blanket, not given in Table 2, was irradiated at a specific power of about 1.2 MW/t, for two cycles of 2 521 and 3 025 days, which correspond to about 3 and 3.6 GW•d/t of burnup, respectively. The inventories at the end of each cycle are obtained using ORIGEN2. Fresh fuel, fuel at end of cycle-1 and fuel at end of cycle-2, each occupy a third of the core at BOEC. At EOEC, fuel at the ends of cycle-1, cycle-2 and cycle-3, each occupy a third of the core. The inventories obtained by ORIGEN2 are converted to number densities for the neutronic parameter estimates at different stages.

1.4.3. *Results*

Table 3 through Table 10 give k_{eff}, prompt neutron life-time, breeding ratio, kinetic parameters viz. delayed neutron fractions and precursor decay constants, and safety-related parameters viz. material worths and Doppler worths in various regions. It may be noted from Tables 3 and 4, that the loss of reactivity of the system with burnup is not steep, since the breeding ratio is moderately high. Table 5 shows decrease of delayed neutron fractions with respect to burnup. Table 6 shows reactivity change ($\Delta k/k$) for 1% increase in fuel concentration, and table 7 shows reactivity change ($\Delta k/k$) for 1% increase in steel concentration. However, the effective delayed neutron fraction observed for the present fuel is higher than that for the PFBR. From Table 8 can be seen that the sodium void worth tends to increase with the core burnup. Thermo physical data used in calculations for PFBR accident analysis in the pre-disassembly phase are shown in Appendix I. For the Doppler worths, the perturbation theory predictions of total worths are compared with the 2k method predictions in Table 9 for the fuel, and in Table 10 for steel. For the fuel, these two predictions are comparable, with the 2k predictions lower in magnitude, irrespective of burnup. On the other hand, the deviation between the two methods, for steel, is quite small for the BOL, widens for BOEC, and slightly shrinks at EOEC. FBR-MA has a cycle length of about 185 full power days in the equilibrium cycle. The fuel composition at BOEC is given Table 11, and the production of actinides during the equilibrium cycle is given in Table 12.

TABLE 3. k_{eff}, PROMPT NEUTRON LIFE-TIME AND BURNUP LOSS OF REACTIVITY

	k-eff	Prompt neutron life-time (μs)	Loss of reactivity (pcm)	
BOL	0.99844	0.3416857	BOL to BOEC	1773
BOEC	0.98071	0.3687211	BOEC to EOEC	1981
EOEC	0.96090	0.3819220	BOL to EOEC	3754

TABLE 4. BREEDING RATIO FOR FRESH CORE

Region	Breeding Ratio
Inner Core	0.33198
Outer Core	0.24315
Lower Axial Blanket	0.12929
Upper Axial Blanket	0.05607
Radial Blanket	0.36604
Total	1.12653

TABLE 5. DELAYED NEUTRON FRACTIONS (β) AND PRECURSOR DECAY CONSTANTS (λ)

Groups →		1	2	3	4	5	6	Total
BOL	β	7.9400E-5	7.4000E-4	6.4110E-4	1.2436E-3	5.5870E-4	1.6850E-4	3.4312E-3
	λ (s^{-1})	1.2974E-2	3.1263E-2	1.3384E-1	3.4291E-1	1.3687E+0	3.7015E+0	
BOEC	β	8.1500E-5	7.3300E-4	6.3490E-4	1.2256E-3	5.4580E-4	1.6440E-4	3.3851E-3
	λ (s^{-1})	1.2947E-2	3.1318E-2	1.3380E-1	3.4229E-1	1.3687E+0	3.6992E+0	
EOEC	β	8.0700E-5	7.2580E-4	6.2930E-4	1.2151E-3	5.4140E-4	1.6300E-4	3.3552E-3
	λ (s^{-1})	1.2942E-2	3.1328E-2	1.3386E-1	3.4239E-1	1.3703E+0	3.7046E+0	

TABLE 6. REACTIVITY CHANGE (Δk/k) FOR 1% INCREASE IN FUEL CONCENTRATION

Region	BOL	BOEC	EOEC
Inner Core	2.322E-03	2.1575E-03	2.2115E-03
Outer Core	2.204E-03	2.2929E-03	2.3141E-03
Lower Axial Blanket	-1.889E-05	-1.0888E-05	-6.3804E-07
Upper Axial Blanket	2.694E-06	4.3654E-06	6.9347E-06
Radial Blanket	-1.962E-05	3.7888E-05	4.8193E-05
Total	4.490E-03	4.4818E-03	4.5800E-03
2k Value	4.247E-03	4.1093E-03	4.4021E-03

TABLE 7. REACTIVITY CHANGE (Δk/k) FOR 1% INCREASE IN STEEL CONCENTRATION

Region	BOL	BOEC	EOEC
Inner Core	-3.79E-04	-3.7757E-04	-3.9990E-04
Outer Core	-7.08E-05	-1.2610E-04	-1.4276E-04
Lower Axial Blanket	2.25E-05	1.8717E-05	1.6658E-05
Upper Axial Blanket	1.23E-05	1.1414E-05	1.1009E-05
Radial Blanket (RB)	5.13E-05	5.0987E-05	4.9949E-05
Axial Plenum	2.20E-06	3.1331E-06	4.0325E-06
Plenum: RB	2.60E-07	6.5468E-07	8.3840E-07
CR Foot	-2.42E-07	-4.1951E-07	-5.3377E-07
RB Bottom	1.49E-08	5.9085E-08	7.9556E-08
SA Top	6.73E-08	1.5350E-07	1.8859E-07
SS Reflector	6.71E-07	6.9260E-06	8.2089E-06
DSR	2.25E-07	1.9337E-07	1.8716E-07
CSR	-2.90E-06	-3.0102E-06	-3.1495E-06
CR Follower	-3.05E-06	-5.3417E-06	-7.1876E-06
Total	-3.67E-04	-4.2020E-04	-4.6237E-04
2k Value	-3.650E-04	-4.0787E-04	-4.3709E-04

TABLE 8. REACTIVITY CHANGE (Δk/k) FOR 1% INCREASE IN SODIUM CONCENTRATION

Region	BOL	BOEC	EOEC
Inner Core	-1.50E-04	-1.5346E-04	-1.6433E-04
Outer Core	-7.12E-06	-3.0540E-05	-3.7865E-05
Lower Axial Blanket	6.77E-06	5.9400E-06	5.7031E-06
Upper Axial Blanket	3.84E-06	3.5212E-06	3.4219E-06
Radial Blanket (RB)	1.45E-05	1.7026E-05	1.7139E-05
Axial Plenum	5.62E-07	1.1691E-06	1.7084E-06
Plenum: RB	8.44E-08	2.8768E-07	3.7363E-07
CR Foot	-1.47E-08	-1.6481E-08	-1.7561E-08
RB Bottom	-6.26E-09	3.3089E-09	6.5681E-09
SA Top	5.02E-09	1.9655E-08	2.5483E-08
SS Reflector	6.85E-08	8.1220E-07	9.6760E-07
DSR	9.40E-08	7.4630E-08	6.8908E-08
CSR	-3.37E-06	-3.4925E-06	-3.6260E-06
CR Follower	5.94E-07	-2.9866E-06	-5.2325E-06
Total	-1.34E-04	-1.6164E-04	-1.8166E-04
2k Value	-1.32E-04	-1.4275E-04	-1.6651E-04

TABLE 9. FUEL DOPPLER WORTHS IN VARIOUS REGIONS

Region	BOL	BOEC	EOEC
Inner Core	-2.514E-3	-2.3282E-03	-2.2921E-03
Outer Core	-1.080E-3	-1.2000E-03	-1.2205E-03
Lower Axial Blanket	-3.594E-4	-5.2056E-04	-6.1166E-04
Upper Axial Blanket	-5.235E-5	-6.8806E-05	-7.6858E-05
Radial Blanket	-3.869E-4	-9.8514E-04	-1.0702E-03
Total:	-4.393E-3	-5.1027E-03	-5.2713E-03
2k Value	-4.313E-3	-5.0239E-03	-5.1839E-03

TABLE 10. STEEL DOPPLER WORTH IN VARIOUS REGIONS

Region	BOL	BOEC	EOEC
Inner Core	-3.947E-04	-3.4233E-04	-3.4912E-04
Outer Core	-2.231E-04	-2.2440E-04	-2.3093E-04
Lower Axial Blanket	-2.334E-05	-2.8039E-05	-3.2755E-05
Upper Axial Blanket	-4.653E-06	-5.3772E-06	-5.8631E-06
Radial Blanket (RB)	-1.705E-05	-3.4488E-05	-3.7387E-05
Axial Plenum	-1.066E-07	-2.8564E-06	-4.0977E-06
Plenum: RB	-4.322E-08	-3.5911E-07	-4.6810E-07
CR Foot	-3.547E-07	-7.2196E-07	-1.0400E-06
RB Bottom	-2.733E-08	-1.9174E-07	-2.5995E-07
SA Top	-1.808E-08	-7.3738E-08	-9.3767E-08
SS Reflector	-7.028E-08	-1.3225E-06	-1.5589E-06
DSR	-2.608E-08	-2.3270E-08	-2.4441E-08
CSR	-2.073E-06	-1.6983E-06	-1.7089E-06
CR Follower	-3.511E-05	-3.9322E-05	-4.0436E-05
Total	-7.016E-04	-6.8120E-04	-7.0575E-04
2k Value	-6.874E-04	-8.0050E-04	-7.9220E-04

TABLE 11. ACTINIDE CONCENTRATIONS (GRAMS) AT BOEC

Nuclide	$T_{1/2}$	Core		Blanket			Total
		Inner	Outer	Lower Axial	Upper Axial	Radial	
Th232	1.4×10^{10}y					1.796E+07	1.796E+07
Th233	22.3m					2.566E+00	2.566E+00
Pa231	32760y					5.339E+02	5.339E+02
Pa233	27d					4.474E+03	4.474E+03
U233	1.6×10^{5}y					5.760E+05	5.760E+05
U234	2.5×10^{5}y	5.538E+01	4.496E+01			8.147E+03	8.247E+03
U235	7×10^{8}y	5.744E+03	6.580E+03	6.030E+03	6.246E+03	1.673E+02	2.477E+04
U236	2.3×10^{7}y	2.584E+02	2.091E+02	1.540E+02	8.832E+01	2.462E+00	7.123E+02
U238	4.5×10^{9}y	2.698E+06	2.946E+06	2.607E+06	2.638E+06		1.089E+07
Np237	2.1×10^{6}y	1.422E+05	1.793E+05	3.556E+01	3.064E+01		3.216E+05
Np239	2.35d	6.898E+02	5.146E+02	4.173E+02	2.284E+02		1.850E+03
Pu238	87.7y	1.547E+04	1.272E+04	2.107E+00	1.029E+00		2.819E+04
Pu239	24119y	4.700E+05	7.757E+05	5.263E+04	2.515E+04		1.323E+06
Pu240	6563y	1.830E+05	3.026E+05	1.329E+03	3.230E+02		4.873E+05
Pu241	14.35y	3.601E+04	6.066E+04	4.301E+01	3.331E+00		9.672E+04
Pu242	3.7×10^{5}y	1.058E+04	1.725E+04				2.783E+04
Am241	433y	9.573E+03	1.244E+04				2.201E+04
Am242m	141y	1.995E+02	2.134E+02				4.129E+02
Am243	7380y	8.390E+03	1.070E+04				1.909E+04
Cm242	162.8d	1.120E+03	1.211E+03				2.331E+03
Cm243	29.1y	2.797E+01	2.262E+01				5.059E+01
Cm244	18.1y	1.665E+03	1.487E+03				3.152E+03
Fuel Total		3.583E+06	4.328E+06	2.668E+06	2.670E+06	1.855E+07	3.180E+07
MA Total		1.632E+05	2.054E+05	3.556E+01	3.064E+01	0.000E+00	3.686E+05

TABLE 12. PRODUCTION OF ACTINIDES (GRAMS) BETWEEN BOEC AND EOEC

Nuclide	$T_{1/2}$	Core		Blanket			Total
		Inner	Outer	Lower Axial	Upper Axial	Radial	
Th232	1.4×10^{10}y	0.0	0.0	0.0	0.0	-50000.0	-50000.0
Pa233	27d	0.0	0.0	0.0	0.0	-344.0	-344.0
U233	1.6×10^{5}y	0.0	0.0	0.0	0.0	43700.0	43700.0
U234	2.5×10^{5}y	80.32	63.34	0.0	0.0	1125.0	1268.66
U235	7×10^{8}y	-930.0	-699.0	-337.0	-219.0	35.50	-2149.50
U236	2.3×10^{7}y	213.80	172.60	90.30	55.68	0.77	533.15
U238	4.5×10^{9}y	-65000.0	-46000.0	-36000.0	-18000.0	0.0	-165000.0
Np237	2.1×10^{6}y	-17600.0	-13800.0	22.23	19.96	0.0	-31357.81
Np239	2.35d	348.20	266.80	152.80	91.90	0.0	859.70
Pu238	87.7y	12280.0	10200.0	2.25	1.12	0.0	22483.37
Pu239	24119y	-19800.0	-40300.0	31040.0	15940.0	0.0	-13120.0
Pu240	6563y	5100.0	5300.0	1261.0	329.70	0.0	11990.70
Pu241	14.35y	-1470.0	-2210.0	64.89	5.35	0.0	-3609.76
Pu242	3.7×10^{5}y	690.0	740.0	0.89	0.0	0.0	1430.89
Am241	433y	-459.0	210.0	1.68	0.12	0.0	-247.20
Am242m	141y	86.30	90.60	0.0	0.0	0.0	176.90
Am243	7380y	-1033.0	-731.0	0.0	0.0	0.0	-1764.0
Cm242	162.8d	-95.0	-173.0	0.0	0.0	0.0	-268.0
Cm243	29.1y	15.54	10.02	0.0	0.0	0.0	25.56
Cm244	18.1y	1118.0	940.0	0.0	0.0	0.0	2058.0
Fuel Total		-86454.84	-85919.64	-3700.96	-1775.17	-5482.73	-183333.3
MA Total		-17967.16	-13453.38	23.91	20.08	0.00	-31376.55
MA produced (%)		-11.0	-6.6	67.2	65.5	0.0	-8.5

There is substantial reduction in the long lived MA, ^{237}Np and ^{243}Am, of about 12% each in the inner core, about 7% each in the outer core, and about 9% each in all, during one equilibrium cycle. The nuclides ^{237}Np, ^{239}Np and ^{241}Am show large fractional increase in the axial blankets, though the increase in terms of mass is relatively very low. The isotopes, ^{243}Cm and ^{244}Cm, having fairly long half-lives, show net production of over 50% during a cycle. The net reductions in the total MA inventory are about 11 and 7%, respectively, in the inner and the outer cores, respectively, and above 8% in all. In other words, out of a total of about 370 kg of MA available at BOEC, about 30 kg are burnt during the cycle. Though production of MA and other higher actinides are inevitable in a reactor, the core of the benchmark seems capable of substantially incinerating the very long-lived MA components of the PHWR discharge-fuel. The use of ThO_2 radial blanket instead of UO_2 ensures no significant production of MA therein. However, there is more than 7% increase in the ^{233}U inventory in the radial blanket.

1.5. Transient analysis

Transient analysis for the transient over power (TOP) and loss of flow (LOF) routes have been done for the FBR-MA. The reactor is divided into 14 axial and 9 radial zones for the calculations (see Fig. 3).

The bottom two and the top two axial zones correspond to the upper and lower axial blankets. The core is radially divided into 6 zones and the last three zones correspond to the radial blanket. Similar zone-wise divisions used for the PFBR calculations are given in Fig. 4.

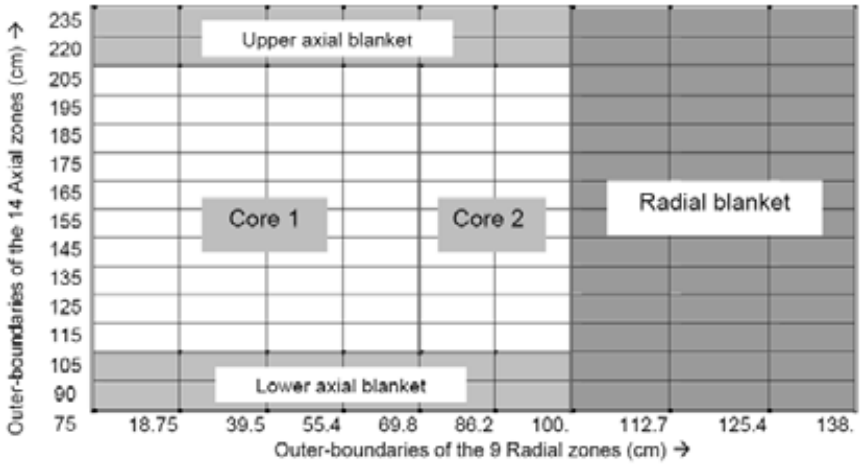

FIG. 3. Zones for the perturbation analysis of FBR-MA.

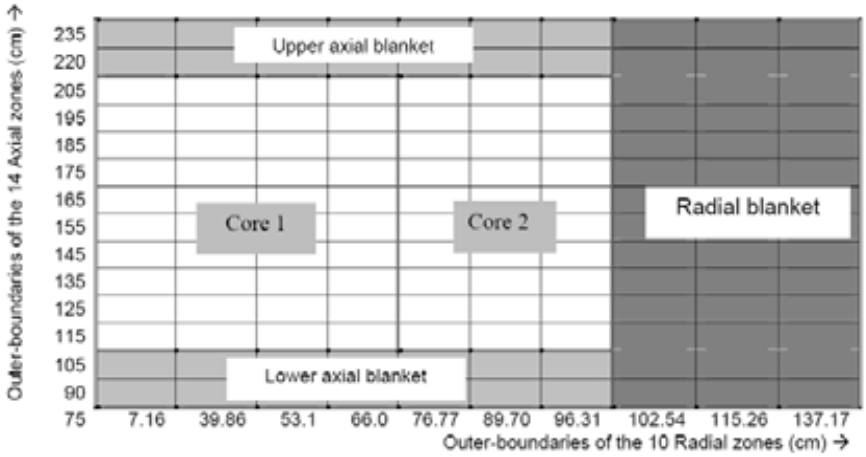

FIG. 4. Zones for the perturbation analysis of PFBR.

The radial zone dimensions of the two models slightly vary, and there are 3 radial zones in core 2 of PFBR, thus making the total radial zones to be 10. The parameters of the core were computed using 2-D diffusion theory and first order perturbation theory [1]. The results are compared with the corresponding parameters of PFBR. For PFBR calculations, the cross-section set CV2M was used. Since CV2M does not give temperature dependent data for iron, steel Doppler worth cannot be estimated using CV2M. Hence, comparison of steel Doppler worths has been omitted. We assume failure of the plant protection system (PPS) both in the TOP and LOF cases. The calculations are carried out in the pre-disassembly phase, using the in-house computer code PREDIS [3]. PREDIS calculations have been validated against the European LOFA benchmark problem [4] and the BN-800 LOFA, TOPA and LOFA/TOPA benchmark problems [5]. PREDIS uses point kinetics for power calculations. Reactivity worths, calculated using perturbation theory, are used as input. Each radial zone is represented by one single fuel pin, which is axially divided as described above. Temperature calculations are carried out using lumped model heat transfer, and are the average values for the fuel and clad. The feedback reactivity is calculated as a sum of the density contributions due to fuel, clad and coolant, Doppler, radial expansion of the core and boundary movement between the inner core and the outer core defined by the different fuel enrichments and between the core and the blankets. Sodium voiding is calculated based on the bulk coolant temperature crossing its saturation temperature at the corresponding pressure. For both the transients initial power of the reactor is taken as 1150 MWt. The thermo-physical constants used for both cases are same and are given in Appendix III. The causes of differences observed in the transient behaviours between FBR-MA and the PFBR include:

1. 5% MA added in the FBR-MA;
2. ThO2 radial blanket in FBR-MA but UO_2 in PFBR;
3. Use of different cross-section sets for the two analyses;
4. Different temperature ranges for the Doppler worth studies.

1.5.1. *Transient over power*

The transient over power is assumed to originate in the uncontrolled withdrawal of a control rod (CR). The CR withdrawal for normal operation in the reactor is 1 mm/s. The peak value of the reactivity addition rate due to CR withdrawal is less than 4 pcm/s, but this value is assumed for the entire transient. The plant protection system (PPS), designed to SCRAM the reactor in the event of CR withdrawal exceeding 40 mm, due to CR discordance, is assumed failed. The uncontrolled CR withdrawal is assumed for a duration of 129 s, which corresponds to a total reactivity input of 1.5 $. This is the reactivity available for the complete removal of the CR from its initial position in the core at full power. Power evolution for the TOP is shown in Fig. 5, for the FBR-MA, along with that for PFBR. It is noted that FBR-MA reaches higher power than PFBR. The reactivity components are shown in Fig. 6, for the FBR-MA and PFBR. The input is a constant ramp, which is partially offset by the negative reactivity due to Doppler and fuel expansion resulting in a small net positive reactivity. The average fuel, clad and coolant temperatures are shown in Fig. 7.

It is found that FBR-MA and PFBR behave almost similarly with respect to fuel temperatures reached. Conductivity and specific heats used are identical in both the cases.

1.5.2. *Loss of flow*

The loss of flow is governed by the fly wheel inertia of the primary pump. The flow coast down is assumed to be with a flow halving time of 8 s. In addition, the plant protection system is assumed to fail leading to a core disruptive accident. The analysis is carried out as described in the section on TOPA. Calculations up to sodium boiling are reported in this paper.

The sequence is radial zones 5, 3, 2, 1, 6 and 4 at 33.02, 33.205, 33.39, 40.02, 50.58, and 68.115 s, respectively, as shown in Table 13. The sequence for PFBR is also included in Table 13.

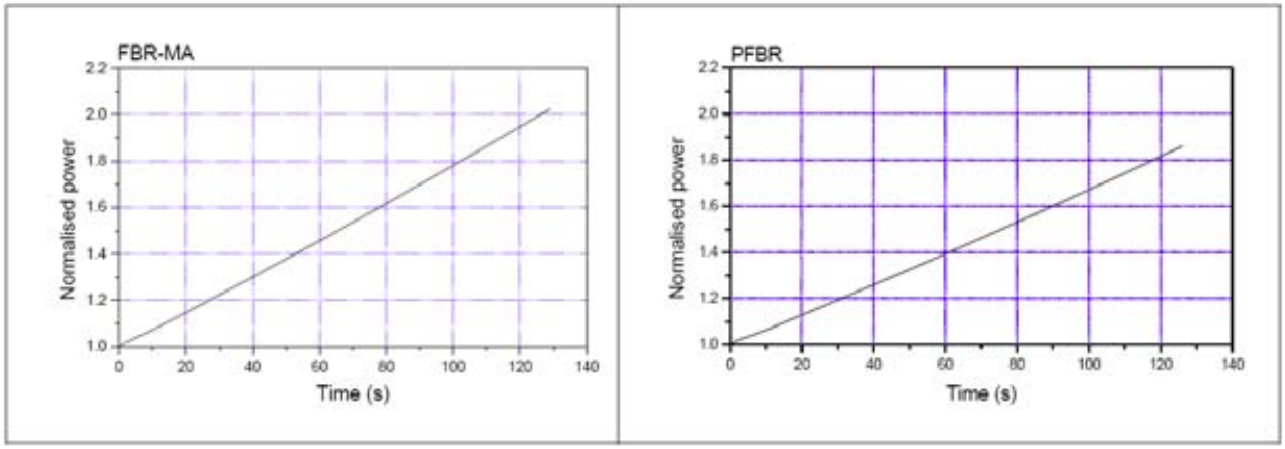

FIG. 5. Power evolution for TOP with reactivity addition rate of 4 pcm/s.

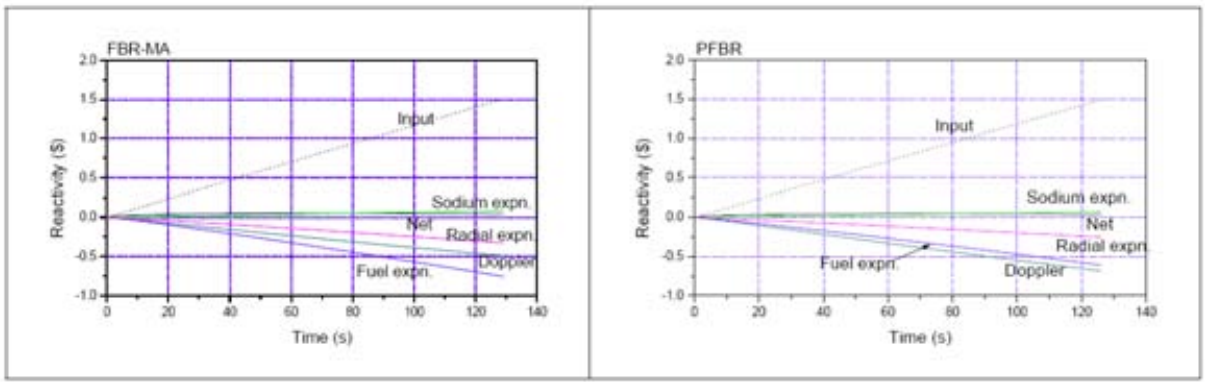

FIG. 6. Reactivity components for TOP with reactivity addition rate of 4 pcm/s.

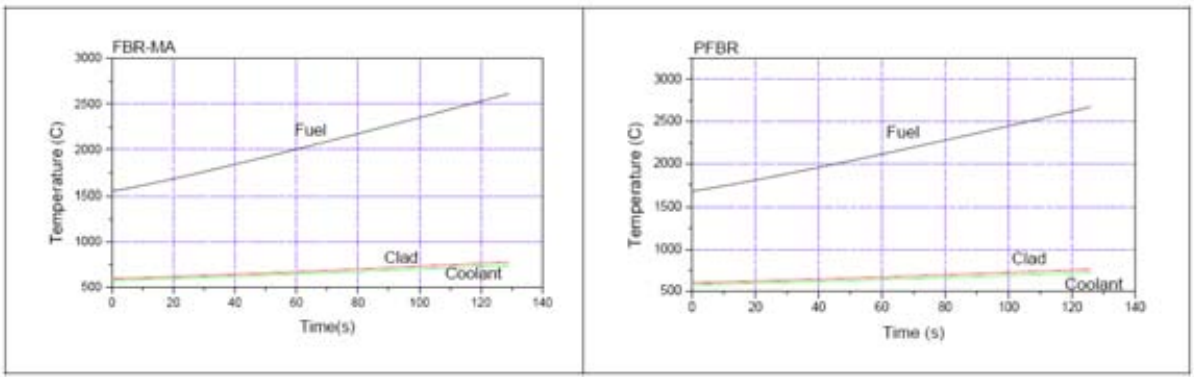

FIG. 7. Average temperatures for TOP with reactivity addition rate of 4 pcm/s.

TABLE 13. INITIATION OF SODIUM BOILING DUE TO LOSS OF FLOW

FBR-MA	Time (s)	33.020	33.205	33.390	40.020	50.580	68.115	
	Channel no.	5	3	2	1	6	4	
PFBR	Time (s)	26.20	29.71	30.25	31.22	42.88	51.23	51.23
	Channel no.	1	3	2	4	5	6	7

The power evolution is shown in Fig. 8. The power falls initially as in a normal LOF. The reactivity components are shown in Fig. 9. In the transient the reactor shuts down but gives rise to a slight positive Doppler feedback due to decrease in fuel temperature. The core starts voiding in the upper part of the core.

The boiling sets in, in all the radial zones of PFBR, in about 53 s. The voiding in the upper regions of the core gives negative reactivity which further brings down the reactivity and hence the power. The fuel, clad and coolant temperatures are shown in Fig. 10. Fuel temperatures reached are lower in FBR-MA.

Thus, from the comparison of safety-related parameters of FBR-MA, under transient overpower and loss of flow conditions, with those of PFBR, the FBR-MA seems to have no serious safety problems. The effects of radial expansion, were studied in academic interest, and the results obtained were not given serious credit.

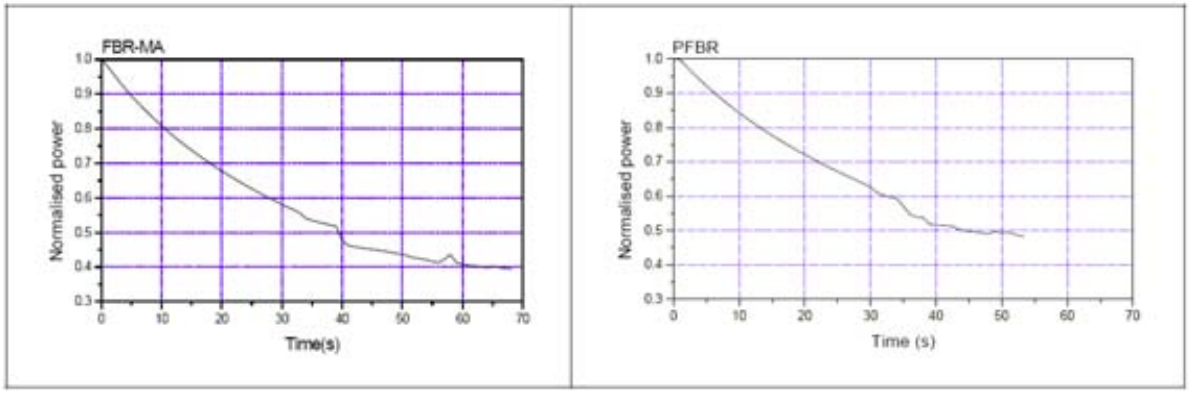

FIG. 8. Power evolution of LOF with fow-halving time of 8 s.

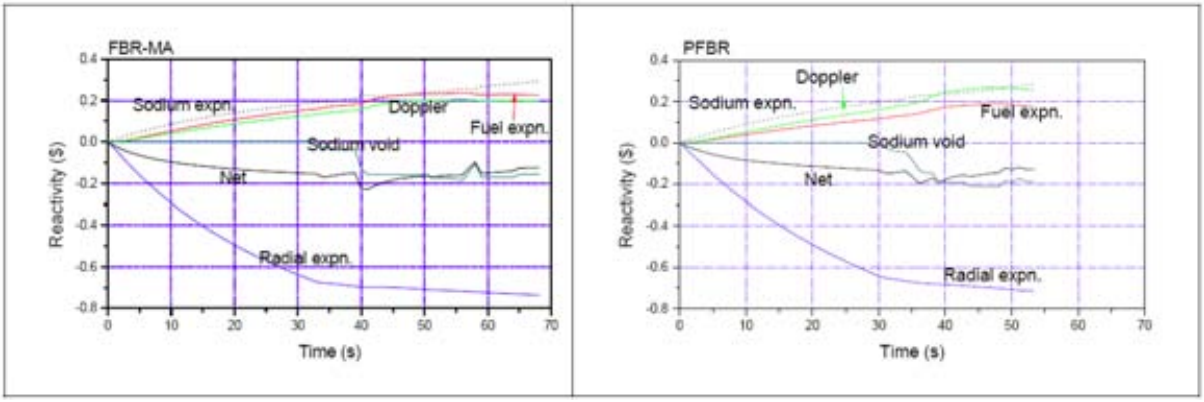

FIG. 9. Reactivity components for LOF with flow-halving time of 8 s.

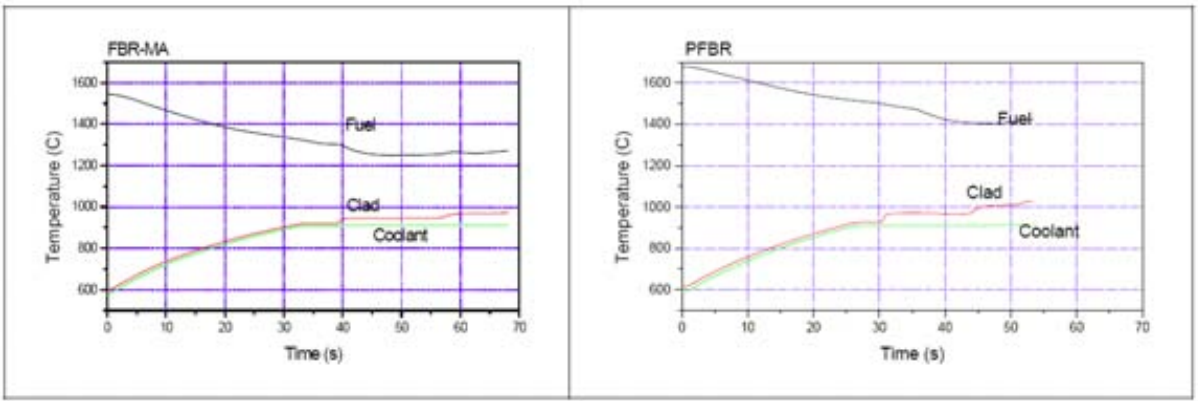

FIG. 10. Average temperatures for LOW with flow-halving time of 8 s.

1.6. Effect of taking MA nuclear data from different evaluations

As mentioned earlier, the PFBR core calculations were based on the CV2M cross-section set. This set does not include data for all MA essential for the present studies, and hence the use of XSET-98, which is more complete than CV2M. All the static and transient analyses carried out for the FBR-MA, whose results are presented above, are based on XSET-98. This report does not touch upon deviations in the results due to differences between XSET-98 and CV2M. The comparison study, whose results are presented in this section, is motivated by curiosity to know the spread in the reactor parameters due to differences in the MA nuclear data in different evaluations, viz. ENDF/B-VI.8, JEFF-3.0 and JENDL-3.3. Toward this, CV2M set is taken as the base set, in the sense that all major materials, including fuel, structural, control and coolant, are taken from CV2M. The actinides viz. ^{233}Pa, ^{234}U, ^{236}U, ^{237}U, ^{237}Np, ^{238}Pu, ^{241}Am, ^{242m} Am, ^{243}Am, ^{242}Cm, ^{243}Cm, and ^{244}Cm are considered from the three evaluations. Thus, for example, in the comparison tables given below, mention of ENDF/B-VI indicates that these 12 actinides are taken from ENDF/B-VI.8 and the rest from CV2M.

Table 14 gives the k_{eff}, the loss of reactivity with burnup, and the effective delayed neutron fractions (β_{eff}), for the FBR-MA, corresponding to the three evaluations.

The spread given in pcm stands for the difference between the maximum and the minimum predictions. In this sense, the predicted k_{effs} agree within a spread of 200 pcm. The k_{eff} shows agreement. The prompt neutron life-times (not shown) are 0.33, 0.356 and 0.37 μs, respectively at BOL, BOEC and EOEC, and show agreement among the three evaluations.

As seen in Table 15, the three evaluations show agreement on the predicted breeding ratios for the fresh-core.

Tables 16 and 17 show material and fuel-Doppler worths, obtained respectively, by perturbation and 2k methods. The spread over the evaluations is given in terms of minimum and maximum deviations from the arithmetic mean value, in each case. Considering all the burnup stages and both the methods together, these worths are within -10 to +6% deviation from the respective mean values.

TABLE 14. K_{EFF}, REACTIVITY LOSS AND DELAYED NEUTRON FRACTIONS

Data Library	k-eff			Reactivity Loss (pcm)		Delayed Neutron Fractions (pcm)		
	BOL	BOEC	EOEC	BOL to BOEC	BOEC to EOEC	BOL	BOEC	EOEC
ENDF/B-VI	1.005570	0.992576	0.977245	1299.4	1533.1	324.18	319.42	316.21
JEFF-3.0	1.005914	0.993711	0.979073	1220.3	1463.9	323.80	318.90	315.54
JENDL-3.3	1.007002	0.993267	0.977383	1373.5	1588.4	325.72	320.86	317.58
Spread (pcm)	143.2	113.5	182.8	74.1	55.3	1.92	1.96	2.04

TABLE 15. BREEDING RATIO FOR FRESH CORE

Region	Breeding Ratio			
	ENDF/B-VI	JENDL-3.3	JEFF-3.0	Spread
Inner Core	0.31682	0.31700	0.31674	0.00026
Outer Core	0.22885	0.22906	0.22884	0.00022
Lower Axial Blanket	0.12340	0.12341	0.12341	0.00001
Upper Axial Blanket	0.04755	0.04760	0.04758	0.00005
Radial Blanket	0.36804	0.36830	0.36821	0.00026
Total	1.08466	1.08537	1.08479	0.00071

TABLE 16. MATERIAL AND DOPPLER REACTIVITY WORTHS FROM PERTURBATION CALCULATION

Case	Data Library	Material worth for 1 % increase			Fuel Doppler Worth
		Fuel	Sodium	Steel	
BOL	ENDF/B-VI	4.3897E-3	-1.4748E-4	-2.7042E-4	-3.3256E-3
	JEFF-3.0	4.3873E-3	-1.4896E-4	-2.7186E-4	-3.3656E-3
	JENDL-3.3	4.3967E-3	-1.5384E-4	-2.7436E-4	-3.3418E-3
	Average	4.3912E-3	-1.5009E-4	-2.7221E-4	-3.3443E-3
	Spread (%)	-0.09 +0.12	-1.74 +2.50	-0.66 +0.79	-0.56 +0.64
BOEC	ENDF/B-VI	4.3619E-3	-1.6865E-4	-3.0950E-4	-4.1250E-3
	JEFF-3.0	4.3562E-3	-1.6947E-4	-3.1006E-4	-3.9875E-3
	JENDL-3.3	4.3777E-3	-1.7680E-4	-3.1505E-4	-3.8495E-3
	Average	4.3653E-3	-1.7164E-4	-3.1154E-4	-3.9873E-3
	Spread (%)	-0.21 +0.28	-1.74 +3.01	-0.65 +1.13	-3.46 +3.45
EOEC	ENDF/B-VI	4.4263E-3	-1.7883E-4	-3.3000E-4	-4.4524E-3
	JEFF-3.0	4.4176E-3	-1.7897E-4	-3.2968E-4	-4.2391E-3
	JENDL-3.3	4.4495E-3	-1.8877E-4	-3.3719E-4	-4.2068E-3
	Average	4.4311E-3	-1.8219E-4	-3.3229E-4	-4.2994E-3
	Spread (%)	-0.31 +0.41	-1.84 +3.61	-0.79 +1.47	-2.15 +3.56

TABLE 17. MATERIAL AND DOPPLER REACTIVITY WORTHS FROM 2K CALCULATION

Case	Data Library	Material worth for 1 % increase			Fuel Doppler Worth
		Fuel	Sodium	Steel	
BOL	ENDF/B-VI	4.2187E-3	-1.4589E-4	-2.6999E-4	-3.3549E-3
	JEFF-3.0	4.5308E-3	-1.4900E-4	-2.7318E-4	-3.3186E-3
	JENDL-3.3	4.2234E-3	-1.5690E-4	-2.7436E-4	-3.0130E-3
	Average	4.3243E-3	-1.5060E-4	-2.7251E-4	-3.2288E-3
	Spread (%)	-2.44 +4.78	-3.13 +4.19	-0.92 +0.68	-6.68 +3.90
BOEC	ENDF/B-VI	4.0645E-3	-1.5887E-4	-2.8960E-4	-4.0394E-3
	JEFF-3.0	4.0820E-3	-1.6946E-4	-3.1403E-4	-3.8895E-3
	JENDL-3.3	4.0943E-3	-1.6285E-4	-3.0968E-4	-3.8895E-3
	Average	4.0803E-3	-1.6373E-4	-3.0444E-4	-3.9395E-3
	Spread (%)	-0.39 +0.34	-2.97 +3.50	-4.87 +3.15	-1.27 +2.54
EOEC	ENDF/B-VI	4.3165E-3	-1.6056E-4	-2.9266E-4	-4.4082E-3
	JEFF-3.0	4.3081E-3	-1.8774E-4	-3.2794E-4	-4.2198E-3
	JENDL-3.3	4.3541E-3	-1.8626E-4	-3.2482E-4	-4.1245E-3
	Average	4.3262E-3	-1.7819E-4	-3.1514E-4	-4.2508E-3
	Spread (%)	-0.42 +0.64	-9.89 +5.36	-7.13 +4.06	-2.97 +3.70

1.6.1. *ThO_2 in the axial blankets*

The design of FBR-MA, as described in the previous sections, has ThO_2 in the radial blanket and UO_2 in the axial blankets. Calculations were redone with UO_2 replaced with ThO_2 in the axial blankets too. This involves replacement of about 5.34 t of uranium by about 4.86 t of Th in the axial blankets in the initial feed, the cores and the radial blankets being unaltered. The fuel composition at BOL and at BOEC is given in Tables 18 and 19, respectively, and the amounts of actinides produced within an equilibrium cycle are given Table 20. For want of space these tables cover only selected actinides. It may be pointed out here that the core has not been re-optimised when the axial blankets are modified. It is assumed to have nearly the same characteristics as the original FBR-MA. The essential differences between the two cases with respect to actinide production during an equilibrium cycle are summarized in Table 21. The change increases ^{233}U production by about 31 kg, but reduces ^{239}Pu production by about 47 kg, thus causing a reduction in the fissile production by about 16 kg. The quantity of MA incinerated increases by 44 g, through reduced production of ^{237}Np.

TABLE 18. FUEL COMPOSITION (GRAMS) AT BOL

Nuclides	Core		Blanket			Total
	Inner	Outer	Lower Axial	Upper Axial	Radial	
Th-232	0.0	0.0	2.426E+06	2.426E+06	1.861E+07	2.346E+07
U-235	6.850E+03	7.415E+03	0.0	0.0	0.0	1.427E+04
U-238	2.770E+06	2.997E+06	0.0	0.0	0.0	5.767E+06
Np-237	1.620E+05	1.955E+05	0.0	0.0	0.0	3.575E+05
Pu-239	4.920E+05	8.239E+05	0.0	0.0	0.0	1.316E+06
Pu-240	1.770E+05	2.959E+05	0.0	0.0	0.0	4.729E+05
Pu-241	3.800E+04	6.354E+04	0.0	0.0	0.0	1.015E+05
Pu-242	9.780E+03	1.637E+04	0.0	0.0	0.0	2.615E+04
Am-241	1.010E+04	1.212E+04	0.0	0.0	0.0	2.222E+04
Am-242m	8.420E+01	1.014E+02	0.0	0.0	0.0	1.856E+02
Am-243	9.640E+03	1.161E+04	0.0	0.0	0.0	2.125E+04
Cm-242	1.260E+03	1.518E+03	0.0	0.0	0.0	2.778E+03
Cm-243	7.530E+00	9.027E+00	0.0	0.0	0.0	1.656E+01
Cm-244	2.750E+02	3.316E+02	0.0	0.0	0.0	6.066E+02
Fuel Total	3.677E+06	4.425E+06	2.426E+06	2.426E+06	1.861E+07	3.156E+07
MA Total	1.8337E+05	2.2119E+05	0.0	0.0	0.0	4.046E+05
MA/Fuel	5 %	5 %				

TABLE 19. FUEL COMPOSITION OF BOEC (SELECTED ACTINIDES)

Nuclide	Core		Blanket			Total
	Inner	Outer	Lower Axial	Upper Axial	Radial	
Th232			2.371E+6	2.390E+6	1.796E+7	2.272E+7
Th233			1.218E+0	1.801E+0	2.566E+0	5.585E+0
Pa231			4.244E+1	5.090E+1	5.339E+2	6.272E+2
Pa233			3.430E+3	2.380E+3	4.474E+3	1.028E+4
U233			4.861E+4	3.479E+4	5.760E+5	6.594E+5
U234	5.538E+1	4.496E+1	2.028E+3	7.743E+2	8.147E+3	1.105E+4
U235	5.744E+3	6.580E+3	4.852E+1	1.252E+1	1.673E+2	1.255E+4
U236	2.584E+2	2.091E+2			2.462E+0	4.700E+2
U238	2.698E+6	2.946E+6				5.644E+6
Np237	1.422E+5	1.793E+5				3.215E+5
Np239	6.898E+2	5.146E+2				1.204E+3
Pu238	1.547E+4	1.272E+4				2.819E+4
Pu239	4.700E+5	7.757E+5				1.246E+6
Pu240	1.830E+5	3.026E+5				4.856E+5
Pu241	3.601E+4	6.066E+4				9.667E+4
Pu242	1.058E+4	1.725E+4				2.783E+4
Am241	9.573E+3	1.244E+4				2.201E+4
Am242m	1.995E+2	2.134E+2				4.129E+2
Am243	8.390E+3	1.070E+4				1.909E+4
Cm242	1.120E+3	1.211E+3				2.331E+3
Cm243	2.797E+1	2.262E+1				5.059E+1
Cm244	1.665E+3	1.487E+3				3.152E+3
Fuel Total	3.583E+6	4.328E+6	2.425E+6	2.428E+6	1.855E+7	3.131E+7
MA Total	1.632E+5	2.054E+5				3.685E+5

TABLE 20. PRODUCTION (GRAMS) OF ACTINIDES BETWEEN BOEC AND EOEC

Nuclide	$T_{1/2}$	Core		Blanket			Total
		Inner	Outer	Lower Axial	Upper Axial	Radial	
Th232	1.4×10^{10}y	0.0	0.0	-23000	-16000	-50000	-89000
Pa231	32760y	1.4E-05	1.1E-05	19.24	15.72	49.90	84.86
Pa233	27d	0.0	0.0	1801.0	1189.0	-344.0	2646
U233	1.6×10^{5}y	0.0	0.0	18370.0	12560.0	43700.0	74630
U234	2.5×10^{5}y	80.32	63.34	559.0	229.70	1125.0	2057.36
U235	7×10^{8}y	-930.0	-699.0	30.15	7.68	35.50	-1555.67
U236	2.3×10^{7}y	213.80	172.60	0.84	0.14	0.77	388.15
U238	4.5×10^{9}y	-65000.0	-46000.0	0.0	0.0	0.0	-111000
Np237	2.1×10^{6}y	-17600.0	-13800.0	0.0	0.0	0.0	-31400
Np239	2.35d	348.20	266.80	0.0	0.0	0.0	615
Pu238	87.7y	12280.0	10200.0	0.0	0.0	0.0	22480
Pu239	24119y	-19800.0	-40300.0	0.0	0.0	0.0	-60100
Pu240	6563y	5100.0	5300.0	0.0	0.0	0.0	10400
Pu241	14.35y	-1470.0	-2210.0	0.0	0.0	0.0	-3680
Pu242	3.7×10^{5}y	690.0	740.0	0.0	0.0	0.0	1430
Am241	433y	-459.0	210.0	0.0	0.0	0.0	-249
Am242m	141y	86.30	90.60	0.0	0.0	0.0	176.9
Am243	7380y	-1033.0	-731.0	0.0	0.0	0.0	-1764
Cm242	162.8d	-95.0	-173.0	0.0	0.0	0.0	-268
Cm243	29.1y	15.54	10.02	0.0	0.0	0.0	25.56
Cm244	18.1y	1118.0	940.0	0.0	0.0	0.0	2058
Fuel Total		-86450.0	-85919.64	-2219.77	-1997.76	-5432.83	-182020.0
MA Total		-17970.0	-13453.38	0.0	0.0	0.0	-31420.54
MA production (%)		-11.0	-6.6	0	0	0	-8.5

TABLE 21. COMPARISON OF ACTINIDE PRODUCTIONS WITH U OR TH AXIAL BLANKETS

Nuclide	Production within an equilibrium cycle (g)		
	Axial U blanket	Axial Th blanket	Difference
U233	43700.00	74630.00	30930.00
U235	-2149.50	-1555.67	593.83
Pu239	-13120.00	-60100.00	-46980.00
Pu241	-3609.76	-3680.00	-70.24
Net Fissile	24820.74	9294.33	-15526.41
Np237	-31357.81	-31400.00	-42.19
Am241	-247.20	-249.00	-1.80
Am242m	176.90	-176.90	0.00
Am243	-1764.00	-1764.00	0.00
Cm242	-268.00	-268.00	0.00
Cm243	25.56	25.56	0.00
Cm244	2058.00	2058.00	0.00
Net MA	-31376.6	-31420.50	-43.99

1.7. Conclusions

Under the IAEA-CRP dealing with options for incineration of radioactive wastes, an FBR model, obtained by suitably modifying the cores and blankets of the 500 MW(e) Prototype Fast Breeder Reactor (PFBR) to include 5% minor actinides of Indian PHWR origin, has been arrived at. The radial blanket is ThO_2. This benchmark burns about 10% of the long lived minor actinides during one equilibrium cycle of its operation. The safety related parameters like the material worths including sodium worth, and Doppler worth have also been predicted, by perturbation and by 2k methods. Transient analysis for the transient over power, and loss of flow conditions has been done. Comparisons with PFBR show that the

reactor is as safe as PFBR. The effects due to the spread in the basic nuclear data in the recent evaluations are also studied, which shows agreement in most of the neutronic parameters, with the material and Doppler worths being well with ±10%. The original model studied has UO_2 axial blanket, but the effect of replacing this with ThO_2 axial blanket also has been studied. As expected, Th in the axial blanket in the place of U enhances ^{233}U production and leads to ^{239}Pu depletion.

REFERENCES TO CHAPTER 1

[1] STANCULESCU, A., et al., Draft Report presented in in the IAEA Research Co-ordination Meeting (RCM) of the Co-ordinated Research Project on Studies of Advanced Reactor Technology Options for Effective Incineration of Radioactive Waste, Forschungszentrum Karlsruhe, Germany, 5-8 November 2002.

[2] MOHANAKRISHAN, P., Physics Design of Core, PFBR/01113/DN/1049 (Rev.C), Indira Gandhi Centre for Atomic Research, Kalpakkam (2004).

[3] DEVAN, K., et al., A Fast Breeder Reactor Model for Incineration of Long-lived Minor Actinides, paper presented in the CRP Meeting at the Institute of Plasma Physics, Chinese Academy of Sciences, 22-26 November 2004, Hefei, Anhui, China.

[4] HARISH, R., et al., A Fast Breeder Reactor Model for Incineration of Long-lived Minor Actinides — Results of Transient Analysis, paper presented in the IAEA CRP Consultancy Meeting, 28 November — 1 December 2005, Vienna, Austria.

[5] a) BYARD, J.P., et al., Specification d'un Code de Diffusion Multigroupe a Deux Dimensions: ALCI, Report CEA-R 2747 (1965).
b) NARAYANAN, R., ALCIALMI, J.T.M., The Computer Code for Solving the Neutron Diffusion Equation in Two Dimensional Geometry, Internal Report RG/RPD/CPS/14 (2000).

[6] GIACOMETTI, C., Specifications du Programme ALEX, Internal Note No. 69/1203 (1969).

[7] JOHN, T.M., NEWPERT — Perturbation Code for Two Dimensional diffusion Equation Internal Report REDG/01150/RP-253 (1984).

[8] DEVAN, K., Theoretical Background of CONSYST Code, Internal Report, RPD/NDS/69 (1998).

[9] TUTTLE, R.J., Review of Delayed Neutron Yields in Nuclear Fission, INDC-NDS-107 Special p 29, International Atomic Energy Agency (1979).

[10] a) CROFF, A.G., ORIGEN2: A Versatile Computer Code for Calculating the Nuclide Composition and Characteristics of Nuclear Materials, Nucl. Tech. 62 (1983).
b) PANDIKUMAR, G., and GOPALAKRISHNAN, V., Adaptation of ORIGEN2 Code for Calculating Isotope Generation and Depletion, Internal Report RPD/NDS/85 (2000).

[11] KATAKURA, J., et al., JENDL FP Decay Data File 2000, JAERI 1343 (2001).

[12] ENGLAND, T.R., RIDER, B.F., ENDF/B-6-FPY, The ENDF/B-6 Fission Product Yield Sublibraries, H.D. Lemmel, Summary Documentation, IAEA-NDS-106, Rev.3, IAEA NDS Report (1995).

[13] CULLEN, D.E., POINT2000 Temperature Dependent ENDF.B-VI Release 7 Cross-sections, CDs obtained from Nuclear Data Section, IAEA, Vienna, Austria.

[14] GOPALAKRISHNAN, V., GANESAN, S., REX1-87: A Code for Multigrouping Neutron Cross-sections from Preprocessed ENDF/B Basic Data File, Internal Report RPD/NDS/13 (1988). An improved version of this code is REX1-99.

[15] HARISH, R., et al., KALDIS: A Computer Code System for Core Disruptive Accident Analysis in Fast Reactors, Internal report, IGC — 208, Kalpakkam (March 1999).

[16] DHARMADURAI, SING Om Pal, Validation of PREDIS Code Against European LOFA Benchmark Problem, FRG/RPS-230 (1983).

[17] INTERNATIONAL ATOMIC ENERGY AGRNCY, Transient and Accident Analysis of a BN-800 Type LMFR with Near Zero Void Effect, IAEA-TECDOC-1139, IAEA Vienna (2000).

CHAPTER 2. DOMAIN-I: IMPACT OF MINOR ACTINIDES BURNING ON SODIUM VOID REACTIVITY EFFECT IN BN 800 TYPE REACTOR WITH (PU TH)O_2 FUEL

2.1. Introduction

Implementation of the declared Russian approach to a fuel cycle, excluding build-up of the excess reactor plutonium and accumulation of minor actinides, and thereby assisting to reducing of radiotoxicity of the radioactive wastes buried, is possible when using fast reactors and burning minor actinides in them. At the present time such a burning is discussed in fast sodium reactors with different core layouts.

In particular, calculation study of possible use of thorium for burning of minor actinides is performing. In such a fuel cycle, build-up of plutonium and own Am and Cm is practically excluded, and built-up uranium can be extracted from irradiated thorium for the subsequent initialization of ^{233}U-Th fuel cycle.

At the second RCM of the CRP 'Study of advanced reactor technologies for effective radioactive wastes burnup' (Hefei, China, November 2004) the report was presented with the results of calculation study [1] of such an option. There was considered a fast sodium reactor of BN-800 type with the fuel on the base of mixture of plutonium and thorium dioxides with an admixture of minor actinide oxides. Possibilities of such a reactor were demonstrated for plutonium utilization and actinides burnup: annual plutonium consumption comprises 1940 kg, actinides — 104 kg from WWER-1000 reactors and 470 kg of its own actinides.

The reactor considered has a reasonable safety properties with the exception of sodium void reactivity effect (SVRE), which is positive and is equal to 1.8% Δk/k when reactor full voiding. In the strict sense, Russian rules of nuclear safety do not require a negative SVRE, but contain the requirements on providing safety in the relevant emergency modes. However, designers usually tend to assure zero or a negative SVRE. It should be noted, that the thorium blanket was considered when performing reactor calculations, instead of sodium plenum, which is currently introduced for assuring a negative SVRE in the standard BN-800 reactor design.

This study is dedicated to a more comprehensive calculation study of SVRE. In particular, an effect of quantity of recycled actinides and their isotope composition on SVRE was under discussion.

2.2. Design and calculation model description

Calculation model of the reactor is based on the traditional design of BN-800 fast reactor considered in paper [2]. For the most part, it coincides with one used at the previous stages of computations [1]. The key distinctions are in the diverse variants of minor actinides (MA) recycling and replacement of upper axial thorium blanket with sodium plenum. Since it is supposed to use the reactor for MA burning simultaneously with ^{233}U building up, so abandoning the upper fertile blanket which results in decrease of ^{233}U breeding may be considered as a loss compared with the variant presented in paper [1]. Radial breeding blanket consists as before of 4 rows of FAs with thorium dioxide. Table 1 presents the main reactor characteristics used in two-dimensional calculation model.

Table 2 gives volume fractions of materials needed for determining of compositions of calculation reactor zones.

The mixture of thorium and plutonium dioxides with dioxides of minor actinides — Np, Am, Cm — was used as a core fuel. Reactor plutonium composition at the moment of reactor loading corresponds to the plutonium content discharged from WWER 1000 reactor after some cooling time and is taken as follows (in weight %) [3]:

^{238}Pu	^{239}Pu	^{240}Pu	^{241}Pu	^{242}Pu	^{241}Am
0.9	61.0	22.0	10.9	4.1	1.1

TABLE 1. BASIC CORE CHARACTERISTICS OF BN-800 TYPE REACTOR (OPERATION CONDITION)

Rated thermal power, MWt	2100
Geometry	hexagonal
Fuel assembly (FA) pitch, cm	10.06
Number of core cells, pieces including: • FAs in low enriched zone (LEZ) • FAs in medium enriched zone (MEZ) • FAs in high enriched zone (HEZ) • neutron source • control rods	547 210 156 150 1 30
Effective core radius, cm	123.6
Core height, cm	96.4
Number of FAs in radial breeding blanket (RBB)	395
Height of bottom breeding blanket (BBB), cm	35.5
Height of sodium plenum	35.5
Height of RBB, cm	167.4
Time interval between reloadings, eff. days	147
Number of reloadings of core and RBB FAs during lifetime	3
Core fuel	ThO_2+PuO_2+MA (Am, Np, Cm) Oxides
Breeding material	ThO_2

TABLE 2. VOLUME FRACTIONS OF MATERIALS IN FUEL ASSEMBLY AND CONTROL ROD CELLS

	Fuel	Absorber	Steel	Sodium
FA of core and BBB	0.388	-	0.228	0.384
FA of RBB	0.585	-	0.171	0.244
Control rod	-	0.296	0.235	0.469
Guide tube for control rod	-	-	0.119	0.881
FA of sodium plenum	-	-	0.228	0.772

In course of core refuellings minor actinides produced in previous reactor cycle are loaded into the core with the fuel. In this case MA radioactive decay during fuel reprocessing and assembly fabrication (3 years) is taken into account. In addition some amount of actinides discharged from WWER-1000 reactor after 3-year cooling time is also loaded into the core. MA composition is taken as follows (in weight %) [3]:

^{237}Np	^{241}Am	^{242m}Am	^{243}Am	^{242}Cm	^{243}Cm	^{244}Cm	^{245}Cm
57.1	27.5	0.05	11.8	0.02	0.03	3.3	0.2

By analogy with a standard BN-800, the core is divided into three radial zones (LEZ, MEZ, HEZ) for flattening power distribution. They have different plutonium content — low, medium and high — in the same ratio as for BN-800 core. Thorium dioxide is the material for radial breeding zones.

Figure 1 demonstrates the scheme of two-dimensional calculation reactor model. Calculations of fuel performance and reactor safety characteristics were carried out by the follows codes:

— Equilibrium composition calculations were made using diffusion RZA [4] code in two-dimensional R-Z geometry with the use of 26-groups constant library BNAB [5] in CONSYST format;
— Calculations of sodium void reactivity effect (SVRE) were carried out by MCNP-4C [6] code taking into account heterogeneous structure of core, upper sodium plenum and lower breeding blanket.

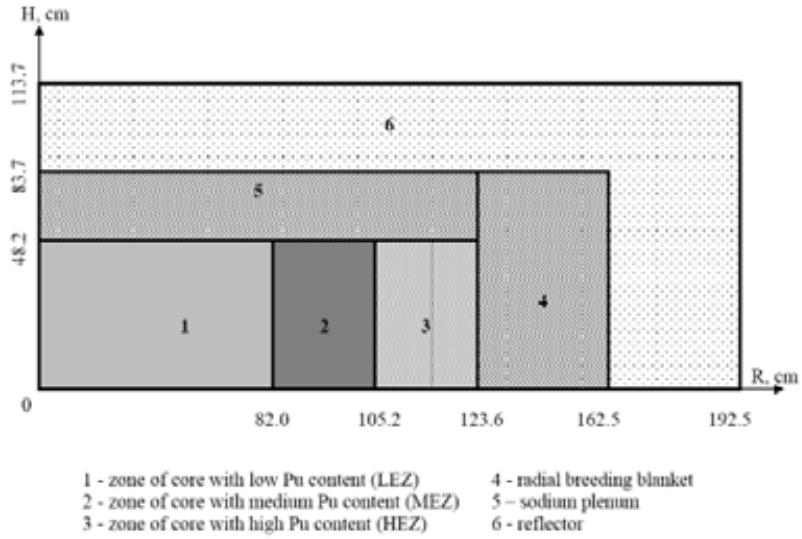

FIG. 1. Calculation reactor model.

2.3. Neutronics characteristics. Results of calculations

An initial plutonium charge of the reactor with ThO_2+PuO_2 fuel was determined from the condition of equality of the k_{eff} value at the end of equilibrium cycle and the same value of k_{eff} in BN-800 reactor with UO_2+PuO_2 fuel. In so doing, the additional quantity of actinides replaces the corresponding quantity of raw material — thorium dioxide. The following variants have been considered.

Variant A — recycle of own actinides only. The variant gives opportunity to evaluate the possibility of project realisation with minimal actinide recycle which makes sense.

Variant B — recycle of own actinides and adding of 52 kg of WWER's actinides at a refuelling. This amount is equal to the result obtained in paper [1] and gives a positive SVRE

Variant C — recycle of own actinides and adding of 13 kg of WWER's actinides at a refuelling. The variant corresponds to some interpolation between variants A and B and gives acceptable SVRE.

Determine general requirements imposed on the reactor:

— Equality of k_{eff} value at the end of equilibrium cycle in BN-800 reactor with ThO_2+PuO_2 fuel to the same value of k_{eff} in BN-800 reactor with UO_2+PuO_2 fuel.
— ^{238}Pu in Pu content taking account cooling time of spent fuel has not to exceed 5%. This amount is considered as acceptable factor from the viewpoint of self-heating of plutonium separated. In order to reduce ^{238}Pu content in spent fuel plutonium is not recycled in the reactor and has to be burned in other reactors.
— Radial power peaking factor ($K_{r\,max}$) should not exceed 1.2.
— SVRE ≤ 0.

Initial plutonium content in three-zoned core with three refuellings during lifetime is shown in Table 3. Table 4 gives the basic neutronic characteristics and heavy metal charge and discharge at reactor refuelling for variants considered (in equilibrium cycle, time interval between refuellings is 147 days, loading factor is 0.8).

TABLE 3. INITIAL PLUTONIUM CONTENT IN FUEL, % MASS

Variants	LEZ	MEZ	HEZ
Variant A	21.76	23.64	31.34
Variant B	21.36	23.09	30.67
Variant C	21.74	23.58	31.15

TABLE 4. BASIC CHARACTERISTICS OF THE REACTOR VARIANTS CONSIDERED

Characteristic	Variant A	Variant B	Variant C
Annual charge of, kg:			
plutonium	2020	1980	2014
actinides*), including	158	560	250
• own actinides	158	456	224
• actinides from VVER	0	104	26
Actinide share in charged fuel , %	1.9	6.9	3.1
Annual discharge of**), kg:			
• plutonium	1530	1580	1545
• actinides	158	452	224
• ^{233}U	533	518	543
^{232}U content in discharged uranium**), ppm			
• from reactor	2935	3072	2968
• from core	5234	5673	5334
• from radial blanket	110	111	110
• from bottom blanket	182	185	183
^{238}Pu share in discharged plutonium**), %	2.0	5.3	2.8
Power fraction , %, (BOC/EOC) in:			
• core	97.9/96.1	98.0/96.2	98.0/96.2
• bottom blanket	0.8/1.6	0.8/1.6	0.8/1.6
• radial blanket	1.3/2.3	1.2/2.2	1.2/2.2
Power peaking factors:			
• radial K_r	1.15	1.15	1.15
• volume K_v	1.42	1.42	1.42
Reactivity shift between refuellings, %Δk/k	1.61	1.21	1.52
β_{eff}, %	0.29	0.27	0.28
Fuel inventory ratio (FIR) for ^{239}Pu, ^{241}Pu, ^{233}U			
• reactor FIR	1.01	1.01	1.01
• core FIR	0.84	0.84	0.84
Burnup, % h.m.			
• average	7.6	8.2	7.7
• maximal	10.8	11.6	10.8

*) actinides: $^{231}Pa+Np+Am+Cm$
**) after 3 years cooling time

Besides, addition calculations were performed for variant C, as best meeting to the SVRE requirements, as follows:

— Calculation of protactinium reactivity effect — reactivity increase due to transition of ^{233}Pa into ^{233}U after power shutdown. Calculation was done with a safety margin, that is at full decay of the end of cycle ^{233}Pa into ^{233}U. Note, that half-decay period of ^{233}Pa is about 27 days. Consequently, about of 88% of ^{233}Pa nuclei will decay in 81 days (3 periods), that is close to refuelling time outage. Maximum value of protactinium effect is +2.2% Δk/k.

— Calculation of control rods efficiency. Calculation was done at equilibrium cycle beginning. In so doing it was adopted that all the rods from natural boron carbide have depth of insertion equal to the core height and when inserted they come out from the sodium plenum, where they are partially placed in cocked position. The MCNP–4 Monte-Carlo code [6] was used for calculations. Calculation result is 6.40±0.19% Δk/k.

From these data and Table 4 data follows that the values of the most parameters of the reactors under consideration are close. They are also close to the variant presented in Ref. [1]. Naturally, actinides charging is an exception. Figures 2 and 3 shows generalized dependences of reactivity shift and delayed neutrons effective fraction β_{eff} on external actinides charge.

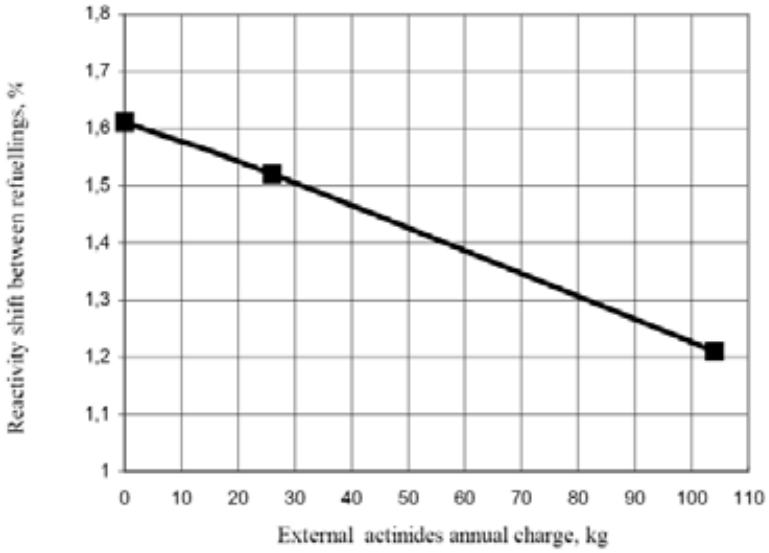

FIG. 2. Reactivity shift Δk/k between refuellings versus external actinide charge.

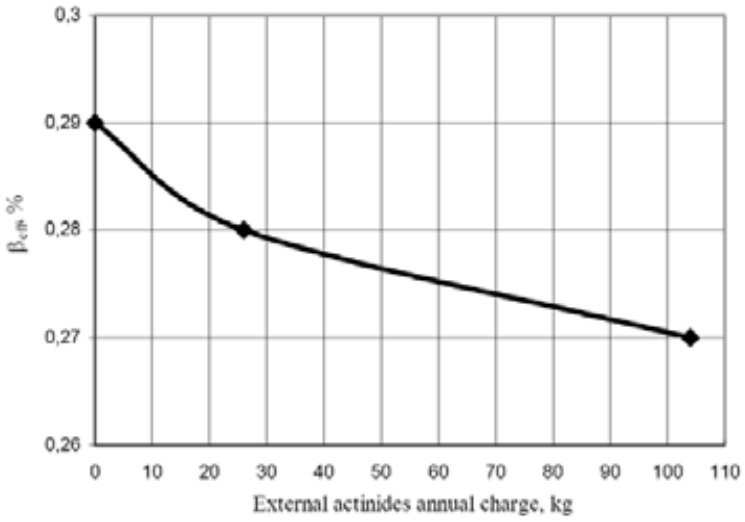

FIG. 3. β_{eff} versus external actinides charge.

2.4. Sodium void reactivity effect

Sodium density decrease is accompanied by reactivity change by the following basic reasons:

— Decrease in macroscopic absorption cross section of sodium (insignificant positive effect);
— Neutron spectrum hardening because of decrease in moderation cross section, sign of effect depends on core composition: in enriched uranium core spectrum hardening results in negative reactivity effect, mixed fuel based on plutonium gives the positive one;
— Probability of neutron leakage from core increases (negative component).

The relationship between components of SVRE depends mainly on sodium volume fraction and dimensions of the reactor. When increasing theese letter leakage component decreases and the role of spectrum effects increases. As this takes place, SVRE can change its sign.

Fast loss of coolant pressure in first circuit accident, in which sodium boiling will start in region of the most high temperature and minimal pressure, that is upon the core, is considered. As boiling is developed, the sodium level upon the core comes down and then is displaced from the core with boiling boundary travelling down.

SVRE was calculated in the reactor with heterogeneous core structure, upper sodium plenum and bottom breeding blanket in actual geometry using MCNP code. Reactivity effect was determined when successive removing sodium from horizontal layers up to full voiding of the reactor. Recall, that upper breeding blanket, which was taken into account in the paper [1], in the present consideration is replaced with sodium plenum, that is, thorium dioxide was completely removed from all the structure elements: fuel claddings, FAs and control rod cans. Besides, the absorber elements were specified in sodium plenum, in so doing they were supposed to be made up of natural boron carbide (^{10}B content is 20%). It should be noted that SVRE was determined at cycle beginning, when it is maximum. Figures 4 and 5 give calculation scheme of the reactor.

Control rod cell in sodium plenum is shown in Fig. 6. Relationship between sodium draining reactivity effect and height of voiding is presented in Fig. 7. It is shown for the variant with upper sodium plenum, own MA recycle and addition of 52 kg of WWER-1000 MA (variant B, where the most positive SVRE should be forthcoming). Interpretation of the result can be as follows. At the first stage, as coolant level in sodium plenum and upper part of the core is coming down, neutron leakage arises resulting in significant negative reactivity.

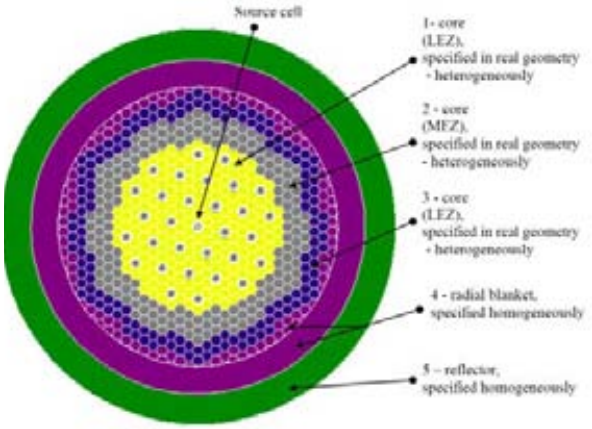

FIG. 4. Reactor layout.

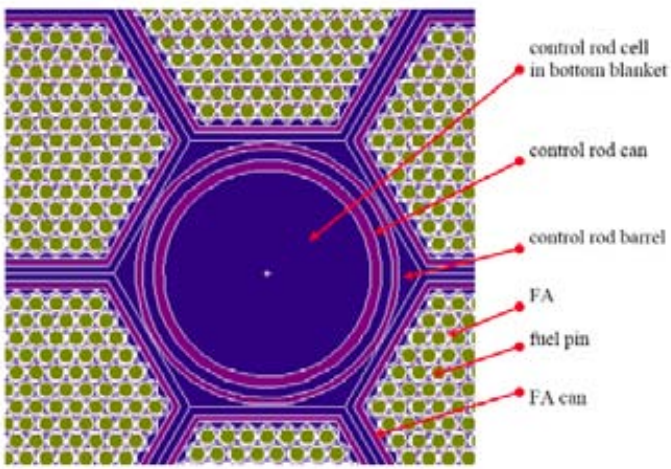

FIG. 5. Control layout.

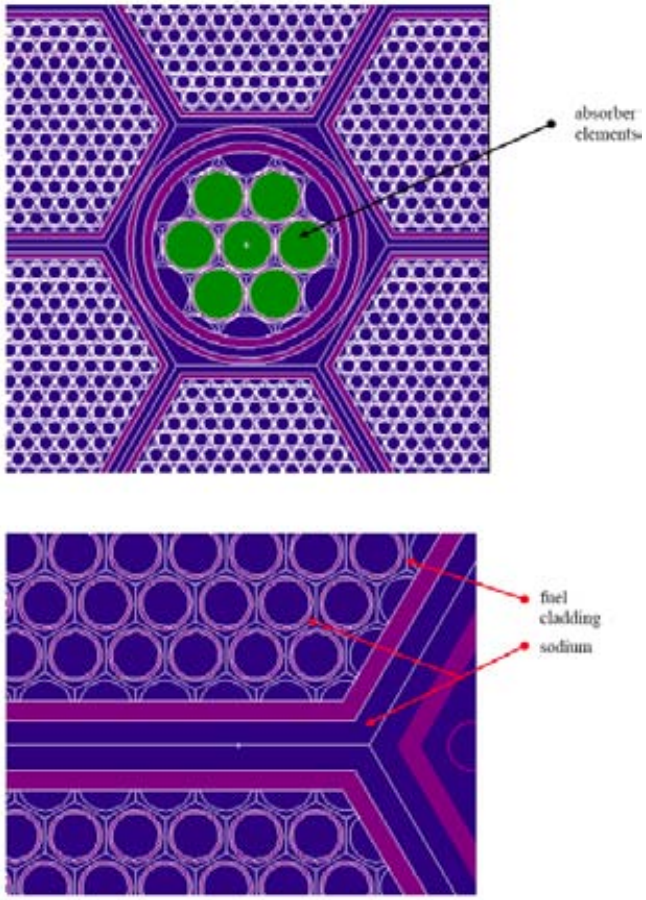

FIG. 6. Details control and fuel assembly.

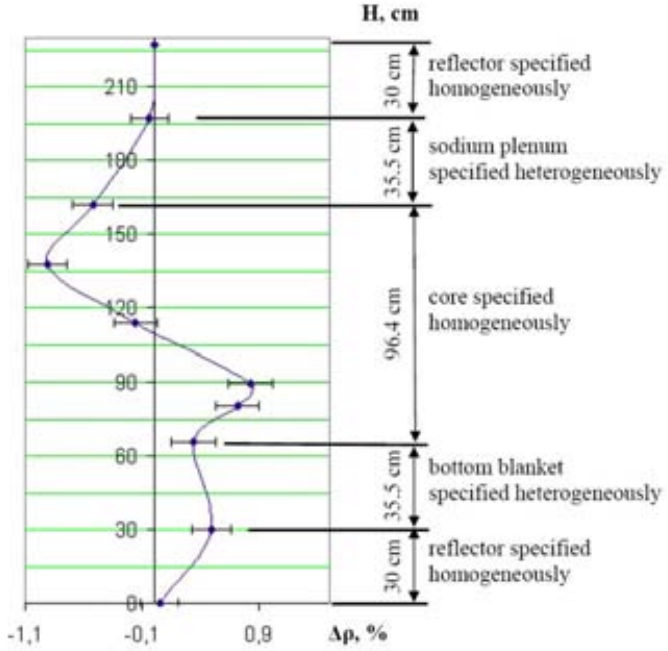

FIG. 7. Sodium void reactivity effect for variant B when coolant draining.

But, with further coolant level lowering in the core, the positive reactivity is introduced, because the more MA giving positive contribution in SVRE are accumulated in the central part of the core. It should be noted, that after passing point of maximum — point of inflection is about 22 cm up from the bottom blanket — neutron leakage through the last one begins to exert significant influence on SVRE. Position of the point of inflection depends on neutron spectrum and medium which determine neutron free path and naturally impact on escape probability from the core. Besides, supplementary distinction between sodium plenum and bottom blanket should be noted: since control rods are cocked, absorber elements which are placed in sodium plenum give negative component in SVRE as neutron leakage increases at the top of core. **For variants A and B** the run of curves of reactivity change at sodium discharge are analogous. So in the point of inflection SVRE has the maximum value and **in variant B** for equilibrium cycle beginning it is

$$0.72\pm0.19\%\Delta k/k,$$

and at full reactor voiding it is

$$0.05\pm0.16\%\Delta k/k.$$

In variant C (with top sodium plenum, recycling of own MA and addition of 13 kg WWER's MA in a charge) maximum SVRE for cycle beginning is

$$0.01\pm0.18\%\Delta k/k,$$

and at full voiding is

$$-0.56\pm0.19\%\Delta k/k$$

At the end of cycle SVRE **in variant C** in the point of it maximum is

$$-0.41\pm0.18\%\Delta k/k.$$

In variant A (with top sodium plenum, recycling of only own MA) maximum SVRE for cycle beginning is

$$-0.54\pm0.18\%\Delta k/k,$$

and at full voiding is

$$-1.14\pm0.20\%\Delta k/k.$$

SVRE change versus external MA addition is plotted in Fig. 8.

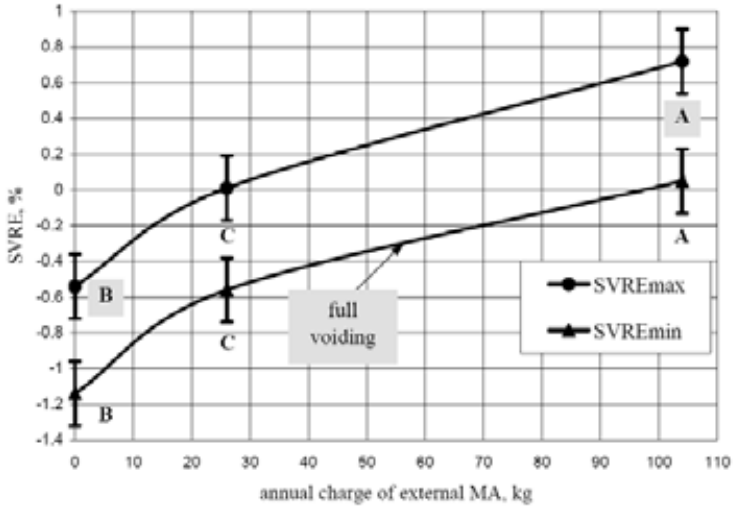

FIG. 8. SVRE versus annual external MA charge.

As may be seen from the results obtained, chosen reactor structure with sodium plenum instead of top blanket and without WWER's MA addition gives the negative SVRE both at full and partial voiding. Annual amount of own MA recycled is about 158 kg.

Maximum value of SVRE becomes close to zero with annual addition of 26 kg from WWER-1000 reactor and at full voiding becomes negative. Total amount of MA annually charged is 250 kg, of which the own ones are 224 kg.

Maximum value of SVRE becomes positive with external MA addition increase up to 104 kg per year and at full voiding close to zero. In so doing the total annual amount of MA charged becomes equal to 560 kg, of which 452 kg are the own ones.

By this means **the variant C** utilizing annually 26 kg of external MA is the most acceptable from the point of view of negative SVRE providing. Note, that WWER-1000 reactor produces annually about 15 kg of MA, that is one fast reactor of the type considered utilizes actinides from about 2 WWER-1000 reactors apart from its own actinides.

With the abandonment of requirement for nonpositivity of SVRE in point of maximum, the amount of MA utilized will significantly increase — up to ~104 kg per year. It is well bear in mind that in this case value of SVRE remains moderate: +0.72%Δk/k. But the possibility for the reactor to operate with such SVRE have to be substantiated in addition.

The estimation of separate MA isotope contributions showed that ^{241}Am, ^{243}Am and ^{237}Np give the positive contribution in SVRE with ^{241}Am majority contribution. The other MA gives the negative contributions (see Fig. 9). The calculations were carried out for equilibrium cycle beginning of the variant B having the largest SVRE by method of the individual isotopes successive removal using MCNP code. Table 5 shows isotope composition of burned MA (discharged from the core and blankets after 3 years cooling time). As may be seen from the data, ^{241}Am fraction is a maximum in the composition under consideration.

The analysis of the results obtained allows directing the ways to increase amount of MA incinerated with simultaneous providing negative SVRE. The most simple and less laborious way is to locate MA (or part of them, for example, relevant to the external ones) in core area giving negative contribution in SVRE.

The other way is separate incineration of elements giving negative and positive components of SVRE. The elements with negative contributions are burned out in the core, and with positive one in definite core parts or in blankets, or outside of critical reactor at all, for example, in ADS. This approach is far and away more challenging from technological side and more economic costly.

However the significant analytical work is still needed to justify the approaches for MA burning increase.

Additional information about fuel fabrication, fuel reprocessing (inclusive aqueous- and pyro-reprocessing) are given in Appendix II.

2.5. Conclusions

The feasibility of minor actinides incineration in the reactor of standard BN-800 design with the fuel in the form of mixtures of thorium and reactor plutonium dioxides with minor actinides — Np, Am, Cm oxides was shown. Simultaneously with own actinides recycling external minor actinides from WWER-1000 reactors are added in the fuel. An impact of the amount of external minor actinides recycled on SVRE was determined.

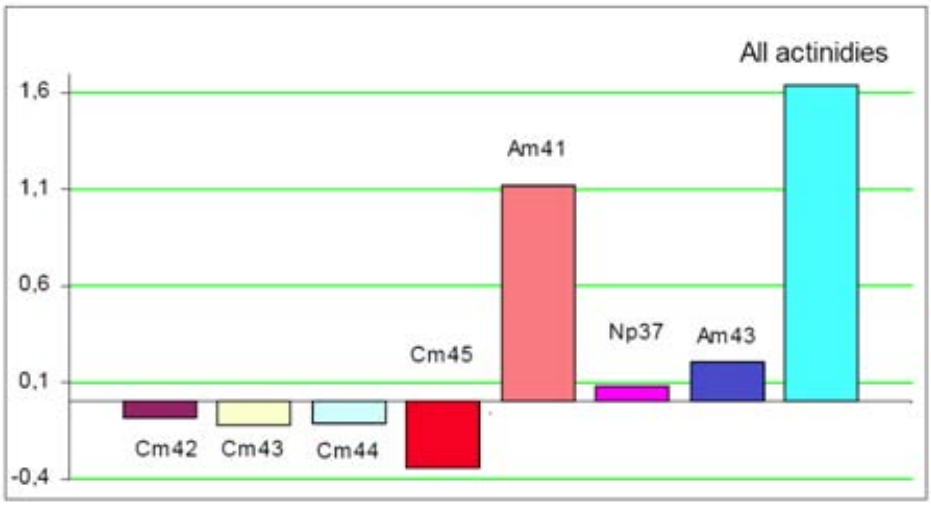

FIG. 9. Individual isotope contributions in SVRE.

TABLE 5. BURNED ACTINIDES COMPOSITION

Nuclide	Mass, kg	%
^{231}Pa	0.199	21.6
^{237}Np	48.82	21.6
^{241}Am	111.8	49.4
^{242m}Am	4.0	1.8
^{243}Am	30.58	13.5
^{242}Cm	0.12	0.1
^{243}Cm	0.86	0.4
^{244}Cm	16.22	7.2
^{245}Cm	5.05	2.2
^{246}Cm	8.43	3.7

It was shown, that nonpositive sodium void reactivity effect with the full draining of coolant and the maximum effect, taking place with partial sodium removal, are achieved with addition in the cycle of no more than 26 kg of external actinides per year. The intimated amount is approximately consistent with annual buildup of minor actinides in two WWER-1000 reactors. It was determined that ^{241}Am, ^{243}Am and ^{237}Np give a positive component in SVRE, with a major contribution of ^{241}Am. Consideration was given to practicable ways of increasing efficiency of external actinides transmutation on retention of negative SVRE.

When abandoning of SVRE nonpositivity requirement in maximum point, the amount of recycled actinides increases significantly — up to 104 kg per year. In this case one reactor of BN-800 type can recycle actinides from 7 WWER-1000 reactors. It should be borne in mind that SVRE value remains moderate: +0.72%Δk/k. However, the feasibility of reactor operation with such SVRE requires additional substantiation.

Calculations of fuel equilibrium composition and some physical characteristics of the reactor were performed. About 2 tons of plutonium are recycled annually, and about 540 kg of ^{233}U are built-up. The built-up ^{233}U can be used for initialization of thorium-uranium fuel cycle of nuclear power.

REFERENCES TO CHAPTER 2

[1] DEKUSAR, V.M., KALASHNIKOV, A.G., CHEBESKOV, A.N., CHIZHIKOVA, Z. N., Feasibility Studies of BN-800 Type Reactor with (Pu-Th)O_2 Fuel for Effective Incineration of Minor Actinides, paper presented in the second RCM of the CRP on Studies of Advanced Reactor Technology Options for Effective Incineration of Radioactive Waste, 22-26 November 2004, Hefei, China.

[2] BAGDASAROV, Yu.E., et. al., Reactor BN-800 — a New Stage in Fast Reactor Development, paper presented in the International Symposium on Fast Breeder Reactors, 22-26 July 1986, Lyon, France, IAEA-SM 284/41.

[3] Evaluation of Data for System Analysis and Calculation of Safety Parameters for WWER Type Reactors with MOX Fuel Loading. Direction № 2. ISTC-369 (1997).

[4] ARTEMIEV, N.I., et. al., Method of multigroup calculation of two-dimensional reactor in slowing down and moderation neutron energy areas and with burning. VANT, Series "Physics and Technic of Nuclear Reactors", issue 2 (1988).

[5] MANTUROV, G.N., NIKOLAEV, M.N., TSIBULYA, A.M., Code for Constant Preparation CONSYST. Description for Use. Preprint IPPE-2828 (Obninsk, 2000) (in Russian).

[6] MCNP — A General Monte Carlo N-Particle Transport Code, LA 12625 M, Version 4B, LANL (March 1997).

[7] DEKUSAR, V.M., et. al., Feasibility Studies on Plutonium Utilization in VVER Type Reactors with Plutonium-thorium Fuel. Preprint IPPE-2986 (Obninsk 2003) (in Russian).

CHAPTER 3. DOMAIN-I: MINOR ACTINIDES BURNING IN FAST LEAD AND SODIUM COOLED REACTORS

3.1. Introduction

The importance of resolving the waste question in the European Union has clearly been demonstrated by the recently conducted EUROBAROMETER poll on nuclear waste [5].

The results show that to the 37% in favor initially to produce energy by nuclear power plants additional 38% of 55% initially opposed could be added, if the issue of nuclear waste was solved (Fig. 1). This would yield 58% in favor and 31% against continuing to utilize nuclear power in the [25]EU.

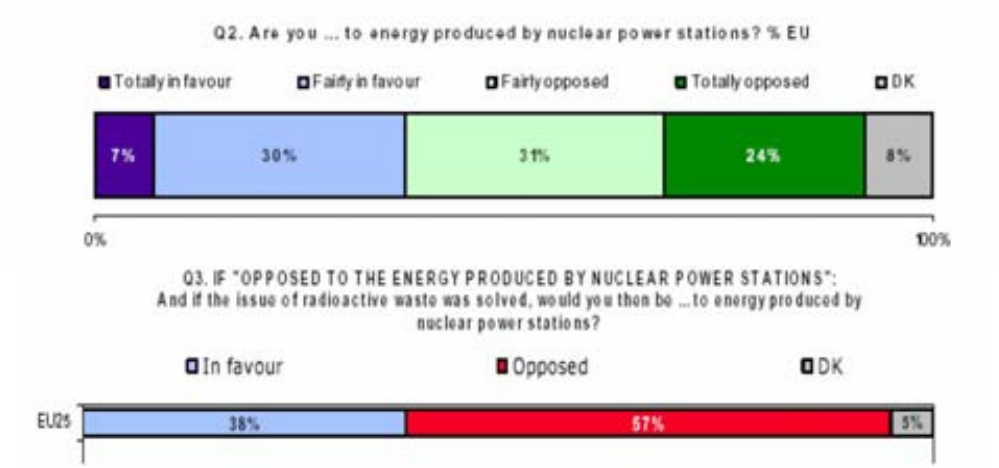

FIG. 1. The results of the ERUOBAROMETER poll on nuclear waste 'DK' = Don't Know.

To resolve the nuclear waste question, to have credibly safe and economical reactors and to assure the long term sustainability of nuclear power requires the early introduction of new fast reactors. The subsequent calculations show that the minor actinides (MAs) can be destroyed in fast reactors without burning plutonium. Moreover, it will be shown that MA burning can even be accompanied by Pu breeding. The latter is important since calculations with the DESAE code show that a four time increase of nuclear power by 2050 would lead to problems with the availability of natural uranium [9]. In order to sustain this four-fold increase of nuclear power, one third of all reactors by 2040 would have to be fast systems. An even earlier introduction, however, is desirable in order to start burning the minor actinides. Critical long lived and water-soluble isotopes, such as ^{129}I and ^{99}Tc, could also be efficiently transmuted in fast systems [8]. The US GNEP program launched by the DOE in 2006 was first aimed at an advanced burner reactor that will burn all the transuranics from spent fuel, including plutonium [6]. This would not meet the criterion of long term sustainability. If one burnt all the currently existing 2600 tons of plutonium in the spent nuclear fuel, not much fast reactor fuel would remain available except for reasonably highly enriched uranium. However, if uranium resources become scarce this fuel would probably become quite expensive because of competition with LWRs. This seems to have been recognized by the US DOE too and the DOE now rather refers to an advanced recycling reactor which appears to imply that they will also preserve the plutonium.

3.2. Method

In this study, we aim at designing 600 MW(e) lead-cooled fast reactor (LFR) and sodium-cooled fast reactor (SFR) cores consuming significant amounts of minor actinides and having, at the same time, a positive plutonium balance. The cores hence accommodate substantial amounts of minor actinides in the actinide vector of the start-up fuel (4-5%). To further improve MA consumption, an option of incorporating minor actinides into axial and radial blankets was also investigated for both SFRs and

LFRs. Apart from increased MA consumption rates, this approach also means that plutonium bred in these blankets is less proliferation-prone. The fraction of minor actinides in the actinide vector of the blankets is 10%.

The special part of our approach is the homogeneous burning of minor actinides (MAs) in the core. However, this makes the neutron spectrum quite hard, which worsens the Doppler reactivity feedback. At the same time, cores with MAs exhibit large positive coolant temperature coefficient due to the higher spectral gradient during coolant heat-up. As a result, the reactivity change of the Doppler becomes smaller than the reactivity increase due to coolant heat-up for an assumed equal temperature increase for both fuel and coolant. To counter this problem a limited number of moderating pins such as CaH_2, $UZrH_{1.6}$, BeO, or Be can be used in all core sub-assemblies.

In this study, $UZrH_{1.6}$ and CaH_2 moderator pins were applied. Moderating power of hydrides is very good, but their relatively low decomposition temperature (~1100 K for CaH_2) excludes their inclusion in the fuel directly. An irradiation of hydride pins (CaH_2) in the Phénix reactor has recently been completed in the frame of ECRIX-H experiment [11].

Only mixed oxide fuel including minor actinides (~5% of the fuel) is used in this study since this fuel can be fabricated and reprocessed using available technologies with enhanced shielding. For the future reprocessing, we envisage the use of the GANEX (Global Actinide Extraction) approach, which is currently in the testing phase [11]. But also the current PUREX reprocessing can be used.

In this paper, also the neutronic performance of 600 MW(e) lead-cooled fast reactors employing Th-based fuels is studied. This investigation considers breeder/burner core configurations incinerating Pu and MAs or Pu alone and generating also significant amounts of ^{233}U, which can subsequently be used to feed thermal breeders with their considerably lower critical mass.

Other important aspects of fast reactors are reliability and safety. In this paper, unprotected Loss-of-Flow (ULOF) and Loss-of-Heat Sink (ULOHS) accidents as well as the decay heat removal in a station blackout condition are investigated for both the SFR and LFR reactors under consideration. These unprotected accidents are of particular interest since fast reactors with their multiple critical masses have a potential for power excursions in core-disruptive accidents.

Table 1 displays design parameters of SFR and LFR cores considered in this study. The characteristics of the cores are derived from established LFR and SFR designs, taking into account thermo-mechanical restrictions with respect to coolant, cladding, structural material, and fuel. Both reactors have a power of 600 MW(e).

TABLE 1. DESIGN PARAMETERS OF SFR AND LFR CORES

Parameter	LFR $(U,TRU)O_2$	LFR $(Th,TRU)O_2$	SFR
Power (MW_e)	600	600	600
Pellet outer radius (mm)	5.0	5.0	3.0
Clad inner radius (mm)	5.1	5.1	3.1
Clad outer radius (mm)	6.25	6.25	3.45
Pellet hole radius (mm)	--	1.5	--
Pitch-to-diameter ratio (P/D)	1.5	1.6	1.2
S/A outer flat-to-flat (cm)	22.20	23.60	14.66
Pins per S/A	127	127	271
Length of upper plenum (cm)	100	100	100
Length of lower plenum (cm)	10	10	10
Active pin length (cm)	200	200	100
Length of upper/lower axial blankets (cm)	50	--	50

The core concept of the SFR is based on a WAC benchmark reactor design, but the power was decreased from 800 MW(e) to 600 MW(e) [12]. The active core length is 100 cm, with 50 cm long upper and lower axial blankets. The allowed maximum velocity of coolant in SFRs is much larger than that for LFRs (8-10 m/s vs. 2-3 m/s), which also means that SFR pin lattices are tighter than those of LFRs. Averaged inlet and outlet sodium temperatures are 653 and 823 K, respectively.

For the LFR, the active pin length is increased to 200 cm. This makes the core geometry compact, which is beneficial for the neutron economy. Correspondingly, pin and pellet dimensions are also larger than for an SFR, guaranteeing stability of the fuel column in a liquid lead environment. The length of axial blankets is the same as for the SFR core. Based on the basic ELSY design parameters the axial temperature increase in the coolant channel is 80 K and the averaged channel outlet temperature 753 K [4]. The maximum operating cladding temperatures thus remain comfortably below the stability limit of protective oxide films (870 K).

For neutronic and depletion analyses, the Monte Carlo code MCB was used. In the calculations, 1-σ statistical uncertainties in k_{eff} were less than 10 pcm [3]. The transuranium (TRU) vector is from spent LWR UOX fuel with a burnup of 41 GW•d/t_{HM} and a subsequent decay of 30 years. Correspondingly, the minor actinide fraction in the TRU vector is 17%. The uranium used was depleted uranium (0.3% ^{235}U). We assumed a 330 days long irradiation period followed by a 35 days refueling period. The fuel cycle length was five years.

The European Accident Code-2 (EAC-2) and Computational Fluid Dynamics code STAR-CD were used for the safety studies [13]. In the Loss-of-Flow (LOF) accidents, the primary coolant flow coast down according to Eq. 1 was used:

$$\frac{G(t)}{G_0} = \frac{1}{1 + t/t_c} \quad , \tag{1}$$

where $G(t)$ and G_0 are coolant flow rates at time t and $t=0$, respectively, t_c equals to 6 s.

3.3. Neutronic and burnup performance of LFRs and SFRs

In this study, moderating pins were placed only in the core sub-assemblies, all of which contain minor actinides. No moderator pins were used in the sub-assemblies of the radial blanket. Note that an introduction of thermalizing pins into core S/As containing Pu and MAs results in an acceptable Doppler reactivity feedback, which is, however, not the case when no moderator pins are used (Table 2).

Both LFR and SFR consume significant amounts of minor actinides in the start-up cores and even breed some plutonium in most cases (Table 3). The highest MA destruction rate is observed in the systems having MAs both in the core and in the blankets. In this case, an SFR transmutes 131 kg of MAs per year while an LFR transmutes annually 104 kg. The latter figure corresponds to an annual production of minor actinides in ~2.2 EPRs.

Placing minor actinides only in the blankets allows a decrease of the U/Pu fraction in the core, which in turn improves breeding. In this case, 198 and 145 kg of plutonium are generated in the SFR and LFR, respectively. Additionally, an SFR destroys annually 65 kg of MAs, but the same figure for an LFR is much lower (15 kg/a). The reason is a larger self-production of minor actinides in the LFR core (~30 kg/a) than in the SFR and a lower neutron flux in the radial blankets leading to lower MA destruction rates.

With respect to MA transmutation, a more attractive option for an LFR thus seems to recycle MAs together in the core and blankets or in the internal part of the core only. In the latter case, about 67 kg of MAs are destroyed annually, while some plutonium (14 kg/a) is still generated. For the SFR, the corresponding figures are slightly lower. Another interesting option for an LFR is to place the blankets inside the core. Our calculations indicate that a similar MA transmutation performance can be obtained as for the homogeneous approach (63 kg/a), but a considerably larger Pu mass is generated (78 kg/a).

TABLE 2. NEUTRONIC AND BURNUP PARAMETERS OF THE 600 MW(e) LFR AND SFR (U,TRU)O_2-FUELLED SELF-BREEDERS: DOPPLER AND COOLANT TEMPERATURE REACTIVITY FEEDBACKS CORRESPOND TO THE INCREASE OF FUEL AND COOLANT TEMPERATURES BY 100 K. DEPLETION PERFORMANCE FIGURES ARE GIVEN AS AN ANNUAL AVERAGE OVER A 5 a START-UP CYCLE

System/Parameter	SFR			LFR		
	MAs only in the core	MAs only in the blankets	MA in the core & blankets	MAs only in the core	MAs only in the blankets	MA in the core & blankets
No. of $UZrH_{1.6}$ moderator pins in a S/A of the core	19	--	19	6	--	6
No. of larger LFR & smaller SFR sub-assemblies (core/blanket)	541/--	547/168	547/168	391/--	397/144	397/144
Actinide mass at BOL core/blankets (t_{HM})	32.1/--	34.6/55.8	32.7/53.5	61.9/--	65.6/68.1	62.9/66.7
Averaged TRU enrichment at BOL, core/blankets (%)	22.7/--	17.0/10	22.7/10	22.6/--	17.0/10	22.6/10
Doppler Δk_D for a 100 K increase (pcm)	–102	–74	–99	–91	–68	–87
Coolant Δk_c for a 100 K increase (pcm)	+56	+62	+55	+62	+44	+46
Actinide burn-up (%FIMA per year)	–1.4	–0.5	–0.5	–0.8	–0.4	–0.4
MA burn-up (%FIMA per year)	–5.3	–1.2	–2.0	–2.9	–0.2	–1.1
Burn-up swing Δk per year ($)	–2.4	–1.3	–2.0	–0.5	–0.2	–0.7

TABLE 3. AMOUNT OF ANNUALLY GENERATED/CONSUMED TRANSURANICS IN LFR AND SFR (U,TRU)O_2-FUELLED SELF-BREEDERS: THE FIGURES CORRESPOND TO THE START-UP CYCLE AND ARE GIVEN AS AN ANNUAL AVERAGE OVER A 5 a CYCLE LENGTH. IN THE SPENT FUEL, ALL ^{242}Cm WAS ASSUMED TO DECAY TO ^{238}Pu

System/Parameter	SFR			LFR		
	MAs only in the core	MAs only in the blankets	MA in the core & blankets	MAs only in the core	MAs only in the blankets (internal blankets)	MA in the core & blankets
Pu generated (kg/y)	–12	+198	+150	+14	+145 (+78)	+110
MA consumed (kg/y)	–66	–65	–131	–67	–15 (–63)	–104

Another type of burner/breeder is an LFR using thorium-based mixed oxide fuels– (Th,TRU)O_2. The plutonium and MA burning capability of such a system is very good since there is very limited self-generation of transuranics from thorium. These systems also breed ^{233}U, which could be used for example as fuel in LWRs or in thermal breeders such as the Indian AHWR [10], CANDUs [1] or MSBRs which have considerable lower critical masses. These combinations of fast reactors and thermal breeders (even if they are just self-breeders) favor the sustainability since much less fissile material is needed.

The neutronic characteristics of LFR Th-fuelled cores are given in Table 4. The beneficial effect of moderator pins on the reactivity coefficients manifests itself in significantly larger negative Doppler feedback in the burner/breeder core than observed for the moderator-free (Th,^{233}U)O_2-fuelled LFR self-breeder (not shown here). In the former case, the Doppler is more than twice larger than the coolant reactivity coefficient.

TABLE 4. NEUTRONIC AND BURNUP PARAMETERS OF THE 600 MW(e) LFR Th-FUELLED BURNER/BREEDER CORES: DOPPLER AND COOLANT TEMPERATURE REACTIVITY FEEDBACKS CORRESPOND TO THE INCREASE OF FUEL AND COOLANT TEMPERATURES BY 100 K. P/D = 1.6. IN THIS CASE, CaH_2 MODERATOR PINS WERE USED.

System configuration / Fuel	Nr. of moder. pins per S/A	Nr. of S/As	Actinide mass at BOL (t_{HM})	Averaged enrichm. (%)	Coolant Δk_D (pcm)	Doppler Δk_c (pcm)	Actinide burn-up (%FIMA per year)	TRU burn-up (%FIMA per year)
Burner/breeder (Th,TRU)O_2	16	265	35.48	29.5	46	–127	–1.3	–3.8
Burner/breeder (Th,Pu)O_2	9	265	39.91	22.0	43	–167	–1.2	–5.1

The burnup behavior of the Th-fuelled systems is more complex than that of reactors operating on uranium-plutonium fuel. This is due to the delay in the ^{233}U production via ^{232}Th → ^{233}Pa (T1/2=26.97 d) → ^{233}U channel. The burnup reactivity swing is exemplified in Figs 2 and 3 for two distinct LFRs: (Th,TRU)O_2 and (Th,Pu)O_2, respectively. The latter system is now much larger (625 core sub-assemblies) than the one presented in Table 4. Consequently, it has a better burnup behavior compared to smaller (Th,Pu)O_2 case, but also to (Th,TRU)O_2-fuelled system. However, in both cases considered in Figs 2 and 3 the reactivity does not change more than 3$ from the initial BOL value for the first 4 years. This is an important factor for limiting reactivity insertion accidents, as the reactivity reserve needed to be present in the shim rods is considerably limited.

Concerning the transmutation performance, TRU-fuelled LFR incinerates 328 kg of Pu and 84 kg of MAs per year, which corresponds to the MA production in ~1.7 EPRs (see Table 5). At the same time, 249 kg of ^{233}U is generated. Such system hence effectively converts plutonium to ^{233}U, which could be used to start new LWRs or even better thermal breeders. The amount of ^{233}U produced is even higher in (Th,Pu)O_2-fuelled system (339 kg/a), which however have the drawback of generating some minor actinides (35 kg/a).

TABLE 5. AMOUNT OF ANNUALLY CONSUMED TRANSURANICS IN LFR BURNER/BREEDERS WITH THORIUM MATRIX FUEL: THE FIGURES CORRESPOND TO THE START-UP CYCLE. IN THE SPENT FUEL, ALL ^{242}Cm WAS ASSUMED TO DECAY TO ^{238}Pu

System	Actinide mass at BOL (t_{HM})	^{233}U generated (kg/y)	Pu consumed (kg/y)	MA generated or consumed (kg/y)
Burner/breeder (Th,TRU)O_2	35.48	+249	–328	–84
Burner/breeder (Th,Pu)O_2	39.91	+339	–480	+35

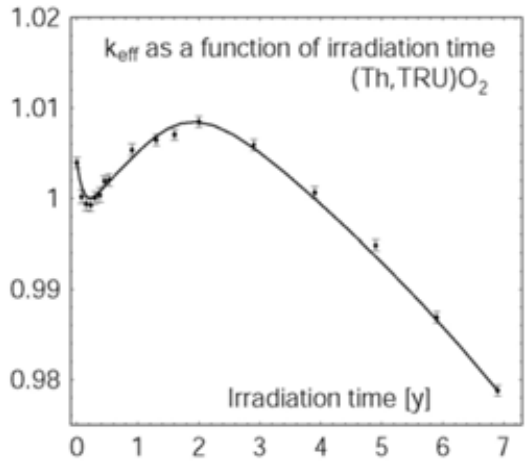

FIG. 2. Effective multiplication factor as a function of irradiation time in the $(Th,TRU)O_2$ LFR burner/breeder. Actinide mass at BOL is 35.48 ton.

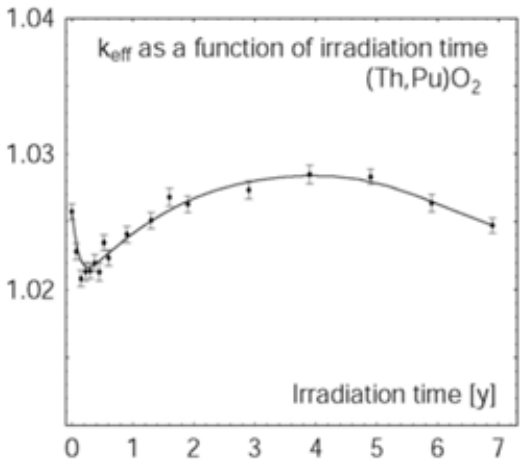

FIG. 3. Effective multiplication factor as a function of irradiation time in the $(Th,Pu)O_2$ fuelled LFR burner/breeder. Actinide mass at BOL is 103.4 ton.

3.4. Severe safety aspects of LFRs

Due to the several critical masses present in the fast cores, the investigation of severe safety characteristics is of particular importance. Ideally, the safety should be provided inherently and/or by passive means. In this respect, lead has several advantages in comparison to other liquid metal coolants. It has high boiling point (2 023 K), high volumetric heat capacity and low chemical activity with water and water vapor. The disadvantages are, however, its relatively large density and susceptibility to corrode structural materials at operating temperatures. Also, the relatively high melting point of lead limits its nominal operating interval to about 670-750 K. Structural resistance of the ferritic/martensitic steels can be guaranteed up to 870 K (using GESA surface coating) and in the future some other promising materials as ODS steels or SiC/SiC may qualify for even higher temperatures. In this study, the unprotected loss-of-flow, unprotected loss-of-heat sink and protected total loss of power (station blackout) accidents were investigated.

The relative power of the $(Th,TRU)O_2$ LFR core in the unprotected loss-of-flow accident is depicted in Fig. 4. The inlet coolant temperature was kept constant at 673 K. Thanks to the low pressure drop, the natural circulation of the coolant is sufficient to remove even the full nominal power (600 MW(e)). Due to the combined negative feedbacks (Doppler and axial fuel expansion), the power decreases to about 85% of nominal 200 s after the commencement of the accident. The corresponding maximum coolant temperature outlet temperature is 900 K (this means an increase of 150 K comparing to the steady-state conditions).

Figure 5 shows relative power in the unprotected loss-of-heat sink. In this case, we assume that the heat exchangers cease to remove the heat in 20 s, but pumps function normally. Again, due to the negative feedbacks from Doppler and axial fuel expansion the relative power diminishes to about 27% of the nominal after 1 000 s. The corresponding maximum outlet temperature is 1 170 K. In the EAC-2 calculation, no lower grid-plate radial expansion could be considered. We assume that this feedback would bring the power down to a decay heat level. The station blackout accident was assumed to be protected, as control rod sub-assemblies would be inserted to the core by a force of gravity when magnets are not powered. The decay heat removal is then facilitated through passive means by a Reactor Vessel Auxiliary (Air) Cooling System (Fig. 6).

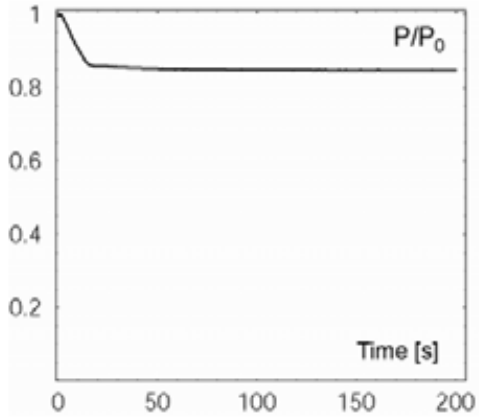

FIG. 4. Relative power in a ULOF accident in a 600 MW(e) (Th, TRU)O_2 fuelled LFR.

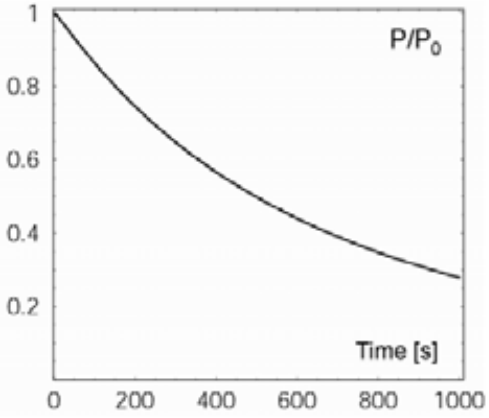

FIG. 5. Relative power in a ULOHS accident in a 600 MW(e) (Th,TRU)O_2 fuelled LFR.

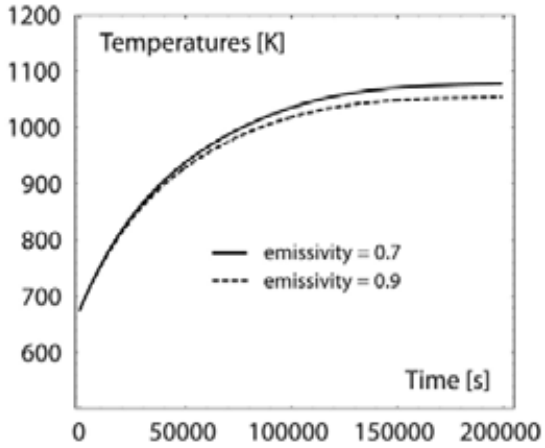

FIG. 6. Temperatures during a TLOP accident in a 600 MW(e) (Th,TRU)O_2 fuelled LFR.

In 200 000 s (~55 h), the coolant temperature will reach 1080 K, which is still about 100 K under the fast creep limit of the reactor vessel. However, an additional or more effective passively operating decay heat removal system might be needed as, e.g. in-vessel reactor auxiliary system, which is also envisioned in the ELSY project Unprotected reactivity or UTOP accidents with a few $'s of reactivity insertion will lead to fuel pin failures in both LFRs and SFRs. An advantage of the LFR appears to be the experience gained from an accident in the first lead-bismuth cooled reactors in Russian ALPHA-class submarines. It was reported that the heavy metal coolant (with a similar density as oxide fuel) led to an extensive fuel sweep-out from the core, which prevented recriticality [7].

3.5. Severe safety aspects of SFRs

During normal operation, the coolant velocities in the sodium-cooled reactor are higher than for the LFR. Therefore the relative velocity reduction during a LOF accident becomes much greater compared to the LFR cores. This fact means that the SFR will have a faster and larger temperature increase. In an unprotected LOF accident this leads to sodium boiling and a power increase as shown in Figs 7 and 8. This case was calculated with the EAC-2 multichannel accident code [13] using a flow halving-time of 6 s (see Eq. 1).

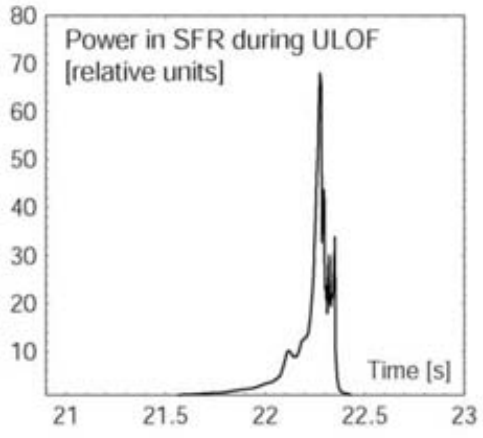

FIG. 7. ULOF in a 600 MW(e) SFR: Sodium boiling cannot be prevented by negative feedbacks. Natural circulation is limited due to the high-pressure drop core and complex flow path. Power increase leads to fuel melting, fuel pin failures and fuel expulsion that shuts the reactor down when about 50% of core is molten.

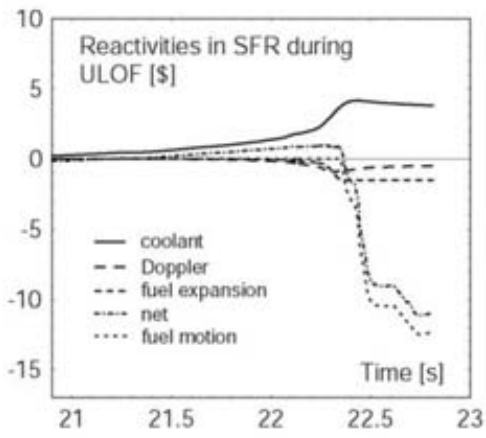

FIG. 8. As can be seen, the sodium voiding leads to a large positive reactivity insertion that causes a large power increase. The axial fuel dispersal leads at least to a temporary shutdown. However, re-criticalities are possible.

Fuel melting, fuel pin failures and axial molten fuel expulsion eventually shut the reactor down. The power burst could be avoided if an additional fast negative feedback due to radial structural expansion could be considered. The latter has been used in recent analyses of larger Russian and Indian designs, but the question is whether the radial expansion feedback can be fast enough to prevent boiling. The IAEA/INPRO considers performing a research project on structural feedbacks in SFRs. Some of the authors of this paper have shown earlier [2] that a significant increase in the pitch-to-diameter ratio of an SFR also avoids boiling, but leads to unacceptably high positive void reactivities. Smaller SFRs as the earlier US PRISM and SAFR designs could also avoid boiling in a ULOF due to a lower positive coolant feedback.

Unprotected Loss-Heat-Sink (ULOHS) accidents in an SFR behave similarly to such an accident in an LFR. However, the cp is only 70% of that of lead and its boiling point is 870 K lower. But the negative reactivity effect of the lower grid plate expansion is probably fast enough to get the power down to the decay heat level for a 600 MW(e) SFR. In reactivity accidents that lead to pin failures, only a limited part of the molten fuel gets swept out in an SFR and the unfragmented fuel will at least partially block the coolant channels of the lead assemblies. Another question is whether the fuel pin failure location is far enough from the core midplane, in order not to get positive reactivity effects from in-pin fuel motion.

REFERENCES TO CHAPTER 3

[1] BERGELSON, B., et al., Thorium self-sufficient fuel cycle of CANDU power reactor, paper presented in International Conference Nuclear Energy for New Europe, 2005, Bled, Slovenia.

[2] CARLSSON, J., et al., Comparison of lead and sodium-cooled reactors — safety, fuel cycle performance, and some economical aspect, European Nuclear Conference, ENC2005, Versailles, France (2005).

[3] CETNAR, J., et al., MCB — a continuous energy Monte Carlo Burnup code, Proc. of Fifth International Information Exchange Meeting, OECD/NEA, Mol, Belgium (1998).

[4] CINOTTI, L., Del Fungo Giera Energia, http://www.delfungogieraenergia.com/, Italy, personal communication (2006).

[5] EUROBAROMETER, Special Eurobarometer, Radioactive Waste, European Commission, June 2005, http://ec.europa.eu/energy/nuclear/index_en.html (2005).
[6] GNEP, Global Nuclear Energy Partnership, Advanced Burner Reactors, http://www.gnep.energy.gov/gnepAdvancedBurnerReactors.html, retrieved on 26 October 2006.
[7] GROMOV, B.F., et al., The analysis of operating experience of reactor installations using lead-bismuth coolant and accidents happened, Proc. of Heavy Liquid Metal Coolants in Nuclear Technology, IPPE, Obninsk, Russia (1998).
[8] OECD/NEA, Physics and Safety of Transmutation Systems, Status Report, NEA No.6090, OECD/NEA (2006).
[9] OMOTO, A., INPRO — Progress since last Steering Committee Meeting, paper presented in 8th INPRO Steering Committee, IAEA/INPRO, Vienna, Austria (2005).
[10] SINHA, R.K., et al., Design and development of the AHWR — the Indian thorium fuelled innovative nuclear reactor, Nuclear Engineering and Design, 236, 683 (2006).
[11] WARIN, D., Status of the French research program for actinides and fission products partitioning and transmutation, Proc. of GLOBAL 2005, Tsukuba, Japan (2005).
[12] WIDER, H.U., et al., Comparative Analysis of a hypothetical Loss-of-Flow accident in an irradiated LMFBR core using different computer models for a common benchmark problem, European Commission, EUR 11925 (1989).
[13] WIDER, H.U., The European Accident Code-2 — overview and status, Proc. Intl Fast Reactor Safety Meeting, Snowbird, Utah (1990).

CHAPTER 4. DOMAIN-II: CRITICAL FAST REACTORS WITH TRANSMUTATION CAPABILITY AND WITH FERTILE-FREE FUELS

4.1. Introduction

Regarding plutonium and minor actinides (MAs) from spent LWR fuel, several fuel cycle scenarios are envisioned. The LWR plutonium can be seen as a long term asset, promoting a rapid expansion of fast (self-)breeders (CR ≥ 1) and transition to a pure fast reactor scheme. On the other hand, if plutonium and minor actinides are rather perceived as a waste and the desire is to destroy them quickly, the reactors will work in a transuranium (TRU) 'burner' mode. These systems will then operate in two-component schemes together with LWRs and/or in a concert with LWRs and sub-critical MA burners in a double-strata scenario. Since the beginning of the nuclear program, about 1 600 tonnes of transuranics have been produced by 2005. Two Generation IV reactors, the sodium-cooled and lead-cooled fast reactors (SFRs and LFRs) are interesting future options that can be used both as (self-)breeders with long burnups and TRU burners. In several countries, the latter could be fast reactors' first mission

4.2. Method

4.2.1. *Design*

This study aims at an indicative comparison of SFR and LFR cores with similar safety coefficients (Doppler, coolant temperature reactivity), which also accommodate large fractions of minor actinides and plutonium in the fuel. The latter then facilitates high MA and Pu consumption rates. Based on the proposal of European Lead-Cooled Fast Reactor (ELSY) project [1], the 600 MW(e) power level was chosen as a basis. However, an up-rated version of an LFR burner (900 MW(e)) was also investigated. For LFRs, the use of the improved supercritical steam cycle was considered, providing a thermal efficiency of 42%. Similarly high thermal efficiency, up to 45%, could be achieved with an SFR employing a supercritical CO_2 Brayton cycle. Design parameters concerning pin and pellet are based on established LFR and SFR core designs and summarized in Table 1.

TABLE 1. DESIGN PARAMETERS OF SFR AND LFR-BURNER CORE-CONCEPTS CONSIDERED IN THIS STUDY

Parameter	LFR	SFR
Power (MW_e)	600 / 900	600
Pellet outer radius (mm)	3.3	3.0
Clad inner radius (mm)	3.4	3.1
Clad outer radius (mm)	4.55	3.45
Pellet hole radius (mm)	--	--
Pitch-to-diameter ratio (P/D)	1.5	1.2
S/A outer flat-to-flat (cm)	20.10	14.66
Pins per S/A	217	271
Length of upper plenum (cm)	100	100
Length of lower plenum (cm)	10	10
Active pin length (cm)	100	100
Number of S/A	625	217
Averaged linear power (kW/m)	11.5 / 17.3	24.3
Peak linear power (assumed) (kW/m)	18.4 / 28.7	40.4

The different core parameters were chosen to comply with restrictions imposed by the thermo-mechanical characteristics of the coolant, cladding, and fuel.

Our SFR core is based on a modified model core for the WAC benchmark reactor [2], where the axial and radial reflectors were removed. As sodium allows for significantly higher coolant velocities (8-10 m/s) than lead (2-3 m/s), SFR pin lattices can be much tighter than those for LFRs. This leads to more compact SFR cores in comparison to LFR cores. The original WAC benchmark reactor had a power of 800 MW(e), whereas the one used here has a reduced power of only 600 MW(e) lowering the linear power by 25%. This is a safety relevant change and facilitates the comparison with the LFR. Averaged inlet and outlet sodium temperatures are 653 and 823 K, respectively.

In order to improve the coolant temperature reactivity coefficient, the concept of a high-leakage, pancake-like core was chosen for the LFR core. Active pin length is 100 cm and the core has the same pin and pellet design as the BREST reactor [3]. An 80 K axial coolant temperature increase in the core is based on the ELSY design. Average coolant outlet temperature is 753 K, which is comfortably below the limit of 870 K, guaranteeing the stability of protective oxide layers under nominal operation. Seismic stability requirements constrain the height of the reactor vessel to 11 m.

The burners operate in concert with LWRs in two-component scheme recycling both Pu and MAs, which are homogeneously admixed to the core fuel. To give an indicative inter-comparison of both systems with (U,TRU)O_2-^{92}Mo fuel, a fuel cycle length of 330 days with 35 days refuelling period was tentatively chosen.

Consideration has been given to the option of including uniformly distributed moderating pins (or thermalizing zones) in fast reactors. The reason is the significant deterioration of the coolant temperature and Doppler reactivity coefficients due to the presence of a sizeable amount of minor actinides. By tailoring of the neutron spectra by moderators, the spectral gradient during coolant heat-up/voiding is diminished. Additionally, more neutrons are scattered down to the resonance region, which profoundly improves the Doppler feedback.

For this purpose, hydrides were considered as moderators, but they have the disadvantage of having relatively low decomposition temperature (e.g. ~1100 K under a H_2 atmosphere for CaH_2), which excludes their incorporation in the fuel directly. In this paper, we investigated introduction of BeO moderators located in dedicated pins within a sub-assembly. It should be noted that, however, that the use of BeO could be problematic due to its high chemical toxicity. Another option would be to use metallic beryllium or $^{11}B_4C$, which was also considered for the CAPRA reactor.

4.3. Computational model

The Monte Carlo code MCB [4] was used in our neutronic and burnup analyses. Doppler reactivity feedback was estimated by evaluating a reactivity change upon the increase of fuel temperature from 300 to 1500 K. Coolant temperature reactivity coefficients correspond to a change in k_{eff} due to a heat-up of coolant in the active core only. The 1-σ statistical deviations in k_{eff} were under 10 pcm. Nuclear data libraries were adjusted for the temperature dependence by the NJOY code. The averaged temperatures of the core components were assumed as follows: 1500 K for fuel, 900 K for cladding, and 600 K for coolant.

The fuel has a burnup of 41 GW•d/tHM and it is assumed to have undergone 30 years of cooling. Correspondingly, Pu/Np/Am fraction is then equal to 83/5/12. Depleted uranium (0.3% ^{235}U) is used in the analyses.

In order to reach reasonable calculation times in MCB, we have chosen to adjust the system parameters (fissile enrichment) such that k_{eff} is one at BOC rather than at EOC. Our calculations thus somewhat underestimate the reactivity burnup swing since the U/TRU fraction would have to be decreased in the latter case. The composition of the actinide vector is that of spent LWR UOX fuel (see Table 2).

TABLE 2. PLUTONIUM AND MINOR ACTINIDE VECTOR CORRESPONDING TO THE LWR UOX SPENT NUCLEAR FUEL WITH BURNUP 41 GW•d/tHM AFTER 30 YEARS OF COOLING

Isotope	Fraction
^{235}U	0.003
^{238}U	0.997
^{237}Np	1.000
^{238}Pu	0.023
^{239}Pu	0.599
^{240}Pu	0.264
^{241}Pu	0.040
^{242}Pu	0.074
^{241}Am	0.871
^{243}Am	0.129

4.4. Neutronic and burnup performance

As already mentioned, CERMET AnO_2-^{92}Mo was chosen as fuel for SFR and LFR burner cores. Volume fraction of ^{92}Mo is kept at 50% due to the reason of fuel fabricability and thermal stability during irradiation. In order to reach considerable TRU consumption rates, TRU fraction should be at least 40-50% (owing to favourable neutronic characteristics). A comparison of neutronic and burnup characteristics of LFR and SFR burners is given in Table 3.

TABLE 3. NEUTRONIC AND BURNUP PERFORMANCE OF SFR AND LFR BURNERS: DOPPLER AND COOLANT TEMPERATURE REACTIVITY FEEDBACK FOR LFR AND SFR BURNER CORES CORRESPOND TO THE INCREASE OF FUEL AND COOLANT TEMPERATURES BY 100 K. BeO MODERATOR PINS WERE USED. THE TWO LFR DESIGNS DIFFER ONLY REGARDING THE POWER LEVEL. THE FUEL CYCLE PERFORMANCE VALUES CORRESPOND TO THE 1st YEAR OF THE START-UP MODE.

Parameter	LFR		SFR
Power (MW_e)	600	900	600
Average TRU fraction in the fuel (%)	50		43
Number of moderator pins per S/A	19		19
Number of core radial channels	14		9
m_{act} at BOL (t_{HM})	17.07		7.56
Doppler Δk (pcm)	−50		−54
Coolant Δk (pcm)	38		36
Burn-up swing ($/y)	−11.7	−16.9	−23.2
Actinide burn-up (% FIMA/y)	−2.7	−4.0	−5.9
TRU burn-up (% FIMA/y)	−3.5	−5.2	−8.1

First, we note that the TRU fraction in the fuel had to be higher for an LFR than SFR in order to attain criticality at BOL despite more than twice the actinide inventory in the LFR. This is due to the better neutron economy of the SFR tight lattice.

Burnup reactivity swing and fuel burnup are approximately inversely proportional to initial actinide inventories. A slight departure from the proportionality can be ascribed to different breeding characteristic of SFR and LFR due to different TRU fractions. The SFR is loosing reactivity twice as fast as the LFR, so its fuel has to be reprocessed more often. However, this also means that the SFR has a larger actinide burnup rate than the LFR. Reactivity coefficients are somewhat better for the SFR, where Doppler is about 50% stronger than the coolant temperature reactivity coefficient.

Due to the large neutron mean free paths (4.2 cm in Pb, 12 cm in Na), the impact of moderator pins on the local power peaking is limited and pin-to-pin local power peaking factor remains below 1.1 at BOL.

Concerning TRU consumption, both 600 MW(e) and 900 MW(e) LFRs perform better than 600 MW(e) SFR (Table 4). While a 600 MW(e) SFR can annually transmute only about 260 kg of TRUs, an LFR of the same power level incinerates over 300 kg/a. Understandably, TRU consumption is higher in an up-rated LFR (900 MW(e)) and equals to about 450 kg, of which 315 kg is plutonium and 134 kg MAs. Observe that due to the self-production of plutonium the destruction rate of MAs in the fuel is in fact higher than what would correspond to their share in the initial load.

TABLE 4. TRANSMUTATION PERFORMANCE OF SFR AND LFR BURNERS EMPLOYING URANIUM-BASED AnO_2-^{92}Mo CERMETs. AN LFR ANNUALLY CONSUMES ABOUT 300 kg OF TRUs THAT IS ROUGHLY THE ANNUAL PRODUCTION OF A 1.1 GW(e) LWR WITH A FUEL BURNUP OF 41 GW•d/tHM. ALL ^{242}Cm WAS ASSUMED TO DECAY TO ^{238}Pu IN THE SPENT FUEL. THE FUEL CYCLE PERFORMANCE VALUES CORRESPOND TO THE 1st YEAR OF THE START-UP MODE.

System	Power (MW_e)	Pu transmuted (kg/y)	Pu transmuted (kg/TWh_e)	MA transmuted (kg/y)	MA transmuted (kg/TWh_e)
LFR	600	−215	−45.2	−88	−18.5
	900	−315	−44.2	−134	−18.8
SFR	600	−178	−37.5	−85	−17.9

In Fig. 1, we compare the transmutation performance of a 600 MW(e) LFR burner with a 600 MW(e) LFR self-breeder (without blankets). The LFR self-breeder employed $(U,TRU)O_2$ mixed oxide fuel (without an inert matrix), average TRU fraction in fuel was 22.6%. We note that in the start-up mode, self-breeder and burner perform similarly concerning the consumption of minor actinides (67 kg/a vs. 88 kg/a for the burner), but while the self-breeder still generates some Pu (14 kg/a), Pu is consumed in the burner (215 kg/a).

It is to be noted that neither of these designs used in the present study were optimized with respect to the burnup reactivity swing performance and fuel management scheme. Particularly, burnup reactivity swing could be reduced for an SFR by increasing fissile inventory through enlarging pin diameter and/or number of core channels. Note, however, that these changes enhance coolant temperature coefficient and void worth and has to be accompanied by a reduction of the MA fraction in the fuel. This would lead to a lower MA consumption rate.

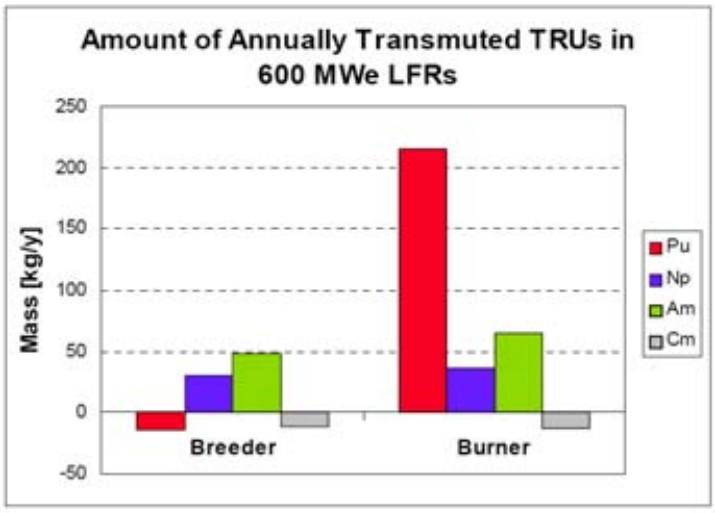

FIG. 1. Amount of annually consumed transuranics in a 600 MW(e) (U,TRU)O_2–^{92}Mo fuelled LFR burner compared to a 600 MW(e) self-breeder employing (U,TRU)O_2 fuel (see Domain-I, JRC/IE contribution). All ^{242}Cm was assumed to decay to ^{238}Pu in the spent fuel.

4.5. Safety aspects of waste burners

With regard to safety aspects of TRU waste burners, most of the aspects presented in Domain-I by JRC/IE also hold here. The only important difference is the lower core height for the LFR TRU waste burner (1 m vs. 2 m for Th-fuelled burners/breeders and U-fuelled self-breeders), which leads to better natural circulation in the ULOF case (Fig. 2).

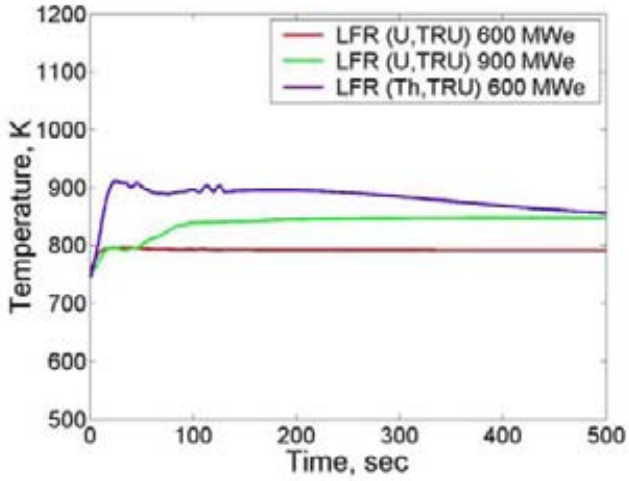

FIG. 2. Temperature evolution during a ULOF accident for three LFR cores: (Th,TRU)O_2– fuelled 600 MW(e) burner/breeder, (U, TRU)O_2–^{92}Mo fuelled 600 MW(e) TRU waste burner, and (U, TRU) O_2–^{92}Mo fuelled 900 MW(e) TRU waste burner. No feedbacks are considered in these STAR-CD calculations.

4.6. Conclusions

In this paper, we first indicated that fuels containing minor actinides and inert matrices could be fabricated and reprocessed. Then, we compared the neutronic, TRU consumption, and safety performance of LFR and SFR burners employing uranium-based CERMET fuels with ^{92}Mo matrices. Minor actinides were homogeneously mixed into the fuel.

Comparing SFR and LFR cores, the SFR core is notably smaller than that of LFR. The reason is twofold. First, lead has lower capability to remove heat from the reactor core (mainly due to lower permissible velocities), which consequently require higher P/Ds for LFR. Second, lead is an excellent neutron reflector, which provides more freedom to the designer to choose the core geometry. For instance, flatter core geometry can be used that offers better safety performance without loosing too many neutrons. In-core moderators employed in the core sub-assemblies were used in order to improve the safety coefficients (Doppler and coolant temperature reactivity). BeO pins were considered for both SFRs and LFRs.

The main conclusion from these calculations, however, is that the large scale burnup of plutonium is counterproductive in a time when a nuclear renaissance is starting and fissile material will become more and more important.

REFERENCES TO CHAPTER 4

[1] CINOTTI, L., Del Fungo Giera Energia, http://www.delfungogieraenergia.com/, Italy, personal communication (2006).

[2] WIDER, H.U., et al., Comparative Analysis of a hypothetical Loss-of-Flow accident in an irradiated LMFBR core using different computer models for a common benchmark problem, European Commission, EUR 11925 (1989).

[3] ADAMOV, E.O., White book of nuclear power, N.A. Dollezhal Research Development Institute of Power Engineering, Moscow, Russian Federation (2001).

[4] CETNAR, J., et al., MCB — a continuous energy Monte Carlo Burnup code, Proc. Fifth International Information Exchange Meeting, OECD/NEA, Mol, Belgium (1989).

[5] LAIDLER, J.J., et al., Development of pyro-reprocessing technology, Prog. Nucl. Energy Vol. 31, 1/2 (1997) pp. 131-140.

[6] LEE, Y.E., et al., Decision-making and nuclear energy policy: application of environmental tool to nuclear fuel cycle, Energy Policy, Vol. 30, 13 (2002).

[7] PONCELET, F., Research at COGEMA: benefits and a future outlook of the nuclear fuel cycle, paper presented in Intl Conf ATALANTE 2004, Nîmes, France (2004).

[8] SERP, J., et al., Electrochemical behaviour of plutonium ion in LiCl-KCl eutectic melts, Electroanal. Chem, Vol. 561, 143 (2003).

CHAPTER 5. DOMAIN-III: HYBRID SYSTEM (ADS) WITH FERTILE FUEL (MYRRHA DESIGN CONCEPT)

5.1. Introduction

Since 1998, the Belgian nuclear research centre, SCK•CEN, in partnership with many European research laboratories, has been carrying out the design studies of MYRRHA, a multipurpose accelerator driven system (ADS), and conducting an associated R&D support programme. MYRRHA is aiming to serve as a basis for the European experimental ADS to provide protons and neutrons for various R&D applications. It consists of a high power Linac accelerator delivering a 350 MeV*5 mA proton beam into a windowless liquid Lead-Bismuth eutectic (LBE) spallation target surrounded by a LBE- cooled, sub-critical core of about 50 MW(th) [1].

Since June 2006, the pre-design studies folder of MYRRHA has been endorsed as the starting point towards the design of the e**X**perimental facility demonstrating the technical feasibility of **T**ransmutation in an **accelerator driven system** (XT-ADS), in the framework of the EC FP6-IP-EUROTRANS project [2]. The main objective of the latter project is to carry out a first advanced design of a 50 to 100 MW(th) XT-ADS and to achieve a generic conceptual design (several 100 MW(th)) of the **E**uropean **F**acility for **I**ndustrial **T**ransmutation (EFIT). The XT-ADS with initial loading of standard MOX fuel, is intended to operate as a test-bench for the main components and for the operation scheme for the EFIT.

In the framework of the present IAEA **C**oordinated **R**esearch **P**roject (CRP) on Studies of Innovative Reactor Technology Options for Effective Incineration of Radioactive Waste, MYRRHA has been taken as the prototype for the benchmark on LBE liquid-cooled sub-critical facilities loaded with solid fuel containing ^{238}U fertile isotope [3] .The CRP benchmarking exercise is focused on the analysis of the behaviour the MYRRHA conceptual design in various accidental conditions.

For the benchmark exercise a 600 MeV protons beam was adopted, as for the XT-ADS instead of 350-MeV, leaving the beam intensity as a free parameter to be adjusted in such a way as to achieve a fission power release of 50 MW(th) within the subcritical core [4]. The beam spot spatial size, as defined by its Full Width at Half Maximum (FWHM), is set to 1.5 cm and is assumed hereafter to have a Gaussian profile. Besides SCK•CEN (Belgium), NRG and JRC (The Netherlands), have been involved in the benchmark either for calculating safety-related neutronics parameters using the input file provided by SCKCEN or carrying out transient and thermal-hydraulic studies using neutronics parameters obtained.

5.2. MYRRHA description and benchmark specifications

Various details on the MYRRHA ADS can be found in the ad-hoc design status report [5]. A pool-type design has been chosen for MYRRHA, not only from a safety point of view (in acknowledgement of the inertia of many hundreds of tons of LBE), but also to provide an extremely flexible core management for the fuel sub-assemblies and the experimental irradiation devices. Also, the design has been made in such a way that all in-vessel components can be removed and replaced during the lifetime of the installation for maintenance.

Figure 1 shows an overview of the machine with its most important components. The hot primary coolant is separated from the cold one by means of the diaphragm which divides the volume of the vessel in an upper hot zone and a lower cold zone. The LBE coolant is circulated from one zone to the other by four primary pumps. It is heated in the core up to 337°C (in nominal conditions) and cooled back to 200°C by means of eight primary heat exchangers (PHX) of which the secondary side is water at 25 bars. Each primary pump delivers the LBE mass flow for two in parallel operating heat exchangers. Four pumps and eight PHXs are installed in four casings at the periphery of the vessel. The secondary cooling is provided by two loops, each one comprising four PHXs.

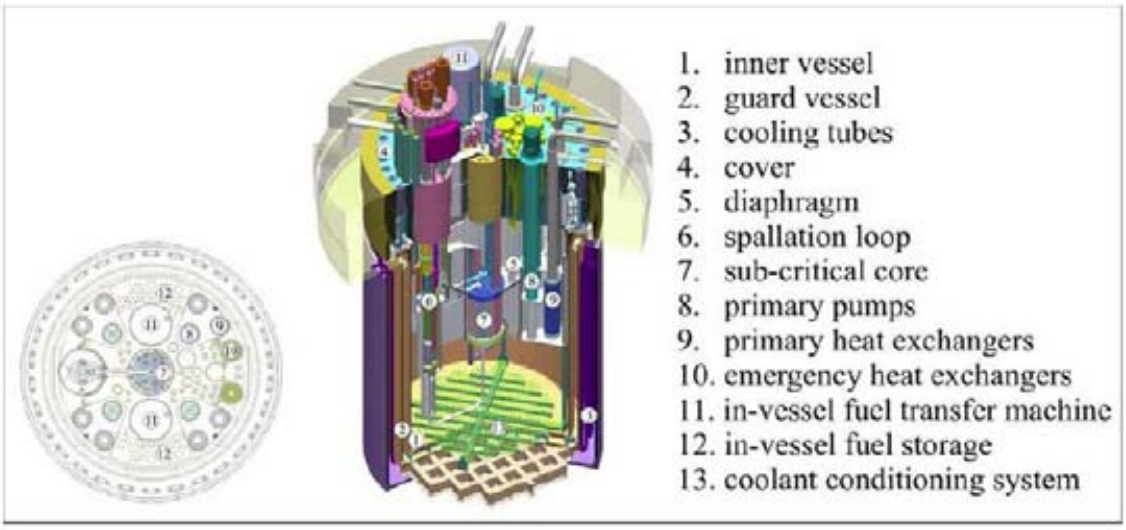

FIG. 1. Bulk cut-views of the MYRRHA ADS.

Surrounding the spallation target, the sub-critical core consists of 99 channels, enabling one to accommodate various loading configurations including fuel sub-assemblies (SA) or experimental devices. To keep the fuel SAs in place, the sub-critical core is enclosed in a core barrel.

The interference of the core with the spallation loop and proton beam line, the fact that the room situated directly above the core will be occupied by lots of instrumentation and irradiation loops penetrations, and core compactness result in insufficient space for fuel handling to (un)load the core from above. Hence, the fuel handling is performed from underneath the core. On a top of that due to the higher density of LBE, the fuel SAs are floating in the core coolant, therefore the fuel assemblies are kept by buoyancy under the core support plate. Because of the presence of the off-centre position of the spallation loop, there are two fuel handling systems that are inserted in penetrations of the reactor cover on opposite sides of the core.

Spent fuel still generates decay heat and must remain in the coolant for some time after the reactor is shut down. To avoid excessive delay between two operation cycles, it was chosen to store the spent fuel at the periphery of the reactor in two dedicated zones and let it cool there. Each of the fuel storage provides sufficient positions to store a full core loading.

The spallation loop is characterized by an off-centre layout (the confinement vessel of the spallation loop is located beside the sub-critical core). Several reasons justify such a configuration, the main one is the need of a high neutron flux in the sub-critical core. The LBE contained in the feed tank flows by gravity in an annular tube surrounding the proton beam tube. The flow rate is determined by the tube geometry and by the height difference between the LBE free surfaces in the feed tank and in the spallation target.

The LBE recirculation in the loop is insured by a mechanical pump. In addition, a magneto hydraulic pump is foreseen to provide the fine tuning of the feed flow. A LIght Detection And Ranging (LIDAR) system measures the vertical position of the target free surface and adjusts the flow of the magneto hydraulic pump in order to keep constant the position of the free surface.

For safety reasons MYRRHA, like any other reactor, is equipped with an Emergency Cooling System (ECS). This ECS is designed to meet all MYRRHA cooling needs, provided that the proton beam is shut off. The residual heat to be evacuated is then composed of the decay heat of the reactor core, the decay heat in the core storage and the heat in the LBE due to the ^{210}Po decay. The most severe situation is a total station black-out where all the normal cooling systems are unavailable. The LBE flow will only be insured by natural convection mechanisms and its cooling will only be provided by

the ECS. Since the ECS is intended to be a strong line of deference, it has the characteristics of being fully redundant and passive. This means that two independent systems are present, each capable of fulfilling the cooling needs. It also implies that the ECS is based on passive principles: no pumps or fans, no power-operated valves, no active pressurize. Each system is basically composed of an emergency heat exchanger (EHX), a check valve at the bottom of the EHX, a closed water circuit operating in natural convection mode, an air cooler and a natural draft chimney.

The core is designed to operate with standard MOX driver fuel but can manage a few minor actinide (MA) oxide fuel sub-assemblies. The reference sub-critical core of MYRRHA after the DRAFT-2 Pre-Design folder [2] is displayed in Fig. 2 (left side picture). It consists of a single-batch of 45 fuel assemblies containing 30wt% Pu-enriched (Pu/HM; HM=Heavy Metal) (U-Pu)O_2 MOX fuel pins. The MOX fuel pellets were assumed to be of 95% of theoretical density (TD) and containing 30 wt.% reactor-graded Pu in the initial heavy metal.

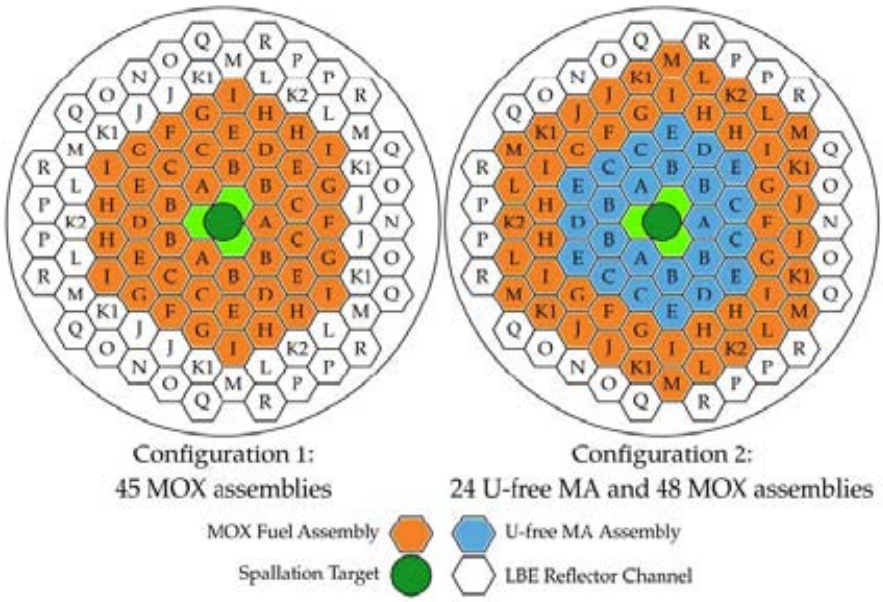

FIG. 2. Core configurations assessed.

Martensitic steel T91 was preliminary chosen as cladding material, taking into account its good mechanical parameters, low irradiation induced swelling of the martensitic 7-10% Cr steels [9] and corrosion resistance in the liquid Pb-Bi eutectic environment at temperatures lower 470°C. The needed assessments were performed to optimise all parameters of the MYRRHA driver fuel pin (fuel type, pellet density and dimensions, cladding diameter and thickness, gas plenum dimensions, etc.).

The triangular lattice of pattern of sub-channels and the closed hexagonal boxes have been adopted as to the fuel assembly design, similar to those widely used in LMFBRs. Each fuel assembly contains 91 fuel rods and the Pb-Bi coolant flow enters from below with the inlet temperature of 200°C. The Pb-Bi mass flow rate is limited by the maximum allowed local velocity that should not exceed 2.0 m/s at normal operation conditions because of possible erosion problems.

The availability of numerous spare channels grants a higher flexibility as to the facility exploitation as an irradiation experimental machine. The core may be indeed adapted to fit out various experimental rigs. Figure 2 (right side picture) shows a typical core configuration dedicated to operate MYRRHA as an experimental small-scale minor actinide (MA) 'transmuter'. It consists of a two-batch U-free MA and MOX core containing 48 previously defined MOX fuel assemblies. The minor actinide load consists of 24 assemblies similar in geometry to the driver ones, but housing the fuel rods containing inert matrix fuel pellets consisting of 45 vol.% ($Pu_{0.5}Am_{0.5}$)O1.88 fuel and 55 vol.% MgO matrix. This

core configuration is also proposed to assess the impact of a realistic load of U-free MA fuel in LBE-cooled ADS.

Two important requirements for the fuel pin design are non-melting of the fuel pellets and non-damage of the cladding by inner or outer stresses during the total fuel life. Given the maximum desired power density in the core, the first criterion will determine the pellet radial dimensions. The second criterion will determine the clad diameter and thickness and the gas plenum volume. A schematic view of the fuel rod and sub-assembly is shown in Fig. 3 wherein the geometry of each of its elements is presented in a simplified way. A fuel pellet design without a central hole has been adopted in order to simplify the fuel production. The leading design parameters of the MYRRHA facility are listed in Table 1.

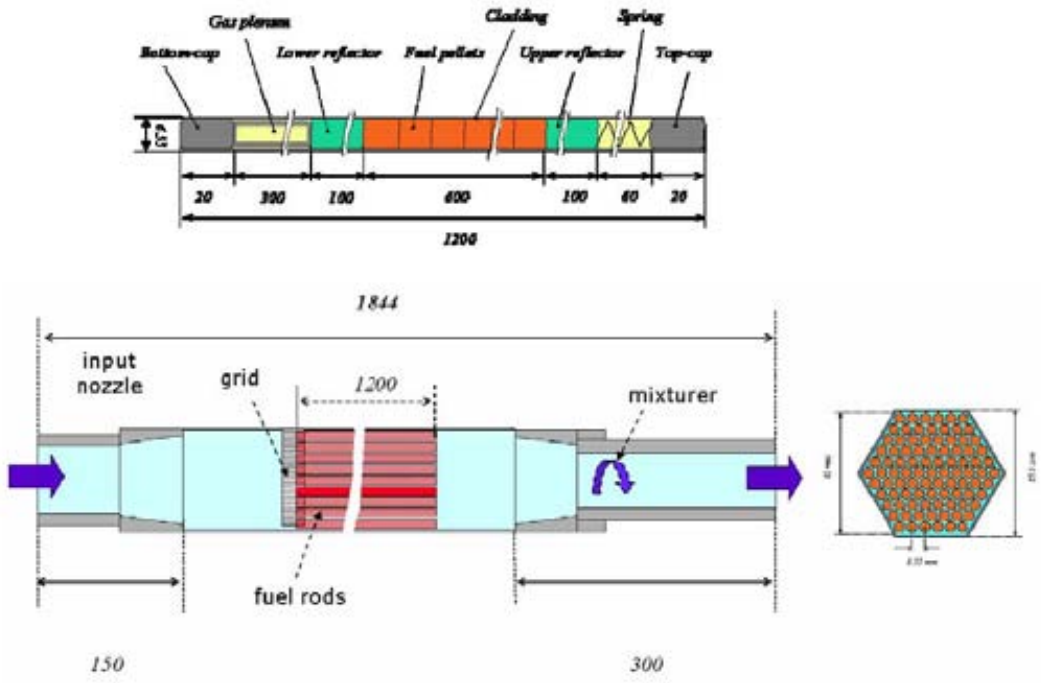

FIG. 3. Schematic view of fuel rod and sub-assembly.

TABLE 1. MYRRHA MAIN CHARACTERISTICS

Proton beam energy	MeV	600
Nominal power	MWth	50
Fuel active length	mm	600
Initial Sub-criticality level	pcm	near -5000
Core diameter	mm	1000
Core height	mm	1800
Vessel inner diameter	mm	4400
Vessel total height (lid not included)	mm	7000
Vessel internal volume	m^3	~100
LBE volume	m^3	~65
Vessel cover thickness	m	~2
Gas plenum height above the coolant	mm	< 500
Primary coolant	LBE	
Coolant pressure	atmospheric + hydrostatic	
Core inlet temperature	°C	200
Core average outlet temperature	°C	337
Coolant average velocity in the core	m/s	2
Primary coolant flow rate (nominal)	kg/s	2500
Secondary coolant	Water or Steam	

5.3. Neutronics analysis

This section presents the results of the reactor physics analysis with a primary focus on the safety-related neutronics parameters namely the power peaking factors, the reactivity coefficients and the kinetics parameters.

5.3.1. *Computer codes and nuclear data*

Within the study of accelerator driven system for transmutation appear aspects that are new for nuclear systems. These include the use of new fuels with much higher content of minor actinides and high mass of plutonium isotopes and the very important role played by unusual isotopes, particularly Pb, Bi and some transuranics (^{241}Pu, ^{242}Pu, Am, Cm, Np).

The computer simulation of the neutronics behaviour of such systems may be affected by many sources of systematic uncertainties, both from the nuclear data and by the methodology selected when applying the codes.

The design of accelerator-driven sub-critical fission machines such as MYRRHA requires powerful simulation tools for the modelling of the high-energy particle cascade, for the neutron source production through various processes and for the transport of the produced neutrons and other particles. The challenge of performing reliable calculations lies in coupling tools designed for the transport of high-energy particles and relying on physical models with tools based upon evaluated data tables and designed for the transport of low-energy (E < 20 MeV) neutral particles.

Since 1999 more and more enhanced and improved versions of the Monte Carlo multi-particle transport code, MCNPX [6-8] have been released by the LANL developer team to address these challenging issues, thanks to the feedback of beta-tester users throughout the world. SCK•CEN, as member of the beta-tester group, has used the various MCNPX code versions to update the MYRRHA design calculations, thereby building a sound expertise in both the use of MCNPX and ADS design studies [9].

The basic feature of MCNPX, from the ADS perspective, is the continuous tracking of neutrons appearing in proton-induced spallation interactions, with kinetic energies up to several MeV, from their birth until their removal from the system by absorption in fuel and structural materials or by leakage. To fill the gap in the energy region between 20 and 150 MeV, where it is known that the physical models are less accurate, the LA150 library was developed at LANL containing tabulated neutron, proton and photonuclear cross-sections up to 150 MeV for a selected set of isotopes.

The use of these higher energy libraries was rather limited until the release of enhanced MCNPX code versions (starting with MCNPX 2.5.c) having the so-called mix-and-match capability. This capability enables one to use, for every nuclide, available nuclear data tables throughout the full energy range along with physics models above the data table upper energy or for missing tabulated data.

To carry out the neutronics analysis, SCK•CEN has used the MCNPX 2.5.0 stable version, as stand-alone or as a part of in-house linkage codes, running in a parallel computer environment with MPI-multiprocessing.

At NRG, the same code version has been used for criticality calculations. NRG has also used an in-house extended MCNP(X) code version to calculate βeff values and to improve the treatment of temperature effects [10].

The core evolution and transmutation calculations have been performed using the ALEPH code, a MC burnup linkage code developed at SCK•CEN [11]. The code uses any version of MCNP or MCNPX for neutron spectra calculations, a slightly modified version of ORIGEN 2.2 [12] for evolution calculations along with nuclear data processed using NJOY 99.112 [13]. Some modifications were made to ORIGEN 2.2 to improve the output accuracy (viz. the number of significant digits was increased from 3 to 5) and to increase memory allocation.

A thorough study on nuclear data for use with MCNP(X) has been launched as well. This ultimately lead to the development of the spin-off code ALEPH-DLG [14] to automate the entire NJOY processing for MCNP(X) and ALEPH libraries. ALEPH-DLG also performs QA tests to insure that the data has been processed correctly (extraction of NJOY warning messages, tests of the unresolved resonance probability tables, …). A new standard library, containing data from JEF 2.2, JEFF 3.0, JEFF 3.1, JENDL 3.3 and ENDF/B-VI.8 at six different temperatures (300, 600, 900, 1200, 1500 and 1800 K, respectively), has now been produced with the aid of ALEPH-DLG.

These libraries have undergone a severe validation program to ensure their quality [15, 16]. After being endorsed by the JEFF group, our processed JEFF 3.1 pointwise library has become one of the official MCNP(X) libraries available at NEA/OECD [17]. The thorough benchmarking studies carried out show large discrepancies for some isotopes (^{209}Bi, Fe) between the various evaluations, in particular between JEF 2.2 and ENDF/B-VI. This benchmarking effort has also shown that the recently released JEFF 3.1 evaluation appears to be the best one (see Fig. 4).

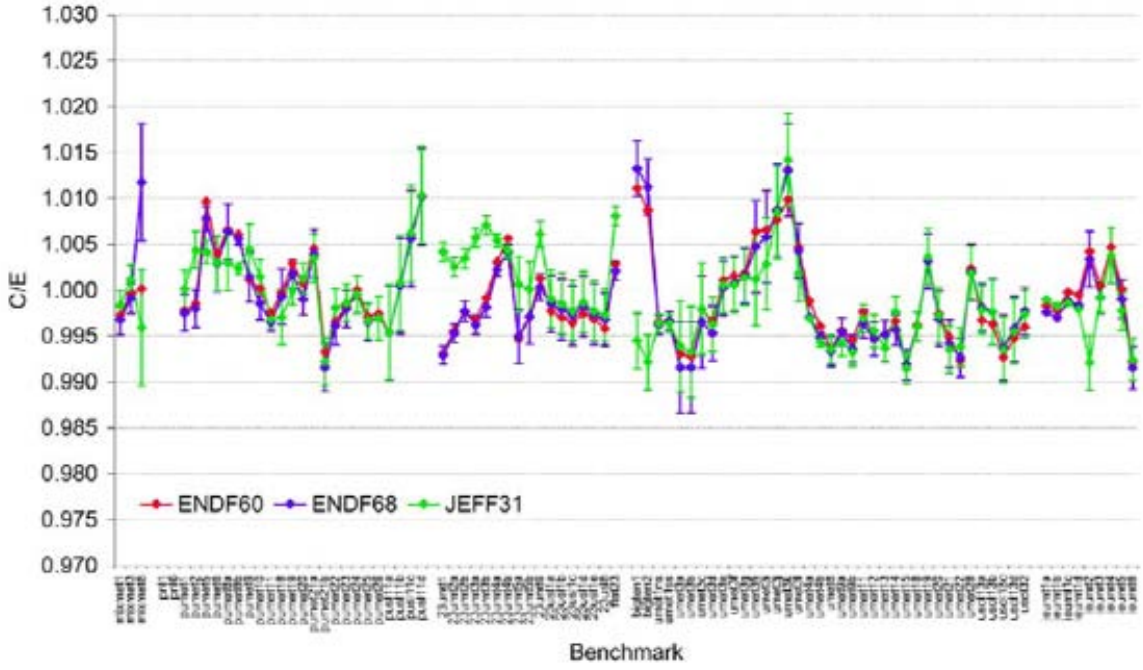

FIG. 4. JEFF 3.1 validation versus criticality benchmarks.

As a matter of fact, SCK•CEN has used the continuous energy libraries JEFF-3.1 for the on-going calculations. The JEFF-3.1 evaluation includes nuclear data up to 200 MeV for Pb, Bi, Fe, O and up to 30 MeV for ^{238}U and ^{239}Pu. For proton transport, the LA150 h library was used in tabular range (1 to 150 MeV) for 41 available isotopes. Beyond this range and for unavailable isotopes, physics models were used. The pions, the muons and other light particles (D, T, He3 and α) were treated only by physics models whereas photons from 1 keV-100 MeV were treated using the standard MCNP libraries.

5.3.2. *Geometrical models for the neutronics calculations*

Figure 5 shows a (r,z) cut-view of the MYRRHA full core geometrical model built for MCNPX calculations along with a close-view onto the fast-core (right side picture). The picture shows among others the fast core and its suspension tube, the spallation loop, the inner and outer vessel as well as the top cover.

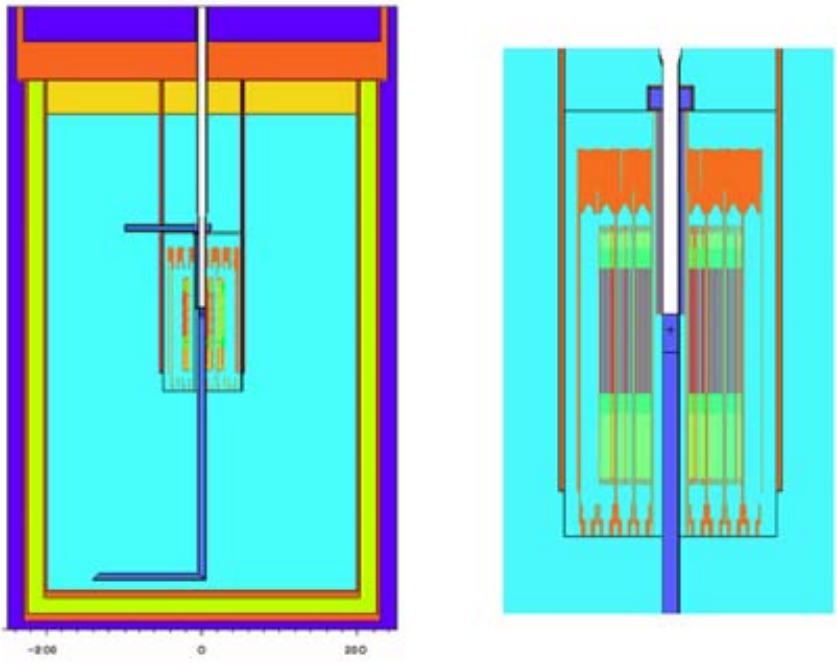

FIG. 5. Cut-view of the full core model (left) with zoom onto the fast core (right).

The tank gas plenum is also shown. The space between the two vessels is filled with air. Beyond the outer vessel, a 22-cm-thickness layer of heavy concrete is assumed. As to the top lid, it is assumed to consist of a 51-cm-thickness steel plate topped by a 45-cm-thickness layer of heavy concrete. The overall size of the model is 800 cm in height and 250 cm in radius. The radial cut of the fast core (Fig. 6) reveals details of the fuel pins within the fuel assemblies (left side picture) and of fuel pin lattice (right side picture). The view of the flow path of LBE from the feed tank down to the spallation free surface as well as the support structure of the spallation target tube are shown in the right hand picture.

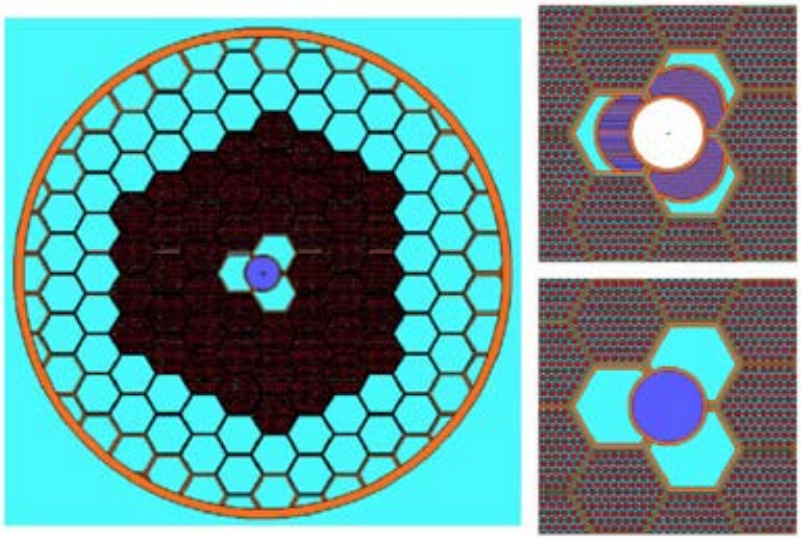

FIG. 6. Radial cut-view of core with close-views at mid-plane (right bottom) and at plane z=100 mm (right top).

5.4. Neutronics parameters and reactivity coefficients

Safety-relevant neutronics parameters include the power coefficients and peaking factors, the inherent reactivity feedbacks as well as kinetics parameters. The main static and steady-state neutronics parameters yielded for both two MYRRHA cores are shown in Table 2.

TABLE 2. OVERVIEW OF NEUTRONICS PARAMETERS

Neutronics parameter		Unit	MYRRHAE core	
			MOX	MOX-MA
Proton beam energy		MeV	600	600
Accellerator current		mA	1.91	2
Proton beam energy		MW	1.20	1.20
Proton beam heating			0.74	0.74
Source neutron yeald per incident proton		np	15.6	15.6
k_{eff}			0.95522	0.95476
Source importance φ*/			1.08	1.09
Thermal power		MW	50	50
Peak linear power (hottest pin)		Wcm	324	182
Axial forum factor			1.21	1.15
Hottest pin-to-core mean pin			1.254	1.242
Hottest pin-to-hotest SA mean pin			1.048	1.080
Hottest SA-to-core meant pin			1.225	1.150
k_{eff} swing with core burnup		Pcm EFPD	-18.12	-11.85
Doppler constant (BOL)		10^3 Tdk/dT	-3.74	-2.72
Coolant temperature reactivity coefficinet		10^5 Tdk/dT	-2.11	-1.48
Effective delay neutrin fraction (β_{eff})		Pcm	349	312
Prompt neutron generation time (Λ		μs	1.49	1.68
Initial fuel mixture		MOX	$(U\text{-}Pu)O_2$	$(U\text{-}Pu)O_2^+$ $(Pu\text{-}Am)O_2$
Initial (HM) fuel mass (m_{fuel})		kg	506.5	660.1
Initial Pu-enrichment	(Pu HM)	at%	30	30
	(Am HM)			60
Avg. core burnup after two 90-EFPDS Sub-cycles + 30 days shutdown in between		MW•d/kgHM	13.6	12.5
Actinide mass balance	U	kg/TW•h/th	-19.3	-13.8
	Pu		-26.1	-26.7
	Am		0.4	-11.9
	Np		2.7	2.5
	Cm		0.0	7.6
	Owerall		-42.3	-42.4

Reactivity effects of importance in ADS design and safety include the reactivity swing from fuel burnup, the Doppler Effect and the effect of the LBE coolant density change.

5.4.1. *Power coefficients and peak factors*

For the sake of steady-state and transients thermal-hydraulics calculations, a power density distribution analysis has been carried out both within the hottest fuel assembly and over the entire core. The distributions are expressed in terms of power coefficients (radial and axial) and in terms of a set of peak-to-average power density ratios called ‘power-peaking factors’.

In Tables 3 and 4, these power coefficients and peak factors are displayed for each one of the core configuration considered at the beginning of the irradiation cycle.

TABLE 3. POWER COEFFICIENTS AND PEAKING FACTORS FOR THE SINGLE MOX BATCH CORE

Channel ID	A	B	C	D	E	F	G	H	I	All core	HOTTEST PIN
	MOX-fuel sub-assemblies										
#S/A per channel	3	6	6	3	6	3	6	6	6	45	
S/A segments											
1	0.170	0.171	0.173	0.174	0.175	0.178	0.179	0.179	0.181	0.175	0.168
2	0.214	0.213	0.211	0.211	0.211	0.209	0.208	0.208	0.207	0.210	0.217
3	0.234	0.231	0.229	0.228	0.227	0.223	0.222	0.222	0.219	0.226	0.238
4	0.212	0.212	0.212	0.212	0.212	0.210	0.210	0.210	0.208	0.211	0.209
5	0.171	0.172	0.175	0.175	0.176	0.180	0.181	0.181	0.184	0.177	0.168
	0.082	0.157	0.145	0.070	0.134	0.062	0.121	0.118	0.111	1.0000	3.135E-04
SA powers (MWth)	1.361	1.308	1.207	1.166	1.119	1.041	1.008	0.981	0.927	50	1.568E-02

Hottest_pin-to-core_mean_pin	1.284
Hottest_pin-to-hottest S/A_mean_pin	1.048
Hottest_S/A-to-core_mean_S/A	1.225

TABLE 4. POWER COEFFICIENTS AND PEAKING FACTORS FOR THE TWO-BATCH (MA+MOX) CORE

Channel ID	A	B	C	D	E	F	G	H	I	J	K1	K2	L	M	All core	HOTTEST PINS MA	HOTTEST PINS MOX
	(MA+Np)-fuel sub-assemblies					MOX fuel sub-assemblies											
#S/A per channel	3	6	6	3	6	3	6	6	6	6	6	3	6	6	72		
S/A segments																	
1	0.165	0.168	0.170	0.171	0.172	0.176	0.176	0.176	0.177	0.180	0.181	0.181	0.181	0.184	0.176	0.161	0.174
2	0.217	0.215	0.214	0.213	0.213	0.210	0.210	0.210	0.209	0.208	0.207	0.207	0.207	0.206	0.210	0.222	0.212
3	0.240	0.236	0.232	0.231	0.230	0.226	0.226	0.226	0.224	0.221	0.220	0.220	0.220	0.217	0.226	0.248	0.228
4	0.212	0.213	0.213	0.213	0.213	0.211	0.211	0.211	0.210	0.209	0.208	0.209	0.208	0.207	0.210	0.210	0.212
5	0.165	0.168	0.171	0.172	0.173	0.177	0.177	0.178	0.179	0.182	0.183	0.183	0.184	0.187	0.178	0.160	0.175
	0.0408	0.0785	0.0749	0.0365	0.0716	0.0491	0.0961	0.0941	0.0898	0.0863	0.0827	0.0412	0.0813	0.0771	1.0000	1.595E-04	1.894E-04
SA powers (MWth)	0.650	0.654	0.624	0.609	0.597	0.819	0.801	0.784	0.748	0.719	0.689	0.686	0.678	0.642	50	7.974E-03	9.472E-03

Hottest_pin-to-core_mean_pin	1.241
Hottest_pin-to-hottest S/A_mean_pin	1.053
Hottest_S/A-to-core_mean_S/A	1.179

5.4.2. *Reactivity and power swings with burnup*

To carry out the core burnup calculations, the 90-day range operational cycle was subdivided into steps of 5 or 10 days over which a constant flux irradiation was assumed. The neutron spectra and total flux for the various fuel assembly positions is updated at each step selecting the isotopes of actinides, of fission products and of activation products such as to account for 99.99%-fractional absorption. The active length of each fuel assembly was divided into three 20 cm length axial segments:

Figure 7 depicts the time-evolution of the reactivity during one operational cycle. Applying linear regression one gets a reactivity loss rate 18.12±0.02 pcm/day) for the compact single batch MOX core,

meaning a loss of 1631 pcm over one full cycle. For the larger two-batch core configuration, one has a smaller reactivity loss rate, viz. 11.85±0.01 pcm yielding a loss of 1 067 pcm.

The corresponding power curves, obtained during the various core burnup steps calculations, are shown in Fig. 8. One observes a power drop of about 25% over one cycle for the full MOX core versus a drop of 18% or the mixed MA-MOX larger core.

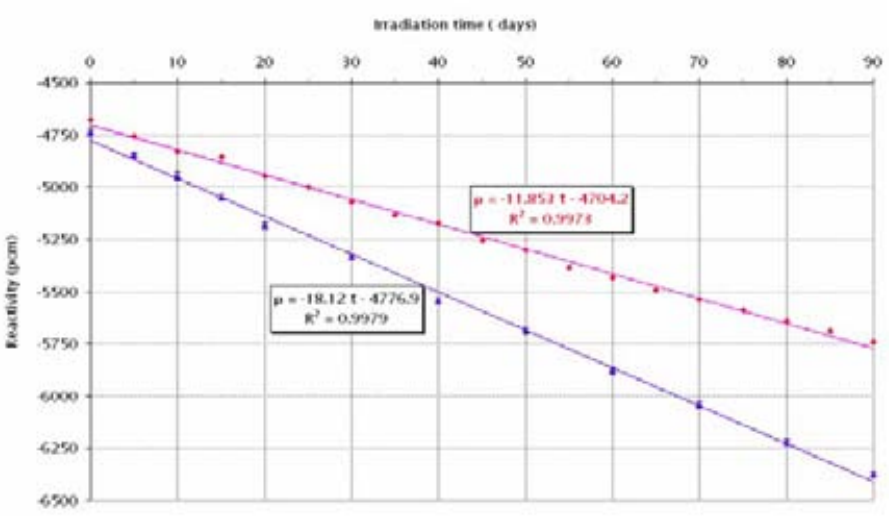

FIG. 7. Reactivity evolution over one operation cycle.

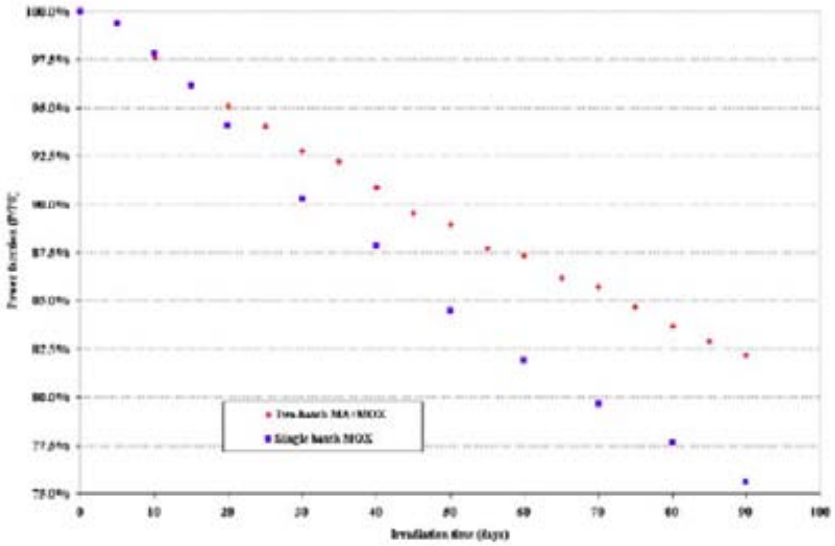

FIG. 8. Power evolution over one operation cycle.

5.4.3. *Doppler reactivity coefficient*

For oxide-fuelled fast reactor, the temperature dependence of the Doppler coefficient, dk/dT, is known to vary with the average fuel temperature [18].

To derive the Doppler constant, CD, we have applied the least-squares regression method to fit a logarithm function through a (T, k_{eff}) set of points obtained carrying out a series of criticality calculations using JEFF3.1 at various temperatures viz. 600, 900, 1200, 1500 and 1800 K, respectively. The quality of such a fit is given by the R2 statistical number. An R2=1.0 would mean

that the model fit the data perfectly, with the line going right through every data point. Figure 9 shows the fitted set of points along with fitting curves for both core configurations. From the equations of the fitting curve one gets for the single-batch MOX core and for the two-batch MA-MOX configuration. For the single-batch MOX core, both SCK•CEN and NRG performed the calculations. All but the 1200 K k_{eff}-values are within the 1-σ standard deviation and yield the same value for the Doppler constant. For the plots in Figs 9 and 10, the point set obtained by SCK•CEN have been used for the full MOX core and those from NRG for the mixed MA-MOX core.

The slope of the k_{eff}-curve at a given temperature gives the corresponding Doppler feedback coefficients. The latter are given in Fig. 10. They are negative and become less and less negative with increasing temperature. For the compact full MOX core, such a small value compared to is expected due harder neutron spectrum and lower for the configuration with U-free MA loading.

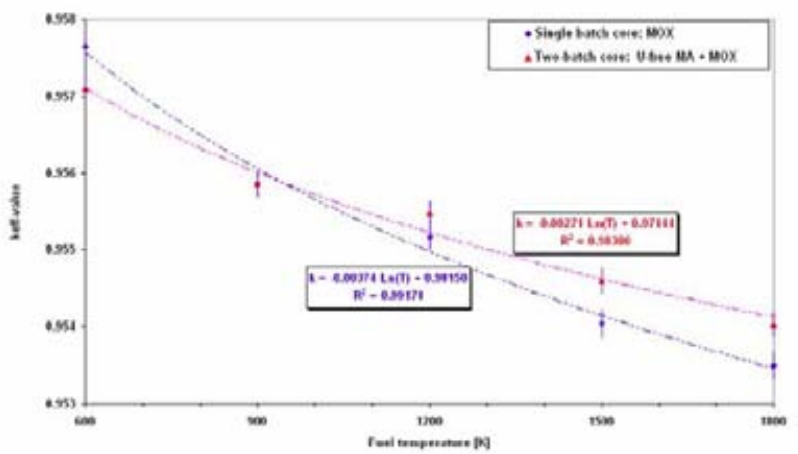

FIG. 9. Variation of k_{eff} as function of average fuel temperature.

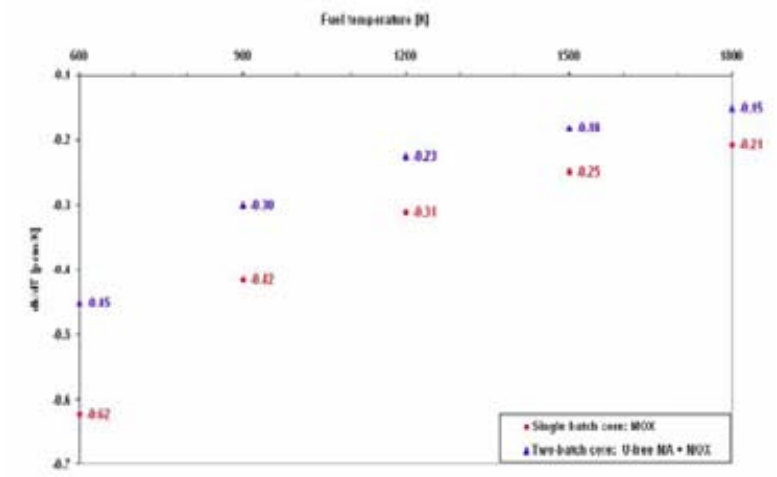

FIG. 10. Doppler coefficient as function of average fuel temperature.

5.4.4. *LBE coolant temperature coefficient*

The reactivity response to the temperature-induced LBE-coolant density changes has been evaluated at the beginning of cycle for temperature ranging from about 130°C (cold core conditions) to about 700°C by performing a series of k_{eff} calculations. The coolant density as a function of the coolant temperature was taken from the RELAP5 database.

A linear regression fit of the set of (T, k_{eff}) points (see Fig. 11) yields a negative coolant temperature coefficient equal to for the full MOX core and of for the MA/MOX core.

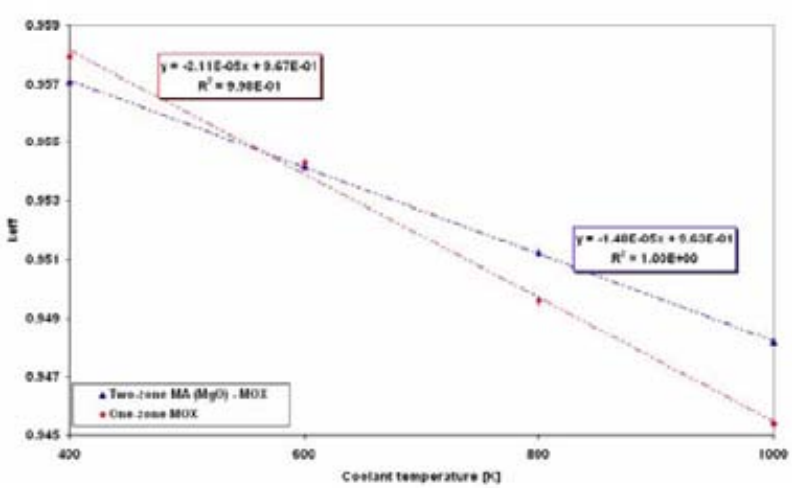

FIG. 11. Variation of k_{eff} as function of LBE-coolant temperature.

5.4.5. *Local coolant void worth*

Voiding of the assembly coolant can generally be expected in case of large temperature increase, higher than the boiling point of the coolant, when vapour bubbles may appear. In a LBE-cooled system such an accidental situation can hardly occur due to the high boiling point of LBE. Moreover LBE is known to have a high specific heat of vaporization. Yet some people have identified a hypothetical scenario that may introduce local void into the core, in a MYRRHA-like design concept, considering a multiple failure of cladding in the core mid-plane and depressurization of the gas plena leading to local voiding in some sub-assembly. The fuel sub-assemblies voiding worth calculated by NRG are given in Table 5 for the various fuel sub-assemblies and for the two core configurations.

For the compact MOX core all voiding worth's are negative. In the large MA-MOX core, voiding of inner sub-assemblies does not yield a significant reactivity change since the calculated reactivity change, even slightly positive, is lower than the standard deviation on the k_{eff}. The voiding reactivity is negative and significantly higher for core peripheral sub-assembly channels. This indicates a dominant void-induced leakage effect in LBE compared to sodium, for instance, where the spectrum-hardening effect and the neutron absorption would prevail. For inner sub-assembly positions, the positive effect of spectrum hardening is large compensating more or less the negative effect due to neutron leakage.

TABLE 5. CALCULATED FUEL SUB-ASSEMBLIES VOIDING WORTH

	Single (MOX) batch		Two (MA + MOX) batches	
SA Channels	Δρ (pcm)	σ	Δρ (pcm)	σ
A	-80	29	5	26
B	-37	28	16	26
C	-77	29	-11	26
D	-111	30	1	26
E	-127	30	-14	26
F	-137	29	-35	27
G	-112	29	-4	26
H	-156	29	-13	26
I	-126	29	-45	26
J			-72	26
K1			-79	27
K2			-101	26
L			-74	26
M			-61	26

5.4.6. *Effective delayed neutron fraction ($ß_{eff}$) and prompt neutron lifetime*

Calculated values of $ß_{eff}$ and of Λ are shown in Table 5. To obtain the effective delayed neutron fraction, the SCK•CEN neutronic team has used the well-known formula [19]:

$$\beta_{eff} = \frac{k}{k_p} - 1$$

In the above formula stands for the k_{eff}-value computed with the fission spectrum accounting for both prompt and delayed neutrons whereas is the k_{eff}-value (re)calculated with the prompt fission spectrum alone. Since the reactivity perturbation induced by delayed neutrons is small, the above first-order approximation formula is accurate enough.

At NRG, the β_{eff} has been calculated using an iterated fission probability method implemented within the in-house MCNP(X) extended. The β_{eff}-values computed by both methods agree to some extend even though the reported 1-σ have different meanings. The prompt neutron lifetime value reported by SCK•CEN has been calculated using the 1/v insertion method where the entire reactor (including the reflector) is perturbed by a dilute and uniform distribution of a purely 1/v neutron absorber [19, 20].

In Table 6 can be seen that the value obtained using this method is of the same order of magnitude but significantly lower than the corresponding value obtained by NRG as the neutron fission lifespan from the criticality run.

TABLE 6. KINETICS PARAMETERS

	ßeff (pcm)		Λ (µs)	
	SCK•CEN	NRG	SCK•CEN	NRG
BOC				
Full MOX	**331 ± 26**	**349 ± 3**	**1.49**	**2.43**
MA + MOX	**337 ± 26**	**312 ± 3**		**2.28**
EOC				
Full MOX	**359 ± 27**			
MA + MOX	**294 ± 27**			

5.5. Safety analysis

5.5.1. *Codes and models*

The analysis of the accidents was performed with two calculation codes: RELAP5 mod 3.2 and SITHER. The RELAP code has been adapted for the use of liquid Lead-Bismuth Eutectic by Ansaldo Nucleare [21]. It is used for transients requiring the simulation of the whole system, like loss of flow and loss of heat sink accidents.

SITHER is a code originally developed by SCK•CEN for simulating the thermal-hydraulic behaviour of core assemblies in LMFBRs, as well in steady state as in transient situations [22]. It is appropriate for the simulation of fast transients for which the core behaviour is the main concern. The inlet conditions (velocity, temperature) are assumed to remain constant during the transients. Typical examples are the overpower transients and sub-assembly blockages.

Alternative calculations have been carried out by JRC/IE (Joint Research Centre of the European Commission, Institute for Energy) for the unprotected LOF and TOP accidents using the European Accident Code 2 (EAC-2) [23]. This is a multi-channel code that includes a steady state and transient fuel pin behaviour module (TRANSURANUS), a thermal hydraulic single and 2-phase module (CFEM), and an in-pin and coolant channel fuel motion and freezing module (MDYN) as well as a point kinetics module that uses reactivity worth tables that were pre-calculated with the HEXNODYN nodal transport code [24]. The RELAP model of MYRRHA can be subdivided into 6 main parts:

1. The lower plenum corresponding to the volume of fluid located below the core level. It is modelled by a branch (volume with multiple connections) receiving the fluid released by the pumps and re-injecting it into the core and medium plenum;
2. The medium plenum containing the volume of fluid around the core barrel, above the lower plenum and below the diaphragm. It represents the leaks through the diaphragm and is modelled by an annular volume linking the lower and upper plena;
3. The upper plenum made up of the hot fluid volumes above the core and the diaphragm. It is modelled by 2 pipes connected by cross flow junctions simulating the flow through the apertures of the core barrel above the core. The top level of this plenum corresponds to the LBE free surface level and it is connected to a time dependent volume fixing the reference pressure;
4. The sub-critical core containing 99 sub-assemblies (SA): 45 MOX SAs + 54 dummy SAs for configuration n°1, 48 MOX SAs + 24 MA SAs + 27 dummy SAs for configuration n°2. The fuel SAs (MOX and/or MA) are subdivided into 9 hydraulic 'group' channels, each one representing a group of SAs, and one single channel corresponding to the hottest fuel pin channel (in order to determine the maximum fuel, clad and coolant temperatures in the core);
5. The main cooling loop including the 4 groups of pump-HX (each group has one pump and 2 PHXs). In order to simulate partial loss of flow and loss of heat sink accidents, one group is modelled separately and the 3 other groups are merged in an equivalent one. The flow is distributed between the groups by means of a fictitious annular volume. The loop includes also the 2 secondary lines, each line being connected to one of the 2 PHXs that each pump-HX group contains;
6. The 2 emergency cooling loops, each one containing the EHX, a secondary water circuit and a tertiary air circuit. The heat is released to the environment via air-coolers. The loops are designed to work fully in natural circulation mode in any circuit (LBE, water, air);
7. In the present version of the model the spallation loop is only modelled as a constant heat source inside the core, when the accelerator is in operation. A schematic representation of this model is provided in Fig. 12.

The SITHER code is based on the single fuel rod channel approximation, i.e. a fuel sub-assembly is represented by only one fuel rod with its associated coolant. For the transients simulated by SITHER the calculations were performed with the hottest fuel pin in the core.

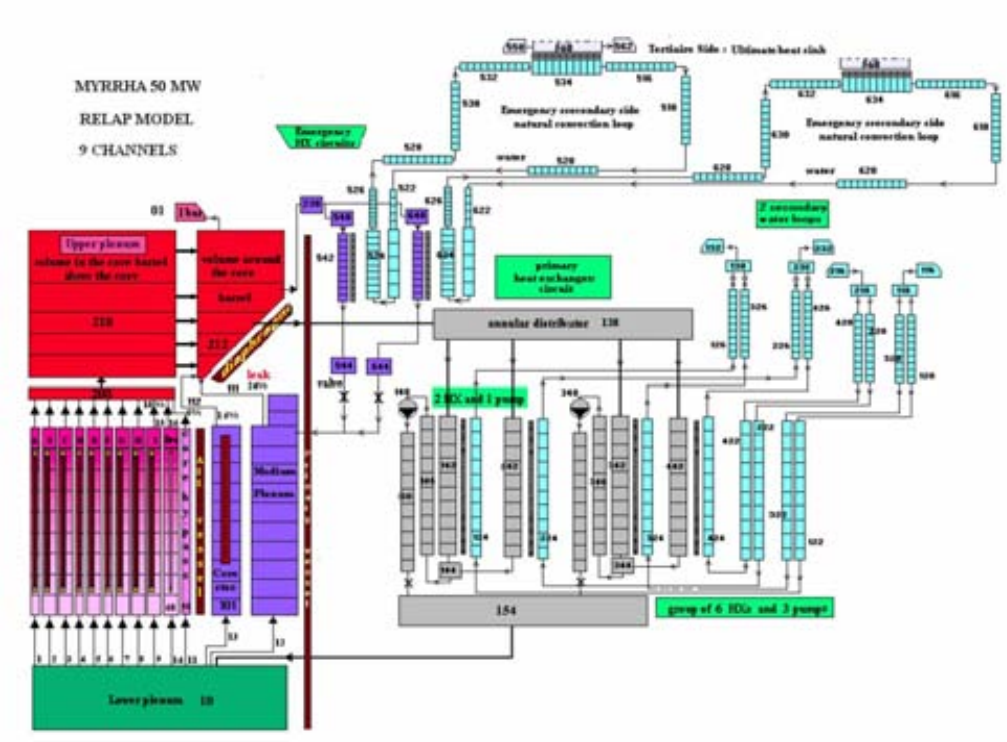

FIG. 12. Schematic representation of the RELAP model.

5.5.2. *List of simulated transients*

The transients simulated by means of RELAP and SITHER are listed in Table 7. A distinction is made between the protected transients and the unprotected transients. For the first category the accelerator is shut down during the transient. A delay of 3 seconds is applied between the accident initiation and the effective proton beam cut off. Unprotected accidents occur in case of failure of the accelerator shut down system and the spallation neutron source is supposed to be maintained to its nominal value. It means in particular that no feedback exists from the primary system thermal-hydraulics to the spallation loop behaviour.

TABLE 7. LIST OF TRANSIENTS

Transient	*Description*	*Code*
Protected TOP	Protected transient overpower at hot full power resulting from a reactivity jump	**SITHER**
Protected LOF	Protected loss of flow resulting from the total loss of circulation pumps in the primary system	**RELAP**
Protected LOH	Protected loss of heat sink resulting from the total loss of the secondary cooling systems	**RELAP**
Protected LOF&LOH	Combination of a protected LOF and LOH (station blackout)	**RELAP**
Protected SAB	Partial blockage at the inlet of one subassembly where the cross sectional area is reduced	**SITHER**
Protected overcooling	Instantaneous water temperature drop from 145°C to 40°C at the inlet of the primary heat exchangers (secondary side)	**RELAP**
Unprotected TOP	Unprotected transient overpower at hot full power resulting from a reactivity jump	**SITHER**
Unprotected LOF	Unprotected loss of flow resulting from the total loss of circulation pumps in the primary system	**RELAP**
Unprotected LOH	Unprotected loss of heat sink resulting from the Total loss of the secondary cooling systems	**RELAP**
Unprotected LOF&LOH	Combination of an unprotected LOF and LOH	**RELAP**
Unprotected SAB	Partial blockage at the inlet of one subassembly where the cross sectional area is reduced	**SITHER**
Unprotected overcooling	Instantaneous water temperature drop from 145°C to 40°C at the inlet of the primary heat exchangers (secondary side)	**RELAP**
BOP	Beam overpower at hot full power	**SITHER**

5.6. Results

Only the most representative results are selected in this section and summarised in Table 8, in particular for transients that can be considered as envelop cases. All the temperatures correspond to the hottest fuel pin (either in the MOX SAs or in the MA SAs).

5.6.1. *Loss of flow and/or loss of heat sink*

5.6.1.1. Full MOX fuel core configuration

The first transient under analysis is the **protected** loss of flow combined with a loss of heat sink (LOF&LOH), consecutive for instance to a station blackout. This is the most severe situation for the protected transients.

The maximum fuel temperature at core mid plane and the maximum clad temperature at core outlet are shown in Fig. 13. They evolve to very safe values: after a short peak up to 522°C, due to the delay between the pump trip and the accelerator shutdown, the clad temperature comes down significantly below its nominal value, whereas the core power drop (see Fig. 14) makes the fuel temperature decrease to low values. Obviously the core integrity is still better guaranteed in case of separate protected LOF or LOH accidents, which are both less severe than the LOF&LOH situation.

Figure 14 compares the power released by the core with the heat rates removed by the secondary and emergency cooling systems (SCS, ECS): the SCS unavailability inherent to the LOH is clearly shown, while the ECS reveals its high capacity of heat removal, indicating that actually only one EHX with its associated circuit is able to insure a sufficient cooling of the primary system. Since the temperatures evolve to low values, the fuel and coolant temperature feedback effects are negligible and are therefore not taken into account for this transient.

The core integrity however is jeopardized in case of unprotected LOF as shown in Figs 15 and 16. During the first phase of the transient, the rate of heat removed by all the heat exchangers (PHXs and EHXs) in free convection mode is much lower than the core power, and the core temperatures (fuel and cladding) grow very quickly as soon as the accident is initiated. The safety criterion on cladding (700°C) is strongly exceeded after a few seconds. Then, due the high temperatures reached by the coolant within the core, natural convection develops much more intensively, the power evacuated by the heat exchangers begins to compensate the core power and the fuel and clad temperatures are stabilizing (note that the core was assumed to stay undamaged during the whole transient).

In order to highlight the fuel and coolant temperature feedback effects, Figs 15 and 16 provide the results with and without feedback. It can be observed that the feedback effects are not negligible (the core power is reduced by 9%), but they are not sufficient to prevent the large and fast excess of the safety criterion on the cladding. As the EHXs are not dimensioned to remove the nominal core power, it is evident that an unprotected LOH can lead to severe core damage. Nevertheless the large thermal inertia of the primary system provides a relatively long grace time before the safety criterion on cladding is exceeded. RELAP calculations (not shown here) estimated this grace time at about 15 minutes. Less severe consequences obviously are not expected in case of unprotected LOF&LOH.

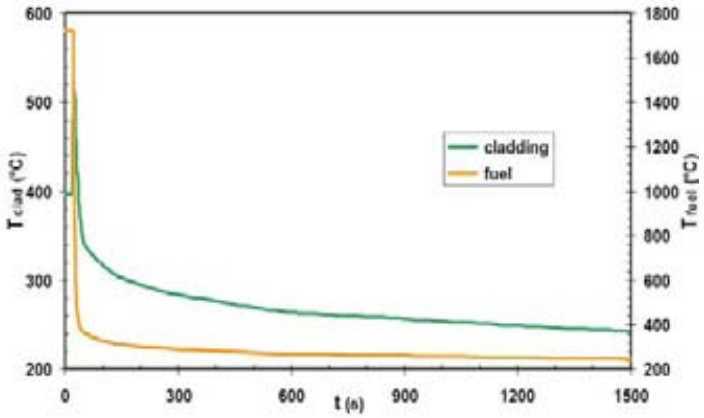

FIG. 13. Full MOX core/protected LOF&LOH — maximul clad and fuel temperatures.

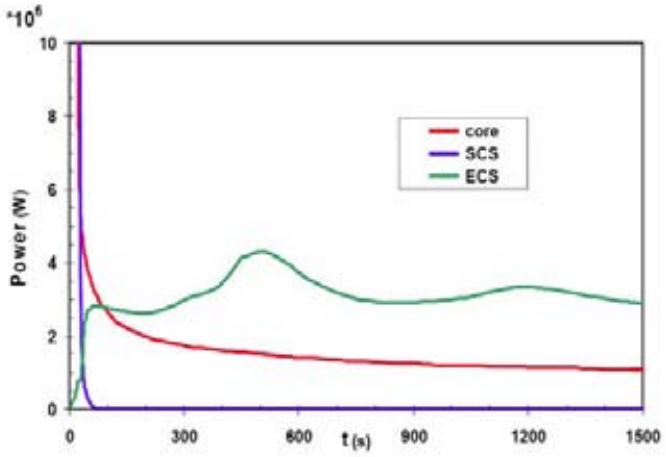

FIG. 14. Full MOX core/protected LOF&LOH — core and cooling systems powers.

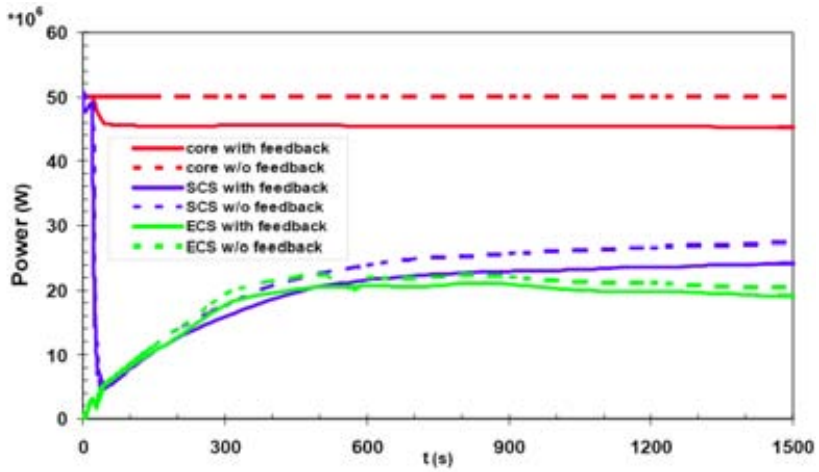

FIG. 15. Full MOX core ULOF — core and cooling systems powers.

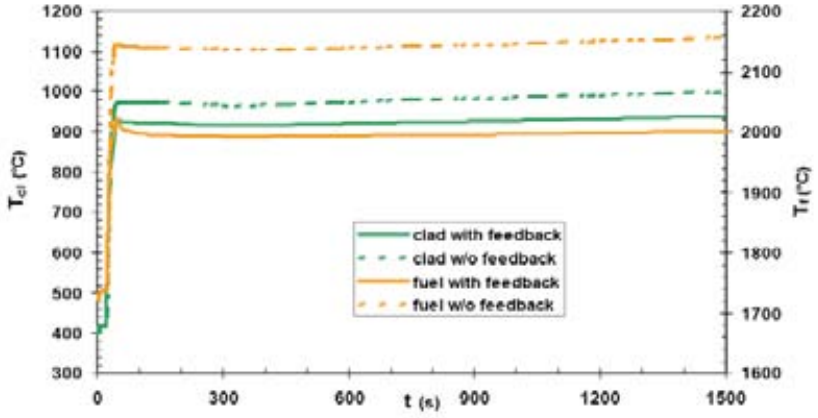

FIG. 16. Full MOX core/ULOF — maximum clad and fuel temperatures.

5.6.1.2. Mixed MOX + MA fuel core configuration

As the power densities are much lower in the second core configuration, we can conclude that the **protected** LOF accidents with or without LOH will bring this core to a still safer state than for the 1st core configuration.

In case of **unprotected** LOF accident (see Figs 17 and 18) the safety criterion on the cladding (700°C) is hardly exceeded. This criterion being conservative, it means that the cladding most likely will withstand a LOF.

Figures 18a, b and c display the results obtained by JRC/IE for the unprotected LOF. For the present calculations 4 channels were considered. A coolant flow reduction was assumed that follows 1/(1+t/3.2 s), where 3.2 s corresponds to the flow halving time of the coolant pumps.

The reactor power in Fig. 18a reduces to about 80% whereas the corresponding power in Fig. 15 reduces only to about 90% of full power. This is probably related to a different treatment of reactivity feedbacks. At any rate the SCK•CEN calculation is more conservative than the JRC/IE calculation.

In these temperature calculations three cladding temperatures are given. Since the fuel mesh starts at node 8 and its last node is 24. So Tclad, 17 is just above the mid-plane, Tclad, 20 is at 3/4 of the 60 cm fuel height and the midpoint of node 24 (Tclad, 24) is just below the top of the fuel pin. It is interesting to note that the cladding temperatures near the mid-plane and at ¾ height rise faster than the exit temperature, probably due to the early fuel temperature increase. The cladding temperatures rise by about 450 K, which is lower than the 550 K in the corresponding Fig. 16. The maximum fuel temperature is about 100 K lower than in Fig. 16, but the initial steady state maximum fuel temperature is about 200 K higher.

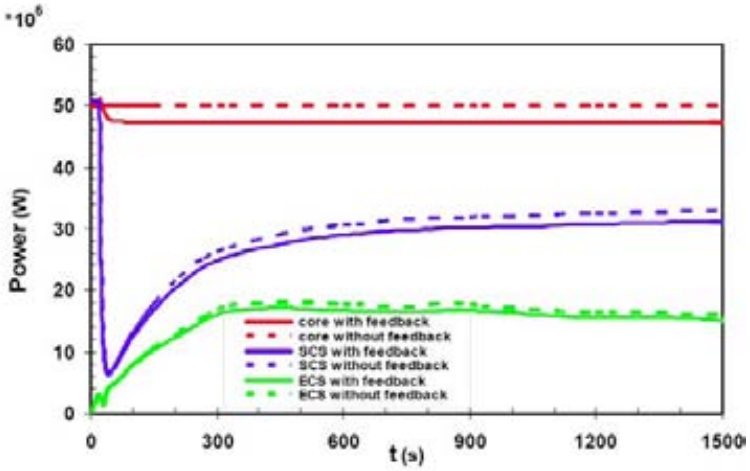

FIG. 17. MOX-MA core: ULOF — core and cooling systems powers.

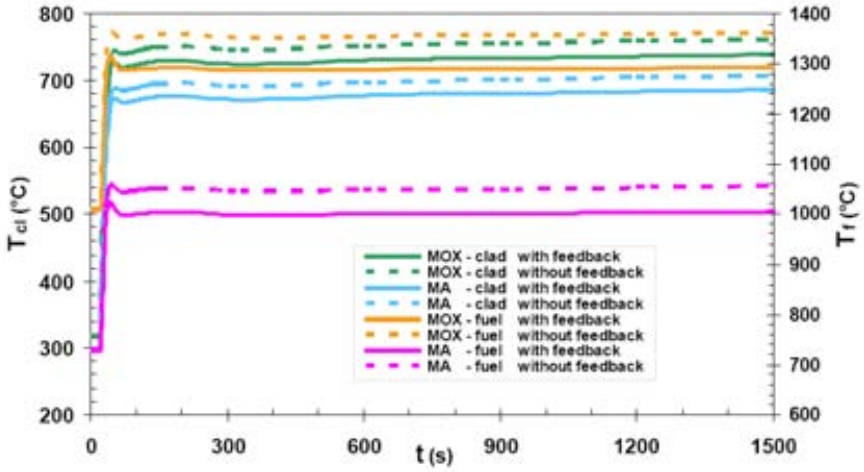

FIG. 18. MOX-MA core/ULOF — maximum clad and fuel temperatures.

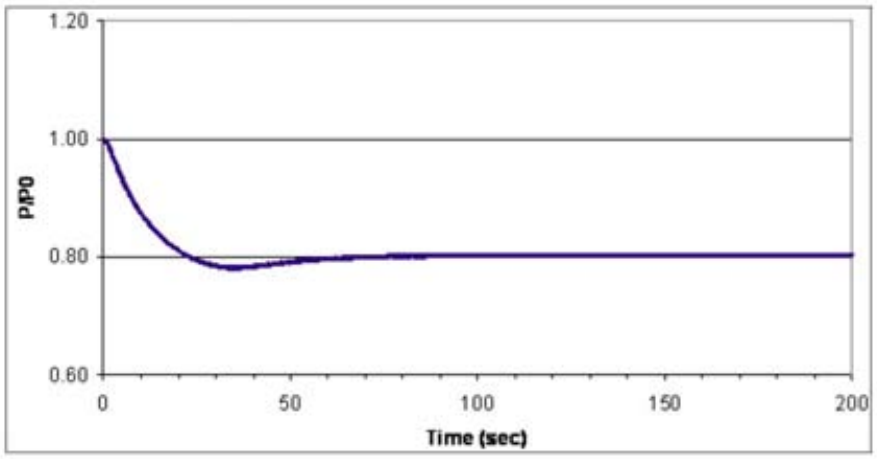

FIG. 18a. Power history in full-MOX core/ULOF: EAC2.

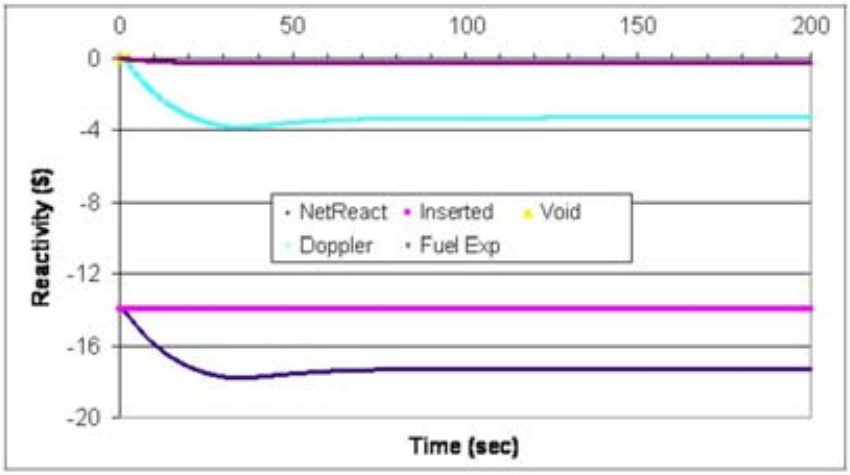

FIG. 18b. Reactivity histories in full-MOX core/ULOF: EAC2.

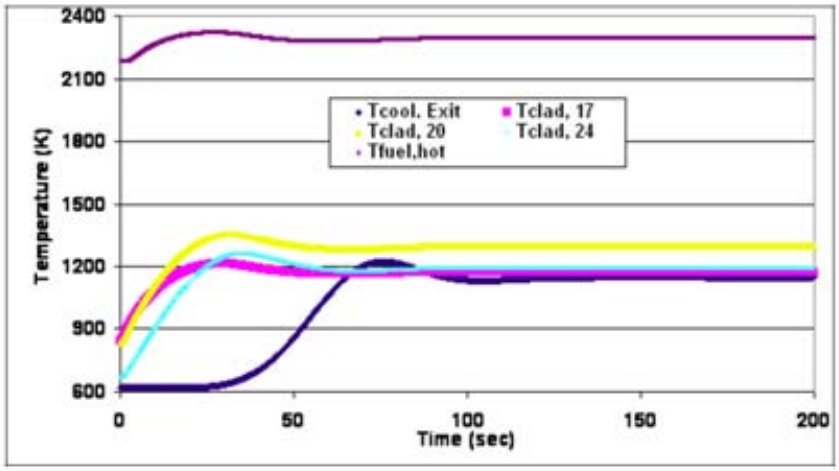

FIG. 18c. Temperatue histories in MOX-MA core/ULOF: EAC2.

If we consider now the unprotected LOF&LOH case, it results from Figs 19 and 20 that clad failure will occur after a certain time. Clad failure, which will also occur in case of unprotected LOH accident, is unavoidable, because in any situation the ECS is not dimensioned to evacuate the nominal power. However the grace time before failure is significantly longer than with the first core configuration.

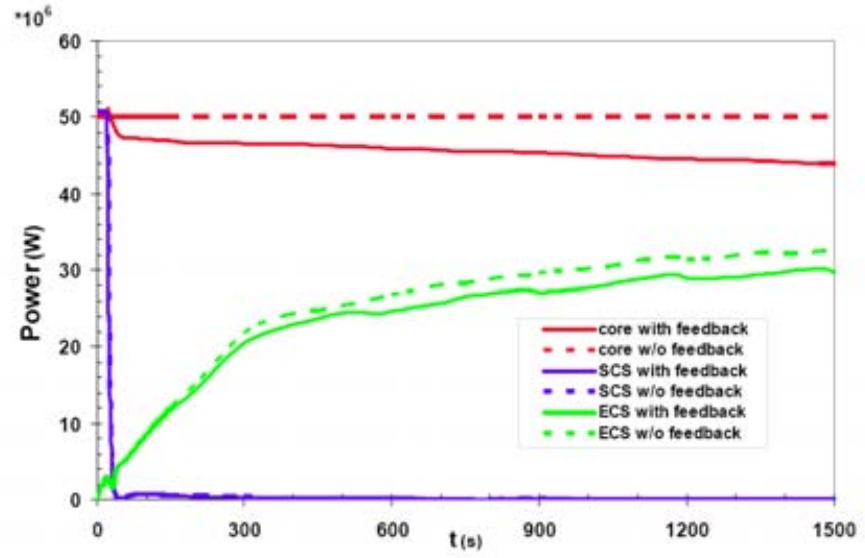

FIG. 19. MOX-MA core/unprotected LOF&LOH — core and cooling systems powers.

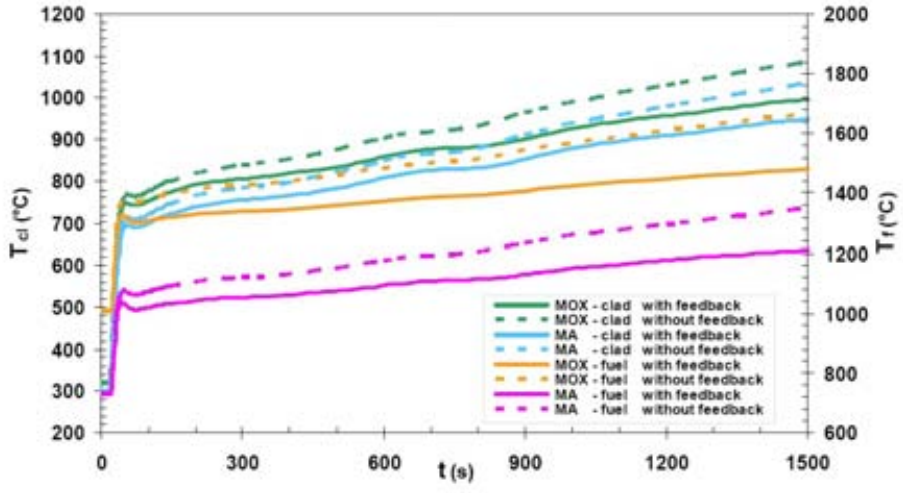

FIG. 20. MOX-MA core/unprotected LOF&LOH — maximum clad and fuel temperatures.

5.6.2. *Overcooling*

The overcooling transient results from a sudden decrease of the water temperature at the inlet of the secondary side of the PHXs. In the present study the water temperature was supposed to drop from 145 to 40°C. The main risk of such an event is LBE freezing inside the heat exchangers with possibility of blockages. The LBE temperatures at the inlet and outlet of the PHXs (primary side) were calculated by RELAP for the full MOX core configuration in the unprotected case and they are plotted in Fig. 21. The LBE outlet temperature is stabilized at 127.5°C, i.e. slightly above the theoretical melting temperature (123.5°C).

Since the presence of impurities may raise this melting temperature by some degrees, blockages of the PHXs by LBE freezing in principle could not be excluded. However when frozen LBE layers begin to develop inside a heat exchanger, the characteristics of this latter one are changing and the RELAP model of the PHXs is not able to take into account these variations. A more sophisticated modelling of LBE freezing in a heat exchanger has been developed in a home-made code [6], showing that a total blockage of the PHXs is only possible with water temperatures significantly lower than 40°C. On the other side, if the overcooling accident is 'protected' (proton beam off), the LBE heating in the core is considerably reduced and a total blockage becomes unavoidable. This means that the term 'protected' is here not really opportune and that the accelerator shutdown **may not** be triggered in this particular case.

Since the transient evolution depends on the core behaviour only via the total core power, these conclusions remain valid for the second core configuration, which develops the same power as the first one.

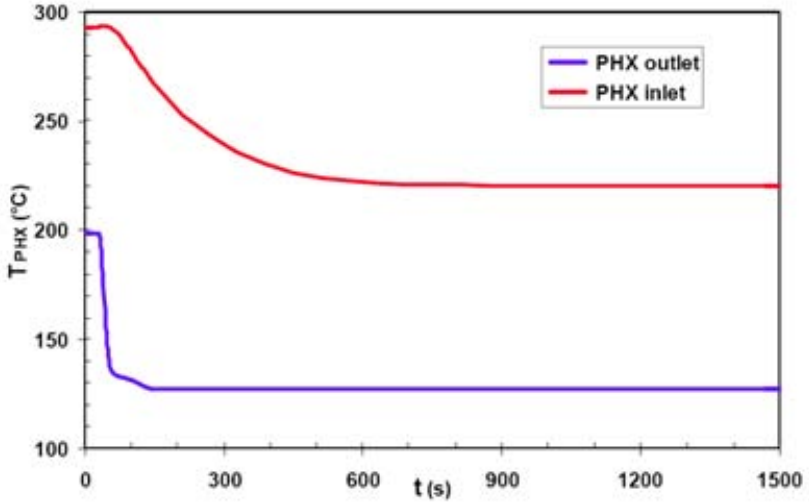

FIG. 21. Full MOX core/unprotected overcooling — LBE temperatures at inlet and outlet of the PHXs.

5.6.3. *Overpower transients*

Overpower transients (TOP) considered in the present study are initiated by accidental insertion of reactivity in the core. One of the main possible causes is the voiding of a specific region of the core. Although MYRRHA is designed to have a negative voiding coefficient in reactivity, voiding of exclusively the inner fuel sub-assemblies however would result in a maximum reactivity insertion $\Delta\rho$ of 410 pcm. This might be due to a HX tube leak, with steam bubbles entering the primary circuit. This amount of reactivity insertion is taken as the basis for an overpower transient in design basis condition (DBC). Liquid water insertion in the core might lead to prompt criticality, this is a design extended condition (DEC) and it has to be proven that sufficient protection exists against this event.

The TOPs were simulated with the SITHER code for the first core configuration. The fuel and coolant temperature feedback effects were introduced in the model. Figures 13 and 20 display the results for the unprotected transients applied to the first core configuration (full MOX). The temperature increase in the fuel rod is very limited for $\Delta\rho$ = 410 pcm (ΔT = 149°C in the fuel, 20°C in the cladding). A reactivity insertion $\Delta\rho$ > 2000 pcm is necessary to exceed the safety criterion on fuel (2500°C), while clad failure has only to be feared for much higher values.

For protected TOPs the clad and fuel temperatures fall very rapidly just after the accelerator shutdown, i.e. in the present case 3 s after the accident initiation. Significantly higher reactivity insertion values can be tolerated with the second core configuration.

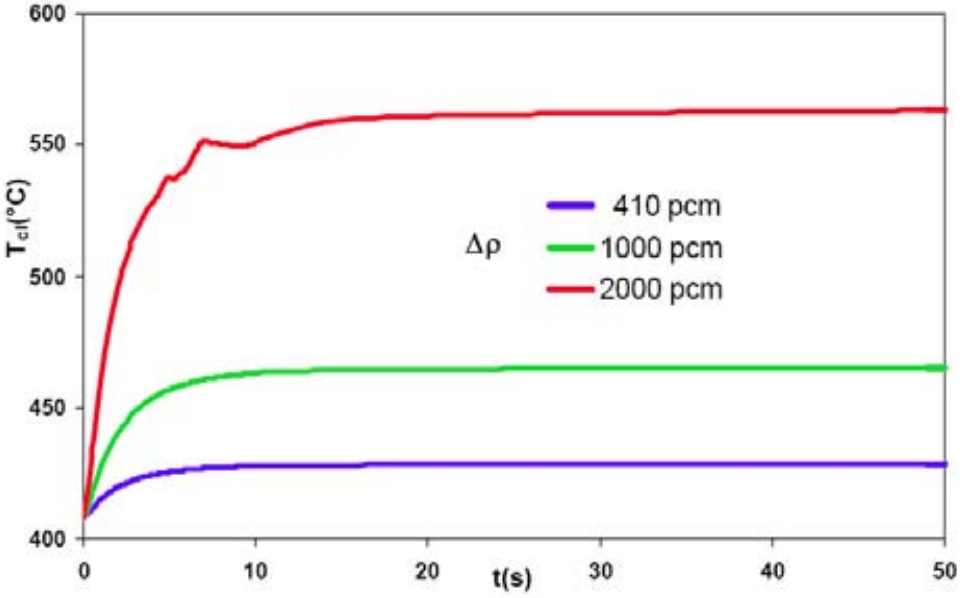

FIG. 22. Full MOX core/unprotected TOP — maximum clad temperature.

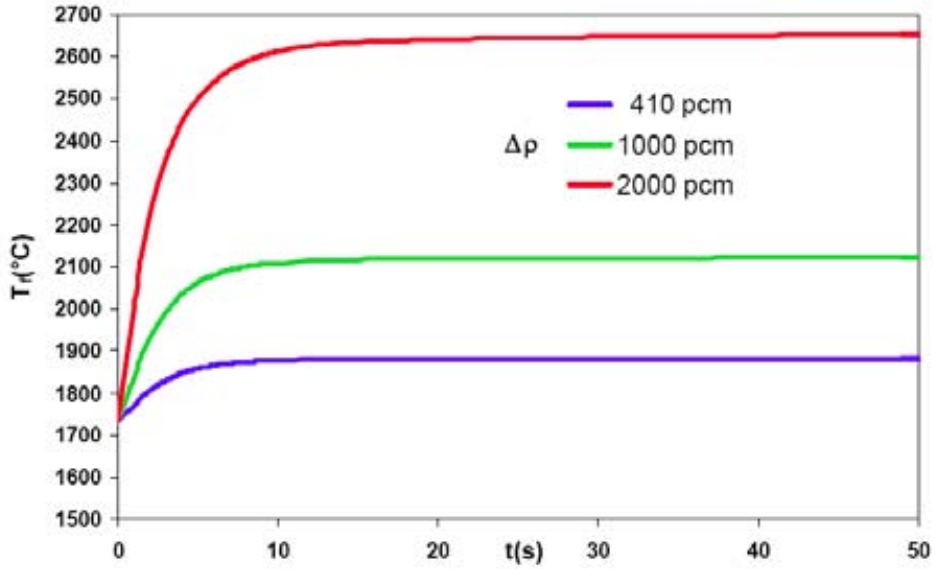

FIG. 23. Full MOX core/unprotected TOP — maximum fuel temperature.

When the two-batch core configuration is considered, reactivity feedbacks cannot be introduced in SITHER, which is not able to handle at the same time two different fuel types. This prevents the evaluation of the average fuel and coolant temperatures over the whole core. These are required for the introduction of the feedback effects in the neutronic point-kinetics model. Nevertheless omitting the reactivity feedbacks provides conservative results. The maximum fuel and clad temperatures are plotted in Figs 24 and 25 for both fuel rod types. Considering the absence of reactivity feedback, we may conclude that reactivity insertions up to 3000 pcm are tolerated by the second core configuration.

Figures 23a and b show the results of alternate calculations carried out using the European Accident Code-2. These calculations consider only the 410-pcm insertion, but it is reassuring to see that the results do not differ very much.

The maximum temperature increases of the cladding are about 25 K whereas it is about 20 K in the SITHER calculations (see Fig. 22). The maximum fuel temperature in Fig. 23b is 2300 K, in Fig. 23 it is 2120 K. The maximum fuel temperature increase is about 100 K both in the EAC-2 and SITHER calculations.

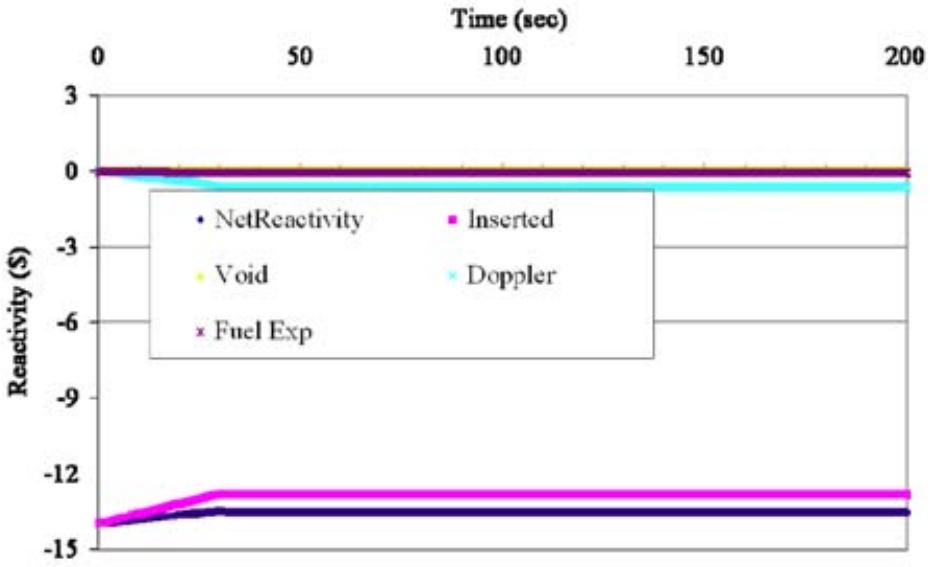

FIG. 23a. Full MOX core/unprotected TOP with a reactivity insertion of 410 pcm.

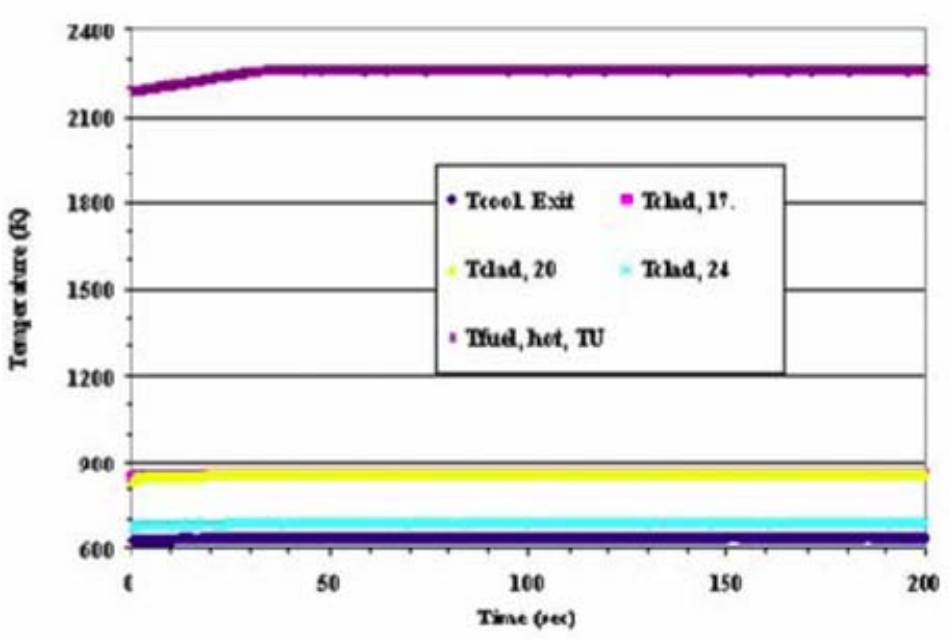

FIG. 23b. Full MOX core/unprotected TOP with a reactivity insertion of 410 pcm temperature histories.

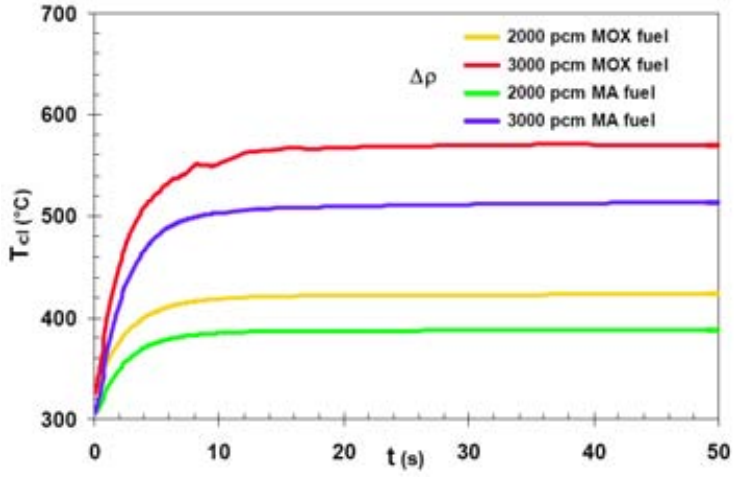

FIG. 24. MOX-MA core/unprotected TOP — maximum clad temperature.

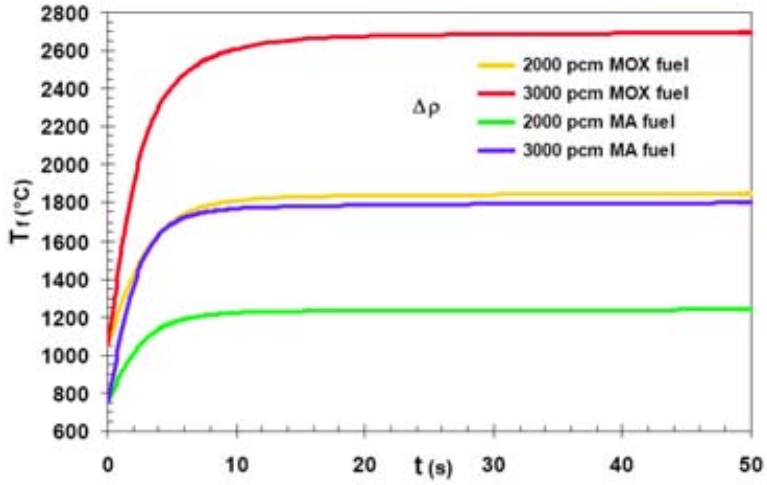

FIG. 25. MOX-MA core/unprotected TOP — maximum fuel temperature.

5.6.4. *Partial blockage in a fuel SA*

Partial blockages of fuel sub-assemblies (SA) were analysed with the SITHER code. The single fuel rod approximation of the model did not allow taking into account radial heat transfer effects. Reactivity feedback effects are not taken into account, because only one SA is involved by the blockage. Several degrees of blockage were considered, each one corresponding to a given value of the flow reduction factor fR.

The results for the unprotected case applied to the first core configuration are shown in Figs 26 and 27. It can be observed that the safety criterion on cladding is exceeded for a flow reduction factor of 40%, whereas the fuel does not yet melt with this value. In the protected situation the temperatures decrease very rapidly just after the accelerator shutdown, i.e. in the present case 3 seconds after the accident initiation.

From Fig. 26 it clearly appears that a very early detection of the blockage is crucial to prevent damage extension in the SA. However it has to be reminded that a simultaneous blockage of several SAs is a very unlikely event and that practically core damage will be limited to only one SA. As expected, the second core configuration tolerates lower values of the flow reduction factor (seeFigs 28 and 29).

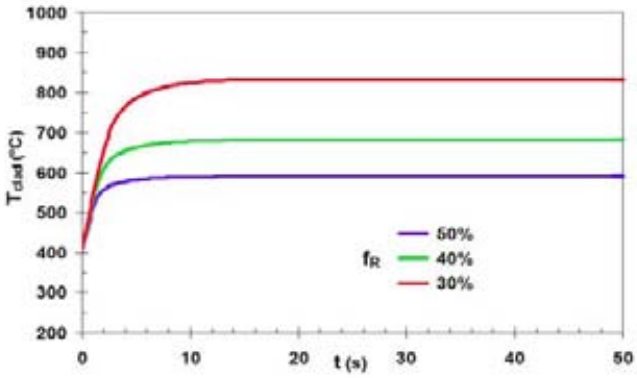

FIG. 26. Full MOX core/unprotected SA blockage — maximum clad temperature.

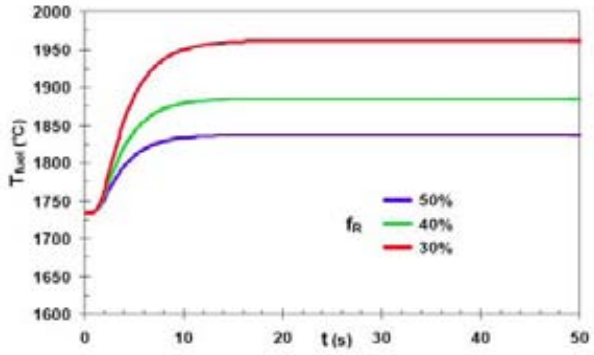

FIG. 27. Full MOX core/unprotected SA blockage — maximum fuel temperature.

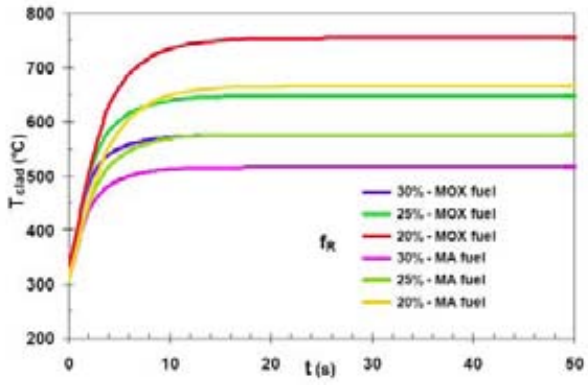

FIG. 28. MOX-MA core/unprotected SA blockage — maximum clad temperature.

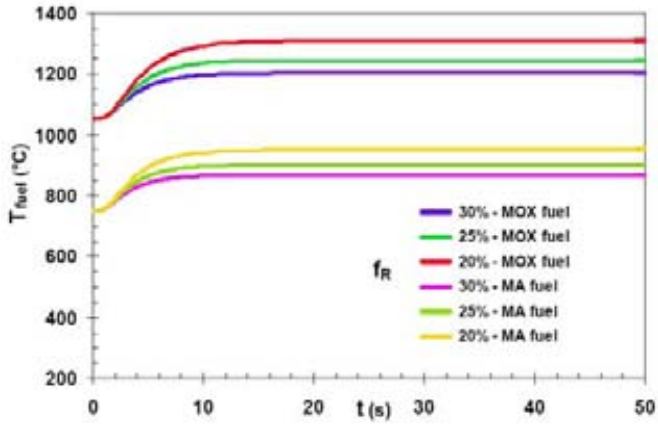

FIG. 29. MOX-MA core/unprotected SA blockage — maximum fuel temperature.

TABLE 8. SUMMARY TABLE OF THE TRANSIENTS ANALYSIS

Transient	Core 1 (MOX)	Core 2 (MOX+MA)
PLOF	😊	😊
PLOH	😊	😊
P(LOF&LOH)	😊	😊
ULOF	☹ Clad failure –grace time: few sec	😐 In principle no clad failure
ULOH	☹ Clad failure – grace time: 10 min	☹ Clad failure – grace time: >10 min
U(LOF&LOH)	☹ Clad failure – grace time: few sec	☹ Clad failure – grace time: few sec
U overcooling	😊	😊
P overcooling	☹ LBE freezing in HX after 1 min	☹ LBE freezing in HX after 1 min
PTOP	☹ Fuel melting for $\Delta\rho$ > 2500 pcm	☹ Fuel melting for $\Delta\rho$ > 3500 pcm
UTOP	☹ Fuel melting for $\Delta\rho$ > 2000 pcm	☹ Fuel melting for $\Delta\rho$ > 3000 pcm
P SA blockage	😐 Clad failure if total and instantaneous blockage Damage limited to the blocked SA	😐 Clad failure if total and instantaneous blockage Damage limited to the blocked SA
U SA blockage	😐 Clad failure for flow area < 40% Damage limited to the blocked SA	😐 Clad failure for flow area < 20% Damage limited to the blocked SA

5.7. Conclusions

The neutronics and safety analysis have been carried out for two typical core configurations of the MYRRHA design concept, adopted as prototype of an LBE-cooled sub-critical reactor. The first configuration consists of a compact core full of (U-Pu)O_2 MOX fuel sub-assemblies whereas the second one is a two-batch fuelled core involving U-free MA sub-assemblies. Both sub-critical cores are designed to deliver the same nominal power (50 MW(th)), but the power densities are significantly lower in the second configuration, which contains more fuel sub-assemblies.

The Doppler coefficient is negative, but a bit smaller than the Doppler effect of oxide-fuelled, Na-cooled reactors, in particular for the larger core where U-free fuel assemblies are loaded in the inner zone.

The core reactivity swing with burnup is limited to about 1000 pcm in the case of mixed MA/MOX core compared to about 1600 pcm for the compact full MOX core.

The hypothetical local voiding of the LBE would yield negative to no significantly positive reactivity effect as would be expected from a sodium–cooled LMFBR.

The thermal-hydraulic behaviour was analysed in several accidental situations considering the two different core configurations. The calculations performed with the RELAP and SITHER have shown that MYRRHA is able to face up very efficiently to protected loss of flow and loss of heat sink accidents, whatever configuration is considered.

In unprotected conditions, the most critical situation for the first configuration is encountered with the loss of flow case, for which the grace time is only a few seconds before the safety criterion on fuel cladding is exceeded.

On the other hand unprotected loss of heat sink accidents allow much longer grace times (~15 minutes). The second core configuration can withstand unprotected loss of flow accidents, but it is not able to prevent clad failure in case of unprotected loss of heat sink, because the emergency cooling system is not dimensioned to evacuate the nominal power (longer grace times however are observed).

Overcooling transients caused by a sudden drop of the water temperature in the secondary circuits do not lead to excessive LBE freezing in the heat exchangers provided that the accelerator is not shutdown. With this condition water temperatures as low as 40°C are acceptable and total blockages of the heat exchangers have not to be feared. This conclusion applies to both core configurations.

Accidental reactivity insertions up to 2000 pcm in the first sub-critical core configuration do not generate core damage, even in unprotected conditions. Under this limit value the maximum fuel temperature stays below 2500°C. Cladding temperatures are much lower than the safety criterion. Higher reactivity insertion values are tolerated by the second core configuration. Partial blockages in core sub-assemblies may lead to cladding failure if the cross sectional area of the flow is reduced to 40% and 20% respectively in the first and second core configurations. A very early detection of the blockage is crucial to mitigate the accident consequences. Nevertheless in any case the core damages will be limited to the affected fuel sub-assembly.

One of the main outcomes of the safety analysis of MYRRHA is the need of an extremely reliable system of accelerator shutdown in order to avoid unacceptable consequences of accidents, especially in the case of LOF. However it has to be emphasized that the windowless concept developed by SCK•CEN for the spallation target could prevent such unprotected situations if an adequate coupling between the primary system and spallation loop behaviour is introduced. Further investigations in that direction are presently under way.

REFERENCES TO CHAPTER 5

[1] AIT ABDERRAHIM, H., KUPSCHUS, P., MALAMBU, E., BENOIT, Ph., VAN TICHELEN, K., ARIEN, B., VERMEERSCH, F., JOGEN, Y., TERNIER, S., VANDEPLASSCHE, D., MYRRHA: a multipurpose accelerator driven system for research & development, Nuclear Instruments & Methods in Physics Research, A 463 (2001) pp. 487-494.

[2] 6th EURATOM Framework Program, EUROpean Research Programme for the TRANSmutation of High Level Nuclear Waste in an Accelerator Driven System, Contract no.: FI6W-CT-2004-516520, Consortium Agreement (March 2005).

[3] MASCHEK, W., STANCULESCU, A., IAEA Coordinated Research Project on Studies of Innovative Reactor Technology Options for Effective Incineration of Radioactive Waste, paper presented in GLOBAL 2005, Tsukuba, Japan 9-13 October 2005.

[4] MALAMBU, E., AOUST, Th., AIT ABDERRAHIM, H., Comparison of MYRRHA Reference Configuration (DRAFT-2) performances to 3 Variants in support to the XT-ADS spallation target design, EUROTRANS/825/05/08, Supplementary deliverable.

[5] AIT ABDERRAHIM, H. et al., MYRRHA Pre-Design File — Draft 2, SCK•CEN Report 4234 (June 2005).

[6] WATERS, L. S., Ed., MCNPXTM User's Manual. Version 2.1.5, TPO-E83-G-UG-X00001, Rev0 (November 1999).

[7] WATERS, L.S., Ed., MCNPX TM User's Manual, Version 2.4.0, LA-CP-02-408, (September 2002).

[8] PELOWITZ, D.B., Ed., MCNPX USER'S MANUAL, VERSION 2.5.0, LA-CP-05-0369, Los Alamos National Laboratory, USA (2005).

[9] MALAMBU, E., AOUST, Th., Strength and weakness of MCNPX: Experience gained from MYRRHA ADS calculations, American Nuclear Society Topical Meeting in Monte Carlo, USA, 17–21 April 2005, Chattanooga, Tennessee, ISBN: 0-89448-695-0.

[10] MEULEKAMP, R.K., VAN DER MAKR, S.C., Calculating the effective delayed neutron fraction with Monte-Carlo, Nucl. Sci. Eng. 152, 2 (142-148).

[11] HAECK, W., VERBOOMEN, B., An Optimum Approach to Monte Carlo Burn-Up. Accepted for publication in Nuclear Science and Engineering, American Nuclear Society (2007).

[12] CROFF, A.G., ORIGEN2: A versatile computer code for calculating the nuclide compositions and characteristics of nuclear materials, Nuclear Technology, Vol. 62 (1983).

[13] MACFARLANCE, R.E., up112 — NJOY version 99.112, Los Alamos Laboratory, USA (2005).

[14] HAECK, W., VERBOOMEN, B., ALEPH-DLG 1.1.0 Creating Cross-Sections Librairies for MCNP(X) and ALEPH, NEA/OECD, JEF/DOC-1125 (2006).

[15] HAECK, W., VERBOOMEN, B., Verification and validation of a multi-temperature JEFF 3.1 library for MCNP(X), NEA/JEFF/DOC-1099, OECD, France (November 2005).

[16] HAECK, W., VERBOOMEN, B., HENDRICKS, J., Validation of Nuclear Data using Lawrence Livermore Pulsed Sphere, Experiments, papere presented in ANS Winter Meeting, Albuquerque, United States, 12-16 November 2006.

[17] HAECK, W. and VERBOOMEN, B., ZZ ALEPH-LIB-JEFF3.1, MCNP Neutron Cross Section Library based on JEFF3.1; http://www.nea.fr/abs/html/nea-1745.html

[18] WALTAR, A.E., REYNOLDS, A.B., Fast Breeder Reactors, Pergamon Press (1981).

[19] HENRY, A.F., The application of reactor kinetic to the analysis of experiments. Nucl. Sci. Eng. 3, 52-70 (1958).

[20] VERBOOMEN, B., HAECK, W. and BAETEN, P., Monte Carlo calculation on the effective neutron generation time, Annals of Nuclear Energy 33, (2006)pp. 911-916.

[21] RELAP5/Mod3 Code Manual, Volume 1: Code Structure, System Models and Solution Methods, NUREG/CR-5535-V1 (June 1995).

[22] ARIEN, B., DANIËLS. J., SITHER: a module for steady and unsteady thermohydraulic calculations in single fuel rod channels, internal report 63-151/80-88, Mol, SCK•CEN, (1980).

[23] WIDER, H., CLUSAZ, A., DEVOS, J., JIRLOV, K, NICHOLSON, R., NGUYEN, H., PETER, G., RYDIN, R., VAN GOETHEM, G., LASSMANN, K., The European Accident Code-2: Overview and Status, paper presented in Intl Conf Fast Reactor Safety Meeting, Snowbird, Utah, USA (August 1990).

[24] BEAUWENS, R., DEVOOGHT, J., MUND, E., RYDIN, R. and WAGNER, R., A 3D multigroup transport kinetics code in hexagonal geometry for fast reactor transient analysis, paper presented in Intl Conf on the Physics of reactors: operation, Design and Computation, 23-27 April 1990, Marseille, France.

CHAPTER 6. DOMAIN-IV: HYBRID SYSTEM (ADS) WITH FERTILE-FREE FUEL FERTILE-FREE HYBRIDE REACTOR BENCHMARK

6.1. Introduction

The incineration of radioactive waste can be performed with critical reactors and accelerator driven systems (ADSs). Depending upon the scenario of nuclear energy utilization in a particular country (or group of countries), different spent fuel (SF) components may be considered as waste. In particular, plutonium (Pu) may be considered as asset in case of a long term nuclear energy utilization strategy assuming a closed fuel cycle, but as waste in once-through or phase-out scenarios. On the other hand, minor actinides (MAs) are always assumed to be dangerous and undesirable SF components due to their high radio-toxicity, decay heat production and reactivity potential, which will pose problems both with respect to MAs utilization as a component of nuclear fuel and with respect to their short-term/long term storage/disposal and the number and/or volume of such repositories. To investigate options for handling MAs and other waste components, several national and international programs [1-3] are currently under way. One of the options is to design innovative nuclear systems, which may be loaded with fuel containing a significant amount of MAs. To achieve the highest radioactive waste incineration rates, the fuel in such a system should ideally consist of pure MAs and Pu, but should contain no fertile nuclides such as ^{238}U or ^{232}Th. The ratio of MAs and Pu may vary considerably depending on the underlying fuel cycle strategy.

Fuels in such a system designed to transmute MAs and plutonium (Pu) are called ‘dedicated’ ones since their composition, chemical state, and fuel form are optimized for this special purpose. Though mixed trans-uranium fuel has been suggested (e.g. (Pu, MA)O_2), it is generally considered that the addition of a non-fissile (inert) support matrix is necessary to dilute the fissile phase and to give mechanical strength to the fuel. The matrix can also help to improve the properties of the fuel, as the omission of uranium (or thorium) as matrix has a penalty due to the fact that the properties of the actinides (melting point, thermal conductivity, chemical stability) gradually decrease along the actinide series going from Th to Am. At present, a wide variety of concepts is considered for dedicated fuels as various combinations of chemical state, fuel state and fuel form are possible. The chemical state can be a metal, nitride or oxide, the fuel state can be a solid solution or a composite (a ceramic fuel-ceramic matrix CERCER, a ceramic fuel-metal matrix CERMET or a metal-metal METMET), fuel form can be a pellet or a (coated) particle. In addition, molten salts could be considered. In the US Accelerator Transmutation of Waste concept a METMET fuel composed of a (Pu, MA, Zr) phase dispersed in a zirconium metal matrix has been suggested [3]. In the Japanese ADS concept of JAERI, a mixed nitride (solid solution) fuel is considered [2]. In Europe, a specialist group has recommended that the European R&D for ADS fuel will concentrate on CERCER and CERMET oxide fuel forms such as inert matrix mixed oxide composites [4].

This ‘dedicated’ fuel is still to be developed; one of the most challenging parts of the mentioned programs being how to fabricate, investigate and test these innovative fuels. A general problem of these fuels is that currently they only exist either in small quantities or on laboratory scale. Naturally, both operational experience and experience under transient conditions is missing. Compared to the wealth of data and knowledge gained in past experimental programs for conventional fast reactor fuels, a safety related database for such new fuels does not exist. Therefore, new safety-related experimental programs have to be foreseen in the future for such innovative fuels. Current safety analyses inevitably suffer from lack of experimental knowledge.

According to the existing experience, a dedicated fuel may suffer from actinide redistribution during irradiation (e.g. AmO_2), radiation impact on the matrix, increased cladding corrosion, higher fission gas release, and pressure build-up due to helium formation (resulting from alpha-decay). The latter aspect has been identified as a unique feature of MA-containing fuels, which has a big impact on the fuel behavior. If helium is released from the fuel during normal operation, the internal pin-pressure will increase. If it is retained in the fuel, burst release can occur during power or temperature excursions. Both cases have to be analyzed carefully for transient conditions as the helium production could have a decisive influence on pin failure mechanisms and is a potential source for initiating a core-voiding transient.

As it will be shown in the following, the utilization of fuels with high MA content will lead to a deterioration of the safety parameters of the core. Besides the almost complete absence of negative Doppler feedback and the degradation of the effective delayed neutron fraction, the reactivity potentials of the steel (clad), of the coolant (void worth) and of the fuel worth are significant in these cores. Operation of such reactors seems only feasible in the subcritical mode, as realized in ADSs. Another typical feature, which significantly increases the safety potential, is the high boiling point of the coolant for the heavy liquid metal (HLM) cooled concept.

Currently, several dedicated fuel options have to be considered in reactor physics and safety studies. The investigations on dedicated ADS cores — described in the following — focus on safety issues and may help to formulate future research and development needs. For the benchmark analysis some important assumptions have been taken during the definition phase and n accordance with the other Domains.

1. For the transients selected, the original intention was not to simulate scenarios with pin breakup and fuel failure. The cases have been designed in such a way. To be on the safe side, it has been decided to switch-off the SIMMER pin failure models for the unprotected loss of flow (ULOF), transient overcurrent (TOC) and unprotected overpower (UTOP) transients. In case of pin failure a gas blow-down would commence and further pin breakup, propagation and fuel sweep-out processes would take place. As no other code is currently available that could model such a scenario, a benchmark analysis would not be possible. In addition, it would give a wrong touch compared to the other Domains to simulate core disruptive accidents only in Domain IV. An exemption is the blockage accident, where a fuel pin disruption is simulated to identify some key safety issues as the fuel and clad sweep-out mechanism investigated in the Kyushu experiments.
2. This decision was also made in the light of the thermal- physical data situation at the start of the benchmark analyses. Especially the MgO matrix fuel was a concern at this time and the caution proved to be reasonable [5, 6]. Thermal-physical data in the report reflect the situation of the year 2004. Now, new data are available and show that for the MgO matrix at temperature levels of 2000-2100 K a problem of dissociation exists in case of failed clad. In addition the thermal conductivity is much lower than the one taken in the current report, espacially in the high temperature damain. This does not jeopardize the benchmark, but has to be kept in mind.
3. Currently a CERMET fuel (^{92}Mo matrix) is favoured as dedicated fuel for ADS. The Zr based solid solution fuel was discarded because of reprocessing problems [6, 24].
4. At the start of the analyses, 316 SS clad was assumed with a protective layer against corrosion and failure data were taken from the fast reactor projects. Currently for ADS the ^{91}T clad is under discussion, which is susceptible to high temperature creep failure at around 1100 K. (pressurized plenum ~50). This failure limits are not taken into account in the current analyses as one can assume that when these innovative fuels are ready to be inserted into an ADS core, also a better clad would be available [23].
5. As coolant Pb/Bi eutectic has been used in the benchmark. Currently due to economic reasons the Pb coolant is generally be preferred.

6.2. Benchmark model description

An example of the ADS [7] with lead-bismuth eutectic (LBE) coolant is shown in Fig. 1. The ADS core is subcritical, the ‘external source’ of neutrons originating as a product of the interaction of protons — accelerated in a LINAC — with target nuclei (usually called spallation process). In the following one considers only the core, target, and relatively small surrounding regions (on the external boundaries of which conventional conditions for neutronics and thermal-hydraulics models are imposed).

The benchmark models investigated in the following are designed by assuming that the core power is 580 MW(th). The power released in the target is ignored in the following: as in many European designs, the target is cooled independently of the core. It is also assumed that the

amplitude of the proton beam current (the energy of protons being 1 GeV) at steady-state conditions is chosen so that the corresponding 'external neutron source' will keep the ADS core power at the specified power level. Two fertile-free fuels are considered: (Pu0.4, Am0.5, Cm0.1)O_2-X+ZrO_2 and (Pu0.4, Am0.5, Cm0.1)O_2-X +MgO. The three-zone (to reduce the radial power peaking factors) core layouts for the ZrO_2-matrix fuel and MgO-matrix fuel options are shown in Figs 2 and 3, respectively, the fuel volume fraction being lower in the inner core and higher in the outer core, while the heavy nuclide isotopic composition is zone-independent at the beginning of life (BOL) conditions. The 2D RZ ADS core model is shown in Fig. 4.

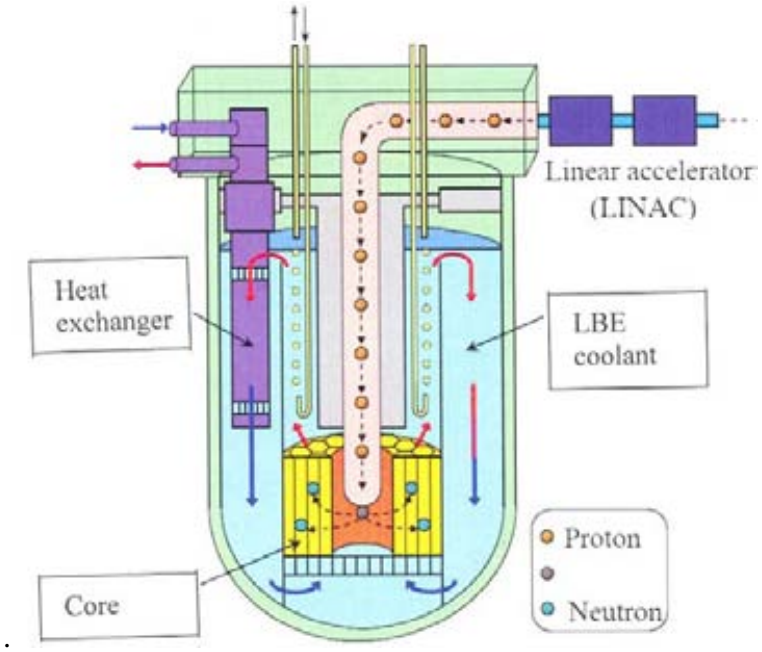

FIG. 1. Example of ADS with major components.

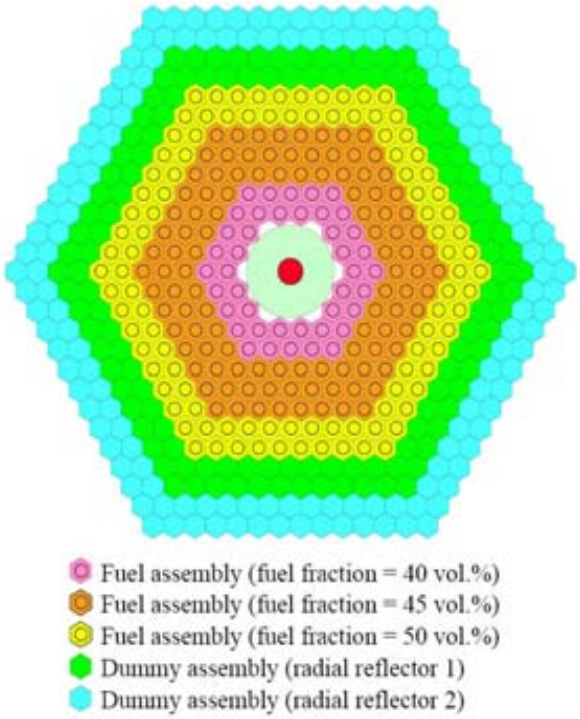

FIG. 2. Three-zone core layout for the ZrO2-matrix fuel.

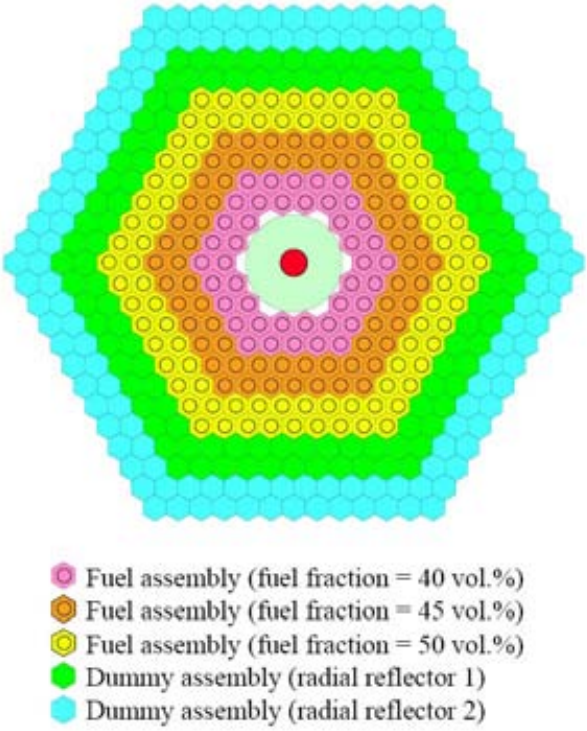

FIG. 3. Three-zone core layout for the MgO-matrix fuel.

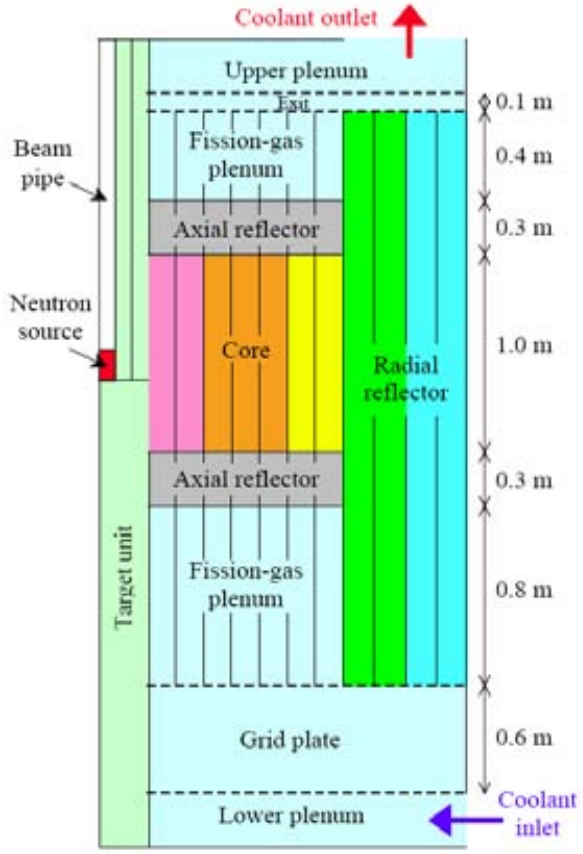

FIG. 4. ADS core model in RZ geometry.

The main core parameters for BOL are given in Tables 1 and 2, respectively, the peak power and temperature values for the k-eff values being specified in the last rows. This core model is employed in thermal-hydraulics analyses. The neutronics calculations (both stand-alone and coupled with thermal-hydraulics ones) are performed for an axially reduced geometry domain. This neutronics model (each HEX ring being represented by a cylinder, the material distribution being assumed to be homogeneous) is defined in Tables 3-6. In Tables 3 and 4 the first row represents the lowest axial 'neutronics' layer, while the last row represents the uppermost one. Compositions 1, 2, 3 correspond to the inner, middle, and outer fuel regions, respectively. Compositions 4, 6, 8, and 11 represent the core surroundings. Compositions 20-22 represent the target region, the 'external' source being located in the geometry regions occupied by Composition 20. Table 3 describes the material distribution in the ZrO_2 core with 14 axial rings, the corresponding thickness values (in cm) being: 8.296 (first column), 13.653, 14.212, 14.300, 14.331, 14.344, 14.352, 14.356, 14.359, 14.361, 14.362, 14.363, 14.364, and 14.365 (last column). The axial layer thickness values are 40 (first row), 15, 15, 10, 10, 10, 10, 10, 10, 10, 10, 10, 10, 15, 15, and 40 (last row). The corresponding values for the MgO core are similar, except that the model contains one only 2 (instead of 3) rings in the middle region. Each composition consists of one or more materials, the corresponding volume fractions being given in Table 5, the nuclear densities being given in Table 6 (by assuming that the temperature of all materials is position-independent and equal to 900 K). For example, the smear density (in 1/(barn*cm)) of ^{238}Pu in the inner ZrO_2 core is 0.000529 times 0.1194.

TABLE 1. MAIN PARAMETERS FOR THE CORE WITH ZrO_2-MATRIX FUEL

Core height	1.00m
Number of pins per SA	169
Number of fuel SAs	252
SA pitch	158.00mm
SA inner width	147.00mm
Fuel pellet diameter	6.00mm
Clad inner diameter	6.20mm
Clad outer diameter	7.00mm
Gap between fuel and clad	0.10mm
Pin P/D	1.6
Hexcan-wall thickness	3.00mm
Mean coolant velocity	0.784m/s
Dynamic pressure drop	1.15 bar
Power	580MWth
Average linear power	136.18W/cm
Power axial form-factor	1.20
Power radial form-factor	1.46
Peak linear power	243.5W/cm
Inlet coolant temperature	573K
Outlet coolant temperature	723K
Peak fuel temperature	1878K
Peak cladding temperature	849K
k-eff at beginning of life (BOL)	0.96706

TABLE 2. MAIN PARAMETERS FOR THE CORE WITH MgO-MATRIX FUEL

Core height	1.00m
Number of pins per SA	169
Number of fuel SAs	198
SA pitch	158.00mm
SA inner width	147.00mm
Fuel pellet diameter	6.00mm
Clad inner diameter	6.20mm
Clad outer diameter	7.00mm
Gap between fuel and clad	0.10mm
Pin P/D	1.6
Hexcan-wall thickness	3.00mm
Mean coolant velocity	0.99m/s
Dynamic pressure drop	1.15 bar
Power	580MWth
Average linear power	173.33W/cm
Power axial form-factor	1.21
Power radial form-factor	1.34
Peak linear power	281.0W/cm
Inlet coolant temperature	573K
Outlet coolant temperature	723K
Peak fuel temperature	1488K
Peak cladding temperature	831K
k eff at beginning of life (BOL)	0.97162

TABLE 3. ZrO_2 CORE MODEL LAYOUT (ASSIGNMENT OF COMPOSITION NUMBERS TO GEOMETRY REGIONS)

22	22	22	6	6	6	6	6	6	6	8	8	11	11
22	22	22	4	4	4	4	4	4	4	8	8	11	11
22	22	22	4	4	4	4	4	4	4	8	8	11	11
22	22	22	1	1	2	2	2	3	3	8	8	11	11
22	22	22	1	1	2	2	2	3	3	8	8	11	11
22	22	22	1	1	2	2	2	3	3	8	8	11	11
22	22	22	1	1	2	2	2	3	3	8	8	11	11
20	22	22	1	1	2	2	2	3	3	8	8	11	11
20	22	22	1	1	2	2	2	3	3	8	8	11	11
21	22	22	1	1	2	2	2	3	3	8	8	11	11
21	22	22	1	1	2	2	2	3	3	8	8	11	11
21	22	22	1	1	2	2	2	3	3	8	8	11	11
21	22	22	1	1	2	2	2	3	3	8	8	11	11
21	22	22	4	4	4	4	4	4	4	8	8	11	11
21	22	22	4	4	4	4	4	4	4	8	8	11	11
21	22	22	6	6	6	6	6	6	6	8	8	11	11

TABLE 4. MgO CORE MODEL LAYOUT (ASSIGNMENT OF COMPOSITION NUMBERS TO GEOMETRY REGIONS)

22	22	22	6	6	6	6	6	6	8	8	11	11
22	22	22	4	4	4	4	4	4	8	8	11	11
22	22	22	4	4	4	4	4	4	8	8	11	11
22	22	22	1	1	2	2	3	3	8	8	11	11
22	22	22	1	1	2	2	3	3	8	8	11	11
22	22	22	1	1	2	2	3	3	8	8	11	11
22	22	22	1	1	2	2	3	3	8	8	11	11
20	22	22	1	1	2	2	3	3	8	8	11	11
20	22	22	1	1	2	2	3	3	8	8	11	11
21	22	22	1	1	2	2	3	3	8	8	11	11
21	22	22	1	1	2	2	3	3	8	8	11	11
21	22	22	1	1	2	2	3	3	8	8	11	11
21	22	22	1	1	2	2	3	3	8	8	11	11
21	22	22	4	4	4	4	4	4	8	8	11	11
21	22	22	4	4	4	4	4	4	8	8	11	11
21	22	22	6	6	6	6	6	6	8	8	11	11

TABLE 5. MATERIAL VOLUME FRACTIONS FOR THE COMPOSITIONS

Composition number	Matrix	Fuel	Steel	LBE	B_4C	Vacuum
1 (ZrO_2, inner)	0.1194	0.0796	0.1369	0.6271	0.0000	0.0000
2 (ZrO_2, mid)	0.1095	0.0895	0.1369	0.6271	0.0000	0.0000
3 (ZrO_2, outer)	0.0995	0.0995	0.1369	0.6271	0.0000	0.0000
1 (MgO, inner)	0.1115	0.0875	0.1369	0.6271	0.0000	0.0000
2 (MgO, mid)	0.1035	0.0955	0.1369	0.6271	0.0000	0.0000
3 (MgO, outer)	0.0915	0.1075	0.1369	0.6271	0.0000	0.0000
4	0.0000	0.0000	0.3729	0.6271	0.0000	0.0000
6	0.0000	0.0000	0.1369	0.6271	0.0000	0.0000
8	0.0000	0.0000	0.0721	0.9279	0.0000	0.0000
11	0.0000	0.0000	0.1369	0.6271	0.2360	0.0000
20	0.0000	0.0000	0.2000	0.8000	0.0000	0.0000
21	0.0000	0.0000	0.0721	0.0000	0.0000	0.9279
22	0.0000	0.0000	0.2000	0.8000	0.0000	0.0000

TABLE 6. NUCLEAR DENSITIES FOR MATERIALS (IN 1/(barn*cm))

ZrO_2 Matrix	O16	Zr			
	0.052383	0.028315			
MgO Matrix	O16	Mg			
	0.053491	0.053491			
Fuel	O16	Pu238	Pu239	Pu240	Pu241
	0.047697	0.000529	0.003946	0.003142	0.001363
	Pu242	Am241	Am243	Cm244	Cm245
	0.001389	0.008602	0.004265	0.002294	0.000254
Steel	Cr	Fe	Ni		
	0.013715	0.055067	0.011387		
LBE	Pb	Bi209			
	0.013246	0.016380			
B_4C	B10	B11	C		
	0.067889	0.045259	0.028287		

6.3. Codes and data used

The analyses presented in the following have been mainly performed with SIMMER-III [8], a safety code, originally developed for liquid metal cooled critical reactors, but extended to accelerator driven systems [9], molten salt reactors [10] and some other reactor types. In addition, a FZK collection of data libraries and stand-alone neutronics codes has applied in this study since it includes more options (compared to SIMMER) for neutronics calculations.

6.3.1. *FZK nuclear data and neutronics code collection*

This collection includes an 11-group nuclear data library [11], the C4P code and data system [12], the ZMIX multigroup cross-section processing system [13], and the DANTSYS neutron transport code [14] coupled with a burnup code TRAIN [15] and few post-processing (e.g. for beta-effective calculations) tools. This code and data package includes also the activation cross-section, fission product yield and decay data libraries used in TRAIN and some other data libraries and codes, which are not used for this study and, therefore, are not mentioned here. This collection is employed at FZK (1) to provide nuclear data for SIMMER, (2) to validate these data by employing them in calculation and experimental benchmarks, (3) to investigate potential options for extension of the SIMMER neutronics part, (4) to compute some SIMMER input parameters, such as 'macroscopic' (i.e. computed for isotope mixtures) beta (delayed neutron fractions) values that are not readily available from nuclear data libraries, and (5) to check the accuracy of SIMMER neutronics calculations by comparing SIMMER results with those provided by this more comprehensive code package.

The 11-group library in the CCCC (ISOTXS and BRKOXS) format has been prepared and used at FZK for more than 10 years mainly for fast-reactor analyses with SIMMER. This library is based on the KFKINR 26-group cross-section set, which has been extended by some more recent data, in particular for Minor Actinides (MAs). For preparing the 11-group library, the 26-group data (including f-factors) were averaged with a weighting function representing the neutron spectrum in a MOX-fueled 300 MW(e)-type Na-cooled fast reactor core.

C4P is code and data system developed at FZK [13], which includes fine-group cross-section libraries in the extended (for taking into account temperature-dependent neutron thermal-scattering 'matrices') CCCC format and related processing tools (in particular for condensation of fine-group data). The fine-group libraries are based on recently evaluated nuclear data files. They are applicable for fast and thermal reactor analyses and include data for 560 energy groups (up to 20 MeV). Alternative libraries corresponding to alternative data evaluations (ENDF, JEFF, JENDL) are available, the JEFF 3.0 data being preferred (after performing a set of benchmark calculations) by now in general. The data can be 'condensed' or 'collapsed' (i.e. reduced to a smaller number of energy groups) by employing a user-defined weighting function. For Domain VI calculations, several (based on ENDF, JEFF, etc.) 30-group cross-section sets (which include f-factors) were derived from corresponding 560-group libraries by using a weighting function that is a fission spectrum at 'fast' energies (above ca. 2.5 MeV), a Maxwellian spectrum at thermal energies, the Fermi spectrum between the fast and thermal energies. The 30-group set boundaries are similar to those of the 26-group set, except the region above 0.4 MeV, where a finer group structure is employed.

ZMIX is a code developed at FZK for calculating the composition-dependent cross-sections on the basis of the CCCC data libraries. The code takes into account cross-section self-shielding and temperature effects by employing f-factors (temperature-dependent thermal-scattering matrices are interpolated vs. temperature as well). The neutron spectrum for a particular composition can be computed by assuming that the composition represents a large homogeneous medium and the neutron flux spectrum is the fundamental mode spectrum in this medium (either a user-defined buckling value or a value that would bring the reactor to criticality can be used). This spectrum can be used for cross-section 'condensation', i.e. for calculation of composition-dependent cross-section for a smaller number of energy groups. For taking into account heterogeneity effects, related to cross-section self-shielding, a technique based on the Bell method [13] can be optionally employed. The composition-dependent cross-sections can be produced in different formats, in particular employed in DANTSYS.

DANTSYS is a Sn transport code developed at LANL. The code was modified at FZK to improve its performance and reliability [16]. A 2D capability of DANTSYS (TWODANT) was employed in the stand-alone (and in SIMMER) calculations.

6.3.2. *The SIMMER-III code*

The SIMMER-III code is developed by JAEA (Japan Atomic Energy Agency, O-arai Engineering Center) in cooperation with Forschungszentrum Karlsruhe, CEA (Commissariat à l'Énergie Atomique, CEN Grenoble and CE Cadarache) and other partners as ENEA, IRSN, PSI, and SCK•CEN. The application of the SIMMER code to ADS is of special interest to the European partners in this cooperation. SIMMER-III is a two-dimensional (RZ, XY), multi-velocity-field, multi-phase, multi-component, Eulerian, fluid-dynamics code coupled with a structure model (fuel pins etc.) and a space-, time-, and energy-dependent neutron dynamics model. SIMMER-III uses an elaborate scheme of equation of state (EOS) functions for fuels, steel, coolants, absorber, and simulation materials (e.g. alumina).

The neutronics part includes a cross-section processing module that computes macroscopic cross-sections from a nuclear data library in the CCCC format, a module for determining the reactivity and flux/power amplitude by the improved quasistatic method [17], these modules interacting with the neutron transport solver based on the DANTSYS code that computes the flux/power shape by the Sn-method, different times steps being employed for the shape (largest steps), reactivity and cross-sections, and amplitude (smallest steps) recalculations.

The key advantage of SIMMER-III/IV is its versatility and flexibility. The code can be used to investigate special effect problems (small scale) as e.g. freeze-out of locally molten fuel on colder structures, but it can also be used to investigate the complex coupled neutronics and thermal-hydraulics behavior of the whole core (medium scale) under transient conditions. Finally on the largest geometric scale, the code can describe core material redistribution within the vessel and beyond e.g. after a fuel release from the core region. This includes both problems related to settling and cooling of fuel within the vessel, but also re-criticality problems in below core structures or in the core catcher can be treated.

6.3.2.1. SIMMER extension for modeling systems with dedicated fuel and LBE coolant

Thermal-hydraulics/fluid-dynamic models of SIMMER were extended some time ago [18] for modeling cores with fertile-free fuel and HLM coolant. For the CRP studies, the EOS model for the LBE coolant has been improved, especially in the high pressure and high temperature region. For ZrO_2-matrix solid-solution fuel ((Pu0.4, Am0.5, Cm0.1)O_2-X+ZrO_2) and MgO-matrix CERCER fuel ((Pu0.4, Am0.5, Cm0.1)O_2-X+MgO), the EOS models have been newly developed as described in the following. An experimental program was carried out to improve/validate the melting-freezing SIMMER model. The gas-blowout model and gas-LBE two-phase flow model was improved as described in the following.

6.3.2.2. SIMMER multiphase model

The SIMMER fluid-dynamics part has been improved so as to describe phenomena of gas Pb/Bi two-phase flows as might occur under core disruptive accident conditions in the Pb/Bi-cooled ADS. The inter-phase drag between bubbles and molten Pb/Bi can be estimated according to the bubble shape [19]. In the original SIMMER-III, the drag coefficient, CD, to evaluate the inter-phase drag is estimated with following equation:

$$C_{\mathrm{D}} = \frac{4}{3}\sqrt{\frac{g\,\Delta\rho}{\sigma}}\left[\frac{1+17.67\left\{f(\alpha)\right\}^{6/7}}{18.67\,f(\alpha)}\right]^2 \quad \text{where} \quad f(\alpha) = \sqrt{1-\alpha}\,\frac{\mu_{\mathrm{f}}}{\mu_{\mathrm{m}}}.$$

This formula was developed for ellipsoidal bubbles shown in normal bubbly flows such as air-water system. However, in the gas-Pb/Bi two-phase flows, cap-shape bubbles were actually identified in the verification experiments. The inter-phase drag for cap-shape bubbles can be expected to be smaller than that for ellipsoidal bubbles. Therefore, the drag coefficient should be also improved in order to estimate the inter-phase drag accurately. Instead of the equation above, we have evaluated CD with

$$C_D = \frac{8}{3}\frac{r_b\, g\, \Delta\rho\,(1-\alpha)}{\rho_f\, v_{gr}^{\,2}} \quad \text{where} \quad v_{gr} = \frac{V_{gj}^{+}}{1-C_0\,\alpha}\left(\frac{\sigma\, g\, \Delta\rho}{\rho_f^{\,2}}\right)^{0.25} .$$

In this equation, Vg j+ is the drift velocity proposed by Kataoka and Ishii/20/.

The impact of the improvement in the fluid dynamics part is presented in Fig. 5. Figure 5 suggests that the improved SIMMER-III has enough accuracy and reliability for the simulation of gas-Pb/Bi two-phase flows. Multiphase flows could be expected e.g. after pin failures leading to a blow-down of fission gases or helium. A model has been adopted for SIMMER based originally on a SAS code formulation [21].

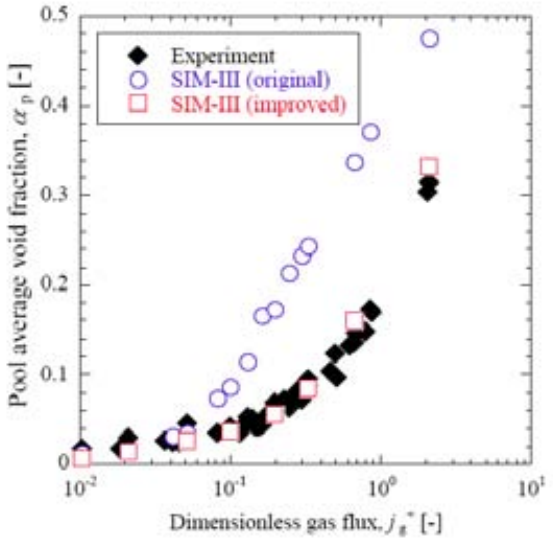

FIG. 5. Code improvement for gas-PB/Bi two-phase flow.

The high boiling point (1943 K) and the high density of Pb/Bi strongly influence the phenomenology under transient and accident conditions. The high boiling point implies that during core disruption caused by a ULOF accident clad melting and pin disruption will occur before coolant boiling.

In the SIMMER-III formulation, chosen for the analyses, the breakup of the fuel pin is determined by a thermal criterion. In this breakup model, the cladding steel will be released into steel particles and molten-steel droplets with a prescribed solid/liquid ratio when the cladding temperature reaches the liquidus temperature. The released steel particles and molten-steel droplets will be assigned to a velocity field, q_1, different from the coolant-flow velocity field, q_2. The behavior of released particles and droplets are mainly governed by inertial force, gravity, buoyancy, and the momentum exchange between q1 and q2. The initial diameter of the particles and droplets are assumed to be 1mm in the present simulation.

The disintegration of the fuel pellet stack is determined by the disappearance of the cladding support. The fuel pellets will be released into free fuel particles immediately when the cladding steel has been broken up in the corresponding computational cells.

6.3.2.3. SIMMER melting freezing model

In severe accidents of LBE-cooled systems, cladding failure in single-phase coolant channels may lead to molten cladding relocation due to buoyancy. This would cause thermal interactions of the molten cladding with colder coolant and upper structures, and result in freezing of the molten cladding into debris and/or onto the structures. In assessing the safety of LBE-cooled systems, it is important to know consequences of such molten-metal freezing phenomena, which may influence the coolant flow rate due to flow area reduction and cause flow channel blockage potentially. This could restrict the fuel dispersal from the core and lessen its effect on reactivity reduction.

In the present study, two types of works were carried out at Kyushu University in order to investigate the freezing behaviors of molten metal during severe accidents of LBE-cooled systems. First, a series of molten-metal freezing experiments was performed to figure out basic characteristics in freezing mode of molten metal onto metal structures. Second, physical modeling for experimental analysis using SIMMER-III was considered to represent the freezing behaviors of molten metal during penetrating onto the metal structures. Verification of the models and methods for the numerical simulation of the observed freezing behaviors of molten metal was also conducted by the experimental analyses.

The major phenomena investigated in this study were melt freezing and debris formation in the coolant, and melt freezing and adherence onto the structure. The present analytical model for the freezing phenomena of molten metal represents the heat and mass transfer among molten metal, metal structure and coolant. The modeling concept of molten-metal freezing behaviors for SIMMER-III is illustrated in Fig. 6. The molten metal flowing on the cold metal structure will lose its heat due to their contact. This will lead to the melt freezing and adherence onto the structure as a crust. In addition, molten metal solidified in fluids is treated as solid particles, which come to debris observed in the experiments. The coolant may significantly contribute to solid-particle formation if there is large heat transfer from the melt to the coolant. In the present experimental analyses using SIMMER-III, these expected freezing behaviors of molten metal were considered based on the heat- and mass-transfer model of SIMMER-III [22].

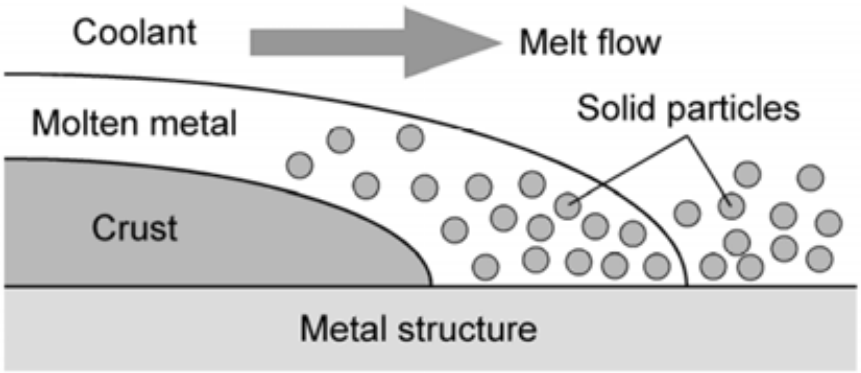

FIG. 6. Modeling concept of molten-metal freezing behaviors.

In the experiments, molten Wood's metal, of which melting point is 78.8°C, as a simulant melt was ejected through a circular nozzle by gravity onto an L-shaped metal structure in a bath filled with stagnant coolant. The structure with 5-mm thickness and 80-cm length was inclined at an angle of 72.5 degree. Two types of nozzles with 1.9-mm and 2.2-mm inner diameter were used to eject the molten metal with different melt flow rates (hereafter, 'N.D.' means the inner diameter of the nozzle). The experiments were conducted to observe the freezing phenomena with different structure materials, stainless steel and brass, in air and water coolant systems. The main experimental conditions are summarized in Table 7.

TABLE 7. SUMMARY OF EXPERIMENTAL CONDITIONS

	Air			Water		
	Coolant temperature	Nozzle diameter (flow rate)	Ejected mass (duration)	Coolant temperature	Nozzle diameter (flow rate)	Ejected mass (duration)
Stainless steel	17 °C	1.9 mm (51.5 g/s)	335 g (6.5 s)	20, 35 and 52 °C	1.9 mm (50.5 g/s)	338 g (6.7 s)
		2.2 mm (60.1 g/s)	337 g (5.6 s)		2.2 mm (59.7 g/s)	340 g (5.7 s)
Brass	17 °C	1.9 mm (51.5 g/s)	335 g (6.5 s)	20, 35 and 52 °C	1.9 mm (50.5 g/s)	338 g (6.7 s)
		2.2 mm (60.1 g/s)	337 g (5.6 s)		2.2 mm (59.7 g/s)	340 g (5.7 s)

The experimental setup is shown in Fig. 7. In the cases of the water coolant experiments, the freezing phenomena were investigated at different initial temperatures of the water. The air coolant experiments were performed under room temperature conditions. In both air and water experiments, the initial melt temperature was controlled within the range of 102-105°C. The melt flow and the freezing behaviors were observed with a high-speed video camera.

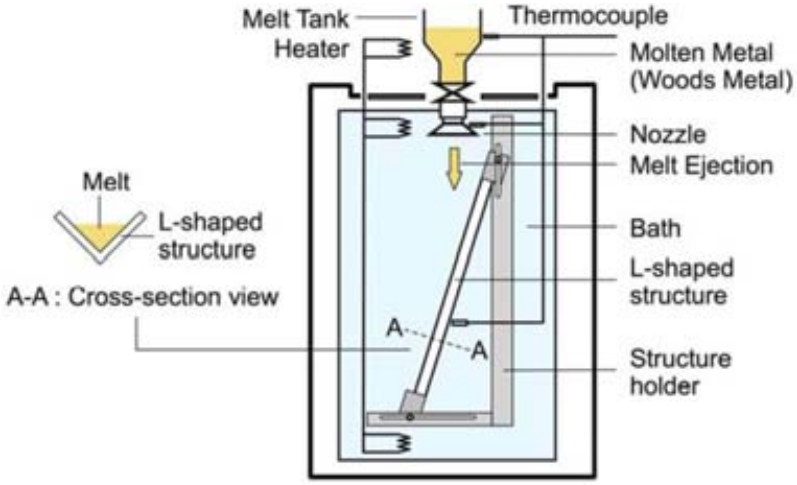

FIG. 7. Schematic view of experimental setup.

Comparisons of transient penetration length between experiment and SIMMER-III simulation are shown in Figs 8 and 9 for the air system and Figs 10 and 11 for the water system. Here, the penetration length is defined as the length of the metal adhered on the structure. Experimental results indicated a bit longer penetration length on the stainless steel structure than on the brass due to the lower thermal conductivity of stainless steel than that of brass. Simulation results of the experimental analyses showed fairly good agreements in the cases of air coolant experiments. On the other hand, under the water coolant conditions, the results suggested that melt cooling was enhanced by effective increase of the contact area between melt and water. The simulation results on the freezing rates of solid formation also indicated that not only crust formation on the metal structure but also particle formation at melt and coolant contact dominated the freezing process. Study of effects of particle formation on melt penetration length suggested that SIMMER-III will overestimate the melt penetration if the particle formation at melt and coolant contact is not considered in the simulation.

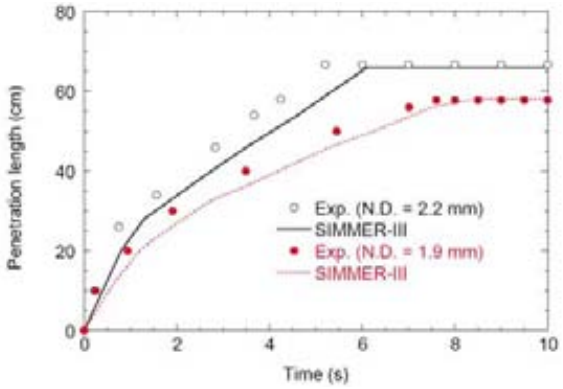

FIG. 8. Transient penetration length of Wood's metal on stainless steel structure in air coolant system.

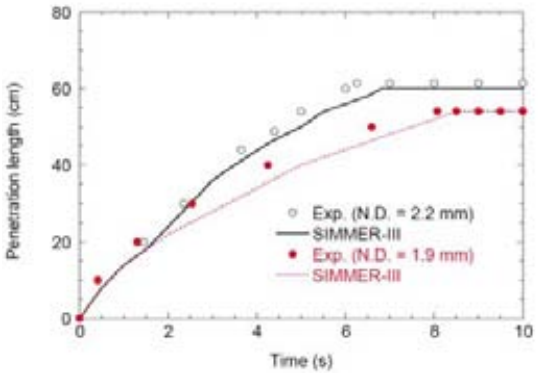

FIG. 9. Transient penetration length of Wood's metal on brass structure in air coolant system.

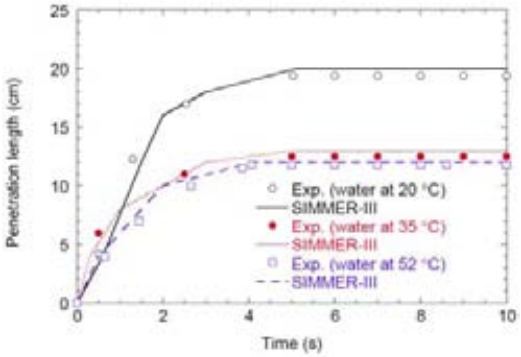

FIG. 10. Transient penetration length of Wood's metal on stainless steel structure in water coolant system (N.D. = 2.2 mm).

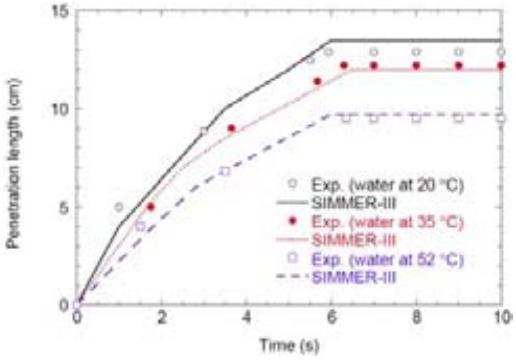

FIG. 11. Transient penetration length of Wood's metal on brass structure in water coolant system (N.D. = 2.2 mm).

Photographs of typical frozen metal observed in the experiments are shown in Figs 12 and 13 for the air and water systems, respectively. In the experiments, a significant amount of particles was formed as debris in the water coolant conditions, whereas in the cases of air coolant most of the frozen metal was adhered on the structure with less particle formation. The formation of debris observed in the water coolant system was due to the high heat transfer of molten metal to water. Figures 14 and 15 show the transient mass distribution of SIMMER-III simulation results for stainless-steel structure in presence of air and water coolant, respectively. These figures indicate that the simulated characteristics of the molten-metal freezing are also in good agreement with experimental observation mentioned above. The present simulation results represent that crust and debris formations are an important sequence of freezing behaviors that contributes to melt quenching and blockage formation in flow channels.

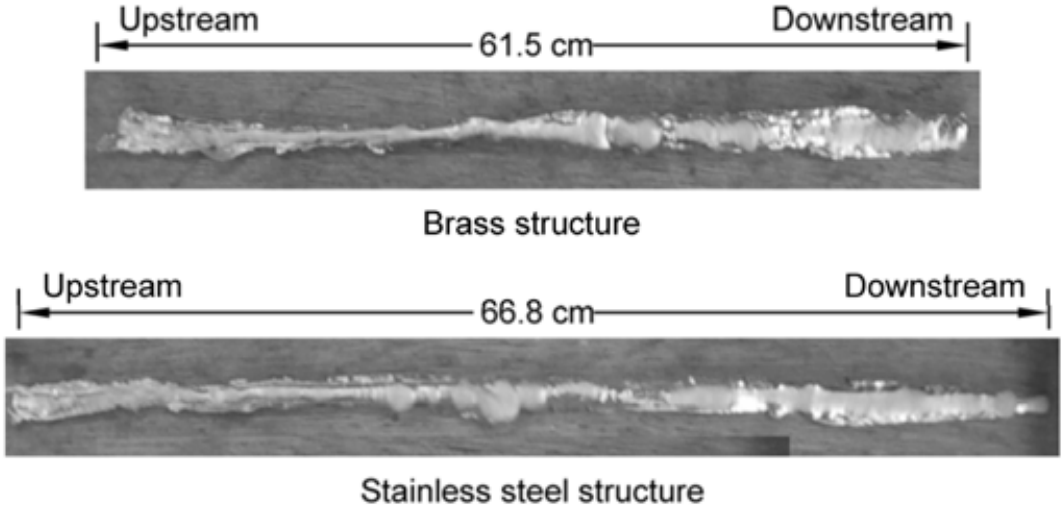

FIG. 12. Photographs of frozen metal adhered on structures in air coolant experiments (N.D. 2.2 mm).

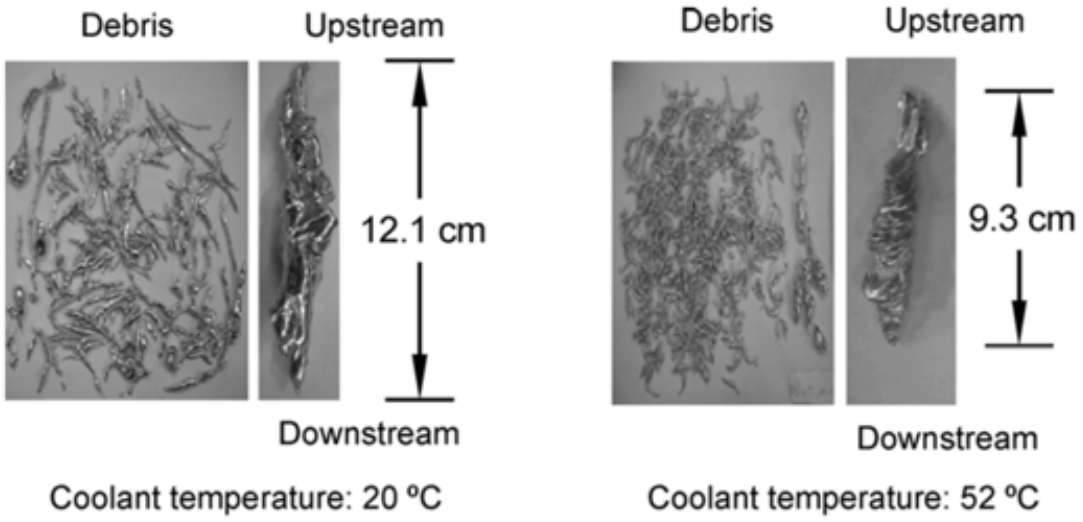

FIG. 13. Photographs of frozen metal into debris and adhered on brass structure in water coolant experiments (N.D. 1.9 mm).

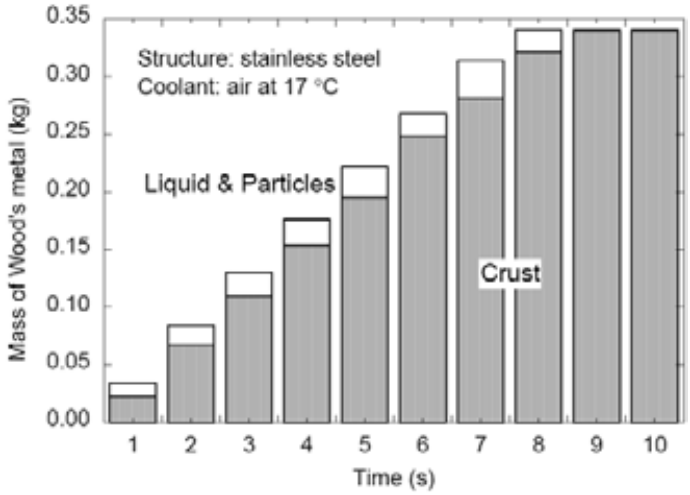

FIG. 14. Transient mass distribution of Wood's metal in air coolant system (the melt flow rate corresponds to that of 1.9 mm N.D. in the experiment).

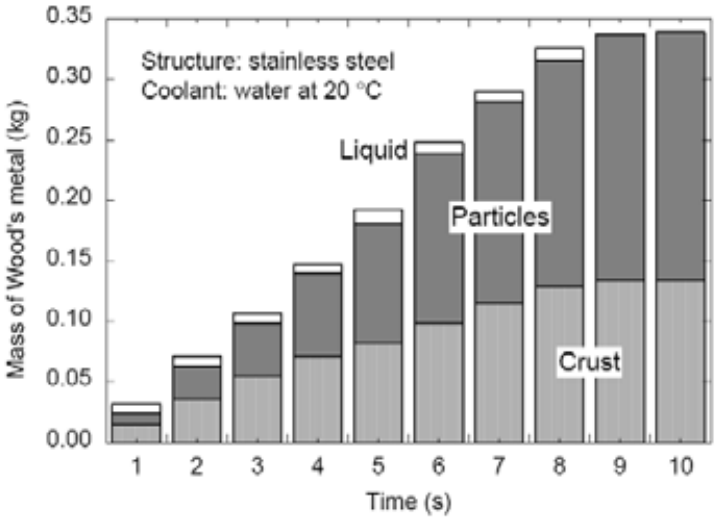

FIG. 15. Transient mass distribution of Wood's metal in water coolant system (the melt flow rate corresponds to that of 1.9 mm N.D. in the experiment).

In this work, a series of fundamental experiments on freezing behaviors of molten metal on metal structures was conducted to verify SIMMER-III. Experimental analyses using SIMMER-III show good agreement with the characteristics of the molten-metal freezing observed in air and water coolant systems. This demonstrates that the basic physical modeling considered for SIMMER-III reasonably represents the freezing behaviors of molten metal during penetrating onto the metal structures. For future work, extended experiments considering geometrical conditions of flow channels in conventional reactors will be performed for more general code verification.

6.3.2.4. SIMMER EOS model for the LBE coolant

The SIMMER EOS model for LBE was improved for the high pressure/temperature domain. LBE vapor is assumed to consist of Pb, Bi and the Bi2, the dimerization of Bi vapor component being taken into account in the EOS derivation. A non-ideal mixture of Pb and Bi in the alloy is assumed that takes into account different Pb and Bi activities. Equation-of-state modeling is based on the theoretical evaluation of the saturation vapor pressure curve, while applying a van-der-Waals type equation for a reacting system (thus taking into account the Bi dimerization). A theoretical estimation of the critical constants has been done, the results being shown in Table 8 (see Figs 16 and 17).

TABLE 8. SUMMARY OF MAJOR PARAMETERS FOR SIMMER EOS FOR LBE

	Present EOS	Remarks
Melting temperature (Tm)	398.15 K	125 °C by Lyon (1952)
Liquid density at Tm	10529 kg/m3	Linear fit by Alchagirov et al. (2003)
Normal boiling point (Tb)	1944 K	1943 K at 98.066 kPa (Russian data)
Heat of vaporization at Tb	713 kJ/kg	182 kJ/mol
Critical temperature	4890 K	Based on generalized van der Waals equation (Martynyuk, 1998)
Critical density	2170 kg/m3	
Critical pressure	87.8 MPa	
Critical compressibility	0.21	

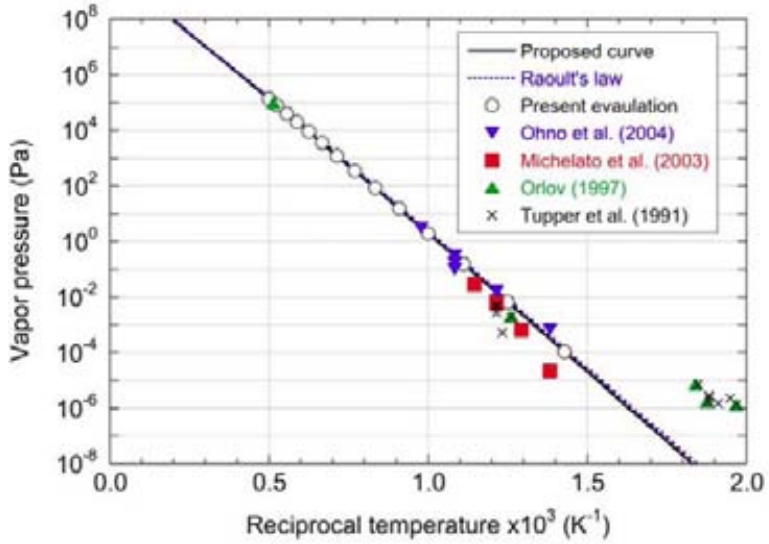

FIG. 16. Proposed vapor pressure curve of saturated LBE.

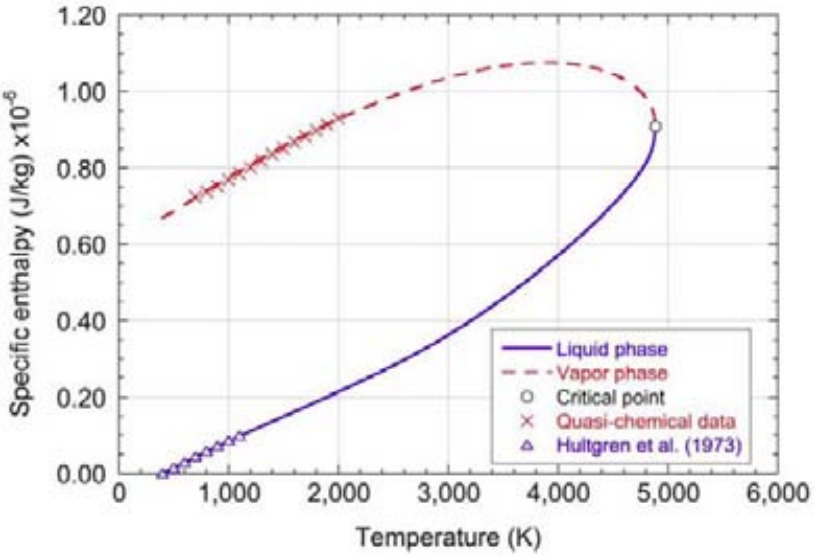

FIG. 17. Specific enthalpy of vapor and liquid LBE on the saturation curve.

6.3.2.5. SIMMER EOS models for dedicated fuels

These models have been developed under the following general assumptions. An ideal mixture of oxide-fuel and matrix components is assumed that implies simulation for a single material component and application of the additivity rule to the mixture. Extrapolation of the MOX data for vapor and liquid phases is assumed to be relevant and representative for the dedicated fuel (Fig. 18). A special treatment for the composite fuel is done with respect to taking into account the eutectic formation that leads to a lowered melting point (i.e. eutectic point) of CERCER with MgO. The effective thermal conductivity is modeled for a fuel mixture, where lower conductivity fuel particles are embedded into a high conductivity matrix (Fig. 19). The summary of advanced fuel properties is given in Table 9.

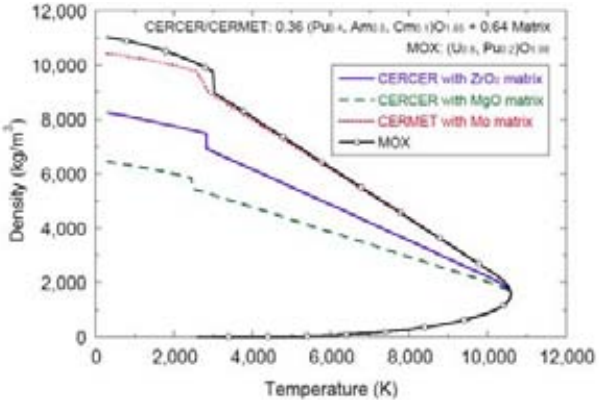

FIG. 18. Solid, liquid and vapor densities of advanced fuels compared to MOX fuel.

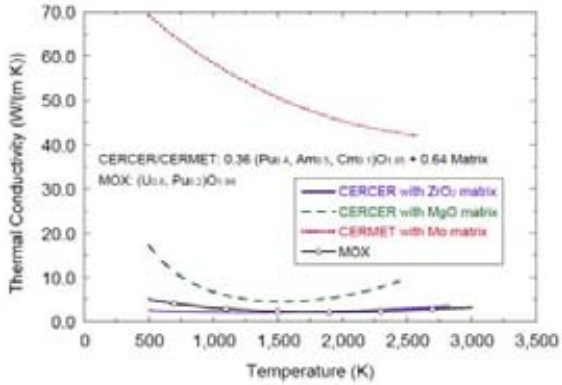

FIG. 19. Thermal conductivities of advanced fuels in the solid state, compared to MOX fuel.

TABLE 9. SUMMARY OF ADVANCED FUEL PROPERTIES

TRU Fuel	$(Pu_{0.4}, Am_{0.5}, Cm_{0.1})O_{1.85}$		
Melting point (estimation)	2588 K		
Conductivity at 1500 K (estimation)	1.8 W/(m K)		
Matrix	ZrO_2	MgO	Mo
Melting point	2950 K	3250 K	2896 K
Conductivity at 1500 K	2.3 W/(m K)	6.6 W/(m K)	97.3 W/(m K)
Advanced fuel (fuel : matrix = 0.34 : 0.64)	CERCER (solid solution)	CERCER (composite)	CERMET (composite)
Melting point (estimation)	2835 K	2442 - 2483 K *	2588 - 2896 K
Conductivity at 1500 K (estimation)	2.1 W/(m K)	4.5 W/(m K)	50.7 W/(m K) *
Remarks		* Eutectic formation	* Effective thermal conductivity

6.3.2.6. SIMMER gas-blowndown and gas-LBE two-phase flow models

The current ADSs with dedicated fertile-free fuels have positive core void worths. Due to LBE's high boiling point, coolant boiling is hardly possible during the initial phase of a hypothetical accident. However, He/fission-gas blowout may trigger a voiding process after local pin failure/failure propagation. The gas-blowout model based on the SAS4A code [21] has been introduced and improved. The gas-LBE two-phase flow model has also been introduced to represent the voiding behavior in LBE-cooled reactors

6.4. Static an steady-state analyses

6.4.1. *Neutronics calculations*

Four data libraries were employed at FZK to compute the k-eff and total core void effect values (though the core may hardly be voided completely, the void effect value is an important parameter that shows the magnitude of reactivity effects in a hypothetical accident that may occur due to pin-failure followed by He/fission gas blowout into the LBE coolant). The results are given in Table 10. The 11-group calculations were performed with the SIMMER code, the 30-group calculations with ZMIX and DANTSYS codes. One may observe significant deviations between results based on different nuclear data. The k_{eff} values related to the 11-group and JEF 2.2 data are significantly (more than 1000 pcm) higher than those related to the JEFF 3.0 and JENDL 3.3 libraries. The void effects exhibit an opposite trend: they are significantly lower in the 11-group/JEF 2.2 cases. The influence of data for particular groups of nuclides is investigated in Tables 11 and 12. In Table 11, the results are obtained with JEF 2.2 data partly replaced by JENDL3.3-based ones for (1) for the Am and Cm isotopes; (2) the Am, Cm, and Pu isotopes; (3) the Am, Cm, Pu, Pb and ^{209}Bi isotopes.

TABLE 10. k_{eff} AND TOTAL CORE VOID EFFECT VALUES

Data library	MgO k-eff/void(pcm)	ZrO_2k-eff/void (pcm)
11 groups	0.97162/6542	0.96706/6594
JEF 2.2, 30 groups	0.96738/6421	0.96297/6385
JEFF 3.0, 30 groups	0.94490/8399	0.95037/7700
JENDL 3.3, 30 groups	0.93982/8337	0.94374/7792

TABLE 11. k_{eff} AND TOTAL CORE VOID EFFECT VALUES OBTAINED FOR JEF 2.2 AND JENDL 3.3 DATA

Replacement in JEF 2.0 data library	MgO k-eff/void(pcm)	ZrO_2k-eff/void (pcm)
Reference; No replacement	0.96738/6421	0.96297/6385
Am,Cm from JENDL 3.3	0.96078/6364	0.95769/6426
Am,Cm,Pu from JENDL 3.3	0.96430/6582	0.96116/6611
Am,Cm,Pu,LBE from JENDL 3.3	0.94466/8134	0.94459/7887

One may note that the main reason for deviations between results based on JEF 2.2 and JENDL 3.3 is due to the LBE nuclear data: replacement by the JENDL 3.3 LBE data leading to increasing of the void effect and decreasing k_{eff} appreciably (more than 1000 pcm). Replacement of data for all TRUs leads to relatively small variations of the parameters, partly because of the compensation of effects of replacement of data for MA and for Pu isotopes.

The results for combinations of JEFF 3.0 and JENDL 3.3 data are given in Table 12. Compared to the previous case, the replacement of the JEFF 3.0 LBE data by the JENDL 3.3 ones leads to much smaller (by magnitude) and different (by sign) variations of the parameters. Replacement of the TRU data leads to and opposite effect compared to the LBE data replacement. That is why the results based on JEFF 3.0 and JENDL 3.3 data are similar.

The results shown in Tables 10-12 are obtained by assuming homogenized media in each S/A, for a relatively small number of energy groups (11 or 30), using isotropic scattering cross-sections and Sn order of 4. The heterogeneity effects are evaluated to be relatively (compared to the void effect) small (less than 500 pcm) in the ADS cores with dedicated fuel. The influence of more refined discretization schemes in energy and angle is shown in Table 13, the values being obtained with JEFF 3.0 data for the MgO core.

TABLE 12. k_{eff} AND TOTAL CORE VOID EFFECT VALUES OBTAINED FOR JEFF 3.0 AND JENDL 3.3 DATA

Replacement in JEFF 3.0 data library	MgO k-eff/void(pcm)	ZrO_2k-eff/void (pcm)
No replacement	0.94490/8399	0.95037/7700
Am,Cm from JENDL 3.3	0.94230/8352	0.94523/8030
Am,Cm,Pu from JENDL 3.3	0.94009/8411	0.94240/8152
Am,Cm,Pu,LBE from JENDL 3.3	0.94022/8334	0.94576/7726

TABLE 13. INFLUENCE OF REFINED CALCULATION SCHEMES ON k_{eff} AND TOTAL CORE VOID EFFECT IN THE MgO CORE

Refinement option	K-eff variation	Void effect variation (pcm)
560 group instead of 30 group	0.0248	-522
P3S16 instead of P0S4	-0.0109	-112

The combined effect of refined (in energy and angle) calculation techniques on k_{eff} is small, the total effect being less that 150 pcm. The void effect is reduction is more significant, being between 600 and 650 pcm, but not exceeding 10 per cent of the calculated effect. In total, refinement of the calculations scheme (with respect to the heterogeneity effects, energy and angle discretization) would most probably decrease the void effect by 10 to 15 per cent, and increase the core reactivity by a value between 500 and 1000 pcm, not exceeding the corresponding uncertainties due to nuclear data.

The presented results show that the SIMMER neutronics model and the 11-group data library offer a reasonable basis for performing transient analyses for the ADSs with dedicated fuel considered in the CRP. One may hardly benefit from more elaborate neutronics models in view of relatively high uncertainties in the basic nuclear data and lack of corresponding experimental data.

Although the uncertainty of the k_{eff} values is relatively high, we may assume that the nominal value is close to 0.97 because of design constraints (that implies that the TRU isotopic vector and/or volume fractions of fuel/matrix can be slightly modified to meet this value). The uncertainties of the void effect values may influence the results of transient simulations appreciably. We may assume, however, that if the 'SIMMER' void effect values (which are already quite high) are exceeded in reality (that we assume to be hardly possible), modifications in the fuel isotopic composition (or other design measures) should be considered: to keep the void effect below a certain value.

The void effect is very large due to high MA content. Since the fission cross-section of the considered MA mixture is relatively small at thermal and intermediate energies, but relatively large at high energies (at 0.1 MeV and higher); the spectral component of the void effect (related to hardening of neutron spectra due to voiding) is very large. The leakage component (increasing of neutron leakage), that is an important contributor to the coolant void effect in conventional fast reactors, plays in this case only a minor role compared to the spectral one. That leads to the large positive coolant void effect. Thus, the inert matrix itself plays a minor role with respect to the void effect. The preliminary evaluations show that the effect would be even higher (by about 10%) if the inert matrix were replaced by the depleted UOX.

The clad removal effect (due to hypothetical replacement of steel by lead) was evaluated by SIMMER, the effect being 3117 pcm for the ZrO_2 core, 2913 pcm for MgO, e.g. about 50% of the coolant void effect.

The Doppler constant was computed (assuming a 1/T dependence) by employing the SIMMER code and 11-group data. The corresponding results are given in Table 14. The inert matrix itself is not the main reason for the low absolute value. Preliminary evaluations show that the Doppler constant would be near -100 pcm: if the matrix were replaced by the depleted UOX. That is also a quite small value. The reason is the low importance of neutrons at 'resonance' energies due to high threshold fission.

Beta-eff values were computed at FZK by employing 30-group the JEFF 3.0 cross-sections and JENDL 3.3 delayed neutron data (since JENDL 3.3 includes delayed neutron data for the largest number of MAs) by employing ZMIX, DANTSYS, and a post-processing code. Isotope contributions to the total β_{eff} value for the MgO core are shown in Table 15. The generation time is about 0.5 μs in both cores.

TABLE 14. β_{eff} AND DOPPLER EFFECT VALUES

Parameter	ZrO_2 core	Mg core
beta-eff, pcm	192	191
Doppler constant, pcm	–17	-19

TABLE 15. ISOTOPE CONTRIBUTIONS TO THE TOTAL β_{eff} VALUE

Isotope	Contribution (%)
Pu238	2.1
Pu239	28.8
Pu240	8.0
Pu241	35.3
Pu242	5.4
Am241	8.6
Am243	5.8
Cm244	3.3
Cm245	2.7

Although the neutron spectrum in the ADS is not much harder than in conventional fast reactors, the 'effective' fraction (that takes into account the neutron importance) of high- energy neutrons is much larger, because a larger fraction of fission events occuring at high energies due to contribution of MA fission with a lower fast fission threshold compared to ^{238}U. Because of (1) the small 'effective fraction' of low-energy neutrons, (2) absence of fertile nuclei, and (3) the fact that the Doppler effect is caused by increasing (with temperature increase) of resonance neutron absorption (that is a negative component) and fission (that is a positive component) of heavy nuclei at lower energies, the Doppler constant is close to zero. Relatively small beta-eff values are due to two reasons: (1) small delayed neutron fractions (beta values) for MAs and (2) softer spectra of delayed neutrons compared to prompt fission ones. The second reason is quite significant: due to the relatively small neutron importance at low energies, the importance-weighted β_{eff} values are significantly lower (by ca. 30%) than beta-sum ones obtained as a simple sum of non-weighted data). This very low beta-sum to $beta_{eff}$ ratio is a particular feature of reactors with high MA content and fast neutron spectrum. Replacement of the inert matrix by the depleted UOX would not change the value appreciably: it would increase by about 15% only.

Additional analyses of criticality, void reactivity effects and burnup performance were performed with new nuclear data evaluated data libraries, such as JEFF 3.1 and ENDF/B-7 at the last phase of investigations. They show that the JEFF 3.1-based k_{eff} and void effect values are close to those obtained with the 11-group library (see Table 10), while the ENDF/B-7-based values are close to those obtained with JEF 2.2.

The burnup performance of both ADS (with MgO and ZrO_2 inert matrices) is quite similar due to the same actinide compositions at BOL and similar fast neutron spectra. The reactivity decreases after 3 years by ca. 4600 pcm in the MgO case and by ca. 4700 pcm in the ZrO_2 case. The reactivity is reduced by about a half of this value after the first 6 months of irradiation.

These burnup analyses results are based on applying JEFF 3.1 nuclear data, including principal cross sections, activation cross-section (including branching ratios), fission product yield and decay data libraries. It should be mention that uncertainties in branching ratios for the ^{241}Am neutron capture reaction (the product of this reaction is either ^{242}Am or ^{242m}Am, the branching ratios being the related probabilities) may affect this result appreciably. Alternative branching ratios as applied by CEA in Domain VII would lead to a smaller reactivity variation (see the Domain VII report for more details). The mass variations for U, Np, Pu, Am, and Cm (4 years means: 3 years irradiation at 580 MW(th) +1 year cooling; 6 years means: 3 years irradiation + 3 years cooling) in reactor fuel are given in Tables 15 (MgO case) and 16 (ZrO_2 case). In the burnup calculations the decay heat is ignored, that means that the reactor power including decay heat was assumed to be higher than 580 MW(th) by a few percents.

TABLE 16. MASS VARIATIONS FOR U, Np, Pu, Am, AND Cm (IN kg PER TWh(th)) IN THE FUEL WITH THE MgO INERT MATRIX: AFTER IRRADIATION AND COOLING

Time (years)	U	Np	Pu	Am	Cm
3	0.3	0.3	-7.0	-46.4	10.1
4	0.4	0.4	-3.2	-46.1	5.7
6	0.8	0.6	-1.5	-45.5	2.8

TABLE 17. MASS VARIATIONS FOR U, Np, Pu, Am, AND Cm (IN kg PER TWh(th)) IN THE FUEL WITH THE ZrO_2 INERT MATRIX: AFTER IRRADIATION AND COOLING

Time (years)	U	Np	Pu	Am	Cm
3	0.3	0.4	-7.0	-46.3	9.8
4	0.5	0.5	-3.1	-45.9	5.1
6	0.8	0.8	-1.3	-45.1	1.8

Both systems are essentially Am burners (while the TRU burning efficiency being ca 43 kg per TWh, the Am burning efficiency being ca. 45 kg per TWh, mass variations of other heavy elements after three years of irradiation and one or more years of cooling being a few kg or less per TWh), similar to other solid fuel fertile-free ADS designs investigated currently worldwide.

Unlike k_{eff} and reactivity effect calculations, the flux calculations for the burnup analyses and for safety analyses reported in the following were performed by solving an external source problem. The cross-sections that characterize interaction of high-energy neutrons (above 20 MeV) with nuclei were assumed to the same as the cross-sections in the first energy group (with the upper boundary up to ca. 20 MeV). This approximation was employed due to absence of high-energy data for some nuclides in the available multi-group data libraries. Since the fraction of the high-energy neutrons is of the order of 10% (with respect to all spallation neutrons) or less (due to their moderation in the target region) and all spallation neutrons constitute ca. 3% of the total (spallation and fission) neutron source (when

k_{eff} is close to 0.97), this approximation does not affect appreciably the spatial distributions of power and other reaction rate profiles in the core, that is indirectly confirmed by benchmark calculations performed in the past. The integral reaction rate values are even more accurate as they are mainly determined by the flux level that is normalized to with respect the specified reactor power, an input parameter (therefore, this approximation does not affect the total power, one of integral reaction rates). These considerations do not undermine the importance of high-energy data that are needed for e.g. obtaining the accurate beam current value. However, the beam current value is not involved in the performed analyses explicitly (contrary to the power and reactions rate profiles) as the target is assumed to be cooled independently upon the core and the heat produced in the target is not taken into account while performing core analyses.

6.4.2. *Thermal-hydraulics core description at steady-state*

Coupled thermal-hydraulics and neutronics calculations were performed for the steady-state conditions with SIMMER. The results for the ZrO_2 core are shown in Figs 20-22. The corresponding results for the MgO core are shown in Figs 23-28.

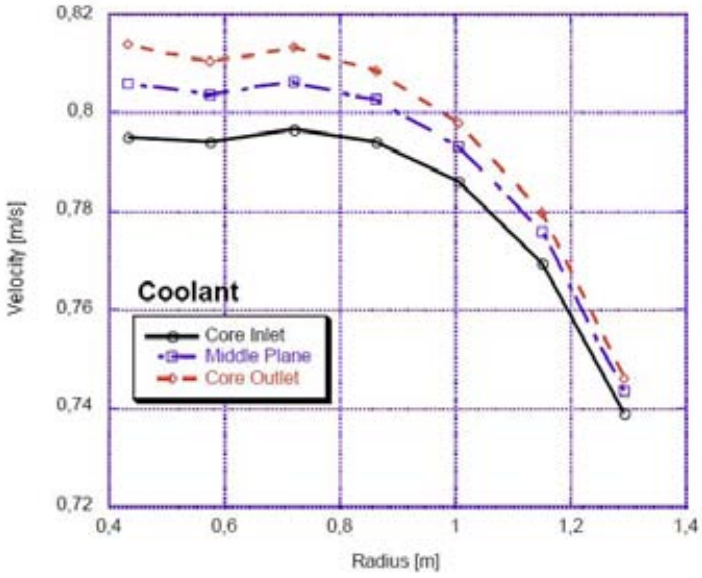

CSA 200741434

FIG. 20. Coolant velocity distribution in the ZrO_2 core.

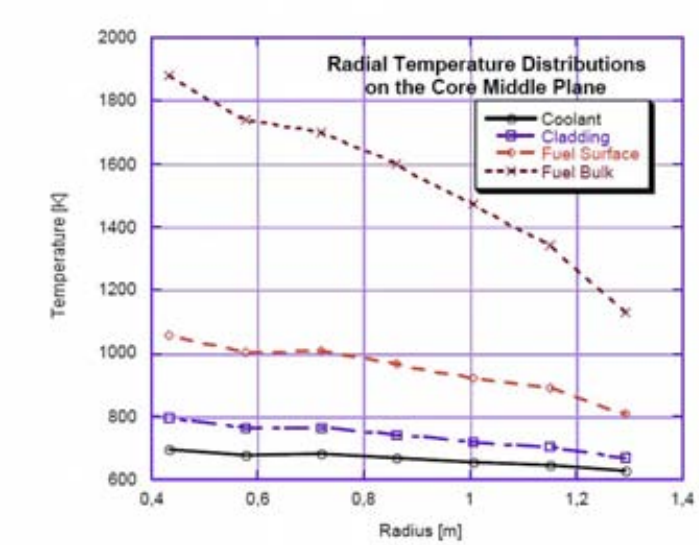

FIG. 21. Radial temperature distributions on the ZrO_2 core mid-plane.

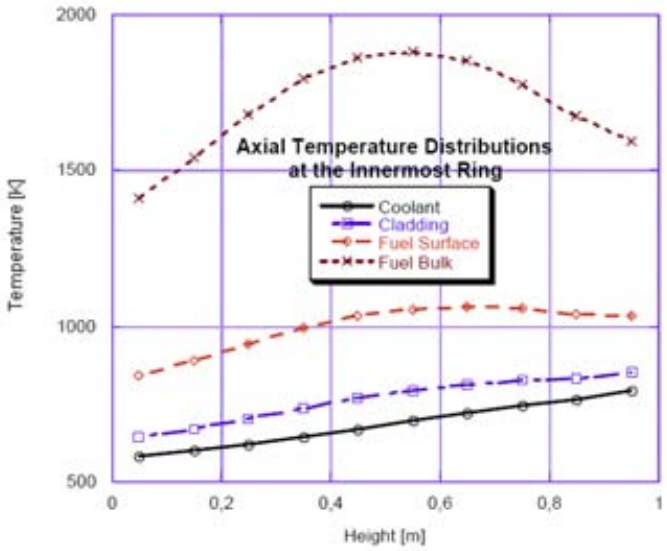

FIG. 22. Axial temperature distributions at the ZrO_2 core innermost fuel ring.

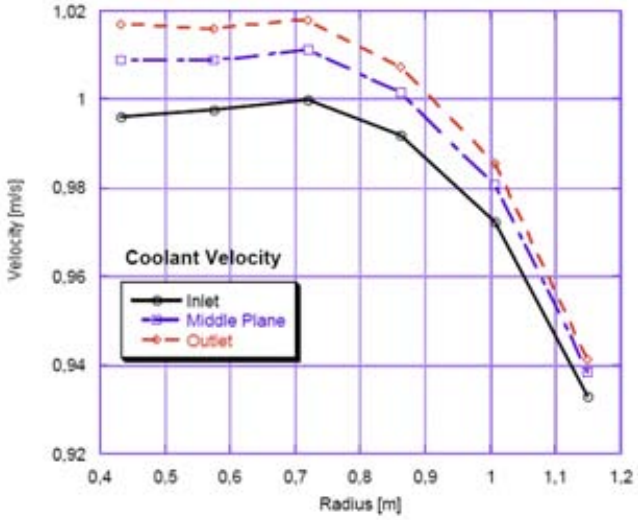

FIG. 23. Coolant velocity distribution in the MgO core.

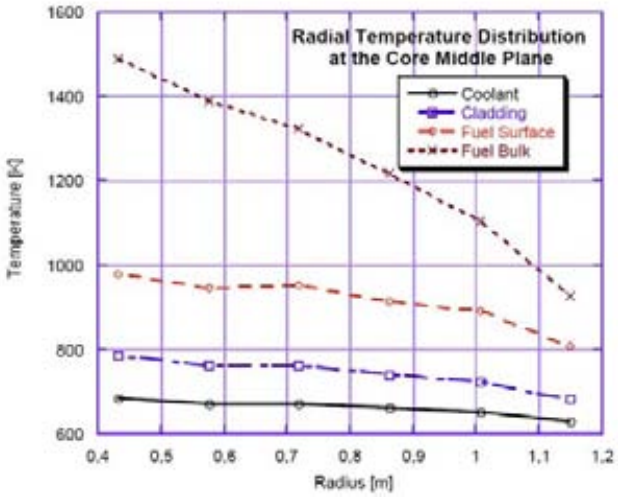

FIG. 24. Radial temperature distributions on the MgO core mid-plane.

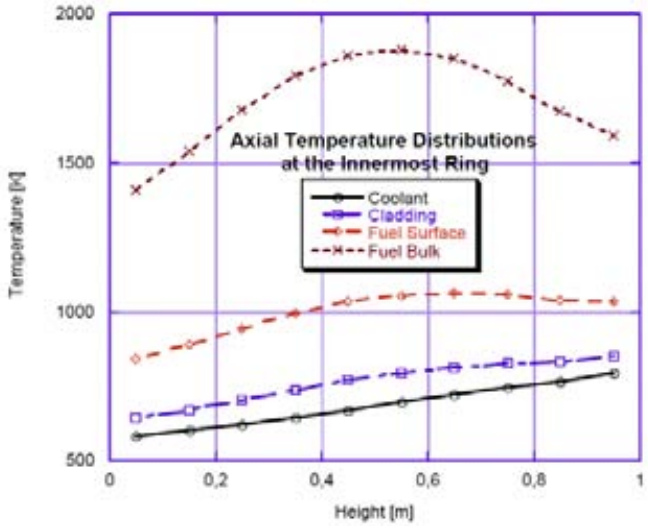

FIG. 25. Axial temperature distributions at the MgO core innermost fuel ring.

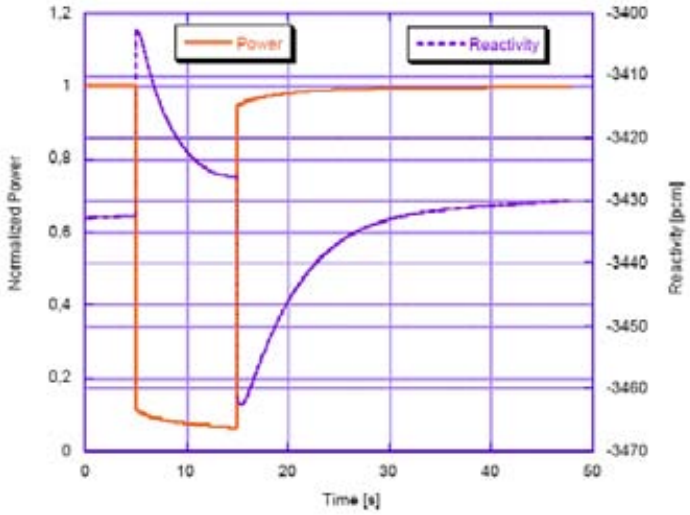

FIG. 26. Power and reactivity traces during a beam trip transient (ZrO_2).

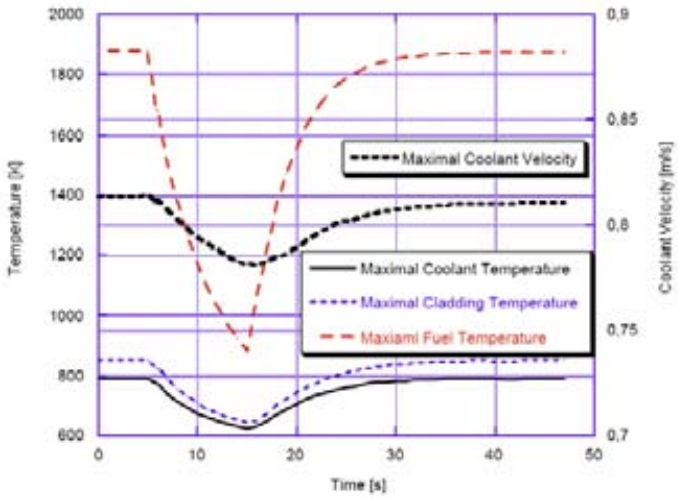

FIG. 27. Temperature distribution and coolant velocity during a beam trip transient (ZrO_2).

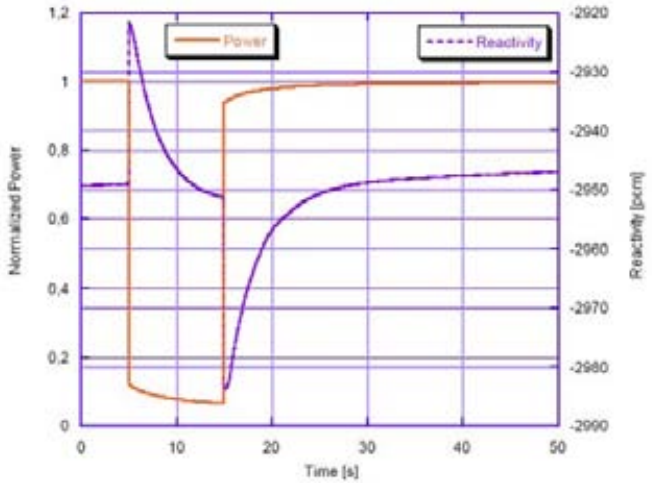

FIG. 28. Power and reactivity traces during a beam trip transient (MgO).

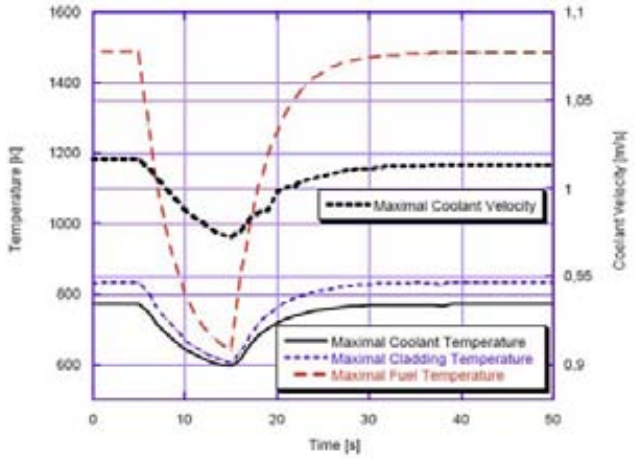

FIG. 29. Temperature distribution and coolant velocity during a beam trip transient (MgO).

The results shown in Figs 20-25 are obtained for systems in which the peaking of the neutron flux in the innermost fuel ring and core mid-plane is more pronounced (compared to conventional critical reactors) due to the influence of the 'external' neutron source. However, employing of a 'buffer' region around the target and of several fuel zones helps to reduce the peaking in the power shape and leads to the acceptable thermal-hydraulics profiles at nominal conditions.

6.5. Transient analyses

Compared to fast reactors studied in the past, the investigated systems are characterized by a nearly missing Doppler feedback and a strong positive void worth. A local void may occur in the system after pin-failure due to He/fission-gas blowout into the coolant, thus increasing the core reactivity. Therefore, transient analyses are important to prove the system safety.

The studies presented in this chapter have been done at FZK. Behavior of the ADS cores - with ZrO_2-matrix solid-solution fuel and MgO-matrix CERCER fuel — under transient conditions has been investigated. In particular, the following accidental transients have been simulated: beam trip transient, transient over current (TOC), unprotected transient overpower (UTOP), unprotected loss of flow (ULOF) and unprotected blockage accident (UBA). 'Unprotected' in the ADS case means no shutdown of the beam coming from the accelerator. For simulating the transients, one set of fuel EOS (corresponding to the fuel fraction of 45%) is applied for 3 fuel zones (40, 45 and 50%, respectively, of fuel content). The gas-blowout criterion temperature is set to 1330 K (the He/fission-gas blowout may start already at 400 K below the melting point of the cladding in relation to a burst-pressure criterion).

6.5.1. *Beam trip transient*

A beam interruption from 5 to 15 s was assumed. This type of transients may occur relatively often: the reliability of the accelerator is still one of the key issues for ADS development. The results of the transient simulation for the core with ZrO_2 matrix are shown in Figs 26 and 27.

After the beam interruption, the power decreases to a level of about 12%. This value is ca. 50% higher (due to presence of the delayed neutron precursors, the 'prompt' fission takes place for some time after beam shut-down) than the value attributed only to the decay heat release (assumed to be 7% in this case, the actual level depends upon the accumulated amount of ^{242}Cm, that appears mainly due to capture of neutrons by ^{241}Am and decay of a product of this reaction, ^{242}Am). Nothing severe occurs in the core, the only concern being the relatively sharp fuel temperature variation. This variation by about 1000 K may influence the fuel performance with respect to its long term operation. The cladding temperature stays far from the gas-blowout criterion. Qualitatively similar results were obtained for the core with MgO inert matrix, these results being shown in Figs 28 and 29.

6.5.2. *Transient over current*

A beam increase by 100% was assumed. This type of transients may occur at BOL if the beam current at BOL is equal to e.g. 50% of its foreseen value at end of fuel cycle (EOC) conditions. A higher current should be foreseen for EOC if the core reactivity goes down significantly with burnup, but the power should stay at the same level. The results of the transient simulation for the core with ZrO_2 matrix are shown in Figs 30 and 31.

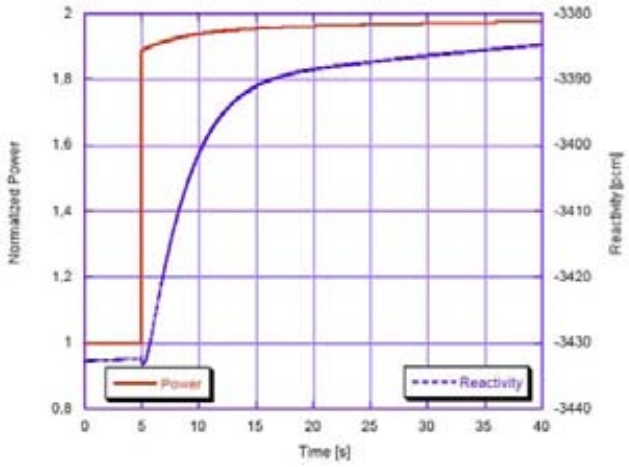

FIG. 30. Power and reactivity traces during TOC (ZrO_2).

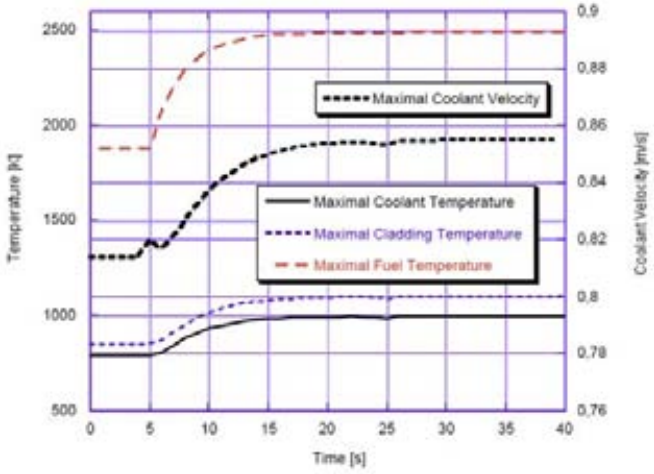

FIG. 31. Temperature distribution, coolant velocity during TOC (ZrO_2).

After 100% beam increase, the core power promptly increases by 95% (not by 100% due to the role of the decay heat and delayed neutron source, which are fairly inertial). Then the power increases relatively slowly due to the slow decay heat and delayed neutron source variations as well as the reactivity variation. The latter is due to the coolant density reduction that occurs because the coolant temperature increases. After several tens of seconds all parameters (power, coolant temperature, reactivity, etc.) reach a new higher level at which they may stay for a long time if no perturbation occurs. The fuel temperature approaches 2500 K, which is still lower than the fuel melting point (≈2730 K). The notable increase of the coolant temperature is significant, but the cross-averaged coolant temperature is still lower than the corrosion limit of LBE. During this transient, nothing severe occurs in the core. Similar results were obtained for the core with MgO inert matrix, these results being shown in Figs 32 and 33.

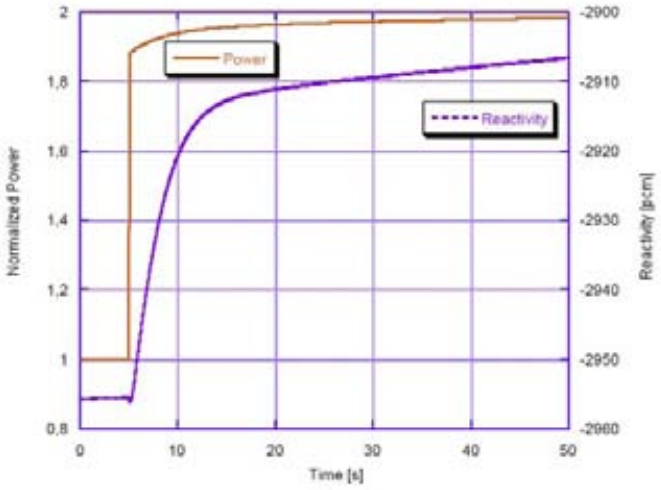

FIG. 32. Power and reactivity traces during TOC (MgO).

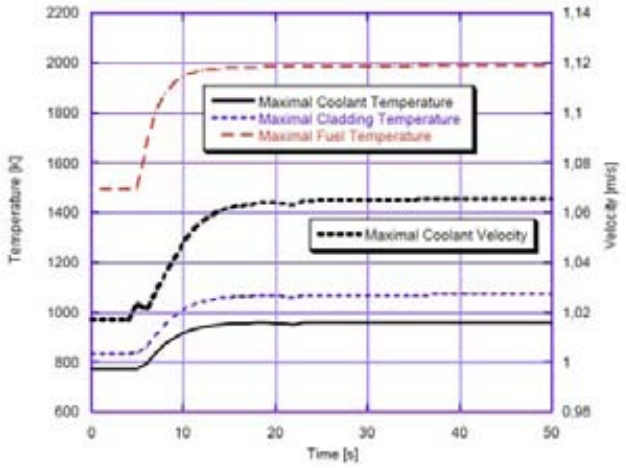

FIG. 33. Temperature distribution, coolant velocity during TOC (MgO).

6.5.3. *Unprotected transient overpower*

In this case, one assumes an instant insertion of a positive reactivity increment into the core resulting in a 'prompt' reactivity jump of 5$ (ca. 950 pcm). The results of the transient simulation for the core with ZrO_2 matrix are shown in Figs 34 and 35.

Due to the low k_{eff} value, the core remains subcritical. The corresponding power variation is limited thus demonstrating the desirable features of ADSs. The increase of the fuel and the cladding temperatures is moderate. No pin failure is observed. During this transient, nothing severe occurs in the core. Similar results were obtained for the core with MgO inert matrix, these results being shown in Figs 36 and 37.

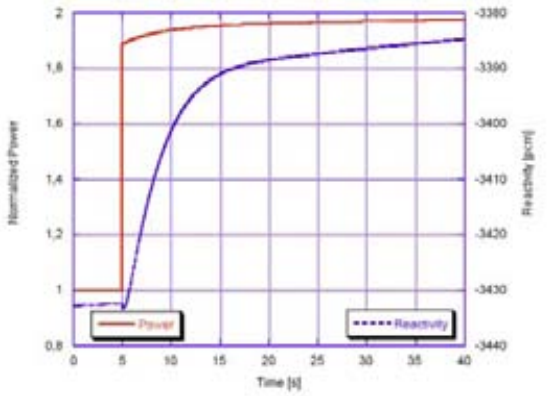

FIG. 34. Power and reactivity traces during UTOP (ZrO_2).

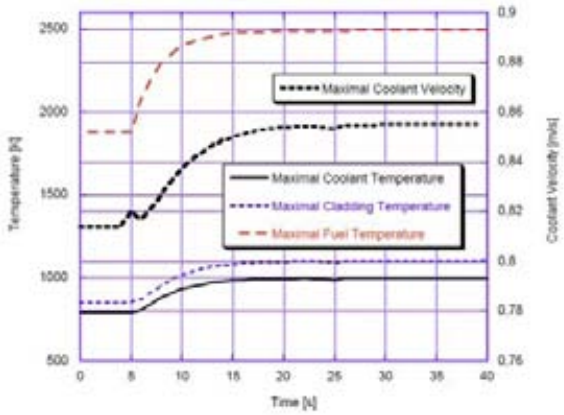

FIG. 35. Temperature distribution and coolant velocity during UTOP (ZrO_2).

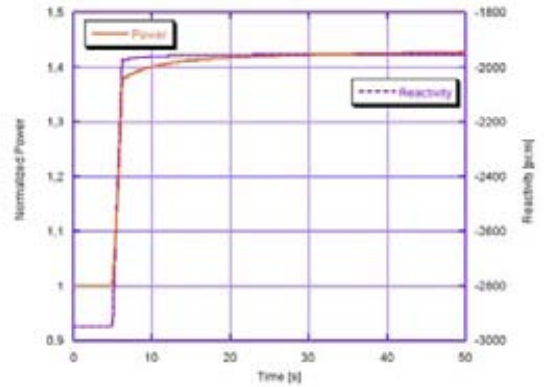

FIG. 36. Power and reactivity traces during UTOP (MgO).

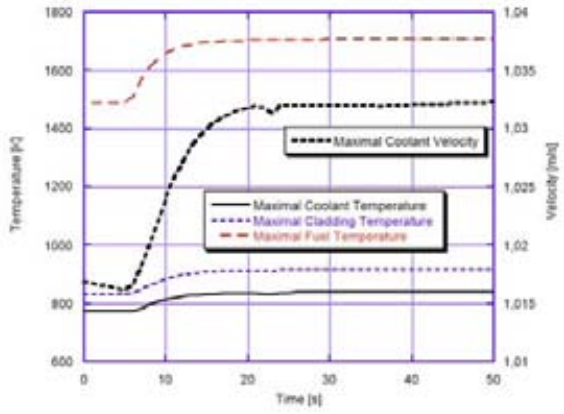

FIG. 37. Temperature distribution and coolant velocity during UTOP (MgO).

6.5.4. *Unprotected loss of flow*

In this case, one assumes a complete loss of forced coolant circulation due to pump coast down. The results of the transient simulation for the core with ZrO_2 matrix are shown in Figs 38 and 39. After ULOF starting at 0 s (half-mass-flow-rate time being about 5 s) the coolant flow rate decreases and approaches a stable value; the fuel and cladding temperatures stay below failure limits. High coolant temperatures are observed. No pin failure takes place because of the strong remaining natural convection. During this transient, nothing severe occurs in the core. Similar results were obtained for the core with MgO inert matrix, these results being shown in Figs 40 and 41.

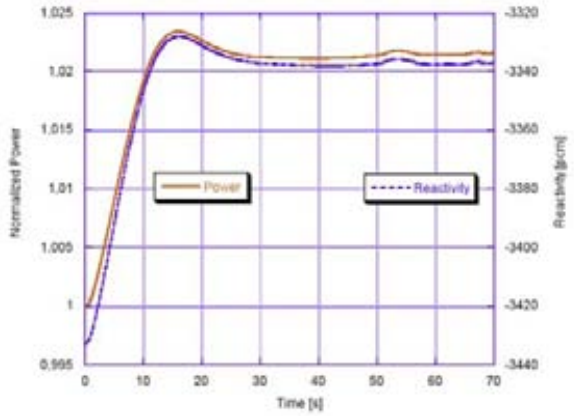

FIG. 38. Power and reactivity traces during ULOF (ZrO_2).

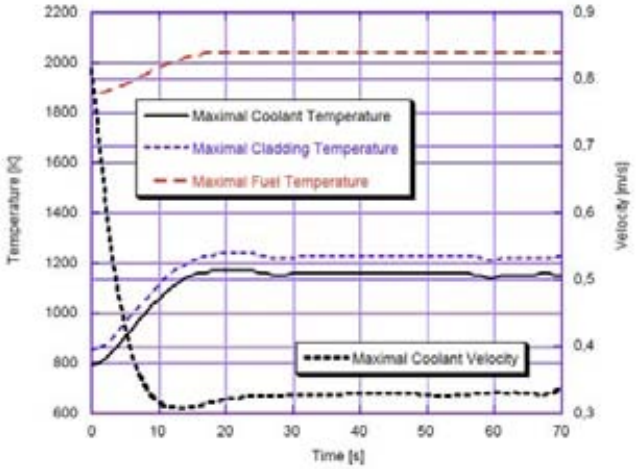

FIG. 39. Temperature distribution and coolant velocity during ULOF (ZrO_2).

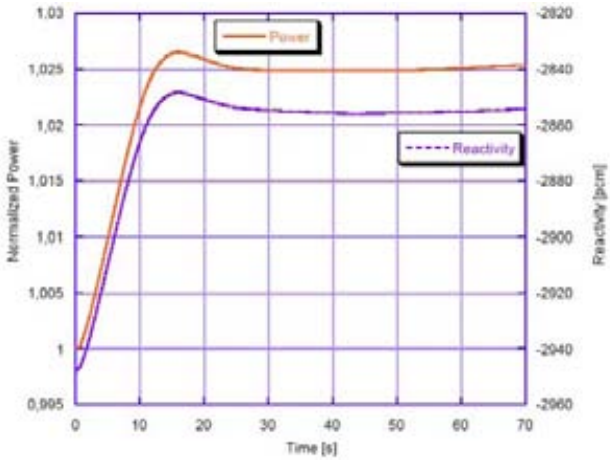

FIG. 40. Power and reactivity traces during ULOF (MgO).

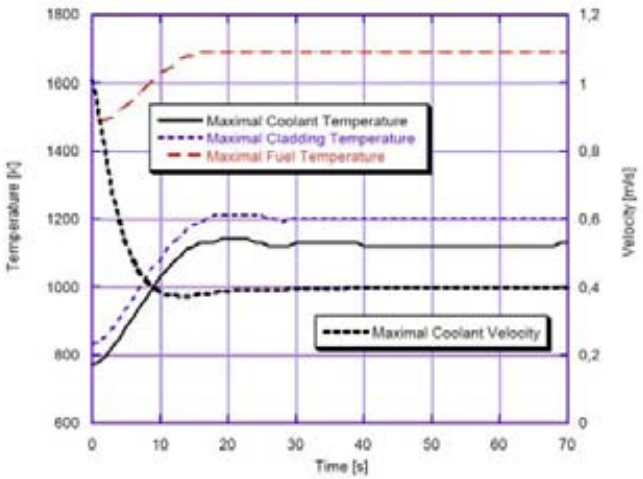

FIG. 41. Temperature distribution and coolant velocity during ULOF (MgO).

6.5.5. *Unprotected blockage accident*

In this case, a coolant flow blockage in one of the hottest assemblies is assumed. The blockage in a single assembly is modeled as a ring blockage because of the 2D simulation in which the coolant flow rate reduces to 16% after UBA (the calculations revealed that for 20% or higher fraction of the nominal flow rate, one may avoid cladding failures and fuel releases into coolant channels in the considered assembly). The results of the transient simulation for the core with ZrO_2 matrix are shown in Fig. 42.

The coolant flow reduction leads to pin failure, then the reactivity increases due to gas blowout. After the gas blow-out the void is eliminated by rushing in coolant and rewetting of the clad. The coolant is heated up further. Finally the clad looses its strenght and the fuel pellets or fuel chunks may be set free and be released. The fuel chunks are expelled out to the region above the core. This fuel relocation decreases the reactivity. The results for the MgO matrix are qualitatively similar. They are shown in Fig. 43.

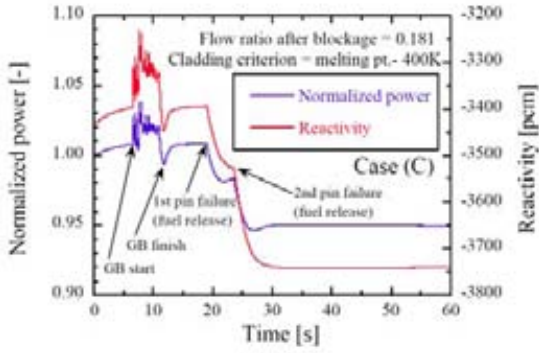

FIG. 42. Power and reactivity traces during UBA (ZrO_2).

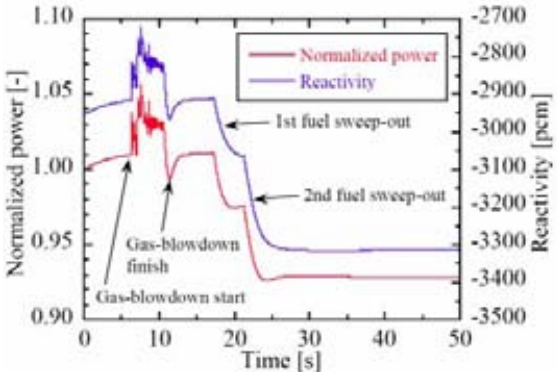

FIG. 43. Power and reactivity traces during UBA (MgO).

Criticality is not reached in this case. However, under a more pessimistic assumption (blockage in several S/As), a higher reactivity variation may occur after gas blowout. This may trigger a more rapid variation of power and reactivity that, in the absence of any negative feedback, would lead to higher power release before the fuel would sweep out. The fuel realease strongly depends on the pellet behavior and on the upper structure behavior, besides other parameters. Therefore, more detailed analyses of related scenarios would be of interest: to investigate in a wider parametric manner the system behavior.

6.6. Conclusions

Systems with solid uranium-free fuel are currently under investigation worldwide as an option for incinerating nuclear waste and to achieve the highest transmutation rate. In particular, fuels with high (up to ca. 50% in the TRU isotopic composition) MA actinide content offer high MA burning-rates. Operation of solid fuel systems with high MA content is not possible in critical reactors due to unfavorable safety characteristics, such as a very high positive coolant void effect, low values of important kinetics parameters ($beta_{eff}$, generation time) and a negligible Doppler effect.

Two ADS models of 580 MW(th) with LBE coolant and dedicated (specially designed for TRU burning) fuel are developed at FZK and studied in the framework of the IAEA CRP. Following the main preference of the European research program, oxide fuel forms are considered, about 50% or more of a fuel element consisting of a non-fissile (inert) support matrix that is necessary to dilute the fissile phase, to give mechanical strength to the fuel, and to improve the properties of the fuel (melting point, thermal conductivity, chemical stability). Thermo-physical data need further benchmarking against a wider set of experimental data.

Two fuel options are considered: TRU oxide mixed with (1) ZrO_2 and (2) MgO inert matrices. Both cores have 3 fuel zones, the TRU composition being the same, the volume fraction of fuel being 40% in the inner core, 45% in the middle core, 50% in the outer core. This zoning was developed to limit power peak factors while assuming that k_{eff} is about 0.97. Due different thermal properties of the fuels, the ZrO_2 core includes an additional ring of S/As in the middle core for the same thermal power. The Pu to MA ratio in the fuel is 40/60, there is no Np in the fuel. The heavy metal content is approximately 9 kg/MW(th) in ZrO_2 core and 7.5 kg/MW(th) in the MgO core.

The SIMMER-III coupled neutronics/thermal-hydraulics safety code, several neutronics data libraries and codes developed at FZK (C4P, ZMIX, TRAIN), and the DANTSYS neutron transport code were applied for reactor static and transient analyses. The SIMMER molten-freezing model and the EOS models for LBE and for the dedicated fuels were developed/improved at the Kyushu University for the CRP studies.

The static neutronics analyses were performed mainly at FZK, k_{eff} values for nominal conditions. Several multi-group (11 to 560 groups) data libraries were employed: an FZK library for SIMMER, JEF 2.2, JEFF 3.0, JEFF 3.1, ENDF/B-7, JENDL 3.3. The results show a relatively high sensitivity of the computed values to employed data libraries. The deviations between more advanced calculation options (fine energy group structure, high order angular orders for scattering matrices and neutron flux, taking into account of S/A heterogeneity) and less advanced ones are not negligible, but smaller (compared to those related to nuclear data), provided that the neutron transport (not diffusion) theory models are applied in both cases. The cross-sections that characterize interaction of high-energy neutrons (above 20 MeV) with nuclei were assumed to the same as the cross-sections in the first energy group (with the upper boundary up to ca. 20 MeV). This approximation does not affect appreciably the accuracy of the computed neutronics parameters,

The Doppler constant in both ADSs is near –20 pcm. The core void effect varies from 6 500 till 8 400 pcm depending upon nuclear data. The core structure removal effect is about a half of the void effect in LBE (3000 + pcm). The β_{eff} is near 190 pcm, the neutron generation time is about 0.5 μs. These parameters are computed at BOL conditions, the k_{eff} being ca. 0.97. Both systems are essentially Am burners (while the TRU burning efficiency being ca 43 kg per TWh, the Am burning efficiency

being ca. 45 kg per TWh, mass variations of other heavy elements after three years of irradiation and one or more years of cooling being a few kg or less per TWh), similar to other solid fuel fertile-free ADS designs investigated currently in many countries. If no fuel reloading occurs, the core reactivity decreases by about 4 500 pcm in 3 years.

By now, almost all benchmark results were obtained at FZK; however the neutronics results are indirectly confirmed by benchmarking of the FZK tools in other Domains. Since the uncertainties (in criticality, coolant/structure reactivity effects and burnup reactivity loss) due to nuclear data are relatively high (being of the order of ca. 20%), more experimental results should be involved in the analyses: to make these uncertainties smaller.

An extended SIMMER-III version was employed for the analyses at BOL conditions. Key transient phenomena relate to potentially strong reactivity increase due to coolant heat-up, gas blow-down after pin disruption and structure removal under accident conditions. Therefore key safety parameters are the high structure and coolant reactivity worth values and a very low Doppler constant. Due to the sub-critical regime, the low β_{eff} value does not influence the safety performance appreciably, but a low value of neutron generation time may potentially lead to higher energy release in case of re-criticality.

Inert matrix affects the neutron spectrum: it is softer compared to a similar system in which the matrix is replaced by UO_2 (depleted). Therefore the inert matrix makes the void effect smaller. On the other hand the Doppler constant would be slightly larger if the inert matrix was replaced by the UO_2. The void and Doppler effect variations (due to the replacement) would not change qualitatively the principal feedbacks and the kinetic parameters: a large void effect combined with a near zero Doppler constant and a low β_{eff} value is due to the high MA content.

The main stabilizing effect comes through the sub-criticality as the Doppler plays no role. The high reactivity worth values of structure and coolant may lead to reactivity increases e.g. in case of S/A blockage. Under ULOF conditions the void worth potential would be more dangerous as the homogeneous elevation of coolant temperatures may involve gross damage propagation under pin failure conditions. The potentially stabilizing role of radial/axial expansion is ignored for the moment; that makes the results conservative. For future studies, these phenomena should be investigated in more detail; while design measures enhancing these phenomena could help to improve the safety.

Several beam-variation and unprotected transient cases with the two fertile-free fuels were studied. The BT and TOC — related to beam power variation — are specific for ADS. Other as ULOF, UTOP and UBA (blockage) are common for LM-cooled systems. Since the beam amplitude controls the power, no CR is present in the system and no CR-withdrawal related transient is considered.

The impact of very fast and cyclic power responses (in μs to ms scale) to beam variations has to be investigated for the innovative fuels and clad materials. Longer time scales (of the order of 10 s) are typical for ULOF and UBA cases.

The transients were simulated up-to and beyond fuel failure. Due to a positive void worth, the simulation of gas-blowout effects is an interesting point to be analyzed and compared with results obtained by other codes. The simulation of the fuel sweep-out effect is an important effect for limiting power excursions. For BT, TOC, UTOP and ULOF cases in MgO and ZrO_2-matrix-fuel cores, the cladding temperature could remain below the assumed gas-blowout criterion. In case of UBA in the hottest assembly, the positive reactivity addition by gas blowout does not directly trigger a power excursion due to incoherence effects. The fuel sweep-out effect finally balances the positive void reactivity addition. In view of a high positive void effect, large uncertainties in the calculated value of the void effect due to nuclear data, and possible blockage in more than in one S/A, more studies are necessary to prove safety of the studied ADS cores. ADS designs need further optimization with respect to the safety and burnup performance.

REFERENCES TO CHAPTER 6

[1] EUROTRANS, EUROpean Research Programme for the TRANSmutation of High Level Nuclear Waste in an Accelerator Driven System, EU Contract FI6W-CT-2004-516520 (2006).

[2] MUKAIYAMA, T., TAKIZUKA, T., MIZUMOTO, M., IKEDA, Y., OGAWA, T., HASEGAWA, A., TAKADA, H. and TAKANO, H., Review of research and development of accelerator-driven system in Japan for transmutation of long-lived nuclides, Progr. Nucl. Energy 38 (2001) p. 107.

[3] A Roadmap for Developing Accelerator Transmutation of Waste (ATW) Technology: A Report to Congress, DOE/RW-0519, USA (1999).

[4] Fuel Fabrication and Processing Subgroup of the Technical Working Group on ADS (2000).

[5] MASCHEK, W. et al., First Results of Safety Analyses for ADTs with CERCER and CERMET Fuels within the EUROTRANS-AFTRA Program, paper presented in the NEA OECD 9th Information Exchange Meeting, Actinide and Fission Product Partitioning & Transmutation, 25-29 September 2006, Nimes France.

[6] MASCHEK, W., CHEN, X., DELAGE, F., FERNANDEZ-CARRETON, A., HAAS, D., MATZERATH-BOCCACCINI, C., RINEISKI, A., SMITH, P., SOBOLEV,V., THETFORD, R., WALLENIUS, J., Accelerator Driven Systems for Transmutation: Fuel Development, Design and Safety, paper presented in the 2nd COE-INES International Symposium on Innovative Nuclear Energy Systems, INES-2, 26–30 November 2006 Yokohama, Japan.

[7] PDS-XADS, Preliminary Design Studies of an Experimental Accelerator-Driven System, 5th Framework Programme of the EU (2001).

[8] KONDO, Sa., MORITA, K., TOBITA, Y and SHIRAKAWA, N., SIMMER-III: An Advanced Computer Program for LMFBR Severe Accident Analysis, Proc. Int. Conference on Design and Safety of Advanced Nuclear Power Plants (ANP'92), No. 40-5, 25-29 October 1992, Tokyo, Japan (1992).

[9] MASCHEK, W., RINEISKI, A., SUZUKI, T., WANG, S., MORI, Mg., WIENGER, E., WILHELM, D., KRETZSCHMAR, F.,TOBITA, Y., YAMANO, H., FUJITA, S., COSTE, P., PIGNY, S., HENRIQUES, A., CADIOU, T., MORITA, K., BANDINI, G., SIMMER-III and SIMMER-IV Safety Code Development for Reactors with Transmutation Capability, paper presented in M&C 2005 Intl Conf, 12-15 September 2005, Avignon, France.

[10] WANG, S., RINEISKI, A., MASCHEK, W., Molten salt related extensions of the SIMMER-III code and its application for a burner reactor, Nuclear Engineering and Design, Vol. 236, Issues 14-16 (August 2006) pp. 1580-1588.

[11] KIEFHABER, E., Updating of an 11-groups nuclear cross section set for transmutation applications. FZKA-6480 (August 2000) p. 582.

[12] RINEISKI, A., SINITSA, V., MASCHEK, W., C4P, a Multigroup Nuclear CCCC Data Processing System for Reactor Safety and Scenario Studies, Proc. Jahrestagung Kerntechnik 2005, 10-12 May 2005, Nürnberg, Germany.

[13] RINEISKI, A., SINITSA, V., MASCHEK, W., WANG, S (2005), Kinetics and Cross-Section Developments for Analyses of Reactor Transmutation Concepts with SIMMER, M&C 2005, 12-15 September 2005, Avignon, France.

[14] ALCOUFFE, R.E., BAKER, R.S., BRINKLEY, F.W., MARR, D.R., O'DELL, R.D., WALTERS, W.F, DANTSYS: A Diffusion Accelerated Neutral Particle Transport Code System, LA-12969-M (1995).

[15] RINEISKI, A., Decay Heat Production in a TRU Burner, paper presente dim the 2nd COE-INES International Symposium on Innovative Nuclear Energy Systems, INES-2, 26-30 November 2006, Yokohama, Japan.

[16] KIEFHABER, E., FZK, private communication (2001).

[17] OTT, K.O., NEUHOLD, R.J., "Nuclear Reactor Dynamics", ANS, La Grange Park, USA (1985).

[18] MASCHEK, W., RINEISKI, A., MORITA, K., KIEFHABER, E., BUCKEL, G., FLAD, M., COSTE, P., PIGNY, S., RIMPAULT, G., LOUVET, J., CADIOIU, T., KONDO, S., TOBITA, Y., SUZUKI, T., SIMMER-III, a Code for Analyzing Transients and Accidents in Accelerator Driven Systems (ADS), paper presented in AccApp'00, Washington D.C., USA (2000).

[19] SUZUKI. T., TOBITA, Y., KONDO, S.A., SAITO, Y., MISHIMA, K., Analysis of Gas-Liquid Metal Two-Phase Flows using a Reactor Safety Analysis Code SIMMER-III, Nuclear Engineering and Design, 220 (2003) pp. 207-223.

[20] KATAOKA, I., ISHII, M., Drift flux model for large diameter pipe and new correlation for pool void fraction, Int. J. Heat Mass Transfer, 30(9) (1987) pp. 1927-1939.

[21] TENTNER, A.M., WEBER, D.P., BIRGERSSON, G., BORDNER, G.L., BRIGGS, L.L., CAHALAN, J.E., DUNN, F.E., KALIMULLAH, K., MILES, J., PROHAMMER, F.G., The SAS4A LMFBR Whole Core Accident Analysis Code, paper presented in the Intl Mtg on Fast Reactor Safety, Knoxville, TN, USA (1985) pp. 989-998.

[22] MORITA, K., YAMANO, H., TOBITA, Y., KONDO, S., SIMMER-III/IV Heat- and Mass-Transfer Model — Model and Method Description, Japan Nuclear Cycle Development Institute, JNC TN9400 2003-047 (July 2003).

[23] MASCHEK, W., CHEN, X., DELAGE, F., FERNANDEZ-CARRETON, A., HAAS, D., MATZERATH-BOCCACCINI, C., RINEISKI, A., SMITH, P., SOBOLEV, V., THETFORD, R., WALLENIUS, J., Accelerator Driven Systems for Transmutation: Fuel Development, Design and Safety, Progress in Nuclear Energy 50 (2008) pp. 333-340.

CHAPTER 7. DOMAIN-IV: HYBRID SYSTEM (ADS) WITH FERTILE-FREE FUEL (THERMOPHYSICAL PROPERTIES OF ADS CORE MATERIALS FOR USE IN IAEA BENCHMARK PROBLEMS)

7.1. Introduction

For accelerator driven systems (ADSs), mixed transuranium (TRU) fuels have been suggested, but at the same time it is generally considered that the addition of a non-fissile (inert) support matrix is necessary to dilute the fissile phase and to give mechanical strength to the fuel. The matrix could also help to improve the properties of the fuel, such as melting point, thermal conductivity and chemical stability. Fuel specifications such as matrix fractions, plutonium/minor-actinide (MA) ratios, pellet densities, thermal conductivities, melting/eutectic points are key issues to assess the reactor transmutation performance and safety behavior of ADSs. However, experimental data in respect to the inert matrix fuels (IMFs) are rather scarce, and few theoretically based recommendations have been made relating to matters necessary for the assessment of reactor performance and safety behavior.

In this report, models to estimate thermophysical properties of IMF will be provided for use in the assessment of reactor performance and safety behaviors of ADS. The estimation will be performed by extrapolating or interpolating known basic properties of oxide fuel and matrix constituents, of which data can be found in open literature. Estimated thermophysical properties will be presented for IMF specified for the IAEA benchmark problems as well as the MOX fuel. Recommendations will also be presented for the thermophysical properties of other ADS core materials such as lead-bismuth eutectic (LBE) and stainless steel.

7.2. Models for fuel properties

In many countries, the actinide oxide fuels are considered as the most promising candidates for the MA transmutation in ADS. Three types of the fuel pellet material are under study now. The first one is a solid solution of actinide oxides in zirconia (or yttria stabilized zirconia), the second is a composite formed by the oxide fuel particles dispersed within a non-fissile MgO ceramic matrix (called below 'CERCER'), and the third is the same kind of composite but with Mo metal matrix (called 'CERMET').

Here, solid properties of inert matrix fuels are estimated using basic properties of each constituent of fuel and matrix. For solid solutions, we apply general assumption of ideal mixture or additivity rule to property calculation. For the composite fuels, their properties are calculated basically by averaging the fuel and matrix properties. In addition, special assumption could be made to cover the material behaviors such as eutectic formation.

7.2.1. *Solid density*

The temperature dependent solid density $\rho_s(T)$ of a solid solution is calculated by the following equation considering the mole-fraction-weighted mean linear expansion with temperature:

$$\rho_s(T) = \frac{\rho_s(T_{ref})}{\left(\sum_M n_M \frac{l_M(T)}{l_M(T_{ref})} \right)^3} \qquad (1)$$

where T_{ref} is ther reference temperature, $l(T)$ and $l(T_{ref})$ are the lengths at the temperatures T and T_{ref}, respectively; $\rho_{s(Tref)}$ is the density at T_{ref}, n is the mole fraction, and the subscript M means a material component in the solid solution. The reference density including the lattice constant of solid solution, which is calculated by Vegard's law, is given by

$$\rho_s(T_{ref}) = \frac{Z}{N_A}\frac{W}{(\sum_M n_M a_M)^3} \tag{2}$$

$$\rho_s(T_{ref}) = \frac{Z}{N_A}\frac{W}{(\sum_M n_M a_M)^3} \tag{2}$$

where N_A is the Avogadro's number, a is the lattice constant, W is the molecular weight and Z is the number of molecules per unit cell. For the actinide stoichiometric dioxides, which have the fluorite type structure, there are four molecules in a cubic lattice, that is $Z = 4$ for type AnO_2 fuels. The molecular weight of the solid solution is calculated by

$$W = \sum_M n_M W_M \tag{3}$$

The density of a composite fuel is calculated as a volume average of actinide oxide fuel and inert matrix densities:

$$\rho_s(T) = \left[(nW)_{\text{fuel}} + (nW)_{\text{matrix}}\right]\left[\left(\frac{nW}{\rho_s}\right)_{\text{fuel}} + \left(\frac{nW}{\rho_s}\right)_{\text{matrix}}\right]^{-1} \tag{4}$$

where the subscripts 'fuel' and 'matrix' mean the actinide oxide fuel and the inert matrix, respectively.

7.2.2. Melting point

The melting temperature T_m of a solid solution can be estimated by additivity rule or mole-fraction-weighted mean:

$$T_m = \sum_M n_M T_{m,M} \tag{5}$$

For composite fuels, the solidus and liquidus temperatures are defined as the minimum and maximum temperatures, respectively, in the melting points of the actinide oxide fuel and the inert matrix. Reduced melting temperatures are also considered for the materials with eutectic formation.

7.2.3. *Solid enthalpy*

The temperature dependent molar enthalpy h of a solid solution is calculated by the additivity rule:

$$h(T) = \sum_M n_M h_M(T) \tag{6}$$

The same rule is also used for the heat of fusion:

$$h_f = \sum_M n_M h_{f,M} \tag{7}$$

For composite fuels, the fusion enthalpy is defined as the sum of the enthalpy difference between solidus and liquidus points of actinide oxide fuel and inert matrix:

$$h_f = n_{fuel}(h_f + h_s)_{fuel} + n_{matrix}(h_f + h_s)_{matrix} \tag{8}$$

where h_s is the sensible enthalpy that is necessary to increase the temperature up to the solidus or liquidus temperature of the composite fuel.

7.2.4. *Thermal conductivity*

The thermal conductivity of a solid solution is roughly approximated as a mole-fraction-weighted mean value of each component in the solid solution:

$$\kappa_s(T) = \sum_M n_M \kappa_M(T) \tag{9}$$

Although in principle Eq. (9) cannot be applied to transport properties (such as thermal conductivity, electric conductivity, diffusivity and viscosity), in the case when a solid solution is composed of similar non-reacting components and in the absence of a eutectic formation, it often gives rather satisfactory results. For composite fuels, Millar's equation is used to evaluate effective conductivity κ_{eff}:

$$\kappa_{eff} = \kappa_{fuel} + \frac{V_{matrix}}{V_{matrix} + V_{matrix}}(\kappa_{matrix} - \kappa_{fuel})\left(\frac{\kappa_{eff}}{\kappa_{matrix}}\right)^{1/3} \tag{10}$$

where V_{fuel} and V_{matrix} are the volumes of actinide oxide fuel and inert matrix in the composite fuel, respectively. The thermal conductivity of the actinide oxide fuel is calculated by Eq. (9). The thermal conductivity of composite fuels depends on not only the matrix volume, but also the shape and distribution of the dispersed fuel particles [2]. However, Eq. (10) considers the contribution of both the actinide oxide fuel and inert matrix components when low conductivity fuel particles are embedded into a high conductivity matrix.

The thermal conductivity of solid fuel decreases with increasing porosity. The well-known Maxwell-Eucken equation is used to correct for this porosity effect [4]:

$$\kappa = \kappa_0 \frac{1-p}{1+2p} \tag{11}$$

where p is porosity and κ_0 is the thermal conductivity of fully dense fuel.

7.3. Properties of actinide oxides and diluents

7.3.1. *Mixed oxides*

7.3.1.1. Thermal expansion

The lattice constants of UO_2 and PuO_2 are 547.04 pm and 539.60 pm, respectively (Katz et al., 1986). Assuming the molecular weights of UO_2 and PuO_2 are 270.01 g mol^{-1} and 271.21 g mol^{-1}, respectively, which are based on the U- and Pu-isotope vectors shown in Table 1, these lattice constants give solid densities of UO_2 and PuO_2 at 293 K of 10956 kg m^{-3} and 11466 kg m^{-3}, respectively.

Since the UO_2, PuO_2 and MOX fuels have very similar thermal expansions, Carbajo et al. [4] recommended employing Martin's correlations [19] for the thermal expansion both of solid UO_2 and MOX fuels:

$$\frac{l(T)}{l(273\text{K})} = 9.9734\times10^{-1} + 9.802\times10^{-6}T - 2.705\times10^{-10}T^2 + 4.391\times10^{-13}T^3$$

$$273 \le T \le 923 \text{ K and} \qquad (12a)$$

$$\frac{l(T)}{l(273\text{K})} = 9.9672\times10^{-1} + 1.179\times10^{-5}T - 2.429\times10^{-9}T^2 + 1.219\times10^{-12}T^3$$

$$923 \text{ K} \le T \le T_m \qquad (12b)$$

where T is in K and T_m is the melting temperature, which is taken as the solidus temperature for the mixed oxide compositions. For the hypostoichiometric MOX fuel, (U, Pu)O_2-x, Carbajo et al. [4] recommended that the thermal expansion is multiplied by a factor of $[1 + 3.9(\pm0.9)x]$ with x being the deviation from stoichiometry. Although this recommendation developed by Martin [19] is valid for the MOX fuels up to 1800 K, we employ it even for other actinide oxide fuels up to their solidus temperatures.

7.3.1.2. Melting point

The melting point of an oxide fuel depends on the fuel composition, O/M ratio or the oxygen content and burnup. Here, for MOX fuels, a correction only for UO_2 and PuO_2 fractions is considered. Carbajo et al. [4] recommended the solidus and liquidus curves of stoichiometric UO_2–PuO_2 solutions given by Adamson [1]. They are expressed by the following polynomial expressions:

$$T_{Sol} = 3120.0 - 655.3y + 336.4y^2 - 99.9y^3 \qquad (13a)$$

$$T_{Liq} = 3120.0 - 388.1y - 30.4y^2 \qquad (13b)$$

where y is the mole fraction of PuO_2. Here, the melting temperatures of stoichiometric, unirradiated UO_2 and PuO_2 are taken as 3120±30 K and 2701±35 K, respectively.

7.3.1.3. Heat capacity and enthalpy

Carbajo et al. [4] recommended the following expressions developed by [9, 10] for the solid enthalpy relative to the solid at 298.15 K:

$$h_s(T) - h_s(298.15\text{K}) = C_1\theta\left(\frac{1}{e^{\theta/T}-1} - \frac{1}{e^{\theta/298.15}-1}\right)$$

$$+C_2\left[T^2 - (298.15)^2\right] + C_3 e^{-E_a/T} \qquad (14)$$

where h_s is in J mol–1 and T is in K. The constants used in the above equation are given as C_1 = 81.613, C_1 = 2.285×10^{-3}, C_1 = 2.36×10^7 and θ = 548.68 for UO_2, C_1 = 87.394, C_1 = 3.978×10^{-3}, C_1 = 0.0 and θ = 587.41 for PuO_2, and E_a = 18531.7. The expression for heat capacity is given by

$$c_{p,s}(T) = \frac{C_1\theta^2 e^{\theta/T}}{T^2(e^{\theta/T}-1)^2} + 2C_2T + \frac{C_3E_a e^{-E_a/T}}{T^2} \qquad (15)$$

where $c_{p,s}$ is in J mol^{-1} K^{-1}.

For liquid PuO_2, Cordfunke and Konings [5] recommended the following value:

$$c_{p,l} = 131.0 \text{ J K}^{-1} \text{ mol}^{-1}$$

The above constant value is used for liquid MOX fuel as an approximation.

7.3.1.4. Heat of fusion

Carbajo [4] recommended the following value for the heat of fusion of UO_2 calculated by Fink [10]:

$$h_f(\text{UO}_2) = 70 \pm 4 \text{ kJ mol}^{-1}$$

For the heat of fusion of PuO_2, we take the following value recommended by Cordfunke and Konings [5]:

$$h_f(\text{PuO}_2) = 67 \pm 15 \text{ kJ mol}^{-1}$$

The heat of fusion value for UO_2–PuO_2 compositions is calculated from the following relationship [8]:

$$h_f(\text{MOX}) = \frac{h_f(\text{UO}_2)}{T_m(\text{UO}_2)} T_m(\text{MOX}) \qquad (16)$$

where T_m is the melting temperature, which is taken as the solidus temperature for the mixed oxide compositions. For the MOX fuels with 20% mole fractions of PuO_2, the above equation yields h_f=66.2 kJ mol^{-1}, which agrees well with 67 ± 3 kJ mol^{-1} measured by Leibowitz et al. [18].

7.3.1.5. Thermal conductivity

Carbajo et al. [4] recommended the following expressions for the thermal conductivity of fully dense fuels:

for UO_2

$$\kappa_s(T) = 1.158\left[\frac{100}{7.5408 + 17.692\tau + 3.6142\tau^2} + \frac{6400}{\tau^{5/2}}\exp\left(-\frac{16.35}{\tau}\right)\right]$$

$$298 \le T \le 3120\ \text{K} \qquad (17)$$

for MOX with PuO_2 concentrations between 3 and 15 %

$$\kappa_s(T,x) = 1.158\left[\frac{1}{2.85x + 0.035 + (-0.715x + 0.286)\times\tau} + \frac{6400}{\tau^{5/2}}\exp\left(-\frac{16.35}{\tau}\right)\right]$$

$$700 \le T \le 3100\ \text{K} \qquad (18)$$

where κ_s is in W m^{-1} K^{-1}, τ is the variable $T/1000$ and T is in K. Equation (17) was developed by [10]. Equation (18) was a combination of the correlations developed by Duriez et al. [7] and Ronchi et al. [21].

The thermal conductivity of solid PuO_2 expressed as a function of temperature by the relationships of the form

$$\kappa_s(T) = \frac{1}{A + BT} \qquad (19)$$

with constants A and B was determined by Gibby [12] and Fukushima et al. [11]. They obtained:

$$A = (0.46 \pm 0.18)\times10^{-2}\ \text{m K W}^{-1} \text{ and } B = (0.0283 = 0.0002)\times10^{-2}\ \text{m W}^{-1}$$

for 97 % TD between 373 – 1873 K (Gibby. 1971)

$$A = (1.64 \pm 0.23)\times10^{-2}\ \text{m K W}^{-1} \text{ and } B = (0.0275 = 0.0002)\times10^{-2}\ \text{m W}^{-1}$$

for 95 % TD between 688 – 1488 K (Fukushima *et al.*, 1981)

where T is in K. Equation (19) using the above two sets of constants agrees well with each other for fully dense solid, which is calculated by Eq. (11), within experimental uncertainty of the measurements. Here, we take the constants determined by Gibby [12].

7.3.2. *Americium dioxide*

7.3.2.1. Thermal expansion

The lattice constant of AmO_2, which has an fcc fluorite-type crystal structure, is 537.72 pm [5]. Assuming the molecular weights of AmO_2 is 271.12 g mol^{-1}, which is based on the Am-isotope vectors shown in Table 4, this lattice constant gives solid densities of AmO_2 at 293 K of 11625 kg m^{-3}.

The thermal expansion of americium oxides has not been reported. Here, we apply the same values as the thermal expansion of solid UO_2 and MOX fuels, which is given by Eq. (12), to that of AmO_2-x in actinide oxide fuels.

7.3.2.2. Melting point

Zhang et al. [27] quoted the following values of the melting points of AmO_2 and $AmO_{1.5}$:

$$T_m = 2448 \text{ K for } AmO_2 \text{ and } T_m = 2478 \pm 15 \text{ K for } AmO_{1.5}$$

Here, we take the value of 2448 K for the melting point of AmO_2-x in actinide oxide fuels.

7.3.2.3. Heat capacity and enthalpy

The estimated heat capacity of solid AmO_2 [24] is given by:

$$c_{p,s}(T) = 84.739 + 1.072 \times 10^{-2} T - 8.159 \times 10^{-7} T^2 - 19.285 \times 10^5 T^{-2}$$

$$298.15 \text{ K} \leq T \leq 2000 \text{ K} \qquad (20)$$

where $c_{p,s}$ is in J K^{-1} mol^{-1} and T is in K. Equation (20) yields the following expression for the enthalpy of AmO_2:

$$h_s(T) - h_s(298.15\text{K}) = -7320.4 + 84.739T + 0.536 \times 10^{-2} T^2$$

$$-2.7197 \times 10^{-7} T^3 + 19.285 \times 10^5 T^{-1}$$

$$298.15 \text{ K} \leq T \leq 2000 \text{ K} \qquad (21)$$

where h_s is in J mol^{-1} and T is in K.

For liquid AmO_2, [27] assumed that its heat capacity have the same constant value as PuO_2 [5]:

$$c_{p,l} = 131.0 \text{ J K}^{-1} \text{ mol}^{-1}$$

7.3.2.4. Heat of fusion

The values of heat of fusion of americium oxides were estimated to be 59±20 kJ mol^{-1} for $AmO_{1.5}$, 61±20 kJ mol^{-1} for AmO_2 and 56±20 kJ mol^{-1} for $AmO_{1.62}$ by Zhang et al. [27]. These values lay

within their uncertainty ranges, and hence we adopt the value of AmO_2 as a standard one for americium oxides:

$$h_f = 61 \text{ kJ mol}^{-1} \tag{22}$$

7.3.2.5. Thermal conductivity

The measured thermal conductivity of americium oxides is quite lower than the thermal conductivity of other actinide dioxides. For example, Bakker and Konings [2] quoted measured values at 333 K: 0.69 W m^{-1} K^{-1} for AmO_2 and 0.82 W m^{-1} K^{-1} for Am_2O_3. On the other hand, the thermal conductivity of AmO_{2-x} can be approximately expressed by the following formula as a function of temperature and oxygen content of americium oxide [2]:

$$\kappa_s(T,x) = \frac{1}{2\times10^{-2} + 1.528(x+0.00931)^{1/2} - 0.1474 + 3.19\times10^{-4}T} \tag{23}$$

Although Eq. (23) overestimates the measured values, Bakker and Konings [2] suggested that this is due to non-stoichiometry of the samples used in the measurement. Therefore, Eq. (23) is used for the rough estimation of the thermal conductivity of AmO_{2-x}.

7.3.3. *Curium dioxide*

7.3.3.1. Thermal expansion

The lattice constant of CmO_2, which has a fluorite-type crystal structure at room temperature, is 535.9 pm [16]. Assuming the molecular weight of CmO_2 is 274.56 g mol^{-1}, which is based on the Cm-isotope vectors shown in Table 4, this lattice constant gives solid densities of CmO_2 at 293 K of 11849 kg m^{-3}.

The fractional change in length of CmO_2 with temperature is expressed by the following equation [16]:

$$\frac{\Delta l(T)}{l(298\text{K})} = -0.3027 + 10.16\times10^{-4}T \qquad 298\text{ K} \le T \le 650\text{ K} \tag{24}$$

where $\Delta l(T)/l(298\text{K})$ is in %, $\Delta l(T)$ is zero at 298 K, and T is in K. CmO_2 becomes unstable above 700 K decomposing via two intermediate compositions to Cm_2O_3. In comparison with MOX fuels, Eq. (12) gives the thermal expansion that is very close to the values obtained from Eq. (24). Here, assuming that the lattice structure of corium oxide in the actinide oxide fuels is similar to those of UO_2 and MOX fuels, we apply Eq. (12) to the thermal expansion of CmO_2.

7.3.3.2. Melting point

Since CmO_2 decomposes above 700 K, its melting point is unavailable. For Cm_2O_3 the following melting point was recommended by Konings [16]:

$$T_m = 2543 \pm 25 \text{ K}$$

We use the above value in the calculation of the melting point of actinide oxide fuels with curium.

7.3.3.3. Heat capacity and enthalpy

Konings [16] gave the following expressions for the heat capacity of curium oxides:

for CmO_2

$$c_{p,s}(T) = 64.871 + 19.152 \times 10^{-3} T - 7.860 \times 10^{5} T^{-2}$$

$$300 \leq T \leq 600 \text{ K} \qquad (25)$$

for Cm_2O_3

$$c_{p,s}(T) = 123.532 + 14.550 \times 10^{-3} T - 1.3489 \times 10^{6} T^{-2}$$

$$298.15 \leq T \leq 1888 \text{ K} \qquad (26)$$

where $c_{p,s}$ is in J K^{-1} mol^{-1} and T is in K. Equation (26) is rewritten for $CmO_{1.5}$:

$$c_{p,s}(T) = 61.766 + 7.275 \times 10^{-3} T - 6.7445 \times 10^{5} T^{-2} \qquad (27)$$

Since Eq. (25) covers only rather low temperature range and there is not large difference between Eqs. (25) and (27), we apply Eq. (27) to the heat capacity of CmO_{2-x} as an approximation. The expression for the enthalpy of CmO_{2-x} is then given by

$$h_s(T) - h_s(298.15\text{K}) = -20679 + 61.766T + 3.3675 \times 10^{-3} T^2 + 6.7445 \times 10^{5} T^{-1}$$

$$(28)$$

where h_s is in J mol^{-1} and T is in K.

There is no heat capacity data for liquid CmO_{2-x}. Here, we assume the same constant value as PuO_2 [5]:

$$c_{p,l} = 131.0 \text{ J K}^{-1} \text{ mol}^{-1}$$

7.3.3.4. Heat of fusion

The heat of fusion of curium oxides has not been reported. Here, we apply the same values as the heat of fusion of MOX fuels, which is given by Eq. (16), to that of CmO_{2-x}, in actinide oxide fuels.

7.3.3.5. Thermal conductivity

The thermal conductivity of CmO_2 has not been measured. Konings [16] estimated the thermal conductivity of CmO_2 as indicative values: 7-10 W m^{-1} K^{-1} at 298.15 K and 3.8-4.6 W m^{-1} K^{-1} at 650 K. For the thermal conductivity of monoclinic Cm_2O_3, Konings [16] also gave the following recommendation:

$$\kappa_s(T) = (0.3629 + 1.78 \times 10^{-4} T)^{-1} \qquad 373 \le T \le 1723 \text{ K} \qquad (29)$$

In comparison with the thermal conductivity of MOX fuels, Eq. (18) with x = 0.0 gives values close to Konings' estimation for CmO_2. On the other hand, for Cm_2O_3, Eq. (18) with x = 0.5 provides rather low thermal conductivity, compared with Eq. (29) in its temperature range of validity. Here, we propose to use Eq. (18) for the thermal conductivity of CmO_{2-x} by replacing x with $0.25x$:

$$\kappa_s(T, x) = 1.158 \left[\frac{1}{2.85 \times 0.25x + 0.035 + (-0.715 \times 0.25x + 0.286) \times \tau} \right.$$

$$\left. + \frac{6400}{\tau^{5/2}} \exp\left(-\frac{16.35}{\tau} \right) \right] \qquad (30)$$

Equation (30) can include reasonably well not only the dependence on the difference from stoichiometry, but also the behavior of oxide fuels at high temperatures as an approximation.

7.3.4. *Magnesium oxide*

7.3.4.1. Thermal expansion

The lattice constant of MgO, which has a cubic crystal structure, is 421.3 pm. This lattice constant gives solid densities of MgO at 293 K of 3580 kg m^{-3} using the molecular weight of 40.30 g mol^{-1}.

Jacobs and Oonk [14] gave the following polynomial fit to the volumetric thermal expansion coefficient of MgO:

$$\alpha(T) = 4.5248 \times 10^{-5} + 8.4711 \times 10^{-10} T - 4.1959 \times 10^{-3} T^{-1} + 2.4984 \times 10^{-12} T^2$$

where α is in K^{-1} and T is in. This equation is related to the linear thermal expansion coefficient by

$$100 \le T \le 3100 \text{ K} \qquad (31)$$

Then, $l(T)/l(T_{ref})$ is expressed by

$$\frac{l(T)}{l(T_{ref})} = \exp[1.50827 \times 10^{-5}(T - T_{ref}) + 1.41185 \times 10^{-10}(T^2 - T_{ref}^2)$$

$$-1.39863 \times 10^{-3} ln\left(\frac{T}{T_{ref}} \right) + 0.2776 \times 10^{-12}(T^3 - T_{ref}^3)]$$

$$100 \le T \le 3100 \text{ K} \qquad (33)$$

7.3.4.2. Melting point

The measured melting point of MgO was reported as T_m = 3250±20 K by Ronchi and Sheindlin [22]. The eutectic formation in binary systems of MgO with plutonium and americium oxides has been estimated by Zhang et al. [27, 28]. The melting temperatures of MgO-PuO_{2-x} and MgO-AmO_{2-x} are expressed by the following equations as a function of oxygen content of actinide oxide:

For MgO-AmO_{2-x} (Zhang *et al*., [27])

$$T_m(x) = -688 + 3053 \times (2-x) - 729 \times (2-x)^2 \quad 1.61 \le 2-x \le 2 \tag{34}$$

for MgO-AmO_{2-x} (Zhang et al., [27])

$$T_m = 1930 \text{ K} \qquad 1.5 \le 2-x \le 1.62$$

$$T_m(x) = 2221(1-N) + 2291N$$

$$+N(1-N) \times [236.6 + 1578.6N - 3478.0 \times N^2 + 1908.8N^3]$$

$$1.62 \le 2-x \le 2 \tag{35}$$

where N is the variable $[(2-x)-1.62]/0.38$. Here, the temperature at which the liquid appears first in the phase diagram is referred to as the melting temperature of the system, which can be the solidus or eutectic temperature. For the MgO-PuO_{2-x} system, the equilibrium oxygen pressure of PuO_{2-x} is much higher than the dissociation pressure of MgO. On the other hand, the melting temperature of the MgO-AmO_{2-x} system becomes very low (1930 K) at low oxygen potentials. This is accompanied by chemical dissociation processes of MgO.

7.3.4.3. Heat capacity and enthalpy

The enthalpy data of solid MgO up to the melting point have been given by Schick [23] and Cox et al. [6] as a set of tabulated data. Here, we adopt the temperature dependent correlation given by Schick [23]:

$$c_{p,s}(T) = 57.4203 - 1.88155 \times 10^{-5} T - 5.93688 \times 10^3 T^{-1}$$

$$298.15 \le T \le 3098 \text{ K} \tag{36}$$

where $c_{p,s}$ is in J K^{-1} mol^{-1} and T is in K. This yields the enthalpy correlation:

$$h_s(T) - h_s(298.15\text{K}) = 1.67133 \times 10^4 + 57.4203T$$

$$-9.40774 \times 10^{-5} T^2 - 5.93688 \times 10^3 ln(T)) \tag{37}$$

where h_s is in J mol^{-1}.

For liquid MgO, Cox et al. [6] gave the following estimation of heat capacity:

$$c_{p,l} = 84.0 \text{ J K}^{-1} \text{ mol}^{-1}$$

7.3.4.4. Heat of fusion

The values of heat of fusion of MgO have been reported by Schick [23] and Cox et al. [6]. These estimations indicate a very close value. Here, we adopt the following value given by Cox et al. [6]:

$$h_f = 77 \text{ kJ mol}^{-1} \tag{38}$$

7.3.4.5. Thermal conductivity

The recommended values of thermal conductivity of MgO have been tabulated by Touloukian et al. [26]. Their data for 98% dense, polycrystalline MgO were used to obtain a thermal-conductivity correlation as a function of temperature. The thermal conductivity of 100% dense MgO was evaluated using the well-known Maxwell-Eucken equation, Eq. (11), and then fitted to the following function in the temperature range 300-2300 K:

$$\kappa_s(T) = 0.53095 + 1.6970 \times 10^4 T^{-1} - 1.6071 \times 10^5 T^{-2}$$

$$-1.4482 \times 10^{-2} T + 7.3536 \times 10^{-6} T^2 \tag{39}$$

where κ_s is in W m^{-1} K^{-1} and T is in K. This equation is extrapolated up to the melting point.

7.4. Material properties of ADS core

7.4.1. *Fuels*

Table 1 shows specifications of the driver MOX fuel used by SCK•CEN in the predesign studies of MYRRHA ADS. Its properties were evaluated mainly based on the recommendations by Carbajo et al. [4]. The basic properties of the driver MOX fuel are summarized in Table 2. The temperature dependent properties are listed in Table 3.

TABLE 1. SPECIFICATIONS OF THE MOX FUEL

Fuel type (solid solution)	$(U_{0.7}, Pu_{0.3})O_{1.97}$	
Density (TD %)	95	
U-isotope vector (wt. %)	^{234}U	0.003
	^{235}U	0.404
	^{236}U	0.010
	^{238}U	99.583
Pu-isotope vector (wt. %)	^{238}Pu	1.27
	^{239}Pu	61.88
	^{240}Pu	23.50
	^{241}Pu	8.95
	^{242}Pu	4.40

TABLE 2. BASIC PROPERTIES OF THE MOX FUEL

Fuel type (solid solution)	$(U_{0.7}, Pu_{0.3})O_{1.97}$
Molecular weight (g/mol)	270.02
Density at 298.15 K (95% TD)	10535 kg/m^3
Density at 1500 K (95% TD)	10141 kg/m^3
Melting temperature	2951 K (solidus) 2994 K (liquidus)
Heat of fusion	245.2 kJ/kg

TABLE 3. TEMPERATURE DEPENDENT PROPERTIES OF THE MOX FUEL WITH 95% TD

Temperature [K]	Density [kg/m^3]	Heat capacity [J/kg·K]	Specific enthalpy* [kJ/kg]	Thermal conductivity [W/K·m]
298.15	10535	238	0.00	5.02
300	10534	239	0.44	5.00
400	10504	271	26.10	4.42
500	10473	289	54.16	3.96
600	10442	300	83.60	3.58
700	10410	307	113.96	3.27
800	10379	313	144.97	3.01
900	10347	317	176.49	2.79
1000	10315	321	208.44	2.60
1100	10282	325	240.76	2.43
1200	10249	328	273.41	2.29
1300	10214	331	306.37	2.16
1400	10178	335	339.66	2.06
1500	10141	338	373.30	1.98
1600	10101	343	407.34	1.91
1700	10060	348	441.89	1.87
1800	10018	355	477.05	1.84
1900	9972	364	512.99	1.84
2000	9925	375	549.92	1.86
2100	9875	388	588.04	1.90
2200	9822	404	627.62	1.95
2300	9767	423	668.93	2.02
2400	9708	444	712.24	2.11
2500	9647	469	757.85	2.21
2600	9582	496	806.05	2.33
2700	9513	526	857.13	2.45
2800	9442	559	911.34	2.58
2900	9367	594	968.95	2.72
2950.99	9327	613	999.71	2.79

* The values are relative to the solid at 298.15 K.

Table 4 shows typical specifications of IMF considered as candidate fuels for transmutation in fast ADS. Its melting temperatures were estimated considering the eutectic formation in the $MgO\text{-}PuO_{2-x}$ and $MgO\text{-}AmO_{2-x}$ systems. For $x = 0.12$, the melting temperatures for $MgO\text{-}PuO_{1.88}$ and $MgO\text{-}AmO_{1.88}$ systems are evaluated as 2 475 and 2 334 K, respectively. Considering the mole factions of constituents, the resultant melting temperatures of the IMF fuel particles and the IMF matrix are given as 2 441 K and 2 482 K, respectively. The basic properties of IMF are summarized in Tables 5 and 6. The temperature dependent properties are listed in Table 7 and 8.

TABLE 4. SPECIFICATIONS OF THE INERT MATRIX FUEL

Fuel type (composite)	$(Pu_{0.4}, Am_{0.5}, Cm_{0.1})O_{1.88}$ + MgO	
Fuel/Matrix volume fraction	40/60, 50/50	
Density (TD %)	90	
Pu-isotope vector (wt. %)	^{238}Pu	5.06
	^{239}Pu	37.91
	^{240}Pu	30.31
	^{241}Pu	13.21
	^{242}Pu	13.51
Am-isotope vector (wt. %)	^{241}Am	66.67
	^{243}Am	33.33
Cm-isotope vector (wt. %)	^{244}Cm	90.0
	^{245}Cm	10.0

TABLE 5. BASIC PROPERTIES OF THE INERT MATRIX FUEL (FUEL/MATRIX VOLUME FRACTION: 40/60)

Fuel type (composite)	40 vol.% $(Pu_{0.4}, Am_{0.5}, Cm_{0.1})O_{1.88}$ – 60 vol.% MgO
Molecular weight (g/mol)	271.34 (fuel) 40.30 (matrix) 96.30 (composite)
Fuel/Matrix mole fraction	0.2424/0.7576
Density at 298.15 K (90% TD)	10408 kg/m^3 (fuel) 3221 kg/m^3 (matrix) 6096 kg/m^3 (composite)
Density at 1500 K (90% TD)	10018 kg/m^3 (fuel) 3060 kg/m^3 (matrix) 5821 kg/m^3 (composite)
Melting temperature	2441 K (fuel) 2482 K (matrix)
Heat of fusion	797.1 kJ/kg (composite)

TABLE 6. BASIC PROPERTIES OF THE INERT MATRIX FUEL (FUEL/MATRIX VOLUME FRACTION: 50/50)

Fuel type (composite)	50 vol.% ($Pu_{0.4}$, $Am_{0.5}$, $Cm_{0.1}$)$O_{1.88}$ – 50 vol.% MgO
Molecular weight (g/mol)	271.34 (fuel) 40.30 (matrix) 115.22 (composite)
Fuel/Matrix mole fraction	0.3243/0.6757
Density at 298.15 K (90% TD)	10408 kg/m^3 (fuel) 3221 kg/m^3 (matrix) 6814 kg/m^3 (composite)
Density at 1500 K (90% TD)	10018 kg/m^3 (fuel) 3060 kg/m^3 (matrix) 6516 kg/m^3 (composite)
Melting temperature	2441 K (fuel) 2482 K (matrix)
Heat of fusion	658.9 kJ/kg (composite)

TABLE 7. TEMPERATURE DEPENDENT PROPERTIES OF THE INERT MATRIX FUEL WITH 90% TD (FUEL/MATRIX VOLUME FRACTION: 40/60)

Temperature [K]	Density [kg/m^3]	Heat capacity [J/kg·K]	Specific enthalpy* [kJ/kg]	Thermal conductivity [W/K·m]
298.15	6096	459	0.00	21.69
300	6095	460	0.90	21.55
400	6076	523	52.43	15.83
500	6055	559	107.91	12.26
600	6034	583	165.90	9.81
700	6012	600	225.64	8.02
800	5990	612	286.70	6.68
900	5967	622	348.79	5.65
1000	5944	631	411.74	4.86
1100	5921	638	475.40	4.26
1200	5897	644	539.69	3.82
1300	5872	649	604.53	3.51
1400	5847	654	669.85	3.32
1500	5821	659	735.63	3.23
1600	5795	663	801.81	3.24
1700	5768	667	868.38	3.34
1800	5740	670	935.30	3.52
1900	5711	673	1002.55	3.78
2000	5682	677	1070.12	4.10
2100	5652	680	1137.99	4.50
2200	5620	682	1206.15	4.96
2300	5588	685	1274.58	5.49
2400	5555	688	1343.27	6.08
2440.67	5541	689	1371.28	6.34

* The values are relative to the solid at 298.15 K.

TABLE 8. TEMPERATURE DEPENDENT PROPERTIES OF THE INERT MATRIX FUEL WITH 90% TD (FUEL/MATRIX VOLUME FRACTION: 50/50)

Temperature [K]	Density [kg/m^3]	Heat capacity [J/kg·K]	Specific enthalpy* [kJ/kg]	Thermal conductivity [W/K·m]
298.15	6814	403	0.00	18.05
300	6814	405	0.80	17.94
400	6792	460	46.61	13.27
500	6770	492	95.72	10.34
600	6747	513	146.93	8.33
700	6723	527	199.61	6.87
800	6699	539	253.41	5.76
900	6674	547	308.10	4.91
1000	6650	555	363.54	4.26
1100	6624	561	419.61	3.76
1200	6598	567	476.23	3.38
1300	6571	572	533.35	3.12
1400	6544	576	590.93	2.94
1500	6516	581	648.92	2.86
1600	6487	585	707.30	2.85
1700	6458	588	766.04	2.91
1800	6427	592	825.12	3.04
1900	6396	595	884.53	3.23
2000	6363	598	944.24	3.47
2100	6329	601	1004.26	3.77
2200	6295	604	1064.56	4.11
2300	6259	607	1125.13	4.51
2400	6221	609	1185.97	4.96
2440.67	6206	610	1210.79	5.15

* The values are relative to the solid at 298.15 K.

7.4.2. *Structure*

Harding et al. [13] reported some recommendations for the thermophysical properties of type 316 stainless steel. They assumed that the composition of the alloy is 65.4% Fe, 17% Cr, 13.5% Ni, 1.7% Mn and 2.4% Mo by weight. The basic solid properties are summarized in Table 9. The temperature dependent properties are listed in Table 10.

TABLE 9. BASIC PROPERTIES OF TYPE 316 STAINLESS STEEL [13]

Composition (wt. %)	65.4 Fe + 17 Cr + 13.5 Ni + 1.7 Mn + 2.4 Mo
Molecular weight	56.05
Density	7964 kg/m^3 (298.15 K) 7396 kg/m^3 (1500 K)
Melting temperature	1683 K (solidus) 1708 K (liquidus)

TABLE 10. TEMPERATURE DEPENDENT PROPERTIES OF TYPE 316 STAINLESS STEEL [13]

Temperature [K]	Density [kg/m^3]	Heat capacity [J/kg·K]	Specific enthalpy* [kJ/kg]	Thermal conductivity [W/K·m]
298.15	7964	471	0.00	14.04
300	7963	471	0.87	15.47
400	7925	492	49.04	16.91
500	7886	513	99.32	18.34
600	7844	534	151.7	19.77
700	7801	556	206.2	21.21
800	7756	577	262.8	22.64
900	7709	598	321.5	24.08
1000	7661	619	382.4	25.51
1100	7611	640	445.3	26.94
1200	7559	661	510.4	28.38
1300	7506	682	577.6	29.81
1400	7452	703	646.8	31.25
1500	7396	724	718.2	32.68
1600	7339	746	791.7	34.11
1683	7291	763	854.3	34.30

* The values are relative to the solid at 298.15 K.

7.4.3. *Coolant*

Thermophysical properties of lead-bismuth binary alloy with a eutectic composition (44.5 weight% lead and 55.5 weight% bismuth) were evaluated up to the critical point based on our recent study [20]. We assumed that the LBE vapor is composed of monatomic lead and bismuth and diatomic bismuth components, and that the liquid LBE is a non-ideal mixture of lead and bismuth. The obtained results are in good agreement with the database of thermophysical properties of the molten LBE used by SCK•CEN [25]. The basic properties of LBE are summarized in Table 11. The temperature dependent properties obtained with EOS developed by Morita et al. [20] are listed in Table 12.

TABLE 11. BASIC PROPERTIES OF LEAD-BISMUTH EUTECTIC

Composition	44.5 wt.% Pb + 55.5 wt.% Bi
Molecular weight	208.2
Melting temperature	398.15 K
Liquid density	10529 kg/m^3 (melting point) 9276 kg/m^3 (1500 K)
Normal boiling point	1944 K
Critical constants	Temperature = 4890 K Density = 2170 kg/m^3 Pressure = 87.8 MPa

TABLE 12. TEMPERATURE DEPENDENT PROPERTIES OF LEAD-BISMUTH EUTECTIC ON SATURATION CURVE

Temperature	Density		Saturation pressure	Specific enthalpy*		Viscosity	Thermal conductivity
[K]	[kg/m^3]		[MPa]	[kJ/kg]		[mPa·s]	[W/K·m]
	(liquid)	(vapor)		(liquid)	(vapor)	(liquid)	(liquid)
398.15	10529	1.065E-19	1.212E-21	0.00	669.76	3.306	10.91
400	10527	1.392E-19	1.591E-21	0.26	670.01	3.277	10.93
600	10300	2.511E-11	4.388E-13	28.19	703.16	1.739	12.96
800	10072	2.732E-07	6.520E-09	55.84	739.54	1.267	15.00
1000	9845	6.412E-05	1.955E-06	83.12	774.96	1.048	17.03
1200	9617	2.265E-03	8.445E-05	109.94	808.64	0.923	(19.07)**
1400	9390	2.749E-02	1.215E-03	136.22	840.54	(0.843)**	(21.11)
1600	9163	1.727E-01	8.843E-03	162.02	870.80	(0.788)	(23.14)
1800	8935	7.035E-01	4.097E-02	187.58	899.53	(0.747)	(25.18)
2000	8708	2.127E+00	1.387E-01	213.29	926.75	(0.717)	(27.21)
2200	8481	5.202E+00	3.744E-01	239.69	952.41		
2400	8253	1.089E+01	8.538E-01	267.34	976.34		
2600	8026	2.029E+01	1.712E+00	296.73	998.36		
2800	7798	3.464E+01	3.104E+00	328.24	1018.22		
3000	7571	5.530E+01	5.199E+00	362.10	1035.65		
3200	7344	8.384E+01	8.163E+00	398.47	1050.37		
3400	7107	1.222E+02	1.216E+01	437.37	1062.06		
3600	6835	1.730E+02	1.735E+01	478.85	1070.33		
3800	6518	2.398E+02	2.387E+01	522.95	1074.72		
4000	6148	3.281E+02	3.185E+01	569.80	1074.56		
4200	5712	4.472E+02	4.140E+01	619.74	1068.86		
4400	5183	6.140E+02	5.263E+01	673.64	1055.87		
4600	4505	8.676E+02	6.564E+01	733.96	1031.87		
4800	3478	1.351E+03	8.050E+01	811.93	983.78		
4890	2170	2.170E+03	8.781E+01	908.08	908.08		

* The values are relative to the liquid at the melting point.
** Parentheses indicate extrapolation beyond range of experimental correlations.

7.5. Conclusion

Thermophysical properties of IMF and MOX fuel were estimated for use in the IAEA benchmark problems. Due to a lack of experimental data published in literature, the basic properties such as the solid density, heat capacity and thermal conductivity were estimated up to the melting point based on empirical and theoretical models extrapolating low temperature data of its constituents. Recommendations were also presented for solid properties of type 316 stainless steel and for liquid and vapor properties of LBE. We expect that the set of thermophysical properties presented here could be utilized as a basis for the development of the standard database for use in the assessment of reactor performance and safety behavior of ADS.

REFERENCES TO CHAPTER 7

[1] ADAMSON, M.G., et al., Experimental and thermodynamic evaluation of the melting behavior of irradiated oxide fuels, J. Nucl. Mater., Vol. 130 (1984) pp. 349–365.

[2] BAKKER, K., KONINGS, R.J.M., On the thermal conductivity of inert-matrix fuels containing americium oxide, J. Nucl. Mater., Vol. 254 (1998) pp. 129–134.

[3] BENEDICT, M., et al, Nuclear Chemical Engineering, MacGraw-Hill, New York, USA (1981).

[4] CARBAJO, J.J., et al., A review of the thermophysical properties of MOX and UO_2 fuels, J. Nucl. Mater., Vol. 299 (2001), pp. 181–198.

[5] CORDFUNKE, E.H.P., KONINGS, R.J.M., Thermochemical Data for Reactor Materials and Fission Products, North-Holland, Amsterdam, Netherlands (1990).

[6] COX, J.D., et al., CODATA Key Values for Thermodynamics, Hemisphere Publishing Corporation, New York, USA (1986).

[7] DURIEZ, C., et al., Thermal conductivity of hypostoichiometric low Pu content (U, Pu)O_{2-x} mixed oxide, J. Nucl. Mater., Vol. 277 (2000) pp. 143–158.

[8] EPSTEIN, L.F., Ideal solution behavior and heats of fusion from the UO_2-PuO_2 phase diagram, J. Nucl. Mater., Vol. 22 (1967) 340–349.

[9] FINK, J.K., Enthalpy and heat capacity of the actinide oxides, Int. J. Thermophys., Vol. 3, (1982) pp. 165–200.

[10] FINK, J.K., Thermophysical properties of uranium dioxide, J. Nucl. Mater., Vol. 279, (2000) pp. 1–18.

[11] FUKUSHIMA, S., et al., Thermal conductivity of $(Pu_{1-x}Nd_x)O_{2-y}$ and $(Pu_{1-x}Y_x)O_{2-y}$ solid solutions, J. Nucl. Mater., Vol. 115 (1983) pp. 118–127.

[12] GIBBY, R.L., The effect of plutonium content on the thermal conductivity of (U, Pu)O_2 solid solutions, J. Nucl. Mater., Vol. 38 (1971) pp. 163–177.

[13] HARDING, J.H., et al., Thermophysical and Thermodynamic Properties of Fast Reactor Materials, Commission of the European Communities Report EUR 12402 EN (1989).

[14] JACOBS, M.H.G., OONK, H.A.J., A new equation of state based on Grover, Getting and Kennedy's empirical relation between volume and bulk modulus. The high-pressure thermodynamics of MgO, Phys. Chem. Chem. Phys., Vol. 2 (2000) pp. 2641–2646.

[15] KATZ, J.J., et al., The Chemistry of the Actinide Elements, Vol. 2, Chapman and Hall, London, UK (1986).

[16] KONINGS, R.J.M., Thermochemical and thermophysical properties of curium and its oxides, J. Nucl. Mater., Vol. 298 (2001) pp. 255–268.

[17] LEIBOWITZ, L., et al., Enthalpy of Molten Uranium-Plutonium Oxides, Argonne National Laboratory Report ANL-8082 (1974).

[18] MARTIN, D.G., The thermal expansion of solid UO_2 and (U, Pu) mixed oxides — a review and recommendations, J. Nucl. Mater., Vol. 152 (1988) pp. 94–101.

[19] MORITA, K., et al., Thermodynamic Properties of Lead-Bismuth Eutectic for Use in Reactor Safety Analysis, Proc. 13th. Int. Conf. Nucl. Eng., Beijing, May 2005. Also available in MORITA, K., et al., Thermophysical properties of lead-bismuth eutectic alloy in reactor safety analyses, J. Nucl. Sci. Tech., Vol. 43 (2006) pp. 1–11.

[20] RONCHI, C., et al., Thermal conductivity of uranium dioxide up to 2900 K from simultaneous measurement of the heat capacity and thermal diffusivity, J. Appl. Phys., Vol. 85 (1999) pp. 776–789.

[21] RONCHI, C., SHEINDLIN, M., Laser-Pulse Melting of Nuclear Refractory Ceramics, Int. J. Thermophys., Vol. 23 (2002) pp. 293–305.

[22] SCHICK, H.L., Thermodynamics of Certain Refractory Compounds, Vol. II, Academic Press, New York, USA (1966).

[23] SILVA, R.J., et al., Chemical Thermodynamics, Vol. 2, Chemical Thermodynamics of Americium, Elsevier, Amsterdam, Netherlands (1995).

[24] SOBOLEV, V., MYRRHA ADS DATABASE: Part I. Thermophysical properties of the molten lead-bismuth eutectic. Report BLG-1014, SCK·CEN, Belgian Nuclear Research Centre, Mol, Belgium (2005).

[25] TOULOUKIAN, Y.S., et al., Thermophysical Properties of Matter, Vol. 2, Thermal Conductivity, Nonmetallic Solids, IFI/Plenum, New York, USA (1970).
[26] ZHANG, H., et al., Melting behaviour of oxide systems for heterogeneous transmutation of actinides. III. The system Am-Mg-O, J. Nucl. Mater., Vol. 250 (1997a) pp. 88–95.
[27] ZHANG, H., et al., Melting behaviour of oxide systems for heterogeneous transmutation of actinides. I. The systems Pu-Al-O and Pu-Mg-O, J. Nucl. Mater., Vol. 249 (1997b) pp. 223-230.

CHAPTER 8. DOMAIN-V: MOLTEN SALT REACTOR WITH FERTILE FUEL

8.1. Introduction

The liquid-fuelled, molten salt MSBR breeder was designed by ORNL at the beginning of the 1970's, in response to the successful operation of an 8 MW experimental molten-salt reactor facility between 1965-69, called MSRE (Molten Salt Reactor Experiment) demonstrating the practicality of molten salts. The objective was to develop the most efficient ^{233}U breeder using the thorium cycle, in the context of strong competition with the development of the LMFBR (Liquid Metal Fast Breeder Reactor).

The overall design of the MSBR concept is shown in Fig. 1 [1]. The fuel salt, a mixture of beryllium, ^{7}lithium, thorium and uranium fluorides, is pumped through a core region consisting of bare graphite stringers and blocks. Passages for salt are formed in the graphite elements.

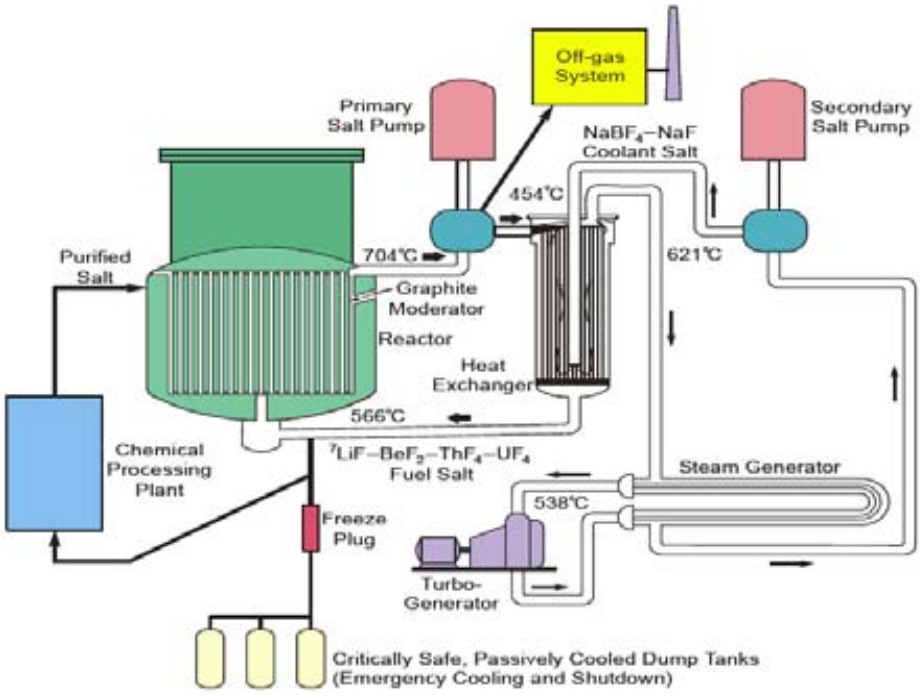

FIG. 1. Schematic of MSBR and AMSTER.

In nominal operating conditions, the salt enters the core at ~565°C, becomes critical due to the moderation by graphite, and leaves the core region at 705°C. Heat is then transferred from the primary fuel salt to a secondary coolant salt in an intermediate heat exchanger. The secondary coolant salt is a mixture of sodium fluoroborate and sodium fluoride, selected because it is less expensive than the ^{7}LiF, BeF_2 coolant used for the MSRE, and has a lower melting point, which is important in order to prevent the salt from freezing when leaving the steam generator.

The coolant salt passes through a steam generator where super-critical steam at 240 atm and 538°C is generated, yielding an overall thermal efficiency of 44%. Thus the MSBR project, designed to generate a thermal power of 2 250 MWt, produces an electrical power of 1 GW(e). All parts of the primary circuit that contact the fuel salt are made of the nickel base alloy, Hastelloy N modified, which has proven to be resistant to the corrosion by fluorides up to 700°C. Three important features of such a system have to be highlighted:

1) A noticeable passive safety feature; in case of an abnormal temperature rise, a freeze plug will melt, draining the salt to tanks, thereby making the system highly sub-critical;
2) Like in MSRE, non soluble fission products (volatile ones like xenon or krypton, or noble metals) are continuously extracted by helium bubbling into an off-gas system;
3) A fraction of the circulating fuel salt is continuously extracted to be chemically processed removing fission products from the primary loop.

The AMSTER concept as designed by EDF [2-3] is based on the MSBR concept assuming different optimization criteria. Whereby the MSBR was designed to optimize the breeding capabilities utilizing the thorium cycle, the AMSTER design (AMSTER-Incinerator) intends to optimize the burning of TRansUranium elements (TRU) with a thorium support base. An additional second AMSTER design variation (AMSTER-breeder) minimizes the amount of long lived nuclear waste sent to the final disposal, with a breeding factor equal to 1 (thus generating as much ^{233}U as is consumed).

These two AMSTER configurations are very similar, except from the core region, which is divided into two core-zones (a fissile and a fertile zone) in the case of AMSTER-breeder.

8.2. Fuel-cycle studies

8.2.1. *Reference scenario: MSBR*

The MSBR operating parameters are as follows:

Thermal/electrical power:	2 250 MWt/1 000 MW(e)
Power density:	87.4 Wcm^{-3}
Fluoride salt composition (mol%):	(HN)F4 12.3%-^{7}LiF 72%-BeF_2 16%
Salt volume inside/outside the core:	25.73 m^3/48.7 m^3
Salt density	3.75-6.68 10-4 T(°C) g cm^{-3}
Fuel and graphite temperature:	635°C
Graphite density:	1.68 g cm^{-3}

The fuel is continuously reprocessed. For the cycle time of uranium, 8 000 days are assumed (equal to the reactor doubling time). For the higher nuclides, a time of sixteen years is assumed. The isotopes are continuously removed, and replaced by an identical mass of a ^{232}Th-^{233}U mixture, with adequate proportions in order to keep the reactor critical.

The fuel composition under irradiation has to be computed time step by time step. At the end of each time step, a fraction of the FP and ^{233}Pa is removed (reprocessing) and replaced by heavy nuclei, whose enrichment is computed to keep the reactor critical while maintaining the heavy nuclides mass constant.

The reaction rates and effective cross-sections are determined using cell calculations with the APOLLO2 transport code with 99 groups CEA 93 library (which is issued from JEF2.2 evaluation), using a Pij (first collision probabilities) to solve the integral transport equation with infinite array hypothesis. The cell geometric model is based on the cylindrisation of the real geometry, which is hexagonal (MCNP calculations showed that the cylindrisation approximation does not have any important effect). After the 99 groups cell computation, a condensation into 6 groups and a homogenisation of the cell are made. The core k_{eff} is calculated using the SN APOLLO2 option, with 6 energy groups. The mean reaction rates in the core are computed, and used for the evolution calculation (equilibrium calculation). The breeding factor computed by ORNL is 1.063, while EDF calculations yielded 1.059.

Calculation results obtained by EDF at equilibrium are summed up in the following table, for 1 GW(e) power reactor producing 7.2 TWhe per year are as follows:

Mass of fuel salt in core:	85 638 kg
Mass of fuel salt in reactor:	162 073 kg
Mass of fission products in reactor:	326 kg
Mass of heavy metal in core/in reactor:	37 947 kg/71 816 kg
Mass of reprocessed fuel per day:	2350 kg
^{233}U production (kg/TWhe):	5.2 kg
^{232}Th consumption (kg/TWhe):	958 kg *
Reactor inventory Pa/Th/U/Np/Pu/Am/Cm/Cf (kg):	7/70143/1622/14/16.5/0.8/2/10^{-3}
Waste per year (Th/Np/Pu/Am/Cm/Cf) (g):	6 130 000/713/848/42/102/0.06
Waste per year: total mass of TRU:	1 700 g
Waste per year: mass of volatile FP:	701 kg

* Thorium losses have been taken into account (6130/7.2= 851 kg/TWh_e)

Only 236 g of TRU per TWh_e (1.7 kg per year) are sent to the disposal: MSBR is a very clean reactor if compared to a PWR, which produces 30 kg of TRU per TWh_e.

In a 1GW(e) power MSBR, there is only 33 kg of TRU at equilibrium, most of them being ^{237}Np (14 kg) and ^{238}Pu (12 kg), and a weak amount of problematic isotopes like ^{244}Cm (1.5 kg) and ^{252}Cf (0.9 g). Moreover, the fissile inventory is limited, with 1 160 kg of ^{233}U and a little less than 100 kg of ^{235}U: compared to fast breeder reactors, which requires about 10 times this mass of fissile isotopes.

We can see that breeding (conversion ratio > 1) is not possible without a significant Pa separation, except for a very fast extraction of fission products (less than 50 days). On the other hand, with a Pa separation good breeding factors can be obtained with a slow extraction time of the rare earths (from 100 to 500 days).

8.2.2. *AMSTER — Incinerator concept*

The AMSTER is a continuously reloaded, graphite-moderated molten salt critical reactor, using a ^{232}Th fuel support, slightly enriched with ^{235}U if necessary. Equilibrium state calculations were done under the hypothesis that the reactor is continuously fed by a mixture of thorium and of transuranium elements issued from PWR spent fuel, i.e. EPR with initial U enrichment of 4.9% and burnup of 60 000 MW•d□/t. the mass composition (%) is following: ^{234}U 0.0187, ^{235}U 0.8195 ,^{236}U 0.7312, ^{238}U 96.9273, ^{238}P 0.0478, ^{239}P 0.6606, ^{240}P 0.3198, ^{241}P 0.2032, ^{242}P 0.1184, ^{241}Am 0.0082, ^{243}Am 0.0350, ^{244}Cm 0.0139, ^{245}Cm 0, ^{237}Np 0.09651, Total 100. The non soluble fission products are supposed to be extracted immediately.

The calculation scheme is the same as for the MSBR but there is only one moderation ratio for the entire core. The cell geometric model is based on the cylindrical model of the real geometry, which is hexagonal. Operating parameters for AMSTER-Incinerator are as follows:

Thermal/electrical power:	2 250 MWt/1 000 MW(e)
Power density:	74 W cm^{-3}
Fluoride salt composition (mol %):	$(HN)F_4$ 12.3% — ^{7}LiF 72% — BeF_2 16%
Salt volume inside/outside the core:	30.4 m^3/18 m^3
Salt density	3.75-6.68×10^{-4} T(°C) g cm^{-3}
Fuel and graphite temperature:	635°C
Graphite density:	1.68 g cm^{-3}
Reprocessing time:	300 days

Calculations at equilibrium for 1 GW(e) power reactor producing 7.2 TWh_e per year (equilibrium) are as follows:

Mass of fuel salt in core:	101 171 kg
Mass of fuel salt in reactor:	161 075 kg
Mass of fission products in reactor:	686 kg
Mass of heavy metal in core/in reactor:	4 4621 kg/71 042 kg
Mass of reprocessed fuel per day:	537 kg
Reactor inventory Pa/Th/U/Np/Pu/Am/Cm/Cf (kg):	71/67451/2023/78/580/162/675/2.3
Waste per year (U/Np/Pu/Am/Cm/Cf) (g)*:	20.3/78/580/162/675/2.3
Waste per year: total mass of TRU:	1497 g
Waste per year: mass of volatile FP **:	357 kg
Waste per year: mass of noble metal FP ***:	143 kg
Waste per year: mass of the other FP:	220 kg

*loss rate= 10^{-3} except from uranium, which is 10^{-5} thanks to a double reprocessing (fluorination + liquid-liquid extraction).
**These gaseous elements (Xe, Kr, He, 3H) are extracted from the salt at the He injection in the pump.
***These noble metal elements (Mo, Se, Te, Tc, Ru, Pd, Ag, Nb) are extracted from the salt at the He injection in the pump.

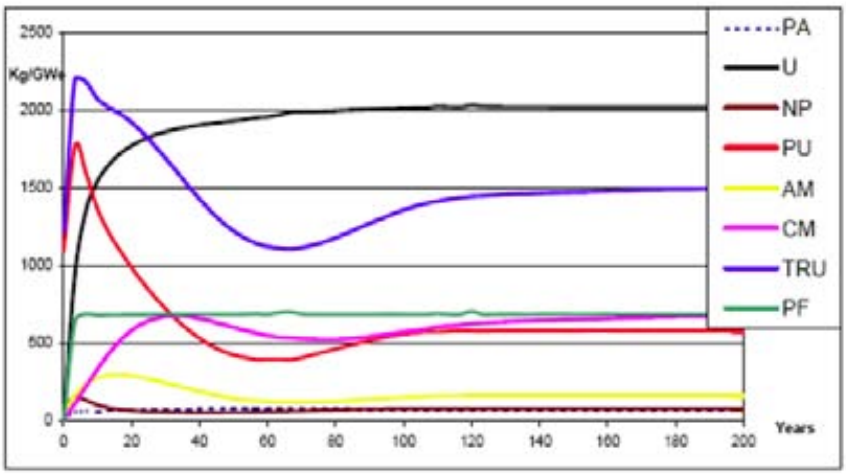

FIG. 2. AMSTER-Incinerator long term evolution of isotopes for 1 GW(e) reactor.

After a short initial rise corresponding to the counter-balancing of the rapid formation of the fission products (which are neutronic poisons), the amount of TRansUranium elements (TRU) in the reactor slowly decreases, because of the ^{233}U formation, which brings an additional source of reactivity (see Fig. 2). In about 70 years, the TRU mass balance starts to increase again, to counter-balance the ^{236}U formation. Equilibrium is reached in about 170 years.

The amount of TRU loaded in AMSTER incinerator per TWhe at equilibrium is ~22.6 kg, with 207 g sent to the final disposal, so the reduction factor is quite good, about 110. But this efficiency is not constant, and is lower between 40 and 170 years (and higher during the 40 first years).

AMSTER is an efficient incinerator concept, but it is important to underline the overwhelming degradation of the TRU isotopic content, leading at equilibrium to large amount of minor actinides, especially curium (350 kg of ^{244}Cm), and even californium (1.6 kg of ^{252}Cf).

In conclusion, AMSTER incinerator looks like an efficient Pu and minor actinides burner, the TRU being totally burnt except from a limited fraction (~1%) sent to the final disposal requiring a very small fissile inventory. On the other side, very large masses of minor actinides at equilibrium, especially ^{244}Cm (350 kg per GW(e)), and ^{252}Cf (1.6 kg), are accumulated implying serious concerns for criticality, safety, reprocessing and maintenance issues.

8.2.3. *AMSTER — breeder concept*

Operating parameters are as follows:

Thermal/electrical power:	2 250 MWt/1 000 MW(e)
Power density:	74 Wcm^{-3}
Fluoride salt composition (mol %):	$(HN)F_4$ 12.3% — ^7LiF 72% — BeF_2 16%
Salt volume inside/outside the core:	30.4 m^3/48.4 m^3
Salt density:	$3.75\text{-}6.68\times10^{-4}$ T(°C) g cm^{-3}
Fuel and graphite temperature:	635°C
Graphite density:	1.68 g cm^{-3}

The fuel is continuously reprocessed. The reprocessing is exactly the same as for the AMSTER-incinerator: 300 efpd removal time for the lanthanides and all actinides (no separation of the Pa stream) is assumed. Preliminary simplified calculations indicated that the reactor was a breeder, but more detailed calculations show now that a separation of Pa is necessary in order to manage breeder option. These new calculations are in agreement with ORNL studies on the impact of reprocessing on the conversion ratio. EDF calculations have confirmed that result, and given a more precise evaluation of the breeding factor, which is equal to 0.95, that will require additional fissile to retain criticality.

AMSTER breeder has been calculated using the APOLLO2 code with a cylindrical description and 16 groups SN computations. The calculation scheme is exactly the same that for the MSBR except that RZ (2D) is replaced by cylindrical model (1D). Calculation results obtained by EDF at equilibrium for 1 GW(e) are as follows:

Power reactor producing 7.2 TWhe per year:	
Mass of fuel salt in core:	101 171 kg
Mass of fuel salt in reactor:	161 075 kg
Mass of fission products in reactor:	662 kg
Mass of heavy metal in core/in reactor:	44 617 kg/71 035 kg
Mass of reprocessed fuel per day:	537 kg
U233 consumption (kg/TWhe):	4.9 kg
Th232 consumption (kg/TWhe):	102.8 kg ****
Reactor inventory Pa/Th/U/Np/Pu/Am/Cm/Cf (kg):	86/68528/2286/46/66/4.3/20/0.09
Waste per year (Th/U/Np/Pu/Am/Cm/Cf) (g)*:	68400/20/46/66/4/20/0.09
Waste per year: total mass of TRU:	245 g
Waste per year: mass of volatile FP **:	357 kg
Waste per year: mass of noble metal FP ***:	143 kg
Waste per year: mass of the other FP:	220 kg

*loss rate= 10^{-3} except from uranium, which is 10^{-5} thanks to a double reprocessing (fluorination + liquid-liquid extraction)
**These gaseous elements (Xe, Kr, He, 3H) are extracted from the salt at the He injection in the pump
***These noble metal elements (Mo, Se, Te, Tc, Ru, Pd, Ag, Nb) are extracted from the salt at the He injection in the pump
**** Thorium losses have been taken into account (9.5 = 68.4/7.2 kg/TWh_e)

As a conclusion, the AMSTER-breeder is actually not quite a breeder (conversion ratio equal to 0.95). However, it has a high conversion ratio, and could be operated as a 'near-breeder' reactor, provided an outside source of ^{233}U is available to close the cycle: only ~5 kg per TWhe are needed, that could be easily produced in a PWR or in a fast breeder reactor (in a thorium radial blankets, for instance). If we want to meet our initial objective, namely to obtain a self-breeder, two alternatives can be envisaged:

1) According to ORNL, ^{233}Pa has to be extracted from the active loop (within 3 to 30 days). A slow extraction of rare earths is required (300 to 500 days). This reactor would then be very close to the MSBR, with comparable requirements on the performance of the on-line fuel salt reprocessing unit.

2) It is possible to increase the size of the reactor in order to decrease the specific power and favour the ^{233}Pa decay to U^{233}.

8.3. Neutronic modeling for liquid-fuelled reactor concepts

In the molten salt reactors the liquid fuel travels from the core region through the loops to the heat exchangers and the pumps, so the fuel spends a significant fraction of time outside the core region. This causes that a significant fraction of the delayed neutrons are emitted either at positions characterized by an importance different from the value at the position where fission took place or outside the core region with an overall reduction of their capability to contribute to the chain reaction. The number of delayed neutrons lost in the loop depends on the residence time of the fuel inside the core region and the time spent outside the core region, in other words, on the flow rate of the fuel, the fuel mass in the core region, and the relative volumes of the core and loop. Consequences appear both in static and time-dependent situations.

Several physical models can be adopted in accounting for the motion of delayed neutron precursors outside the core region. In all models a modification of the balance equation for delayed precursors is introduced.

8.4. The reference model

The reference model correctly describing the balance of neutrons and precursors is constituted by the Boltzmann transport equation for neutrons associated to a balance for delayed neutron precursors including the streaming term due to the motion in the fluid fuel [4]. A spatial first order term is thus appearing also in the equations for precursors, and the full model can be given the form of the following system of equations:

$$\begin{cases} \dfrac{\partial n(\mathbf{r},E,\mathbf{\Omega},t)}{\partial t} = \left[\hat{\mathrm{L}}(t)+\hat{\mathrm{M}}_p(t)\right] n(\mathbf{r},E,\mathbf{\Omega},t) + \displaystyle\sum_{i=1}^{R} \mathscr{E}_i(\mathbf{r},E,t) + S(\mathbf{r},E,\mathbf{\Omega},t), \\ \dfrac{1}{\lambda_i}\dfrac{\partial \mathscr{E}_i(\mathbf{r},E,t)}{\partial t} + \dfrac{1}{\lambda_i}\nabla\cdot(\mathbf{u}(\mathbf{r},t)\mathscr{E}_i(\mathbf{r},E,t)) = \hat{\mathrm{M}}_i(t) n(\mathbf{r},E,\mathbf{\Omega},t) - \mathscr{E}_i(\mathbf{r},E,t), \\ \qquad\qquad i=1,2,...,R, \end{cases} \tag{1}$$

where leakage, prompt and delayed multiplication operators are introduced and the delayed neutron equations are written in terms of delayed emissivities, rather than in terms of concentrations. Proper boundary conditions accounting for the flow in the external circuit are introduced for both neutrons and delayed precursors. The velocity field u(r,t) requires the introduction of further equations to describe the fluid-dynamics of the fissile material. The resulting model turns to be quite complicated and challenging from the numerical point of view. Different levels of approximation can be introduced, depending on the physical configuration of the system under study.

A first simplification amounts to the assumption of a velocity field established independently from the neutronic field. In that case u(r,t) is a given quantity. For systems of the AMSTER type where the fluid is flowing in parallel tubes inside the graphite matrix the further assumption of a fully axial flow with no radial dependence (slug flow) can be made. In this case the streaming term involves only an axial derivative of the delayed neutron flow.

For the peculiar situation of an externally imposed velocity field the system of equations can be reduced by a numerical technique that can be considered as a natural extension of the classic separation-projection procedure of reactor physics. Consequently, consistent kinetic equations are derived, with a mathematically founded definition of the kinetic parameters.

8.4.1. *Kinetic equations and kinetic parameters*

It is useful for the engineering evaluations of the system to generalize the kinetic equations of reactor physics to molten salt systems. This extension requires a time phase-space separation for both neutron density and delayed neutron emissivities [4]. To carry out the projection a weight function needs to be determined. As usual, the solution of the stationary adjoint problem is chosen, introducing also importance functions associated to delayed neutrons. The adjoint model can be given the following form:

$$\begin{cases} \left[\hat{\mathrm{L}}_0^\dagger + \hat{\mathrm{M}}_{p,0}^\dagger\right] N_0^\dagger(\mathbf{r},E,\mathbf{\Omega}) + \sum_{i=1}^{R} \hat{\mathrm{M}}_{i,0}^\dagger \mathscr{E}_{i,0}^\dagger(\mathbf{r},E) + S_0^\dagger(\mathbf{r},E,\mathbf{\Omega}) = 0, \\ \dfrac{1}{4\pi} \oint \mathrm{d}\mathbf{\Omega} N_0^\dagger(\mathbf{r},E,\mathbf{\Omega}) + \dfrac{1}{\lambda_i}\mathbf{u}_0 \cdot \mathbf{V}\left(\mathscr{E}_{i,0}^\dagger(\mathbf{r},E)\right) - \mathscr{E}_{i,0}^\dagger(\mathbf{r},E) = 0, \quad i = 1,2,\ldots,R. \end{cases} \tag{2}$$

with boundary conditions symmetrical with respect to the direct problem. When the projection of the time dependent equations (1) is taken upon the adjoint, the following point-like system of equations is readily obtained:

$$\begin{cases} \dfrac{\mathrm{d}A}{\mathrm{d}t} = \alpha A + \sum_{i=1}^{R} \mu_i G_i + \tilde{S}, \\ \dfrac{\mathrm{d}G_i}{\mathrm{d}t} = \vartheta_i A - \Lambda_i G_i, \quad i = 1,2,\ldots,R \end{cases} . \tag{3}$$

As it is clearly seen the kinetic parameters take a special form, to account for the fuel flow, with the introduction of extra terms with respect to the standard model. Of particular significance is the definition of the effective delayed neutron fraction, which plays a very important role in determining the time-dependent characteristics of the system:

$$\tilde{\beta}_i = \frac{\left\langle \mathscr{E}_{i,0}^\dagger \middle| \hat{\mathrm{M}}_i n \right\rangle}{\sum_{i=1}^{R} \left\langle N_0^\dagger \middle| \mathscr{E}_i \right\rangle + \left\langle N_0^\dagger \middle| \hat{\mathrm{M}}_p n \right\rangle} . \tag{4}$$

It is clear that the definition of effective □ consistently with the reduction of the original full model requires a weighting process. Therefore, this parameter has a dynamical meaning, and as such it may change during a transient owing to a change in the spatial distributions of neutron and precursors. In fact, the point model (3) is used in conjunction with quasi-static schemes that can produce accurate predictions of the space-energy-time evolution of the neutron flux during a transient. This remark should help avoiding any confusion between an effective quantity and quantities evaluated on the basis of static considerations. Concerning delayed neutrons, the reduction of their role is described also by the reduction of static reactivity induced by fuel motion. However, this parameter is obviously different from what is evaluated by a weighting procedure and must be used in generalized methods for the kinetic evaluation, with special connection to quasi-statics.

An alternative definition of kinetics parameters is employed in the SIMMER spatial kinetics model [8]. The effects related to the precursor movement are taken into account by introducing additional (negative at nominal conditions due to ‘loss’ of delayed neutrons in the loop, i.e. outside of the core) source terms in the shape and amplitude equations. The reactivity and effective delayed neutron fractions are determined independently upon the salt flow rate, i.e. similarly to a solid fuel system. As a consequence, the reactivity in a MSR is positive at nominal conditions (contrary to ADS in which the reactivity is negative, but the source term is positive at nominal conditions).

8.4.2. *A heuristic point model*

The effect of non-stationary liquid-fuel on neutron kinetics can be illustrated in a relatively simple manner by a heuristic approach, through a generalization of the usual point kinetic model by the introduction of proper terms to account for the fuel motion. This approach is explained in the following.

8.4.2.1. Point kinetic model of stationary fuel

$$\begin{cases} \dfrac{dn}{dt} = k_{eff}\left(\dfrac{k_{eff}-1}{k_{eff}} + \rho(t) - \tilde{\beta}\right)\dfrac{n}{l_{pr}} + \sum_i \lambda_i C_i^{core} + Q \\ \dfrac{dC_i^{core}}{dt} = k_{eff}\dfrac{\beta_i}{l_{pr}} n - \lambda_i C_i^{core} \end{cases} \tag{5}$$

where the normal nomenclature has been adopted as found in any nuclear engineering textbook. The second equation above describes the generation and loss of neutron precursors (normally six groups of precursors are adopted) inside the core region.

In case the fuel is non-stationary, an additional set of precursor equations has to be set up to describe the time-dependence of the precursor concentration C^{loop} in the external loop regions.

8.4.2.2. Point kinetic model for liquid-fuelled reactor concepts

$$\begin{cases} \dfrac{dn}{dt} = k_{eff}\left(\dfrac{k_{eff}-1}{k_{eff}} + \left(\rho(t) + \rho_{lost}\right) - \tilde{\beta}\right)\dfrac{n}{l_{pr}} + \sum_i \lambda_i C_i^{core} + Q \\ \dfrac{dC_i^{core}}{dt} = k_{eff}\dfrac{\beta_i}{l_{pr}} n - \lambda_i C_i^{core} + C_i^{loop}\left(\dfrac{w}{M_{loop}}\right)\left(\dfrac{V_{loop}}{V_{core}}\right) - C_i^{core}\left(\dfrac{w}{M_{core}}\right) \\ \dfrac{dC_i^{loop}}{dt} = C_i^{core}\left(\dfrac{w}{M_{core}}\right)\left(\dfrac{V_{core}}{V_{loop}}\right) - C_i^{loop}\left(\dfrac{w}{M_{loop}}\right) - \lambda_i C_i^{loop} \qquad i = 1,\ldots,R \end{cases} \tag{6}$$

Normally the external loop is sub-divided in various nodes. In the SIM-ADS code [5], as used in the following transient analysis section, the external loop has been divided into 10 nodes.

8.4.3. *Effect of fuel mixing phenomena on the kinetic behavior of molten salt reactors*

The models presented above aim to simulate the change in the distribution of the delayed neutron precursors in liquid-fuel reactors due to the fuel circulation, as this has an important effect on the kinetics behavior of the reactor. However, for the proper determination of the distorted delayed neutron precursors distribution, besides the circulation of the fuel, which shifts the distribution along the flow direction, one has to consider the fuel mixing effect, as well, which can result in a dispersion of the original shape of the distribution. The importance of this effect has been shown in the MSRE pump start-up transient of the MOST project [2], where some simulations showed oscillations not observed during the experiment. In reality, the fuel mixing in the primary loop due to the turbulent flow diminishes these oscillations. Therefore, in the calculations care should be taken to the simulation

of dispersion, which can be done by the insertion of a diffusive term in the precursor-concentration equations:

$$\frac{\partial C_i'}{\partial t} = \frac{\partial C_i}{\partial t} + \nabla\left(u(z,t)K(z,t)\nabla C_i\right) \tag{7}$$

where u and K are the fuel velocity and the dispersion coefficient at a given point of the primary circuit [6]. At the same time one should minimize the numerical dispersion by defining a proper number of control volumes or using an improved discretization scheme, e.g. a Total Variation Diminishing scheme [6]. Otherwise the numerical dispersion can override the physical phenomena.

Calculations indicate [7] that the fuel dispersion effect may be governed by the fuel mixing in the large volume components of the primary loop (e.g. heat exchanger, etc) and not in the pipings. This means that proper estimation for the dispersion coefficients can be expected only from measurements or from detailed, 3D analysis of the flow.

8.5. Transient studies

8.5.1. *Introduction*

The safety issue associated with a particular reactor design is typically expressed in its dynamic behaviour, or transient response to typical malfunctions which the reactor might experience during its operation. Various transient initiators have been defined which are believed to be representative malfunctions such as loss of flow due to failure of a pump, inadvertent insertion of a positive reactivity ramp, over-cooling of the primary side due to some failure in the secondary loop, and failure of the heat sink.

ORNL performed dynamic studies of the ORNL MSBR design using analog computers. On account of the severe computational resources limitations imposed by these machines at those times (1960s), a detailed, high fidelity simulation of the dynamic behaviour was very difficult to achieve. A large number of simplifications in the modelling were necessary in order to accommodate the limited computational resources. The dynamic calculations performed at ORNL were thus of limited utility. More modern computational tools however allow a much more precise prediction of the transient reactor behaviour.

In order to be able to study the transient response of the reactor design to typical plant transient initiators, design data of sufficient detail is required in order to perform these analyses. These data include not only typical reactor and plant design data, but also reactor and fuel cycle specific neutronic data such as reactivity feedback coefficients and nuclear kinetic data.

Taking into account the fact that total temperature coefficients for both MSBR and AMSTER are positive, thereby rendering these reactors intrinsically unstable, all transient calculations were also performed with the hypothesis of adding ^{167}Er to the graphite matrix (to assure that the total temperature coefficient becomes negative). This allows comparison of two configurations (without and with ^{167}Er).

The AMSTER has a single zone core, whereas the MSBR core is divided into a central fissile zone and a fertile region, each having different moderation ratios, and thus also quite different reactivity feedback coefficients.

8.5.2. *Input data sets for transients calculations*

In this section, we have collected all the data required for the performance of transient analyses with code SIM-ADS. The SIM-ADS code [5] has been benchmarked against actual transient reactor data as documented by ORNL during the operation of the 8 MW MSRE experimental reactor facility in the

years 1965-69. Transient analyses are performed for the MSRE and the two AMSTER concepts, assuming with and without ^{167}Er in the graphite matrix.

8.5.2.1. Geometry –thermohydraulics data

The reactors design, material property and thermo-hydraulic design data used for the transient calculations are summarized in Table 1.

TABLE 1. SUMMARY OF IMPORTANT DATA FOR MSBR AND AMSTER

	MSBR	AMSTER - B	AMSTER - I
In core salt volume (m^3)	30.4	30.4	30.4
Total salt volume (m^3)	48.7	48.4	48.4
Core height (m)	3.96	4	5
Salt channel radius (cm)	3.49	4	4
Graphite volume (m^3)	160		235
Graphite thickness (cm)	3	7.82	7.82
Salt flow (m^3/s)	3.48	3.48	3.48
Core inlet salt temperature (C)	566	566	566
Nominal thermal power (MW)	2250	2250	2250
Salt fuel specific heat (J/kg/C)	1357	1357	1357
Salt fuel density (kg/ m^3)	3.752-6.68 10^{-4}T(C)	3.752-6.68 10^{-4}T(C)	3.752-6.68 10^{-4}T(C)
Salt fuel conductivity (W/m/C)	1.23	1.23	1.23
Salt fuel viscosity (Poiseuille)	1.09 10^{-4} exp(4090/T+273)	1.09 10^{-4} exp(4090/T+273)	1.09 10^{-4} exp(4090/T+273)
Graphite specific heat (J/kg/C)	1750	1750	1750
Graphite density (kg/ m^3)	1898.7	1680	1680
Graphite conductivity (W/m/C)	3763 $T^{-0.7}$	3763 $T^{-0.7}$	3763 $T^{-0.7}$

For the MSBR and the AMSTER reactor designs, the fuel flow rate is in the transitional flow regime. In the report ORNL-4541, the thermal-hydraulic design data of MSBR is calculated based on the Coburn correlation for the Nusselt number, namely

$$Nu = 0.023 * \mathrm{Re}^{0.8} * \mathrm{Pr}^{0.33}$$

We will retain the Coburn correlation in our MSBR and AMSTER transient studies for the sake of data consistency. A more realistic, molten-salt specific correlation for the Nusselt number was proposed by Cox. This correlation is based on actual experimental data generated by ORNL (Cox, 1969, ORNL-4449, p.85 and ORNL-4396, p.119) using MSBR salt, namely:

$$Nu = 0.089 * (\mathrm{Re}^{2/3} - 125) * \mathrm{Pr}^{0.33} * \left(\frac{\mu_{bulk}}{\mu_{surf}} \right)^{0.14}$$

The Cox correlation above provides a ~20% lower heat transfer coefficient than the Coburn correlation.

TABLE 2. MSRE AND MSBR THERMO-HYDRAULIC DATA

	Nomenclature	Units	MSRE	MSBR
fission power	P_fiss	watt	7.270E+06	2.160E+09
decay heat	P_decayheat	watt	6.973E+04	9.000E+07
fraction of fission deposited in graphite matrix	f_gr	fraction	0.075	0.048
graphite heat conduction length	L_graph	cm	1.970E+05	1.139E+07
thermal conductivity of graphite	k_graph	W/mK	30.0	31.2
mass of graphite matrix	M_graph	kg	3767	399500
specific heat of graphite	cp_graph	J/kg*K	1750	1760
heat transfer area of graphite	A_graph	m^2	63.96	1507
flow rate of fuel	w	kg/s	181.6	11822
core outlet enthalpy of fuel	h_core_outlet	kJ/kg*K	1296.76	1357
core inlet enthalpy of fuel	h_core_inlet	kJ/kg*K	1256.33	768.06
mass of fuel in core region	M_core_fuel	kg	1550	962.11
specific heat of fuel	cp_fuel	J/kg*K	1982.5	1357
thermal conductivity of fuel	k_fuel	W/mK	1.440	1.23
viscosity of fuel	nu_fuel	kg/m*s	7.738E-03	9.85E-03
hydraulic diameter of graphite channells	D_hyd	m	0.01582	0.00762
length of graphite channels	L_channel	m	1.6637	
coolant flow area	A_flow	m^2	0.40795	1.2816
coolant velocity	vel	m/s	0.1967	2.76
ratio	DL		0.00951	-----
Reynold number	Re		910.1	7138
Prandl number	Pr		10.7	10.86
Nusselt number	Nu		7.21 (Mart.-Boelter)	61.16 (Coburn)
convection heat transfer coefficient graphite/fuel	h_s	W/cm^2*K	0.0656	0.9872
temperature drop graphite/fuel interface	delta_T_film	C	12.99	6.97
temperature drop in bulk graphite	delta_T_graph	C	9.3	30.4
average fuel temperaute	T_fuel	C	643.9	637.5
graphite surface temperature	T_graph_surf	C	656.9	644.5
graphite bulk temperature	T_graph_bulk	C	666.2	674.9
thermal heat transfer	R	W / C	4.20E+04	1.488E+07

8.5.2.2. Decay heat data

The data used for the decay heat is summarized in Fig. 3. It is recognized that molten salt reactors have different decay heat characteristics than typical LWR's on account of some of the fission products and other materials being continuously removed during the reprocessing of the liquid fuel. The data used for the molten salt reactors corresponds to the data recommended by ORNL, as listed in ORNL-4541, p. 43, Fig. 3.25, curve E, which models the afterheat produced by fission products which remain dispersed in the primary salt after removal of Kr and Xe gases by the off-gas system.

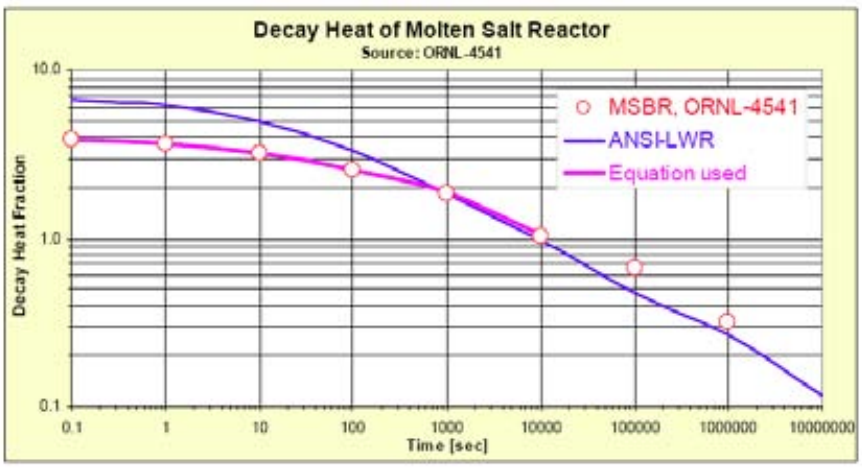

FIG. 3. Decay heat distribution used for transient analysis of molten salt reactors.

8.5.2.3. Delayed neutron precursor data

Neutron precursor data uded for the transient calculations were calculated by Apollo (see Table 3).

TABLE 3. NEUTRON PRECURSOR DATA USED FOR THE TRANSIENT CALCULATIONS

Neutron Precursor Data		Total	Group 1	Group 2	Group 3	Group 4	Group 5	Group 6
λ_i (sec^{-1})			0.01272	0.03174	0.116	0.311	1.4	3.87
MSBR	BOL	**303.6**	23.9	59.1	62.6	115.5	31.6	10.9
	BOL with erbium	**303.6**	23.9	59.1	62.6	115.5	31.6	10.9
	Equilibrium	**330.9**	23.8	63.2	66.4	126.1	35.7	15.7
	Equilibrium with erbium	**330.6**	23.7	63.4	66.3	125.7	35.3	16.2
AMSTER Incinerator	Equilibrium	**327.4**	18.7	66.2	62.1	121.9	38.7	19.8
	Equilibrium with erbium	**327.4**	18.7	66.2	62.1	121.9	38.7	19.8
AMSTER Breeder	Equilibrium	**341.4**	23.3	65.2	67.6	129.7	36.9	18.7
	Equilibrium with erbium	**341.4**	23.3	65.2	67.6	129.7	36.9	18.7

8.5.2.4. Feedback reactivity coefficients

The most important data determining the transient response of any reactor are the reactivity feedback coefficients. It is particularly important to determine these nuclear parameters to a relatively high degree of fidelity. These data has been determined by a detailed modelling of the reactor core using the APOLLO code system. Input data into these codes are the precise core geometries and material compositions. The reactivity coefficients as a function of the graphite and salt temperature for the cases with and without ^{167}Er are displayed in graphical form the Figs 4-6. As can be observed from these figures, some of the data points do not fall on a smooth curve (red curves). This data was then approximated by using a polynomial curve fit (black curves).

If we consider the case of MSBR without erbium addition in graphite (Fig. 4), we can verify that for nominal operating condition (average salt temperature ~650°C, average graphite temperature ~700°C), the total coefficient is positive: the graphite coefficient is +2.07 pcm/°C, the fuel salt coefficient is -1.77 pcm/°C, yielding a total of +0.4 pcm/°C. The salt coefficient is more sensitive to temperature, the total coefficient becoming thereby more positive for higher core temperatures, a tendency that worsens the core unstable tendencies. Addition of erbium into the graphite matrix changes the sign of the graphite coefficient from positive to negative, rendering the total coefficient significantly negative thereby making the core intrinsically stable.

AMSTER-incinerator without erbium in graphite (Fig. 5) presents quite different characteristics. At nominal operating conditions, the total coefficient is positive: the graphite coefficient is +1.3 pcm/°C, the fuel salt coefficient is -0.8 pcm/°C, the total coefficient being +0.5pcm/°C, similar to MSBR. But in case of a temperature increases, the AMSTER-incinerator coefficients show stronger variations than the MSBR coefficients. The differences to MSBR coefficients is due to the different fuel composition, the large amount of plutonium isotopes at equilibrium in the AMSTER-incinerator core, with important absorption resonances in the neutron thermal energy range (especially ^{240}Pu) , playing a role very similar to erbium, thereby rendering the graphite coefficient less positive. Of course, further addition of erbium in graphite enhance this tendency, thus ensures core stability. AMSTER-breeder (see Fig. 6) present characteristics quite similar to those of MSBR, but with a lower graphite temperature, due to the fact that the weighing of the fertile zone (which is taken into account in the global reactivity coefficients calculation) is larger (in the AMSTER breeder, the slower fission products extraction and no ^{233}Pa extraction (thereby decreasing the effect of ^{233}U) has to be compensated by an increase of the fertile part of the core, and thus favours a less positive graphite effect. Theoretically, this feature should improve the reactor stability, even without erbium. Moreover, any rise in temperature from the nominal operating conditions would favour the salt negative reactivity effect and so improve reactor stability.

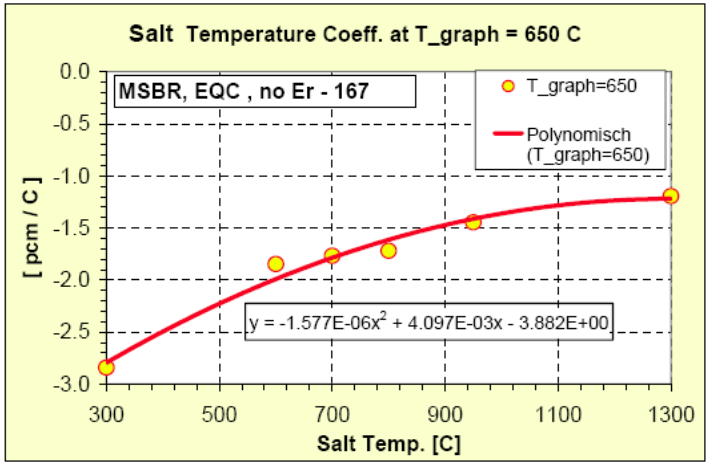

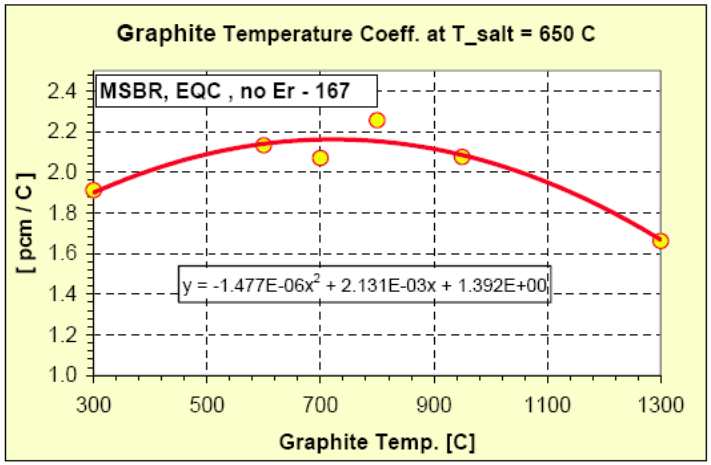

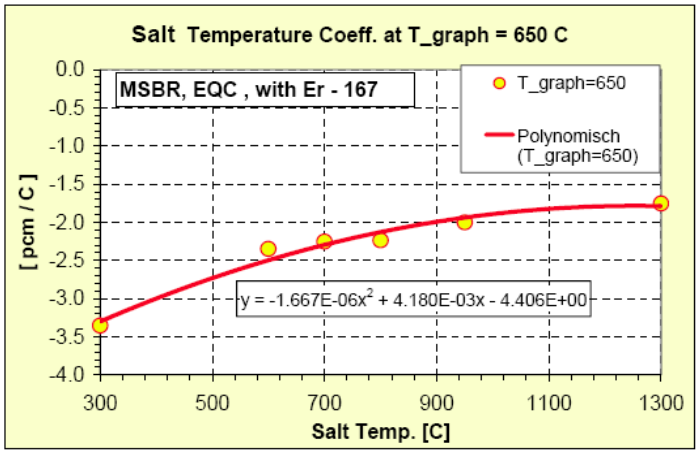

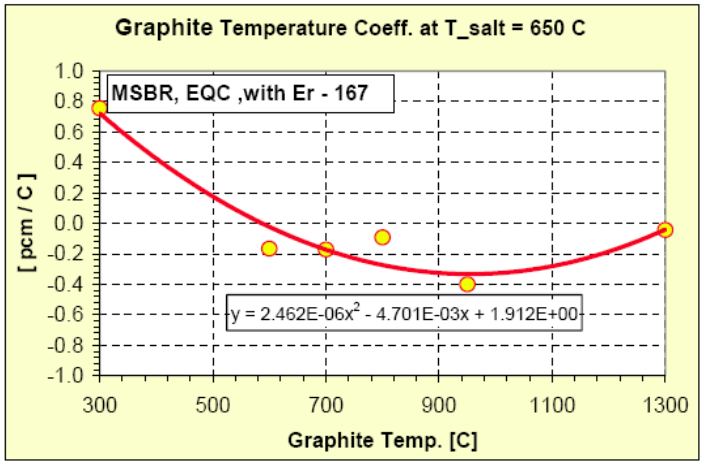

FIG. 4. Reactivity coefficients for MSBR with and without ^{167}Er.

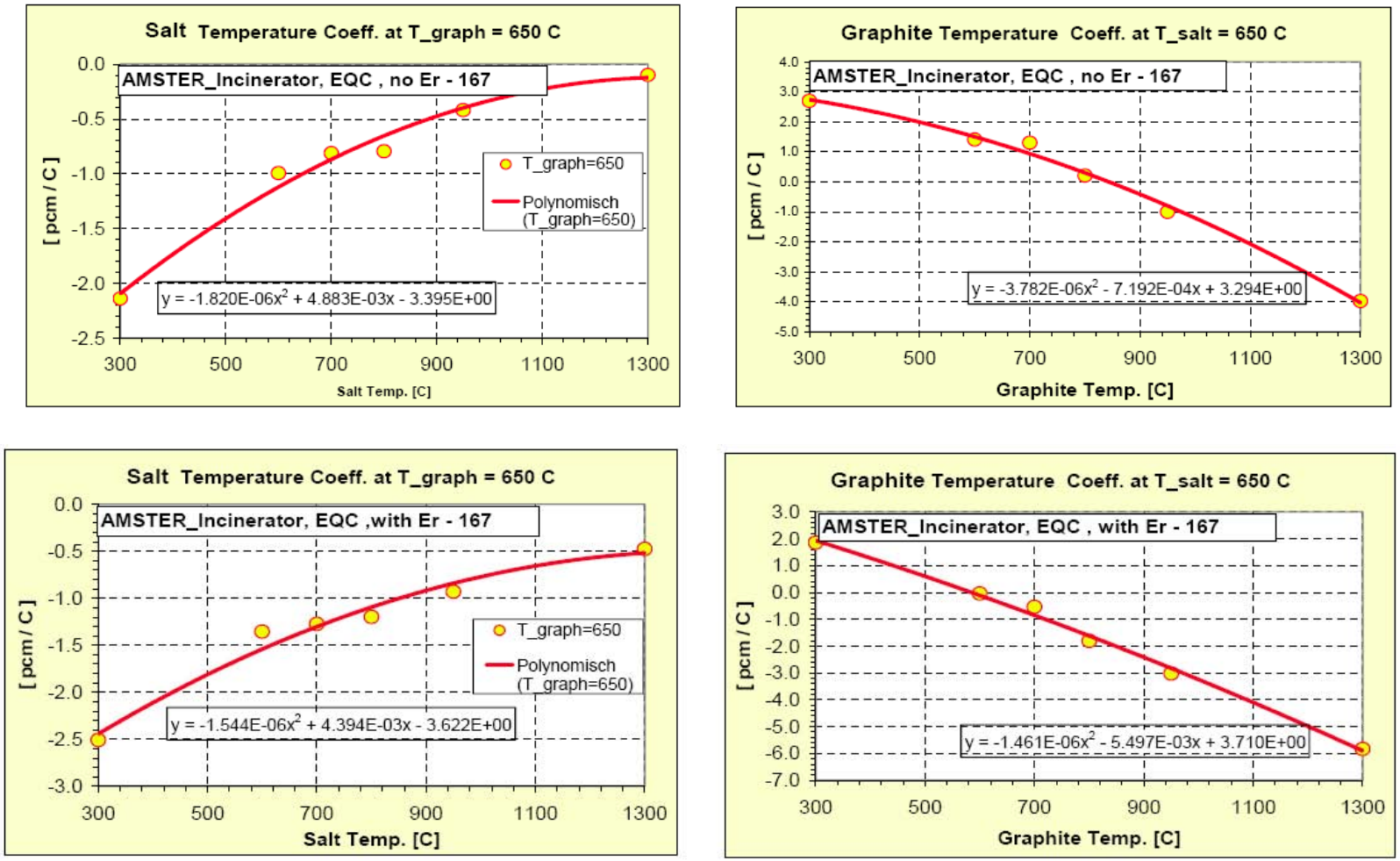

FIG. 5. Reactivity coefficients for AMSTER-Incinerator with and without ^{167}Er.

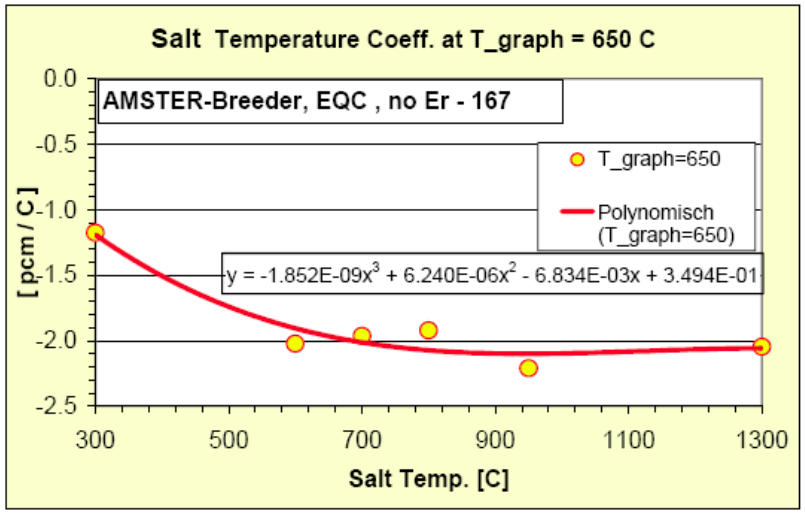

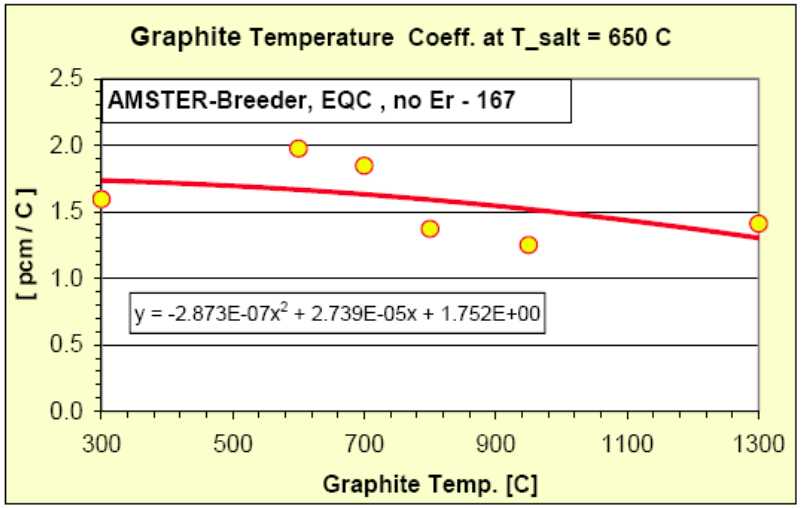

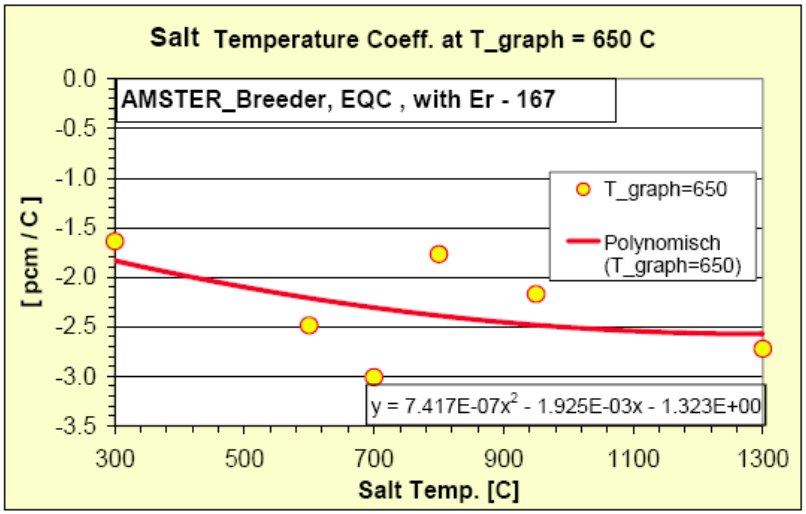

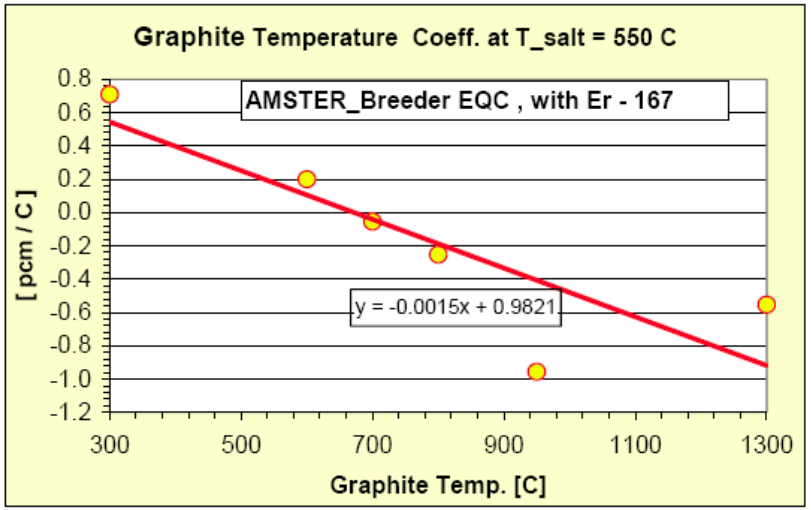

FIG. 6. Reactivity coefficients for AMSTER-Breeder with and without ^{167}Er.

8.5.3. *Transients analyzed*

Four basic transients have been analyzed:

— Unprotected Loss of Flow (ULOF), assuming loss of forced circulation in the primary system due to pump failure. The core inlet temperature is assumed to remain constant. The mass flow rate of the fuel salt is assumed to stabilize after 7 s at about 5% of its nominal value (natural convection);

— Unprotected transient over power (UTOP) due to a +300 pcm jump in reactivity; a fissile fuel particle dislodged from the loop walls (fissile fuel agglomeration) is assumed to become lodged inside the core region, the core inlet temperature is assumed to remain constant during this transient;

— Unprotected primary circuit Overcooling transient, with the inlet temperature reduced by 50°C in 50 s.

— Unprotected Loss of Heat Sink (ULOH) in which the heat sink is assumed to totally fail;

The transient initiators selected for detailed analysis are listed in Table 4. Also listed in the table are the underlying assumptions under which the specific transients were analyzed.

8.6. Results

8.6.1. *MSBR transients*

The results of the unprotected loss of flow (ULOF), the unprotected transient over power transient (UTOP), overcooling transient and unprotected loss of heat sink (ULOH) of the core are displayed in Figs 7-10.

For each transient two figures are provided. In the first figure (top), the dynamic response of the normalized thermal reactor power, neutron flux, and mass flow rate are displayed. In the second figure (bottom), the dynamic response of the molten salt core outlet -, average core -, core inlet -, and average bulk graphite — temperatures are shown.

8.6.1.1. MSBR ULOF transient

For the ULOF transient without ^{167}Er, Fig. 7a, the mass flow rate drops to the natural convection flow rate (about 5% of nominal flow is assumed) very shortly after pump failure. Control rods are postulated not to insert into the core. The loss of flow rate in circulating fuel reactors implies an insertion of positive reactivity. In the case of MSBR, with β_{eff} static = 330.9 pcm, this reactivity insertion due to the loss of fuel circulation is +83.8 pcm (β_{loss} = -83.8 pcm), or +25%.

The average fuel temperature is observed to rise very rapidly to ~750°C as results of the fast decreasing mass flow rate. Since the temperature coefficient of the fuel is strongly negative, namely ~ -1.8 pcm/°C (see Fig. 4), sufficient negative reactivity is being inserted into the reactor to counterbalance the positive reactivity increase associated with the loss of fuel circulation. The net effect is a fast decrease in the power level to below 10% after 120 s into the transient.

Concurrent with the fast rise in the average fuel temperature is the relatively slow rise in the bulk graphite temperature. Due to the positive graphite reactivity coefficient of ~ +1.85 pcm/°C, a positive reactivity is now slowly inserted into the core, and after about 500 s into the transient, the net reactivity becomes positive because of the decreasing average fuel temperature after ~80 s. After 300 s into the transient, both average fuel temperature and bulk graphite temperature assume about the same value. The net reactivity, i.e. the sum of the fuel and the graphite coefficient, is now positive, namely ~ +0.3 pcm/°C. This leads now to a gradual increase in reactor power, which itself again increases both the average fuel and bulk graphite temperatures resulting in a positive feedback loop. After about 3 000 s the reactor power has risen to 18% and the corresponding average fuel and graphite temperature are close to 800°C (see Fig. 7a). The core outlet temperature is seen to rise briefly above 940°C during the initial phase of the transient, decreasing to around 820°C at ~300 s into the transient, and subsequently rising continuously to above 1 000°C at 3 000 s into the transient.

TABLE 4. LIST OF TRANSIENTS ANALYZED

Number	Transient	Description
1. MSBR		
U - 1a	ULOF	loss of forced circulations in primary and secondary system, core inlet temperature remains constant
U - 1b	ULOF with Er-167	loss of forced circulations in primary and secondary system, core inlet temperature remains constant
U - 2a	UTOP	300 pcm jump in reactivity at HFP, coolant inlet will remain constant
U - 2b	UTOP with Er-167	300 pcm jump in reactivity at HFP, coolant inlet will remain constant
U - 3a	over-cooling of primary side	core inlet drops by 50 C in 50 sec
U - 3b	over-cooling of primary side with Er-167	core inlet drops by 50 C in 50 sec
U - 4a	ULOH	loss of heat sinks (HX)
U - 4b	ULOH with Er-167	loss of heat sink (HX)
2. AMSTER - Incinerator		
U - 1a	ULOF	loss of forced circulations in primary and secondary system, core inlet temperature remains constant
U - 1b	ULOF with Er-167	loss of forced circulations in primary and secondary system, core inlet temperature remains constant
U - 2a	UTOP	300 pcm jump in reactivity at HFP, coolant inlet will remain constant
U - 2b	UTOP with Er-167	300 pcm jump in reactivity at HFP, coolant inlet will remain constant
U - 3a	over-cooling of primary side	core inlet drops by 50 C in 50 sec
U - 3b	over-cooling of primary side with Er-167	core inlet drops by 50 C in 50 sec
U - 4a	ULOH	loss of heat sinks (HX)
U - 4b	ULOH with Er-167	loss of heat sink (HX)
3. AMSTER - Breeder		
U - 1a	ULOF	loss of forced circulations in primary and secondary system, core inlet temperature remains constant
U - 1b	ULOF with Er-167	loss of forced circulations in primary and secondary system, core inlet temperature remains constant
U - 2a	UTOP	300 pcm jump in reactivity at HFP, coolant inlet will remain constant
U - 2b	UTOP with Er-167	300 pcm jump in reactivity at HFP, coolant inlet will remain constant
U - 3a	over-cooling of primary side	core inlet drops by 50 C in 50 sec
U - 3b	over-cooling of primary side with Er-167	core inlet drops by 50 C in 50 sec
U - 4a	ULOH	loss of heat sinks (HX)
U - 4b	ULOH with Er-167	loss of heat sink (HX)

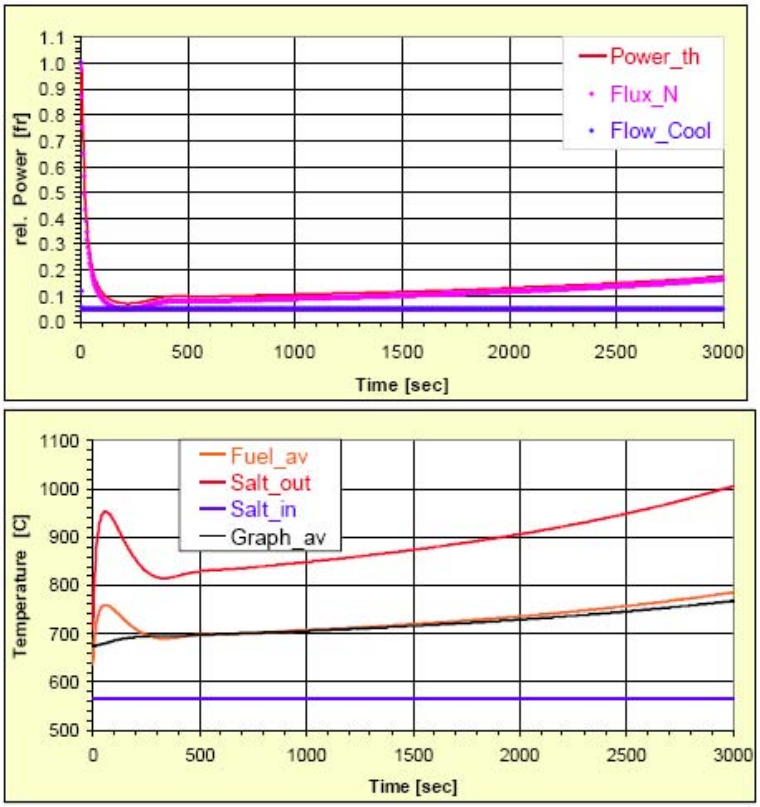

FIG. 7a. Unprotected Loss of Flow (ULOF) for MSBR without ^{167}Er.

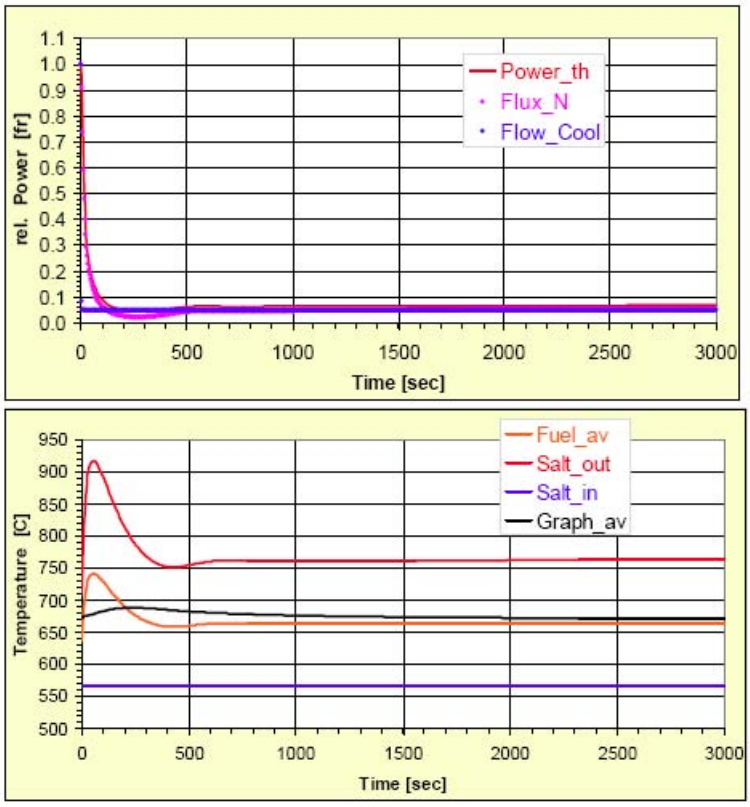

FIG. 7b. Unprotected Loss of Flow (ULOF) for MSBR with ^{167}Er.

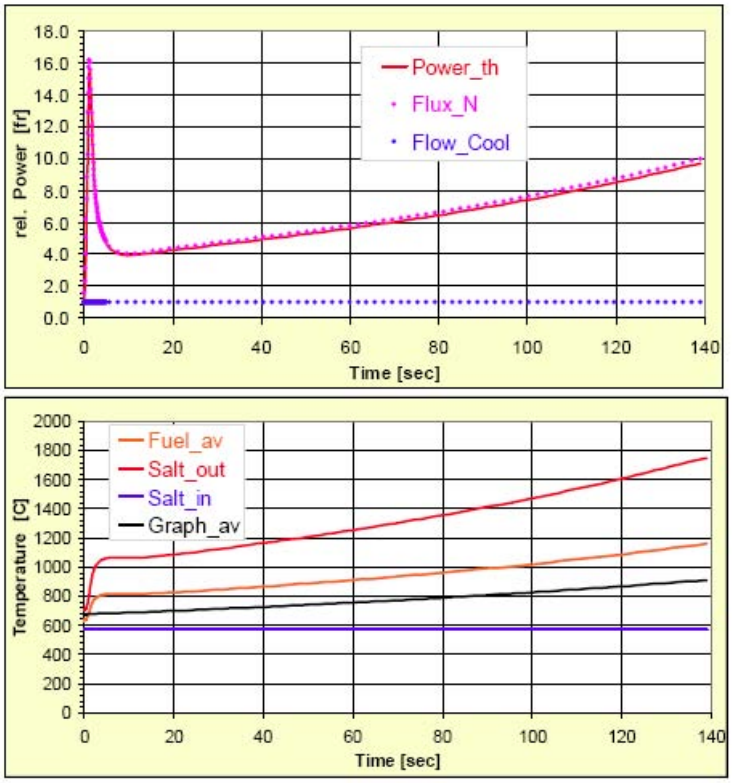

FIG. 8a. Unprotected TOP (+300 pcm insertion) for MSBR without ^{167}Er.

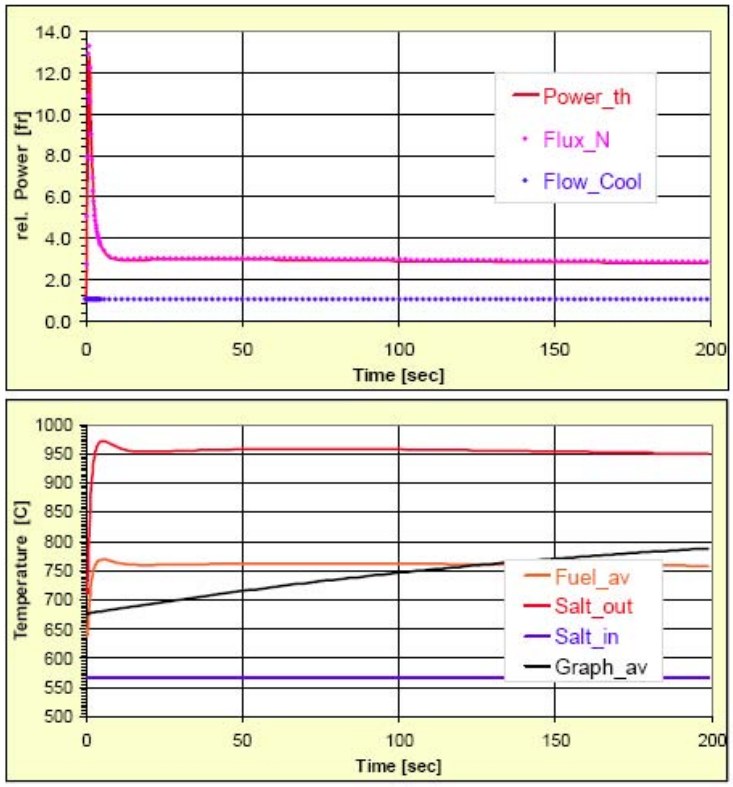

FIG. 8b. Unprotected TOP (+300 pcm insertion) for MSBR with ^{167}Er.

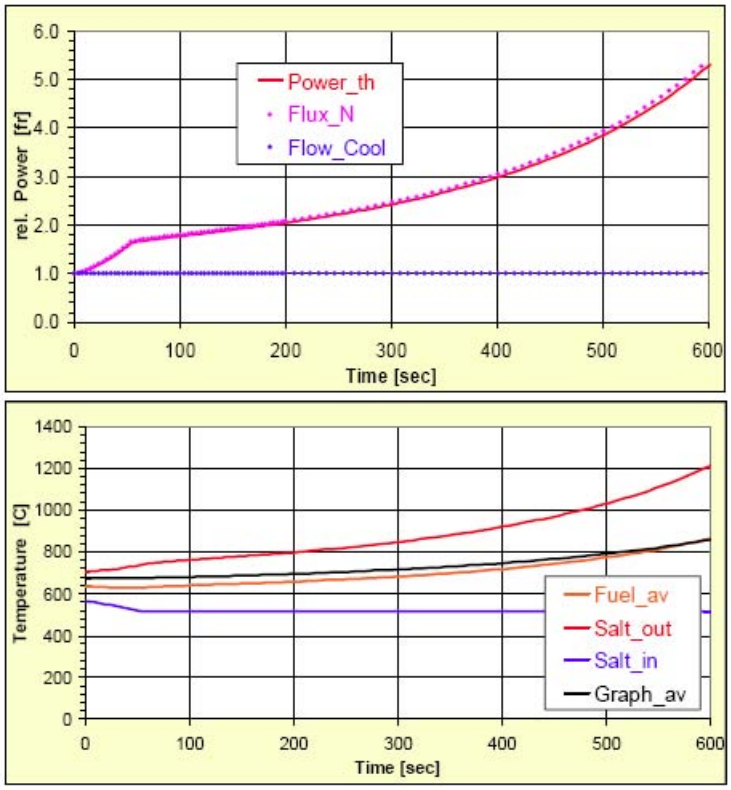

FIG. 9a. Unprotected Over-Cooling Transient for MSBR without ^{167}Er.

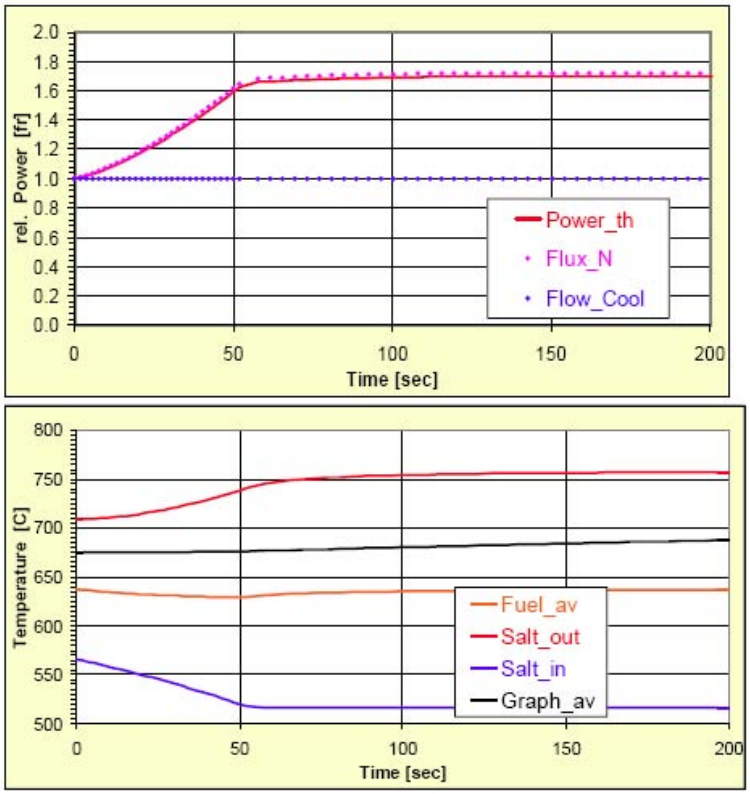

FIG. 9b. Unprotected Over-Cooling Transient for MSBR with ^{167}Er.

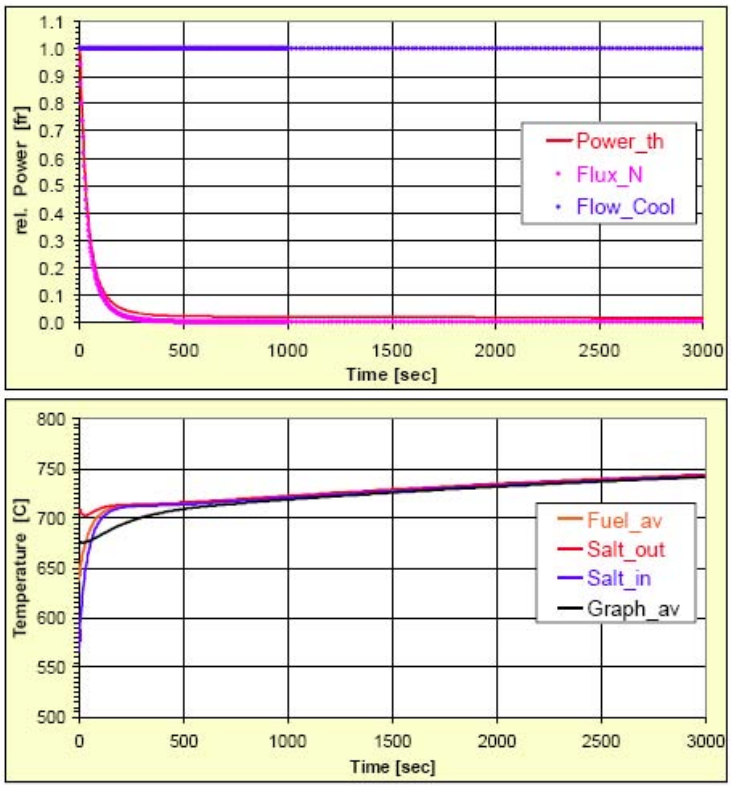

FIG. 10a. Unprotected Loss of Heat Sink (ULOH) for MSBR without ^{167}Er.

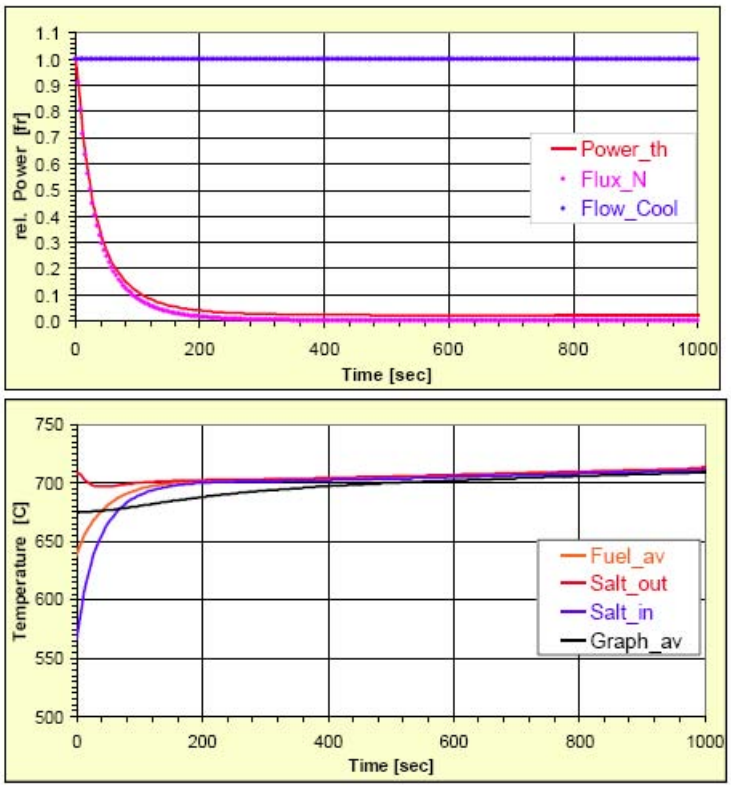

FIG. 10b. Unprotected Loss of Heat Sink (ULOH) for MSBR with ^{167}Er.

For the ULOF transient with ^{167}Er in the graphite, (see Fig. 7b), the mass flow rate follows the same characteristic as observed for the ULOF case without ^{167}Er. Since the fuel temperature coefficient is ~ -2.35 pcm/°C, an increasing average fuel temperature will lead to a large insertion of negative reactivity depressing the power level to below 10%. During the first 200 s the transient response of both average fuel and outlet temperature follow the same pattern as in the previous case, namely a short rise with a subsequent drop to around 750°C for the outlet and 670°C for the core average fuel temperature. Since the graphite temperature coefficient is however slightly negative in this case, namely ~ -0.17 pcm/°C, an increase in graphite temperature will now insert additional negative reactivity. Under these conditions, power and temperatures will stabilize, as can be observed, implying that this reactor design is inherently stable. The power levels off around 5% nominal, average fuel and the graphite temperatures stabilize around 670°C, and the core outlet temperature remains at ~760°C. Adding ^{167}Er to the graphite makes this reactor design under ULOF transient condition inherently safe.

8.6.1.2. MSBR UTOP transient

In the case of the overpower transient without ^{167}Er, (see Fig. 8a), the insertion of +300 pcm reactivity, or 90 cents, leads to a power spike of factor 16.2. The fast rise in average and outlet temperatures add quickly negative reactivity into the core, bringing the power back down to a factor 4 at about 10 s into the transient. The increasing graphite temperature now inserts positive reactivity which leads to a slow increase in reactor power again. The core outlet temperature exceeds now 1 100°C after 20 s into the transient, the average fuel temperature being continuously above 820°C. After about 140 s into the transient, the outlet temperature reaches above 1700°C and failure of the reactor system must be anticipated beyond that point in time.

In the case of the overpower transient with ^{167}Er (see Fig. 8b) the observed power spike is now only to a factor 13, dropping down to a factor 3 after 10 s into the transient. The fuel outlet temperature quickly rises to around 950°C within 10 s after the initiation of the transient, and stabilizes thereafter at about that level. The core average temperature quickly rises to 750°C and stabilizes thereafter. The graphite temperature is observed to increase continuously, adding negative reactivity since its reactivity coefficient is slightly negative (see Fig. 4). This again demonstrates that the addition of ^{167}Er stabilizes the UTOP transient at acceptable temperatures.

8.6.1.3. MSBR Overcooling transient

In the case of the overcooling transient without ^{167}Er, (see Fig. 9a), the decreasing core inlet temperature leads to a decrease in the average fuel temperature. Since the reactivity coefficient of the fuel is negative (see Fig. 4), a positive reactivity is inserted into the reactor leading to a power rise to a factor 1.6 about 50 s into the transient. Due to the gradual increase in the temperature of the bulk graphite, additional positive reactivity is inserted into the core leading to a continuous power rise up to a factor of 5.2 at 600 s into the transient. Correspondingly, the core outlet temperature increases to 1 200°C at 600 s into the transient and the core average temperature to 850°C. The reactor system must now be expected to fail on account of excessive temperatures. The reactor design is this not inherently stable under this transient.

In the case of the overcooling transient with ^{167}Er, (see Fig. 9b), the decreasing core inlet temperature leads to a decrease in the average fuel temperature. Since the reactivity coefficient of the fuel is negative (see Fig. 4), a positive reactivity is inserted into the reactor leading to a power rise to a factor 1.6 about 50 s into the transient, almost the same as without ^{167}Er. In this case, however, power and all temperatures stabilize; the core outlet temperature stabilizes around 750°C, and both average fuel and graphite temperatures remain below 700°C because of the negative graphite temperature coefficient.

8.6.1.4. MSBR ULOH transient

For the ULOH transient without ^{167}Erb, (see Fig. 10a), the heat transfer into the secondary system is assumed to fail at t = 0. Control rods are postulated not to insert into the core. The loss of heat sink implies the core inlet temperature will increase on account of lack of cooling via the heat exchangers. The only heat sink remaining will be radiation via the vessel surface to the reactor containment atmosphere. As can be observed in Figs 10a, the core inlet temperature will increase from 570°C to about 700°C within 150 s after transient initiation (pumps are assumed to remain active). As a result, the core average

fuel temperature will also increase from 640 to 710°C within 150 s into the transient causing negative reactivity to be inserted into the core on account of the strongly negative fuel reactivity coefficient, namely ~ -1.77 pcm/°C (see Table 4). The net effect is a fast decrease in the power level to below 10% after 100 s into the transient. By 200 s into the transient, the nuclear power is below the decay heat power level. Since the power level decreases, the core fuel outlet temperature does not rise above 710°C. As can be observed in Fig. 10a, all fuel temperatures reach an asymptotic level of about 740°C about 3000 s into the transient. The graphite temperature gradually increases from 675 to 710°C beyond 500 s injecting positive reactivity into the core on account of its positive reactivity coefficient, namely ~ +2.08 pcm/°C. While the total reactivity coefficient remains negative, the temperatures in the system are not expected to go significantly beyond the 740°C in this transient because the continued decreasing decay heat power level and the 23 MW being lost via radiation of the vessel walls serving as a heat sink.

At the asymptotic temperature of ~750°C, the total reactivity coefficient becomes slightly positive (~ +0.4 pcm/°C) but the reactor is still sub-critical by about -50 pcm. The average fuel and bulk graphite temperature would need to increase by another +120°C for the core reactivity level to become positive and nuclear power to increase again. Without the radiation heat sink, this temperature increase would occur. Additional negative reactivity would then have to be inserted into the core via the control rod systems in order to assure a continued nuclear shut-down.

Furthermore, should the fuel temperatures decrease substantially below the asymptotic level of ~750°C, a positive reactivity insertion due to the decreasing fuel temperature will lead to a renewed rise in nuclear power. In order to prevent this, additional negative reactivity will need to be inserted into the core at some point into this transient in order to assure continued nuclear power shut-down.

For the ULOH transient with ^{167}Er in the graphite, (see Fig. 10b), a similar behaviour is seen as has been observed for the ULOH case without ^{167}Er. Since the fuel temperature coefficient is ~ -2.3 pcm/°C, an increasing average fuel temperature after the loss of heat sink will lead to a large insertion of negative reactivity depressing the power level within 100 s to below 10%. During the first 200 s, the transient response of all fuel temperatures follows the same pattern as in the previous case, namely a fast rise with a subsequent levelling off at around 720°C. Since the graphite temperature coefficient is however slightly negative in this case, namely ~ -0.2 pcm/°C, an increase in graphite temperature will now insert additional negative reactivity assuring continued nuclear shutdown.

The total temperature coefficient will remain negative throughout this transient for this reactor design. There will thus be no concern that nuclear power production will revitalize at some time into this transient on account of the increasing bulk graphite temperature. This implies that this reactor design is inherently safe.

All relevant temperatures are observed to be below 730°C for 1 600 s into transient. Beyond this time, the temperatures are not expected to exceed 750°C since the decay heat generation, which is the dominant heat production source at this time into transient, will continue to decrease. Again, about 23 MW of heat are being lost from the primary system via radiation from the vessel walls, providing a heat sink for the system. Should the fuel temperatures drop below the asymptotic temperatures during this transient, positive reactivity will be inserted into the reactor due to the reactivity coefficients. This could revitalize nuclear power generation. In order to prevent this, some form of additional negative reactivity will need to be inserted into the core at some point into this transient in order to assure continued nuclear power shut-down. Adding ^{167}Er to the graphite adds to the safety margin of this reactor design under ULOH transient condition.

8.6.1.5. Summary of MSBR transients

The above transients have demonstrated that the MSBR design without ^{167}Er added to the graphite matrix is inherently unstable on account of its positive graphite temperature reactivity coefficient. For this reactor design to be stable under unprotected transient conditions for long transient time-scales, ^{167}Er should be added in the graphite matrix to assure a negative graphite temperature coefficient. One positive attribute associated with graphite is its very large thermal inertia, assuring a sluggish transient behaviour due to the slow heat-up of graphite. This sluggishness provides sufficient response time for the reactor operators to counteract the failed control rod system that has been assumed not functional for all of the above investigated transients.

8.6.2. *AMSTER Incinerator transients*

The results of the Unprotected Loss of Flow (ULOF), the Unprotected Transient Over Power Transient (UTOP), Overcooling Transient and Unprotected Loss of Heat Sink (ULOH) of the core are displayed in Figs 11-14.

For each transient two figures are provided. In the first figure (top), the dynamic response of the normalized thermal reactor power, neutron flux, and mass flow rate are displayed. In the second figure (bottom), the dynamic response of the molten salt core outlet -, average core -, core inlet -, and average bulk graphite — temperatures are shown.

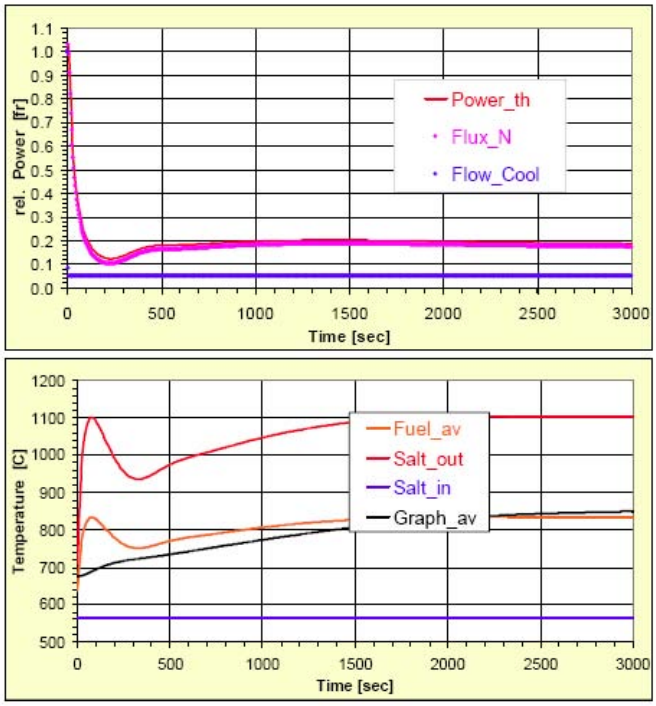

FIG. 11a. Unprotected Loss of Flow (ULOF) for AMSTER-Incinerator without ^{167}Er.

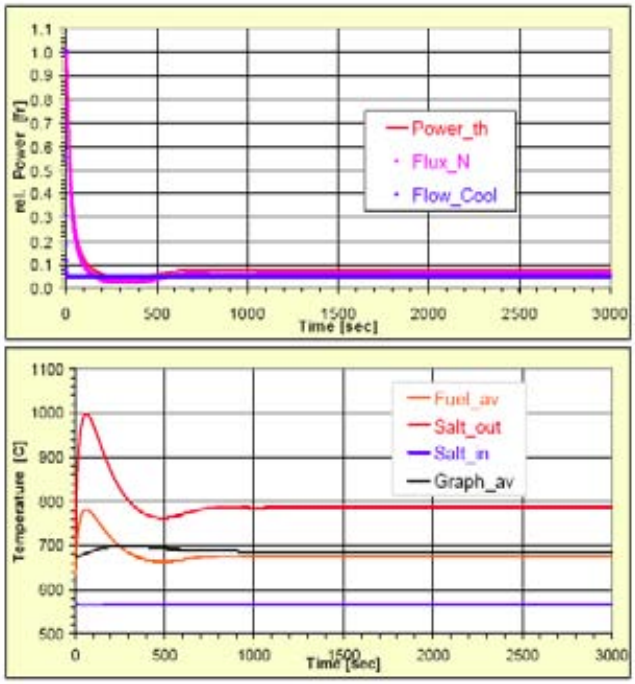

FIG. 11b. Unprotected Loss of Flow (ULOF) for AMSTER-Incinerator with ^{167}Er.

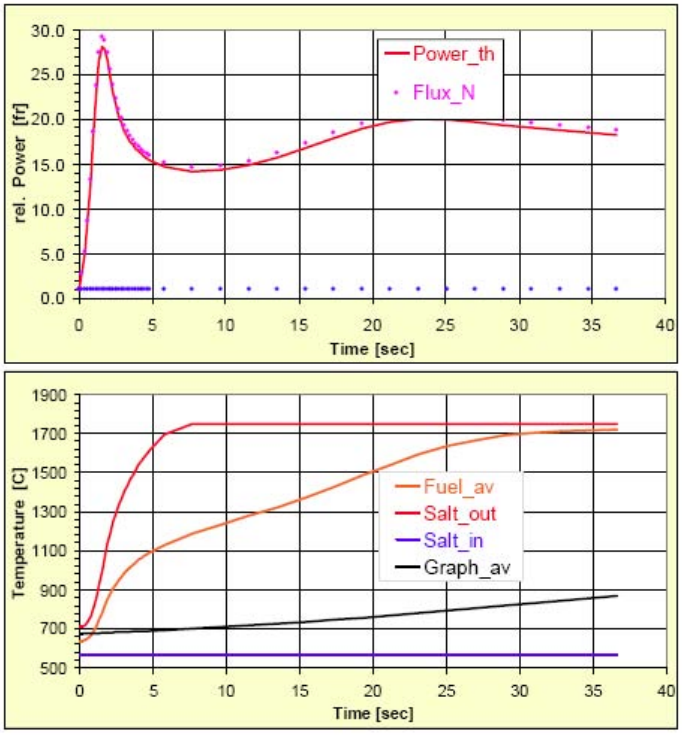

FIG. 12a. Unprotected TOP (+300 pcm insertion forAMSTER-Incinerator without ^{167}Er.

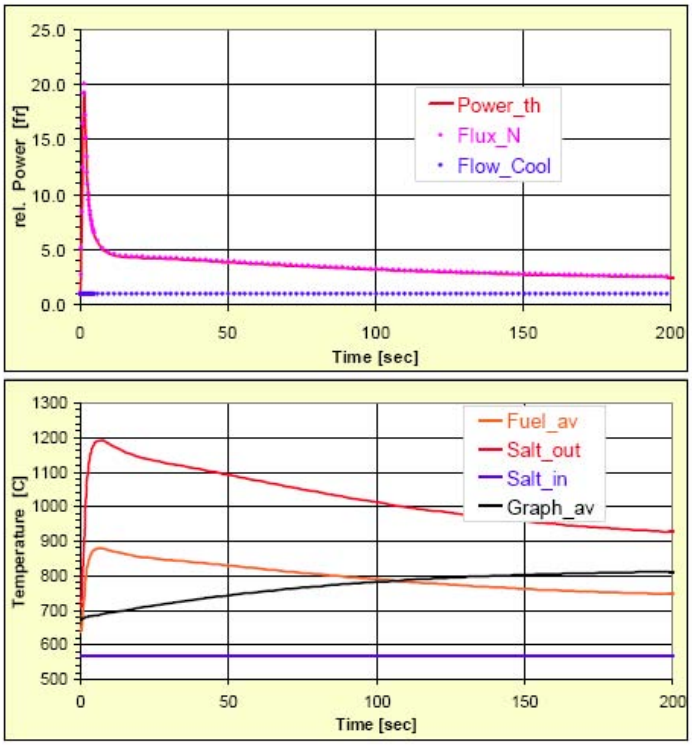

FIG. 12b. Unprotected TOP (+300 pcm insertion) for AMSTER-Incinerator with ^{167}Er.

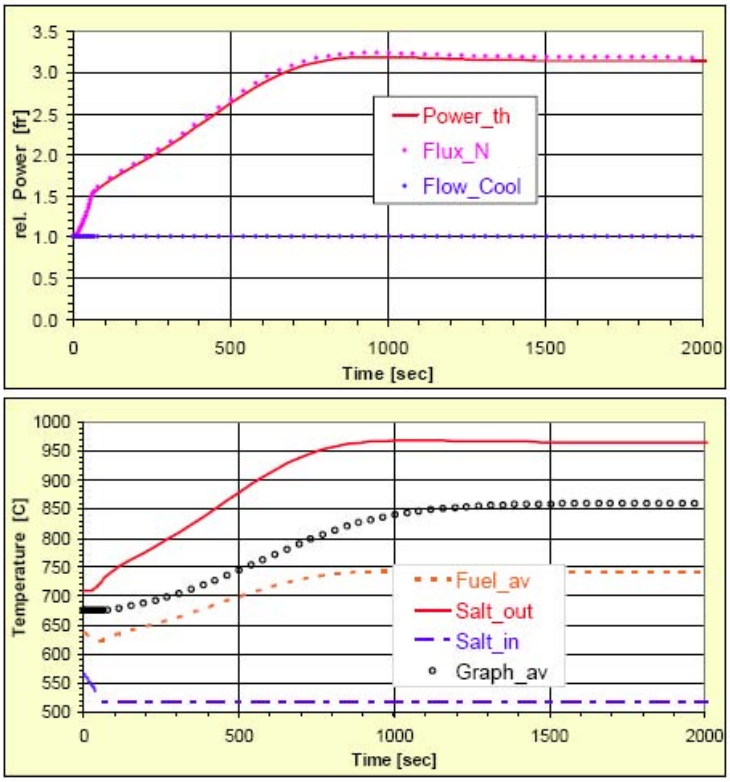

FIG. 13a. Unprotected Over-Cooling Transient for AMSTER-Incinerator without ^{167}Er.

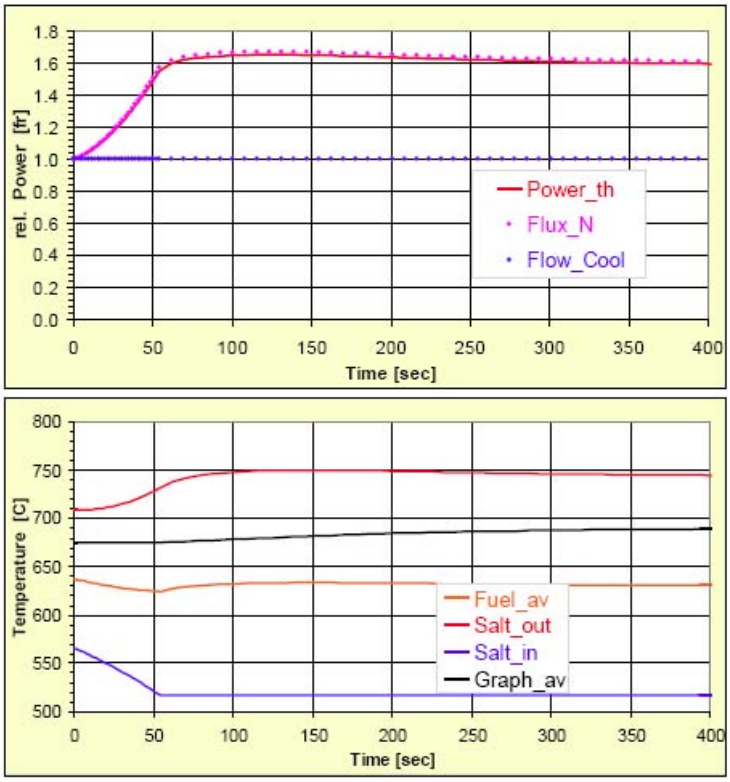

FIG. 13b. Unprotected Over-Cooling Transient for AMSTER-Incinerator with ^{167}Er.

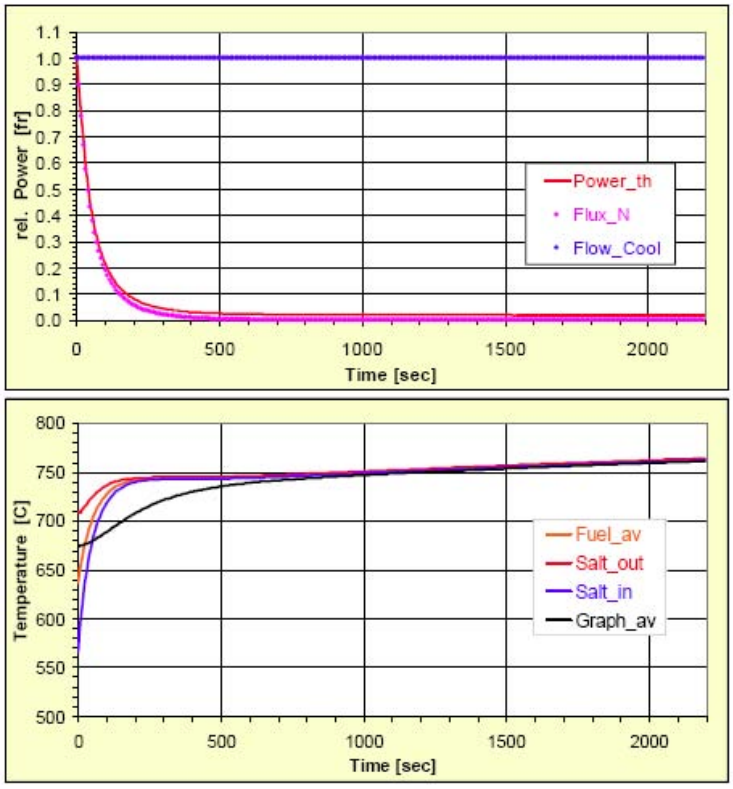

FIG. 14a. Unprotected Loss of Heat Sink (ULOH) for AMSTER-Incinerator without ^{167}Er.

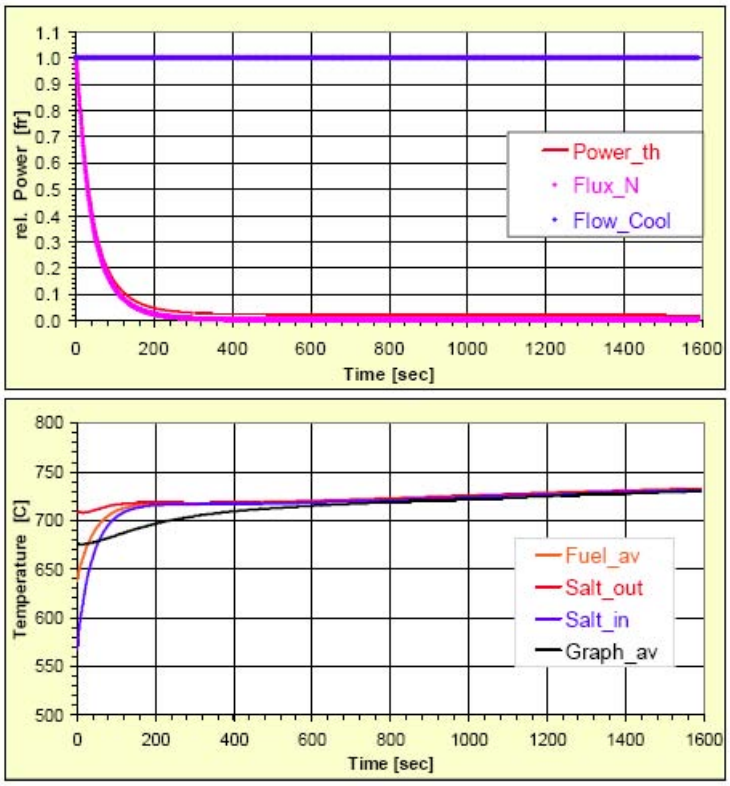

FIG. 14b. Unprotected Loss of Heat Sink (ULOH) for AMSTER-Incinerator with ^{167}Er.

8.6.2.1. AMSTER-Incinerator ULOF transient

For the ULOF transient without ^{167}Er, (Fig. 11a), the mass flow rate drops to the natural convection flow rate (about 5% of nominal flow is assumed) very shortly after pump failure. Control rods are postulated not to insert into the core. The loss of flow rate in circulating fuel reactors implies an insertion of positive reactivity. In the case of MSBR, with $\beta_{eff}\ static = 327.4\ pcm$ (see Fig. 5), this reactivity insertion due to the loss of fuel circulation is + 82.9 pcm (β_{lost} = -82.9 pcm), or -25%. The average fuel temperature is observed to rise very rapidly to ~840°C as a result of the fast decreasing mass flow rate. Since the temperature coefficient of the fuel is small negative, namely ~ -0.9 pcm/°C (see Table 5), insufficient negative reactivity is being inserted into the reactor to counterbalance the positive reactivity increase associated with the loss of fuel circulation during the first 10 s of this transient. The power level rises briefly to 104%. Thereafter, continuously increasing fuel temperature eventually inserts sufficient negative reactivity to compensate for the positive flow reactivity. The power level slowly drops to 12% 200 s into the transient. Concurrent with the fast rise in the average fuel temperature is the relatively slow rise in the bulk graphite temperature. Due to the positive graphite reactivity coefficient of ~ +1.4 pcm/°C, a positive reactivity is now slowly inserted into the core, and after about 300 s into the transient, the net reactivity becomes positive because of the decreasing average fuel temperature after ~80 s. This leads to a gradual increase in reactor power from 12 to 20% 1 200 s into the transient. After 750 s into the transient, both average fuel temperature and bulk graphite temperature continuously rise until the graphite temperature increase above the fuel temperature at ~2200 s into the transient. But while the fuel salt temperature coefficient keeps the same level, around — 1 pcm/°C, the graphite temperature coefficient decreases significantly (to less than +0.3 pcm/°C when graphite temperature is above 800°C, resulting in a negative total reactivity coefficient. That explains why the power seems to level off and even decrease slightly again. After about 3 000 s the reactor power stabilized at 18% and the corresponding average fuel and graphite temperature are close to 800°C. The core outlet temperature is seen to rise briefly to 1 100°C, decreasing to around 940°C at ~300 s into the transient, and subsequently rising and stabilizing to above 1 100°C at 3 000 s into the transient.

So AMSTER-incinerator without erbium has a quite different behaviour than MSBR in case of ULOF, since the core power stabilizes due to a total reactivity coefficient which becomes negative when the graphite temperature should exceed 800°C. This difference in the graphite reactivity effect is due to the difference of fuel composition, the large amount of plutonium isotopes at equilibrium in the incinerator core, with important absorption resonances in the neutron thermal energy range (especially ^{240}Pu), playing a role very similar as the one played by erbium.

For the ULOF transient with ^{167}Er in the graphite, (see Fig. 11b), the mass flow rate follows the same characteristic as observed for the ULOF case without ^{167}Er. Since the fuel temperature coefficient is ~ -1.35 pcm/°C, an increasing average fuel temperature will lead to an insertion of negative reactivity depressing the power level to below 10%. During the first 200 s the transient response of both average fuel and outlet temperature follow the same pattern as in the previous case, namely a short rise with a subsequent drop to around 780°C for the outlet and 670°C for the core average fuel temperature. Since the graphite temperature coefficient is however slightly negative in this case, namely ~ -0.2 pcm/°C, an increase in graphite temperature will now insert additional negative reactivity. Under these conditions, power and temperatures will stabilize, as can be observed, implying that this reactor design is inherently stable. The power levels off around 8% nominal, average fuel and the graphite temperatures stabilize around 680°C, and the core outlet temperature remains at ~780°C. Adding ^{167}Er to the graphite makes this reactor design under ULOF transient condition inherently safe.

8.6.2.2. AMSTER-Incinerator UTOP transient

In the case of the overpower transient without ^{167}Er, (see Fig, 12a), the insertion of +300 pcm reactivity, or 92 cents, leads to a power spike of factor 28. The fast rise in average and outlet temperature add quickly negative reactivity into the core, bringing the power back down to a factor 14 at about 8 s into the transient. The increasing graphite temperature now inserts positive reactivity which leads to a slow increase in reactor power again. The core outlet temperatures exceed very rapidly 1 700°C after 7 s into the transient (saturation temperature was assumed to be 1 750°C), the average fuel temperature also

continuously rising to 1 700°C 30 s into the transient. Failure of the reactor system must be anticipated beyond that point in time.

In the case of the overpower transient with ^{167}Er, (see Fig. 12b), the observed power spike is now only to a factor 19, dropping down to a factor 5 after 8 s into the transient. The fuel outlet temperature quickly rises to around 1 200°C within 10 s after the initiation of the transient, and decreases thereafter continuously to below 950°C. The core average temperature quickly rises to 880°C and decreases thereafter to around 750°C at 200 s into the transient. The graphite temperature is observed to increase asymptotically to 810°C, adding negative reactivity since it's reactivity coefficient becomes increasingly more negative (see Fig. 5). This demonstrates that the addition of ^{167}Er stabilizes the UTOP transient at acceptable temperatures.

8.6.2.3. AMSTER-Incinerator overcooling transient

In the case of the overcooling transient without ^{167}Er, (see Fig. 13a), the decreasing core inlet temperature leads to a decrease in the average fuel temperature. Since the reactivity coefficient of the fuel is negative (see Fig. 5), a positive reactivity is inserted into the reactor leading to a power rise to a factor 1.6 about 60 s into the transient. Due to the gradual increase in the temperature of the bulk graphite, additional positive reactivity is inserted into the core leading to a power rise up to a factor of 3.2 at 800 s into the transient. Correspondingly, the core outlet temperature increases to 970°C at 800 s into the transient and the core average temperature to 740°C. Due to the fact that the graphite coefficient becomes negative above 820°C the power will stabilize at a power factor of 3.1 with an core outlet temperature stabilizing at 970°C. The average fuel temperature remains below 750°C while the graphite temperature levels off at 850°C. The reactor design is thus inherently stable at elevated temperatures under this transient even without ^{167}Er.

In the case of the overcooling transient with ^{167}Er, (see Fig. 13b), the decreasing core inlet temperature leads to a decrease in the average fuel temperature. Since the reactivity coefficient of the fuel is negative (see Fig. 5) a positive reactivity is inserted into the reactor leading to a power rise to a factor 1.6 about 60 s into the transient, almost the same as without ^{167}Er. In this case, however, power and all temperatures stabilize; the core outlet temperature stabilizes around 750°C, and both average fuel and graphite temperatures remain below 700°C because of the negative graphite temperature coefficient.

8.6.2.4. AMSTER-Incinerator ULOH transient

For the ULOH transient without ^{167}Erb, (see Fig. 14a), the heat transfer into the secondary system is assumed to fail at t = 0. Control rods are postulated not to insert into the core. The loss of heat sink implies the core inlet temperature will increase on account of lack of cooling via the heat exchangers. The only heat sink remaining will be radiation via the vessel surface to the reactor containment atmosphere. As can be observed in Fig. 14a, the core inlet temperature will increase from 570 to about 740°C within 200 s after transient initiation. As a result, the core average fuel temperature will also increase from 640 to 740°C within 200 s into the transient causing negative reactivity to be inserted into the core on account of the negative fuel reactivity coefficient, namely ~ -1.0 pcm/°C. The net effect is a fast decrease in the power level to below 10% after 150 s into the transient. By 300 s into the transient, the nuclear power is below the decay heat power level. Since the power level decreases, the core fuel outlet temperature does not rise above 750°C. As can be observed in Fig. 14a, all fuel temperatures reach an asymptotic level of about 760°C about 2200 s into the transient. The graphite temperature gradually increases from 675 to 760°C beyond 800 s injecting positive reactivity into the core on account of its positive reactivity coefficient, namely ~ +1.2 pcm/°C. While the total reactivity coefficient remains negative, the temperatures in the system are not expected to go beyond the 770°C in this transient because the continued decreasing decay heat power level and the 23 MW being lost via radiation of the vessel walls serving as a heat sink.

At the asymptotic temperature of ~760°C the total reactivity coefficient becomes slightly positive (~ +0.2 pcm/°C) but the reactor is still sub-critical by about -40 pcm. The average fuel and bulk graphite temperature would need to increase by another +200°C for the core reactivity level to become positive

and nuclear power to increase again. Without the radiation heat sink, this temperature increase would occur. Additional negative reactivity would then have to be inserted into the core via the control rod systems in order to assure a continued nuclear shut-down.

Furthermore, should the fuel temperatures decrease substantially below the asymptotic level of ~760°C, a positive reactivity insertion due to the decreasing fuel temperature will lead to a renewed rise in nuclear power. In order to prevent this, additional negative reactivity will need to be inserted into the core at some point into this transient in order to assure continued nuclear power shut-down.

For the ULOH transient with ^{167}Er in the graphite, (see Fig. 14b), a similar behaviour is seen as has been observed for the ULOH case without ^{167}Er. Since the fuel temperature coefficient is ~-1.36 pcm/°C, an increasing average fuel temperature after the loss of heat sink will lead to a large insertion of negative reactivity depressing the power level within 120 s to below 10%. During the first 200 s, the transient response all fuel temperatures follow the same pattern as in the previous case, namely a fast rise with a levelling off at around 720°C. Since the graphite temperature coefficient is however negative in this case, namely ~ -0.63 pcm/°C, an increase in graphite temperature will now insert additional negative reactivity assuring continued nuclear shutdown.

The total temperature coefficient will remain negative throughout this transient for this reactor design. There will thus be no concern that nuclear power production will revitalize at some time into this transient on account of the increasing bulk graphite temperature. This implies that this reactor design is inherently safe.

All relevant temperatures are observed to be below 740°C for 1 600 s into transient. Beyond this time, the temperatures are not expected to exceed 750°C since the decay heat generation, which is the dominant heat production source at this time into transient, will continue to decrease. Again, about 23 MW of heat are being lost from the primary system via radiation from the vessel walls, providing a heat sink for the system.

Should the fuel temperatures drop below the asymptotic temperatures during this transient, positive reactivity will be inserted into the reactor due to the reactivity coefficients. This could revitalize nuclear power generation. In order to prevent this, some form of additional negative reactivity will need to be inserted into the core at some point into this transient in order to assure continued nuclear power shut-down. Adding ^{167}Er to the graphite adds to the safety margin of this reactor design under ULOH transient condition.

8.6.2.5. Summary of AMSTER-Incinerator transients

The above transients have demonstrated that the AMSTER-Incinerator design without ^{167}Er added to the graphite matrix can be stable when graphite temperatures exceed 800°C because the graphite temperature coefficient becomes negative above these temperatures. For this reactor design to be stable for long transient time-scales under all conceivable unprotected transient conditions, ^{167}Er should be included in the graphite matrix to assure a negative graphite temperature coefficient even at lower graphite temperature (~600°C). One positive attribute associated with graphite is its very large thermal inertia, assuring a sluggish transient behaviour due to the slow heat-up of graphite. This sluggishness provides sufficient response time for the reactor operators to counteract the failed control rod system that has been assumed not functional for all of the above investigated transients.

8.6.3. *AMSTER Breeder transients*

The results of the Unprotected Loss of Flow (ULOF), the Unprotected Transient Over Power Transient (UTOP), Overcooling Transient and Unprotected Loss of Heat Sink (ULOH) of the core are displayed in Figs 15-18. For each transient two figures are provided. In the first figure, the dynamic response of the normalized thermal reactor power, neutron flux, and mass flow rate are displayed. In the second figure, the dynamic response of the molten salt core outlet -, average core -, core inlet -, and average bulk graphite — temperatures are shown.

8.6.3.1. AMSTER-Breeder ULOF transient

For the ULOF transient without ^{167}Er, Fig. 15a, the mass flow rate drops to the natural convection flow rate (about 5% of nominal flow is assumed) very shortly after pump failure. Control rods are postulated not to insert into the core. The loss of flow rate in circulating fuel reactors implies an insertion of positive reactivity. In the case of MSBR, with (see Fig. 6), β_{eff} static = 341.4 pcm this reactivity insertion due to the loss of fuel circulation is +85.8 pcm (β_{loss} = -85.8 pcm), or -25%.

The average fuel temperature is observed to rise very rapidly to ~750°C as a result of the fast decreasing mass flow rate. Since the temperature coefficient of the fuel is strongly negative, namely ~ -2.0 pcm/°C (see Fig. 6), sufficient negative reactivity is being inserted into the reactor to counterbalance the positive reactivity increase associated with the loss of fuel circulation. The net effect is a fast decrease in the power level to below 10% after 100 s into the transient.

Concurrent with the fast rise in the average fuel temperature is the relatively slow rise in the bulk graphite temperature. Due to the positive graphite reactivity coefficient of ~ +1.90 pcm/°C, a positive reactivity is now slowly inserted into the core, and after about 400 s into the transient, the net reactivity becomes slightly positive because of the decreasing average fuel temperature after ~80 s. After 300 s into the transient, both average fuel temperature and bulk graphite temperature assume about the same value. The net reactivity, i.e. the sum of the fuel and the graphite coefficient, is now close to zero because the fuel coefficient becomes more negative and the graphite coefficient less positive as temperature increase. This leads now to the stabilization in reactor power. After about 3 000 s the reactor power remains below 10% and the corresponding average fuel and graphite temperature are close to 700°C. The core outlet temperature is seen to rise briefly above 940°C, decreasing to around 820°C at ~300 s into the transient, and subsequently levelling off at that temperature.

For the ULOF transient with ^{167}Er in the graphite, Fig. 15b, the mass flow rate follows the same characteristic as observed for the ULOF case without ^{167}Er. Since the fuel temperature coefficient is ~ -2.5 pcm/°C, an increasing average fuel temperature will lead to a large insertion of negative reactivity depressing the power level to below 10%. During the first 200 s the transient response of both average fuel and outlet temperature follow the same pattern as in the previous case, namely a short rise with a subsequent drop to around 930°C for the outlet and 750°C for the core average fuel temperature. Since the graphite temperature coefficient is however close to zero in this case, an increase in graphite temperature will now insert negligible reactivity. Under these conditions, power and temperatures will stabilize, as can be observed, implying that this reactor design is inherently stable. The power levels off around 7% nominal, average fuel and the graphite temperatures stabilize around 670°C, and the core outlet temperature remains at ~765°C. There is no need to add ^{167}Er to the graphite in this reactor design under ULOF transient condition since it is inherently safe without it.

8.6.3.2. AMSTER-Breeder UTOP transient

In the case of the overpower transient without ^{167}Er, Fig. 16a, the insertion of +300 pcm reactivity, or 90 cents, leads to a power spike of factor 15. The fast rise in average and outlet temperature adds quickly negative reactivity into the core, bringing the power back down to a factor 3.8 at about 7 s into the transient. The increasing graphite temperature now inserts positive reactivity which leads to a slow increase in reactor power again. The core outlet temperatures exceed now 1 100°C after 60 s into the transient, the average fuel temperatures being continuously above 800°C. After about 60 s into the transient, the outlet temperature reaches above 1 100°C and failure of the reactor system should be anticipated beyond that point in time.

In the case of the overpower transient with ^{167}Er, Figs 6b, the observed power spike is now to a factor 13, dropping down to a factor 3 after 10 s into the transient. The fuel outlet temperature quickly rises to around 950°C within 10 s after the initiation of the transient, and stabilizes thereafter at about that level. The core average temperature quickly rises to 760°C and stabilizes thereafter. The graphite temperature is observed to increase continuously, adding negative reactivity since its reactivity coefficient becomes slightly negative above 700°C (see Fig. 6). This again demonstrates that the addition of ^{167}Er stabilizes the UTOP transient at acceptable temperatures.

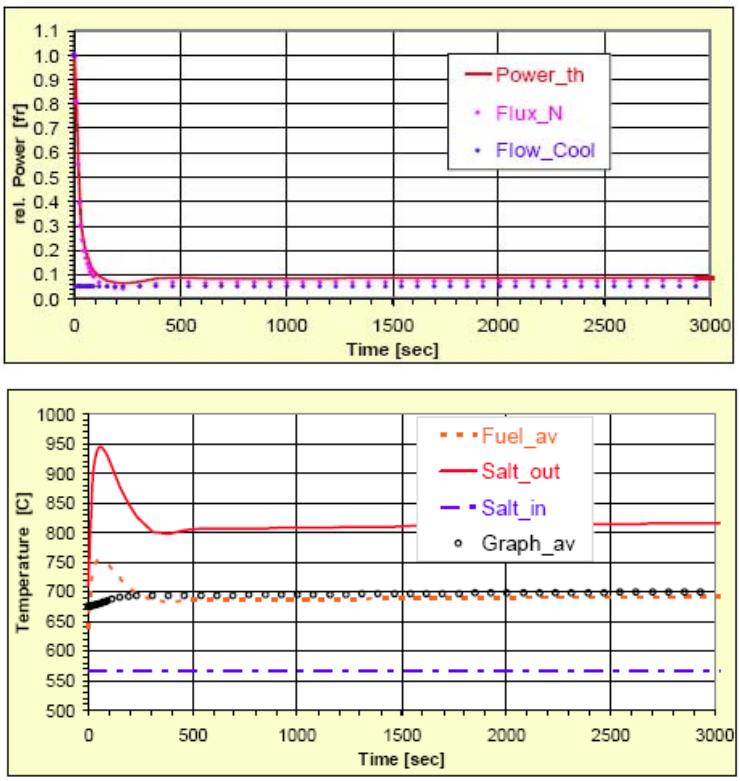

FIG. 15a. Unprotected Loss of Flow (ULOF) for AMSTER-Breeder without ^{167}Er.

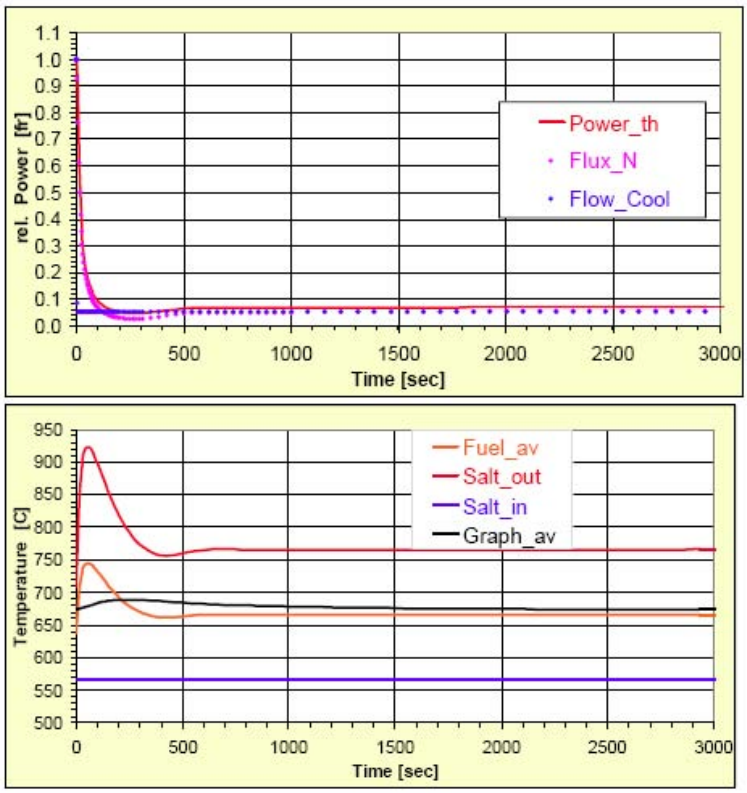

FIG. 15b. Unprotected Loss of Flow (ULOF) for AMSTER- Breeder with ^{167}Er.

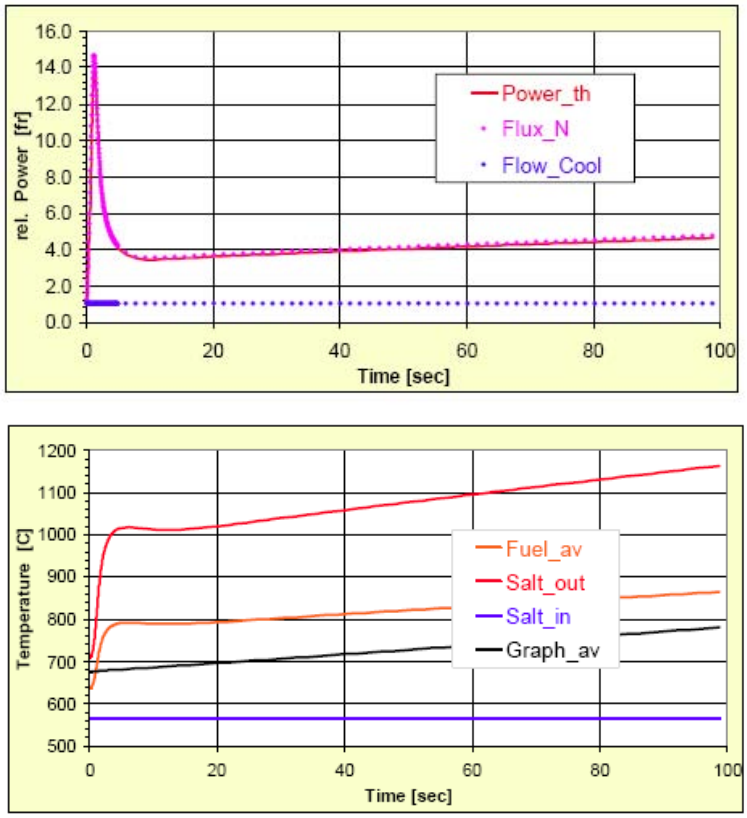

FIG. 16a. Unprotected TOP (+300 pcm insertion) for AMSTER-Breeder without ^{167}Er.

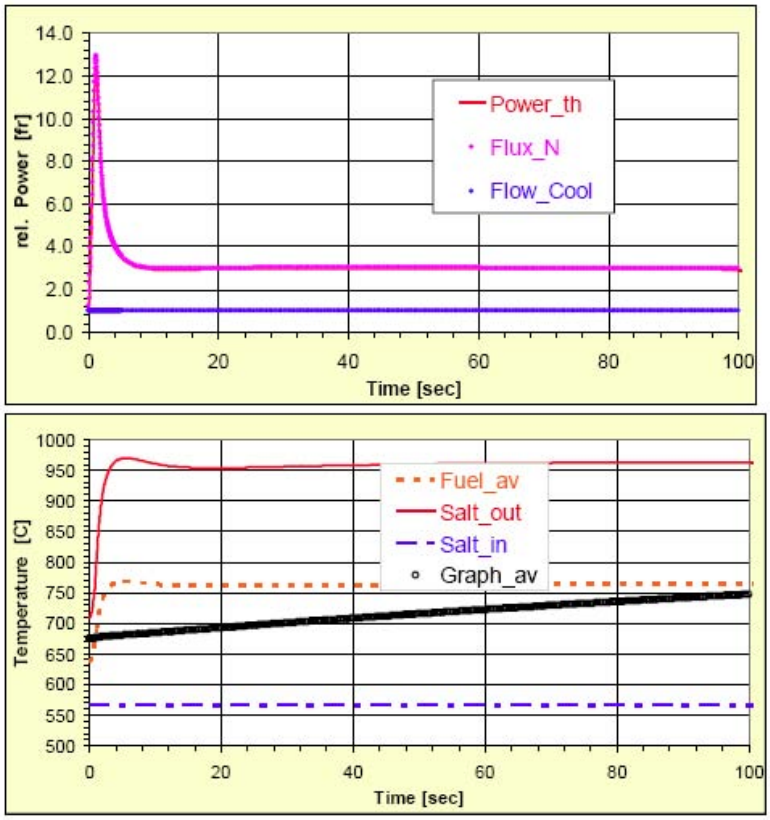

FIG. 16b. Unprotected TOP (+300 pcm insertion) for AMSTER-Breeder with ^{167}Er.

8.6.3.3. AMSTER-Breeder bvercooling transient

In the case of the overcooling transient without ^{167}Er, Fig. 17a, the decreasing core inlet temperature leads to a decrease in the average fuel temperature. Since the reactivity coefficient of the fuel is negative (see Fig. 6), a positive reactivity is inserted into the reactor leading to a power rise to a factor 1.6 about 50 s into the transient. Due to the gradual increase in the temperature of the bulk graphite, additional positive reactivity is inserted into the core leading to a continuous power rise up to a factor of 11 at 5 000 s into the transient when the power levels off due to the total reactivity coefficient becoming positive. The core outlet temperature increases above 1 740°C at 2 500 s into the transient and the core average temperature levels off at 1 300°C. The graphite temperature gradually increases to 1 700°C within 5 000 s into the transient. Even though the reactor stabilizes during this transient, excessively high temperatures will lead to reactor system failure at some point beyond 2 000 s.

In the case of the overcooling transient with ^{167}Er, Fig. 17b, the decreasing core inlet temperature leads to a decrease in the average fuel temperature. Since the reactivity coefficient of the fuel is negative (see Fig. 6), a positive reactivity is inserted into the reactor leading to a power rise to a factor 1.7 about 60 s into the transient, almost the same as without ^{167}Er. In this case, however, power and all temperatures stabilize; the core outlet temperature stabilizes around 760°C, and both average fuel and graphite temperatures remain below 700°C because of the negative graphite temperature coefficient.

8.6.3.4. AMSTER-Breeder ULOH transient

For the ULOH transient without ^{167}Er, Fig. 18a, the heat transfer into the secondary system is assumed to fail at t = 0. Control rods are postulated not to insert into the core. The loss of heat sink implies the core inlet temperature will increase on account of lack of cooling via the heat exchangers. The only heat sink remaining will be radiation via the vessel surface to the reactor containment atmosphere. As can be observed in Fig. 18a, the core inlet temperature will increase from 570°C to about 710°C within 150 s after transient initiation. As a result, the core average fuel temperature will also increase from 640 to 710°C within 150 s into the transient causing negative reactivity to be inserted into the core on account of the strongly negative fuel reactivity coefficient, namely ~ -1.95 pcm/°C (see Table 6). The net effect is a fast decrease in the power level to below 10% after 150 s into the transient. By 200 s into the transient, the nuclear power is below the decay heat power level. Since the power level decreases the core fuel outlet temperature does not rise above 720°C. As can be observe in Fig. 18a, all fuel temperatures reach an asymptotic level of about 740°C about 2 500 s into the transient. The graphite temperature gradually increases from 675 to 710°C beyond 500 s injecting positive reactivity into the core on account of its positive reactivity coefficient, namely ~ +1.86 pcm/°C. While the total reactivity coefficient remains negative, the temperatures in the system are not expected to go beyond the 740°C in this transient because the continued decreasing decay heat power level and the 23 MW being lost via radiation of the vessel walls serving as a heat sink.

At the asymptotic temperature of ~750°C, the total reactivity coefficient remains slightly negative (~ -0.1 pcm/°C) with the reactor being sub-critical by about –100 pcm. There will thus be no concern that nuclear power production will revitalize at some time into this transient on account of the increasing bulk graphite temperature. This implies that this reactor design is inherently safe during this particular transient. Should the fuel temperatures decrease substantially below the asymptotic level of ~750 C, a positive reactivity insertion due to the decreasing fuel temperature will lead to a renewed rise in nuclear power. In order to prevent this, additional negative reactivity will need to be inserted into the core at some point into this transient in order to assure continued nuclear power shut-down.

For the ULOH transient with ^{167}Er in the graphite, Fig. 18b, a similar behaviour is seen as has been observed for the ULOH case without ^{167}Er. Since the fuel temperature coefficient is ~ -2.5 pcm/°C, an increasing average fuel temperature after the loss of heat sink will lead to a large insertion of negative reactivity depressing the power level within 100 s to below 10%. During the first 200 s, the transient response of all fuel temperatures follows the same pattern as in the previous case, namely a fast rise with a subsequent levelling off at around 710°C. Since the graphite temperature coefficient is however slightly negative in this case, namely ~ -0.1 pcm/°C, an increase in graphite temperature will now insert additional negative reactivity assuring continued nuclear shutdown.

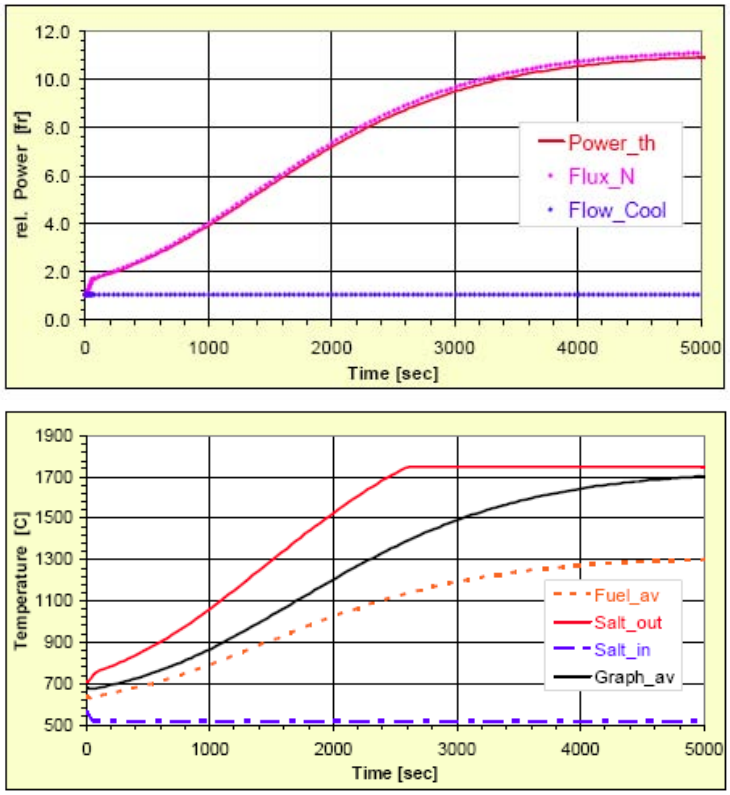

FIG. 17a. Unprotected Over-Cooling Transient for AMSTER-Breeder without ^{167}Er.

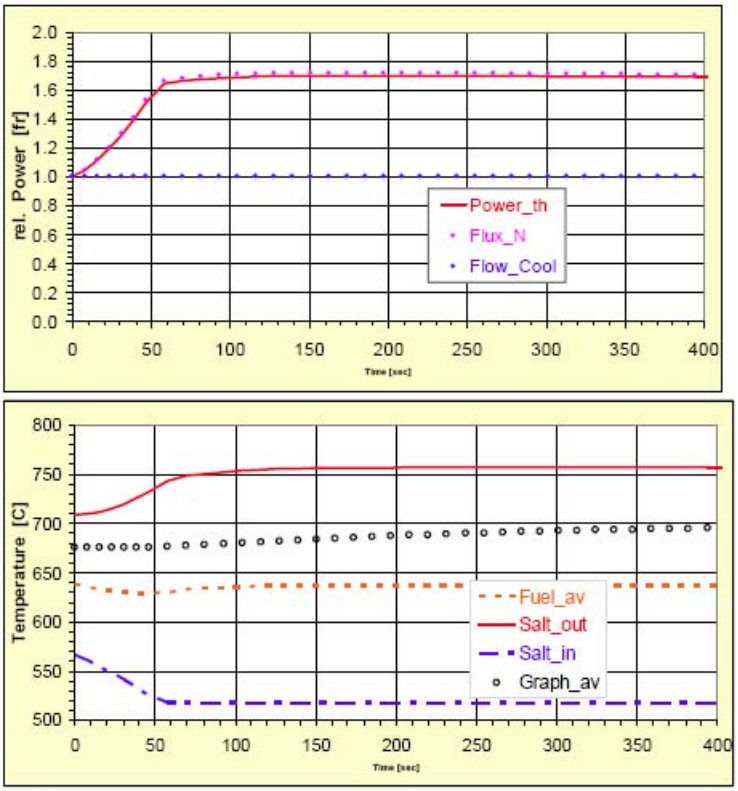

FIG. 17b. Unprotected Over-Cooling Transient for AMSTER- Breeder with ^{167}Er.

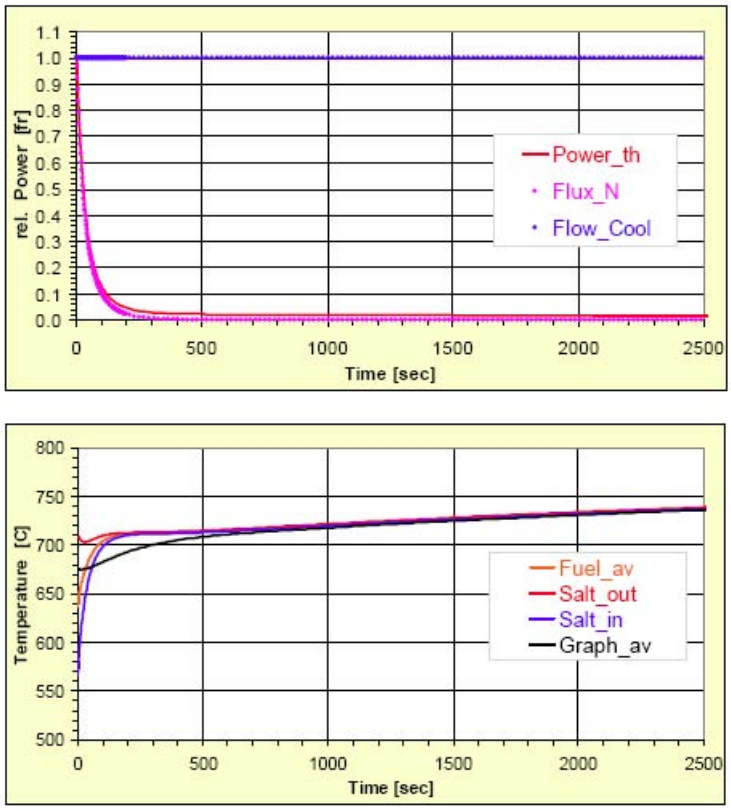

FIG. 18a. Unprotected Loss of Heat Sink (ULOH) for AMSTER-Breeder without ^{167}Er.

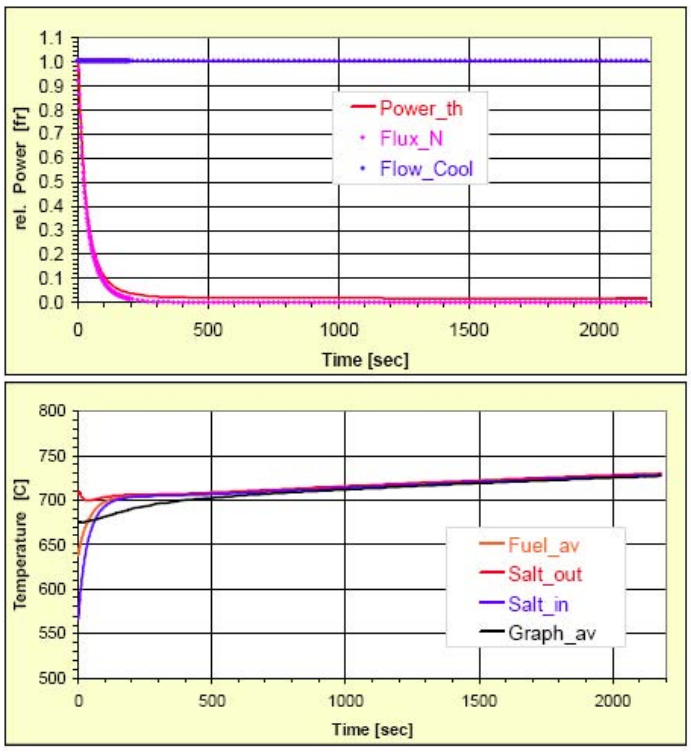

FIG. 18b. Unprotected Loss of Heat Sink (ULOH) for AMSTER-Breeder with ^{167}Er.

The total temperature coefficient will remain negative throughout this transient for this reactor design. There will thus be no concern that nuclear power production will revitalize at some time into this transient on account of the increasing bulk graphite temperature. This implies that this reactor design is inherently safe during this particular transient.

All relevant temperatures are observed to be below 740°C in 2 200 s into transient. Beyond this time, the temperatures are not expected to exceed 750°C since the decay heat generation, which is the dominant heat production source at this time into transient, will continue to decrease. Again, about 23 MW of heat are being lost from the primary system via radiation from the vessel walls, providing a heat sink for the system.

Should the fuel temperatures drop below the asymptotic temperatures during this transient, positive reactivity will be inserted into the reactor due to the reactivity coefficients. This could revitalize nuclear power generation. In order to prevent this, some form of additional negative reactivity will need to be inserted into the core at some point into this transient in order to assure continued nuclear power shut-down. Adding ^{167}Er to the graphite adds to the safety margin of this reactor design under ULOH transient condition.

8.6.3.5. Summary of AMSTER-breeder transients

The above transients have demonstrated that the AMSTER-breeder design without ^{167}Er added to the graphite matrix is inherently unstable on account of its positive graphite temperature reactivity coefficient, although its behavior is better than MSBR one, due to the fact that its design, with a more important fertile zone, favors a less positive total reactivity coefficient. For this reactor design to be stable under unprotected transient conditions for long transient time-scales, ^{167}Er should be included in the graphite matrix to assure a negative graphite temperature coefficient. One positive attribute associated with graphite is its very large thermal inertia, assuring a sluggish transient behavior due to the slow heat up of graphite. This sluggishness provides sufficient response time for the reactor operators to counteract the failed control rod system that has been assumed not functional for all of the above investigated transients.

8.6.4. *Spatial effects and transients*

Spatial and fluid-dynamics effects can be important for the physics evaluations of molten salt systems. To investigate this aspect full space kinetics analyses have been performed on the system, using the code DYNAMOSS [V.4], specifically developed for the study of fluid-fuel systems in a slug-flow regime. It is especially interesting and physically worth-while to evidence the large differences in the spatial distributions of delayed neutron precursors with respect to the case of solid fuel. This effect can be clearly seen by the observation of Fig. 16.

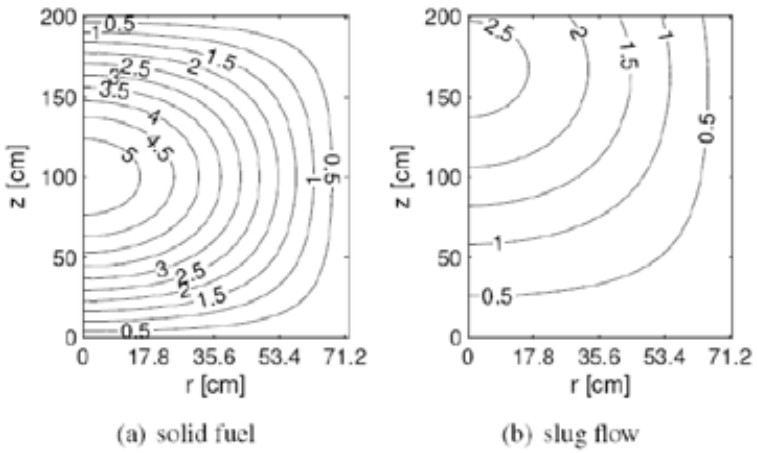

FIG. 16. Level curves for precursor distributions in the MSRE reactor and effects of the motion of the fuel for a family characterized by λ=0.116s-1.

For the time-dependent analysis the presence of spatial effects is now investigated. Results are obtained for a channel-type reactor with the use of the DYNAMOSS code, coupled with a channel thermal model. The core is subdivided into four radial zones, numbered from 1 to 4, starting from the axis outward, in each of which a full temperature calculation is performed. Figure 17 reports both the axial linear power distribution radially-averaged over the zone corresponding to each channel and the axial temperature profiles.

A localized positive reactivity insertion amounting to 200 pcm is considered. The system stabilizes on a power level 36% higher than the initial one. The temperature distributions at different instants during the transient are reported in Fig. 18.

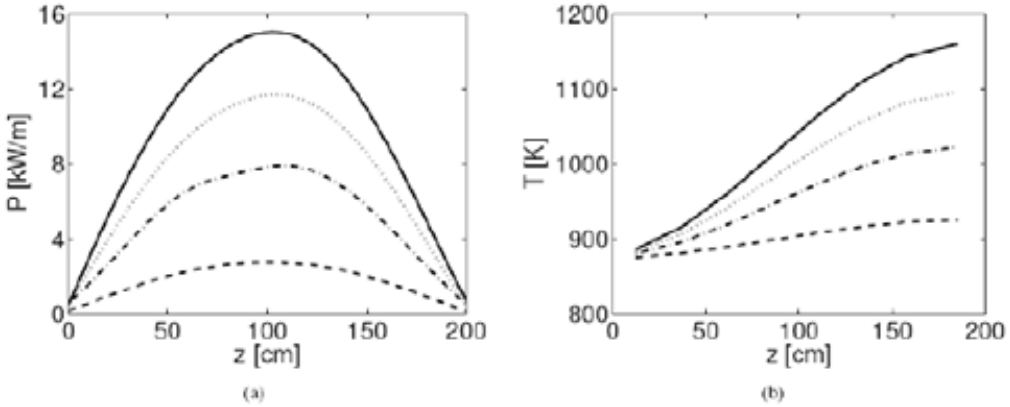

FIG. 17 Axial linear power distribution in the four channels on the left (full line: channel 1; dotted line: channel 2; dash-dotted line: channel 3; dashed line: channel 4). Axial temperature distribution in the channels on the right.

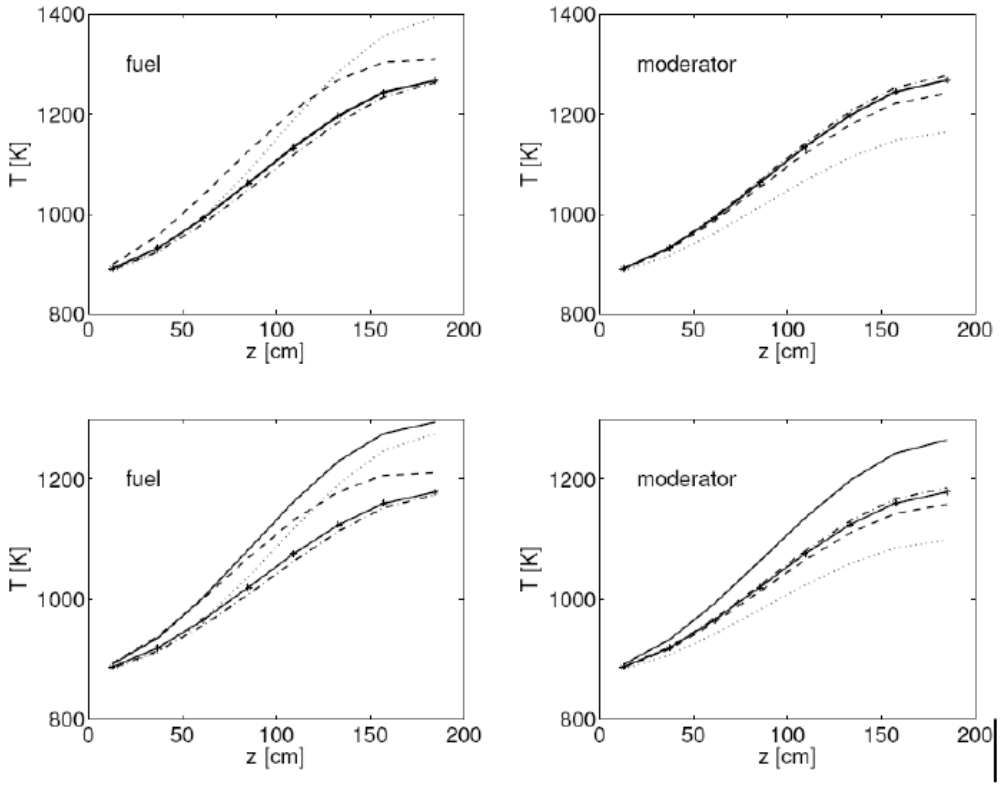

FIG. 18 Time evolution of fuel and graphite temperatures for channels 1 and 2. Solid line: 5 s; dotted line: 20 s; dashed line: 75 s; dash-dotted line: 150 s; starred line: 300 s.

8.7. Fuel salt cleanup for thorium-uranium MSR

Molten-salt reactor (MSR), which is considered to be a non-classical nuclear reactor type, exhibits some very specific features coming out from the use of liquid fuel circulating in the MSR primary circuit. Even though this features cause serious technical problems of the MSR technology, which must be solved, they simultaneously bring the main advantages of this reactor type. The MSRs can be operated either as thorium breeders within the ^{232}Th-^{233}U fuel cycle or as actinide transmuters incinerating transuranium fuel. MSR is classified as a non-classical reactor system as the fuel is in the liquid form, dissolved in the reactor primary circuit. Essentially, the main attractiveness of MSR comes out from the prerequisite, that this reactor type should be directly connected with the 'on-line' reprocessing of circulating liquid (molten-salt) fuel. This principle should allow very effective extraction of freshly constituted fissile material (^{233}U) and removal of fission products. Besides, the on-line fuel salt cleanup is necessary within a long run to keep the reactor in operation. As a matter of principle, it permits to clear away typical reactor poisons like xenon, krypton, lanthanides etc. and possibly also other products of burned plutonium and transmuted minor actinides. The fuel salt cleanup technology should be linked with the fresh MSR fuel processing to continuously refill the new fuel (thorium or transuranics) into the reactor system. On the other hand, the technologies of transuranium molten-salt fuel processing from the current LWR spent fuel and of the on-line reprocessing of MSR fuel represent two killing points of the whole MSR technology, which have to be successfully solved before MSR deployment in the future. Whilst the 'fresh' transuranium fuel processing for MSR burner, similarly as the fresh thorium for MSR breeder, can be prepared outside the reactor site, the MSR on-line reprocessing must be tightly connected with the MSR primary (fuel) circuit technology. Furthermore, the separation technology used for on-line reprocessing can strongly influence the reactor core chemistry. Therefore the choice of separation processes has to be done carefully.

The MSR fuel cycle chemistry and technology were studied intensively during the Molten-Salt Reactor Experiment (MSRE) and Molten-Salt Breeder Reactor (MSBR) projects in ORNL during 1960s and beginning of 1970s, the liquid fuels for MSR were processed, and however, the MSR spent fuel reprocessing was never fully realized either in a pilot scale. For all that, considerable effort was carried out in radiochemical laboratory research to develop separation processes for uranium, thorium, protactinium and rare earth elements from the carrier molten salt. Also the basic flow-sheeting work was done during the MSBR program to design main principles of MSBR spent fuel on-line reprocessing [1].

Nowadays, based on the new requirements of sustainable development of nuclear power, the MSR technology is under revival of interest in the frame of the development of advanced nuclear reactor types. However, it is necessary to realize that the knowledge and experience of the Molten-Salt Reactor technology is not well proportioned. Whereas the knowledge of the MSR performance is quite comprehensive, the MSR fuel cycle technology, including the on-line reprocessing, represents one of the poorest developed and verified areas.

Main fuel processing and reprocessing technologies proposed for MSR fuel cycle are generally pyrochemical or pyrometallurgical, majority of them are fluoride technologies. This is caused by the fact that MSR fuel is constituted by a mixture of molten fluorides. As the preparation of fresh thorium fuel is generally known and adequately experimentally verified, the processing of transuranium fuel for MSR and the spent MSR fuel cleanup technology are still under the laboratory development [2]. There are three main pyrochemical separation techniques generally proposed for reprocessing of MSR fuel:

— Fluoride volatilization processes;
— Molten salt/liquid metal extraction processes;
— Electrochemical separation processes.

In addition to these pyrochemical techniques also the gas extraction from the fused salt (often called as He — bubbling method) could be one additional step of MSR fuel salt cleanup.

The development of on-line reprocessing (fuel salt cleanup) technology represents a very specific problem affecting even the MSR design, reactor core chemistry and a choice of structural materials.

Particularly the link to reactor core chemistry is close because the chemical reactions rate and theirs character in the reactor have to be compensated by the reprocessing technology. (The nuclear fission in the molten salt fuel medium is an oxidizing process, nevertheless the red — ox potential in the reactor must be kept in slightly reductive range to protect the reactor core and primary circuit structural materials — nickel alloys and graphite.) Special attention should be paid to the selection of carrier molten salt, which must exhibit several basic properties (e.g. good thermal conductivity, appropriate melting point, low vapor pressure, radiation stability, sufficient solubility of actinides and last but not least the reprocessability by adequate separation techniques). Based on these requirements, the $^{7}LiF - BeF_2$ eutectics remains the basic carrier salt candidate among several others, sometimes considered or proposed molten salt mixtures, for this purpose.

As the molten-salt/liquid metal extraction processes dedicated to actinide/lanthanide separation were intensively studied during the MSRE and MSBR projects, the electrochemical separation represents the other possible and promising partitioning technique suitable for on-line reprocessing of MSR spent fuel.

The general spirit of MSR on-line reprocessing is to keep the reactor in steady-state conditions by continuous cleaning-up of the primary (fuel) circuit salt. It means, that some part of the salt circulating in the primary circuit is piped to the reprocessing unit, where the fission products are extracted and then moved to waste, whereas the separated actinides are dissolved again in the carrier salt and returned back into the primary circuit. As there is all the time the same concentration of fission products in the primary circuit, the removal of these elements in reprocessing unit need not be absolute, however no actinides can be moved into the waste stream. The general principle of MSR on-line reprocessing is shown in Fig. 19. Distribution of main fission product groups and corresponding separation times are shown in Table 7.

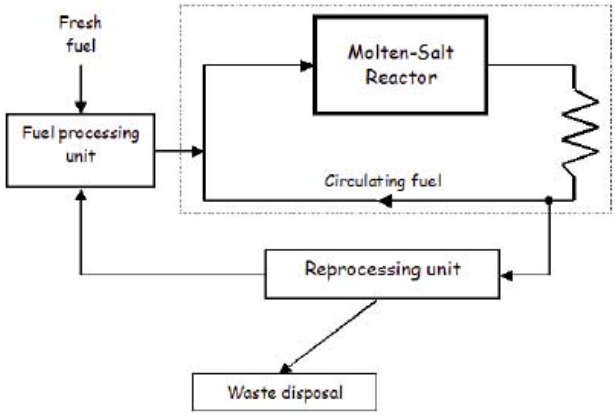

FIG. 19 General scheme of MSR on-line reprocessing principle.

TABLE 7. DISTRIBUTION OF MAIN FISSION PRODUCT GROUPS ACCORDING TO THEIR REMOVAL TIME DEMAND IN MSR

Chemical element	Removal time	Main extraction technology
Noble gases (Kr, Xe)	1 min.	Gas extraction process (He bubbling) in primary circuit impeller
Noble metals (Nb, Mo, Ru, Sb, Se, Te, …	2 – 3 hours	Gas extraction process (He bubbling) in primary circuit impeller
Actinides, Lanthanides	300 days	Liquid metal extraction and Electroseparation

The AMSTER-Incinerator flow-sheet concept comes out from the former results achieved by ORNL team during MSRE and MSBR projects and from the current electrochemical separation studies described above. The reprocessing technology is based on primary non-selective molten-salt/liquid metal reductive extraction and subsequent selective electrochemical separation processes. Li and molten Bi is proposed to be used as reduction and extraction agents, respectively.

8.8. Conclusions

The basic transient behaviour of these particular reactor designs can be characterised by the mismatch in the temperature response of the fuel (fast acting) and the graphite (slow acting). After the initial transient phase, during which the average fuel temperature dominates the transient response, the graphite temperature catches up and impose its characteristics onto the plant dynamic behaviour thereafter.

In general, however, all transients are observed to be very sluggish due to the very large thermal inertia associated with the graphite in the core.

The long term dynamic behaviour of the reactor becomes unstable under unprotected transient conditions if the total reactivity coefficient of the system should be positive. The long term reactor power level will not stabilize under these conditions. Should the total temperature coefficient be negative, the reactor will stabilize at a certain power level with corresponding temperatures.

The total temperature coefficients for the three different molten-salt reactor concepts studied (MSBR, AMSTER-Incinerator, AMSTER-Breeder), all have values close to zero, if erbium is not added to the graphite matrix. Moreover, both fuel and graphite coefficients display non-negligible variations with temperature, leading to quite complex and unpredictable long term transient behaviour (if the operator does not intervene, of course).

The sluggish transient behaviour of this reactor design, however, provides sufficiently response time for the reactor operators to counteract the failed control rod system that has been assumed not functional during all of the above transients analyzed. Since the initial phase of all transients is dominated by the negative reactivity coefficient associated with the fuel temperature, the reactor can be basically characterized as safe.

Successful solution of the MSR spent fuel reprocessing technology development seems to be one of crucial steps before industrial deployment of MSR systems. As the MSR reprocessing technology must meet special demands (like radiation resistance, compactness, exclusion of moderating agents, compatibility with the carrier molten salt type and with the structural material of MSR primary circuit, acceptable process reaction rate and process workability by remote handling), the pyrochemical separation processes seems to be the only technologies, which can be generally applied. The pyrochemical fluoride separation processes seems to be the most promising ones. However, the development of individual separation technique must be realized in association with the flow-sheeting research. The close cooperation with reactor physicists is necessary as well. Current R&D effort and achieved results in pyrochemical separation methods offer the realistic preconditions that the MSR on-line reprocessing technology could be solved successfully. Then the MSR systems can significantly contribute to the sustainable development of nuclear power.

REFERENCES TO CHAPTER 8

[1] Conceptual design study of a single fluid molten salt breeder reactor, Report ORNL-4541, Oak Ridge (1971).

[2] Reactor physics study, design review and nominal operating conditions, non proliferation issues, Final MOST-Project Report, Brussels (2004).

[3] LECARPENTIER, D., Le concept AMSTER, aspects physiques et sûreté, PhD Thesis, Conservatoire National des Arts et Métiers, Paris (2001).

[4] DULLA, S., RAVETTO, P., ROSTAGNO, M.M., Neutron kinetics of fluid–fuel systems by the quasi-static method, Annals of Nuclear Energy, 31, (2004) pp. 1709-1733.

[5] SCHIKORR, W.M., Assessment of the Kinetic and Dynamic Transient Behavior of Sub-Critical Systems (ADS) in Comparison to Critical Reactor Systems, Nuclear Engineering and Design, 210 (2001) pp. 95-123.

[6] LATHOUWERS; D., Modeling and Simulation of Turbulent Bubbly Flow, PhD thesis, Delft University of Technology, (1999).

[7] KÓPHÁZI, J., LÉGRÁDI, G., et al.; Effect of fuel mixing phenomena on the kinetic behaviour of molten salt reactors, 19th International Conference on Transport Theory, Budapest, 24-29 July 2005 (to be published in: Transport Theory and Statistical Physics)

[8] RINEISKI, A., SINITSA, V., MASCHEK, W., WANG, S., Kinetics and Cross-Section Developments for Analyses of Reactor Transmutation Concepts with SIMMER, paper presented in M&C 2005, 12-15 September 2005, Avignon, France.

CHAPTER 9. DOMAIN-VI: MOLTEN SALT REACTOR WITH FERTILE-FREE FUEL

9.1. Introduction

Recent years have demonstrated a growing interest in the nuclear energy systems employing the technology of molten salt fluorides. Among the systems selected in GIF generation iv, molten salt reactors (MSR) presents a promising flexible option in response to the goals and criteria assigned to future nuclear systems: fuel cycle sustainability, safety, environmental impact, proliferation resistance, diversity of applications and economics.

Molten salt reactor (MSR) systems have been under development since 1947 and extensive experience with fluoride based salts has been accumulated [1]. Various compositions of UF_4 and ThF_4 dissolved in ^{7}LiF-BeF_2 system have been considered for fuel salt. The most likely choice for reference Molten Salt Breeder Reactor (MSBR) designs was dealt with ^{72}LiF-$^{16}BeF_2$-$^{12}ThF_4$ (mole%) mixture. TRU burning was not the original development goal for the MSBR concept. Main questions arising from TRU fueling include: evaluation of alternative fuel salt composition with adequate TRU solubilities, advanced core configuration, new redox buffer for systems without uranium, analytical chemistry instrumentation, corrosion and container chemistry, suitable fuel processing, waste form development and safety aspects.

One of the systems studied within the CRP framework is molten salt actinide recycler & transmuter (MOSART) concept with fertile-free fuel developed at RRC-KI [2]. This study include neutronics analyses, in particular, benchmarks on computing safety parameters (reactivity coefficients, effective delayed neutron fraction, etc.) and (2) transient analyses, which are supported by neutronics studies, for simulating relevant hypothetical accidents.

9.2. General description of MOSART concept

In our study focus is placed on double component scenario, in which Na,Li,Be/F MOSART is used as TRU burner system of the LWR long lived radioactive wastes. The start up and feed fuel material for MOSART critical core is typical composition of TRU's from UOX spent fuel of a commercial PWR (60 GW•d/tU – 4.9% $^{235}U/U$; after 1 year cooling, see Appendix V, Table V.1). Physical properties of fuel salt are given in Appendix VI.

There is, of course, not one possible arrangement of MOSART unit. Figures 1 and 2 show the preliminary design configuration that is used here to evaluate its neutronics and thermal hydraulics feasibility. As in well established MSBR case the fluoride fuel salt mixture is circulated through the reactor core by four pumps operating in parallel. Pumps circulate salt through heat exchangers and return it to a common plenum at the bottom of the reactor vessel. Provisions are made for maintaining fission products at low required level by continuous fuel salt processing. Methods and cycle times for fission products removal and TRU recycling used in our study are given described in details in Appendix V. To minimize actinide losses in reprocessing we considered removal time about 300 edpf for soluble fission products (rare earth trifluorides). Possible front-end fuel cycle of MOSART is given in Appendix VI.

Basic characteristics of MOSART used in our study are as follows [2]:

— 2 400 MWt MOSART system has the cylindrical core having an intermediate to fast energy spectrum of neutrons. No solid material is present in the core of this reactor as moderator, only as external reflector;
— Fuel salt is molten ^{58}NaF-^{15}LiF-$^{27}BeF_2$ (mole%) mixture with 479°C melting temperature and addition of about 1.05 mole% of ($TRUF_3$ +LnF_3) with mass proportion at equilibrium for chosen fuel cycle scenario with soluble fission product removal cycle 300 epdf (see Appendix III, Table III.2);
— The salt inlet temperature in core is assumed as 873 K. At that temperature solubility of (TRUF3 +LnF_3) is about 2 mole%;
— The diameter (D)/height (H_{eff}) of the cylindrical core is about 3.4 m/3.6 m (V_{core}= 32.67m^3);
— Fuel salt volume out of the core is V_{loop} =18.40 m^3. M_{loop} =2140*18.4 = 39 363kg;
— The fuel salt specific power is about 47 W/cm^3 (2 400/(32.67+18.40));

— The effective flux of such system is near 1.1015 n/cm^2/s;
— The core salt mass flow rate G = 10000 kg/s. Average axial velocity of stream in core is equal about 0.5m/s ;
— The fuel salt enters the core through 0.5 m inlet radial window at the bottom of core;
— The fuel salt leaves the reactor vessel through 1 m diameter outlet pipe attached to the top conic reflector. At core outlet pipe with diameter 1m, it was increased up to 7 m/s;
— Out core circulation time M_{loop}/G = 39 363/10 000 =3.94 s;
— Optimal thickness for removable radial and axial graphite reflectors accounts for 0.2 m. Thermal conductivity and density of the graphite reflectors was accepted equal to the following values: λ_C = 57 Wm^{-1} K^{-1} and ρ_C = 1 800 kg/m^3;
— About 1% of the reflector volume is the fuel salt. Owing to relative power in graphite reflectors (2.2%) the total fuel salt flow rate through reflectors was chosen 275 kg/s (2.75% from the total flow);
— In addition, between reflector and reactor vessel, 30 cm width steel blocks with (1% of fuel salt) are installed to reduce the damage flux arriving at surface of the 5cm reactor vessel wall made of Ni based alloy Hastelloy NM. To minimize the reactor vessel wall temperature the 5mm fuel salt annulus is assumed between iron blocks and reactor vessel;
— Melting temperature of the primary circuit material Hastelloy NM is 1 644 K. The Hastelloy NM is designed to operate at temperature up to 1 023 K and pressure up to 500 000 N/m^2 [1].

Design parameters of MOSART fuel circuit are as follows:

Thermal capacity, MWt	2 400
Reactor vessel ID, m	6.77
Vessel wall thickness, cm	5.5
Vessel design pressure, N/m^2	5.2×10^5
Core height, m	3.6
Radial thickness of reflector, cm	20
Volume fraction of salt in core	1
Average core power density, MW/m^3	75.0
Peak core power density, MW/m^3	163
Average neutron flux, ncm^{-2}s^{-1}	10^{15}
Max. graphite damage flux, ncm^{-2}s^{-1}	1.45×10^{14}(>180 keV)
Graphite temperature at max. graphite damage, K	1084
Estimated useful life of graphite, yrs	3-4
Total weight of graphite in the reactor, t	20
Average flow velocity of salt in core, m/s	0.5
Total fuel salt in reactor vessel, m^3	40.4
Outer diameter of one heat exchanger, D_2, m	1.05
Total number of tubes in four heat exchangers, N	18591
Length of one heat exchanger, l, m	6.6
Total volume of fuel salt in heat exchangers tubes, V, m^3	6.2
Heat transfer coefficient, α_1, Wm^{-2}K^{-1}	17 100
Heat transfer coefficient, α_2, Wm^{-2}K^{-1}	17 656
Overall heat transfer coefficient, K_Σ, Wm^{-2}K^{-1}	5 700
Pressure drop in heat exchangers, ΔP_h, kPa	660
Pressure drop in core, kPa	3.7
Pressure drop in main circulation pipes, kPa	180
Total pressure drop in the fuel circuit, kPa	840

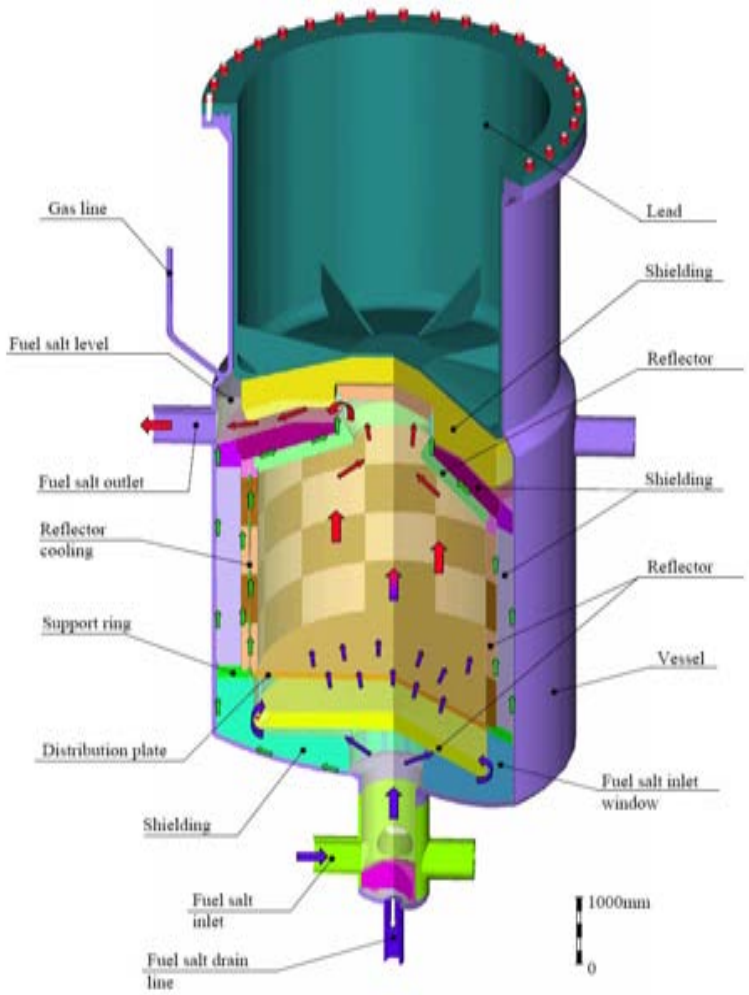

FIG. 1. MOSART core (option 1).

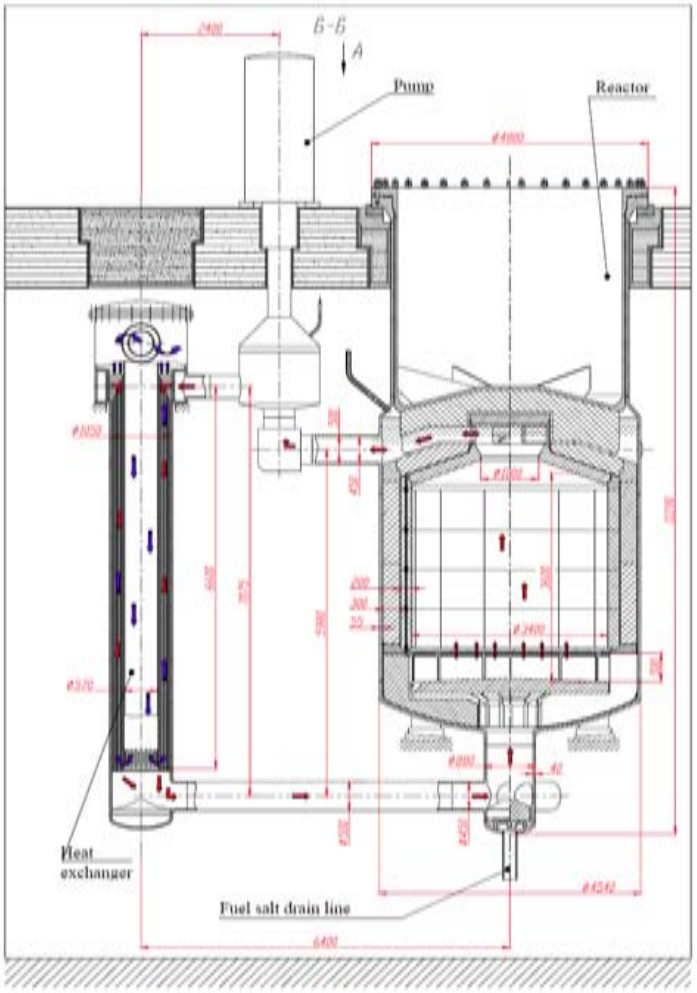

FIG. 2. MOSART fuel circuit (option 1).

9.3. Neutronic analyses

9.3.1. *Data and codes for neutronic analyses*

Several nuclear data libraries (in particular ENDF/B-VI, JEF 2.2, JEFF 3.0, JEFF 3.1, JENDL 3.3) were used for performing the analyses. Both multigroup deterministic and Monte-Carlo models (with 'point-wise' nuclear data libraries) were employed. Participants from BME, NRG, RRC-KI, SCK●CEN made computations with different versions of the MCNP [4] or MCNPX [5] codes. The NRG version of MCNP includes an extension [6] for computing β_{eff}, the effective delayed neutron fraction.

In addition to MCNP, BME employed a 1D Sn code, XSDRNPM [7] and a corresponding 172-group library based on JEFF 3.1. This code relies on a buckling (that is computed on the basis of the core height) correction technique in 2D that may bring a significant uncertainty into computed k_{eff} values in the 2D case. However, the computed 172-group spectra are assumed to be accurate for computing few-group macroscopic group cross-sections.

The computed by XSDRNPM 4-group macroscopic cross-sections (for different reactor sub-regions, at different temperatures) were employed at Polito with a 2D diffusion code DYNAMOSS [8]. This code computes k-eff and neutron flux and takes into account the effect of fuel movement on the delayed neutron precursor concentrations (if the fuel velocity distribution is known).

At FZK, a 560-group cross-section library [9] (several version of the library are available: for JEFF 3.0, JENDL 3.3, etc) was employed for (1) computing composition-dependent cross-sections and (2) producing a smaller cross-section libraries (which include, in particular, f-factors) with 172 and 9 energy groups. 2D 560-group neutron transport calculations were performed with the DANTSYS code [10]. Coupled neutronics (9-group) and thermal-hydraulics calculations were performed with the 2D SIMMER-III code [3] in order to obtain the velocity distribution and evaluate the effect of the delayed neutron precursor movement at steady-state conditions. In addition to MCNP, RRC-KI employed another Monte-Carlo code, MCU, which takes nuclear data from a related code library, MCUDAT [11].

9.3.2. *Burnup calculations*

For chosen scenario of finite core loading, with the help of MCNP-4B+ORIGEN2.1 code with library received on the basis of ENDF/B version 5,6, calculation of transition to equilibrium was carried by RRC-KI. For core with 0.2 m graphite reflector (see Fig. 3) the fuel salt power density – q_v = 47 W/cm^3 and soluble fission product removal time – τ_{Ln} = 300 efpd the initial AnF_3 concentration in the fuel salt is about 0.46 mole%.

Transient to equilibrium needs about ten years. At equilibrium state AnF_3 concentration in fuel salt is 1.03 mole% (0.6 mole% for infinite core). Note, that at equilibrium, AnF_3 concentration (in mole%) is about one order of magnitude higher than that of LnF3 in fuel salt. Mass fractions of heavy elements for initial and equilibrium critical loadings for chosen scenario are given in Fig. 4.

The schedule of fuel integral loadings for scenario under consideration, including the initial critical loading for 2 400 MWt MOSART operating with soluble fission product removal time 300 efpd is shown in Table 1.

This table also includes the integral quantities of TRUs burned in MOSART core during its operation. Mass of TRU in primary circuit at equilibrium according MCNP calculation for scenario under consideration is 6 280 kg. For this case the specific mass of TRU burned in MOSART is 303 kg/GWt/a. The MCNP input for the equilibrium state used in benchmark is given in Appendix III.

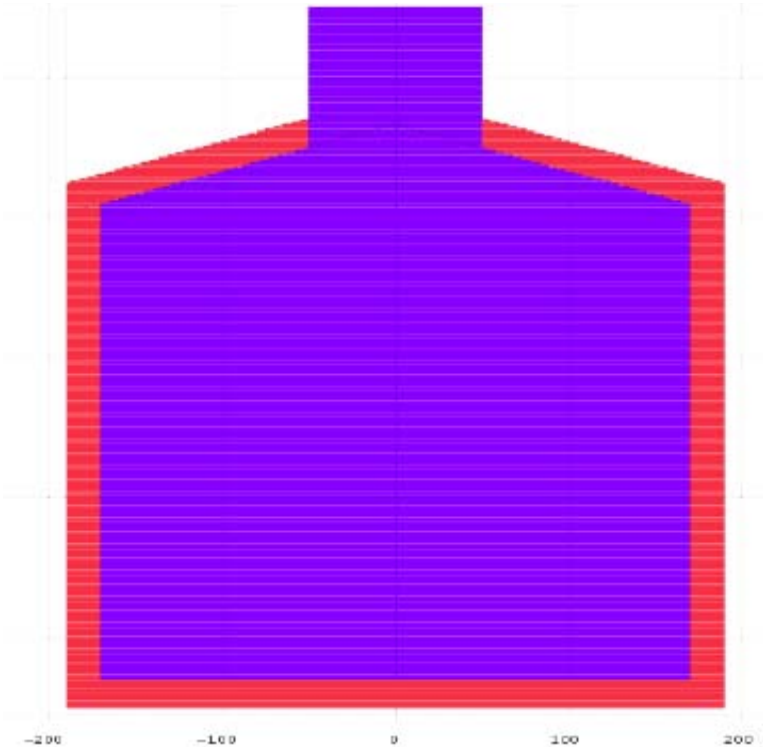

FIG. 3. MOSART core: model for neutronic studies — cylindrical geometry.

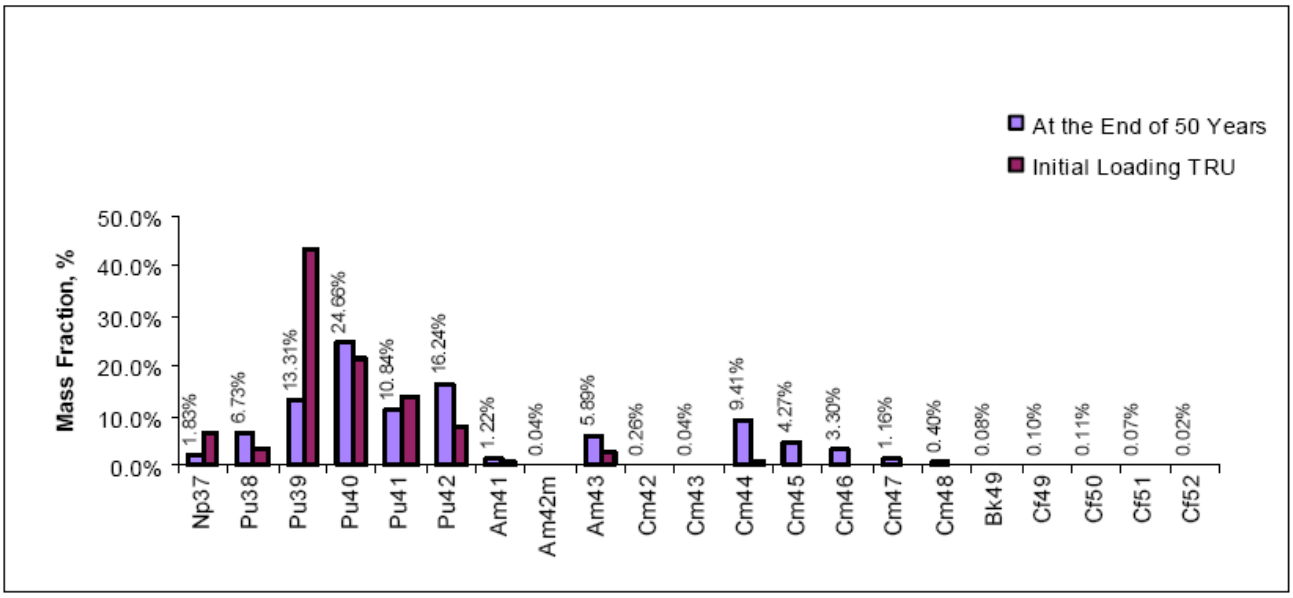

FIG. 4. Mass proportion for TRU in MOSART core model.

TABLE 1. FUEL LOADING AND FUEL BURNING SCHEDULE FOR MOSART PRIMARY CIRCUIT

Year	$N^{TRU}(t)$, TRU loaded, kg	$N_F^{TRU}(t)$, TRU burned, kg
0[a]	2746	0
1	4104	730
2	5321	1459
3	6437	2188
4	7357	2918
5	8377	3646
6	9339	4376
7	10189	5104
8	11065	5832
9	11879	6560
10	12710	7288
11	13520	8015
12	14367	8742
13	15144	9469
14	15923	10196
15	16705	10923
16	17526	11650
17	18258	12376
18	19064	13102
19	19840	13828
20	20626	14555
21	21359	15281
22	22130	16007
23	22907	16733
24	23624	17459
25	24387	18184
26	25196	18911
27	25902	19636
28	26675	20362
29	27378	21088
39	28107	21813
31	28911	22539
32	29611	23265
33	30383	23990
34	31123	24716
35	31838	25442
36	32558	26167
37	33356	26892
38	34046	27618
39	34822	28344
40	35555	29069
41	36316	29794
42	37052	30519
43	37774	31244
44	38476	31970
45	39206	32695
46	39993	33421
47	40706	34146
48	41439	34872
49	42137	35595
M_E	6280 kg	
K_G	0.845	

9.3.3. *Static neutronic analyses*

The principal benchmark results for isothermal core with equilibrium loading are given in Table 2. The k_{eff} calculations were performed with the core/reflector temperature values of 900/950 K. All values in Table 2 are obtained by assuming no inlet in the radial and top reflectors. A simplified 2D model (a right cylinder without axial reflectors) was used at Polito. Thus, the BME (1D) and Polito k_{eff} results include an uncertainty that is related to the approximate geometry treatment. Assuming that the error related to the 172-group approximation applied by XSDRNPM (for discretization in energy) is minor (that aspect is discussed later), one may conclude (by comparing the k_{eff} results of BME and Polito with those of other participants) that the corresponding geometry approximations may have a minor influence on the computed reactivity effects and kinetics parameters.

TABLE 2. MOSART MAIN REACTIVITY AND KINETICS PARAMETERS

	BME MCNP4C +JEFF 3.1 /1D 172 gr. +JEFF 3.1 /MCNP4C +JEF 2.2	FZK 2D 560 gr. JEFF 3.0 /JENDL3.3 /ENDF 6.8 /JEF 2.2	NRG MCNP4C JEFF 3.1 /JEFF 3.0	Polito 2D 4 gr. JEFF 3.1	RRC-KI MCNP4B +ENDF5,6 /MCU+ MCUDAT	SCK•CEN MCNPX250 JEFF 3.1
k-eff	1.00905 /1.01984 /0.96462	0.99285 /1.01023 /0.98474 /0.96498	1.00887 ±0.00030 /0.99335 ±0.00041	0.99595	0.99791 /0.98930	1.00904/ 0,96581
α-total, pcm/K	/-3.86	-3.86 /-3.82 /-3.86	-3.75	-3.78	-3.71 /-3.41	-3.66
α-Doppler, pcm/K	/-1.67	-1.52 /-1.53 /-1.46	-1.42	-1.73	-1.62 /-1.09	-1.69
α-reflector, pcm/K	/-0.05	-0.05		-0.04		
Generation time, μs		8.3 /8.2	11.66*) /11.36±0.03	8.8		8.7
β-eff, pcm (static)		/340	323±4.4 /294.3±4.6			320 ± 10

(*) it gives the neutron removal time, determined with the NRG evaluator which coincides with the MCNP neutron lifespan.

The Monte-Carlo and 560-group based k-eff values, obtained using the JEF2.2 nuclear library are in excellent agreement (the deviations are about 50 pcm or smaller, that is similar to the statistical uncertainty of the MCNP k_{eff} results) provided that the same nuclear data are used. That is in line with previously published results [8] on using the 560-group data for k_{inf} studies of graphite-free molten salt systems with MSRE-type [11] salts (with major fertile nuclide being either ^{232}Th or ^{238}U). On the other hand, these studies have shown a very large sensitivity of the computed k_{inf} values to the group structure (e.g. the 172 group results overestimated k-inf values at high temperatures by about 3000/1000 pcm in the ^{238}U/^{232}Th cases compared to the 560-group and MCNP results) and to the energy threshold (the error was about 600/200 pcm if this value was lower than 30 eV), above which the upscattering effects (in particular for neutron scattering on ^{19}F) are ignored. By generating a 172-group library from the 560-group one and comparing the 560-group and 172 group k_{eff} results, only a minor deviation (of about 200 pcm) was observed at FZK; similarly the mentioned 'upscattering' effects were much smaller. The reason for better performance of the simplified energy discretization model (with 172 groups) in the MOSART case is that there is no single fertile nuclide (like ^{238} Uand ^{232}Th) in the system. Since the neutron spectrum in MSR's (without graphite in the core) includes a significant fraction of neutrons with energies above a few eV (see Fig. 5), a quite accurate modelling of neutron interaction with nuclei (in particular heavy nuclides and ^{19}F) at energies near the major resonance peaks of the fertile nuclides is required if neutron absorption by these fertile elements contributes significantly to the overall neutron balance.

Though the spectra shown in Fig. 5 indicates a higher fraction of lower energy neutrons near the core and reflector boundary (R=170 cm) due to moderation in the graphite reflector, the neutron spectrum can be considered to be essentially a fast one, a very important feature for a transmutation reactor.

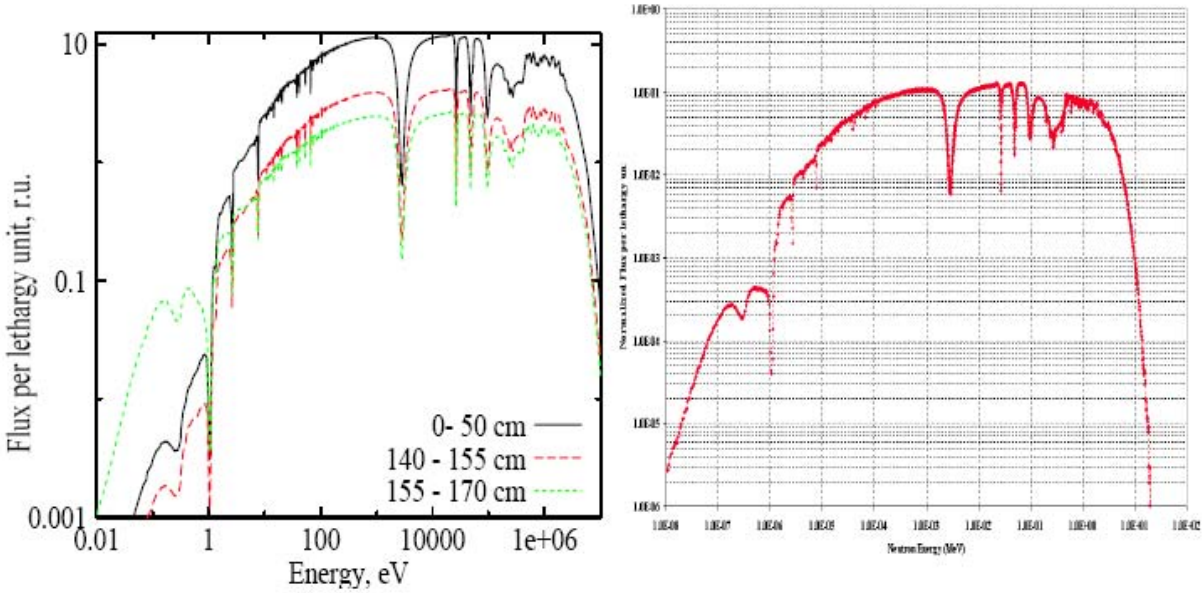

FIG. 5. Axially averaged flux spectra in MOSART at different radial locations; calculation of FZK (left) and SCK CEN (right).

Criticality values computed with different nuclear data may differ significantly. In particular a strong difference can be seen between the JEFF 3.1 and JEF 2.2 cases. The reasons for this difference were investigated at BME by considering originally all data from JEFF 3.1 and then replacing data for particular nuclides by those from JEF 2.2. The results of this study are presented in Table 3. One may see in Table 3 that the major contributions (to the difference between the JEFF 3.1 and JEF 2.2 results) come from Cm isotopes, ^{9}Be and ^{19}F. This result underlines importance of using new evaluated data (which are assumed here to be more accurate) for the mentioned non-heavy nuclides in the molten salt case.

TABLE 3. EFFECT OF SUCCESSIVE DATA REPLACEMENT (JEFF-3.1 DATA REPLACED BY JEF 2.2 ONES)

Isotopes from JEF 2.2	k-eff	Standard deviation
None	1.00905	0.0003
Pu238	1.00576	0.00029
+ Pu239	1.00172	0.0003
+ Pu240	0.99699	0.00029
+ Pu241	1.00517	0.0003
+ Pu242	1.00438	0.0003
+ Cm245	1.01095	0.00031
+ Cm247	0.99613	0.0003
+ Be9	0.97842	0.00029
+ Li7	0.9773	0.00028
+ F19	0.96595	0.00028
+ Na23	0.96635	0.00028
+ B10	0.96661	0.00028

All α coefficients (total, Doppler, reflector) shown in Table 2 are related to heating up the core and reflector by 600 K (from the state, at which the k_{eff} values were computed). The α total coefficient is the total reactivity effect divided by 600. The α-Doppler one is determined similarly, except that the salt density is assumed to be temperature-independent. The α reflector coefficient takes into account the temperature variation in the reflector only. The temperature coefficients are favourable for the

reactor safety (unlike the case with solid fuel transmutation reactors, which may require a subcriticality and an external neutron source for coping with safety problems), in particular due to strong density and Doppler effects. The reflector coefficient plays a minor role. The reactivity coefficients obtained by different participants are in reasonable (for the purpose of safety analyses) agreement, except that the underestimation of the MCU results (in particular due to the fuel Doppler effect) compared to other ones.

Results of all participants show a similar trend in temperature dependence of the coefficients. Though the Doppler coefficient varies appreciably (up to 20% if a smaller temperature shift, e.g. 100 K or 300 K, instead of 600 K, is considered), a relatively weak variation (less than 5%) of the total α-coefficient is observed. The reflector coefficient shows stronger variation (it can be lower or higher by ca. 50% at lower or higher salt and reflector temperatures) but the absolute value remains well below 0.1 pcm/K in all considered cases.

Generation time values computed at Polito are higher than those computed at FZK (see Table 2), the first values increasing with temperature (by ca. 20% after heating up the core by 600 K) while the latter ones remaining almost unchanged. This can most probably be attributed to different cross-section generation options employed in each case.

The β_{eff} values shown in Table 2 and computed by assuming no delayed neutron precursor movement were calculated at FZK, SCK CEN and NRG. They agree reasonably well taking into account use of different nuclear data and Monte-Carlo statistical uncertainties (approx. 5 pcm). According FZK results, major nuclide contributions come from ^{241}Pu (ca. 60%), ^{239}Pu (approx. 17%), ^{245}Cm (approx. 9%) and ^{247}Cm (approx. 4%).

For the core with 20cm graphite reflectors 3D power distribution maps have been obtained. These calculations have been done for the core design with the help of MCU and MCNP codes at RRC-KI (Fig. 6) and at SCK CEN by MCNPX JEFF3.1 (Fig. 7).

For calculations with a conic top reflector in Fig. 6 was entered function of relative power distribution $k(r, x)$, referred to peak power. The local power density was defined as:

$$q_v = q_v^{\max} \, k(r, x).$$

For the case with the graphite reflector: $q_v^{\max} = 163 \; MW / m^3$

— in core: $k(r, x) = k(r) \cdot k(x)$,

$$k(r) = \begin{cases} 0.476 + 0.571\cos(1.23\,r), & r \le 1.49 \\ -7.06 + 8.37\,r - 2.29\,r^2, & r > 1.49 \end{cases}$$

$$k(x) = \begin{cases} -0.680\,x + 0.553, & x < 0.325 \\ 0.599 + 0.426\cos(1.342\,x - 2.683), & 0.325 \le x \le 3.675 \\ 0.44\,x - 1.29, & x > 3.675, \quad r \ge 0.5 \\ 0.338, & x > 3.675, \quad r < 0.5 \end{cases}$$

— in top and bottom axial reflectors:

$$k(r) = \begin{cases} 0.0277 + 0.0249\cos(1.072\,r + 0.433), & r \le 1.503 \\ -0.0427 + 0.0393\,r, & r > 1.503 \end{cases}$$

— in top reflector: $k(x) = 11.53 - 0.742\ r - 2.23x$,

— in bottom reflector: $k(x) = 2.85\ e^{3.7x}$,

— in radial reflector: $k(r) = 504.8\ e^{-3.7x}$,

$$k(x) = \begin{cases} 0.0260 - 0.0529x + 0.0779x^2, & x < 0.6 \\ -0.0509 + 0.099\cos(0.525x - 1.052), & 0.6 \le x \le 3.4 \\ 1.061 - 0.571x + 0.0779x^2, & x > 3.4 \end{cases}$$

Comparison of calculated and approximated values of function $k(r, x)$ for the core and graphite reflectors is shown in Fig. 6. As can seen from Figs 6 and 7 for graphite reflectors there is significant power growth on the boundary of the fuel salt and graphite reflector due to thermal neutrons return to the core.

The total power outputs due to n+γ radiation for the graphite and nickel reflectors have been obtained. According RRC-KI [2] calculations relative power in graphite reflectors is respectively 2.2% of total core power. In whole power densities distributions received by different codes are in agreement. The asymmetry of a power density distributions received in the top part of core reflects the account of a conic top reflector and outlet pipe. It should be noted that RRC-KI calculations [2] of reactivity coefficients have been done not only for isothermal core, but also for core operating at nominal power, on base of 3D temperature distributions received in thermal hydraulic calculation. The account of temperatures distribution in the core operating at nominal power, make temperature reactivity coefficients more negative (-4.125 pcm/K for equilibrium critical loading), compared to isothermal core.

Additionally the effect of the fuel salt gas release system work on the MOSART safety characteristics was investigated. This system is based on the very low solubility of the gaseous fission products in the fuel salt. These products rapidly migrate to the boundary gas-salt and transform to gas phase. For the increasing of the gas phase part of the fuel salt passes through the bypass loop in which the sparging of helium bubbles into the fuel salt takes place. In the normal reactor operation process the concentration of the helium bubbles in the fuel salt is from 0.2 to 1 vol.%. As it can be seen from Table 2 the density reactivity coefficient (α-density = α total ~ α-Doppler) for the homogeneous MOSART core is negative. Any increasing of the gas fraction in the fuel will lead to the fuel salt exit from the core and corresponding decrease of the core reactivity. Thus any changes of pressure in the system (e.g. to change of pump speed) will change the core void fraction and lead to the inserting of the negative reactivity. Thus at 1 vol.% the voids in the MOSART, additionally inserted reactivity is -40 pcm. Due to ORNL estimations a complete depressurization of fuel system, which would allow these bubbles to expand by a factor of 2 to 3, and as result to move part of the fuel outside the core, would cause a reactivity decrease of about 0.1 δk/k.

9.3.4. *Transmutation efficiency*

Data obtained as a result of the burn up calculations permit to determine the integral parameters, characterizing system as TRU transmuter. The following two parameters have been used to evaluate MOSART transmutation ability:

TRU transmutation output: $N_F^{TRU}(t)$ — full amount of TRU nuclides burned during period t. This parameter is proportional to the core thermal power and reaches its maximum in critical system of MOSART type fuelled by only TRUs.

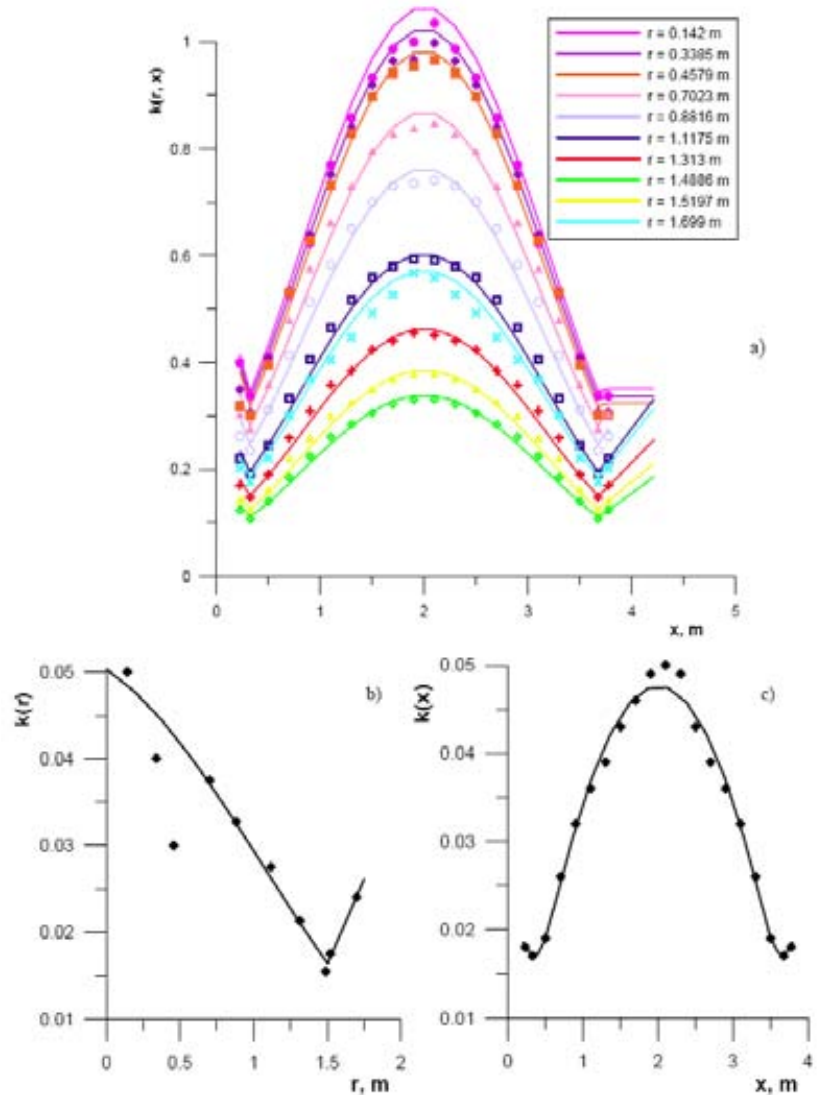

FIG. 6. 2 400 MWt MOSART core power distributions: comparison of calculated and approximated values of function $k(r, x)$: a — core, b — axial reflectors, c — radial reflector; symbols — calculated values, lines — approximated values, calculation of RRC-KI [2].

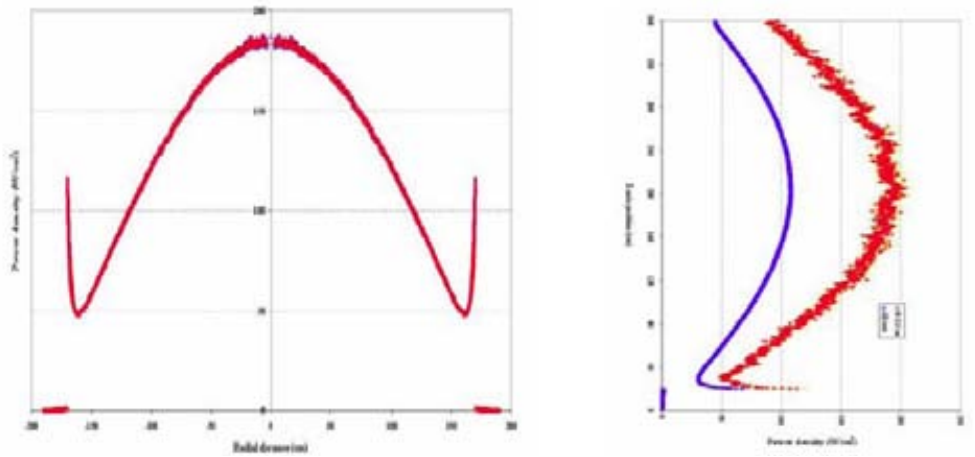

FIG. 7. MOSART power density distribution in w/cm3: radial (left) and axial (right) profiles in cm; calculation of SCK CEN by MCNPX JEFF3.1.

TRU transmutation efficiency:

$$K_G(t) = \frac{N_F^{TRU}(t)}{N^{TRU}(t)},$$

where $N^{TRU}(t)$ — full amount of loaded TRU nuclides during t period.

If we deal with the critical system loaded by only TRUs with relatively small transition to equilibrium time:

$$\frac{1}{K_G(T)} = 1 + \frac{M_E}{P} E_f \left(\frac{z}{\tau} + \frac{1}{T} \right),$$

where T — lifetime of the fuel loading, ME — equilibrium TRU loading, P — thermal power of the system, E_f — fission energy, $1/\tau_i$ – FP removal rate, z_i – losses to waste.

K_G aspires to maximal meaning for the systems with long lifetime T, minimal possible equilibrium specific loading (ME/P) and minimal losses to waste in fission products removal process (z/τ). The meanings of K_G determined by specific equilibrium loading (ME/P) for two types of 2 400 MWt MOSART loadings are given in the last line of Table 1 (for the case of actinides losses to waste stream in single pass $z=10^{-3}$). The K_G factor responsible for transmutation efficiency and equal 0.95 for the infinite in radial direction core loaded by scenario 1 is decreased for the case of 3D finite core down to 0.845.

9.4. Thermal hydraulics of core with reflectors

Two options were considered in the CRP studies by now: (1) the fuel salt enters into the core through a radial window of 0.5 meter height (as shown in Fig. 1) or (2) enters from the top into the peripheral salt annulus or 20 cm thick. In both cases, the salt leaves the core through a pipe (of 1 m diameter) of the top conic reflector (see Fig. 9a).

On the basis of 3D power distributions received at RRC-KI [2] from neutronics core calculations for 2400 MWt MOSART core with reflectors, the thermal hydraulics calculations are carried out. Calculations are executed by Russian commercial code Flow Vision [2]. The connected task was considered: core thermal hydraulics and process of thermal conductivity in reflectors. Calculations of the connected thermal hydraulics task (core with graphite reflectors, see Fig. 1) have allowed due to increase of height of a radial fuel salt inlet window from 0.1 up to 0.5 m and uses top conic reflector, instead of a flat one, to carry out alignment of core velocity distribution. However in the bottom part on periphery of core small recirculation area was still kept. Introduction of the distribution plate at core inlet with porosity of 32% has allowed: completely to remove recirculation areas of flow and to keep the maximal temperature of fuel salt to a level 1036 K, that only 48 K higher than average fuel salt temperature at core outlet (see Fig. 8). In Fig. 10 the longitudinal velocity change Vx along reactor height X for different radius R is also given. Pressure drop on the distribution plate has made 3.7 kPa. The temperature of a radial reflector has decreased down to 1087 K.

The temperature and velocity distributions for the second design option (computed at steady-state by employing the SIMMER [3] code) are shown in Fig. 9b, the temperature (from 752.15 to 1180.6 K) and velocity (3 m/s) scales being given. This flow profile was obtained after trying several distribution plate arrangements: to avoid stagnant regions and reverse flow; otherwise the maximum salt temperature could be appreciably higher than shown in Fig. 9b. As can see from Figs 8-10 optimized MOSART core configurations satisfy the two most important thermal hydraulic considerations: (1) the maximum temperature of solid reflectors is low enough to allow it use for suitable time and (2) regions of reverse or stagnant flow are avoided. It should be noted that for first option the maximal temperature of fuel salt is 150 K below compared to second one.

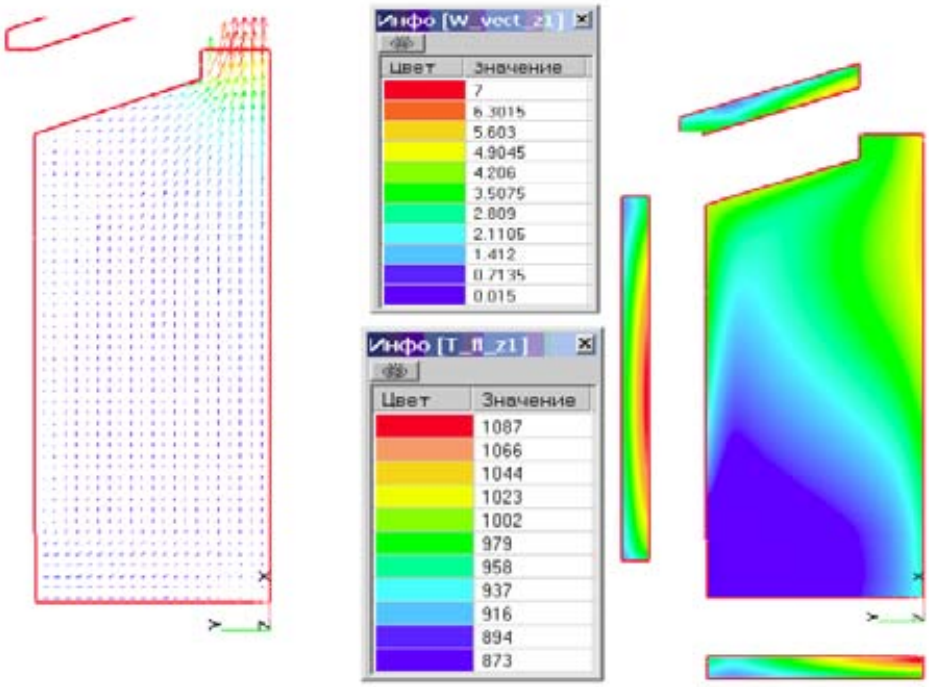

FIG. 8. Velocity (left, in m/s) and temperature (right, in K) distributions in longitudinal section for core with graphite reflector, H_{in}=0.5 m and inlet porous distribution plate) [2].

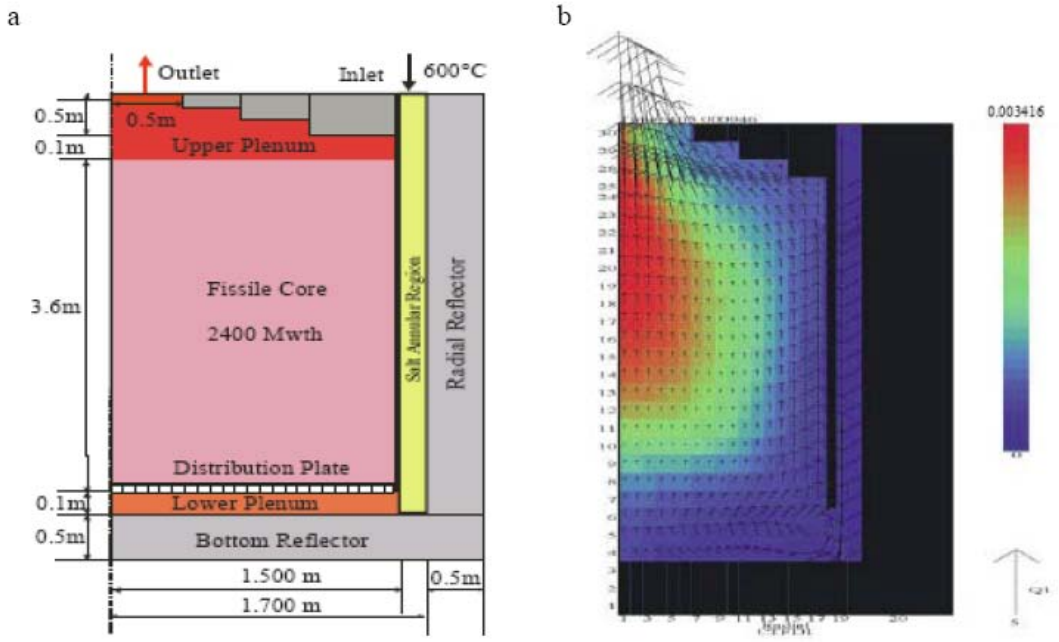

FIG. 9. Sectional view of MOSART geometric model for option 2 (a) and temperature & velocity distribution in the core (b) calculated by SIMMER-III.

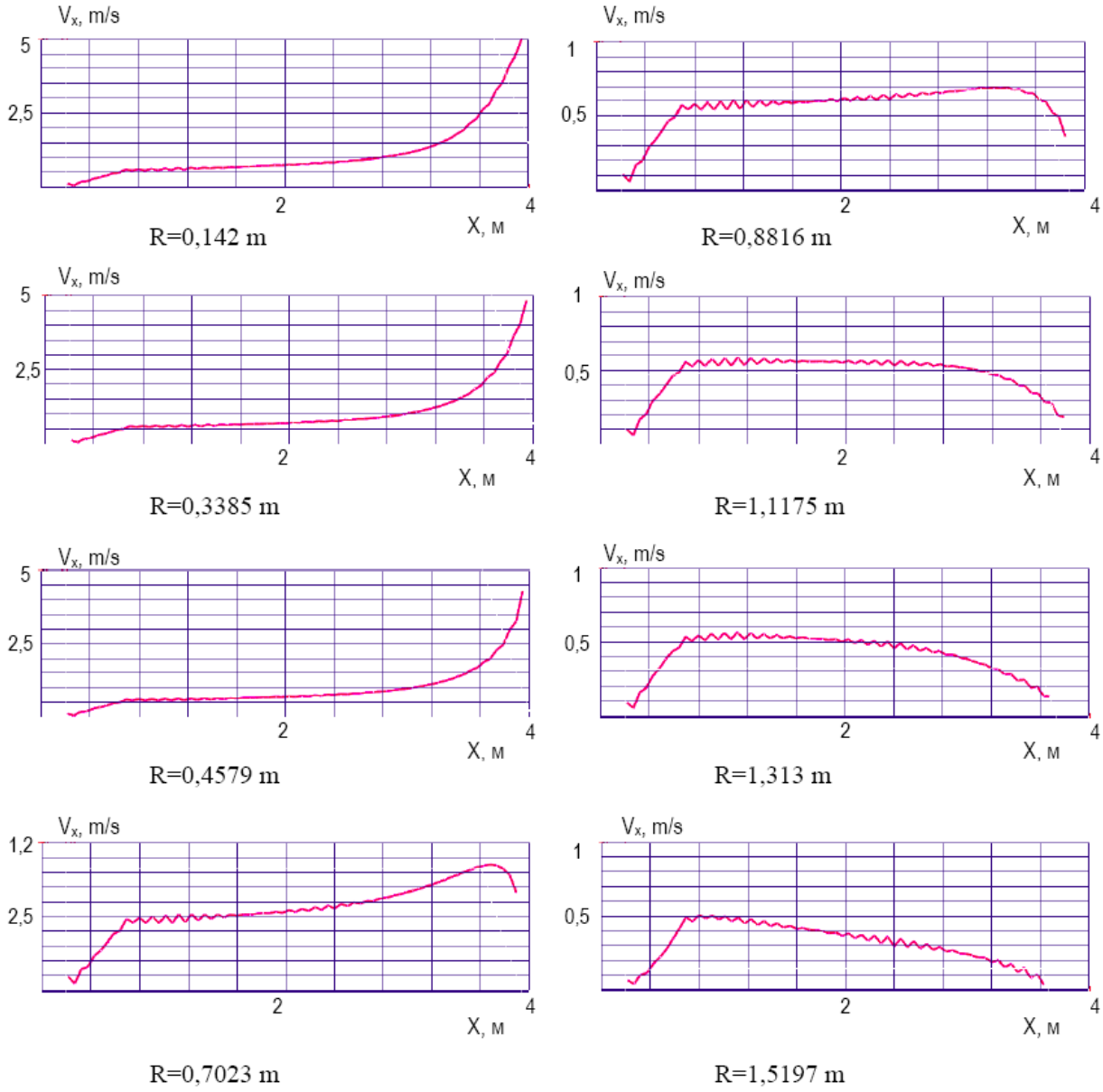

FIG. 10. Longitudinal velocity distributions Vx along core height X for different radius R, m/s.

9.5. Damage neutron fluence on the graphite reflector

Temperature distributions in graphite reflectors of MOSART core model (see Fig. 8), were used for specification of damage neutrons fluence on radial and axial reflectors. The following results by the MCNP code for damage neutrons with energy above 0.18 Mev fluxes on the core center were received by RRC-KI [2]:

Damage neutrons flux on a radial reflector — 1.30E+14 n/(cm^2 s);
Damage neutrons flux on axial reflector — 1.45E+14 n/(cm^2 s).

The temperature of graphite, according our results, is 960-1 100 K for the bottom axial reflector and 900-1100 K for a radial reflector (on the center of the core). In Fig. 11 damage neutrons critical fluences dependence from graphite temperatures, used for an estimation of the GR220/GR280 graphite lifetime at the Russian channel uranium — graphite reactor plant is resulted. According to data given in the Fig. 11 life-time for graphite reflector of MOSART core may be appreciated as 3.5-4.0 years.

Primary requirement for the MOSART concept is also to provide the lifetime expectancy of the reactor pressure vessel to the full 50-year plant lifetime. As noted above, between the reflector and reactor vessel, 30-50 cm width iron blocks with (1% of fuel salt) should be installed to reduce the damage flux arriving at surface of the 5 cm reactor vessel wall made of Ni based alloy Hastelloy NM. To minimize the reactor vessel wall temperature the 5 mm fuel salt annulus is assumed between iron blocks and reactor vessel. All these constructional features are supposed to be included in the calculation scheme on the stage of more detailed design.

Further specification of thermal hydraulics characteristics of core and reflectors may be received by use of two-temperature model of a porous body. Also it will be necessary to take into account reactor vessel protection required, by e.g. 30 cm width iron blocks with (1% of fuel salt) installed to reduce the damage flux arriving at surface of the 5 cm reactor vessel wall made of Ni based alloy Hastelloy NM. To minimize the reactor vessel wall temperature the 5 mm fuel salt annulus would be assumed between iron blocks and reactor vessel.

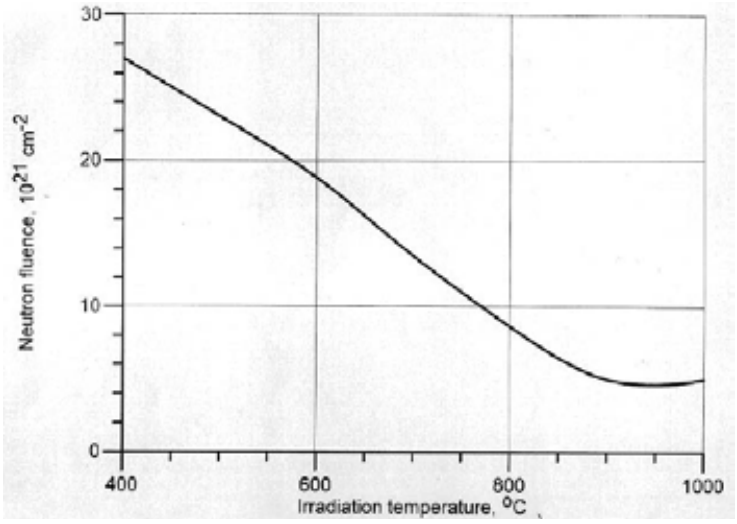

FIG. 11. Damage neutrons critical fluence vs. graphite temperature.

9.6. Effect of delayed neutron precursors movement at steady-state

The effect of the delayed precursor movement at steady state was evaluated at FZK and Polito. Different salt velocity profiles and different geometry models were employed. The velocity profile (together with the precursor distributions) was computed at FZK by SIMMER (see Fig. 9 b) for the 'top inlet' option as a result of a 100 s 'transient' simulation that brings an initially 'non-equilibrium' (determined by input code parameters for a 'coarse' geometry mesh) core reasonably close to steady-state conditions (the velocity profile as well as the reactor power varied significantly during this simulation). The velocity profile employed at Polito was computed at RRC-KI for the 'radial inlet' option (see Fig. 10). Both profiles show similar features: a higher salt velocity closer to the centre. An additional difference in modelling comes due to the geometry approximation applied at Polito: simulating the flow in the right cylinder leads to higher salt residence time in the core (ca. 8 s) compared to the FZK case (ca. 7 s). Since in both cases, the 'loop' time is similar (ca. 4 s), the relative fraction of the 'loop' time (during which the precursors decay being outside the core) compared to the total salt circulation time differs by ca. 9% in these two cases.

We assume that the effect of the precursor movement (relative variation of the effective fraction of delayed neutrons due to salt flow, β_{eff}-lost/β_{eff}-static) differs mainly due to the mentioned deviation in modelling. This effect is ca. 50% in the FZK case and 42% in the Polito case. These results are currently considered as preliminary and should be confirmed by future studies.

The computed 'movable precursor' effects in MOSART seem to be relatively strong compared to MSRE (ca. 33% according to the experiment). Note, that the residence times in the (1) MSRE core, (2) plena below/above the core and (3) in the loop are ca. (1) 8.2, (2) 4.3, and (3) 12.4 s. Thus the MSRE 'loop' time fraction is larger compared to the MOSART, but the effect in the MSRE is smaller. To get a deeper understanding of the situation, calculations with the flat velocity profile (similar to that one assumed in the MSRE case) were performed at Polito. Using the flat profile (instead of the 'real' one) reduced the 'movable precursor' effect to 33% (from 42%). This happened due to higher salt velocities (in the 'real' flow profile) in the center where the fission source is at maximum. Thus the 'effective' salt residence time in the core decreases when the 'real' non-flat MOSART velocity profile is employed. One should also consider effects of the axial shape of fission source in the MOSART and MSRE cores. Preliminary evaluations show that the MSRE one is more flat in average, thus increasing the 'effective' salt residence time and decreasing the 'movable precursor' effect. These evaluations should be confirmed in the future.

Since it appears that the effect of the motion of delayed neutron precursors is important for the physics of the system, the study of the coupling of fluid-dynamic models with the neutronic equations, in both steady-state and transient situations, is of particular relevance. Since the power generation affects the thermal and fluid-dynamic field a comprehensive description of the system would require the simultaneous solution of the neutronic equations coupled with the fluid-dynamic equations. As explained in the above, models usually employed solve the problem in a decoupled fashion, by imposing a velocity field in the streaming term appearing in the delayed neutron precursor balance equations. However, the coupling may play a very important role for the when dealing with the MOSART system. The usual assumption of a pure slug-flow condition may turn out to be totally inadequate.

It is therefore worth-while to assess the effect of fluid-dynamics on the neutronic behaviour. To that end, different velocity fields can be imposed and studied in a two-dimensional cylindrical reactor. The multigroup neutron diffusion equations are then solved in steady-state and transient conditions using the code DYNAMOSS, developed at Polito. The direct consequence on the effective delayed neutron fraction is particularly evident considering the Table 4. In the table a comparison of the values of the effective delayed neutron fractions is shown together with the reactivity reductions associated to various velocity fields. The usual slug-flow assumption, characterized by a flat radial velocity profile, is compare to a parabolic radial distribution and to a velocity field as computed by the RRC-KI (see Fig. 12).

The observation of the contour plots for the delayed neutron precursor distribution indicates the importance of different flow-regimes on the physical behaviour of the system, as can be seen in Fig. 13. The delayed neutron precursor family characterized by an about-average value of the decay constant is considered. The effect of the velocity field is immediately appreciable. Physical analysis clearly demonstrates the importance of fully modelling the MOSART system with a coupled neutronic and thermal hydraulic system of equations. The accurate solution of such system requires a quite significant computational effort and sophisticate numerical techniques. Some work is well under way to obtain results even with a few simplifying physical assumptions.

TABLE 4. EFFECT OF THE DELAYED NEUTRON PRECURSOR MOTION FOR VARIOUS VELOCITY FIELDS

Velocity fields	$\Delta\rho$ [pcm]	β_1 [pcm]	β_2 [pcm]	β_3 [pcm]	β_4 [pcm]	β_5 [pcm]	β_6 [pcm]	β_{tot} [pcm]	β_{loss} [pcm]
Solid fuel	0.0	7.8	77.2	54.9	118.1	61.0	20.8	339.8	0.0
Flat	-115.2	3.7	37.3	28.9	78.4	56.4	20.5	225.2	114.6
Parabolic	-131.8	3.6	36.4	27.1	69.3	53.0	20.1	209.5	130.3
RRC-KI data	-143.4	2.8	29.4	24.1	68.5	53.1	19.9	197.8	142.0

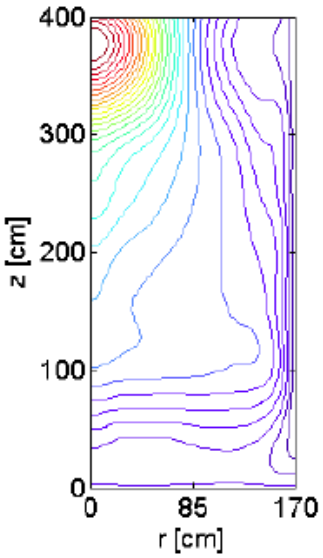

FIG. 12. Spatial velocity distribution as computed by RRC-KI.

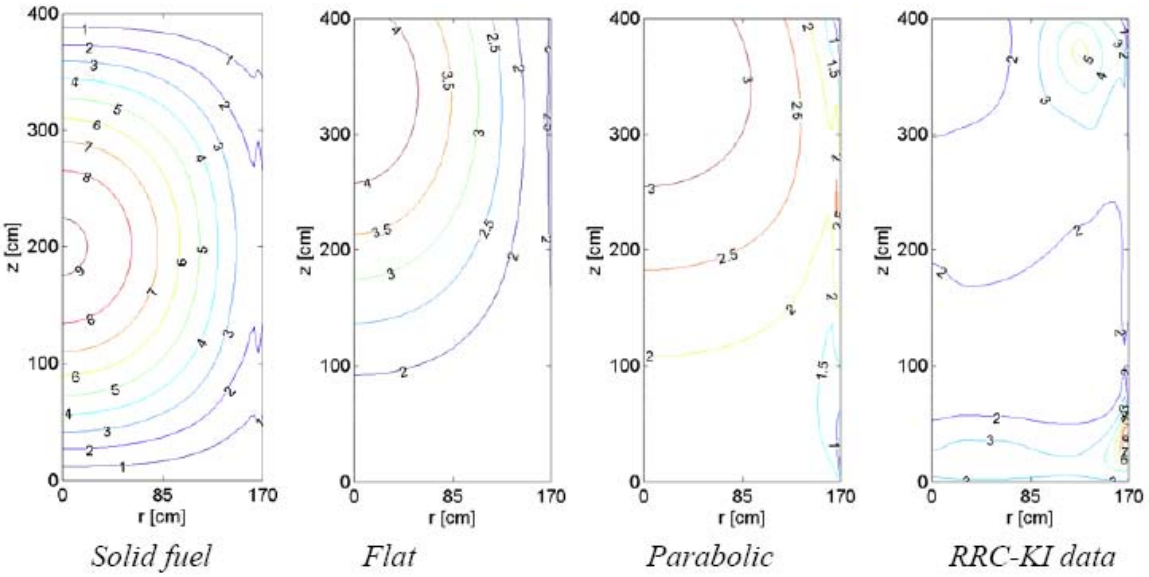

FIG. 13. Contour plots of the distribution of delayed neutron precursors for the third family.

9.7. Transient analysis

9.7.1. *Possible transient initiators for detailed analysis*

The general principles of nuclear safety in MSR are the as for all reactors. Small fluctuations in reactivity should produce only highly dumped power oscillations. Large, rapid increases in reactivity should be difficult to produce and be easily controlled before the resulting power excursions produce damaging temperature or pressure excursions. The continuous removal of fission products and the adjustment of fissile inventory in the fuel salt during operation of the MSR minimize amount of excess reactivity that must be compensated by control rods and hence limit the potential for rapid increases in reactivity associated with this excess.

— Change of the effective delayed neutron fraction due to the stopping and starting fuel circulation;
— Increase of the fissile materials concentration in the fuel;
— Changes in the fuel composition and density (voiding of fuel channels, changes in the gas fraction in the fuel and a primary circuit overcooling).

In all of these transients, we can assume that the xenon continuous extraction from the salt was ~100% efficient, so that no significant amount of xenon remains inside the fuel salt.

A unique consideration in fluid-fuel reactors is the possibility of inhomogenity of the fissile material in the circulating fuel. Specifically of concern is gradual segregation of fissile material outside the core, followed by rapid introduction with the incoming stream. The MSR fuel salt, is quite stable over a range of conditions much wider than the anticipated deviations. In Th-U MSR segregation of uranium could conceivably be produced by introduction of reducing agents or oxygen into the salt, but adequate protection against this should be provided in the MSR (e.g. gettering action of the ZrF_4 for H_2O major impurity). The principle components of MOSART fuel mixture do not form intermediate compounds with PuF_3. It is anticipated therefore that in concentrations at which PuF_3 would be used, it would not be deposited preferentially from the bulk salt during the inadvertent freezing, nor at locations such as in freeze valves.

MOSART operation would require routine additions of fresh fissile fuel in the amount of about 20 kg per week. Also, the fissile material in the processing systems amounts to about 1% of the reactor inventory. If these materials could be added to the reactor, the excess reactivity would be increased up to 500 pcm or even less. Furthermore, conceivable rates of introduction are quite inconsequential, and any unwanted reactivity increase from these sources can easily be stopped.

The response of the nuclear power to reactivity increases is governed by the temperature coefficients of reactivity and the action of the control rods and safety rods. Because the delayed neutron fraction will be unusually small in case of U-Th system and TRU transmuter, the MSR power responds rapidly to reactivity increases.

In MOSART core fluid fuel expansion due to a rise in temperature in the reactor core reduces not only fluid density, but also the amount of fissile material in the core thus reducing reactivity. The system without moderator offered the prospect therefore have being self-regulating and the reactor experiments that were operated showed that the classical control rod absorber system was not necessary.

9.7.2. *Transients analyzed for MOSART with the SIM-ADS code*

Four basic transients have been analysed with the SIM-ADS code in the MOSART concept for design option 1 [12]:

— An Unprotected Loss of Flow (ULOF), assuming loss of forced circulation in the primary system due to pump failure. The core inlet temperature is assumed to remain constant. The mass flow rate of the fuel salt is assumed to stabilize after 7 s at about 4% of its nominal value (natural convection);
— An Unprotected Loss of Heat Sink (ULOH) in which the heat sink is assumed to totally fail;
— An Unprotected primary circuit Overcooling transient, with the inlet temperature reduced by 100°C in 60 s;
— Several Unprotected Transients Over Power (UTOP) due to a +200 and a +500 pcm reactivity insertion. This transient is assumed initiated by a particle becoming dislodged from the walls of the loop (fissile fuel agglomeration due to precipitation); two different cases will be investigated. In one case, the particle is assumed to become lodged inside the core region (this case is somewhat hypothetical in the MOSART design since no surface areas inside the core region are foreseen aside of possible flow diverters and the reflector surfaces); the second case assumes that

the particle transits repeatedly the core region; the core inlet temperature is assumed to remain constant during all UTOP transients.

The transient initiators selected for detailed analyses are listed in Table 5. Also listed in the table are the underlying assumptions under which the specific transients were analyzed. The results of the Unprotected Loss of Flow (ULOF), Unprotected Loss of Heat Sink (ULOH, Overcooling Transient of the core, and the Unprotected Transient Over Power Transient (UTOP) are displayed in Figs 14 to 18.

For each transient two figures are provided. In the first figure, the dynamic response of the normalized thermal reactor power, neutron flux, and mass flow rate are displayed. In the second figure, the dynamic response of the molten salt core outlet -, average core -, core inlet -, and average bulk graphite — temperatures are shown.

9.7.2.1. MOSART ULOF Transient

For the ULOF transient, Fig. 14, the mass flow rate drops to the natural convection flow rate (about 4% of nominal flow is assumed) shortly after pump failure. Control rods are postulated not to insert into the core. The loss of flow rate in circulating fuel reactors implies an insertion of positive reactivity. In the case of MSBR, with β_{eff}-static = 340 pcm, this reactivity insertion due to the loss of fuel circulation is + 82.9 pcm (β_{loss} = -82.9 pcm), or +24.4%.

Both fuel average and fuel outlet temperatures are observed to rise rapidly to ~740°C and ~880°C respectively at about 50 s into the transient as a result of the fast decreasing mass flow rate. Since the temperature coefficient of the fuel is strongly negative, namely ~ -4.125 pcm/°C, sufficient negative reactivity is being inserted into the reactor to counterbalance the positive reactivity increase associated with the loss of fuel circulation. The net effect is a fast decrease in the power level to below 10% after 50 s into the transient.

TABLE 5. LIST OF TRANSIENTS ANALYZED

Number	Transient	Description
MOSART		
U - 1	ULOF	loss of forced circulations in primary and secondary system, core inlet temperature is assumed to remain constant
U - 2	ULOH	loss of heat sinks (HX failure)
U - 3	over-cooling of primary side	core temperature inlet drops by 100 C in 60 sec
U - 4a	UTOP	200 pcm jump in reactivity at HFP due to an acclomerated fissile particle that is assumed to remain lodged inside the core region, coolant inlet temperature will remain constant
U - 4b	UTOP	200 pcm jump in reactivity at HFP due to an acclomerated fissile particle that is assumed to repeatedly transit the core region, coolant inlet temperature will remain constant
U - 5a	UTOP	500 pcm jump in reactivity at HFP due to an acclomerated fissile particle that is assumed to remain lodged inside the core region, coolant temperature inlet will remain constant
U - 5b	UTOP	500 pcm jump in reactivity at HFP due to an acclomerated fissile particle that is assumed to repeatedly transit the core region, coolant inlet temperature will remain constant

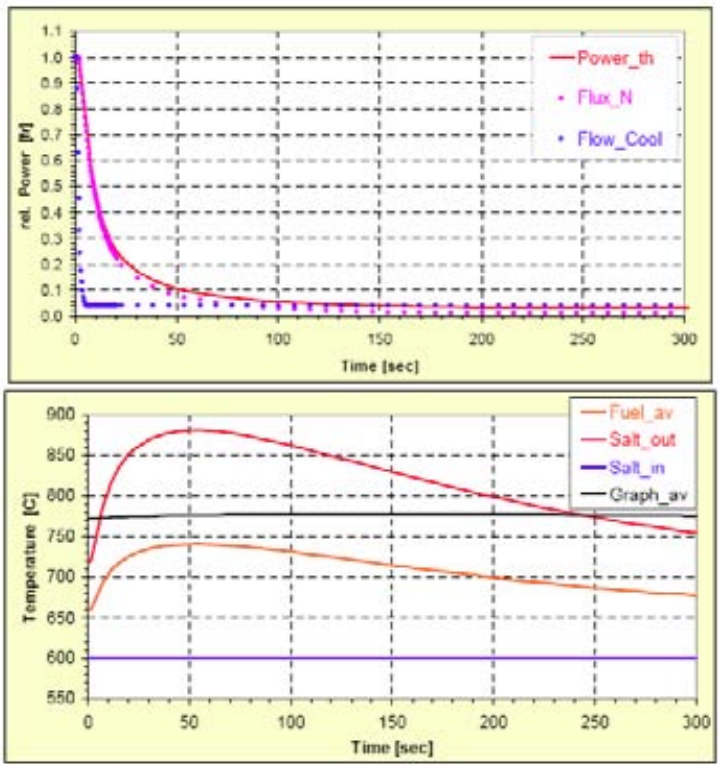

FIG. 14. Unprotected Loss of Flow (ULOF) for MOSART.

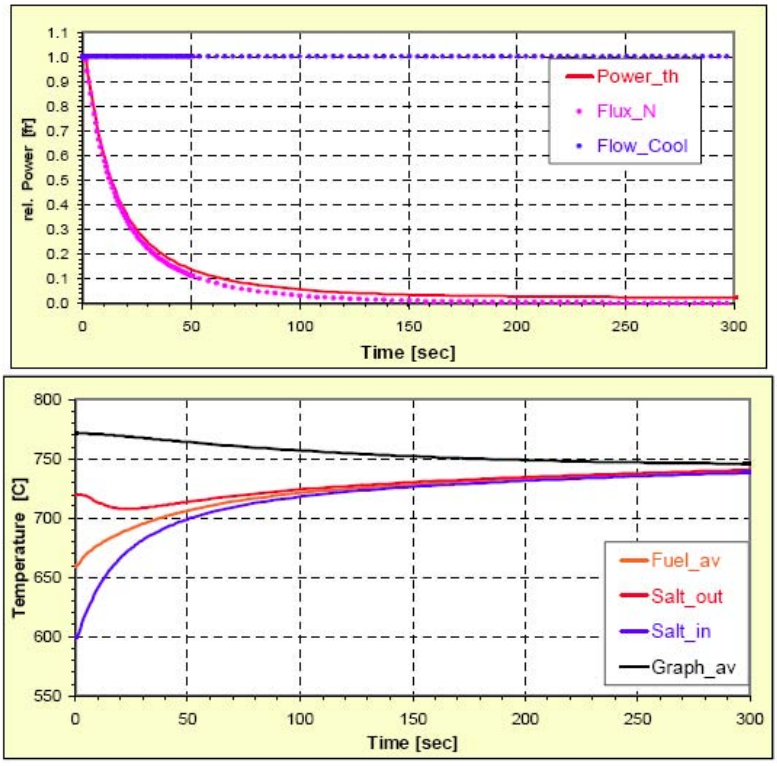

FIG. 15. Unprotected Loss of Heat Sink (ULOH) for MOSART.

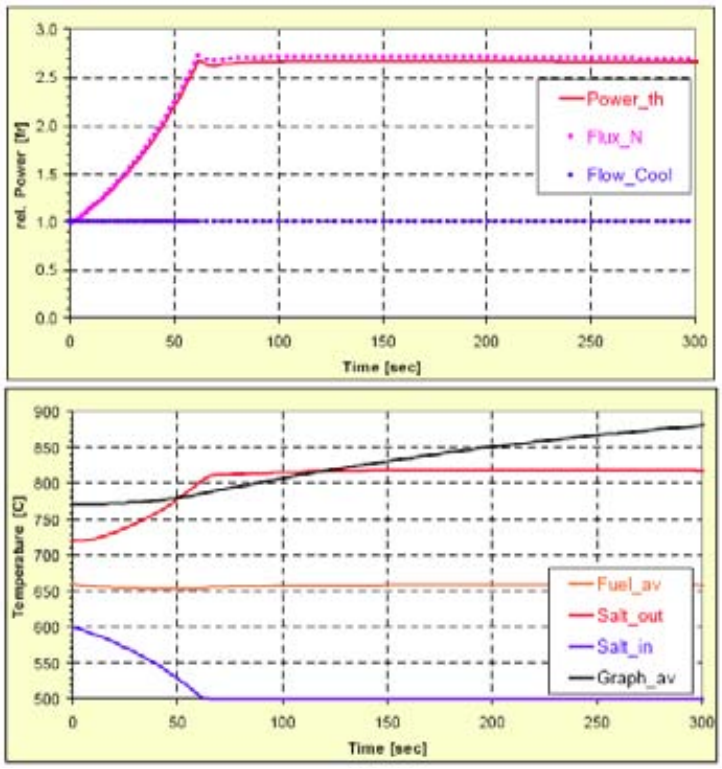

FIG. 16. Unprotected Over-Cooling Transient for MOSART.

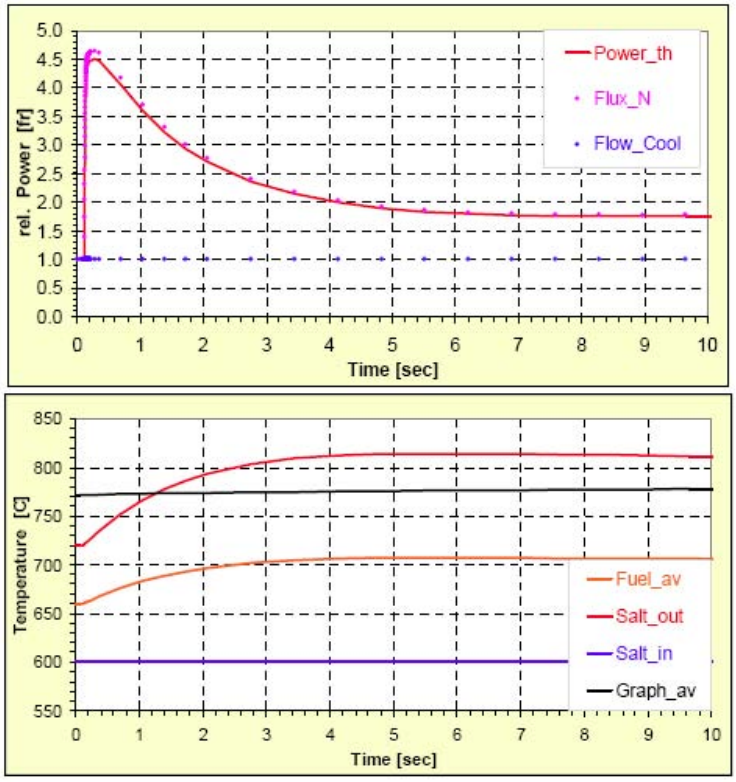

FIG. 17a. Unprotected Overpower Transient (UTOP + 200 pcm) for MOSART agglomerated fuel particle assumed to remain lodged inside core region.

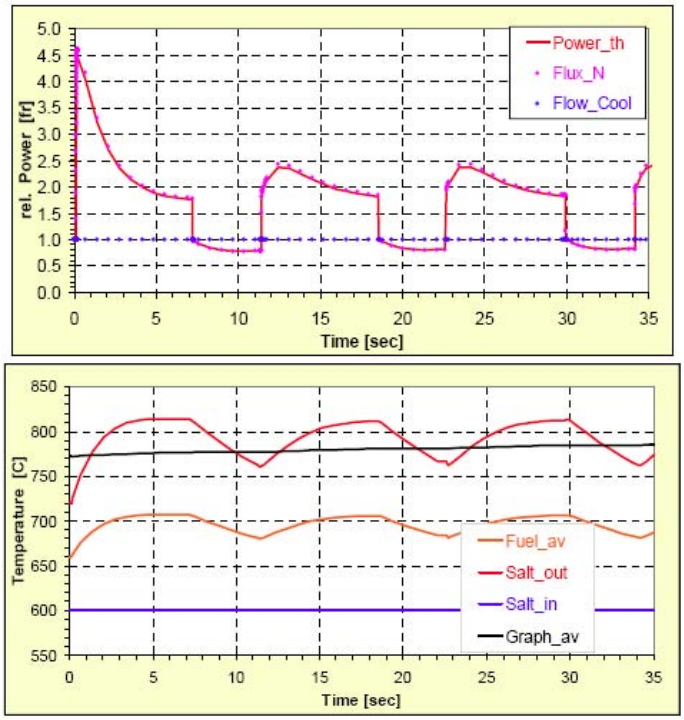

FIG. 17b. Unprotected Overpower Transient (UTOP + 200 pcm) for MOSART agglomerated fuel particle assumed to swept through core region.

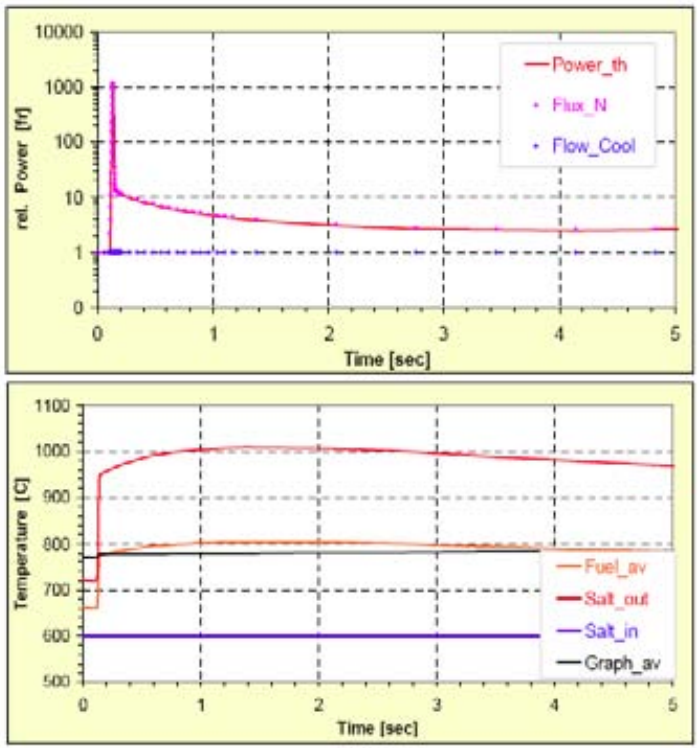

FIG. 18a. Unprotected Overpower Transient (UTOP + 500 pcm) for MOSART agglomerated fuel particle assumed to remain lodged inside core region.

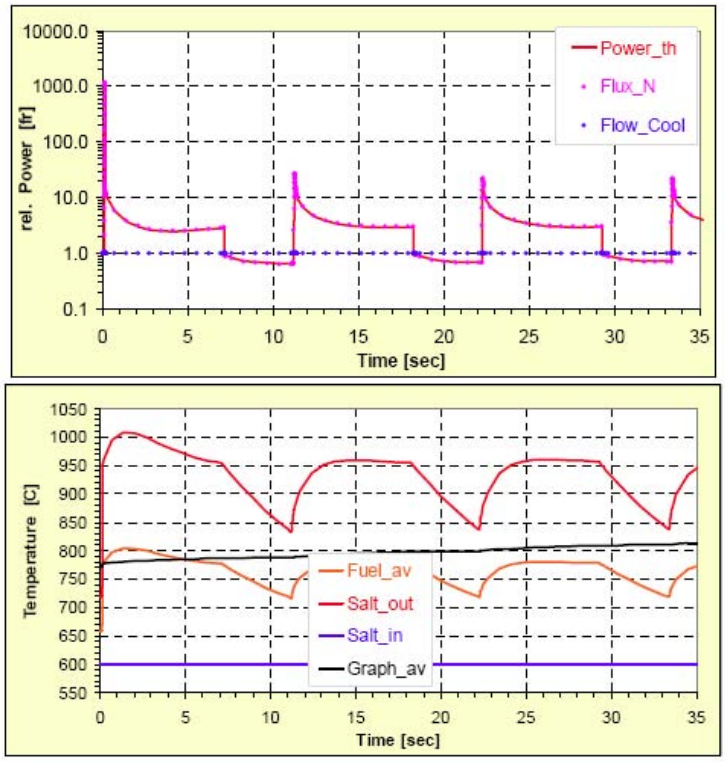

FIG. 18b. Unprotected Overpower Transient (UTOP + 500 pcm) for MOSART agglomerated fuel particle assumed to swept through core region.

Concurrent with the initial fast rise in the fuel temperatures is the relatively slow rise in the reflector graphite temperature. Due to the negative graphite reactivity coefficient of ~ -0.04 pcm/°C, another negative reactivity is now slowly inserted into the core. After 240 s into the transient, both outlet fuel temperature and bulk graphite temperature assume about the same value, namely 770°C. The net reactivity, i.e. the sum of the fuel and the graphite coefficient remains negative, namely ~ -4.165 pcm/°C. This assures a continued decrease in reactor power with a concurrent decrease of both fuel average and outlet temperatures after the peak temperatures 50 s into the transient have been reached.

Temperature exposure of the vessel and the outlet loop exceeding 850°C is observed to be limited in time to ~130 s. The system is expected not be seriously challenged by this transient since all temperatures will be below nominal temperatures after ~ 350 s after initiation of this transient.

9.7.2.2. MOSART ULOH transient

For the ULOH transient, Fig. 15, the heat transfer into the secondary system is assumed to fail at t = 0. Control rods are postulated not to insert into the core. The loss of heat sink implies the core inlet temperature will increase on account of lack of cooling via the heat exchangers. The only heat sink remaining will be radiation via the vessel surface to the reactor containment atmosphere. As can be observed in Fig. 15, the core inlet temperature will increase from 600°C to about 740°C within 300 s after transient initiation. As a result, the core average and outlet fuel temperatures will be at ~740°C within 150 s into the transient causing negative reactivity to be inserted into the core on account of the strongly negative fuel reactivity coefficient, namely ~ -4.125 pcm/°C. The net effect is a fast decrease in the power level to below 10% after 60 s into the transient. Since the power level continues to decrease, the core fuel temperatures do not rise above 750°C. As can be observe in Fig. 15, all fuel temperatures reach an asymptotic level of about 740°C in approx. 300 s into the transient. The graphite temperature gradually also decreases from 770 to 740°C.

9.7.2.3. MOSART Overcooling transient

In the case of the overcooling transient, Fig. 16, the decreasing core inlet temperature leads to a decrease in the average fuel temperature whereas the fuel outlet temperature increases from 720 to ~ 830°C. Since the reactivity coefficient of the fuel is negative, a positive reactivity is inserted into the reactor leading to a power rise of a factor 2.7 about 60 s into the transient. Due to the gradual increase in the temperature of the bulk graphite, additional negative reactivity is inserted into the core leading to a levelling off of the power level at a factor of 2.7. Correspondingly, the core outlet temperature remains constant at ~820°C. The mechanical integrity of the hot loop must now be carefully monitored on account of potential long-term exposure of vessel and loop components exceeding temperatures of 800°C unless rectifying countermeasures are activated at some reasonable time into this transient. The reactor design is however inherently stable under this transient condition.

9.7.2.4. MOSART UTOP transients

In the case of the unprotected overpower transient caused by an assumed agglomerated fissile fuel particle to become lodged inside the core region, Fig. 17a, the insertion of +200 pcm reactivity, or ~60 cents, leads to an initial power spike of factor 4.5. The correspondingly fast rise in average and outlet fuel temperatures add quickly negative reactivity into the core, reducing the power to a factor 1.8 at about 6 s into the transient. The slowly increasing graphite temperature inserts additional negative reactivity which will cause the power level to become stabilized. The core outlet temperature reaches about 820°C and stabilizes at ~810°C. These temperatures are only ~100°C above nominal conditions and no serious challenge to the mechanical integrity of the system is expected under these transient conditions assuming rectifying countermeasures are activated at some reasonable time into this transient (several minutes).

Unless power is reduced (by control rod shutdown or reduction of the fuel inlet temperature) some reasonable time after transient initiation (i.e. several minutes) in order to reduce fuel outlet temperatures, piping or vessel failure at the core outlet must be anticipated at some point into this transient.

In the case of the overpower transient caused by a fuel particle (+200 pcm) sweeping through the core region in ~7 s to return in another ~4 s (loop time) a cyclic power spiking will be observed (see Fig. 17b). The power spikes subsequent to the first power cycle (power factor ~4.5) are dampened (power factor ~2.4) because of the lower power level (below nominal) from which these power spikes are initiated (the drop in power below nominal after particle transit is due to elevated average fuel temperatures). Fuel outlet temperatures quickly rise to ~820°C within 1 s after the initiation of the transient, and decrease to ~760°C after the particle has left the core region. The fuel outlet temperature cycles between these limits during subsequent particle transits through the core region. These temperatures are only ~100°C above nominal conditions and no serious challenge to the integrity of the system is expected under these transient conditions.

In the case of the unprotected overpower transient caused by an assumed agglomerated fuel particle to become lodged inside the core region, Fig. 18a, the insertion of +500 pcm reactivity, or ~ +1.5$, leads to an sharp power spike of factor ~1000. The correspondingly fast rise in average and outlet fuel temperatures add quickly negative reactivity into the core, reducing the power to a factor ~3 at about 3 s into the transient. The slowly increasing graphite temperature inserts additional negative reactivity which will cause the power level to become stabilized. The core outlet temperature reaches a maximum of ~1010°C to decrease thereafter. These temperatures are ~300°C above nominal conditions presenting a possible challenge to the mechanical and structural integrity of the upper vessel and loop components. Since the time duration of these excessive temperatures is relatively short (several seconds) the system is not expected to fail catastrophically since rectifying countermeasures are assumed to be activated at some reasonable time into this transient (several tens of seconds).

In the case of the unprotected overpower transient caused by a +500 pcm fuel particle repeatedly sweeping through the core region in ~7 s to return in another ~4 s (loop time), a cyclic power spiking

(power factor ~1000) will be observed (see Fig. 18b). Again, the power spikes subsequent to the first power spike are dampened (power factor ~30) because of the lower power level (below nominal) from which these power spikes are initiated (the drop in power below nominal after particle transit is due to elevated average fuel temperatures). Maximum fuel outlet temperatures quickly rise to ~1010°C within 1 s after the initiation of the transient, and decrease to ~840°C after the particle has left the core region. In subsequent power cycles, the temperatures range from 960 to 840°C. These temperatures are ~300°C above nominal conditions presenting a possible challenge to the mechanical and structural integrity of the upper vessel and loop components. Rectifying countermeasures should be activated soon after initiation of this transient (several minutes) in order to assure long term structural integrity of the hotter parts of the systems. Short term catastrophic system failure is however not expected in this transient.

9.7.3. *Transient analyzed for MOSART with the SIMMER-III code*

The extension of neutronics module of SIMMER coupled with the thermal hydraulic part was applied by FZK for the transient calculations of an unprotected loss of flow (ULOF) in the MOSART concept (option 2) [13]. The RZ fluid-dynamics mesh is 20×30, the neutronics mesh is 60×90. The calculation was first performed with keeping the total fuel flow rate constant until the steady condition was obtained. Then, the ULOF was performed from the steady state (in this calculation the pump coast-down begins from t=105 s). Those pump coast-down data were taken from [14] (see Fig. 17). The pump coast-down begins immediately after t=105 s, and relative pump power goes to zero until t=125 s, then the calculation was continually performed until t=165 s.

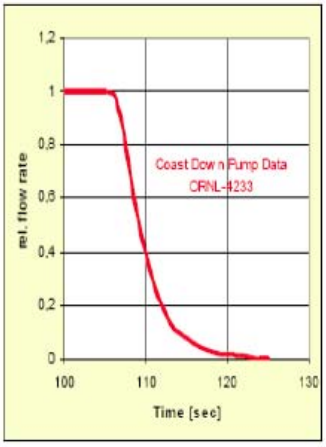

FIG. 19. Pump and fuel coast down transient [14]

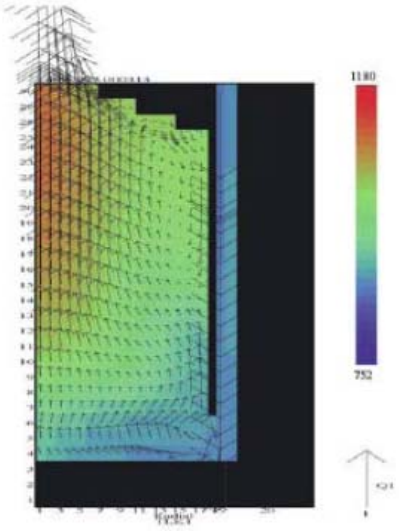

FIG. 20. 2D distribution of molten salt temperature at t=125s, velocity vector is 1 m/s.

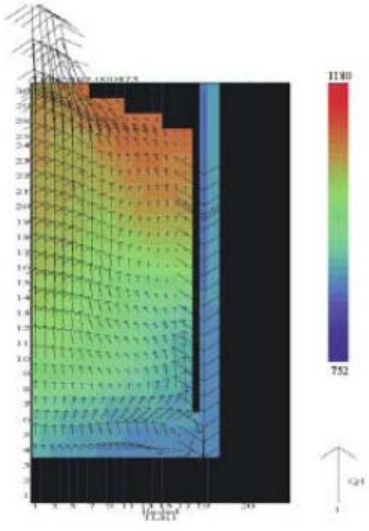

FIG. 21. 2D distribution of molten salt temperature at t=165s, velocity vector is 1 m/s.

Figures 9b, 18, and 19 give the evaluation of molten salt temperature and velocity distribution during the ULOF. Figure 8b shows the steady state at t=105 s. The maximal fuel temperature region is near the reactor axis and in the reactor midplane, and furthermore, the maximal molten salt temperature is about 1180 K. The salt temperature and velocity distribution at t=125 s is given in Figs 12 and 13 shows the salt temperature and velocity distribution at t=165 s. The highest liquid fuel temperatures can be observed in this upper-right corner region, where the precursor accumulates during the ULOF. Though there is no pump power to drive the liquid fuel, the fuel flows continually because of the natural convection.

9.8. Conclusions

1. In this domain main attention has been paid to single fluid Na,Li,Be/F MOSART system with design objective to provide safely the fissile concentration and geometry of the fuel salt to obtain heat release of about 2 400 MWt at conditions affording the effective transmutation of TRU's from UOX LWR spent fuel without U-Th support.

2. It is important from technical point of view that for molten Na,Li,Be/F system, was found quite wide range with minimal of LiF (17-15 mole%) and BeF_2 (25-27mole%) content in the ternary composition, which provide fuel salt able to get solubility of PuF_3 from 2 to 3 in mole% at 600°C, to keep adequate melting point (<500°C) and very low vapour pressure, to have good nuclear properties (neutron transparent salt), low activation, suitable transport properties, to be well compatible with the materials in the system and moderately expensive (about 25$ per kg).

3. 2400 MWt MOSART core of homogeneous configuration can satisfy most important neutronic and thermal–hydraulic considerations: (1) the AnF_3+LnF_3 concentration in fuel salt is truly within the solubility limit for molten ^{58}NaF-^{15}LiF-$^{27}BeF_2$ (mole%) at minimum fuel salt temperature in primary circuit of 600°C for fuel cycle scenario under consideration; (2) core with 0.2 m graphite reflector in the temperature range 900-1600 K has strong negative temperature reactivity coefficients (-4.125 pcm/K for the scenario of the equilibrium critical loading); (3) regions of reverse, stagnant or laminar flow are avoided and (4) the maximum temperature of solid reflectors is low enough to allow it use for suitable time.

4. Mass of TRU in primary circuit at equilibrium according MCNP calculation for scenario under consideration is 6280 kg. For this case the mass of TRU burned in MOSART core is 303 kg/GWt/a. TRU transmutation output of MOSART concept will be several times higher than that of the subcritical molten salt system or critical one with fertile materials. In the case of 100 years lifetime MOSART can provide TRU transmutation efficiency KG for the case of 3D finite core equal to 0.83. The proportion of 2 400 MWt MOSART units in a PWR nuclear fleet needed to burn its TRU production is less than 25%.

5. Several nuclear data libraries, codes, and computation models were employed to compute safety-related neutronics parameters for 2400MWt MOSART system. The results show that the parameters are favorable for reactor safety, mainly due to the strong density and fuel Doppler effect. The results are in principal agreement with respect to the major reactivity effects.

6. A simplified procedure — based on using few-group cross-sections obtained from the 172-group library by employing 1D spectra — was shown to be appropriate for reactivity effect and transient analyses in the considered reactor model.

7. 560-group deterministic and Monte-Carlo k_{eff} results are in excellent agreement (provided that the same nuclear data are employed) giving a higher confidence to the results. The influence of different nuclear data options on the k_{eff} values is quite strong. Comparison of different data sets revealed a strong contribution from data differences for Cm isotopes and light (^{9}Be, ^{19}F) elements, the latter being present in large quantities in the carrier salt.

8. Major kinetics parameters computed by different participants agree reasonably well taking into account data and modeling differences. Major contributions to β_{eff} come from ^{241}Pu (ca. 60%), ^{239}Pu (ca. 17%), ^{245}Cm (ca. 9%) and $Cm2^{47}$ (ca. 4%).

9. Preliminary evaluations of the effect of delayed precursor movement at steady-state show a relatively high reduction of the effective delayed neutron fraction (by ca. 40 to 50%). This effect (as well as the temperature distribution in the core) strongly depends upon the velocity profile that in its turn depends at upon the distribution plate design and may vary strongly during the transient. Additional effort should be paid to confirm the computed effect. The results of the transient calculations have mostly performed with the simplified models of the SIM-ADS code,

where these space-time effects are not included. The results have therefore to be regarded with some caution.

10. Any changes of pressure in MOSART reactor system will lead to helium bubbles fraction increasing and due to negative value of density reactivity coefficient to the inserting of negative reactivity.

11. Preliminary calculations of kinetic and dynamic characteristics of the MOSART system indicate that it would exhibit high levels of controllability and safety. System would also posses inherent dynamic stability and would require only modest amounts of reactivity control capability.

12. The transient study has shown that the MOSART design is an inherently stable reactor design on account of its large, negative fuel temperature coefficient (-4.125 pcm/°C) in combination with its negative graphite reflector reactivity coefficient (-0.04 pcm/°C). The MOSART reactor is expected not to be seriously challenged by the major, unprotected transients such as ULOF, ULOH, overcooling, or even UTOP. The system was shown to buffer reactivity insertion of up to +1.5$. System temperatures are expected to rise only ~300°C above nominal under such severe transient conditions. The mechanical and structural integrity of the system is not expected to be impaired assuming countermeasures are activitated within a reasonable time period after initiation of the 1.5$ UTOP transient (several minutes).

13. A full safety analysis of MOSART has not been performed because it would require a much more comprehensive design than is currently available.

14. Preliminary consideration of environment effects indicate that MOSART system could have attracted performance and TRU transmutation efficiency features while providing lower total materials inventories and waste compared to prior MSR designs, including MSBR (e.g. it allows significantly reduce to the order mass flows of graphite and ^{7}Li enriched of 99.99 % in the design).

15. While a substantial R&D effort would be required to commercialize MOSART, there are no killing unresolved issues in the needed technology. The major technical uncertainties in the conceptual design are in the area of tritium confinement, fuel salt processing and behavior of some fission products.

REFERENCES TO CHAPTER 9

[1] WEINBERG, A., et al., Collection of Papers on the Molten Salt Reactor Experiment, Nuc. App. Technol., Vol. 8 (1970).

[2] IGNATIEV, V., et al., Integrated Study of Molten Na,Li,Be/F Salts for LWR Waste Burning in Accelerator Driven and Critical Systems, paper presented in GLOBAL 2005, 9-13 October 2005, Tsukuba, Japan.

[3] MASCHEK, W., RINEISKI, A., SUZUKI, T., WANG, S., MORI, Mg., WIEGNER, E., WILHELM, D., KRETZSCHMAR, F., TOBITA, Y., YAMANO, H., FUJITA, S.,COSTE, P., PIGNY, S., HENRIQUES, A., CADIOU, T., MORITA, K., BANDINI, G., SIMMER-III and SIMMER-IV Safety Code Development for Reactors with Transmutation Capability, M&C 2005, 12-15 September 2005, Avignon, France.

[4] BRIESMEISTER, J.F., (ed.), MCNP-A General Monte Carlo N-Particle Transport Code, Version 4C, LA-13709-M, Los Alamos National Laboratory (2000).

[5] PELOWITZ, D.B., (ed.), MCNPX, VERSION 2.5.0, LA-UR-05-0369, LANL, USA (2005).

[6] VAN DER MARCK, S.C., KLEIN MEULEKAMP, R.., Calculating the Effective Delayed Neutron Fraction with Monte Carlo, Nucl. Sci. Eng., Vol. 152, 42 (2006).

[7] GREENE N. M., L. M. PETRIE, XSDRNPM: A One-dimensional Discrete-Ordinates Code for Transport Analysis, Oak Ridge National Laboratory, NUREG/CR-0200 Volume 2, Section F3 (March 2000).

[8] DULLA, S., RAVETTO, P., Interactions between Fluid-Dynamics and Neutronic Phenomena in the Physics of Molten-Salt Systems, Nuclear Science and Engineering, Vol. 155 (3) (2007).
[9] RINEISKI, A., et al., Kinetics and Cross-Section Developments for Analyses of Reactor Transmutation Concepts with SIMMER, paper presented in M&C 2005, 12-15 September 2005, Avignon, France.
[10] ALCOUFFE, R.E., et al., DANTSYS: A Diffusion Accelerated Neutral Particle Transport Code System, LA-12969-M (June1995).
[11] GOMIN, E.A., MAIOROV, L.V., The MCU Monte Carlo Code for 3-D Depletion Calculation, papaer presented in M&C 1999, Madrid, Spain (1999).
[12] SCHIKORR, M., Assessment of the Kinetic and Dynamic Transient Behavior of Sub-Critical Systems (ADS) in Comparison to Critical Reactor Systems, Nuclear Engineering and Design, Vol. 210 (2001) pp. 95-123.
[13] WANG, S., RINEISKI, A., MASCHEK, W., IGNATIEV, V., Transient analysis for molten salt transmutation reactor using the extended SIMMER-III code, paper presented in ICONE-14 International Conference on Nuclear Engineering, 17-20 July 2006, Miami, Florida, USA.
[14] PRINCE B. E., et al., Zero-Power Physics Experiments on the Molten Salt Reactor Experiment, ORNL-4233 (February 1968).
[15] UHLÍŘ J., SOUČEK, P., MODOLO, G., WALLE, E., NANNICINI, R., EC/EURATOM report of the FP5 project MOST, FIKWT-CT-2001-00096, 08/2003 MOST-D7F.
[16] PYROCHEMICAL SEPARATIONS IN NUCLEAR APPLICATIONS — A Status Report, OECD-NEA No. 5427, OECD (2004).
[17] IGNATIEV, V. et. al., Progress in Integrated Study of MOlten Salt Actinide Recycler & Transmuter System, paper presented in 9th OECD/NEA IEM on Partitioning & Transmutation, Nimes, France, September 2006.
[18] IGNATIEV, V., et. al., Experience with Alloys Compatibility with Fuel and Coolant Salts and their Application to MOlten Salt Actinide Recycler & Transmuter, paper presented in the ICAPP '06, Reno, NV USA, June 2006.
[19] ROBERTSON R, S., Conceptual design study of a single fluid molten salt breeder reactor, ORNL-4541, USA, June (1971).
[20] ENGEL, J.R. et. al., Conceptual design characteristics of DMSR with once-through fueling, ORNL/TM-7207, USA (1980).

CHAPTER 10. DOMAIN-VII: GAS COOLED HBRIDE (ADS) SYSTEM WITH FERTILE-FREE FUEL

10.1. Introduction

Partitioning and Transmutation (P&T) of nuclear waste has been proposed to reduce the amount of high-level waste inventory and the associated radiotoxicity inventory in the final repository. This can alleviate the burden on the final repository and improve public acceptance, contributing to ease nuclear waste management and help the sustainability of nuclear energy as a future energy source.

The objective of the full long lived nuclear waste transmutation is really meaningful only if the plutonium, which represents nearly 90% of the radiotoxic inventory in the open cycle, is also correctly managed. On the other hand, recycling of plutonium inevitably produces minor actinides, which decrease the potential benefits in mass and radiotoxicity that Pu management could bring.

In France, the law voted in 1991 on this issue, has generated much R&D on the subject. Different detailed comparisons of various modes of transmutation and waste management in different types of reactor have been investigated. In Germany, the investigation of nuclear waste incineration options is one of most important topics in the nuclear field. Other European countries also pay a significant attention to this topic.

To obtain the transmutation of actinides, we can consider two ways: the fission reaction where the nucleus is transformed in fission products (with short life of 50 years) or the capture reaction. In this last case, the nucleus is transformed in another nucleus without necessarily a significant reduction of the radiotoxicity and the minor actinide mass inventory. However, these isotopes generated can be also transmuted by fission or capture. To obtain an efficient transmutation, it is really necessary to prioritize the fission way. In this case, the examination of the cross sections underlines the advantage of the fast spectrum and the different studies carried out these last years have confirmed the interest using the fast spectrum with regard to the thermal spectrum to optimize the transmutation. In this context, two types of reactors can be used: the fast critical reactors and the sub-critical reactors dedicated to the transmutation (accelerator driven system, ADS or accelerator driven transmuter, ADT). An accelerator feeding a sub-critical core is a way to produce a neutron surplus, more or less expensive depending on the sub-criticality level that determines the fraction of the produced energy that is necessary to feed the accelerator. Sub-criticality is interesting from the safety viewpoint in the case of reactors containing large amounts of minor actinides and having poor reactivity coefficients. Waste (Am, Cm, Long lived fission product) can be concentrated in a ‘stratum’ of the fuel cycle disconnected from the part managing U, Pu. Studies, which were performed in the past for the PDS-XADS concept, are under process in Europe to optimize an ADS picture able to absorb the flow of minor actinides from the PWR fleet and to multirecycle them.

In this context, a gas cooled ADS core neutronics benchmark has been proposed by the Commissariat à l’Energie Atomique (CEA) and investigated in cooperation with FZK, NRG and SCK-CEN for an IAEA Coordinated Research Project (CRP) on Studies of Advanced Reactor Technology Options for Effective Incineration of Radioactive Waste. The benchmark is to help in clarifying the future issues associated to the improvement of the core designs with more reliable and accurate tools.

10.2. Benchmark description

The study of the He cooled ADT with dedicated Minor Actinide fuels has been performed in the past at CEA and demonstrated that the size of the 80MW(th) core (proposed for a MOX-fuelled ADS) is too small to achieve an acceptable transmutation rate. On the other hand, it has been shown that there is a good compromise between transmutation and core performances of the Helium cooled ADT for a core having a power between 200 and 400 MW(th). So in the framework of this CRP, the CEA proposed a benchmark on a 400 MW(th) gas-cooled ADT with fertile-free fuelled. The specifications of this benchmark are presented in this chapter. Table 1 presents the basic specification of the 400 MW(th) GC-ADT core for the neutronics benchmark. The GC-ADT core is a traditional concept with a fuel pin bundle with steel cladding roughened to enhance cooling with the coolant.

TABLE 1. ADT CHARACTERISTICS

Core Thermal Power	400MWth
Coolant	He
ΔT coolant	250°C
Input Temperature	200°C
Coolant pressure	60 bars
Pressure drop	0.5 bar
Proton beam	600 MeV
Fuel	(Pu, Np, Am, Cm)O_2
Matrix	MgO
Fuel/Matrix Volume Ratios	34/66
Clad	Steel
Fuel S/A residence time	1450 EFPD
Max. power per unit volume	94 W/cm^3
Average power per unit volume	44 W/cm^3
Pu/(Pu+AM) (weight%)	36.38%

The detailed data on conditions are described in Tables 2 and 3: temperature of each homogeneous region, the composition of the fresh fuel (corresponding to the He pressure of 60 bar). The geometrical description (2D RZ core geometry) is given in Fig. 1. The description of the source is given in Table 4.

TABLE 2. REGION-WISE TEMPERATURE DATA

Region	Temperature (°C)
Core [1]	993
Target [2]	325
Spn [3]	325

N of mesh points	ORDINATES, cm												
114	569,077	Void	Target	Target	Spn	Spn	Spn	Spn	Spn	Spn	Spn	Spn	Spn
83	413,234	Void	Target	Target	Core	Core	Core	Spn	Spn	Spn	Spn	Spn	Spn
76	378,044	Void	Target	Target	Core	Core	Core	Spn	Spn	Spn	Spn	Spn	Spn
69	342,854	Source	Target	Target	Core	Core	Core	Spn	Spn	Spn	Spn	Spn	Spn
62	307,664	Target	Target	Target	Core	Core	Core	Spn	Spn	Spn	Spn	Spn	Spn
55	272,473	Target	Target	Target	Core	Core	Core	Spn	Spn	Spn	Spn	Spn	Spn
48	237,283	Target	Target	Target	Spn	Spn	Spn	Spn	Spn	Spn	Spn	Spn	Spn
48	237,283	Target	Target	Target	Spn	Spn	Spn	Spn	Spn	Spn	Spn	Spn	Spn
1	0	Target	Target	Target	Spn	Spn	Spn	Spn	Spn	Spn	Spn	Spn	Spn
	ABSCISSAE,cm	0- 6, 355	16, 814	27, 701	63, 994	118, 655	131, 934	148, 203	166, 697	189, 334	190, 309	230, 480	247, 263
	N of mesh points	1- 2	4	6	13	24	27	30	34	39	40	48	51

Source: position in the target

FIG. 1. Geometrical description (operating conditions).

TABLE 3. SMEARED NUCLEAR DENSITIES FOR REACTOR COMPOSITIONS AT BOL

Nuclides	Core [1]	Target [2]	Spn [3]
Np-237	2.83748E-04		
Np-239	3.21250E-10		
Pu-238	4.83303E-05		
Pu-239	3.60774E-04		
Pu-240	2.82879E-04		
Pu-241	1.05878E-04		
Pu-242	1.20737E-04		
Am-241	7.24609E-04		
Am-242m	4.86855E-06		
Am-243	3.87889E-04		
Cm-242	1.86325E-08		
Cm-243	1.84719E-06		
Cm-244	1.73726E-04		
Cm-245	2.71601E-05		
Cm-246	2.38544E-06		
O	1.24180E-02		
Mg	7.41875E-03		
Fe-54	2.92058E-04	9.12351E-04	8.13117E-04
Fe-56	4.43568E-03	1.38565E-02	1.23493E-02
Fe-57	1.04118E-04	3.25251E-04	2.89875E-04
Fe-58	1.54185E-05	4.81654E-05	4.29266E-05
Cr-50	1.19626E-04	3.73697E-04	3.33051E-04
Cr-52	2.23562E-03	6.98378E-03	6.22418E-03
Cr-53	2.50064E-04	7.81165E-04	6.96200E-04
Cr-54	6.11684E-05	1.91082E-04	1.70298E-04
Ni-58	4.27441E-03	1.33527E-02	1.19003E-02
Ni-60	1.59597E-03	4.98558E-03	4.44332E-03
Ni-61	7.49757E-05	2.34214E-04	2.08739E-04
Ni-62	2.16002E-04	6.74760E-04	6.01369E-04
Ni-64	6.63171E-05	2.07166E-04	1.84633E-04
Mo	2.80231E-04	8.75402E-04	7.80187E-04
Ti	2.28123E-04	7.12626E-04	6.35116E-04
Cu	3.93239E-05	1.22843E-04	1.09481E-04
Si	8.97449E-05	2.80351E-04	2.49858E-04
Mn	3.05867E-05	9.55487E-05	8.51561E-05
He-4	8.15259E-05	3.86463E-05	7.64723E-05
Pb		2.51939E-03	
Bi-209		3.05397E-03	

Unit E24/cm3

TABLE 4. SOURCE CHARACTERISTICS

Group Number	Upper Energy (eV)	Source (n. s^{-1}. cm^{-3})
1	1.96E+07	5.91E+17
2	1.00E+07	6.04E+17
3	6.07E+06	9.44E+17
4	3.68E+06	1.25E+18
5	2.23E+06	1.25E+18
6	1.35E+06	9.95E+17
7	8.21E+05	6.59E+17
8	4.98E+05	4.00E+17
9	3.02E+05	2.31E+17
10	1.83E+05	1.30E+17
11	1.11E+05	7.25E+16
12	6.74E+04	4.02E+16
13	4.09E+04	2.22E+16
14	2.48E+04	1.24E+16
15	1.50E+04	6.90E+15
16	9.12E+03	3.76E+15
17	5.53E+03	1.97E+15
18	3.35E+03	9.60E+14
19	2.03E+03	4.52E+14
20	1.23E+03	2.04E+14
21	7.49E+02	1.03E+14
22	4.54E+02	3.58E+13
23	3.04E+02	2.95E+13
24	1.49E+02	8.78E+12
25	9.17E+01	2.08E+12
26	6.79E+01	3.51E+12
27	4.02E+01	1.44E+12
28	2.26E+01	3.19E+11
29	1.37E+01	3.19E+11
30	8.32E+00	7.98E+11
31	4.00E+00	1.60E+11
32	5.40E-01	0.00E+00
33	1.00E-01	0.00E+00
	1.10E-04	

The calculation items are listed below and to be calculated at BOL and EOL for a single batch of 1450 Equivalent Full Power Days (EFPD) simulating a 3-batch cycle scheme of 1 450 (≈3×483) EFPD:

— Criticality (effective multiplication factor);
— Kinetic parameter (β_{eff});
— Current (A) for a power set to 400 MW(th) with.

$$I(A) = \frac{P \times q \times \left(1 - k_{eff}\right) \times \nu}{\varphi^{*} \times E_{f} \times k_{eff} \times Z}$$

P: Thermal power (in W(th)),
φ*: importance of the source,
q: proton charge (=1.6×10-19°C),
E_f : energy release per fission (3.2×10-11 J),
k_{eff}: effective multiplication factor without the source,
ν: number of neutrons produced per fission (2.9),
Z: number of neutrons produced by spallation (about 14 for a Pb-Bi target hit by a 600 MeV proton).

— Transmutation Rate (kg/TW•h/th) for neptunium, americium, curium, plutonium isotopic vectors for discharged Pu, Am, Cm and mass balance;
— Reactivity insertions:
  (i) Temperature effect, calculated between T_fuel = 993°C and T_fuel = 180°C (in fact, this correspond at the change between cold and hot state of the core; note that media being described as homogeneous, all elements should be considered at the same fuel temperature);

Coolant depressurization reactivity (He density = 3.057×10E-06 at 1024/cm^3; for a 1 bar pressure with only core zones depressurized);

  (ii) Core compaction;
  (iii) In this case, the size of the core is reduced with a new R_{ext}=131.60867 cm instead of R_{ext}=131.93492 cm (see Fig. 1). The new homogeneous compositions data for the core is described in the Table 5.

TABLE 5. CORE COMPACTION: NEW CORE COMPOSITIONS DATA AT BOL

Nuclides	Core [1]
Np-237	2.85219E-04
Np-239	3.22917E-10
Pu-238	4.85810E-05
Pu-239	3.62645E-04
Pu-240	2.84346E-04
Pu-241	1.06427E-04
Pu-242	1.21363E-04
Am-241	7.28367E-04
Am-242m	4.89380E-06
Am-243	3.89901E-04
Cm-242	1.87292E-08
Cm-243	1.85677E-06
Cm-244	1.74627E-04
Cm-245	2.73010E-05
Cm-246	2.39782E-06
O	1.24824E-02
Mg	7.45723E-03
Fe-54	2.93573E-04
Fe-56	4.45869E-03
Fe-57	1.04658E-04
Fe-58	1.54985E-05
Cr-50	1.20247E-04
Cr-52	2.24722E-03
Cr-53	2.51361E-04
Cr-54	6.14856E-05
Ni-58	4.29658E-03
Ni-60	1.60424E-03
Ni-61	7.53646E-05
Ni-62	2.17122E-04
Ni-64	6.66611E-05
Mo	2.81684E-04
Ti	2.29307E-04
Cu	3.95279E-05
Si	9.02104E-05
Mn	3.07453E-05
He-4	8.15259E-05

Unit E24/cm3

TABLE 6. RESULTS

	BOL (0 EFPD)	EOL (1450 EFPD)
Reactivity, k_{eff}	Yes	Yes
Kinetics parameter, β_{eff} (pcm)	Yes	No
Current (mA)	Yes	No
Reactivity insertions		
- Fuel temperature effect, $\Delta\rho_{doppler}$ (pcm)	Yes	Yes
- Coolant depressurization, $\Delta\rho_{coolant}$ (pcm)	Yes	Yes
- Core compaction (pcm)	Yes	No
Mass balance		
- M_U (kg)	Yes	Yes
- M_{Pu}(kg)	Yes	Yes
- M_{Np} (kg)	Yes	Yes
- M_{Am} (kg)	Yes	Yes
- M_{Cm} (kg)	Yes	Yes
Isotopic vector: N_i/N_{tot} (%)		
- Pu8/Pu9/Pu0/Pu2 (%)		Yes
- Am1/Am2m/Am3 (%)		Yes
- Cm2/Cm3/Cm4/Cm 5/Cm6 (%)		Yes
Transmutation rate		
- ΔM_U (kg/TW•h/th)		
- ΔM_{Pu} (kg/TW•h/th)		
- ΔM_{Np} (kg/TW•h/th)		
- ΔM_{Am} (kg/TW•h/th)		
- ΔM_{Cm} (kg/TW•h/th)		

10.3. Participants, codes and data used

10.3.1. *Participants*

Four participants provided results for this benchmark by using several combinations of Monte-Carlo and deterministic codes with four data libraries (JEF2.2, JEFF3.1, JENDL3.3, ENDF/B-VI). The complete list of combinations of codes and libraries employed by different benchmark participants is given in Table 7.

1) Commissariat à l'Energie Atomique, CEA, Cadarache (France)
Participants: C. Chabert, Y. Peneliau, G. Rimpault, D. Plisson-Rieunier, J. Tommasi
Codes: ERANOS2.0, TRIPOLI4, MCNP4C
Nuclear Data: JEF2.2, JEFF3.1

2) Nuclear Research and Consultancy Group, NRG, Petten (Netherlands)
Participant: D. Da Cruz
Codes: OCTOPUS (MCNP4C3-FISPACT)
Nuclear Data: JEF2.2, JEFF3.1, JENDL-3.3, ENDF/B-VI.8

3) Belgian Nuclear Research Center, SCK CEN, Mol (Belgium)
Participant: E. Malambu
Codes: MCNPX.2.5.0
Nuclear Data: JEF2.2, JEFF3.1

4) Forschungszentrum Karlsruhe, Germany
Participant: A. Rineiski
Codes: C^4P-ZMIX-DANTSYS-TRAIN
Nuclear Data: JEF2.2, JENDL3.3

TABLE 7. COMBINATIONS OF CODES AND LIBRARIES OF THE DIFFERENT SOLUTIONS

	JEF2.2	JEFF3.1	JENDL3.3	ENDF/B-VI.8
	Deterministic Codes			
ERANOS2.0	CEA	CEA		
C^4P-ZMIX-DANTSYS-TRAIN	FZK		FZK	
	Monte-Carlo Codes			
TRIPOLI4	CEA (Bi209: ENDF/B-VI.4)	CEA		
MCNP4C MCNP4C-FISPACT	CEA NRG	CEA NRG	NRG	NRG
MCNPX.2.5.0	SCK	SCK		

10.3.2. *ERANOS code*

ERANOS is a system of neutron and gamma-transport codes developed by CEA [1]. Fast reactor core, shielding and fuel cycle calculations can be performed with this code system. ERANOS is a deterministic code, so neutron physics calculations are performed in two steps: at the cell/lattice level and at the core level.

The cell/lattice code ECCO is fed by libraries that are in a direct access format in various energy meshes: 1968 groups (all-purpose), 175 groups (shielding purposes), the 172-group XMAS scheme (refined in the low energy range), and 33 groups (energy mesh generally used for core calculations). Four sets of libraries can be used: JEF2.2, ERALIB1 (obtained from the JEF2.2 libraries by a statistical fitting on integral experiments), JEFF3.1 and ENDF/B-VI.8.

The ECCO code takes into account resonance self-shielding effects on multigroup neutron cross-sections by using the sub-group method and computing, with a collision probability method, a fine-group solution of the transport integral equation. The cross-sections can be condensed and homogenized. The resulting broad-group cross sections, corresponding to an equivalent homogeneous cell, can then be used in core calculations.

The core calculations carried out by ERANOS, include reactivity, flux, spatial power distribution, reactivity coefficients, burnup and control rod worth. Moreover, for very different applications, traditional, generalized and harmonics perturbation modules are available.

10.3.3. *C4P, ZMIX, DANTSYS and TRAIN codes*

FZK employed four code/data systems for this benchmark. C^4P [2] is an FZK code and data system that manages nuclear data libraries in the CCCC format (resonance self-shielding is taken into account by the f-factor method). The master C^4P library contains data for 560 energy groups (in the energy range below 20 MeV). C^4P can condense these libraries into smaller ones. 172-group libraries were produced from the 560-group ones (JEF2.2 and JENDL3.3) and used for this study.

ZMIX [3] is an FZK code that computes composition dependent cross-sections from data libraries generated by C4P. The cross-sections are computed for the same or lower number of energy groups, in the latter case ZMIX employs computed spectra for each homogeneous media and employs them for condensation of cross-sections. The 33-group cross-sections were computed by ZMIX and used in DANTSYS and TRAIN for this benchmark.

DANTSYS [4] is an Sn transport code developed at LANL. We employed a 2D capability of DANTSYS (TWODANT). One should mention that ERANOS includes 2D Sn transport model, BISTRO, that is similar to TWODANT in many respects.

TRAIN [5] is an FZK code for burnup analyses. It employs fluxes computed by DANTSYS, multigroup cross-sections produced by ZMIX and data from JEFF3.1 activation, decay and fission product yield files. Thus, the branching ratios are assumed to be energy-dependent as they are computed from JEFF3.1 activation file.

In the following C^4P and ZMIX will not be mentioned (as they are always employed for preparing the cross-sections for DANTSYS and TRAIN): we will mention DANTSYS (if C^4P, ZMIX and DANTSYS are employed) or DANTSYS-TRAIN (if TRAIN is employed in addition).

10.3.4. *TRIPOLI4 code*

TRIPOLI4 is a computer code simulating the 3D transport of neutrons, photons, electrons and positrons with the Monte-Carlo method [6]. The code has been validated through several hundred benchmarks as well as measurement campaigns and is used by the French nuclear industry.

TRIPOLI is directly compatible with point-wise cross-sections produced by the NJOY processing code system. It may also be run with homogenized multigroup cross-sections and multigroup cross-sections with probability tables.

It computes the following quantities: flux, current, reaction rates, dose equivalent rates, deposit of energy, recoil energy and multiplication factor. The associated types of estimator are collision, track length, surface and point detectors.

The geometry may be described by predefined shapes combination and/or surface equations. Complex lattices and lattices of lattices are available. The source description is factorized in space, energy, direction and time, providing the user with an extended choice through tabulated or analytical laws. The code has perturbation estimation capabilities (concentration, density), using the correlated sampling technique.

10.3.5. *OCTOPUS code system*

All the calculations have been performed with the NRG's code system OCTOPUS [7, 8], a modular system that permits the coupling of several spectrum and burnup codes. The exchange of data between the codes is accomplished by means of the so-called binary interface files. The structure of this code system is flexible enough to allow the coupling of other type of codes as well, like uncertainty analysis codes, or codes for generation of nuclear databases required for full core reactor simulation. For this study MCNP4C3 [9, 10] has been used (as spectrum code) in combination of FISPACT [11] (as burnup code). For each burnup step, the flux distribution is calculated using MCNP, and in a separate OCTOPUS module the cross sections for each active isotope (taken from the MCNP point cross section library) are collapsed to few-group cross sections using the spectrum in each burnup zone. For each burnup zone a separate FISPACT run computes the new isotopic composition using these few-group cross sections. The flux to be used by FISPACT is calculated before each burnup step from the total reactor power, the isotopic composition of each burnup zone, the flux distribution, and the energy released per fission and capture for each nuclide. The same normalization factor is also applied to scale the flux and energy production tallies produced by MCNP. In this study the nuclear data for all actinides and fission products are from JEFF-3.1 evaluated nuclear data file, except for the fission yield data and cross section data, which has not been used in the transport process in MCNP and taken from the JEF2.2 nuclear data file.

10.3.6. *MCNPX code*

MCNPX is a general-purpose Monte-Carlo radiation transport code for modeling the interaction of radiation with matter. MCNPX stands for Monte-Carlo N-particle extended. It extends the capabilities of MCNP4C3 [10] to nearly all particle types, to nearly all energies, and to nearly all applications without additional computational time penalty. MCNPX is fully three-dimensional and time dependent. It utilizes the latest nuclear cross section libraries and uses physics models for particle

types and energies where tabular data are not available. Applications range from outer space (the discovery of water on Mars) to deep underground (where radiation is used to search for oil). MCNPX is used for nuclear medicine, nuclear safeguards, accelerator applications, nuclear criticality and much more.

10.4. Calculation results

10.4.1. *Core reactivity (k_{eff}) results*

The results along with the computational tools are displayed in Table 9. Concerning the deterministic codes, the method/approximations used are summarized in Table 8.

TABLE 8. METHOD USED IN DETERMINISTIC CODES

	ERANOS	DANTSYS
Transport options	P0 S4 inconsistent	P3 S8
Group cell calculation	1968 groups	172 groups
Group core calculation	33 groups	33 groups

TABLE 9. RESULTS FOR THE REACTIVITY AT BOL BY PARTICIPANT

	Code	JEF2.2	JEFF3.1	ENDF/B-VI.8	JENDL3.3
	Deterministic				
CEA	ERANOS	0,96533	0,99315	-	-
FZK	DANTSYS	0,98390	-	-	0,98544
	Monte-Carlo				
NRG	MCNP	0,98253 ± 0,00013	0,99731 ± 0,00018	1,01935 ± 0,00016	0,98995 ± 0,00012
SCK	MCNPX	0,98398 ± 0,00016	0,99689 ± 0,00011	-	-
CEA	TRIPOLI4	0,98233 ± 0,00076	0,99847 ± 0,00079 (T=300K)	-	-

The most of results are obtained using the European JEF2.2 and JEFF3.1 libraries. First, we can notice a good agreement between the different Monte-Carlo calculations performed by NRG, SCK and CEA. The Monte-Carlo TRIPOLI4 code developed by CEA gives results consistent with those of MCNP. A sensitivity study was made by NRG (with MCNP): to explain the origin of the discrepancies between JEF2.2 and JEFF3.1 on the initial reactivity (Table 10) and also between JEF2.2 and ENDF/B-VI.8 (Table 11).

TABLE 10. DISCREPANCIES BETWEEN JEF2.2 AND JEFF3.1 — SENSITIVITY STUDY WITH MCNP

	Δk (pcm)
All JEFF3.1	-
JEFF3.1 with only Np from JEF2.2	-276
JEFF3.1 with only Pu from JEF2.2	-988
JEFF3.1 with only Am from JEF2.2	-1084
JEFF3.1 with only Cm from JEF2.2	402
JEFF3.1 with only MgO from JEF2.2	740
JEFF3.1 with only structure+He+LBE from JEF2.2	-580
All JEF2.2	-1690

TABLE 11. DISCREPANCIES BETWEEN JEF2.2 AND ENDF/B-VI.8 — SENSITIVE STUDY WITH MCNP

	Δk (pcm)
All JEF2.2	-
JEF2.2 with only Np from ENDF/B-VI.8	537
JEF2.2 with only Np, Pu from ENDF/B-VI.8	710
JEF2.2 with only Np, Pu, Am from ENDF/B-VI.8	3248
JEF2.2 with only Np, Pu, Am, Cm, MgO from ENDF/B-VI.8	3616
JEF2.2 with only Am241 from ENDF/B-VI.8	1742
JEF2.2 with only Am242m from ENDF/B-VI.8	279
JEF2.2 with only Am243 from ENDF/B-VI.8	630
All ENDF/B-VI.8	3682

A large reactivity effect (-1084 pcm) is due to different Am data in JEF2.2 and JEFF3.1. A large effect is also observed between JEF2.2 and ENDF/B-VI.8 because of these data. Deviations in Pu data have also an impact on the reactivity (-988 pcm between JEF2.2 and JEFF3.1). A reactivity of 740 pcm is due to the change in Mg nuclear data from JEF2.2 and JEFF3.1.

In fact, in the JEF2.2 library, includes only the cross sections for the Mg natural element, while the ^{24}Mg, ^{25}Mg and ^{26}Mg cross section are available in JEFF3.1. Interesting values also presented by NRG to illustrate the reactivity discrepancies between JEF2.2 and JEFF3.1 (Figs 2-4).

10.4.2. *Discussion on DANTSYS results*

A good agreement is observed with regard to DANTSYS and Monte-Carlo results whichever library is used. FZK employed JEF2.2 and JENDL3.3 nuclear data for preparing multigroup cross-sections used for computing the criticality (k_{eff}), major reactivity effects, source importance. β_{eff} vas computed with JENDL3.3 data only (since delayed neutron data for some minor actinides are not available in the JEF2.2 library).

Computations were performed with 172-group and also 560-group data libraries produced earlier at FZK from the mentioned evaluated data libraries. The 172-group library was used for computing all parameters, the self-shielding calculations being performed with the 172-group data, the resonance self-shielding 172-group cross sections being condensed to 33-group cross sections by employing composition-dependent spectra calculated in B2 approximation. The 33-group cross sections were used further in 2D neutron transport calculations. The 560-group library was employed for checking the accuracy of this procedure (with respect to k_{eff} value only). For that purpose, 560-group self-shielded cross sections were produced from the 560-group library and used in 560-group 2D neutron transport calculations.

The transport calculations in 33 and 560 groups were performed with the DANTSYS code. In both, 172/33 and 560-group cases, the cross sections for DANTSYS were generated by the ZMIX code. DANTSYS calculations were performed in the P3S8 approximation for the mesh specified in the benchmark description. To evaluate angle/space discretization uncertainties (with respect to k_{eff} value only), computations in the P5S16 approximation with 2 times finer spatial mesh were also performed. Computations with more energy groups, finer spatial and angular approximations may be considered as ‘corrections’ to be applied for results obtained with less number of groups and meshes. Table 12 summarizes these corrections related to different approximations. We can observe that these corrections are small.

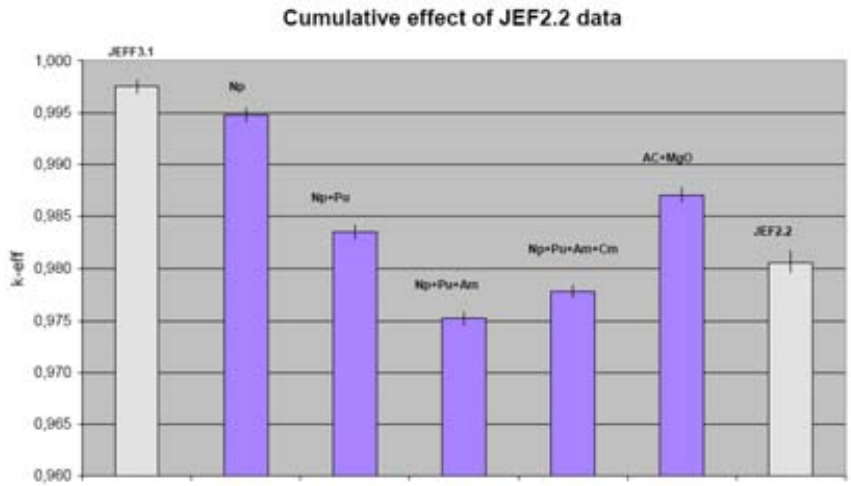

FIG. 2. Cumulative effect of JEF2.2 data obtained by NRG with OCTOPUS system.

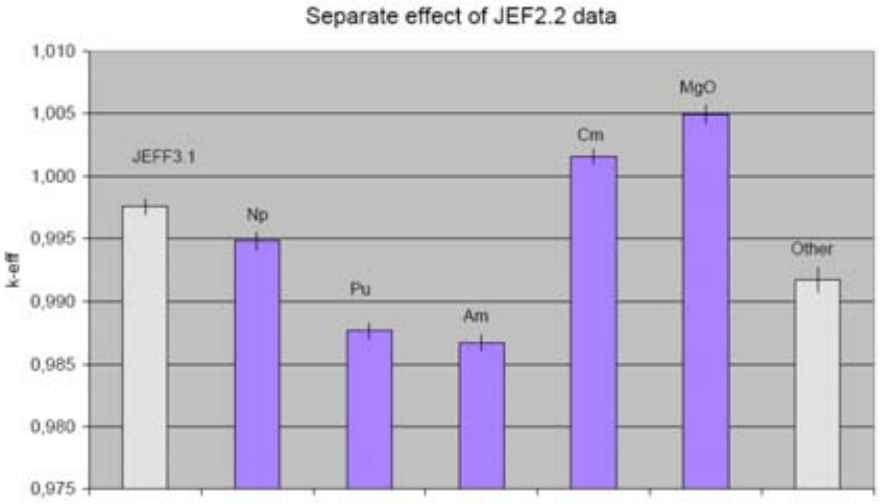

FIG. 3. Separate effect of JEF2.2 data obtained by NRG with OCTOPUS system.

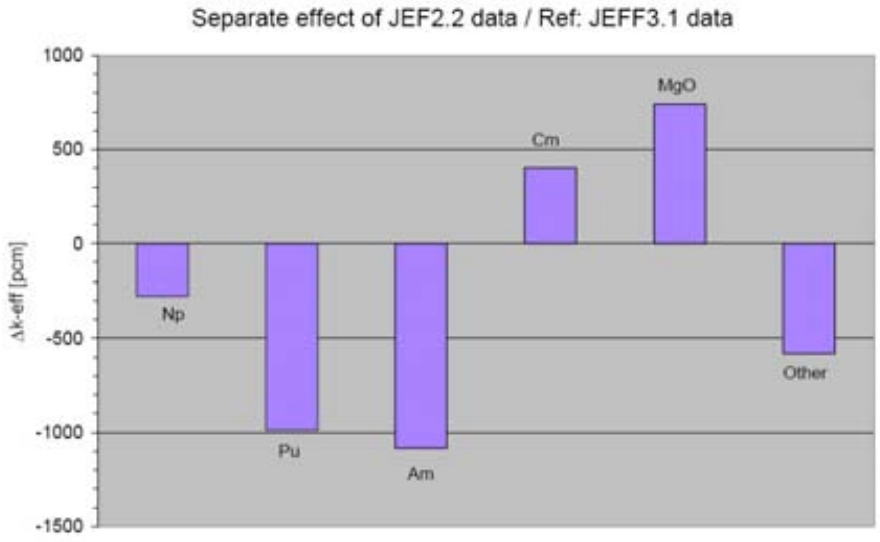

FIG. 4. Separate effect of JEF2.2 data obtained with OCTOPUS system/Ref: JEFF3.1.

TABLE 12. Corrections obtained at FZK for k_{eff} values computed with the DANTSYS code

P5S16 – P3S8 (pcm)	-11
Fine_mesh – Coarse_mesh (pcm)	+7
560 groups – 172/33 groups	-109
Total (pcm)	-113

10.4.3. *Discussion on ERANOS results*

Several calculations (using different methods and libraries) must be done to get finally good agreements between ERANOS and Monte-Carlo results with respect to the core reactivity at BOL. Initially a large discrepancy was observed (see Table 9, result with JEF2.2/ERANOS), but after appropriate corrections the results were in a better agreement (see Table 9, result with JEFF3.1-ERANOS).

Table 9 shows a discrepancy between ERANOS and Monte-Carlo results while using JEF2.2: of about 1800 pcm. In this case, the ERANOS calculation is performed with the method approximations described in Table 8; namely, a homogeneous cells representation in ECCO with a flux calculations performed in 1968 energy groups with subsequent condensation and homogenization, thus providing 33-group cross-sections for the whole core calculation. CEA used the 'inconsistent' equations, approximating leakage by a non-leakage factor and current by a Fick-like law. In standard fast reactor analyses, the inconsistent approximation is quite accurate, but looses validity in case of important anisotropic scattering by light nuclides. The BISTRO 2D Sn transport module is then used for whole core calculation, in RZ geometry with S4 angular discretization and P0 approximation for the scattering matrix. To reduce the discrepancies observed, CEA performed several calculations by employing different approximations. The results are presented in Table 13.

It appears that the a better agreement with other codes with respect to criticality prediction for the ADT core cannot be obtained by employing one of the investigated approximations. Analyses were also performed by comparing TRIPOLI4 and ERANOS results in more detail: to bring the problem into focus. This study consisted in calculation of the discrepancies due to variations in the fuel composition. The results are presented in the Table 14. Based on this analysis, it appears that the discrepancy is mainly due to ^{241}Am and ^{243}Am.

Analyses were also done for a simplify geometry (only fuel core with void around). They showed that the same problem still exists (Table 15). For this study, ECCO calculation were performed with 1968-group data, which were then condensed to 33-group cross-sections employed in the whole core calculation. Another model was a fuel cell analyzed by ECCO and TRIPOLI4. The results are summarized in Tables 16 and 17 (with JEF2.2 and JEFF3.1 libraries respectively).

TABLE 13. METHOD AND MODELING EFFECTS ON THE K_{EFF} USING JEF2.2-ERANOS

Library order P1 → P5	-98 pcm
Transport → Diffusion	-550 pcm
Group cell calculation 1968g → 33g	+153 pcm
Group core calculation 33g → 172g	+42 pcm
P0 → P1	-271 pcm
S4 → S8	+110 pcm
Inconsistent → Consistent	+100 pcm

TABLE 14. INITIAL REACTIVITY DISCREPANCIES BETWEEN ERANOS AND TRIPOLI4 USING DIFFERENT FUEL CORE COMPOSITION

			Discrepancies (pcm) (ERANOS/TRIPOLI4)
ADT benchmark			-1792 (+/- 76)
Pu without Minor Actinides			+199 (+/- 105)
Pu+Am	Am241 Am242m Am243	3642.6 kg 24.5 kg 1966.1 kg	-1926 (+/- 77)
Pu+Am241	Am241	5184.2 kg	-1272 (+/- 77)
Pu+Am243	Am243	4347.9 kg	-1993 (+/- 73)
Pu+Cm	Cm243 Cm244 Cm245 Cm246	29.7 kg 2810.9 kg 441.2 kg 38.9 kg	+6 (+/- 98)
Pu+Np237			-924

TABLE 15. DISCREPANCIES BETWEEN TRIPOLI AND ERANOS WITH A SIMPLIFY GEOMETRY

ERANOS initial reactivity	-5167 pcm
TRIPOLI4 initial reactivity	-3368 pcm
Discrepancy	1799 pcm

TABLE 16. DISCREPANCIES BETWEEN ECCO AND TRIPOLI4 FOR THE FUEL CELL (JEF2.2 LIBRARY)

Code	Group number	k-inf
TRIPOLI4	Point-wise	1.16650 +/- 56 pcm
ECCO	1968 g **(1)**	1.14024
	33 g	1.14434
	172 g **(2)**	1.16807
	STEP_1 172 g (diffusion initialization step) STEP_2 1968 g (transport step)	1.14217

TABLE 17. DISCREPANCIES BETWEEN ECCO AND TRIPOLI4 (JEFF3.1 LIBRARY) FOR THE FUEL CELL

Code	Group number	k-inf
TRIPOLI4	Point-wise	1.18102 +/- 46 pcm
	Probability tables (TABPROB) 1968 g	1.17904 +/- 46 pcm
ECCO	172 g **(3)**	1.18357
	1968 g for isotopes only present at 1968 g in JEF2.2 library (*) **(4)**	1.16401
	1968 g for all isotopes except Mg isotopes and Am243 **(5)**	1.16519
	1968 g for all isotopes except Mg **(6)**	1.16631
	1968 g for all isotopes **(7)**	1.17697

A good agreement (with respect to k_{inf}, infinite multiplication factor) between TRIPOLI4 and ECCO with 172-group data seems to be not-consistent with other results. In fact, the 172-group structure is obtained by a condensation of 1968-group data by employing a thermal spectrum while the benchmark is to model a fast fuel cell. One may assume that this result keeps compensation phenomena. The same conclusion can be obtained while using the JEFF3.1 library.

To understand these results, it is also essential to take into account that the JEF 2.2 based 1968-group data library includes data for the following isotopes only: ^{235}U, ^{238}U, ^{237}Np, ^{239}Pu, ^{240}Pu, ^{241}Pu, ^{242}Pu, ^{241}Am, ^{245}Cm, ^{54}Fe, ^{56}Fe, ^{57}Fe, ^{58}Fe, ^{50}Cr, ^{52}Cr, ^{53}Cr, ^{54}Cr, ^{58}Ni, Ni60, ^{61}Ni, ^{62}Ni, ^{64}Ni, ^{16}O, ^{4}He. Thus, data for Mg and ^{243}Am isotopes are not included in this 1968-group library, but 33-group data being employed for these nuclides. On the other hand, the JEFF3.1-based 1968-group library includes data for Mg and ^{243}Am. This fact is very important for understanding the results of the benchmark. If we look at the results obtained with the JEFF3.1 library (see Table 9), one can notice that the discrepancy between the Monte-Carlo and ECCO results depends on whether the mentioned isotopes are included in the 1968-group library. It appears that it is very essential to treat in ECCO the considered fuel cell with 1968-group data for all cell components, in particularly for the Mg isotopes, oxygen and minor actinides such as ^{243}Am. In this case, one can notice that the ECCO calculation (with 1968-group data for all isotopes) gives a good agreement with the TRIPOLI4 results (based on the probabilities table option); the discrepancy is about 150 pcm. Sensitivity studies were performed with the Perturbation method of ECCO to better understand this problem (see Table 18). Taking into account these results, we present in Table 19 a summary of results provided by ERANOS and TRIPOLI4 for the ADT core benchmark.

TABLE 18. SENSITIVE STUDY WITH ECCO USING PERTURBATION METHOD (TO UNDERSTAND THE RESULTS, ONE SHOULD KNOW SOME 33-GROUP BOUNDARIES, gr5: 2.23 MeV AND 1.35 MeV, gr6: 1.35 MeV AND 0.802 MeV, gr7: 0.802 MeV and 0.497 MeV, gr8: 0.497 MeV AND 0.302 MeV, gr9: 0.302 MeV and 0.183 MeV)

Library	JEF2.2	JEFF3.1	JEFF3.1	JEFF3.1	JEFF3.1
Sensitive study between	**(1) and (2)**	**(3) and (4)**	**(3) and (7)**	**(6) and (7)**	**(5) and (7)**
Variation	2089 pcm	1426 pcm	475 pcm	774 pcm	858 pcm
Mg	1266 pcm (elastic: gr5-9)	-	-	-	-
Mg24	-	390 pcm (elastic: gr9 206pcm)	153 pcm (elastic: gr7,9,10)	221 pcm (elastic: gr9 141pcm)	232 pcm (elastic: gr9 142pcm)
Mg25	-	64 pcm (elastic)	4 pcm	58 pcm	60 pcm (elastic)
Mg26	-	83 pcm (elastic)	12 pcm	67 pcm	68 pcm (elastic)
O16	314 pcm (inelastic: gr6,7)	376 pcm (elastic: gr6 114 pcm) (elastic: gr7 289 pcm)	141 pcm (elastic: gr7 120 pcm)	203 pcm (elastic: gr6 117 pcm) (elastic: gr7 153 pcm)	218 pcm (elastic: gr6 119 pcm) (elastic: gr7 158 pcm)
Am243	178 pcm (inelastic: gr6)	69 pcm (fission: gr6,7: 48 pcm) (elastic: 12 pcm) (inelastic: 9 pcm)	3 pcm	23 pcm	66 pcm (fission: gr6,7: 37 pcm) (elastic: 12 pcm) (inelastic: 6 pcm) (capture: 10 pcm)
Am241	55 pcm (fission: gr6,7)	80 pcm (fission: gr 6,7)	28 pcm	52 pcm	52 pcm (fission)

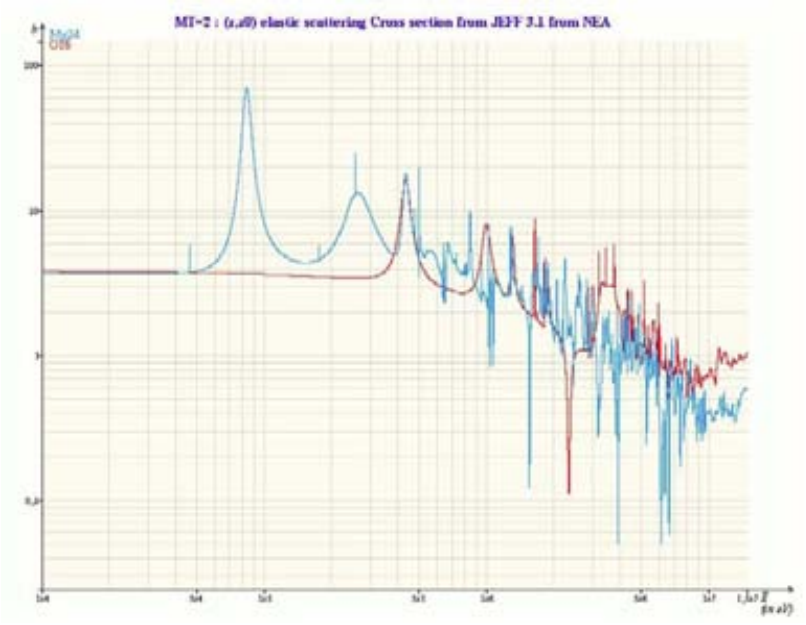

FIG. 5. ^{24}Mg (blue) and ^{16}O (red) elastic scattering cross sections from JEFF3.1.

TABLE 19. INITIAL REACTIVITY COMPUTED BY ERANOS AND TRIPOLI4 BENCHMARK

ERANOS – JEF2.2 (1968g)	0.96533
TRIPOLI4 – JEF2.2	0.98233 +/- 0.00076
ERANOS – JEFF3.1 (1968g for isotopes only described at 1968g in JEF2.2)	0.98359
ERANOS – JEFF3.1 (1968g for all isotopes)	0.99315
TRIPOLI4 – JEFF3.1 (300K)	0.99847 +/- 0.00079

Thus, for studying with ERANOS, cores with large content of MgO and minor actinides, the recommendation is to treat Mg, O and minor actinides at the fine group level. This is necessary because it is the only library to include both nuclides in fine groups (Mg isotopes are not available in 1968-group in JEF2.2) and therefore allows a correct treatment of the overlapping of Mg and O resonances (Fig. 5). It includes also the most up-to-date evaluations for minor actinides.

In case one cannot apply with library with ERANOS, the JEF2.2 172 group library may provide reasonable answer, partly due to compensation effects.

10.4.4. *Kinetic parameter, beam current and reactivity effect results*

The results for the kinetic parameters, Doppler effect, coolant depressurization reactivity, core compaction and current are shown in Tables 20 and 21 at BOL and EOL, respectively. The Doppler constant is in the range from -20 to -40 pcm. For β_{eff}, good agreement is observed between the different calculations except the MCNP-JEF2.2 results. Reasonable results are also obtained for the coolant depressurization reactivity effect at BOL. However, due to some deviation in these results, it appears necessary to improve agreement between them within the framework of another project.

TABLE 20. COMPARISON OF THE KINETIC PARAMETER, CURRENT, REACTIVITY INSERTIONS AT BOL

BOL	ERANOS JEF2.2	ERANOS JEFF3.1	DANTSYS JEF2.2	DANTSYS JENDL3.3	TRIPOLI4 JEF2.2	MCNP JEF2.2	MCNP JEFF3.1
	CEA	CEA	FZK	FZK	CEA	NRG	NRG
βeff (pcm)	173	172.7	-	178	-	143.5 ± 1.9	179 ± 3
Δρ Doppler (pcm) 993°C → 180°C	12.4	64.3	42	57	-	40 ± 21	19 ± 31
Δρ Coolant (pcm) 60 bars → 1 bar	254.4	247.7	248	239	238 ± 21	289 ± 18	244 ± 31
Core compaction (pcm)	70	-	78	77	43 ± 21	101 ± 19	53 ± 23
Current (mA)	18.8	3.6	8.5	7.9	-	10 ± 0.2	2.4 ± 0.1

TABLE 21. COMPARISON OF THE KINETIC PARAMETER, CURRENT, REACTIVITY INSERTIONS AT EOL

EOL	ERANOS JEFF3.1	MCNP JEFF3.1
	CEA	NRG
Δρ Doppler (pcm) 993°C → 180°C	74.4	92 ± 40
Δρ Coolant (pcm) 60 bars → 1 bar	235.8	306 ± 40

10.4.5. *Depletion calculation results*

Several depletion calculations have been performed with different code systems and different libraries by NRG, FZK and CEA. FZK employed DANTSYS-TRAIN with two libraries: JEF2.2 and JENDL3.3. CEA used the ERANOS code with JEF2.2 and JEFF3.1. The NRG results are also very interesting because they perform depletion results obtained with a Monte-Carlo code in combination of FISPACT as burnup code. In this last case, the library used is JEFF3.1. The different tables below (Tables 22-27) present comparisons of the results computed with theese different system at the fuel EOL (burnup reactivity loss, fuel inventory in kg, isotopic vectors in %, transmutation rate in kg/TW•h/th).

It is not easy to conclude about the discrepancies (between the results) because the libraries and the methods are different. For example, fine-group data for some isotopes like Mg, are not available in the JEF 2.2 library of ERANOS, that leads to an inaccurate core reactivity.So it is more suitable to compare the reactivity loss. In this case, one can observe good agreement between the ERANOS calculations based on 2 different data libraries. The reactivity loss is about 1 900 pcm. This deviates significantly from other results. The design scheme of ERANOS uses 6 lumped fission products. These pseudo cross-sections are aimed at simulating the absorption of the individual solid fission products in the reactor core, which originate mostly from ^{235}U, ^{238}U, ^{239}Pu, ^{240}Pu, ^{241}Pu, and ^{242}Pu. In the other codes used to calculate this benchmark (OCTOPUS and TRAIN system), a larger number of explicit fission products can be described. For example 77 FP can be used in OCTOPUS. TRAIN may use up to several hundreds fission products (though for some types of fast reactor analyses only one lumped FP can be applied, that is often sufficient). A more detailed investigation may show the role of using different approximation in different types of analyses and to understand whether using of lumped fission products for MAs (such as ^{241}Am, ^{242m}Am, ^{243}Am, ^{243}Cm, ^{244}Cm, ^{245}Cm) may affect the accuracy appreciably.

TABLE 22. COMPARISON OF THE BURNUP REACTIVITY LOSS IN THE DEPLETION CALCULATION BENCHMARK

	JEF2.2-ERANOS CEA	**JEF2.2-DANTSYS-TRAIN** FZK	**JENDL3.3-DANTSYS-TRAIN** FZK	**JEFF3.1-ERANOS** CEA	**JEFF3.1-OCTOPUS** NRG
k-eff at BOL	0.96533	0.98390	0.98544	0.99315	0.99731
k-eff at EOL	0.94735	0.95579	0.95697	0.97415	0.96994
Reactivity loss (pcm)	1798	2811	2847	1965	2737

TABLE 23. COMPARISON OF THE MASS BALANCE IN THE CORE AT EOL (kg)

EOL	**JEF2.2-ERANOS** CEA	**JEF2.2-DANTSYS-TRAIN** FZK	**JENDL3.3-DANTSYS-TRAIN** FZK	**JEFF3.1-ERANOS** CEA	**JEFF3.1-OCTOPUS** NRG
U	10,0944	10,13		9,80	10,04
Np	885,473	884,64	883,28	886,28	882,7
Pu	3419,57	3424,17	3416,1	3393,13	3411
Am	3557,97	3527,15	3546,22	3589,85	3554
Cm	834,139	833,42	823,68	819,62	825,3

TABLE 24. COMPARISON OF THE ISOTOPIC MASS BALANCE IN THE CORE AT EOL (kg)

EOL	**JEF2.2-ERANOS** CEA	**JEF2.2-DANTSYS-TRAIN** FZK	**JENDL3.3-DANTSYS-TRAIN** FZK	**JEFF3.1-ERANOS** CEA	**JEFF3.1-OCTOPUS** NRG
Np237	885,47	884,6	883,28	886,28	883
Pu238	465,20	481,78	470,39	443,32	460,82
Pu239	1092,56	1087,51	1092,81	1095,30	1089,81
Pu240	1091,38	1088,2	1089,73	1095,32	1094,59
Pu241	289,19	283,86	283,88	284,69	282,43
Pu242	481,24	482,8	479,28	474,51	483,33
Am241	2253,94	2253,84	2265,32	2278,35	2268,16
Am242m	61,54	40,56	39,36	57,94	37,31
Am243	1242,28	1232,38	1241,53	1253,37	1248,52
Cm242	42,42	44,67	42,91	39,15	42,83
Cm243	6,60	6,08	5,85	5,87	5,94
Cm244	669,20	668,65	652,35	646,10	647,2
Cm245	104,50	102,84	109,63	115,29	116,03
Cm246	11,23	11	12,6	12,78	12,87
Cm247	1,81E-01	1,66E-01	4,12E-01	0,42	4,12E-01

TABLE 25. COMPARISON OF THE ISOTOPIC VECTOR AT EOL (%)

	EOL	JEF2.2-ERANOS CEA	JEF2.2-DANTSYS-TRAIN FZK	JENDL3.3-DANTSYS-TRAIN FZK	JEFF3.1-ERANOS CEA	JEFF3.1-OCTOPUS NRG
Pu	Pu238	13,60	14,07	13,77	13,07	13,51
	Pu239	31,95	31,76	31,99	32,28	31,95
	Pu240	31,92	31,78	31,9	32,28	32,09
	Pu241	8,46	8,29	8,31	8,39	8,28
	Pu242	14,07	14,1	14,03	13,98	14,17
Am	Am241	63,35	63,9	63,88	63,47	63,82
	Am242m	1,73	1,15	1,11	1,61	1,05
	Am243	34,92	34,94	35,01	34,91	35,13
Cm	Cm242	5,09	5,36	5,21	4,78	5,19
	Cm243	0,79	0,73	0,71	0,72	0,72
	Cm244	80,23	80,23	79,2	78,83	78,42
	Cm245	12,53	12,34	13,31	14,07	14,06
	Cm246	1,35	1,32	1,53	1,56	1,56
	Cm247	0,02	0,02	0,05	0,05	0,05
	Cm248	0	0	0	0	0

TABLE 26. COMPARISON OF THE TRANSMUTATION RATES AT EOL (kg/TW•h/th)

EOL	JEF2.2-ERANOS CEA	JEF2.2-DANTSYS-TRAIN FZK	JENDL3.3-DANTSYS-TRAIN FZK	JEFF3.1-ERANOS CEA	JEFF3.1-OCTOPUS NRG
U	0,7	0,7	0,7	0,7	0,7
Np	-10,1	-10,2	-10,3	-10,1	-10,3
Pu	3,8	4,2	3,6	2,0	3,2
Am	-40,5	-42,9	-41,5	-38,3	-40,8
Cm	4,9	4,9	4,2	3,9	4,3
Total	-41,2	-43,3	-43,3	-41,8	-42,9

TABLE 27. DISCREPANCIES OF THE MASS BALANCE WITH DIFFERENT LIBRARIES AND CODES

EOL	JEF2.2-ERANOS CEA (1)	JEFF3.1-ERANOS CEA (2)	JEFF3.1-OCTOPUS NRG (3)	Discrepancies (2)/(1) in %	Discrepancies (2)/(3)) in %
U234	9,34	9,07	9,29	-2,86	-2,38
U235	3,21E-01	2,89E-01	2,98E-01	-9,87	-3,06
U236	4,35E-01	4,38E-01	4,54E-01	0,66	-3,59
U238	3,32E-03	3,30E-03	3,34E-03	-0,59	-1,05
Np237	885,47	886,28	883	0,09	0,37
Np239	1,07E-03	1,08E-03	1,08E-03	0,58	-0,10
Pu238	465,20	443,32	460,82	-4,70	-3,80
Pu239	1092,56	1095,30	1089,81	0,25	0,50
Pu240	1091,38	1095,32	1094,59	0,36	0,07
Pu241	289,19	284,69	282,43	-1,56	0,80
Pu242	481,24	474,51	483,33	-1,40	-1,82
Am241	2253,94	2278,35	2268,16	1,08	0,45
Am242m	61,54	57,94	37,31	-5,86	55,28
Am243	1242,28	1253,37	1248,52	0,89	0,39
Cm242	42,42	39,15	42,83	-7,70	-8,58
Cm243	6,60	5,87	5,94	-11,05	-1,17
Cm244	669,20	646,10	647,2	-3,45	-0,17
Cm245	104,50	115,29	116,03	10,32	-0,64
Cm246	11,23	12,78	12,87	13,77	-0,69
Cm247	1,81E-01	0,42	4,12E-01	131,26	1,67
Cm248	2,45E-03	0,01	8,54E-03	233,68	-4,40

Concerning the mass balance values, the different results seem to be consistent, no dramatic discrepancies being observed. However, we can point out a little difference between the CEA results and those of FZK and NRG related to the ^{242m}Am and ^{242}Cm production. For example (Table 24), a discrepancy of about 34% is observed on the amount of ^{242m} Am between JEF2.2-ERANOS and JEF2.2-DANTSYS-TRAIN results. The origin of this difference can be attributed to the ^{241}Am branching ratio toward this isotope which is different in the two cases. FZK took the branching ratio from the JEFF3.1 activation file. This value is ca. 8.4% for ^{242m}Am in this system (in the FZK case the ratio is energy-dependent and therefore its integral value is reactor-dependent), while CEA specifies 15% in the ERANOS input (NRG effectively employs 8.3% this values is based on EAF data which are similar to JEFF 3.1 activation data). A small difference is observed also for the amount of ^{242}Pu and ^{242}Cm produced from ^{242}Am; CEA uses a value of 16% for ^{242}Pu when FZK and NRG employ 16.8 and 17.3%, respectively. These results underline the importance of improving the knowledge of the branching ratios.

Table 25 summarizes the discrepancies between JEF2.2 and JEFF3.1 while using the ERANOS code and also discrepancies between the deterministic code ERANOS and the OCTOPUS system (MCNP-FISPACT) with the same library JEFF3.1. Large discrepancies can be observed between the two libraries on the prediction of the amount of almost all of minor actinides. In JEFF3.1, the ^{241}Am, ^{243}Am capture cross sections are lower compared to JEF 2.2, while the ^{244}Cm, ^{245}Cm, ^{246}Cm, ^{247}Cm capture cross sections seem to be higher. The most discrepancies between ERANOS and OCTOPUS come from deviations in the branching ratios and decay data.

An interesting result obtained by NRG with OCTOPUS system present the evolution of mass actinides during the time irradiation (see Fig. 6). In general, however, the mass balance calculation seems to be correct with regard to the precision necessary for an ADS project study.

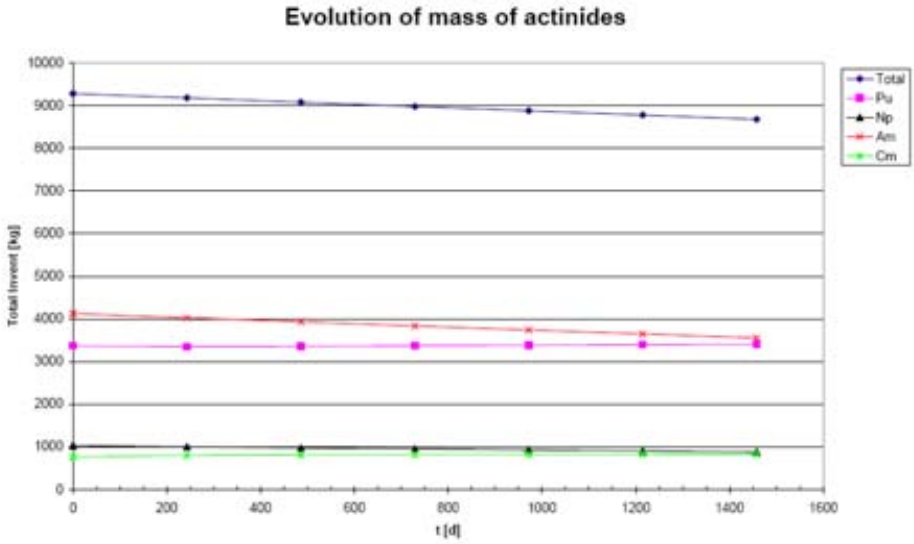

FIG. 6. Evolution of mass of actinides obtained by NRG with OCTOPUS-JEFF3.1.

10.5. Conclusions

A neutronics benchmark based on the 400 MW(th) gas cooled accelerator driven system design has been described. The system contains ca. 23.4 kg of heavy metal, HM nuclei per MW(th), that is relatively large compared to the values for LBE-cooled systems (7.5 or 9 depending on the inert matrix type): due to relatevely low power density in this gas-cooled system. Pu/MA weight fractions in the HM part of the fuel (NP is present in the MA part contrary to the systems of Domain IV) are 36/64. The fuel/matrix (MgO) volume fractions are 34/66.

This ADS system (similar to others with fertile-free fuel considered in Domain IV) shows the maximum possible TRU burning potential, in the range from 42 to 43 kg/TWh (th), almost all burned TRU's being MAs, in particular Am.

Four institutions took part in the analysis, by using two deterministic code systems (ERANOS and C4P-ZMIX-DANTSYS-TRAIN) and Monte-Carlo codes as MCNP/MCNPX, OCTOPUS and TRIPOLI4. The nuclear data are based on the JEF2.2, JEFF3.1, ENDF/B-VI.8 and JENDL3.3 evaluations.

A comparison has been carried out for the following parameters: reactivity, Doppler effect, coolant depressurization effect, core compaction, kinetic parameter β_{eff}, mass inventory at EOL that characterizes the transmutation rate.

Initially a large discrepancy was observed between results on the core reactivity at BOL provided by different participants; in particular, the ERANOS results deviated from those by computed by other codes. Sensitive studies were performed to understand the reason of deviations. It was found that fine-group data should be used in the ERANOS calculation scheme to compute parameters for cores with a large content of MgO and Minor Actinides. In particular, it is important to treat Mg, and O and minor actinides at the fine group level, this option being available with the JEFF3.1-based ERANOS library. This is the only library for ERANOS that includes both nuclides Mg and O at the fine group level. At this level, one may take into account the overlapping of Mg and O resonances. This library also includes the most up-to-data evaluations for minor actinides.

The sensitivity of reactivity at the end of cycle to the fission product treatment (using of a few lumped fission products, or several tens, or several hundreds individual fission products, FPs) was not investigated. It would be interesting to evaluate the related effect. An option for these studies is offered by ERANOS (that may employ a few lumped FPs or of 87 individual FPs), OCTOPUS (77 FPs) and TRAIN (single lumped FP or up to several hundreds individual FPs).

The uncertainties (in criticality, coolant/structure reactivity effects and burnup reactivity loss) due to nuclear data remain relatively high: deviations with respect to particular isotopes (^{242}Am, ^{242m}Am, ^{242}Cm, ^{242}Pu) due to different branching ratios, mainly due to the branching ratios for ^{241}Am>^{242}Am/^{242m}Am (8-9% for ^{241}Am>^{242m}Am for non-CEA: coming from JEFF 3.1/EAF; 15% for CEA). The branching ratios also influence the reactivity loss per cycle: ca. 2 800 pcm after 1 450 EFPD for non-CEA vs. ca. 1 900 pcm for CEA. This reactivity loss is lower (500 to 700 pcm per year) than one for considered LBE-cooled systems (ca. 1 500 pcm per year) due to higher relative (per unit power) fuel inventory. Thus, a particular attention should be paid to the branching ratio of the ^{241}Am capture reaction, as uncertainties in this value influence significantly the reactivity loss due to fuel burnup.

It would be also interesting too to improve the calculation scheme for computing the beam current value, core compaction and coolant depressurization effects: by using a more refined geometry model and by involving the high-energy data directly in the calculations scheme.

One may notice a good agreement on the mass balance prediction between the deterministic and Monte-Carlo codes, the deviations are not appreciable with regard to the precision necessary for an ADS project study The Doppler constant is in the range from -20 to -40 pcm. The core void effect: ca. 250 pcm (as He pressure drops from 60 to 1 bar). Core structure removal effect is not evaluated, but should be appreciably higher than the core void effect. $Beta_{eff}$ is in the range from 170 to 180 pcm.

Though the safety is not investigated, lost of He pressure can be considered as the main safety case. It is not clear whether the system may withstand this accident. The main stabilizing effect comes through the sub-criticality as the Doppler plays no role.

The high reactivity worth of structure may lead to a dramatic reactivity increase in case of loss of coolant and subsequent clad melting and relocation. The impact of potential fuel relocation is difficult to predict without performing computer simulations. Until the clad is failed, reactivity variations are small

compared to the sub-criticality level. Doppler plays no role as in other fertile-free systems, the coolant void worth is much smaller compared to LM-cooled fertile-free systems, other reactivity effects (related to structure) are assumed to be similar to other fertile-free systems. Constructive measures that improve safety feedbacks (due to e.g. core geometry variations) may help, but this point needs a more detailed study.

Very fast power response (in μs to ms scale) to beam variations may potentially shorten life of reactor materials, but should bring no safety problems. Longer time scales (of the order of 10 s) should be typical for other cases.

The available codes are at sufficiently high level in general to investigate the key phenomena. Additional efforts should be paid to perform trasnient analyses, for that purpose additional codes and dabases should be used, these codes may need benchmarking and/or extension for gas-cooled reactor application. Nuclear data for MAs are still associated with high uncertainties; ADS designs optimisation may improve their safety and burnup performance, in particular a higher unit power could be considered.

REFERENCES TO CHAPRTER 10

[1] RIMPAULT, G., The ERANOS code and data system for fast reactor neutronic analyses, paper presented in PHYSOR 2002, 7-10 October 2002, Seoul, Republic of Korea.

[2] RINEISKI, A., SINITSA, V., MASCHEK, W., "C4P, a Multigroup Nuclear CCCC Data Processing System for Reactor Safety and Scenario Studies", Proc. Jahrestagung Kerntechnik 2005, 10-12 May 2005, Nürnberg, Germany.

[3] RINEISKI, A., SINITSA, V., MASCHEK, W, WANG, S., "Kinetics and Cross-Section Developments for Analyses of Reactor Transmutation Concepts with SIMMER", paper presented in M&C 2005, 12-15 September 2005Avignon, France.

[4] ALCOUFFE, R.E., BAKER, R.S., BRINKLEY, F.W., MARR, D.R., O'DELL, R.D, and WALTERS, W.F., DANTSYS: A Diffusion Accelerated Neutral Particle Transport Code System, LA-12969-M (1995).

[5] RINEISKI, A., Decay Heat Production in a TRU Burner, paper presented in 2nd COE-INES International Symposium on Innovative Nuclear Energy Systems, INES-2, 26-30 November 2006, Yokohama, Japan.

[6] BOTH, JP., LEE, Y., MAZZOLO, A., PENELIAU, Y., PETIT, O., ROESSLINGER, B., SOLDEVILA, M., A three dimensional polykinetic particle transport Monte-Carlo code, paper presented in Intl Conf on supercomputing in Nuclear Applications, 22-24 September 2003, Paris, France.

[7] OPPE, J., KUIJPER, J.C., OCTOPUS_TNG Reference Guide, NRG Report 20748/03.54103/C (November 2004).

[8] MISU, S., TIMM, W., BURDICK, B. and HOGENBIRK, A., Qualification of nuclide density predictions for high burnup MOX and UO2 fuel, Proceedings Jahrestagung Kerntechnik 2000, Inforum Verlag (May 2000).

[9] BRIESMEISTER, J.F., ed., MCNPTM- A General Monte Carlo N-Particle Transport Code Version 4C, LA-13709-M, Los Alamos National Laboratory (2000).

[10] HENDRICKS, J.S, MCNP4C3 — 3/22/01, Report X-5:RN(U)-JSH-01-17, Los Alamos National Laboratory (13 April 2001).

[11] FORRESTER, R.A., The European Activation System: EASY-2001 overview, UKAEA FUS 449 (2001).

CHAPTER 11. DOMAIN-VIII: FISSION-FUSION HYBRID REACTOR (TANDEM MIRROR CONCEPT)

The AGH University of Science and Technology in Cracow contributed to the benchmark model of a Tandem Mirror Transmutation System. The coupling of fission and fusion with the objective of transmutation/incineration appears to be advantageous from basic principles, since the fission process is energy rich and neutron poor (80 MeV/n), while the fusion process is neutron rich and energy poor (17.6 MeV/n). Therefore, the fission fraction of the energy released in a fusion-driven sub-critical system can be very high (up to 90%) already at low values of k_{eff} (as low as 0.6). For such a system also the value of the plasma energy gain (Q) can be low, depending upon the efficiency of the electricity self-consumption and its fraction of the total energy produced by the fusion-driven sub-critical system. It can be concluded that the requirements regarding the plasma Q can be significantly relaxed in the case of a fusion-driven sub-critical system, down to levels achievable in small Tandem Mirror Concepts. For the Tandem Mirror Concept, the group has performed neutronics analyses, of which the following main results have been obtained so far: approximately 0.5 MW/m^2 neutron wall load; uniform distribution of the nuclear heating due to the introduction of fission power; the worst credible accident scenario (collapse of the Tandem Mirror System) does not lead to super-criticality; higher neutron multiplication in the first generation and, consequently, increased energy release and enhanced neutron source; satisfactory incineration rates for plutonium.

The fusion/fission hybrid benchmark proposed by ASIPP is based on a preliminary tokamak fusion/fission hybrid concept called FDS-I, whose missions are plutonium breeding, as well as incineration and transmutation of minor actinides and long lived fission products. To reach these objectives, the requirements for the plasma core are relaxed, compared to a fusion reactor: the FDS-I plasma core has a fusion power of approximately 150 MW, major and minor radii of about 4 and 1 m, respectively, and an elongation factor of 1.7. The neutron wall load is approximately 0.5 MW/m^2. The sub-critical 'waste' blanket is cooled by helium and lithium-lead eutectic [dual-cooled waste (DWT) blanket] and contains the various zones (incineration of MAs, transmutation of long lived fission products, plutonium breeding). In addition to FDS-I, ASIPP is also proposing the model of a spherical tokamak system called FDS-ST. The advantage of such a system is its compactness, making it more suitable for incineration and transmutation applications. For this benchmark exercise, the following main transient scenarios were retained: ramping of fusion power, plasma disruption, quench of super-conducting in the field coils, loss of flow accidents (LOFA), loss of cooling accidents (LOCA), loss of heat sink accident (LOHS), overpower transient, and possibly other transient scenarios considered in ADS. Preliminary results were obtained for dynamics calculations that were performed for a few transients, such as LOFA, LOCA and overpower transient. The sub-critical blanket static calculations were performed with the help of the in-house ASIPP-developed multi-purpose (transport, burnup, activation, etc) neutronics code system called VisualBUS. For these calculations the nuclear data library HENDL1.0 was used.

First, some basic problems of the nuclear power are sketched then the question of transmutations and their physical preconditionings are discussed. It has been reminded that any form of closed fuel cycle cannot avoid dealing with large quantities of radioactive materials. It is indicated that closing of the fuel cycle is not easy since the Minor Actinides (MA), unavoidably produced then in significant quantities, show disadvantageous physical properties (intense radioactivity, heat release, positive reactivity coefficients). In search for solutions subcritical Fusion-Driven Incinerator system (FDI) have been suggested. Next the problems of nuclear fusion have been addressed and the ways of solution with use of fission energy contained in actinides of spent nuclear fuel have been proposed. The main positive of that option of fusion power,/thanks to energy release from fissions/, is the prospect of a radical reduction of necessary plasma energy gain Q to levels achievable in much smaller i.e. much more economic devices. No less important advantages of the FDI system are: reduced load of the FW with 14 MeV neutrons as well as tritium consumption and homogeneous heating distribution. (The radiation damage also of neutronic origin is one of the main sources of material difficulties in fusion technology. Then it has been suggested that one of the most viable incineration concepts is a symbiotic nuclear energy system, consisting of a transuranics (Pu, Np and Am) incinerator and a number of co-operating Light Water Reactors (LWRs). Summarising, the concept of

actinides incineration in fusion-driven subcritical systems significantly heightens safety of nuclear power systems.

In conclusion, the option of fusion presented herewith as a means to solve the problems inherent to fission based nuclear energy may change the attitude of the fusion community regarding the fission power — perceiving it not as a competitor but an ally of fusion that can facilitate its development.

11.1. Introduction

The strong objections against any symbiosis of fusion with fission, which one could observe for over two decades, seem to be based upon the ignorance of the public unaware of the common nuclear roots of both processes. It is not a kinship of fusion to fission energy that is the greatest threat for its deployment but the real difficulties it is still facing. Meanwhile, they can be effectively relaxed while shifting the heavy burden of energy production to the energy rich fission process. Then, one should be conscious that in any closed fuel cycle one cannot avoid dealing with large quantities of radioactive materials. It is true that the radiotoxicity of the FDI system must be larger than that of a pure fusion system alone. But the whole radiotoxicity issued from the symbiotic system, consisted of a FDI of transuranics (Pu, Np and Am) and of associated LWRs the fission waste is received from, will be lower than that from the latter and the pure fusion system.

11.2. Global energy problems

The longstanding forecast of end of cheap organic fuels (oil and gas) seems finally to come true. Since at present nearly one third of the world population lives outside of electrified areas within the next quarter of century the number of electricity consumers will double. Calmed by often spectacular energy savings in modern electronics (per device) one neglects its avalanche expansion in numbers (e.g. of the mobile phones and PCs). The related power demand is particularly troublesome due to its characteristic load distinct by the 3^{rd} and next uneven harmonics, generated in alternate-to-direct current converters. Besides, many households in the world are only going to be equipped with microwave ovens, air conditioners, (de)humidifiers, etc. Having all the above in mind, one can anticipate a global permanent increase in the electricity consumption. Such demand must not be met with organic fuels that threaten with further heightening of CO_2 concentration in the atmosphere (Kyoto Protocol). The opinion that a deployment of renewables is very desirable does not give rise to any doubts. Unfortunately, the present quite important share of hydroenergy (nearly 1/5) in the world electricity production cannot be significantly increased. In turn, the possibilities of other renewables/solar, wind/, because of physical/low power density/and practical limitations/low disposability/are by far insufficient. Therefore, the only option the contribution of which is meaningful and has a potential to increase fast is nuclear energy.

11.2.1. *Problems of nuclear power*

Unfortunately, the existing i.e. fission based nuclear power provokes considerable social objections originating from subjective perception of potential risk associated with. These are:

1) Contingency of uncontrolled supercriticality in extreme accidents.
   An intuitive factor of safety is the remoteness of the system state from the super prompt criticality [1]. This distance of a critical system is determined by the Nature's bounty — the delayed neutrons, quantitatively, by their effective fraction β_{eff} specific for each composition of nuclides and neutron spectrum in the system. A safety margin larger than β_{eff} is thinkable, but can occur solely in subcritical systems that can operate in a steady state provided an external neutron source is continuously filling the neutron deficit in each generation.

2) Highly radioactive, long lived nuclear waste.
   High radiotoxicity of nuclear spent fuel is the cause why finding a way of its definitive neutralisation has become a necessary condition of social acceptance of nuclear power. Meanwhile the problem is aggravating.

At current level of world deployment of nuclear energy (ca. 370 GW(e)l installed civilian capacity) the yearly global yield of spent fuel exceeds 10 000 metric tonnes, whereas the global inventory of civilian spent nuclear fuel (including the reprocessed fraction) amounts to over 200 000 t [2] that contain nearly 4 000 tonnes of fissile nuclides.

The global problem of waste has not been resolved until now in an indisputable way. Spent nuclear fuel at present is stored either at the plant or in interim engineered installations. Up to now, a disposal in geological formations is assumed as the main way of final solution of the problem. In view of the required properties of the repository that should guarantee the retention of the waste during millions of years, sufficient for decay of its longest lived radioisotopes and its permanent safeguarding, this concept is not inexpensive. Instead, one must not neglect the enormous energy content of actinides, (200 MeV/atom *2500 MW_t.a/.ton) equal to a striking number 8×1020 J in the world yearly spent fuel i.e. more than twice the total world's annual energy consumption. Moreover, the energy contained in the global/civilian only/inventory amounting to 2×1022 J is equal to the consumption of energy/at present rate/in all forms by the whole humankind during 50 years. To bury such enormous amount of energy would be really deplorable. One should consider a duty of present generations to assure for the future ones the use of that precious energy source.

Simultaneously, it should be reminded that only fissioning is a definitive way of getting rid of radiotoxic actinides, since other nuclear reactions with exchange of only several nucleons leave the nucleus to remain an actinide one. As regards fission products, since their transmutations bring no energy bonus this option is not considered in this part. One should remember that toxic metals (Pb, Hg, Cd, As, Cr etc.) and CO_2 dispersed by humankind in the environment in enormous quantities do not decay at all ($T_{1/2} = \infty$!), while over 90% of fission products are short lived or stable.

Finally, it may be hoped that indispensable social acceptance of nuclear energy can be facilitated by the possibility of definitive destruction of nuclear waste, thus adding an important social value to this concept. The development of a fusion-driven incinerator (FDI) is a major step in this direction.

11.2.2. *Problems of nuclear fusion*

The worldwide antinuclear phobia has not left untouched also the field of nuclear fusion. On the part of the fusion community one has been generally observing the avoidance of mentioning any relationship of fusion to fission. Yet, the specialists, though aware of the important differences between these two forms of nuclear energy cannot perceive fusion as having nothing in common with radioactivity, not mentioning the general public, usually allergic about. Thus, we are sceptical about the effectiveness of opposing the fusion energy to the fission, so as to make the public to like the former. We believe that there are other, better arguments and concepts demonstrating the fusion power as an environmentally benign energy source.

The fusion reactor can be used as a device for safe incineration of the waste produced by fission based nuclear energy [3]. The fact that the LWR costs seem to determine the future electricity prices together with high investment costs of the fusion reactor put in doubt whether its mere energy production, even at reduced radioactive waste level, proves sufficient for making it economically competitive. But its additional use and thus income from secure/as free of criticality dangers/incineration of actinides in a fusion-driven device can resolve this question. At present the fusion technology is not ready, yet, the problem of actinide waste seems prolonged enough, that the fusion technology — operating relaxed due to fission component — is ready in time.

11.3. Physical preconditions

11.3.1. *General characteristics*

Figure 1 shows that the exploitation of nuclear fuel is coupled with a variety of processes generating significant quantities of large number of nuclides. It is so, since many of them instead of fissioning are transmuted into heavier Minor Actinides (MA) as a result of successive neutron captures. Quantitatively it is given in Table 1 [5, 6].

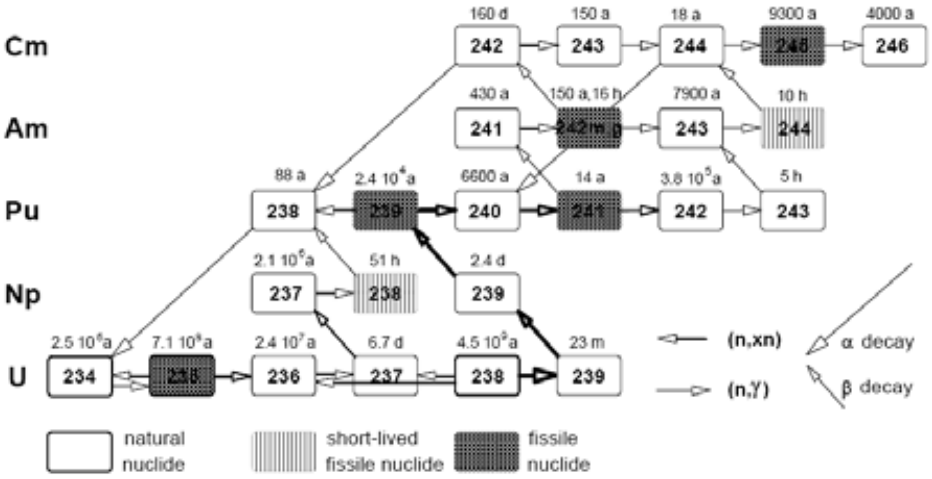

FIG. 1. Main trajectories of nuclear transformations in the U-Pu nuclear fuel cycle [4] /for clarity, all prolonged α decays as being less significant are not shown/.

TABLE 1. AVERAGE COMPOSITION OF SPENT NUCLEAR FUELS (MAIN RADIONUCLIDES/1 GWelyr)

Actinides				Fission products[2]			
Nuclide	$T_{1/2}$ [a]	Mass [kg]		Nuclide	$T_{1/2}$ [yr]	Mass [kg]	Isotope fraction [%]
		U fuel	MOX[1]				
^{235}U	$7.0 \cdot 10^8$	280	50	^{85}Kr	10.8	0.4	
^{236}U	$2.3 \cdot 10^7$	120	20	^{90}Sr	29	14	
^{238}U	$4.5 \cdot 10^9$	$2.8\ 10^4$	$2.7\ 10^4$	^{137}Cs	30	32	
^{237}Np	$2.1 \cdot 10^6$	15	10	^{151}Sm	93	0.3	
^{238}Pu	88	6 (2%)	25 (3.5%)	^{79}Se	$6.5 \cdot 10^4$	0.2	10
^{239}Pu	$2.4 \cdot 10^4$	170 (57%)	350 (47.5%)	^{93}Zr	$1.5 \cdot 10^6$	23	20
^{240}Pu	6600	70 (23%)	200 (27%)	^{99}Tc	$2.1 \cdot 10^5$	25	100
^{241}Pu	14	40 (13%)	80 (11%)	^{107}Pd	$6.5 \cdot 10^6$	7	16
^{242}Pu	$3.8 \cdot 10^5$	15 (5%)	80 (11%)	^{126}Sn	$1.0 \cdot 10^5$	1	31
^{241}Am	430	7	30	^{129}I	$1.6 \cdot 10^7$	6	75
^{242m}Am	141	0.1	0.2	^{135}Cs	$2 \cdot 10^6$	10	14
^{243}Am	7370	3	25				
^{244}Cm	18	0.7	15				
^{245}Cm	8500	0.1	3				

[1] approximate values [2] ^{235}U

On the basis of the Table 1 one can state that ca. 7% of the fissioned mass is transmuted into Long Lived Fission Products (LLFP). One should also notice that the amount of transplutonic MAs: Am and Cm in the MOX spent fuel is much higher than in the uranium one, while the fraction of uneven (i.e. fissile) Pu isotopes is lower.

It should be added that the content of heavier MAs/Am and Cm/still increases with further burnup (approaching 10% of the fissioned Pu).

Therefore, a full recycling of Pu in LWRs i.e. in thermal spectra, unavoidably leads — in addition to the Pu degradation — to the transmutation of its significant part into highly radiotoxic nuclides (see Table 2) less convenient as a fuel (Table 3). The data in Table 2 indicate that in the case of MOX spent fuel actinides is the main source of radiotoxicity from the beginning, whereas for uranium fuel they become after less than a hundred years (i.e. after a partial decay of ^{90}Sr and ^{137}Cs). From Table 3 can be seen that the MAs are distinct by a minute fraction of delayed neutrons.

TABLE 2. COMMITTED EFFECTIVE DOSES (CED) OF SELECTED NUCLIDES WHEN INGESTED BY ADULTS [11]

Actinide	CED [Sv·kg^{-1}]	Fission product	CED [Sv·kg^{-1}]
^{235}U	3.8	^{85}Kr	-
^{236}U	110	^{90}Sr	$1.4\cdot10^{8}$
^{238}U	0.5	^{137}Cs	$4.3\cdot10^{7}$
^{237}Np	$2.8\cdot10^{3}$	^{151}Sm	$9.2\cdot10^{5}$
^{238}Pu	$1.5\cdot10^{8}$	^{79}Se	10^{2}
^{239}Pu	$5.7\cdot10^{5}$	^{93}Zr	90
^{240}Pu	$2.1\cdot10^{6}$	^{99}Tc	$4\cdot10^{2}$
^{241}Pu	$1.9\cdot10^{7}$	^{107}Pd	0.7
^{242}Pu	$3.5\cdot10^{4}$	^{129}I	$7\cdot10^{2}$
^{241}Am	$2.6\cdot10^{7}$	^{135}Cs	95
^{242m}Am	$7.3\cdot10^{7}$		
^{243}Am	$1.5\cdot10^{6}$		
^{244}Cm	$3.7\cdot10^{8}$		
^{245}Cm	$1.3\cdot10^{6}$		

TABLE 3. APPROXIMATE VALUES OF FISSION PARAMETERS: DELAYED NEUTRON FRACTION *, NUMBER OF NEUTRONS PER FISSION * AND PER ABSORPTION η OF SELECTED ACTINIDES/BASED ENDF/B-VI, JENDL-3/

Nuclide	β [%]	ν (thermal spectr.)	η 0.025eV	η fast*
^{232}Th	2.4*	2.2*	~0	0.11
^{233}U	0.4	2.5	2.29	2.34
^{235}U	0.7	2.42	2.07	2.08
^{238}U	1.7*	2.6*	~0	0.13
^{237}Np	0.4*	3.0*	~0	0.82
^{238}Pu	0.14*	3.1*	~0	2.06
^{239}Pu	0.26	2.88	2.12	2.63
^{240}Pu	0.30*	3.0*	~0	1.38
^{241}Pu	0.55	2.9	2.17	2.70
^{242}Pu	0.65*	3.0*	~0	1.13
^{241}Am	0.12*	3.4*	0.02	0.56
^{242m}Am	0.18	3.3	2.93	3.22
^{243}Am	0.23*	3.5*	~0	0.68
^{244}Cm	0.13	3.3	~0	1.34
^{245}Cm	0.16	3.6	3.12	3.33
^{246}Cm	0.24*	3.7*	~0	1.07

*fiss. neutrons spectrum

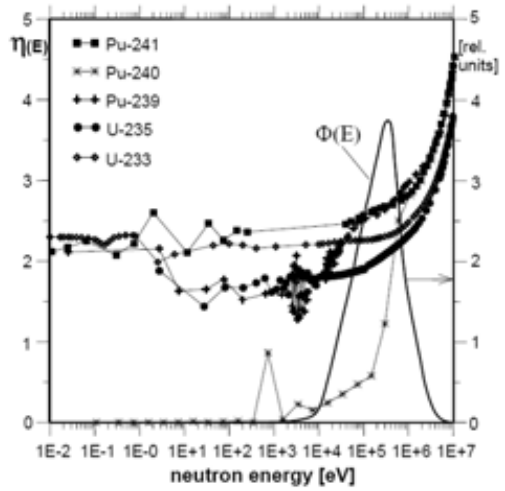

FIG. 2. Parameter η(E) of some nuclides vs. energy and the neutron fast spectrum Φ(E) in a Pb cooled system [6].

Figures 3 and 4 show: 1) the striking prevalence of capture over fission processes for thermal spectrum and much less important for a hard one, thus the generation of heavier and heavier nuclides in thermal neutron flux; 2) the advantage of fast spectrum is paid with minute values of cross-sections that in turn draws behind a need of higher nuclide inventories.

On this basis one can state that the present common preference of hard spectra is justified, though in some cases, e.g. for Pu incineration without fissile regeneration a soft spectrum may prove more advantageous. Finally, it should be remembered that the rate of actinide transmutation i.e. by fissioning has a well-fixed intensity (per energy unit). Thus its rate per power unit is nearly constant and the yield is directly determined by the size i.e. the power of the device. As concerns incinerations of LLFP, this energy poor process though possible in principle (Fig. 5) is not easy — seeing the cross sections and deteriorating the neutron balance. Here one should mention an alternative to the U-Pu fuel cycle i.e. the Th-U cycle (Fig. 6) [4].

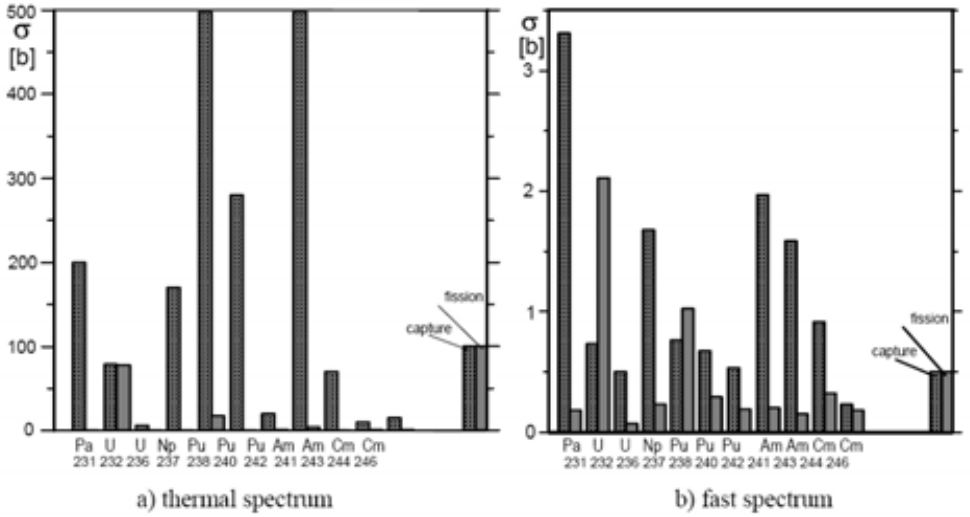

FIG. 3. Transmutation related neutron cross-sections of selected actinides.

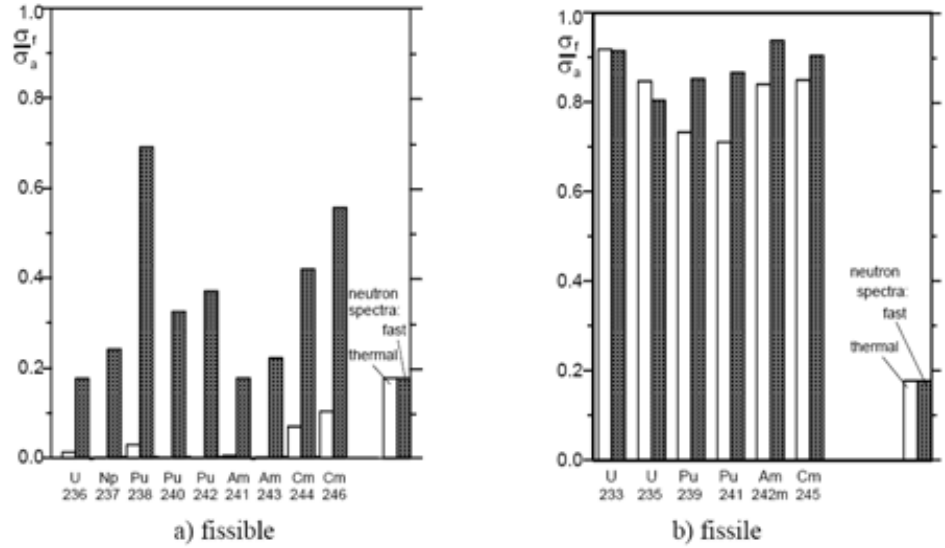

FIG. 4. Probability of fissioning of selected actinides after absorption of a neutron (thermal or fast one).

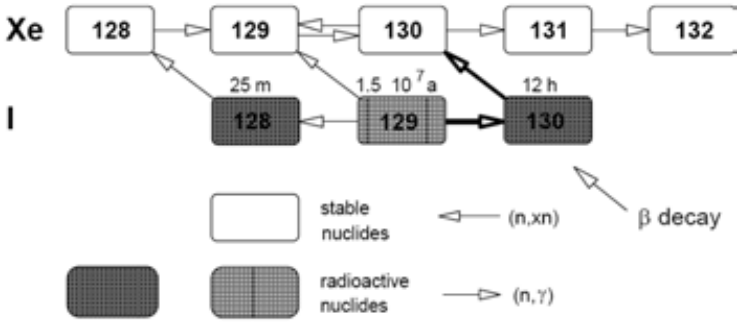

FIG. 5. Example of fission product transmutations/^{129}I/.

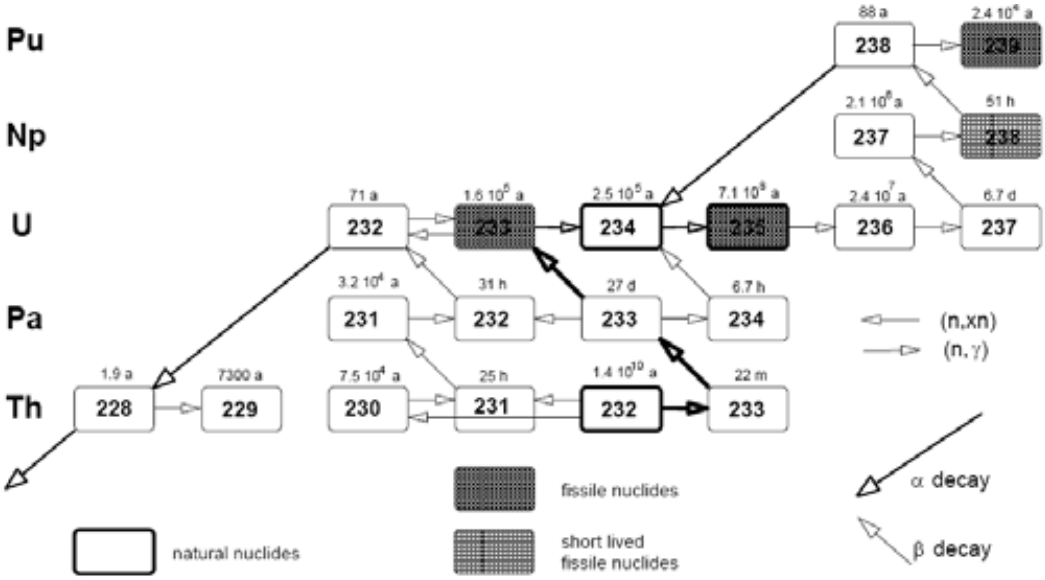

FIG. 6. Main trajectories of nuclear transformations in the Th-U fuel cycle.

Figure 6 suggests that the generation of Pu and first of all of transplutonics in the Th-U cycle is very minute, thus proving its advantages (see also Fig. 11). Another important question that must be addressed here regards the proliferation. Some actinide properties significant in view of the possible use as nuclear explosives are shown in Table 4.

One must not forget also that there is no way to incinerate spent nuclear fuel without its reprocessing. In this regard, recalling the saying: 'one cannot have eaten the cake and still to have it', inversely — there is no possibility to destroy completely nuclear waste and not to manage with it at all. Thus, the recycling must be carried out so that to prevent a diversion of processed fissile materials.

The ambivalence of the properties of ^{238}Pu, Am and Cm is worth to notice. High: spontaneous fission neutron yield, heat release and gamma activity make MA a very troublesome material for nuclear explosives. Alpha heating of many hundred watts corresponding to critical masses disintegrates the chemical explosive, spontaneous fission neutrons provoke a predetonation that significantly reduces the energy of explosion and — more important — make even small amounts of MA easily detectable, whereas the large ones may prove deadly (e.g. ^{233}Pa, Cm) — if handled unprotected. In connection with the Th-U cycle a diversion also faces difficulties. The tremendous heating of ^{233}Pa (40 W/g) hinders chemical separations of even small quantities of this isotope, thus imposing, say, and yearlong cooling times. Meanwhile, a chain stemming from ^{232}U and emitting very penetrating gammas (^{208}Tl, Eγ=2.6 MeV) develops with the time constant 2.7 a (^{228}Th). On the other hand all these effects make of MA inconvenient materials for the fuel too as requiring a remote handling during all the fabrication and transport.

TABLE 4. NON-PROLIFERATION SIGNIFICANT PARAMETERS OF ACTINIDES (SPECIFIC HEATING, γ DOSE RATE, SPONTAN FISSION NEUTRONS, ETC.)

Nuclide	Specific heating [W/kg]	γ dose rate [mSv·m²/(kg·h)]	Spontaneous fissions		Neutron yield from (α,n) in H_2O		Bare critical mass[1] [kg]
			Yield [n/(kg·s)]	Dose rate [mSv·m²/(kg·h)]	Yield [n/(kg·s)]	Dose rate [mSv·m²/(kg·h)]	
^{233}Pa	$4\cdot10^{4}$	$1.6\cdot10^{8}$	-	-	-	-	k_∞<0.5
^{233}U (.06%^{232}U)	0.2	$1.2\cdot10^{2}$	0.6		$2\cdot10^{4}$		17÷15.5
^{237}Np+^{233}Pa	-	6	0.2	-	$2\cdot10^{3}$	-	60÷62.7
^{238}Pu	$6\cdot10^{2}$	12	$3.6\cdot10^{6}$	<0.1	$7\cdot10^{7}$	0.7	10÷8.2
^{239}Pu	2	3	20	-	$2\cdot10^{5}$	-	10÷10.1
^{240}Pu	7	2.5	$1.6\cdot10^{6}$	<0.1	$8\cdot10^{5}$	-	33÷37
^{241}Pu	30	-	3	-	-	-	12÷13
^{242}Pu	0.1	-	$2.3\cdot10^{6}$	<0.1	$1\cdot10^{4}$	-	55÷85.3
^{241}Am	120	$1.2\cdot10^{3}$	$2.5\cdot10^{3}$	-	$1.5\cdot10^{7}$	0.1	75÷60
^{242m}Am+^{242}Cm	$15+4\cdot10^{2}$	$4\cdot10^{2}+5\cdot10^{2}$	$6\cdot10^{4}+8\cdot10^{7}$	0.8	$5\cdot10^{7}$	0.5	17÷9.1
^{243}Am	8	80	$8\cdot10^{2}$	-	$7\cdot10^{5}$	-	150÷209
^{242}Cm	$1.1\cdot10^{5}$	$1.5\cdot10^{5}$	$2.2\cdot10^{10}$	$2.2\cdot10^{2}$	$1.5\cdot10^{10}$	$1.5\cdot10^{2}$	350
^{244}Cm	$3\cdot10^{3}$	1	$1.3\cdot10^{10}$	$13\cdot10^{2}$	$4\cdot10^{8}$	4	21÷27
^{245}Cm	6	40	$1.2\cdot10^{5}$	-	$8\cdot10^{5}$	-	12÷9.2
^{246}Cm	10	20	$1\cdot10^{8}$	1	$1.5\cdot10^{6}$	<0.1	40÷41

[1]range

More important is to hinder a misuse of recycled Pu. But a significant 'contamination' of Pu can be done when associating Pu with ^{237}Np. This mixture subject to neutron flux results in a higher content of ^{238}Pu in the final composition, due to the reaction (n,γ). The very high heat release of this isotope (~0.6 kW/kg) makes Pu containing above 5-7% of ^{238}Pu hardly suitable for military purposes [8]. Thus, it seems that a closing of the fuel cycle does not provide more proliferation problems as those in the acknowledged and used technology of the MOX fuel cycle. Finally, the decades long experience of many thousand tons of spent fuel reprocessed in the UK and France indicates that a reliable Pu accountancy, safeguarding and diversion prevention are possible.

The fundamental advantage of subcritical systems is their significantly higher level of safety as compared with typical nuclear reactors, as a rule operating critical. Due to the negative reactivity, thus a much larger distance of the system from the super prompt criticality the latter is practically excluded. As could be concluded from all the above, a fusion reactor could be the external neutron source for subcritical system [9].

11.3.2. *Fusion-driven incinerator*

The process of fission is energy rich and neutron poor: 200 MeV/2.5n = 80 MeV/n whereas the process of fusion is neutron rich and energy poor: 17.6 MeV/n thus a coupling of both processes is worth consideration e.g. for incineration of actinides. Therefore an option appears of nuclear waste incineration with the help of fusion technology, i.e. an attractive possibility to picture fusion as a mean to resolve the problems caused by fission based nuclear energy. This application of fusion is deeply pro-environmental, though the hazard caused by the FDIs alone is higher than by pure fusion reactors, since the overall environmental load the fission waste + FDI is effectively reduced [10]. Besides, it seems doubtful that the society — biased, sceptic and unaware that the fusion-driven nuclear energy is really safer — is ready to accept its significantly higher costs. In turn, the scarcity of fossil fuels in the next decades, should effectively assure the survival of LWRs. In conclusion, a net energy producing FDI symbiotic with a number of LWRs and contributing to solve their waste problem seem to be an attractive option. Obviously, any other variants of this approach to the waste solution are also desirable. At this early stage of development of this new technology with many aspects still remaining insufficiently known, any selection of directions of research is premature.

A satisfactory power level of externally driven subcritical system requires high number of source neutrons and a high neutron multiplication factor k_{eff}. In FDI both demands are difficult to be satisfied,

since at the same time not too low plasma Q and k_{eff} are needed. The difficulties in attaining plasma Q high enough are evident, whereas the upper limit to the k_{eff} can be theoretically set by assuring the system to remain subcritical in spite of any conceivable rearrangements. Even at normal operation step-wise changes in this value are inevitable, following e.g. a necessary fuel shuffling or simply a system reloading, thus lower values of k_{eff} are by far more preferable. Therefore, a specific objective appears: maintenance of the energy gain of the system at lowest k_{eff}. Fortunately, there is an effect apparently increasing the k_{eff} due to the driving source.

The respective factor G_n reflects the number of extra neutrons over those born in the k_{eff}-based fundamental mode, mostly in the first cycles of the multiplication chain (Fig. 7). The – 14 MeV generated fast fission and (n,2n) neutrons — relax the demand for higher, less safe k_{eff} while assuring the needed number of fissions in the system.

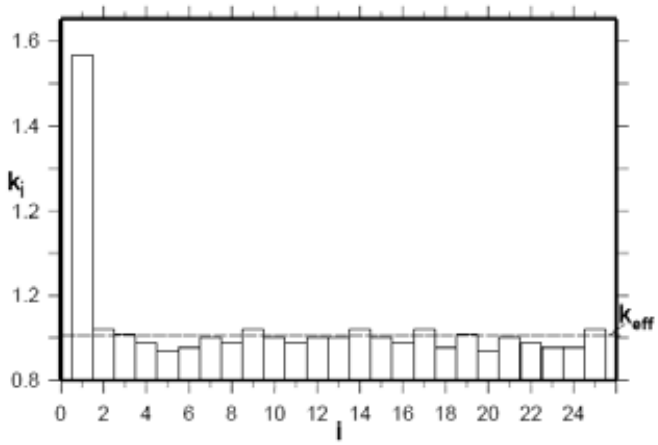

FIG. 7. Example of neutron multiplication vs. number **i** *of successive neutron generations.*

In this way the energy gain can be sufficient for a significant reduction in the plasma Q. This can be done by placing of fissionable materials close to the first wall (FW). However, a superfluous accumulation of fissile material directly at the FW may easily lead to an excessive energy release in there. Thus, in designing the system one is limited by the admissible power density and its peaking. On the other hand, the presence of fissile material deeper in the blanket increases the volume of nuclear heating, thus allowing for achieving the sufficient power of the system at reduced area of the first wall. Thus, the question is what values of k_{eff} would be needed that the necessary energy gains due to fissions are achieved. The contribution of fission to the total energy released in an FDI system is shown in the Fig. 8 [12].

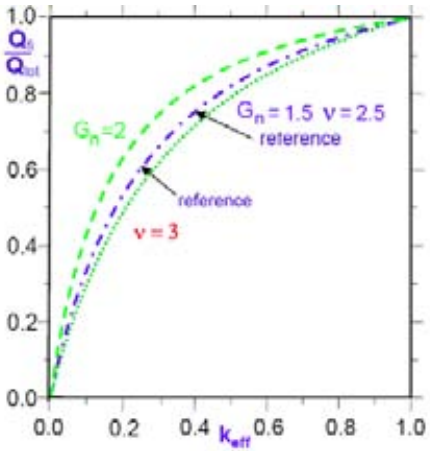

FIG. 8. Fission fraction of energy release in the FDI system vs. k_{eff}. Reference values: Fusion energy Q_{fu} =17.6 MeV, fission energy Q_{fi} =200 MeV, self-consumed power fraction c_{ps}=0.25, conversion efficiency of self-consumed power c_p = 0.16, G_n =1.5, n./fission ν = 2.5.

It can be seen that the values of the k_{eff} necessary that to contribute significantly to the FDI energy balance is not to be lower than 0.6-0.7. The several curves in the picture reflecting the dispersion of the values of most significant parameters correspond to different variants of the system.

Figure 9 demonstrates that at unaffected power of the FDI system, a radical drop in the value of Q, down to a level 0.3 achievable in small devices, (spherical assembly or tandem mirror), is feasible./e.g. for k_{eff} = 0.85 plasma Q = ca. 0.5 seems sufficient/.

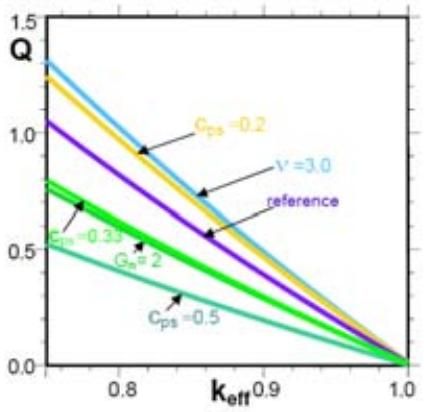

FIG. 9. Plasma **Q** *reduction in FDI systems for given fixed power vs. k_{eff} [12].*

Another key problem of fusion is the radiation damage. Its main sources are: charged particle flux from plasma to materials directly exposed to (first of all the divertor) and neutron induced/both in the First Wall (FW) and in the divertor/: gas production, DPA and to a degree — transmutations. The use of fissions for energy production fructifies with drastic reduction in the alpha and 14 MeV neutron yield. The attenuation of the radiation (charged particles and photons) from plasma may be taken as proportional to the reduction in the fusion component in the FDI system. Though instead of D-T neutrons load the fission neutrons appear, yet in much lesser number (Fig. 10). Besides it should be emphasized that the destructive potential of the latter are much lesser (Figs 11 and 12). Thanks to fissions the 14 MeV neutron yield can be reduced by factor of several tens, e.g. 50.

11.3.3. *Radiation damage*

Exemplary pertinent cross-sections illustrate the nuclear conditions of gas production (Fig. 11). Figure 11 shows that — as expected — the thresholds of gas production reactions are pretty high, mostly confined within the range from a few to ~12 MeV. More data can be seen in Fig. 12. From Fig. 12 can be seen that the gas production by the fission neutrons (energy ca. 1 MeV) is rather exceptional — limited to H and particular isotopes (e.g. ^{58}Ni).

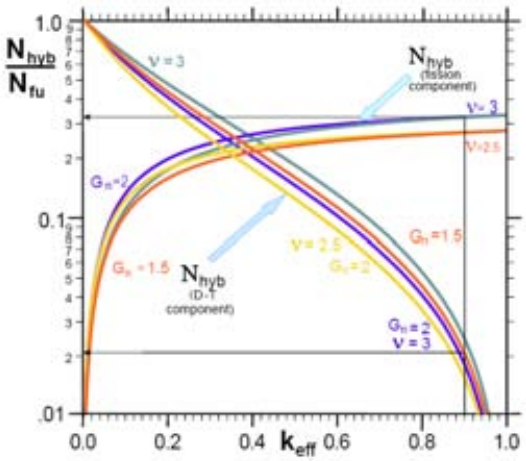

FIG. 10. Neutron yield reduction in FDI systems for given fixed power vs. k_{eff}.

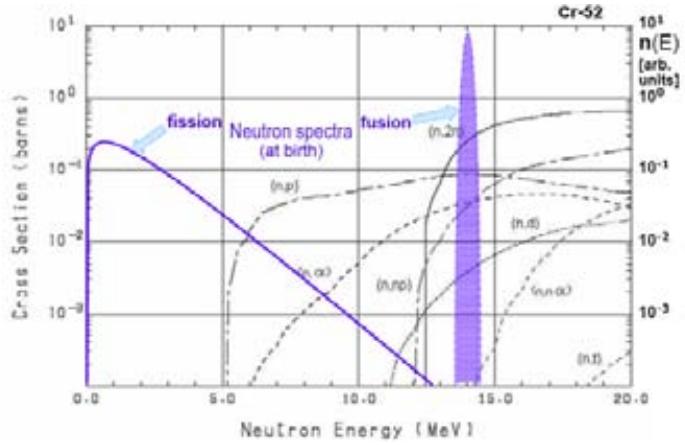

FIG. 11. Example of metal typical reaction cross-sections (gas production including) [13].

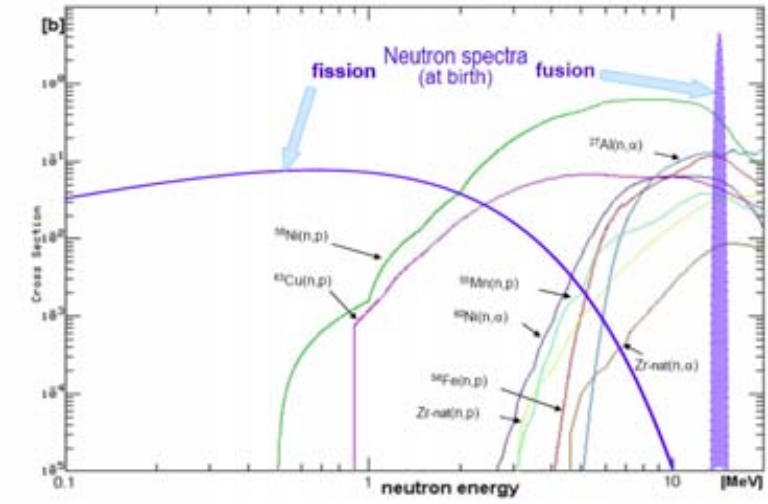

FIG. 12. Neutron source spectra and cross-sections for gas production in some construction materials [14].

As regards the DPA, one should look at the efficiency of fission neutrons and of 14 MeV ones in displacing the atoms of main components of construction materials in Fig. 13. Figure 13 indicates that the destructive displacing of the atoms by 14 MeV neutrons is also much more intensive than that of fission ones.

Summarising, one may foresee that in the most sensitive zones of the FDI (divertor, FW) the gas production component of the radiation damage can be reduced by the same factor as the D-T neutron yield, i.e. by several tens times (Table 5), whereas the reduction of DPA (non-threshold reaction) seems to be lesser. In view of all the above the size of FDI can be radically reduced as compared with the pure fusion reactor — usually a Tokamak (Fig. 14) [16].

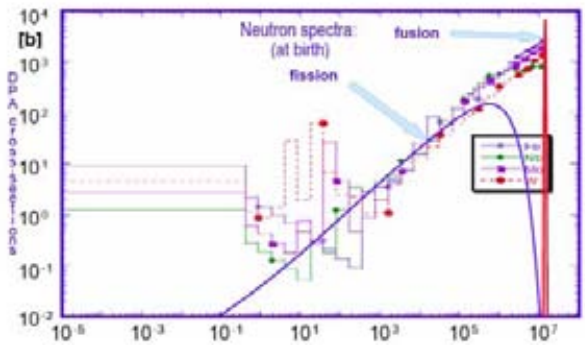

FIG. 13. DPA cross-sections of several elements of construction materials [15].

TABLE 5. COMPARISON OF MCNP EVALUATED RADIATION DAMAGE EFFECTS IN THE FIRST WALL (PURE FUSION REACTOR VS. FDI OF THE SAME POWER)

Effect / Option	E – energy per source n. [MeV]	tot. H prod. [nuclei/ (source n.*cm^3*E)]	tot. He prod. [nuclei/ (source n.*cm^3*E)]	dpa [events/ (source n.*E)]
Fusion Reactor	22.4	2.69E-07	5.08E-08	6.21E-07
FDI	1100	5.94E-09	1.06E-10	4.05E-08
FDI/FR ratio	49.1	0.0225	0.0208	0.0652

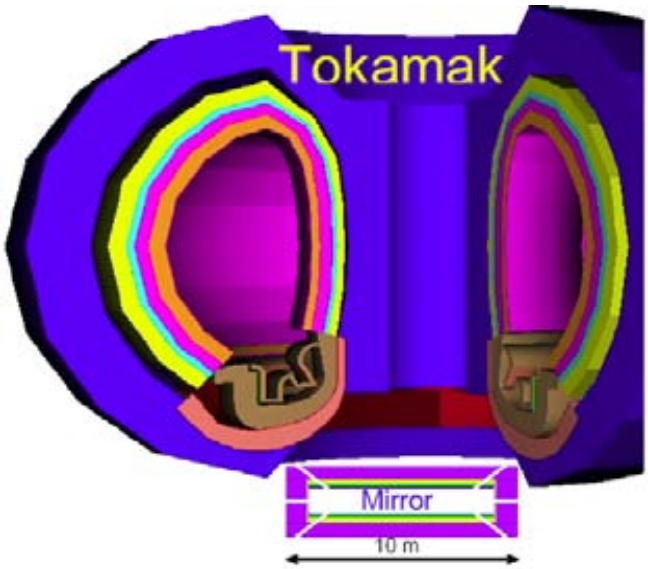

FIG. 14. Size of fusion reactors: a Tokamak vs. a Mirror device.

One sees that a Mirror based FDI can be incomparably smaller than a pure fusion system.

On the other hand one should be conscious that there is an important question of the trade-off: system size vs. radiation damage reduction. The latter by need not be recognized as the supreme objective. One can safely recognize a relaxing of the radiation load by the factor of say, 5 as very satisfying. This signifies still a reduction of the FW dimensions by one order of magnitude. From the pure geometrical considerations results that since the volume as compared to surface decreases with the 3/2 exponent, a reduction in the volume of the hybrid device by the factor of 30 can be expected in these conditions. Obviously, a decision where lies the optimum i.e. what is the most advantageous size of the hybrid system at acceptable radiation damage level can be made only after a detailed study in the multiparameter phase space consisted of technical, economical and safety dimensions. Besides, the selected at present concept of a Mirror system is not at all a definitive choice. It has been taken rather for demonstration of the long time underestimated potential of fusion technology for incineration of actinides. The reduction in size draws behind a reduction in mass inventories of various materials. Namely, the total mass within shield of a Mirror system amounts to ~1500 t, whereas the one of ITER, which still is not a full scale pure fusion reactor equals to 25 000 t. The ratio of masses of tritium breeding material (^{17}Li^{83}Pb) 30 t to 6 000 t in the DEMO fusion reactor is much more striking.

11.3.4. *Tritium*

Another aspect favorising the fusion hybrid system is linked to questions associated with tritium. One should not forget that the inventories of tritium in the whole fusion fuel cycle system are not minute and are measured in kilograms. The tritium inventories can be divided in two categories: the first, resulted from the undesirable but unavoidable solubility of tritium in all the materials remaining with

it in contact and the second one — the planned storage assuring the undisturbed tritium flow in case of never-to-be-excluded failures of some elements of the fuel cycle chain. Full scale pure fusion reactor (3 000 MW(th)) would consume ca. 0.5 kg of tritium per day. Having taken all the above into consideration, one can hardly imagine the total tritium inventory not exceeding 10 kg. Instead, the fission-fusion system can be sustained at the consumption rate of the order of 10g per day. Though in the fusion hybrid the unwanted inventory won't be proportionally reduced, the total one — well below 1 kg can expected. This numbers get importance when seeing the present tritium prices 33 000 U$/g, that correspond to the circumstances of equilibrated demand and supply on the tritium civilian market. Appearance of an enormous buyer at the time of launching of fusion reactor(s) can dramatically rocket the tritium price, especially when the available world civilian stocks (Canada) are estimated equal to ca. 22 kg. Thus the sum needed for the birth of fusion power at present prices attaining (> 3.3 108 i.e. perhaps ≥ half of billion U$ may prove prohibitive. In view of this the fusion hybrid seems to the only solution.

11.3.5. *Safety*

The most widely known advantage of fusion over fission power is the higher safety of the former. This opinion is based upon the fact that pure fusion systems by definition are free of the danger of supercriticality. The meltdown of such reactors is also highly improbable since in case of emergency, the scram of fusion reactor can be performed very fast by injection of (relatively) heavy particle beam (e.g. Ar) into plasma. The argon atoms or ions (non-corrosive!) cool the plasma down and stop the energy release in the system. These properties of pure fusion plants must not be undermined in fusion hybrids by a threat of supercriticality in case of a worst accident to be considered for a FDI — reactor meltdown (Fig. 15) [12]. Thus, the MCNP calculation model of the FDI in question has been completed with the configuration of the molten core.

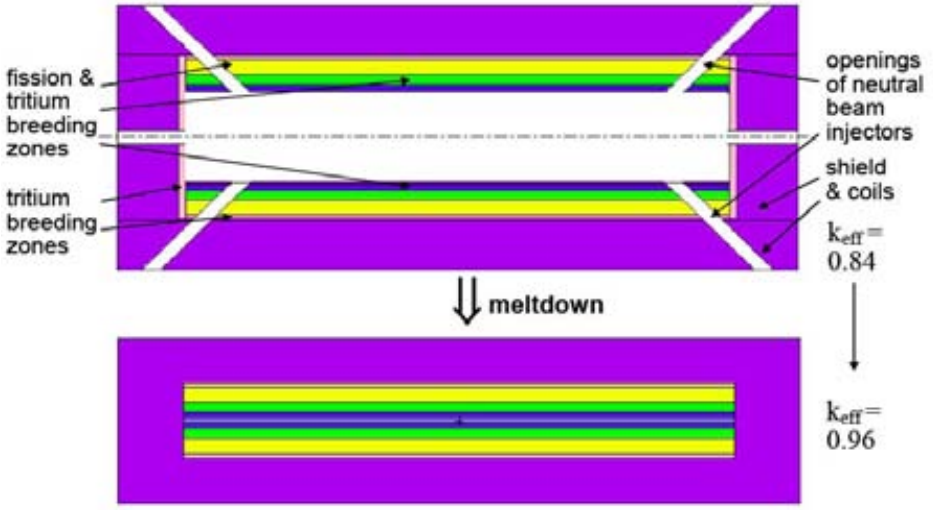

FIG. 15. MCNP model of the Mirror FDI system in operation and after meltdown.

The FDI system is safe — the assembly after collapse remains subcritical (k_{eff} = 0.96)

Both the processes — fissile incineration and breeding are not uniform in space and time, running at different rates within the system volume in the course of the transmutation cycle. The local transmutation rates vary very significantly that draws behind the necessity of compensation of the resulted very inhomogeneous nuclear heating by adjustment of the respective fissile concentrations. The achieved this way (in an earlier study [10]) quite effective power flattening (Fig. 16) illustrates the superiority of the heating distribution in the FDI as compared with a pure fusion reactor. At the same time the need of the fuel shuffling is confined to that associated with routine removal of the incinerated material and its replacement with a fresh one.

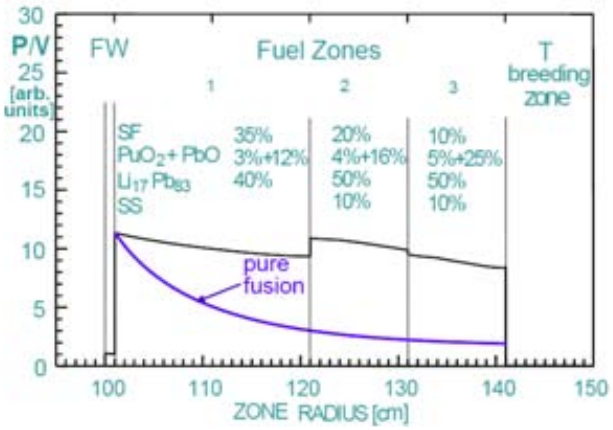

FIG. 16. Flattening of heating in FDI system and a pure fusion reactor blanket.

The results of the recent MCNP calculations of another Mirror FDI system are shown in Table 6 [10].

Table 6 demonstrate the numbers indicating very advantageous characteristic of the FDI system: the needed plasma Q is quite small, similarly the neutron FW load, k_{eff} value is safe and the power flattening has been achieved. The incineration of particular nuclides is given in Table 7.

TABLE 6. GENERAL PERFORMANCE OF THE FDI SYSTEM

Gross thermal power	500 MW_t
Electric power	170 MW_{el}
Self-consumed power	42 MW_{el}
Efficiency of plasma heating	0.5
Plasma Q	0.6
Neutron FW load	0.32 MW/m^2
k_{eff}	0.84
zone 1 specific power	21.4 MW/m^3
zone 1 specific power	21.9 MW/m^3
zone 1 specific power	22.4 MW/m^3

TABLE 7. INCINERATION OF TRANSURANICS IN THE FDI SYSTEM

Nuclide	Inventories (BOC) [t]	Net Incineration rate [kg/500MW*yr] (BOC)	Fission rate [kg/500MW*yr] (BOC)
^{237}Np	0.21	8.49	1.56
^{238}Pu	0.29	1.83	5.6
^{239}Pu	4.28	149.3	121.2
^{240}Pu	2.36	5.28	17.7
^{241}Pu	0.87	20.9	33.9
^{242}Pu	0.87	4.8	4.8
^{241}Am	0.60	23.0	3.56
^{242m}Am	0.004	-19.3	0.1
^{243}Am	0.53	14.0	2.4
Total	10.004	208.3	190.8

First it should be reminded here that efficiency of the incineration is predominantly affected by the composition of the inventory of incinerated actinides. On this basis one can distinguish whether the destruction of given nuclide signifies its transmutation into some other actinide or is a real destruction of an actinide nuclide by fissioning. Such composition, however, cannot be chosen arbitrarily, as being determined first of all by the composition of spent fuel to be incinerated. In addition, as it was mentioned due to the technical reasons it was decided to neglect Cm in the initial inventory above.

It is interesting to look at the differences between the net incineration rates and the fission rates. One sees, for instance, that ^{237}Np is effectively incinerated rather apparently, since its fissioning contributes to the incineration only in less than 20%. To the contrary ^{240}Pu is fissioned quite efficiently, but the net incineration is rather low as the captures in ^{239}Pu supply a 'fresh' ^{240}Pu.

Unfortunately, high incineration of ^{243}Am signifies production of ^{244}Cm, that cannot be destroyed at that moment at all (similarly ^{242m}Am, nearly absent in the input is net produced — until build-up). Yet, the incineration of Pu and Np in general is very efficient, that of Am can be so qualified too, but provided that Cm is incinerated also.

11.4. Proposed conceptual solutions

In general, two primary objectives of transmutations can be considered:

— Incineration of actinides and only if reasonable, of other radwaste;
— In addition to current exoergic actinide destruction, a supply of fuel for future use.

A number of options of power systems with transmutation unit have been proposed, principally distinct by different assumptions of primary objectives. One can aim either at a more farsighted objective of designing a self-sustaining nuclear power system with closed fuel cycle or confine oneself to a development of technology of incineration of nuclear waste (the global amount of which anyway will continue to grow during next half century). The example (Fig. 17) of a symbiotic system: LWRs-incinerator, illustrates an option recommended here while leaving open the alternatives of material flows and their quantitative estimations. That choice has been made in belief that assisting the present mature and economically competitive nuclear power technology to close the fuel cycle has most chances of being realized in a foreseeable future.

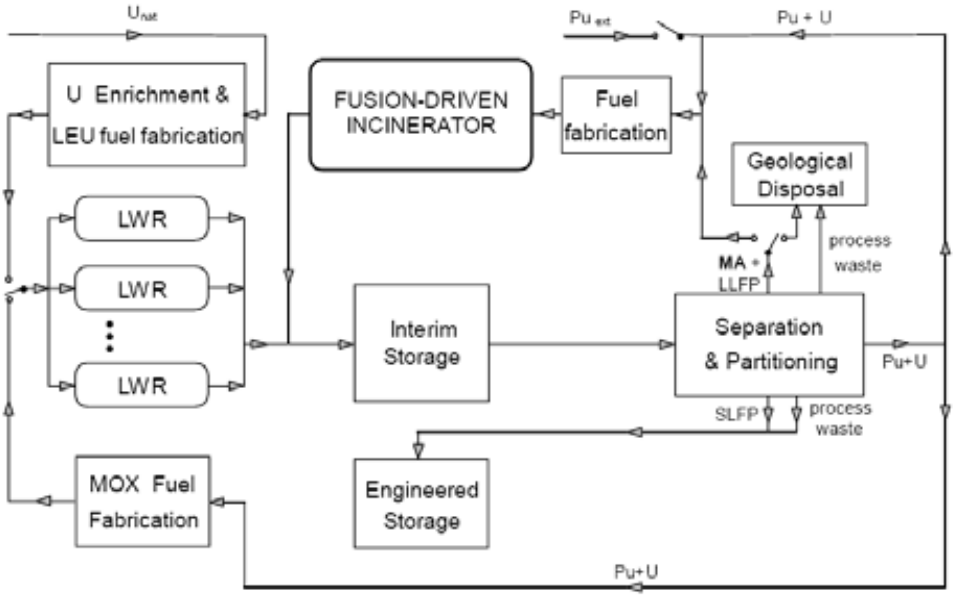

FIG. 17. Symbiotic nuclear power system/U-Pu cycle/with fusion-driven subcritical unit/LEU — Low Enriched Uranium, SLFP — Short Lived Fission Products/.

Another reason results from the French studies indicating a successful admixing of sole ^{237}Np to the regular LWR fuel [17]. Seeing that, Pu, Np and of Am have been accepted in the MA input but not Cm since its small fractions of 0.25% heighten the γ and neutron background respectively by two orders of magnitude, thus drawing behind an inadmissible increase in the fabrication costs.

In the frame of a symbiotic system two extreme variants can be noted:

1. Conservative — waste incinerating system (e.g. stored Pu and MA) without regeneration of fissile nuclides;
2. Optimistic — self-sustaining nuclear power system (more precisely, assuming a replenishment of incinerated actinides in the system with natural or depleted uranium or thorium) and restrained to use only self-generated fissile materials (except of initial inventory).

Between these extremes there are plenty of intermediate options; in any case a long perspective of low uranium prices gives at present no premises for the extreme future-oriented variant.

There are a number of concepts of devices for transmutations mostly of a hard spectrum as e.g. the pool type reactors cooled with liquid Pb or Pb-Bi eutectics, descending from Russian submarine propulsion units. The advantage of this solution is that it excludes a core melt. However, fast water-cooled systems as based upon the most common technology deserve mentioning too [18].

Qualitatively, the principal material flow is to be as follows: the LWRs can be supplied with both types of fuel — the LEU or the MOX. In spent fuel recycling, U and Pu are separated first, then the MAs from the rest, i.e. from the fission products. In thermal spectra, Pu can be recycled at most twice because of incineration of fissile isotopes ^{239}Pu and ^{241}Pu. Therefore, Pu must be regularly 'refreshed' in a harder spectrum, in the transmuting unit together with other MAs, namely Am and Cm. The regenerated Pu returns as a MOX fuel associated with Np to the LWRs. This optimistic picture is unfortunately darkened by the threat of positive void reactivity coefficients (due to a spectrum hardening as a result of moderator dilatation [19] that due to the relation and shape of fission and capture cross-sections of MA favours the former. According to some authors [5], in thermal systems the fraction of MA should not exceed 5% in the inventory of actinides to be transmuted. Thus, for safety reasons, the asymptotic composition of incinerated actinides should be very well known and its reactivity coefficients reliably checked. This composition, however, depends on many factors that cannot be determined at present. Though a decisive choice among particular concepts already now would be premature, there are good grounds for doubts if the equilibrium actinide compositions can have safe reactivity coefficients at the neutron balance assuring criticality. Therefore, it should be expected that the whole transmutation process will not be licensed in critical reactors, thus the use of subcritical systems may prove indispensable.

Another objective is not only to keep the neutron multiplication factor k_{eff} below a certain value recognised as safe one but also maintain a quasi-steady k_{eff} over the whole fuel campaign. Such a stabilisation of k_{eff} in subcritical systems would allow for keeping the energy gain of the system constant that is desirable in order to have always the optimum load of its fusion component. While expecting a difficult neutron balance, no use of burnable poisons is recommended in response to changing actinide composition (and content) in the system. An example of evaluations of asymptotic composition is shown in Fig. 18. On the other hand, since fissile incineration and breeding are not uniform in space and time, an adequate shuffling of the fuel within the assembly may prove indispensable requiring, in turn, elaboration of a respective shuffling procedure. The information about the composition of recycled fuel is important also for radiochemists charged with development of partitioning methods on industrial scale without which a closed fuel cycle would remain out of question.

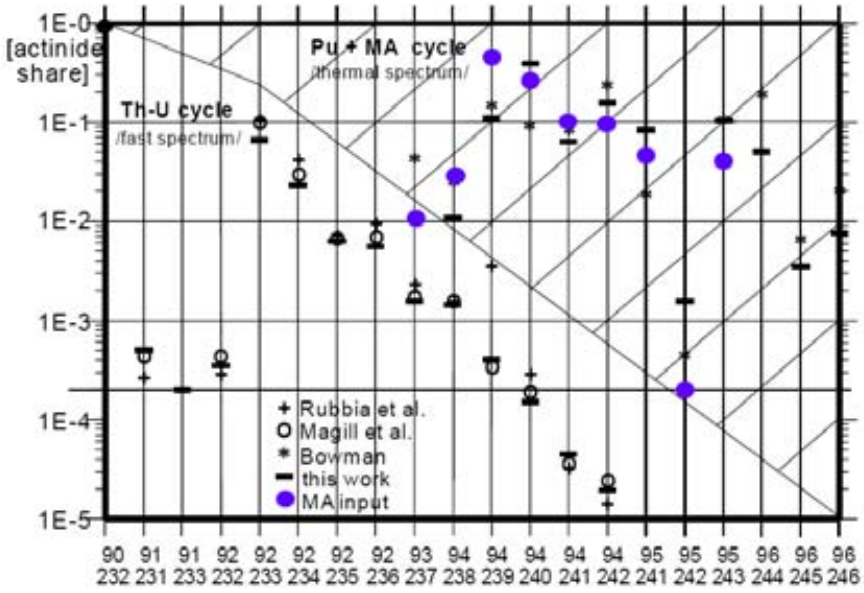

FIG. 18. Examples of equilibrium actinide compositions [20-22].

The fair agreement of the results obtained here with those given in Refs [20, 21] is fully satisfying, when remembering that in the present calculations the unknown details of referenced ones could not be reflected. Besides the advantages of Th-U cycle lying in ca. 3 orders of magnitude lower Pu content and still much lesser of transplutonics are quantitatively shown.

The hitherto noticeable lack of motivations for research of subcritical systems can explain why not all their properties can be recognised yet as thoroughly known. For instance, weakly coupled subcritical systems deserve some more investigations [23]. The significance of respective research is based upon the expectation of achieving much higher system power without heightening of its k_{eff}, i.e. at unaffected safety of the system. A need of flexibility in fuel compositions (there are options of homo-and-heterogeneous recycling) draws behind necessity of separating of all actinides (mutually) and from fission products. Meanwhile, chemical affinity of lanthanides and MA makes these processes difficult with classical chemical methods. Thus, one needs to apply more sophisticated ways e.g. pyrometallurgy and electrorefining. Yet, the assumption that separation processes can be carried out at exactly 100% efficiency is over-optimistic. Separation factors though well exceeding 0.99 (even so high values as 0.9995 can be noticed in the pertinent bibliography) still do not assure null concentrations in the depleted fractions. It signifies that at present, one can expect final reduction of actinide waste by more than two orders of magnitude, but not to zero.

On such a background has appeared the concept of applying of fusion-driven systems (FDI) for the neutralisation of nuclear waste with power production.

11.5. Conclusions

The concept of fusion-driven incinerator system provides a feasible way of radical reduction of necessary plasma Q of fusion reactors. Thanks to fission component the 14 MeV neutrons yield can be reduced by factor of several tens, thus, among others, the neutron induced radiation damage in the system. First of all in the first wall but also in the divertor due to a general reduction of the fusion component in the system. The distribution of nuclear heating is well flattened.

Symbiotic character of the proposed nuclear energy system composed of a fusion-driven subcritical assembly and existing LWRs does not urge to a revolutionary turning point in development of nuclear energy by pretending to replace all the present power plants. The FDI applied for transmutations of actinide waste thus associated with energy production seem to be a most attractive emerging option of nuclear power. While incinerating the most toxic long lived actinide waste realization of this concept

can efficiently shorten the duration of related hazard. The fissioning of materials that could not be licensed in critical systems (i.e. transplutonics) makes this operation safe in subcritical assemblies, thus promising to achieve a closed fuel cycle. Moreover, it must emphasized that radical abatement of actinides i.e. of the main source of heat in the long range, facilitates and reduces costs and scale of the waste disposal in geological repositories.

Thus, the fusion-driven incinerator concept — small, simple and cheaper deserves consideration — also as an intermediate step towards the Pure Fusion.

Summarizing, on the basis of the presented discussion and evaluations, one can state that the concept of fusion-driven subcritical systems for transmutations should approach deployment of fusion energy, as being just a technology that reduces environmental impact of present nuclear energy thus having a positive social undertone.

REFERENCES TO CHAPTER 11

[1] TACZANOWSKI, S., Transmutations of radioactive nuclides in accelerator-driven subcritical systems, Postepy Techniki Jadrowej, Vol. 41 (1998) pp. 437-41 (in Polish).

[2] BRAET, J., et al., Perspectives on the Use of Civil Plutonium, Trans. of Am. Nucl. Soc., 78 (1998) pp. 57-58.

[3] LIDSKY, L.M., Fission-Fusion Systems: Hybrid, Symbiotic and Augean, Nuclear Fusion, Vol. 15 (1975) pp. 151-172.

[4] TACZANOWSKI, S., 'Transmutations of nuclear waste in accelerator-driven subcritical systems', Applied Energy, 75 (2003) pp. 97-117.

[5] ABRAHAMS, K., et al. Transmutation of Nuclear Waste in Nuclear Reactors, IV Eur. Conf. on Management and Disposal of Radioactive Waste, EUR 17543 EN (March 1996) pp. (71-85).

[6] YOSHIDA, H., et al. A strategic study of the partitioning and transmutation system, Proc. Int. Conf. Emerging Nucl. Energy Syst., ICENES'93, Chiba, Japan, World Scientific (September 1993) pp. 463-467.

[7] Euratom N° 96/29, Official Journal of the European Communities, Vol. 39 (1996).

[8] MASSEY, J.V., SCHNEIDER, A., The Role of Plutonium-238 in Nuclear Fuel Cycles, Nucl. Techn., 56 (1982) pp. 55-71.

[9] TACZANOWSKI, S., HARMS, A.A., Flux spectrum extremisation criteria for blankets sustained by exogenous neutrons, Atomkernenergie, Vol. 41, 99 (1982).

[10] TACZANOWSKI, S., CETNAR, J., DOMAŃSKA, G., Fusion-driven transmutations of nuclear waste — a misconception or an incentive for promotion of fusion energy?, Fus. Eng. & Des. 41 (1998) pp. 455-460.

[11] TACZANOWSKI, S., Neutronic Study of Nonproliferation Oriented Options of Fusion- and Accelerator-driven Transmutation Systems, Proc. ICENES'96 Obninsk (June 1996) pp. 701-714.

[12] TACZANOWSKI, S., JANCZYSZYN, J., POHORECKI, W., Transmutation of Transuranics in Tandem Mirror Subcritical Blanket, paper presented in Research Coordination Meeting of the CRP on Studies of Advanced Reactor Technology Options for Effective Incineration of Radioactive Waste", 22–26 November 2004, Hefei, China.

[13] http://www.ndc.tokai-sc.jaea.go.jp/j33fig/findex.htm

[14] http://atom.kaeri.re.kr/cgi-bin/endfform.pl

[15] YOUSSEF, M., UCLA, paper presented in 6th APEX and FHPD Workshop, UCLA, 16-19 February 1999.

[16] TACZANOWSKI, S., POHORECKI, W., KOPEC, M., Activation of the divertor region as a function of different designs and configurations, Poland/TW4-TRP-002D2f, Power Plant Conceptual Study (2005).

[17] BERNHARD, H., PRUNIER, C., Future Nuclear Fuels for Plutonium and Minor Actinides Recycling, Proc. GLOBAL'97, Intl Conf on Future Nuclear Systems, Yokohama, Japan (October 1997) pp. 518-522.

[18] TAKAHASHI, H., ZHANG, J., Accelerator-driven light water fast reactor, paper presented in III Int. Conf. on Accelerator-Driven Transmutation Technology & Applications, Prague, CD ROM Tu-O-F21, June 1999.

[19] SALVATORES, M., et al., Role of Accelerator-Driven Systems in Waste Incineration Scenarios, Proc. GLOBAL'97, Intl Conf on Future Nuclear Systems, Yokohama, Japan (October 1997) pp. 561-567.

[20] RUBBIA, C., et al., Conceptual Design of a Fast Neutron Operated High Power Energy Amplifier, CERN/AT/95-44ET (1995).

[21] BOWMAN, C., Accelerator-driven systems for nuclear waste transmutation, Annu. Rev. Nucl. Part. Sci. 1998. 48 (1998) pp. 505-556.

[22] MAGILL, J. et al., Inherent Limitations in Toxicity Reduction Associated with Fast Energy Amplifiers, Proc. of II ADTTA, Kalmar, Sweden (1996) pp. 1114-1120.

[23] TACZANOWSKI, S., Selected Properties of Asymmetrically Coupled Subcritical Systems for Transmutations, IAEA Tech. Com. Meeting, Madrid, September 1997, IAEA TC-903.3, (1999) pp. 403-428.

[24] TACZANOWSKI, S., Transmutations of Long Lived Radioactive Nuclides of the Spent Nuclear Fuel, Summer School of Nuclear Energy, Warsaw, Rep. IEA-71/A (2001) p.197 (in Polish).

CHAPTER 12. DOMAIN–VIII: FISSION-FUSION HYBRID REACTOR (TOKAMAK CONCEPT)

12.1. Introduction

The conventional fission nuclear industry has been problematic as there has been no conclusion about how to solve the shortage of nuclear resources and how to effectively deal with the high level waste (HLW) in addition to nuclear safety issues and proliferation. The fusion-driven subcritical system (a kind of fusion-fission hybrid reactor) has very attractive advantages because of its potential ability to achieve effective transmutation of long lived radioactive wastes from spent fuel of fission industry, efficient breeding of fissile fuel to supply for fission industry and other near term applications based on feasible fusion plasma physics and technology. A series of design activities on the fusion-driven subcritical system (the reference design is named FDS-I), which consists of the fusion neutron driver with relatively easy-achieved plasma parameters and the subcritical blanket used to transmute long-lived nuclear wastes and to generate energy on the basis of self-sustaining of tritium needed for fusion reaction in plasma core and plutonium needed for neutron multiplication in the subcritical blanket, have been being carried out to evaluate and optimize the concept in China [1-6].

An overview of the FDS-I design is presented and the summary of FDS-I conceptual study activities were summarized in Ref. [2], which the main reference parameters of the FDS-I design were given covering plasma physics and engineering of the fusion neutron driver, blanket neutronics, blanket thermal-hydraulics, safety & environmental impact and cost & benefit analysis etc. An overview of the FDS-I reference model is shown in Fig. 1.

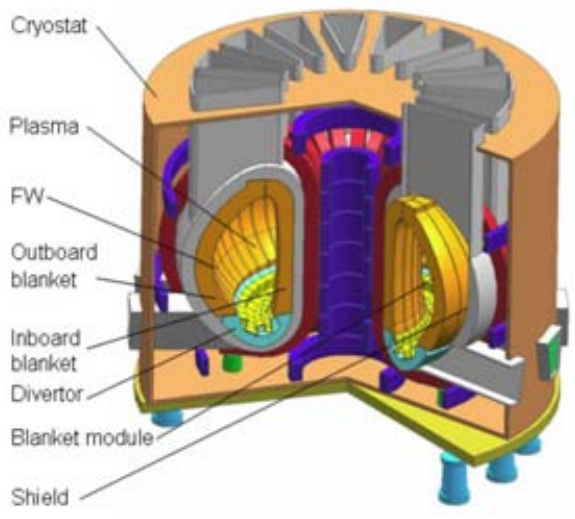

FIG. 1. Overview of FDS-I reference model.

12.2. FDS-I conceptual design

12.2.1. *Fusion core*

The major objective of FDS-I is to demonstrate the feasibility of early application of fusion energy technology. The plasma physics and engineering parameters of FDS-I are selected on the basis of considering the progress in recent experiments and associated theoretical studies of magnetic confinement fusion plasma and the progress in studies of blanket concepts optimization to reduce the requirement for neutron source intensity and subsequently plasma technologies. A set of plasma-related parameters of FDS-I are given in Table 1, as well as those of the International Thermonuclear Experimental Reactor (**ITER**) [7] for the purpose of comparison. It is understandable that the FDS-I requirement for plasma technology could be met by the development of ITER. More details on design optimization of fusion plasma core are being carried out.

TABLE 1. MAIN CORE PARAMETERS OF FDS-I

Parameters	Design	
	FDS-I	ITER
Fusion power (MW)	150	500
Major radius(m)	4	6.2
Minor radius(m)	1	2
Aspect ratio	4	3.1
Plasma elongation	1.7	1.7
Triangularity	0.4	0.33
Plasma current (MA)	6.3	15
Toroidal field on axis (T)	6.1	5.3
Safety factor /q_{95}	3.5	3
Auxiliary power /Padd(MW)	50	73
Energy multiplication /Q	3	≥10
Average neutron wall load($MW \cdot m^{-2}$)	0.5	0.57
Average surface heat load ($MW \cdot m^{-2}$)	0.1	0.2

12.2.2. Blanket concept and reference module

The general idea of a fusion-fission subcritical system is to have the subcritical blanket which is to interact with a copious source of fusion neutrons provided by the fusion core to achieve its multi-functions such as nuclear waste transmutation, fissile fuel and tritium breeding. The FDS-I blanket design focuses on the technology feasibility and concept attractiveness to meet the requirement for fuel sustainability, safety margin and operation economy. A series of design scenarios, with emphasis on circulating particle or pebble bed fuel forms considering geometry complexity of tokamak, frequency of fuel discharge and reload (including design of an emergency fuel discharge sub-system to improve the safety potential of the system), are being evaluated and optimized considering various blanket module structure and fuel forms. A design and its analysis on the helium-gas and liquid lithium-lead (LiPb) eutectic Dual-cooled Waste Transmutation **(DWT)** blanket with **C**arbide heavy nuclide **P**article fuel in circulating **L**iquid LiPb coolant (named **DWT-CPL**) are presented in this report. Other concepts such as the **DWT** blanket with **O**xide heavy nuclide **P**epper pebble bed fuel cooled in circulating helium-**G**as (named **DWT-OPG**) and with **N**itride heavy nuclide **P**article fuel in circulating helium-**G**as (named **DWT-NPG**) are also being investigated.

The basic concept of the DWT-CPL blanket has been presented previously in Ref. [1.8], in which helium gas was adopted to cool the structural walls and long lived **F**ission **P**roduct (**FP**:^{99}Tc, ^{129}I, ^{135}Cs) transmutation zones(**FP-zones**), **L**iquid **M**etal (**LM**) LiPb eutectic with tiny particle long lived fuel to self-cool Actinide **(AC**: MA, Pu, U etc.**)** zones (**AC-zones or LM-zones)**including **M**inor **A**ctinides (**MA**: ^{237}Np, ^{241}Am, ^{243}Am, ^{244}Cm) transmutation zones (**MA-zones**) and **U**ranium-loaded fissile fuel breeding zones (**U-zones**). LiPb in **AC**-zones serves as coolant, tritium breeder and fuel circulating carrier. Pb is also a kind of neutron multiplier. High energy neutrons from D-T fusion reactions and AC fission reactions are moderated in FP-zones with graphite. In the current design, only plutonium (**Pu**) isotopes from the spent fuel of fission power plants e.g. **PWR** is loaded into the blanket as neutron multiplier instead of part of Pu coming from U-zones, that is, the U-zones are replaced with additional MA-zones, which results in a fertile-free blanket. The reduced activation ferritic-martensitic steel (**RAFM** e.g. **CLAM**) [9] is considered as an alternative structural material because of its good performance in the highly corrosive environment of most intense radiation. The AC appears in the form of the TRISO (TRi-ISOtropic)-like carbide particles coated with SiC suspending in the LiPb slurry. The circulating fuel form has the advantages of good compatibility with complex geometry, easy control of fuel cycle and fast response to emergency fuel removal etc. The reference module, basic material compositions and radial sizes of DWT-CPL blanket at the tokamak mid-plane of FDS-I are given as in Fig. 2 and Table 2.

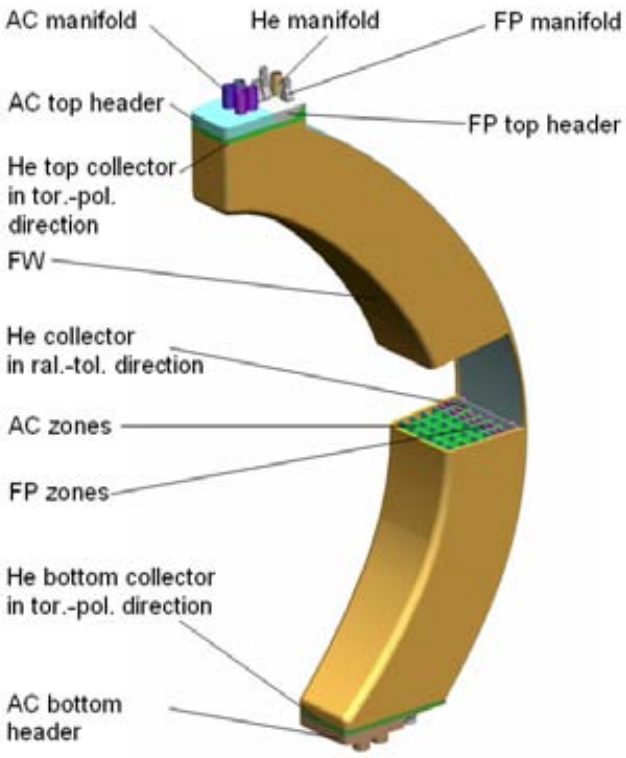

FIG. 2. Reference module of DWT-CPL blanket.

TABLE 2. MATERIAL COMPOSITIONS AND RADIAL SIZES OF DWT-CPL BLANKET

Zones	Material composition (vol.%)	Thickness (cm)
Inboard blanket		
FW	CLAM(54.64%); He(45.36%)	3
Tritium breeding zone	LiPb (100%)	11/11
Structural walls	CLAM (60%); He(40%)	1/1
Neutron reflector	Graphite (100%)	13
Helium manifold	CLAM (31.8%); He(68.2%)	10
Shield layer	CLAM (75%); H_2O(25%)	30
Outboard blanket		
FW	CLAM(54.68%); He(45.32%)	3
AC-1/AC-2/AC-3	(MAC)C(0.649%); (PuC)C(5.38%); Li17Pb83(93.971%)	10/10/10
Structural walls	CLAM steel(60%); He(40%)	1/1/1/1/1
FP(CsCl/ NaI/ Tc)	FP(1.22%/0.7033%/0.7858%); graphite(60%); He(38.78%/39.3%/39.2%)	12/12/12
Helium manifold	CLAM(38.3%); He(61.7%)	11
Shield layer	CLAM(75%); H_2O(25%)	60

FDS-I is an innovative nuclear system with new features, some of which are related to its transient safety characteristics caused by using the dedicated fuel, although inherent and passive safety measures may be integrated into the defense lines. Transient accidents of the FDS-I may occur due to the perturbation of external neutron source, the failure of functional device, and occurrence of the uncontrolled event, though 'critical' accident can be avoided by the inherent safety characteristic of deep subcriticality. So the analysis of transient scenarios needs to be performed to meet the safety requirements of the engineering design and the human environment. Moreover, inherent features are valuable means for minimizing public concern and gaining public perception on new reactor concepts. There is a consensus among reactor designers, supporting the value of passive safety designs.

12.3. Computational models, codes and data

12.3.1. *Calculation models*

12.3.1.1. Neutronics models

There were three neutronics models, one-dimensional (1D) sphere, two-dimensional (2D) cylinder and three-dimensional (3D) cylinder, had been applied to the neutronics analyses. The three geometry models were created by neutronics automatic modeling programs MCAM [10, 11] and SNAM [12].

The 1D calculations are based on a sphere geometry model with a uniform neutron source extended in all directions shown in Fig. 3(a) and (b). The 2D modeling is needed to properly account for the poloidal heterogeneity. Due to the limitation of 2D modeling, the model is assumed to have a uniform height of 6.6 m. The section and stereograms drawing of 2D model are shown in Fig. 4(a) and (b), respectively.

Because of symmetry, only 1/16 of the chamber is modeled in 3D modeling with reflecting boundaries, shown in Fig. 5 (a) and (b). The 3D model is used considering the effects of upper port and mid-plane port. The toroidal angle of upper port and mid-plane port is 7.5° and poloidal dimension of mid-plane port is 130 cm. The top view of upper port and mid-plane port are given in Fig. 5 (c) and (d).

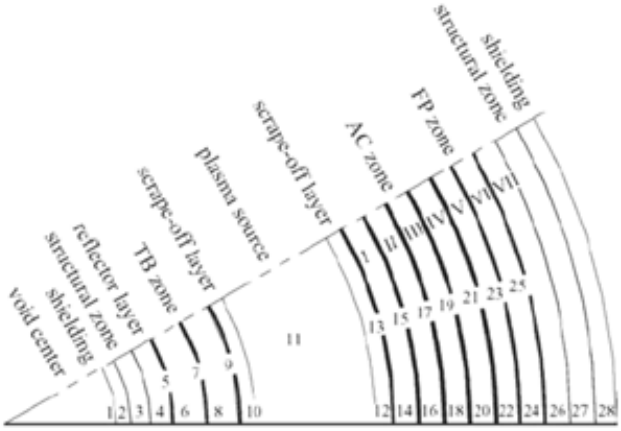

FIG. 3(a). The section drawing of 1D sphere geometrical model.

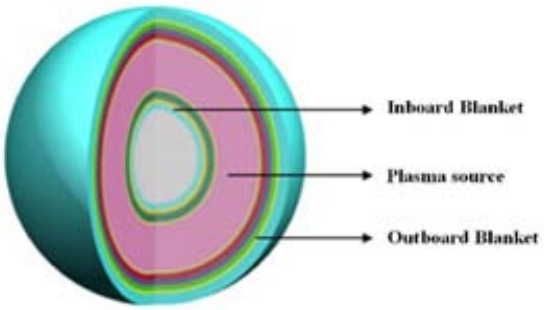

FIG. 3(b). 1D sphere geometrical model in MCAM and SNAM.

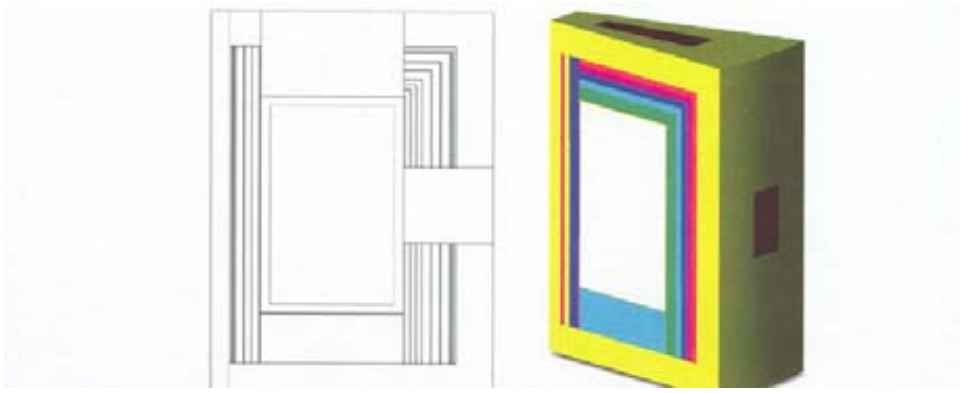

FIG. 4(a) The section drawing of 2D cylinder geometrical model.

FIG. 4(b) 2D cylinder geometrical model in MCAM and SNAM.

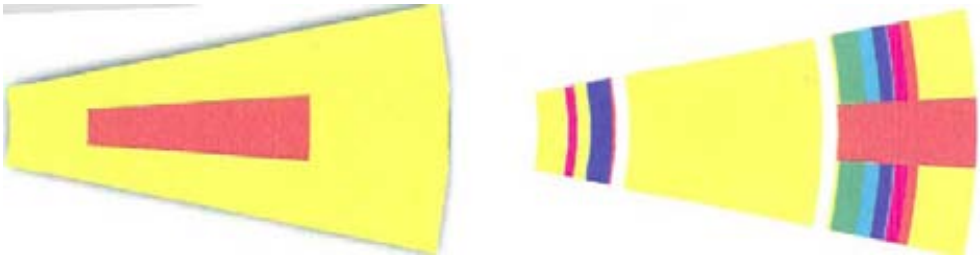

FIG. 5(a) The top view of upper port by MCAM.

FIG. 5(b) The top view of mid-plane Port by MCAM.

12.3.1.2. Accident analysis model

The principal design parameters of the FDS-I for accident analysis are displayed in Table 3. The calculation model is simplified according to the functions and material compositions. The geometric model for FDS-I/DWT-CPL analysis is illustrated in Fig. 6. The present simulation is assumed to be 2D symmetric in toroidal direction. In the IB for breeding tritium, the LiPb flows from bottom to top. In the OB for waste transmutation, the two phase fluid model of fuel particle/LiPb is adopted. The reflect zones and shield zone locate in the OB. All of the fertile fuels are loaded in the AC zones in the OB, which are the most important zones for safety analysis. The temperatures of the coolant and fuel particles in the OB, and the reactivity and power of the system in the transients scenarios as well, are the key parameters for analysis.

TABLE 3. PRINCIPAL DESIGN PARAMETERS OF FDS-I/DWT-CPL

Space dimension	2D R-Z
External neutron source	D-T neutron (14MeV)
Fusion power	150 MW
Initial Thermal power	4.2 GW
Fuel type	MAC, PuC (coated particle)
Tritium breeder	LiPb
Coolant	Liquid LiPb/Helium gas
Inlet LiPb velocity	2 m/s
Inlet LiPb temperature	523 K
Outlet LiPb pressure	1MPa

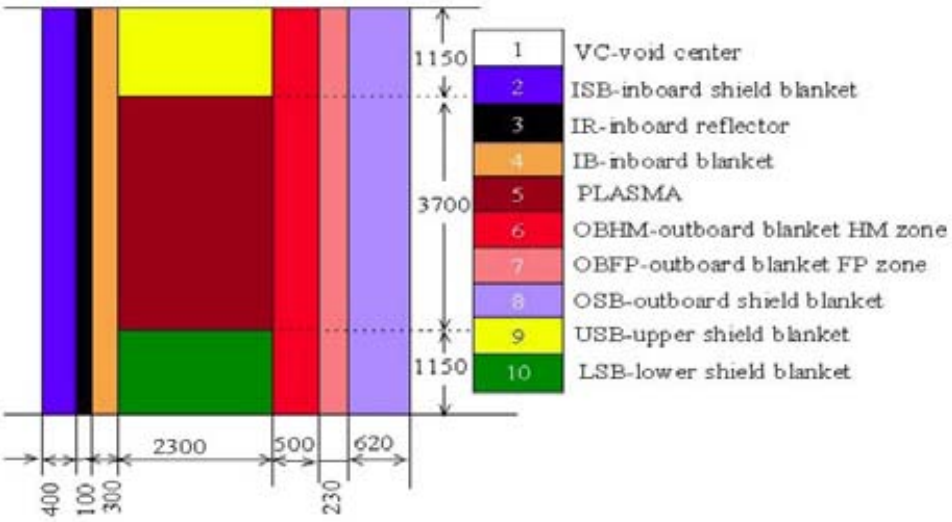

FIG. 6. Geometric model for accident analyses.

12.3.2. *Codes*

The static neutronics parameters and the burnup results are calculated by VisualBUS2.0[2.4], which is the home-developed multi-dimensional transport and burnup calculation code. The kinetics parameters are calculated by MCNP [14]. The transient analysis of typical accident scenarios was performed with a home-developed neutronics thermo-hydraulics coupling code NTC2D [15].

12.3.2.1. Integrated multi-functional neutronics analysis system — VisualBUS

An integrated software system for shielding calculation and modeling, VisualBUS, has been developed by FDS Team, Institute of Plasma Physics, China Academy of Sciences. VisualBUS, as a multi-functional neutronics analysis system, includes calculation modules, modeling modules and nuclear data libraries. Calculation modules consist of transport, burnup, activation and thermal-hydraulics calculations, which can be coupled or streamed together to run in a batch way or interactively started. Transport calculation for shielding analysis can be simulated by using either the Monte Carlo (MC) method, Discrete Ordinates (SN) method or MC-SN coupled method on the basis of the multi-dimensional geometry models.

VisualBUS has three modeling functional modules, MCAM (Monte-Carlo Automatic Modeling), SNAM (SN Automatic Modeling), and RCAM (Radiation Coupled Automatic Modeling). Nuclear database HENDL [16, 17] (Hybrid Evaluated Nuclear Data Library) is also included.

MCAM, developed by FDS Team to address the Monte Carlo particle transport modeling predicament, is an integrated interface program between commercial CAD systems and Monte Carlo codes. With the progress of computer science, especially computer graphics and CAD technology, besides the accurate bidirectional conversion between CAD and neutronics models, MCAM also supports model creating, CAD model fixing, neutronics model analyzing and editing, which make it an integrated modeling environment for Monte Carlo particle transport simulation codes. MCAM can be used for shielding analyses of fusion/fission/hybrid reactors and accelerator systems, criticality safety, nuclear safeguards, radiation detector, nuclear well logging, health physics, medical physics, aerospace, etc.

MCAM can be used for shielding simulation of fusion/fission/hybrid reactors and accelerator systems, criticality safety, nuclear safeguards, radiation detector, nuclear well logging, health physics, medical physics, aerospace, etc. Currently, MCAM had been successfully applied in FDS series fusion power plants designs [18], nuclear analyses of ITER joint international research and development project such as the Upper Ports [19], neutronics design of CREST[20] and shielding analysis of EAST [21].

SNAM, developed by FDS Team, is an integrated interface program between CAD systems and SN codes. It can convert CAD engineering model created in commercial CAD software system to neutronics model, and then automatically generate the input file for SN codes. Moreover, the existing input files, created for SN codes, can also be automatically parsed and converted to CAD model by SNAM. SNAM can also visualize the real-time or post-process calculating results of SN codes, which facilitates the user to analyze the physics essentials.

RCAM combines the modeling function of MCAM and SNAM for combined MC-SN simulation of a complex and large nuclear system and could seamlessly cooperate with the simulation codes in the background to carry out the actual coupled calculations according to users' requirements. In this case, the region with complex geometry representation can be processed and simulated by MC method and the region with the simple geometry representation and large size can be processed and simulated by SN method. A transitional region with optimized size can be defined to achieve the boundary combination of MC and SN simulations.

12.3.2.2. Neutronics thermo-hydraulics coupling code — NTC2D

NTC2D is a two-dimensional, multi-velocity-field, multiphase, multi-component, Eulerian, fluid-dynamics code coupled with a space-dependent and energy-dependent neutron kinetics model for transient safety analysis of reactor. The reactor neutronics behavior is predicted by solving discrete ordinates neutron transport equation of space, energy, and time-dependent. Temperature and background effects are based on Bondarenko formalism (self-shielding factor approach). The thermal-hydraulics calculation solves multi-component, multiphase, multifield equations for mass, momentum, and energy conservation. Neutronics and Thermo-hydraulics calculations are coupled by feedback of nuclear heating, temperature and density of fuel and coolant.

12.3.3. *Data libraries*

12.3.3.1. Hybrid evaluated nuclear data library — HENDL

To meet the need for calculation and optimization of fusion, fission and fusion-fission hybrid systems, a hybrid evaluated nuclear data library which named HENDL has been developed by FDS Team. It is a compilation of nuclear data selected from the various national and international evaluated nuclear data files. Several working libraries are prepared, e.g. the coupled neutron gamma-ray multi-group library HENDL/MG for the SN transport calculation and continuous point-wise neutron data library HENDL/MC for the MC transport calculation as well as those for burnup and activation calculations. Some special purpose working libraries e.g. for self-shielding effects analysis are also custom-tailored. A series of data test analyses have been performed to validate and qualify the HENDL working libraries.

12.3.3.2. Thermal physical properties data library

For safety analysis of reactor, thermodynamic properties of reactor materials are needed over a very wide temperature and pressure ranges. The method is used to be based on generalized Van-der-Waals equation with the most reliable experiment data of liquid phase density and vapor pressure to obtain critical parameters, and then the EOS parameters are determined from the characteristic of the critical point and vapor thermodynamic states which are represented by using MRK equation. Further more, internal energy and enthalpy of vapor and liquid are calculated with the evaluated EOS. And the speed of sound in liquid materials, which is required to calculate liquid compressibility, is also estimated.

12.4. Static analyses

FDS-I is an advanced reactor system which has the characteristics of a strong anisotropic neutron flux distribution, wide range of neutron energy, and spatial non-uniformity of the power density distribution caused by the external neutron source and the heterogeneous material distribution. To assess the modeling approach for neutronics models, the same material compositions cases for multi-dimensional

neutronics models are firstly analyzed, where the material compositions in each corresponding zone for different models are kept the same. The static neutronics parameters of the multi-dimensional neutronics models with the same material compositions are shown in Table 4. Values have been calculated and analyzed here for the FDS-I/CPL DWT blanket concept with the system VisualBUS (SN method) and data library HENDL/MG with 175-group neutron and 42-group gamma.

TABLE 4. MATERIAL COMPOSITIONS AND DIMENSIONS FOR 1D/2D/3D MODELS

Zones	Material compositions (vol.%)	Dimensions (cm)
Inboard blanket		
FW	CLAM(54.64%); He(45.36%)	3
Tritium breeding zone	LiPb(100%)	11/11
Structural walls	CLAM(60%); He(40%)	1/1
Neutron reflector	C(100%)	13
Helium manifold	CLAM(31.8%); He(68.2%)	10
Outboard blanket		
FW	CLAM(54.68%); He(45.32%)	3
AC-1/AC-2 /AC-3	(MAC)C(0.649%); (PuC)C(5.38%); Li17Pb83(93.971%)	10/10/10
Structural walls	60%CLAM; 40%He	1/1/1/1/1
FP(CsCl/ NaI/ Tc)	FP(1.22%/0.7033%/0.7858%); graphite(60%); He(38.78% /39.3% /39.2%)	12/12/12
Helium manifold	CLAM(38.3%); He(61.7%)	11
Shield	CLAM(75%); H2O(25%)	60
Divertor		
W-plate	W(100%)	1
Cu-plate	Cu(100%)	1
divertor	CLAM(25%); He(75%)	83

The neutronics parameters analyzed here include three types:

— Characteristic parameters of the system: effective neutron multiplication factor (k_{eff}), energy deposition(P_{th}), energy gain(M);

— Reaction rates: tritium breeding ratio(TBR), waste transmutation ratio(WTR: the ratio of the transmutation number of waste nuclides (long lived actinides or fission products) induced by one external neutron to the initial number);

— Distribution parameters: power density distribution, flux distribution in the specific zones.

The characteristic parameters of the system and reaction rate parameters of 1D sphere/2D cylinder/3D cylinder models with the same material compositions are shown in Table 5.

12.4.1. *Characteristic parameters*

As shown in Table 35, the k_{eff} in the 2D/3D models are much lower than that in the 1D sphere model. For example, the k_{eff} in the 3D cylinder model at the beginning of operation is 0.737, but it is 0.947 in the 1D sphere model. Accordingly, the energy gain in the 3D cylinder model decrease rapidly to 17, which is only 12% of that in the 1D sphere model. Firstly, this is due to the leakage effects caused by the divertor and the ports in the 2D/3D models. Second, the loading inventories in the 2D/3D models are much less than that in the 1D sphere model so as to reduce the k_{eff} value greatly. The loading inventories and zone volumes in the 1D/2D/3D models are displayed in Table 6. The AC zone volume in the 2D cylinder model is ~62% of that in the 1D sphere model, while the AC zone volume in the 3D cylinder model is only ~52% of that in the 1D sphere model. Due to the same material compositions, the loading inventory in 3D model is ~52% of that in the 1D model.

TABLE 5. STATIC NEUTRONIC PARAMETERS OF 1D/2D/3D NEUTRONICS MODELS

Parameters	1D sphere	2D cylinder	3D cylinder
Systemic characteristic parameters			
K_{eff}	0.947	0.841	0.737
P_{th} (MW)	17211	5084	2067
M	143	42	17
Reaction rate parameters			
TBR	3.83	1.20	0.50
WTR_{LLMA} (AC-1/2/3)	0.26 (0.09/0.09/0.08)	0.08 (0.03/0.03/0.02)	0.03 (0.01/0.01/0.009)
WTR_{Pu} (AC-1/2/3)	9.77 (3.08/2.98/3.71)	2.78 (0.86/0.86/1.06)	1.08 (0.36/0.33/0.39)
$WTR_{^{135}Cs}$ (FP-1)	0.75	0.18	0.06
$WTR_{^{129}I}$ (FP-2)	0.39	0.12	0.04
$WTR_{^{99}Tc}$ (FP-3)	2.40	0.67	0.23

TABLE 6. WASTE LOADING INVENTORY AND THEIR ZONE VOLUME IN DWT BLANKET

	1D sphere		2D cylinder		3D cylinder	
	Loading inventory(kg)	Zone volume(m^3)	Loading inventory (kg)	Zone volume(m^3)	Loading inventory (kg)	Zone volume(m^3)
LLMA	5650	107.54	3518	66.96	3015	57.39
Pu	46850	107.54	29171	66.96	25003	57.39
^{135}Cs	1801	46.79	1136	29.51	986	25.62
^{129}I	1074	49.00	682	31.11	596	27.18
^{99}Tc	4675	51.26	2986	32.74	2625	28.78

12.4.2. *Reaction rates*

The TBR is 3.83 in the 1D sphere model, which is much higher than tritium sustainability design limit 1.1 [22]. The large tritium inventory generated can not only satisfy the self-sustaining of tritium, but also support other fusion reactors. The TBR in the 2D cylinder model is 1.2 which can also meet the requirement of self-sustaining of tritium. But the TBR in the 3D cylinder model is as low as 0.5 due to its low k_{eff} value, which can not meet the requirement of self-sustaining of tritium. Meanwhile, the difference of transmutation ratios in the AC zone and FP zone in the different dimensional models has the same tendency as TBR.

Regarding WTR, the Pu transmutation rate is higher than LLMA. Since ^{239}Pu, which is the main isotope in Pu, has rather large fission cross sections at low and moderate energy neutrons, but fission cross sections for LLMA are large only at high energy neutrons, the fission reactions are mainly from the fission of ^{239}Pu induced by low energy neutrons. As shown in Figs 7-9, there are large differences among the neutron spectrum of the three AC zones at low energies. The low energy neutron flux density is higher in the AC-3 zone than that in the AC-1/AC-2 zone which make Pu transmutation rate higher. The neutron spectrum in the three AC zones for the 1D/2D/3D models are displayed in Figs 7-9. From Figs 7-9 can be found that:

(1) Due to its similar distribution of space and material in the different models, the shapes of neutron spectrum are similar. The distance from the reactor core is longer, the shapes of neutron spectrum are more similar. This demonstrates that the difference of spatial distribution of flux density among the different models will decrease with increasing the distance from the neutron source;
(2) There are large differences among the neutron spectra in the 1D sphere/2D cylinder/3D cylinder models because of their different loading inventories and geometries. For example, the neutron flux density in the 1D sphere model is 4~6 times higher than that in the 3D cylinder model at high energies.

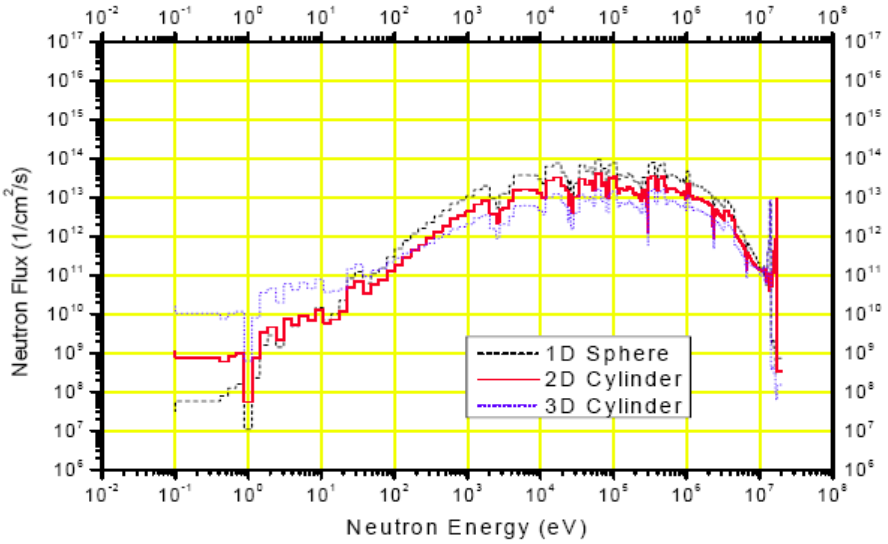

FIG. 7. Neutron spectrum in the AC-1 zone.

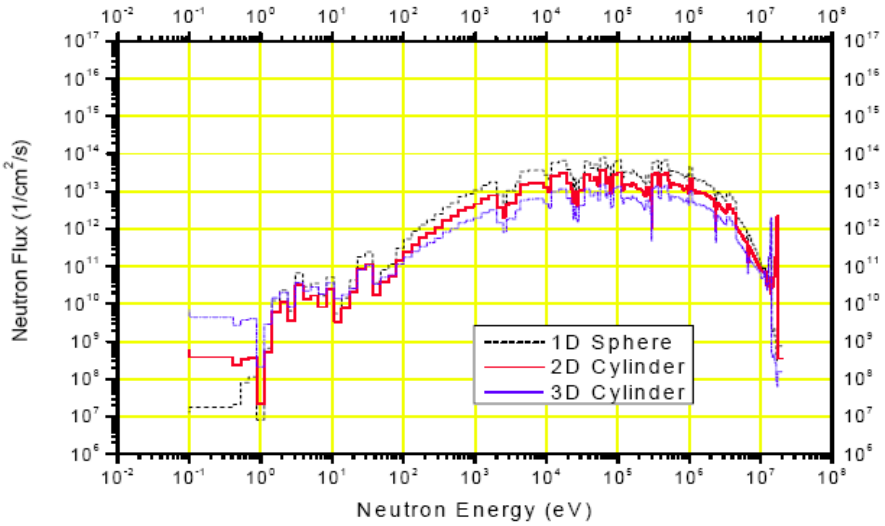

FIG. 8. Neutron spectrum in the AC-2 zone.

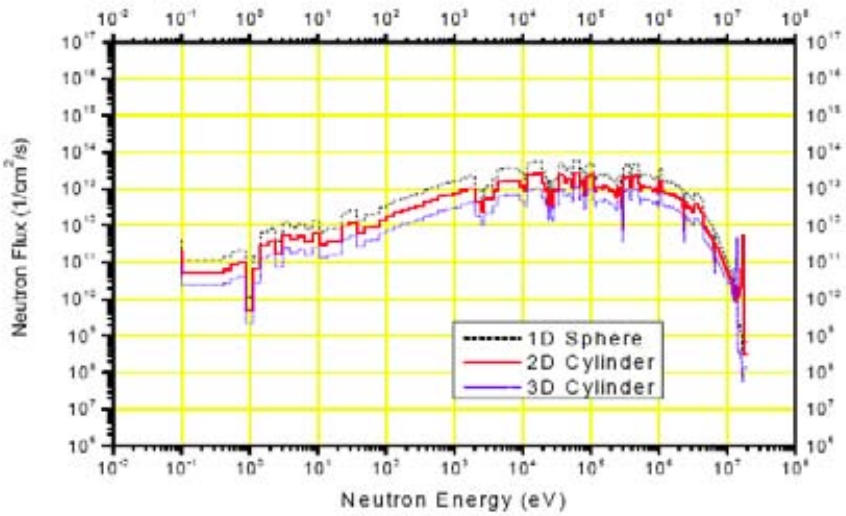

FIG. 9. Neutron spectrum in the AC-3 zone.

The three FP zones are filled with long lived fission products ^{99}Tc, ^{129}I and ^{135}Cs, respectively. The results of the FP transmutation ratio in the 1D sphere model are taken as an example to assess the transmutation ratio in the FP zones below. Figure 10 gives the neutron energy spectrum in the 3 FP zones of the 1D sphere model at the beginning of operation. The neutron flux densities in the FP zones at low energy are high. Meanwhile, the long lived FP products have much larger (n,γ) cross section at low energy than that at high energy [3.2] as shown in Table 7 and the FP transmutation rate depend on the (n,γ) reaction rates. So the thermal neutrons do much contribution to the FP transmutation.

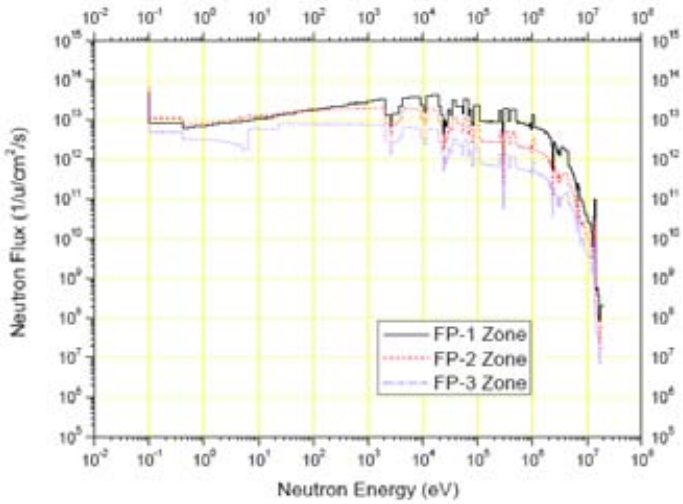

FIG. 10. Neutron spectra in three FP zones of the 1D sphere model.

TABLE 7. CAPTURE CROSS SECTIONS □(n,□) [b] OF ^{99}Tc, ^{129}I AND ^{135}Cs FOR FAST AND THERMAL NEUTRON SPECTRUM

Nuclide	fast spectrum (E_n=0.2MeV, Φ=10^{15}n/cm^2·S)	Thermal spectrum (E_n=1eV, Φ=10^{14} n/cm^2·S)
^{99}Tc	0.2	4.3
^{129}I	0.14	4.3
^{135}Cs	0.07	1.3

12.4.3. *Distribution parameters*

The power density distribution in the outboard blanket is displayed in Fig. 11. The power density distribution is very non-uniform and the distribution trends are similar for all the multi-dimensional models. Because that energy generated in the blanket is mainly from the fission reactions of Pu and MA in the AC zone, the power densities in the three AC zones are very high, while those in the FP zones, FW and helium manifold are 1~2 orders of magnitude lower. Since the material compositions in the AC zones are the same and the zones are close to each other, the power densities are close. Due to the maximal transmutation rate in AC-3 zone, the power density in AC-3 zone is highest with the value ~164 MW/m^3, which can still be taken away by the coolant in the AC zones.

Although the 1D sphere model can give some system parameters and radial distribution parameters approximately, it can not display axial distribution of parameters. Figures 12 and 13 give the axial distributions of power density in the three AC zones, FWs and tritium breeding zones of the 2D cylinder model, respectively. Due to highest flux density in the equator, the power density in the equator is highest.

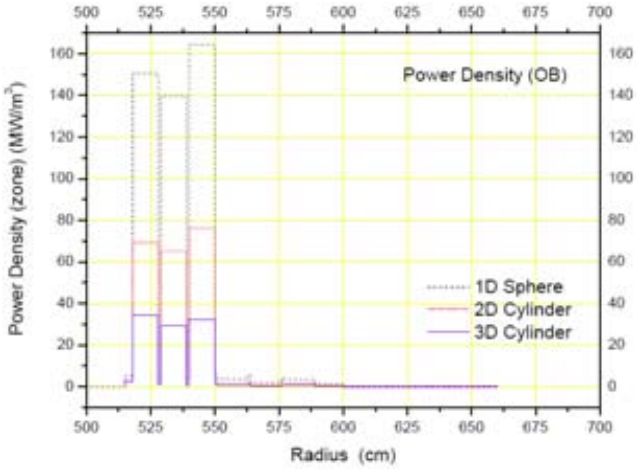

FIG. 11 Radial distribution of power density in the OB of 1D/2D/3D models.

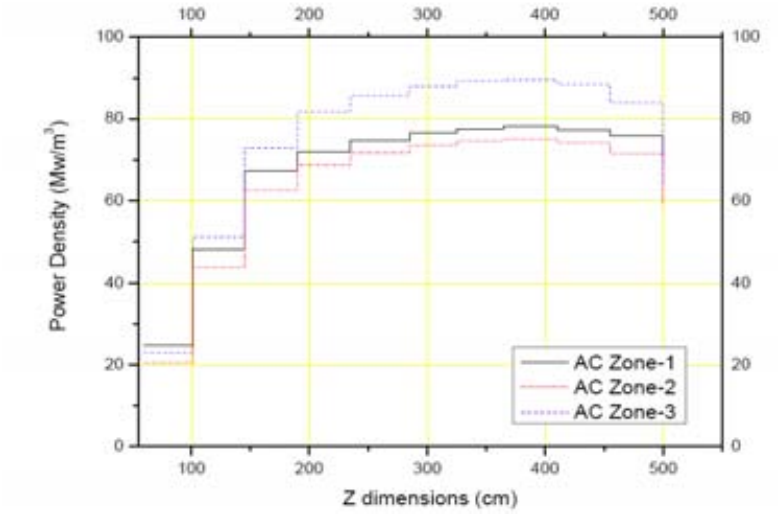

FIG. 12. Axial distribution of power density in the three AC zones of 2D cylinder model.

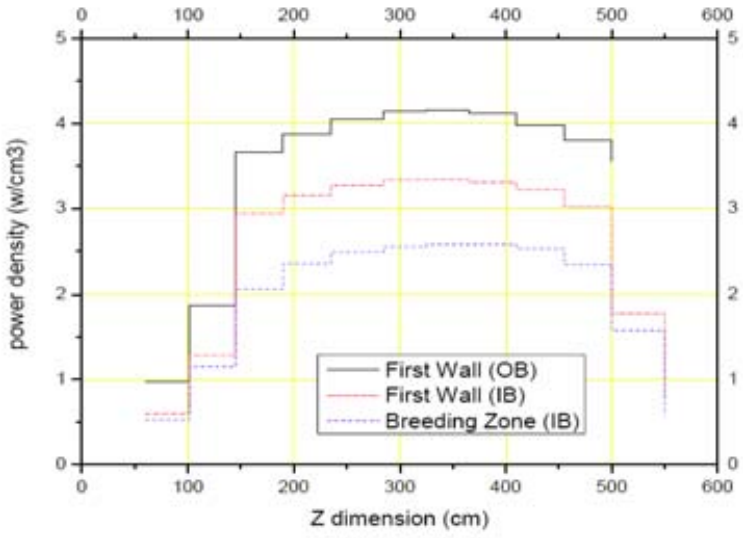

FIG. 13. Axial distribution of power density in the FWs and inboard first breeding zone of 2D cylinder model.

From the analyses above, the most important conclusions are the following:

(1) When the material compositions are the same for the 1D/2D/3D models, the characteristic parameters of the system in the 2D/3D models, such as k_{eff}, TBR and WTR, are much lower than that in the 1D model due to their less loading inventories and leakage effects caused by the divertor and the ports.
(2) The distributions of flux and power density in the FDS-I are very nonuniform both in the radial and axial direction. It is necessary to carry out the neutronics calculation based on the 2D/3D models to analyze the integrated parameter distributions in the system.
(3) It is not reasonable to get the precise calculation results in the 2D/3D models by analogy with the results in the 1D model under the same material compositions. So the modeling method needs to be improved to minimize the differences among multi-dimensional models.

12.5. Dynamic analyses

12.5.1. *Kinetics parameters*

Based on the simplified 1D spherical geometry model shown in Fig. 3(a) and (b), the kinetics parameters calculation of the FDS-I/DWT-CPL is performed with MCNP/4C and data library HENDL/MC. The material compositions and neutronics parameters are listed in Table 8, where the unit of UPWR means the annual production of waste from a 3 000 MW PWR (after 10 years decay) and the detailed compositions are given in Table 9.

TABLE 8. MAIN NEUTRONICS PARAMETERS OF FDS-I/DWT-CPL

parameters		BOC
Fuel material		MAC/PuC; C; SiC
Fuel fraction (vol.%)		10.76:89.24 (MA:Pu)
Fuel mass (kg/UPWR)	MA	5629/162
	Pu	46604/162
	FP	7498/180
K_{eff}		0.969

TABLE 9. THE ANNUAL PRODUCTION OF WASTE FROM A 3 000 MW PWR (AFTER 10 YEARS DECAY)

Waste	Isotope	UPWR (kg)	
LLMA	^{237}Np	14.5	34.7
	^{241}Am	16.6	
	^{243}Am	3.0	
	^{244}Cm	0.6	
Pu	^{238}Pu	4.5	288.1
	^{239}Pu	166.0	
	^{240}Pu	76.7	
	^{241}Pu	25.4	
	^{242}Pu	15.5	
LLFP	^{99}Tc	25.69	41.65
	^{129}I	5.96	
	^{135}Cs	10	

12.5.1.1. Temperature coefficients

Temperature affects the reactivity during the startup or stable operation of a reactor, such as the resonance self-shielding effects in the fuel materials and the densities of the liquid moderator or coolant. The liquid LiPb eutectic and the helium gas serve as the coolants in the FDS-I/DWT-CPL blanket. The interaction between the helium gas and the neutron is negligible and the temperature effect of the liquid LiPb coolant is important in the reactor. The most important temperature effects arising in the FDS-I/DWT-CPL reactor are the fuel Doppler effect and the coolant density effect, i.e. the void effect.

The fuel Doppler effect is the prompt response to the reactor power. The fuel Doppler reactivity worth is likely to be a significant feedback parameter in the safety of a reactor. According to the temperature design of the inlet and outlet temperature of the liquid coolant LiPb eutectic in the AC zones of the blanket for the FDS-I/DWT-CPL reactor, 700 K is assumed as the referred temperature to calculate the Doppler coefficients, shown in Table 10, in the beginning of cycle (BOC) of the FDS-I/DWT-CPL reactor. Though the positive Doppler effect lead to the positive feedback to the reactor so as to increase the multiplication factor, the supercritical accidents cannot happen because the small coefficients have little influence on the subcritical system and the subcritical margin is deep enough even in the BOC.

In the AC zones, a lot of nuclear heat generated from the dedicated fuel fission may result in the boiling of the local region to leave a void, namely void effect (the fraction of fuel particle is assumed to be consistent in the calculation). Because the neutron absorption cross-section of LiPb is high, the macroscopic cross-section decreases for the left void in the LiPb coolant. The fission probability is improved to enhance the *k*-eigenvalue so that the positive void coefficient is expected in the reactor as shown in Table 10.

TABLE 10. TEMPERATURE COEFFICIENTS

	Doppler coefficients (pcm/dk/kk'dT)	Void coefficients (pcm/%)
	700K[a]	700K[a]
BOC	1.206	413.4

[a] Reference temperature

12.5.1.2. External neutron source effects

The FDS-I/DWT-CPL is a subcritical system driven by fusion neutron and the effective neutron multiplication factor is affected by the external neutron source. The effective neutron multiplication factor k_s of a subcritical system is defined as the ratio of fission neutron population and total neutron population (consisting of fission neutron and external neutron).

$$k_s = \frac{W\nu}{W\nu + S_0}$$

Where S_0 is the external source neutron number per second; W is defined as the fission times per second in the fusion-driven subcritical system; v is the average neutron number per fission. Though the reactor is operating in the subcritical state, the continuous external neutron source is supplied to sustain the chain fission reaction. If the external neutron source is shutdown, the chain fission reaction will stop so that there is the inherent and passive safety in a subcritical system. The k_s in the BOC is ~0.997. The big value of k_s indicates the more frequency of the fission reaction and the higher transmutation availability of the incinerator system.

12.5.1.3. Delayed neutron fraction

A critical reactor period is mainly decided by the prompt neutron lifetime and the delayed neutron lifetime. The prompt neutrons lifetime is very short because they are emitted from fission promptly. The delayed neutrons emitted with appreciable time delay are extremely important for time behavior of a reactor. Hence delayed neutrons substantially increase the time constant of a reactor to make the effective control possible. The effective lifetime of neutrons is given by the prompt neutron lifetime l plus the additional delay time of the decaying precursor. The prompt neutron lifetime is l_p~1.6E−5 s in the FDS-I/DWT-CPL reactor. The chain fission reaction cannot be sustainable by the neutrons emitted from fission and the delayed precursor for the subcritical margin of the FDS-I reactor. The external neutron source is needed. If the external neutron fraction is omitted, the calculated delayed neutron fraction β_{eff} is ~285 pcm. The neutronics response time is determined by the half-life for decay of delayed neutron precursors in a typical critical reactor. For a source-driven subcritical system, the external neutron source will dominate the system.

12.5.2. *Accident analysis*

The transient analysis of typical accident scenarios was performed with a code NTC2D with 11-group nuclear data library to evaluate the safety features of the He-gas/liquid lithium-lead DWT blanket with carbide heavy nuclide particle fuel in circulating liquid LiPb coolant (named DWT-CPL).

As typical transient scenarios, the following cases were analyzed: unprotected plasma overpower (UPOP), unprotected loss of flow (ULOF), unprotected transient overpower (UTOP) and collapse accident [24]. In addition, to cover some core-melt situations and investigate the potential for super-criticalities, so-called hypothetical accident with all of the blanket rupture was also investigated.

12.5.2.1. Unprotected Plasma Over Power (UPOP)

This specific accident to FDS-I means the rapid increase of the external neutron source power (i.e. the fusion plasma power). An example for a source perturbation is given in Fig. 14, where the neutron source strength is constant initially; then it is rapidly tripled within 4 s and keeps it on. The power and reactivity of the FDS-I for UPOP simulation are presented in Fig. 14.

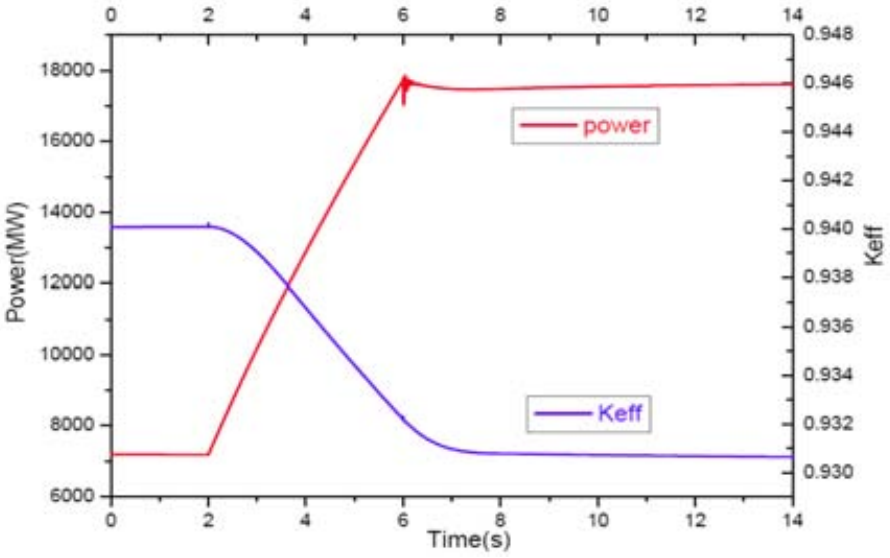

FIG. 14. Power and reactivity in UPOP.

As a result of the 200% increase of the neutron source power within 5 s, the reactor power was increased by about 144% (from 7.2 to 17.6 GW). Reactivity decrease about 1080 pcm was caused by the coolant temperature increase and the fuel particle fraction decrease as shown in Fig. 15, which is a negative feedback to the plasma power increase. The maximum coolant temperature induced by the rapid increase of the neutron source power was 1050 K. Thus, even if the external neutron source power is tripled without a plasma shutdown, FDS-I system still remains acceptable temperature levels below the limits of failure. Negative reactivity feedback is an advantage due to the fuel form of circulating particles in FDS-I.

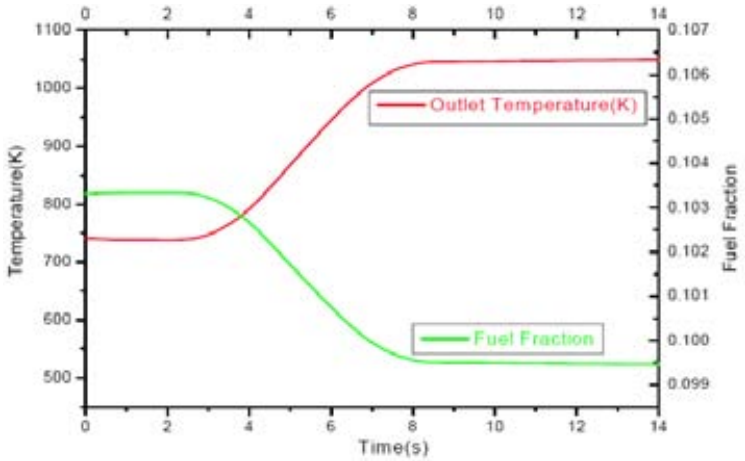

FIG. 15. Power density, coolant temperature and fuel particle fraction in UPOP.

12.5.2.2. Unprotected loss of flow (ULOF)

An unprotected loss of flow transient has been chosen to initiate a severe accident scenario that might end in fuel disruption and core melting. A pump coastdown with a flow-halving time of 6 s is simulated with a plasma-on situation. Natural convection flow is taken into account, which makes the flow rate keep 10% of normal operation. Figure 16 shows the reactor power and k_{eff} excursion. The power decreased from 7.2 to 4.8 GW. The k_{eff} decreased form 0.9395 to 0.9116 and reactivity decreased about 3238 pcm. Figure 17 shows the velocity and temperature of coolant, fuel particle fraction in ULOF at the inlet, middle and outlet of the flow channel respectively. It can be seen that the coolant outlet temperature increases with the flow rate decreases. But the maximum temperature (1920 K) is still less than the melting point of fuel particle material (~2773 K). The simulation showed that the remaining natural convection of the coolant would prevent the structural steel from melting the within 30 s. The fraction of fuel particle in coolant decreases with the temperature increases, which results in the nuclear power and the k_{eff} decrease. So the reactivity feedback is negative at the ULOF.

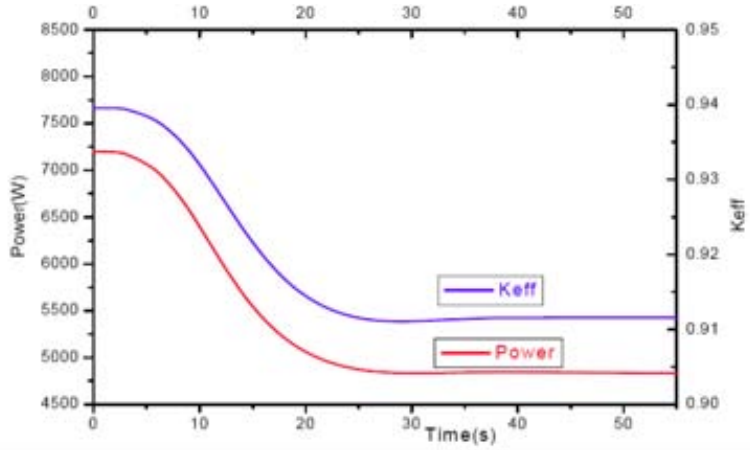

FIG. 16. Power and reactivity in ULOF.

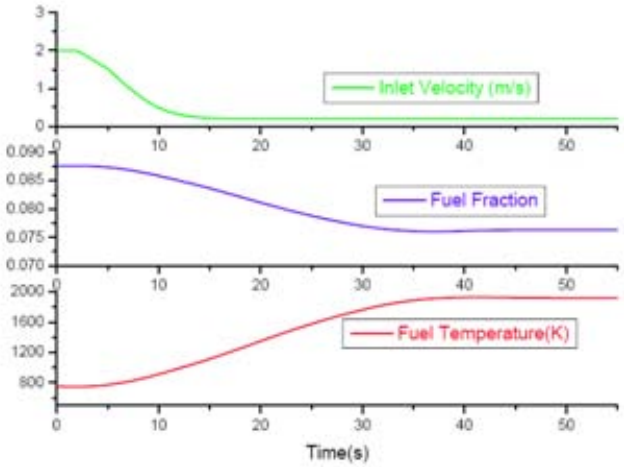

FIG. 17. Velocity and temperature of coolant, fuel particle fraction in ULOF.

12.5.2.3. Unprotected transient over power (UTOP)

An unprotected transient over power might be caused by an instant insertion of positive reactivity to the core. As no control rods are used in FDS-I, the core must survive certain reactivity increases. For the current design of FDS-I, a positive reactivity addition of 1000 pcm was investigated in the present study. The results of the power and k_{eff} for UTOP are displayed in Fig. 18, where the reactivity insertion was installed in 0.01 s and then kept it on. The increase of power after the reactivity insertion was about 15%. Figure 18 shows the transient of LiPb coolant outlet temperatures and power density and the fuel particle fraction respectively. With the UTOP, the maximum increases in LiPb coolant temperature was only 40 K. Since particle fuel is used in the present simulation, this fuel fraction decreases with the temperature increase, which caused a slight decrease in reactivity after 2 s as shown in Fig. 19.

12.5.2.4. Collapse accident

The Collapse Accident is to evaluate the possibility of super-criticality of the subcritical blanket system in hypothetical severe accidents, i.e. the LiPb coolant with fuel particles are assumed to fully or partially enter the fusion plasma region of tokomak while the divertor channel would be blocked. If only one of the blanket modules collapsed, the k_{eff} is still subcritical about 0.977. When the number of collapsed blanket is 3, the k_{eff} will be 0.994. So the supercriticality could be avoided if the number of collapsed blankets is less than 3.

12.5.3. *Burnup analyses*

The neutronics parameters vary with the burnup of fuel in the AC zones and FP zones. It depends on two factors to draw analogous results among the 1D/2D/3D models: energy spectrum and material compositions. As described in the Section 3, the neutronics parameters in the 2D/3D models do not have an analogy to those in the 1D model under the condition of same material compositions. So the modeling method of making k_{eff} at the same level in the multi-dimensional models is adopted here to draw an analogy between the calculation results in the 2D/3D models and 1D model.

The k_{eff} and transmutation rate of the system mainly depend on the spent fuel (Pu and MA) inventory in the AC zones. Keeping the same volume fraction proportion between PuC and MAC, the total volume fractions of PuC and MAC were modified in the multi-dimensional models to make the k_{eff} to be the same level as 1D model. The material compositions in all the other zones are kept to be the same. In order to make the k_{eff} at the same level of ~0.95, the volume fractions of PuC and MAC in the AC zones of the 2D cylinder model are ~1.24 times as large as those of the 1D sphere model as shown in Table 11. Meanwhile, the volume fractions of PuC and MAC in the AC zones of the 3D cylinder model are ~1.55 times as large as those of the 1D sphere model.

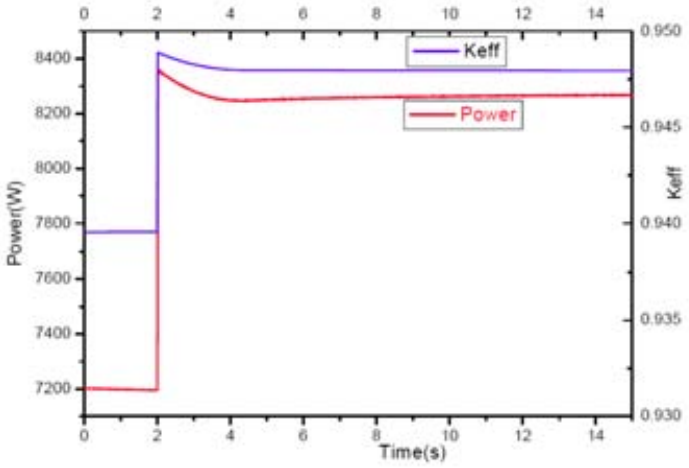

FIG. 18. Power and reactivity in UTOP.

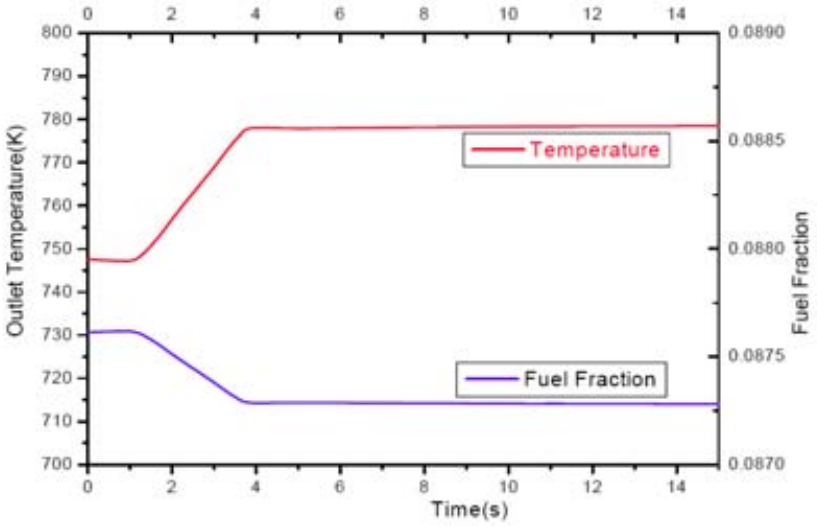

FIG. 19. Nuclear power density, coolant temperature and fuel particle fraction in UTOP.

TABLE 11. SPENT FUEL VOLUME FRACTIONS AND LOADING INVENTORY IN THE AC ZONES OF THE 1D/2D/3D MODELS

	1D sphere	2D cylinder	3D cylinder
MAC volume fraction (vol.%)	0.650	0.807	1.011
PuC volume fraction (vol.%)	5.400	6.693	8.394
LLMA loading inventory (kg)	5671	4374	4702
Pu loading inventory (kg)	47019	36290	39010

The following neutronics parameters have been calculated and analyzed with the code system VisualBUS (SN method) and data library HENDL/MG here to study the burnup discipline of the system:

(1) Characteristic parameters: k_{eff}, energy deposition (P_{th}), energy gain (M);
(2) Reaction rates: TBR, WTR;
(3) Distribution parameters: power density distribution, flux distribution in specific area;
(4) Burnup parameters: waste transmutation fraction (WTF: the ratio of the transmuted mass of waste nuclides (Minor Actinides or Fission Products) to the initial number).

12.5.3.1. Characteristic parameters

Assuming that the cycle length is 1 year, the calculation results at the BOC and end of cycle (EOC) are displayed in the Table 12. At the BOC, all the k_{eff} in the 1D/2D/3D models are 0.949 and the total energy depositions in the system are 17 800, 17 513 and 13 793 MW, respectively. After one full power year of operation, the k_{eff} in the 1D sphere model decreases to 0.84 when it in the 2D cylinder model and 3D cylinder model decrease to 0.82 and 0.85, respectively.

TABLE 12. NEUTRONICS PARAMETERS IN THE 1D/2D/3D MODELS (k_{eff}~0.95)

Parameters	1D sphere		2D cylinder		3D cylinder	
Cycle length	1 year					
	BOC	EOC	BOC	EOC	BOC	EOC
Systemic characteristic parameters						
K_{eff}	0.949	0.842	0.949	0.820	0.949	0.849
P_{th} (MW)	17800	5661	17513	4491	13793	4432
M	148	47	146	37	115	37
Reaction rate parameters						
TBR	3.95	1.43	3.25	1.02	1.95	0.76
WTR_{LLMA}	0.09/0.09	0.03/0.03	0.10/0.11	0.03/0.03	0.08/0.09/	0.03/0.03/
(AC-1/2/3)	/0.08	/0.02	/0.09	/0.02	0.08	0.03
WTR_{Pu}	3.18/3.09	1.01/0.95	2.92/3.07	0.94/0.92	2.29/2.45/	0.89/0.87/
(AC-1/2/3)	/3.85	/1.04	/3.80	/1.03	2.92	0.95
$WTR_{^{135}Cs}$ (FP-1)	0.77	0.23	0.55	0.16	0.34	0.11
$WTR_{^{129}I}$ (FP-2)	0.41	0.12	0.35	0.10	0.22	0.07
$WTR_{^{99}Tc}$ (FP-3)	2.48	0.77	2.06	0.61	1.29	0.45

12.5.3.2. Reaction rates

At the beginning of operation, the TBR in the 1D sphere model and 2D cylinder model are 3.95 and 3.25, respectively, which are much higher than tritium sustainability limit 1.25. Because there are 16 upper ports and 16 equatorial ports in the 3D model which occupy a lot of space, the TBR in the 3D model is 1.95 which is only ~60% of that in the 2D model.

Since the k_{eff} in the 1D/2D/3D models are the same, the neutron energy spectra in the AC zones, as shown in Figs 20-22, are rather similar in the models except at very low energies so that the transmutation rates are similar. Due to the ports are filled with 25% water in the 3D model, the neutron flux densities at low energies in the 3D model are rather higher than those in the 1D/2D models.

12.5.3.3. Waste transmutation fraction

After a year of operation, the waste transmutation fraction and mass depletion for the LLMA, Pu and LLFP are given in Table 13.

It should be noticed here that the above depletion values do not signify the net incineration of the whole of actinides in the system, but of the ones present at the BOC. The nonnegligible (of the order of one ton) contribution of reactions other than fission/i.e. mostly (n,γ), but also, e.g. (n,2n)/to the depletion, lies in the transmutation of some actinides into other ones.

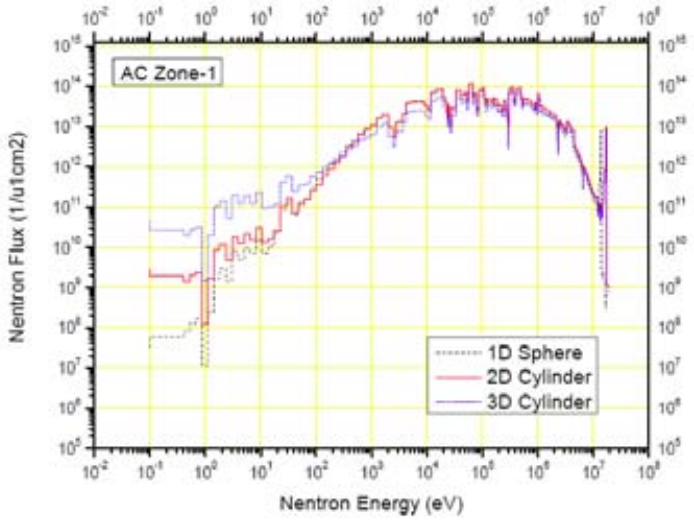

FIG. 20. Neutron spectrum in the AC-1 zone at the BOC.

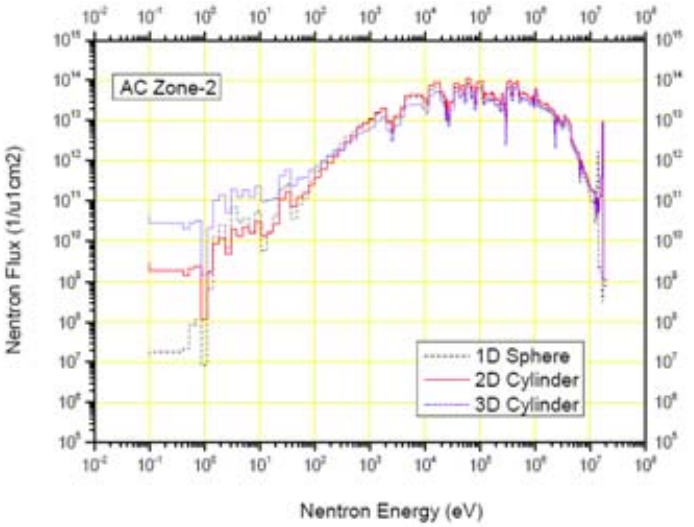

FIG. 21. Neutron spectrum in the AC-2 zone at the BOC.

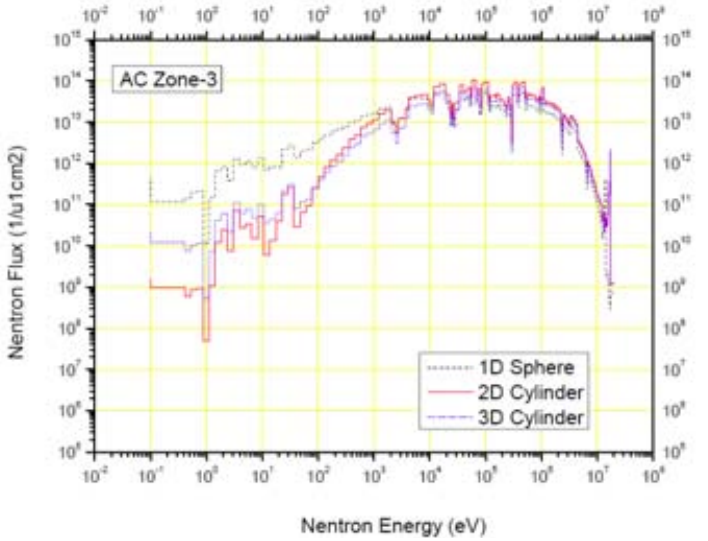

FIG. 22. Neutron spectrum in the AC-3 zone at the BOC.

TABLE 13. WASTE TRANSMUTATION FRACTION IN THE 1D/2D/3D MODELS (BOC: K_{EFF}~0.95)

Parameters	1D sphere		2D cylinder		3D cylinder	
	WTF (%)	Depletion (kg)	WTF (%)	Depletion (kg)	WTF (%)	Depletion (kg)
LLMA						
AC-1 zone	8.75	159	11.19	155	6.63	98
AC-2 zone	7.87	149	11.26	164	6.63	104
AC-3 zone	10.67	210	14.75	225	9.33	154
Pu						
AC-1 zone	11.98	1800	14.41	1661	11.02	1356
AC-2 zone	11.23	1760	14.45	1748	11.19	1454
AC-3 zone	12.84	2096	16.35	2074	12.21	1675
LLFP						
$WTF_{Cs\text{-}135}$ FP-1 zone	12.03	216	15.82	180	11.40	112
$WTF_{I\text{-}129}$ FP-2 zone	12.54	135	16.53	113	12.00	71
$WTF_{Tc\text{-}99}$ FP-3 zone	13.29	621	17.27	516	12.65	331

12.6. Conclusions

1. The fusion-driven subcritical system proves very attractive due to its potential of effective transmutation of long lived radioactive wastes (i.e. spent fuel) from fission based nuclear power plants. While achieving these objectives, the requirements regarding the plasma are relaxed, compared to a pure fusion reactor.

2. Since the spatial distribution of neutronics parameters is nonuniform, there are still some differences among the results in the 1D/2D/3D models even under the same k_{eff} level at the beginning of operation. But the differences are not very obvious for most parameters, such as TBR, WTR, WTF. Therefore, it is a good way to study the discipline of neutronics parameters in the 2D/3D models by analogy with the results in the 1D model under the same k_{eff} level.

3. Taking the 1D model as an example, the k_{eff} decreases rapidly from 0.949 to 0.842 after a full power year of operation so as to cause that the energy deposition, TBR and WTR decrease rapidly, too. But this is very uneconomical. Therefore, fuel cycle design need to be further optimized.

12.7. Summary

A concept of Fusion-Driven (Tokamak) subcritical System (FDS-I) has been analyzed. The fusion power of FDS-I plasma amounts approximately to 150 MW, major and minor radii to about 4 and 1 m, respectively, and an elongation factor equals to 1.7. The neutron wall load is approximately 0.5 MW/m^2. The subcritical 'waste' blanket is cooled by helium and lithium-lead eutectic (dual-cooled waste transmutation (DWT) blanket) and contains the various zones (incineration of long lived MAs, transmutation of long lived FPs, plutonium breeding).

The static and dynamic neutronics parameters of the multi-dimensional neutronics models have been calculated and analyzed for the FDS-I/CPL DWT blanket concept. The FDS-I/CPL DWT blanket concept used to transmute long lived nuclear wastes and to generate energy on the basis of self-sustainable fusion fuel cycle was proved to be feasible. But its economic assessment and further detailed design and analyses are needed as a next step.

The following main transient scenarios were analyzed: unprotected plasma over power (UPOP), unprotected loss of flow (ULOF), unprotected transient over power (UTOP) and collapse accident. The reactivity temperature coefficient is negative due to the fuel inventory decreased in the blanket while the coolant expanding. There is no severe accident occurred under any protected accident and UTOP and UPOP. For the ULOFA and ULOHS, the structure melting might cause the CA, but the supercriticality could be avoided if the number of collapsed blankets is not more than 3. A very reliable Emergency Fusion Power Shutdown System (EFPSS) is necessary. And the design needs to be optimized to avoid supercriticality under any conditions if possible.

Summarizing, the fusion-driven subcritical systems are prospective option of effective transmutation of long lived radioactive wastes (spent fuel) from present i.e. fission based nuclear energy.

REFERENCES TO CHAPTER 12

[1] WU, Y.C., QIAN, J.P, YU, J.N, The fusion-driven hybrid system and its material selection, Journal of Nuclear Materials (2002) pp. 307-311 and pp. 1629-1636.

[2] WU, Y, ZHENG, S., ZHU, X, et al., Conceptual design of the fusion-driven subcritical system FDS-I, Fusion Eng. Des. 81 (2006) pp. 1305-1311.

[3] ZHU, X., ZHENG, S., LI, J., Analysis on fuel cycle schemes in the fusion-driven subcritical system, (FDS-I), Fusion Eng. Des. 81 (2006) pp. 851-857.

[4] ZHENG, S., WU, Y., Neutronic safety analysis in severe transients of the dual-cooled waste transmutation blanket for the FDS-I, Fusion Eng. Des. 81 (2006) pp. 1425-1429.

[5] BAI, Y., CHEN, H., KE, Y., et al., Preliminary transient thermal analysis for safety of the dual-cooled waste transmutation blanket for the FDS-I, Fusion Eng. Des., 81 (2006) pp. 1397-1401.

[6] HU, L., WU, Y., Probabilistic safety assessment of the dual-cooled waste transmutation blanket for the FDS-I, Fusion Eng. Des. 81 (2006) pp. 1403-1407.

[7] Summary of the ITER Final Design Report, G A0 FDR 401-06-28 R 0.2 (uly 2001).

[8] WU, Y., ZHU, X., ZHENG, S., et al., Neutronics analysis of the dual-cooled waste transmutation blanket for the FDS, Fusion Eng. Des. 63-64 (2002) pp. 133-138.

[9] HUANG, Q., LI, C., LI, Y., et al., Progress in Development of China Low Activation Martensitic Steel for Fusion Application, J. Nucl. Mater. (2007) 367-370 (2007) pp. 142-146.

[10] WU, Yican., XU, X.George., The Need for Further Development of CAD/MCNP Interface Codes, Transactions of American Nuclear Society, Vol. 96, TRANSAO 961-882, ISSN: 0003-018X (2007).

[11] WU, Y., LI, Y., LU, L., et al., Research and development of the automatic modeling system for Monte Carlo particle transport simulation, Chinese J. Nuclear Science & Engineering, Vol. 26, No. 1 (2006) pp. 20-27.

[12] HU, H., LI, J., LI, Y., et al., Study on Key Issues of Automatic Modeling for the SN-method Based Particle Transport Simulation Codes Program, Nuclear Physics Review, Vol. 23 No. 2, 2006 (pp. 134-137).

[13] WU, Y., LI, J., LI, Y., et al., Integrated Multi-functional Neutronics Calculation and Analysis Code System: VisualBUS, Chinese J. Nuclear Science & Engineering, to be published in Vol.27 No. 4 (2007).

[14] BRIESMEISTER, J.F., (Ed.), MCNP4C general Monte Carlo Nparticle transport code, Los Alamos National Laboratory, LA- 13709-M (2000).

[15] KE, Ya., Study on Transient Safety Characteristics for the Fusion Driven Sub-critical Reactor, doctoral dissertation of graduate university of Chinese Academy of Sciences (2006).

[16] GAO, C., XU, D., LI, J., et al., Integral Data Test of HENDL1.0/MG and VisualBUS with Neutronics Shielding Experiments (I), Plasma Phys. Technol., 6 (5) (2004) pp. 2507-2513.

[17] GAO, C.J., XU, D.Z., LI, J.J, et al., Integral Data Test of HENDL1.0/MG with Neutronics Shielding Experiments (II), Plasma Phys. Technol. 2004, 6 (6), 2598-2600.

[18] WU, Y., FDS Team, Conceptual design activities of FDS series fusion power plants in China, Fusion Engineering and Design, 81 (2006) pp. 2713-2718.

[19] ZHENG, S., WU, Y., Nuclear analysis of the Upper Port-Dose rate analysis of the upper port to confirm sufficiency of shielding capacity of final port geometry, ITER international analysis report, ID: ITA 73-01.
[20] HUANG, Q., ZHENG, S., LU, L., et al., Neutronics Analysis for A Compact Reversed Shear Tokamak CREST, Fusion Engineering and Design, 81 (2006) pp. 1239-1244.
[21] ZHENG, S., CHEN, M., LI, J., et al., Neutronics Analysis for the Test Blanket Modules proposed for EAST and ITER, Nuclear Fusion 47 (2007) pp. 1053-1056.
[22] WU, Y., ZHENG, S., ZHU, X., WANG, W., etc., Conceptual design of the fusion-driven subcritical ystem FDS-I, Fusion Engineering and Design, 81 (2006) pp. 1305-1311
[23] SALVATORES, M., SLESSAREV, I., TCHISTIAKOV, A., The Transmutation of Long-Lived Fission Products by Neutron Irradiation. Nuclear Science and Engineering, 130, (1998) pp. 309-319.
[24] BAI, Y, KE, Y., WU, Y, Preliminary analysis of typical transients in fusion driven subcritical system (FDS-I), paper presented in 15th Intl Conf on Nuclear Engineering, 22-26 April 2007, Nagoya, Japan.

CHAPTER 13. COMPARATIVE ASSESSMENT OF ALL DOMAINS

13.1. Domain-I: critical fast reactors with transmutation capability and with fertile fuel

Investigations under the 'Domain-I' approach the CRP theme through the fast reactor option for incineration of radioactive waste. By the CRP classification, a Domain-I reactor (1) is a fast reactor, (2) uses solid fuel, and (3) uses fertile breeder material in the core/blanket. The minor actinides (MA), viz. the isotopes of Np, Am, and Cm, are the main radioactive waste (from thermal reactors) considered for incineration in the fast reactor flux, and so the domain-I reactors consist of some proportion of MA intentionally mixed with the feed fuel. A common characteristic of the Domain-I reactors is the preference of Th to ^{238}U as fertile, obviously to reduce production of MA. The CRP participants have independently designed fast reactor models under this domain and studied their static and transient safety related neutronic behavior. The models and contributions of IGCAR and IPPE are based on an existing power reactor design, with variations accommodated for the specific need of MA incineration. Salient features of these designs are given below.

The reactor model proposed by IGCAR is a modification of the 500 MW(e), sodium cooled, Prototype Fast Breeder Reactor (PFBR), presently under construction. The model is called FBR-MA in this report. The PFBR core features are almost maintained. The depleted UO_2 radial blanket is replaced with ThO_2, and the fresh fuel consists of 5% of MAs with composition corresponding to the (uncooled) discharge fuel from the Indian PHWRs. During an equilibrium cycle length of about 180 days, the MA inventory reduces by about 32 kg, from about 369 kg, indicating nearly 10% incineration of long lived MAs. Static and transient analyses of FBR-MA have shown that the model reactor is found as safe as the PFBR. The effect of spread in the MA nuclear data in different recent evaluations on the predicted material and Doppler worths, has been found to be within ±10%. The study also has been extended to replace the UO_2 axial blanket with ThO_2.

The model proposed by IPPE, is a sodium-cooled fast breeder reactor of the Russian BN-800 type, with the fuel replaced with a mixture of oxides of Pu, Th, and MAs. The MAs come from WWER-1000 reactors after a cooling period of 3 years. The design specifically concentrates on MA incineration and the associated safety and fuel economy aspects. The MAs produced during the burnup are recycled. The model accepts significantly larger proportion of MAs in the fuel than the IGCAR model, and the upper limit of MAs is determined by the ^{238}Pu content in the spent fuel, which is limited to 5% to avoid self-heating. The study mainly aims at assessment of sodium void reactivity effect (SVRE), in the presence of MAs, in three variants (Variant A, B and C) with different MA inventories. Fuel cycle studies are done to assess the incineration potential. No transient analyses are reported. In the extended study of a few variants with respect to MA recycling, replacement of upper axial thorium blanket with a sodium plenum is also considered. The sodium plenum is meant to reduce SVRE towards negative. Maximum burning of about 104 kg of recycled actinides, per year, is achieved in the variant where the SVRE is permitted to be positive. Thus, this variant can recycle MAs from 7 WWER-1000 reactors per year. The annual production of 540 kg of ^{233}U is justified for use in the Th-U fuel cycle.

The JRC model finally considers the design of a lead-cooled fast reactor (LFR) and a sodium-cooled fast reactor (SFR), of 600 MW(e) power class. The cores contain about 5% MA at startup. An option of including about 10% MA in the axial and radial blankets is also investigated. The neutron spectrum being hard due to MA burning, the Doppler feedback is too small to compensate for the reactivity increase due to coolant heat-up under transient conditions. Incorporation of a limited number of moderating pins such as CaH_2, UZrH1.6, BeO, or Be, is considered to counter the above problem. In the LFR model, uranium and thorium based fuels are studied. Transients such as ULOF and ULOHS are also studied in detail. It is shown that systems having MA in the core and blankets have much higher MA incineration rate, compared to the systems having MA in the core alone.

Key parameters and key data and results of critical fast reactors with transmutation capability and with fertile fuel are shown in Table 1.

TABLE 1. KEY PARAMETERS AND KEY DATA AND RESULTS OF CRITICAL FAST REACTORS WITH TRANSMUTATION CAPABILITY AND WITH FERTILE FUEL

Key Parameter	**Key Data and Results**		
Reactors analyzed	Variation of 500 MW(e) Indian PFBR with 5% MA loading in core and thoria radial blanket. Reactor power: 1150 MW(th) (460 MW(e)) .	Variation of Russian BN-800 with 5% MA loading in core with (Pu-Th) MOX core and thoria radial blanket. Reactor power: 2100 MW(th) (800 MW(e)) .	600 MW(e) lead/sodium cooled FR with hydride moderating pins in SA. Reactor power: 1430 MW(th) (600 MW(e)) .
Transmutation potential	MA Burning during 1 equilibrium cycle: ^{237}Np 9.8%; ^{243}Am 9.2%; Net MA burning 8.5%. ^{237}Np, ^{241}Am and ^{243}Am are major contributors to MA in PHWRs (99.1%) and burn over a cycle; ^{242m} Am, ^{243}Cm and ^{244}Cm increase by about 50% — but negligible in quantity. About 30 kg of MA burns out of 370 kg loading.	MA Burning limited by condition of maximum positive void worth. Three variants considered : Variant A = only own MAs burnt Variant B = own MAs plus 52 kg/a added Variant C = own MAs plus 26 kg/a added Variant C with 26 kg of external MAs/a is acceptable from SVRE condition being negative. The paper gives details of effects of different MA on SVRE, done by successive removal of individual isotopes using MCNP — Negative reactivity components are given by Cm, while Am and Np give positive contribution.	MA Burning for MAs both in core and blankets : SFR: 131 kg/a LFR: 104 kg/a MA in core only : SFR: 66 kg/a LFR: 67 kg/a
Fuel masses and configurations, inventories	Core: (DU+Pu) MOX Rad. Bl.: Uranium oxide Ax. Bl.: Thorium oxide (in a variant) DU - Depleted uranium about 0.3wt% ^{235}U MA Loading: 5% in fuel (only inner & outer cores).	(Pu-Th) MOX Thorium oxide Variant A considers 1.9 MA loading (only own MA); Variant B 6.9% MA; Variant C 3.1% MA; Variants A and B: own MA+ MA from WWER; correspondingly Pu and Th charge varies.	LFR and SFR with (DU+TRU), (Th+TRU) DU — Depleted Uranium about 0.3wt% ^{235}U MA — loading: MA are 17% of TRU.
Safety coefficients and kinetic data (Doppler, structure, coolant, β_{eff})	β_{eff}. pcm/lifetime (μ sec) BOL 343/0.342 BOEC 338/0.369 EOEC 335/0.382.	Beta-eff varies between 270 to 290 pcm — 270 pcm due to high MA loading (variant B) Lower value of β_{eff} is due to Th-Pu fuel.	Beta-eff in LFR (DU,TRU) 295 pcm for MA in C only 332 pcm for MA in B only LFR (Th,TRU): 268 pcm SFR (DU,TRU) 343 pcm for MA in B only Due to presence of MAs in the fuel, the JRC core design has very hard n-spectrum, leading to low

			Doppler and high positive coolant heat-up reactivities. Hydride pins are used to increase absolute value of the negative Doppler and decrease positive coolant heat-up reactivity coefficients.
Transients analyzed	ULOF UTOP	None	ULOF ULOHS Protected Station Black-out
Result of transient analyses	Standard Indian FBR (PFBR) and FBR-MA are compared : UTOP: uncontrolled CSR withdrawal without SCRAM: (1.5$ in 129 s); PFBR & FBR-MA give similar results. LOF: pump trip with fly-wheel action, without SCRAM — followed up to Na boiling; Power drops faster in MA loaded core; Na boiling occurs later for FBR-MA; Doppler and axial expansion dominates the feed-back.	None	LFR: For ULOF & ULOHS power decreases — power reaches a lower value for ULOF; power asymptotically decreases for ULOHS. For station blackout, CRs are inserted on LOP; decay heat removal is passive, but slow (vessel air cooling system) — Pb temperature reaches about 1080 K. SFR: ULOF leads to power excursion. Sodium boiling cannot be prevented by assumed negative feedbacks. Natural circulation is limited due to the high-pressure drop core and complex flow path. Power increase leads to fuel melting, fuel pin failures and fuel expulsion that shuts the reactor down when about 50% of core is molten' (disassembly). ULOHS is similar to LFR.
Key transient phenomena and key safety parameters	ULOF in sodium cooled reactor have the potential to lead to power excursion via sodium boiling.		ULOF in sodium cooled reactor leads to power excursion. In lead cooled reactor with significant natural convection potential due to the possible lager pitch/diameter ratio a ULOF can be survived.
Feedback mechanisms	Doppler Worth: BOL -439 pcm BOEC -510 pcm EOEC — 527 pcm Na void worth for 1% change in concentration: BOL 13.4 pcm BOEC 16.2 pcm	Only SVRE dependence on MA loading is dealt with.	Doppler/Coolant Δk in pcm/100 K SFR(DU,TRU): -74 to -102/+55 to +62 LFR(DU,TRU): -68 to -91/+44 to +62

	EOEC 18.2 pcm Expansion coeffs.: Fuel axial: -0.46 pcm/°C Clad axial: +0.05 pcm°C Sodium expansion reactivity: +0.37pcm/°C.		LFR(Th,TRU): -127/+46 LFR(Th,Pu): -167/+43.
Typical timescales of transients	Typical timescales are in sec in case of no power excursion.		Typical timescales are in sec in case of no power excursion. In case of a power excursion, transient time scales are in the msec range.
Control systems	Control Rods: 9 CSR SD System: 9 CSR 3 DSR (B_4C; 65% ^{10}B in B) 19 pins/SA.	Control rods: 30.	Simplified core design model without explicitly modelling CR channels.
Static neutronics codes	ALCIALMI (for 2D diffusion neutronics); CONSYST & EFCONSY (for n-data); ALEX (for BR, power distribution etc.) NEWPERT (perturbation code for Doppler etc.) ORIGEN2 (for nuclide evolution with burnup).	Core calculation with code RZA MCNP-4C for SVRE.	Monte Carlo burnup code — MCB.
Transient codes	Accident Analyses performed with PREDIS code.	None.	Accident Analysis with European Accident Code — EAC-2 and CFD code STAR-CD.
Data basis nuclear	XSET-98 (A version ABBN-93) CV2M (updated Cadarache Ver.2 set); Databases of ORIGEN updated with JNDC-FP-2000 for decay data; ENDF/B6-FPY for FP yields (both from IAEA NDS).	26 group BNAB Library in CONSYST format.	Temperature adjusted continuous energy cross-section library JEF2.2.
Data basis thermalhydraulics (EOS) etc.	In-house.		In-house.
Results of benchmarking activity in this CRP and lessons learned	MA burning in operating FBR feasible at 8-10% per eqbm cycle; Effect of MA nuclear data spread on material/Doppler worth within 10%; ThO_2 is preferred blanket.	Dependence of SVRE on MA loading One FR-MA (Variant B — 29 kg loading) can burn annual MA discharged (about 15 kg) from 2 WWERs. Taking into account limits given by sodium void worth limit is given with 26 kg of external MAs/a.	Superior behaviour of LFR system under ULOF accident conditions.

Status of methods, tools and data and further needs for development	General needs for theoretical and experimental work (e.g. data, transients, experiments….). PHWR discharge MA after a few years of cooling needs to be studied.		Needs for updating code description on structural feedbacks. Code updating on pin behavior under accident conditions and heavy liquid metal flow.
Long term general needs for theoretical and experimental work	General needs for theoretical and experimental work. Development of advanced coupled accident code.		General needs for theoretical and experimental work. Development of advanced coupled accident code.

13.2. Domain-II: critical fast reactors with transmutation capability and with fertile-free fuel

The Domain-II analyzed critical reactors with solid non-fertile fuel. A comparison of a sodium cooled fast reactor (SFR) versus a lead cooled fast reactor (LFR), both as Pu and MA burners has been performed. Both systems are fuelled with CERMET fuel based on a fertile-free ^{92}Mo matrix, and are rated at 600 MW(e). Both cores contain BeO moderator pins to improve the safety related characteristics, and have sufficiently negative Doppler coefficients (in the range -0.9 to -1 pcm/K) and similar positive coolant temperature reactivity coefficients (in the range 0.5 to 0.6 pcm/K). The lead cooled fast reactor core is larger than the sodium cooled one. The lead cooled fast reactor utilizes approximately 300 kg of actinides (Pu and MAs) per year (corresponding to the yearly production of actinides of 1.1 GW(e) LWR capacity), compared to approximately 260 kg in the case of the sodium cooled fast reactor (corresponding to the yearly production of actinides of 0.95 GW(e) LWR capacity). However, it must be kept in mind, that the utilization rate of MAs is about 1.8 times higher in the sodium cooled fast reactor than in the lead cooled one, due to the lower mass inventory in the former. An obvious consequence of these neutronics characteristics is found in the burnup reactivity swing of the two cores, which is almost 2.9 times higher in the case of the sodium cooled fast reactor, as compared to the lead cooled one. With regard to the transient characteristics, the relatively larger lead cooled fast reactor core can cope with the ULOF event (increase of the lead outlet temperature less than 150 K) due to its natural circulation characteristics, while in the case of the sodium cooled core, which does not have sufficient negative feedbacks to compensate for its lesser natural circulation characteristics, sodium boiling cannot be avoided. However, the ULOF analysis did not take into consideration the negative structural feedback effects, which would avoid sodium boiling, provided they were fast acting. Key parameters and key data and results of critical fast reactors with transmutation capability and with fertile-free fuel are shown in Table 2.

TABLE 2. KEY PARAMETERS AND KEY DATA AND RESULTS OF CRITICAL FAST REACTORS WITH TRANSMUTATION CAPABILITY AND WITH FERTILE-FREE FUEL

Key Parameter	**Key Data and Results**	
Reactors analyzed	LFR	SFR
Transmutation potential	The LFR burners operate in concert with LWRs in two-component scheme recycling both Pu and MAs, which are homogeneously admixed to core fuel. Transmutation rates: LFR: Pu – 45 kg/TWhe, MA – 19 kg/TWhe	The SFR burners operate in concert with LWRs in two-component scheme recycling both Pu and MAs, which are homogeneously admixed to core fuel. Transmutation rates: SFR: Pu – 38 kg/TWhe, MA – 18 kg/TWhe

Key Parameter	Key Data and Results	
Fuel masses and configurations, inventories	Homogeneous core with moderator pins (BeO) to increase absolute value of the negative Doppler and decrease positive coolant temperature reactivity coefficients. Actinide mass at BOL: LFR: 17.07 t_{HM}, TRU mass at BOL: LFR: 8.56 t_{HM}	Homogeneous core with moderator pins (BeO) to increase absolute value of the negative Doppler and decrease positive coolant temperature reactivity coefficients. Actinide mass at BOL: SFR: 7.56 t_{HM} TRU mass at BOL: SFR: 3.26 t_{HM}
Safety coefficients and kinetic data (Doppler, structure, coolant, β_{eff})	LFR: Doppler $\Delta k = -50$ pcm Coolant $\Delta k = +38$ pcm $\beta_{eff} = 256$ pcm Temperature reactivity feedbacks correspond to an increase of fuel and coolant temperatures by 100 K.	SFR: Doppler $\Delta k = -54$ pcm Coolant $\Delta k = +36$ pcm $\beta_{eff} = 295$ pcm Temperature reactivity feedbacks correspond to an increase of fuel and coolant temperatures by 100 K.
Transients analyzed	— Unprotected loss-of-flow accident (ULOF) with assumed primary coolant flow halving time of 6 s — Unprotected loss-of-heat-sink (ULOHS) accident TLOP, total loss-of-power (station blackout) accident assuming that the safety rods will be inserted under gravity when the electromagnets that hold them are no longer powered.	
Result of transient analyses	The LFR showed advantages over SFR regarding behaviour in severe accidents like ULOF, ULOHS and TLOP. This is due to the better natural circulation behaviour of an LFR design and the much higher boiling temperature of lead. In an ULOF accident, coolant outlet temperature increases only by 100-150 K in an LFR, while in a SFR sodium may boil and voiding may commence. A drawback of the LFR is that for present steels a protective oxide layer or a coating is needed to minimize erosion during normal operation. These oxide layers deteriorate the heat transfer and are sensitive to coolant temperatures above 870 K for prolonged periods of time.	
Key transient phenomena and key safety parameters	A sizable negative radial expansion feedback of the structure is necessary to prevent sodium boiling in unprotected loss-of-flow accident (ULOF) in an SFR. These large and fast radial structural feedbacks do not have to be present in an LFR, which overcomes an ULOF by combined effect of prompt negative Doppler and axial fuel expansion feedbacks only. Further safety advantages of LFRs in comparison to SFRs are 30% larger volumetric heat capacity of lead, its higher boiling point and good natural circulation of the coolant due to low pressure drop.	
Feedback mechanisms	Unprotected reactivity or UTOP accidents with a few dollars of reactivity insertion will lead to fuel pin failures in both reactors. Fuel sweep-out from the core and nuclear shut-down the LFR might exist. Some information available from an accident in the first lead/bismuth cooled reactors in Russian ‘Alpha’ class submarines. It was reported that the heavy metal coolant (with a similar density to oxide fuel) led to an extensive fuel sweep-out from the core, which prevented recriticalities. Impact on decay removal systems in a commercial LFR unknown.	
Control systems	Reactor Vessel Auxiliary Cooling System (RVACS) Fast shut-down mechanism and ultimate shut-down rod	

Key Parameter	Key Data and Results
Static neutronic codes	MCB 2b
Transient codes	EAC-2, STAR-CD
Data basis nuclear	JEF-2.2, JEFF-3.1, ENDF/B-VI.8
Data basis thermal-hydraulics (EOS) etc.	Handbook on Lead-bismuth Eutectic Alloy and Lead Properties, Materials Compatibility, Thermal-hydraulics and Technologies, OECD/NEA, 2007. Incropera, F.P., Fundamentals of Heat and Mass Transfer, John Wiley & Sons, 1996. Etherington, H., Nuclear Engineering Handbook, McGraw-Hill, 1958.
Results of benchmarking activity in this CRP and lessons learned	Needs for development of accident code with proper description of CERMET fuel behaviour under high temperature and failure conditions.
Status of methods, tools and data used and further needs for development	Neutronic analyses were done by Monte Carlo Burnup code MCB, which allows in-flight calculation of reaction rates. Fuel cycle analyses were performed for start-up cycle scenario where burner uses high quality LWR TRUs. A use of beryllium oxide moderator pins was assumed due to much higher melting point of BeO compared to other moderator materials such as metallic beryllium or hydrides. Effect of moderator pins on the local power peaking within the sub-assembly is to be studied further. Severe safety characteristics are calculated by multi-channel code EAC-2, which needs to be benchmarked and its modelling capabilities further improved and refined. This concerns mainly implementation of radial and improvement of axial structural feedbacks and implementation of primary circuit thermal hydraulic model, including heat exchangers and pumps.
Long term general needs for theoretical and experimental work	Investigation of structural feedback effects fast and strong enough to prevent sodium boiling and avoid subsequent power increase with loss of core integrity as a result. The concept of fast negative radial feedback has been demonstrated experimentally only for small reactors (20 MW(e) EBR-II) and it remains to be seen whether a similar performance can be expected even for large power reactors (~100 s of MW(e)). As regards behaviour in severe accident scenarios, the wide-pitch LFRs have an advantage over SFRs for all severe accident initiators. The EAC code has to be further benchmarked for lead cooled systems, especially the pin behaviour with advanced CERMET fuels. The same holds for the description of the BeO pins. Experiments are also needed to confirm whether description of the expulsion of molten fuel from ruptured pins is adequate and leads to fuel sweep-out, which would reduce likelihood of recriticalities.

13.3. Domain-III: hybrid system (ADS) with fertile fuel

These benchmark exercises are based on the MYRRHA concept, as originally developed by SCK•CEN within EURATOM's 5th Framework Program. MYRRHA is a lead-bismuth eutectic cooled 50 MW(th) sub-critical reactor driven by a spallation source. Two configurations were analyzed: a reference sub-critical core configuration consisting of 45 MOX fuel assemblies (30 wt% Pu enrichment), and a core with 24 uranium-free assemblies containing MAs embedded in an MgO matrix plus 48 MOX assemblies. Static neutronic calculations were performed by different participants using the MCNPX.2.5.0 code based on the JEFF3.1 data file. Burnup calculations were done with the help of the ALEPH code that couples MCNPX with ORIGEN2.2. The static results show that the Doppler reactivity coefficient is slightly lower, β_{eff} of the same order of magnitude, and the neutron generation time ($1.49\text{-}2.43\times10^{-6}$ s) an order of magnitude larger than in sodium cooled fast reactor. The larger core containing MOX and MAs assemblies has a reduced burnup reactivity swing. The core void reactivity effect is negative. Depending on the data and method used, the β_{eff} of

the reference configuration lies in the range of 331 to 349 pcm, and 312 to 337 in the core containing MOX and MAs. The transient studies were performed with the help of the codes RELAP and SITHER. The following transients were analyzed (both protected and unprotected): LOF (loss of forced circulation in primary cooling system), LOH (loss of secondary cooling system), concomitant LOF and LOH, Overcooling (inlet temperature to secondary cooling system drops instantaneously to 40°C), TOP (reactivity jump at hot full power conditions — maximum insertion of 2 000 pcm and 2 500 pcm in the unprotected and protected case, respectively), and Assembly Blockage (up to 30% and 50% reduction of the flow area in the hottest assembly in the unprotected and protected case, respectively). Additionally, the unprotected Beam Overpower transient (beam power jump corresponding to a neutron source increase by up to 175% at hot full power conditions) was mid plane and at core outlet, respectively) for the LOF transient in the MOX core show that no melting occurs (safety criteria for fuel and cladding temperatures are 2 500°C and 600-700°C, respectively). The only exception is the Assembly Blockage transient that leads to limited damage for assembly flow area reduction factors larger than 30%. For unprotected transients, for which major problems occur with regard to the maximum cladding temperature, the envelope case is given by the MYRRHA MOX core, since the MAs plus MOX core features significant safety improvements for all unprotected transients. In the MOX core case, total ULOF results in maximum cladding temperatures of close to 1 000°C and pin failure, with a grace time of about 7 s until 700°C are reached. ULOH is slightly better, since the grace time before reaching the fuel pin failure safety criteria is increased to about 600 s. The most penalizing case is concomitant ULOF and ULOH: cladding temperatures are higher than 1 200°C, with 7 s grace time before reaching 700°C. The unprotected Overcooling transient results in a relatively large grace time (14 m) before attaining freezing temperature (124°C) of the bismuth-lead eutectic. As for the unprotected Beam Overpower transient, the outcomes are benign for beam power jumps at hot full power conditions corresponding to a neutron source increase by up to 160%. Key parameters and key data and results of hybrid systems (ADS) with fertile fuel are shown in Table 3.

TABLE 3. KEY PARAMETERS AND KEY DATA AND RESULTS OF HYBRID SYSTEMS (ADS) WITH FERTILE FUEL

Key Parameter	Key Data and Results
Reactor analyzed	ADS with fertile fuel
Transmutation potential	MYRRHA is a small scale ADS. It is not optimised as a MA transmuter. Assessment performed for the fuel inventory of two typical core loadings. One with only driving (U-Pu)O_2 MOX subassemblies and another core including partially U-free dedicated (Am-Pu)O2 MA subassemblies. The fuel mass inventory after two 90 days irradiations subcycle has yielded a transmutation potential of 42 kg/TW•h/th in both cases.
Fuel masses and configurations, inventories	The IAEA-CRP MYRRHA benchmark considers two sub-critical core configurations: a typical core configuration composed only of (U-Pu)O_2, 30% Pu-enriched, MOX fuel assemblies and another one including additional U-free minor actinides fuel assemblies, the latter one being dedicated to operate MYRRHA as an experimental small-scale minor actinides (MA) 'transmuter'. The core consists of a triangular lattice of closed hexagonal boxes, typical to LMFBRs, each fuel assembly containing 91 fuel rods. The Pb-Bi coolant flow enters from below with the inlet temperature of 200°C. The heavy metal masses at BOL are about 508 kg and 660 kg, respectively for the reactor reference full MOX, core and for the mixed MOX-MA core.
Safety coefficients and kinetic data (Doppler, Structure, coolant, β_{eff})	β_{eff}=349 pcm Prompt neutron lifetime (Λ)= 1.5 μs Doppler reactivity constant Tdk/dT=-3.74×10^{-3} Coolant temperature reactivity coefficient: -2.1 pcm/°K Partial loading of U-free MA slightly deteriorates these safety related parameters.

Key Parameter	Key Data and Results
Transients analyzed	— PTOP: Protected transient overpower at hot full power resulting from a reactivity jump — PLOF: Protected loss of flow resulting from the total loss of circulation pumps in the primary system — PLOH: Protected loss of heat sink resulting from the total loss of the secondary cooling systems — PLOF&PLOH: Combination of a protected LOF and LOH (station blackout) — PSAB: Partial blockage at the inlet of one subassembly where the cross sectional area is reduced — Protected overcooling: Instantaneous water temperature drop from 145 to 40°C at the inlet of the primary heat exchangers (secondary side) — UTOP: Unprotected transient overpower at hot full power resulting from a reactivity jump — ULOF: Unprotected loss of flow resulting from the total loss of circulation pumps in the primary system — ULOH: Unprotected loss of heat sink resulting from the total loss of the secondary cooling systems — ULOF&ULOH: Combination of an unprotected LOF and LOH — Unprotected SAB: Partial blockage at the inlet of one subassembly where the cross sectional area is reduced — Unprotected overcooling: Instantaneous water temperature drop from 145 to 40°C at the inlet of the primary heat exchangers (secondary side) — BOP: Beam overpower at hot full power.
Result of transient analyses	A distinction is made between the protected transients and the unprotected transients. For the first category the accelerator is shut down during the transient. A delay of 3 seconds is applied between the accident initiation and the effective proton beam cut off. Unprotected accidents occur in case of failure of the accelerator shut down system and the spallation neutron source is supposed to be maintained at its nominal value. It means in particular that no feedback exists from the primary system thermal-hydraulics to the spallation loop behaviour. The calculations performed with the RELAP and SITHER have shown that MYRRHA is able to face up very efficiently to protected loss of flow and loss of heat sink accidents, whatever configuration being considered. In unprotected conditions, the most critical situation for the full MOX core configuration is encountered with the loss of flow case, for which the grace time is only a few seconds before the safety criterion for fuel cladding is exceeded. On the other hand the unprotected loss of heat sink accidents allow much longer grace times (~15 minutes). The second core configuration, with partial load of U-free (Am-Pu)O_2 subassemblies, can withstand unprotected loss of flow accidents, but it is not able to prevent clad failure in case of unprotected loss of heat sink, because the emergency cooling system is not dimensioned to evacuate the nominal power (longer grace times however are observed). Overcooling transients caused by a sudden drop of the water temperature in the secondary circuits do not lead to excessive LBE freezing in the heat exchangers provided that the accelerator is not shutdown. With this condition water temperatures as low as 40°C are acceptable and total blockages of the heat exchangers have not to be feared. This conclusion applies to both core configurations. Accidental reactivity insertions up to 2 000 pcm in the first sub-critical core configuration do not generate core damages, even in unprotected conditions. Under this limit value the maximum fuel temperature stays below 2 500°C. Cladding temperatures are much lower than the safety criterion. Higher reactivity insertion values are tolerated by the second core configuration. Partial blockages in core sub-assemblies may lead to cladding failure if the cross sectional area of the flow is reduced to 40 and 20% respectively in the first and

Key Parameter	Key Data and Results
	second core configuration. A very early detection of the blockage is crucial to mitigate the accident consequences. Nevertheless in any case the core damages will be limited to the affected fuel sub-assembly.
Key transient phenomena and key safety parameters	Pool type systems cooled by heavy liquid metals have the capability of removing the core decay heat in natural convection mode, so that a total loss of the primary pumps can be managed successfully in a passive way. Unprotected transients however cause major problems in many accidental situations like loss of flow and loss of heat sink accidents. This implies the necessity of a very high reliability of the accelerator shutdown system. A correct dimensioning of the emergency cooling system is also essential to insure the system integrity for the most severe transients. An overcooling transient may result from a sudden decrease of the water temperature at the inlet of the secondary side of the primary heat exchangers. The main risk of such an event is LBE freezing inside the heat exchangers with possibility of blockages if the water temperature is significantly lower than 40°C. The accelerator shut-down should be prohibited in case of such an overcooling event since the coolant heating in the core would be considerably reduced making a total blockage unavoidable. So in case of overcooling, the 'protected' mode (proton beam off) is the more harmful.
Feedback mechanisms	Only Doppler and cooant voiding effects were taken into account. Feedback resulting from the coupling between primary system and spallation loop should be introduced for a better simulation. The Doppler and coolant voiding feedbacks have significant effects for the transients leading to high temperatures in the fuel and consequently in the coolant, i.e. more particularly for the unprotected transients
Typical timescales of Transients	Time scales very dependent on the type accident (few seconds for LOF or TOP up to tens of minutes for LOH): range is a few sec to 10 minutes.
Control systems	Beam shutdown Emergency cooling systems
Static Codes	MCNPX (2.5 versions); ALEPH (MCNPX +ORIGEN2.2)
Transient Codes	RELAP for simulation of whole system behaviour SITHER for simulation of core behaviour EAC-2 for simulation of core behavior
Data basis nuclear	Continuous-energy JEFF3.1 neutron library
Data basis thermal-hydraulics (EOS) etc.	Handbook on Lead-bismuth Eutectic Alloy and Lead Properties, Materials Compatibility, Thermal-hydraulics and Technologies, OECD/NEA, 2007
Results of benchmarking activity in this CRP and lessons learned	One of the main outcomes of the safety analysis of MYRRHA is the need of an extremely reliable system of accelerator shutdown in order to avoid unacceptable consequences of accidents, especially in the case of LOF. However it has to be emphasized that the windowless concept developed by SCK•CEN for the spallation target could prevent such unprotected situations if an adequate coupling between the primary system and spallation loop behaviour is introduced. Further investigations in that direction are presently under way.
Status of methods, tools and data used and further needs for development	Uncertainties on natural convection (LOF) simulation with RELAP → need of CFD simulation (under way at SCK•CEN with FINE\HEXA). Unprotected accidents consequences should be reassessed by taking into account the spallation loop. In case of clad or fuel damage the used codes must be able to assess the consequences of the core damage. Thus other codes than used in the benchmark exercise have to be applied.

Key Parameter	Key Data and Results
Long term general needs for theoretical and experimental work	Necessity of a very reliable beam cut-off system to avoid unprotected situations Optimization of the emergency cooling system (realized in XT-ADS with a better utilization of the primary heat exchangers in LOF and LOH accidents). Coupling of the primary system to the spallation loop (e.g. strong reduction of ULOF probability if the primary pumps and the spallation loop pump have the same electrical supply, due to the: instability of the spallation target free surface in absence of flow). Codes must be further developed to cope with coupled system. Further, other codes have to be used for assessing the consequences of transients with the potential of core damage.

13.4. Domain-IV: Hybrid system (ADS) with fertile-free fuel

The Domain IV analyzed an accelerator driven subcritical system with solid fertile-free fuel. Fertile-free cores are characterized by the lack of the prompt stabilizing Doppler temperature feedback, very small βeff, and considerable fuel, coolant, and cladding material density reactivity effects. In an ADS, sub-criticality offers a means to design cores that would cope with such fuels. While not caused by boiling (boiling point of lead bismuth eutectic is 1940 K), but rather by events like pin failure and release of fission gases and helium from the transmutation process, or a steam generator tube rupture accident with steam ingress into the core, coolant void reactivity effects would normally exceed the built-in sub-criticality (about 3000 pcm) and impact the transient behaviour of these ADSs. SIMMER-III, MCNP, ERANOS and DANTSYS codes were used to perform the neutron static calculations. SIMMER-III uses an 11-group data library based on FZK data (processed with the C4P code system): Benchmarking was done against cross section libraries based on JEF2.2, JEFF3.0, JENDL3.3 and ENDF/B-IV.8. The results show satisfactory agreement, and uncertainties in the Pb and Bi nuclear data were identified as major source of the discrepancies between the results obtained with different data files. For instance, results obtained for the CERCER (both ZrO_2 and MgO inert matrix) fuelled core void reactivity effect range from 6 500 pcm (FZK-11 groups, JEF2.2, 30 groups) to 7 700 pcm (JENDL3.3, 30 groups) and 8 300 pcm (JEFF3.0, 30 groups). Within the framework of the CRP, SIMMER-III validation efforts were made based on experimental data provided by the Kyushu University group for important accident modeling phenomena, in particular related to molten clad freezing subsequent to an assembly blockage accident. The following transients were analyzed: ULOF, UTOP, unprotected Beam Overpower transient (150 and 200% proton beam overpower at reactor hot full power conditions, respectively), and the unprotected Assembly Blockage transient. The results with SIMMER-III for the ULOF transient in the case of the CERCER fuelled (MgO matrix) core show that maximum fuel temperatures are below 1 800 K, well below the temperature limit of 2 100 K for which recent investigations have indicated the possibility of the MgO matrix disintegration in case of pin failure. Key parameters and key data and results of hybrid systems (ADS) with fertile-free fuel are shown in Table 4.

TABLE 4. KEY PARAMETERS AND KEY DATA AND RESULTS OF HYBRID SYSTEMS (ADS) WITH FERTILE-FREE FUEL

Key Parameter	Key Data and Results
Reactor analyzed	ADS with fertile-free fuel
Transmutation potential	The ADS system of a power class of 580 MW(th) with fertile-free fuel and shows the maximum possible TRU burning potential, in the range from 42 to 43 kg/TW•h/th, almost all burned TRU's being MAs, in particular Am (ca. 45 kg/TW•h/th).
Fuel masses and configurations, inventories	Heavy metal content: ca. 7.5 kg/MW(th) for MgO, ca. 9 kg/MW(th) for ZrO_2 Pu/MA ratio (no Np): 40/60, Fuel/Matrix (Volume fractions): 40/45/50.

Key Parameter	Key Data and Results
Safety coefficients and kinetic data (Doppler, Structure, coolant, β_{eff})	Doppler constant: near -20 pcm Core void effect: from 6 500 till 8 400 pcm depending upon nuclear data. Core structure removal effect is ca. 50% compared to the void effect in LBE; $ß_{eff}$: ca. 190 pcm, neutron generation time: ca. 0.5 µs. k_{eff} at beginning of life: ca 0.97, reactivity variation after 3 years (assuming no fuel reloading) near 4500 pcm.
Transients analyzed	BT and UTOC — related to beam power variation — are specific for ADS. Other as ULOF, UTOP and UBA (blockage) are common for HLM-cooled systems
Result of transient analyses	ULOF is survived due to significant natural convection flow. UTOP can be survived due to limited reactivity potentials and UTOC can be survived on the short term but needs a final beam-shut-down. UBA represents a route into core damage. Currently no damage propagation envisioned due to limited gas release and rewetting by coolant. Beam shut-down needed for all transients.
Key transient phenomena and key safety parameters	Except UBA, the system is stable due to the sub-criticality. Key transient phenomena relate to potentially strong reactivity increase due to coolant heat-up, gas blow-down after pin disruption and structure removal under accident conditions. Therefore key safety parameters are the high structure and coolant reactivity worth values and a very low Doppler constant; Due to the sub-critical regime, low β_{eff} value does not influence the safety performance appreciably. The lack of the prompt acting Doppler effect , the low β_{eff} and a low value of neutron generation time may potentially lead to significant energy release in case of criticality.
Feedback mechanisms	The main stabilizing effect comes through the sub-criticality as the Doppler plays no role. The high reactivity worth values of structure and coolant may lead to over-criticality in case of S/A blockage; The potentially stabilizing role of radial/axial expansion is ignored for the moment that makes the results conservative. LBE voiding gives a very high reactivity potential. Inert matrix affects the neutron spectrum: it is softer compared to a similar system in which the matrix is replaced by UO_2 (depleted). Therefore the inert matrix makes the void effect smaller. On the other hand the Doppler constant would be slightly larger if the inert matrix was replaced by the UO_2. The void and Doppler effect variations (due to the replacement) would not change qualitatively the principal feedbacks and the kinetic parameters: a large void effect combined with a near zero Doppler constant and a low β_{eff} value is due to the high MA content.
Typical timescales of transients	Very fast power response (in µs to ms scale) to beam variations. Longer time scales (of the order of 10 s) are typical for ULOF and UBA cases
Control systems	Beam controls the power
Static neutronic codes	C^4P-ZMIX-DANTSYS-TRAIN(FZK), deterministic
Transient codes	SIMMER-III Code
Data basis nuclear	JEF 2.2, JEFF 3.0, JEFF3.1, ENDF/B-7, JENDL 3.3 11 groups for SIMMER, 30 to 560 groups for FZK static codes
Data basis thermal-hydraulics (EOS) etc.	SIMMER-III EOS was established for fuels (included in report). Basis for heavy liquid metal coolants is the Handbook on Lead-bismuth Eutectic Alloy and Lead Properties, Materials Compatibility, Thermal-hydraulics and Technologies, OECD/NEA, 2007.

Key Parameter	Key Data and Results
Results of benchmarking activity in this CRP and lessons learned	— The necessity to study in detail potential consequences of UBA is highlighted; — The uncertainties (in criticality, coolant/structure reactivity effects and burnup reactivity loss) due to nuclear data remain relatively high, the relative uncertainty being ca. 20% Benchmark results from FZK only; however the neutronics results are indirectly confirmed by benchmarking of FZK tools in other Domains.
Status of methods, tools and data and further needs for development	— The available codes are at sufficiently high level in general to investigate the key phenomena — For the moment, 2D transient analyses are routinely possible with respect to computer time, even going into core disruption as in the UBA; 3D analyses are more time-consuming and require very long computer times for simulating transient that last much longer than 1 minute (as e.g. the UBA transient when following the complex material redistribution after pin damage). — Thermal expansion of reactor structure is either simulated with primitive models or ignored. —
Long term general needs for theoretical and experimental work	Nuclear data for MAs and partly for 'new' reactor materials (Pb) are still associated with high uncertainties; Uncertainties of lower magnitude are assumed to be related to not taking into account nuclear data above 20 MeV and using of homogeneous models in the cross-section processing in SIMMER and FZK static neutronics codes;Thermo-physical data need benchmarking against a wider set of experimental data. ADS design optimization may improve safety and burnup performance. A key issue is the behavior of the fuels under irradiation, high temperature conditions and accidental conditions. Both experimental evidences has to be provided in the future and significant code development has to be performed in this direction.

13.5. Domain-V: Molten salt reactor with fertile fuel

The Domain V analyzed a critical molten salt reactor with fertile fuel of the 2 250 MW(th) power class. The benchmark is based on the Li/Be/Th-F AMSTER (Actinides Molten Salt TransmutER) incinerator concept, originally proposed by EdF as part of EURATOM's 5th Framework Program MOST Project. AMSTER is based on ORNL's Molten Salt Breeder Reactor (MSBR) design (proposed in the 1970s to optimize breeding in a thorium cycle), and comprises a 'burner' concept utilizing the actinides originating from PWRs and a 'breeder' concept having a conversion factor close to 1.0 designed to reduce the amount of long lived waste. The benchmark participants relied on experimental results obtained in the 1960s within the framework of tests performed at ORNL in the 10 MW Molten Salt Reactor Experiment (MSRE). A pump start-up and coast-down (which leads to a reactivity increase in the molten salt reactor, due to the moving neutron precursor nuclides) experimental data have been used to perform inter-comparisons between code systems such as SimADS, SIMMER, and DYNAMOSS. The reactivity coefficients were calculated for the AMSTER 'burner' concept using APOLLO2 and WIMS8a. An important result is that the addition of ^{167}Er is required to achieve a negative graphite reactivity coefficient (and, thus, long term stable reactor conditions), in the range of 600-800°C. The benchmark participants analyzed the following unprotected transient events: ULOF, ULOHS, UTOP, and the unprotected overcooling of the primary molten salt fuel. The comparison of the results confirms that the large thermal inertia associated with the graphite leads to a very 'sluggish' transient behavior of such transmutation systems, ensuring sufficient grace time for effective operator intervention. Key parameters and key data and results of molten salt reactor with fertile fuel are shown in Table 5.

TABLE 5. KEY PARAMETERS AND KEY DATA AND RESULTS OF MOLTEN SALT REACTOR WITH FERTILE FUEL

Key Parameter	Key Data and Results
Reactor analyzed	AMSTER –I Molten Salt System
Transmutation potential	The Li,Be,Th/F AMSTER is a continuously reloaded, graphite-moderated molten salt critical reactor, using a ^{232}Th fuel support, slightly enriched with ^{235}U if necessary. Equilibrium state calculations were done under the hypothesis that the reactor is continuously fed by a mixture of thorium and of TRUs issued from PWR spent fuel. TRU burned rate is ~22.6 kg/TW•h/th
Fuel masses and configurations, inventories	The cell geometric model is based on the cylindrical model of the real geometry, which is hexagonal. Mass of heavy metal in the reactor: 71 042 kg Mass of TRU at equilibrium: 1497 kg
Safety coefficients and kinetic data (Doppler, Structure, coolant, β_{eff})	AMSTER-incinerator without erbium in graphite presents quite different characteristics. At nominal operating conditions, the total temperature coefficient is positive: the graphite coefficient is +1.3 pcm/°C, the fuel salt coefficient is -0.8 pcm/°C, the total temperature coefficient being + 0.5pcm/°C.
Transients analyzed	Unprotected Loss of Flow (ULOF), assuming loss of forced circulation in the primary system due to pump failure. The core inlet temperature is assumed to remain constant. The mass flow rate of the fuel salt is assumed to stabilize after 7 s at about 5% of its nominal value (natural convection); Unprotected Transient Over Power (UTOP) due to a +300 pcm jump in reactivity; a fissile fuel chunk dislodged from the loop walls (fissile fuel agglomeration) is assumed to become lodged inside the core region, the core inlet temperature is assumed to remain constant during this transient; Unprotected primary circuit Overcooling Transient (UOT), with the inlet temperature reduced by 50°C in 50 s. Unprotected Loss of Heat Sink (ULOHS) in which the heat sink is assumed to totally fail. Special initiating events, which could lead to the reactivity changes in MSR can be summarized as: (i) Change of the effective delayed neutron fraction due to the stopping and starting fuel circulation; (ii) Increase of the fissile materials concentration in the fuel; (iii) Changes in the fuel composition and density (voiding of fuel channels, changes in the gas fraction in the fuel and a primary circuit overcooling).
Result of transient analyses	The above transients have demonstrated that the AMSTER-Incinerator design without ^{167}Er added to the graphite matrix can be stable when graphite temperatures exceed 800°C because the graphite temperature coefficient becomes negative above these temperatures. For this reactor design to be stable for long transient time-scales under all conceivable unprotected transient conditions, ^{167}Er should be included in the graphite matrix to assure a negative graphite temperature coefficient even at lower graphite temperature (~600°C). One positive attribute associated with graphite is its very large thermal inertia, assuring a sluggish transient behaviour due to the slow heat-up of graphite. This sluggishness provides sufficient response time for the reactor operators to counteract the failed control rod system that has been assumed not functional for all of the above investigated transients.
Key transient phenomena and key safety parameters	The basic transient behaviour of these particular reactor designs can be characterised by the mismatch in the temperature response of the fuel (fast acting) and the graphite (slow acting). After the initial transient phase, during which the average fuel temperature dominates the transient response, the graphite temperature catches up and impose its characteristics onto the plant dynamic behaviour thereafter.

Key Parameter	Key Data and Results
	Addition of erbium into the graphite matrix changes the sign of the graphite coefficient from positive to negative, rendering the total coefficient significantly negative thereby making the core intrinsically stable.
Feedback mechanisms	In general, all transients are observed to be very sluggish due to the very large thermal inertia associated with the graphite in the core. The long term dynamic behaviour of the reactor becomes unstable under unprotected transient conditions if the total reactivity coefficient of the system should be positive. The long term reactor power level will not stabilize under these conditions. Should the total temperature coefficient be negative, the reactor will stabilize at a certain power level with corresponding temperatures. The total temperature coefficients for the AMSTER-Incinerator, have values close to zero, if erbium is not added to the graphite matrix. Moreover, both fuel and graphite coefficients display non-negligible variations with temperature, leading to quite complex and unpredictable long term transient behaviour (if the operator does not intervene). The sluggish transient behaviour of this reactor design, however, provides sufficiently response time for the reactor operators to counteract the failed control rod system that has been assumed not functional during all of the above transients analyzed. Since the initial phase of all transients is dominated by the negative reactivity coefficient associated with the fuel temperature, the reactor can be basically characterized as safe.
Typical timescales of transients	10-100 s depending on the out core circulation time
Control systems	Control rods Subcritical drain tanks Decay heat removal systems
Static neutronic codes	APOLLO2 transport code
Transient codes	DYNAMOSS code, coupled with a channel thermal model, SIM-ADS, SIMMER-III
Data basis nuclear	99 groups CEA 93 library (which is issued from JEF2.2 evaluation)
Data basis thermal-hydraulics (EOS) etc.	ORNL's Molten Salt Breeder Reactor (MSBR)
Results of benchmarking activity in this CRP and lessons learned	Major lessons (e.g. Erbium addition) already found in MOST project
Status of methods, tools and data used and further needs for development	The further acceleration of neutronics module of SIMMER coupled with the thermal hydraulic part as applied to AMSTER design. The use of space-time kinetics with separately moving precursor groups is recommended.
Long term general needs for theoretical and experimental work	A full safety analysis of AMSTER –I has not been performed because it would require a much more comprehensive design than is currently available. Successful solution of the MSR spent fuel reprocessing technology development seems to be one of crucial steps before industrial deployment of AMSTER-I system.

13.6. Domain-VI: Molten salt reactor with fertile-free fuel

The benchmark case investigated in this area is based on the Na/Be/Li-F MOlten Salt Advanced Reactor Transmuter (MOSART) concept that is investigated within the framework of the ISTC project #1606. The benchmark considers the MOSART concept as incinerator of actinides from LWR spent fuel. Hence, actinide (An) composition (6.42% Np, 3.18% ^{238}Pu, 43.93% ^{239}Pu, 21.27% ^{240}Pu, 13.52% ^{241}Pu, 7.88% ^{242}Pu, 0.55% ^{241}Am, 2.33% ^{243}Am, 0.92% Cm) of the MOSART start-up and feed fuel correspond to the composition of the unloaded commercial PWR UOX fuel (4.9% ^{235}U, 60 GW•d/tU burnup, 1 year cooling time). MOSART is a 2 400 MW(th) system with a cylindrical core, and has an intermediate to fast neutron spectrum. The reactor core is surrounded by a solid 0.2 m thick graphite reflector, which proved to be the optimum as far as minimum equilibrium actinide concentrations are concerned. There is no solid material in the core of the reactor. The molten salt fuel carrier mixture (mol%) 58NaF-27BeF_2-15LiF has a melting point of 479°C and is fuelled by 1 mol% of AnF_3, which is well below the solubility limit of 1.9 mol% for PuF_3 at 600°C. The molten fuel salt enters the core at 600°C through a 0.5 m radial window at the bottom of the core and leaves the core through a 1 m diameter pipe in the top conic reflector. The average neutron flux is 10^{15}n×cm^{-2}s^{-1}, peak and average power densities are 163 and 75 MWm^{-3}, respectively. The molten fuel salt has an average flow velocity of 0.5 ms^{-1}, and its flow rate is 103 kg^{-1}. The static neutronics calculations were performed using multi-group deterministic codes (DANTSYS, SIMMER, XSDRNPM) and Monte-Carlo codes (MCNP, MCNPX, MCU). The cross sections were obtained from various nuclear data libraries (ENDF/B-VI, JEF 2.2, JEFF 3.0, JEFF 3.1, JENDL 3.3). The results indicate a 2.5% spread in k_{eff} due to the different libraries. Strong contributions to this spread stem from Cm data, but also light elements (^{9}Be and ^{19}F) introduce large uncertainties. When the same data library is used, deterministic and Monte Carlo results are in excellent agreement. The agreement between the results obtained for the major kinetics parameters is satisfactory. The major contributions to the effective delayed neutron fraction β_{eff} come from ^{241}Pu, ^{239}Pu, ^{245}Cm, and ^{247}Cm (60, 17, 9, and 4%, respectively). The agreement between the results obtained for the main temperature reactivity effects (Doppler and material density) is also good: in the range 600-1 300°C, the temperature reactivity effect is strongly negative (approximately -4 pcm/K). The CRP participants used the SIMMER and the DYNAMOSS code to analyze the effect of the movement of the delayed neutron precursors. Preliminary results indicate a relatively high reduction of β_{eff} in steady state conditions by 40 to 50%, as compared to stationary fuel. This effect, as well as the temperature distribution in the core strongly depends upon the molten salt velocity profile, which, in turn, depends upon the design of the distribution plate. It is also important to note that these effects may also vary strongly during a transient. The benchmark exercise included the analyses of the following transients: UTOP, ULOF, and ULOHS. The simulation with SimADS of ULOF transients in reactors with circulating fuel implies positive reactivity insertion. In the case of MSBR (with 340 pcm static β_{eff}) the reactivity insertion due to the loss of fuel circulation was calculated to be 83 pcm. However, due to the strong negative temperature effects, the transient leads to a power reduction. Key parameters and key data and results of molten salt reactor with fertile-free fuel are shown in Table 6.

TABLE 6. KEY PARAMETERS AND KEY DATA AND RESULTS OF MOLTEN SALT REACTOR WITH FERTILE-FREE FUEL

Key Parameter	Key Data and Results
Reactor analyzed	MOSART
Transmutation potential	Single fluid Na,Li,Be/F MOSART system with design objective to provide safely the fissile concentration and geometry of the fuel salt to obtain heat release of about 2400 MW(th) at conditions affording the effective transmutation of TRU's from UOX PWR spent fuel without U-Th support. TRU burned rate is 43 kg/TW•h/th

Key Parameter	Key Data and Results
Fuel masses and configurations, inventories	Homogeneous core without moderator, Mass of TRU at equilibrium 6280 kg
Safety coefficients and kinetic data (Doppler, structure, coolant, β_{eff})	α total = -3.7 pcm/K α-Doppler = -1.6 pcm/K α reflector = -0.05 pcm/K α density = α total – α-Doppler β_{eff} (static) = 320 pcm
Transients analyzed	— An Unprotected Loss of Flow (ULOF), assuming loss of forced circulation in the primary system due to pump failure; — An Unprotected Loss of Heat Sink (ULOHS) in which the heat sink is assumed to totally fail. — Several Unprotected Transient Over Power (UTOP) due to a +200 and a +500 pcm reactivity insertion. Special initiating events, which could lead to the reactivity changes in MSR can be summarized as follows: — Change of the effective delayed neutron fraction due to the stopping and starting fuel circulation. — Increase of the fissile materials concentration in the fuel. — Changes in the fuel composition and density (voiding of fuel channels, changes in the gas fraction in the fuel and a primary circuit overcooling).
Result of transients	The transient study has demonstrated that the design is an inherently stable reactor design on account of its large, negative fuel temperature coefficient in combination with its negative graphite reflector reactivity coefficient. The MOSART reactor is expected not to be seriously challenged by the major, unprotected transients such as ULOF, ULOHS, overcooling, or even UTOP. The system was shown to buffer reactivity insertion of up to +1.5$. System temperatures are expected to rise only ~300°C above nominal under this severe transient conditions. The mechanical and structural integrity of the system is not expected to be impaired assuming countermeasures are activated within a reasonable time period after initiation of the 1.5$ UTOP transient (several minutes). Preliminary calculations of kinetic and dynamic characteristics of the MOSART system indicate that it would exhibit high levels of controllability and safety. System would also posess inherent dynamic stability and would require only modest amounts of reactivity control capability.
Key transient phenomena and key safety parameters	In core fluid fuel expansion due to a rise in temperature in the reactor core reduces not only fluid density, but also the amount of fissile material in the core thus reducing reactivity. The system without moderator offered the prospect therefore of being self-regulating and the reactor experiments that were operated showed that the classical control rod absorber system was not necessary.
Feedback mechanisms	In core fluid fuel expansion due to a rise in temperature in the reactor core reduces not only fluid density, but also the amount of fissile material in the core thus reducing reactivity. Any changes of pressure in MOSART reactor system will lead to helium bubbles fraction increasing and due to negative value of density reactivity coefficient to the inserting of negative reactivity.
Typical timescales of transients	10-100 s depending on the out core circulation time
Control systems	Subcritical drain tanks Decay heat removal systems

Key Parameter	Key Data and Results
Static neutronic codes	BME: MCNP4C+JEFF 3.1/1D 172 gr. +JEFF 3.1/MCNP4C+JEF 2.2 FZK: 2D 560 gr. JEFF 3.0/JENDL3.3/ENDF 6.8/JEF 2.2 NRG: MCNP4C JEFF 3.1/JEFF 3.0 Polito: 2D 4 gr.JEFF 3.1 RRC-KI: MCNP4B +ENDF5,6/MCU+ MCUDAT SCK•CEN: MCNPX250 + JEFF 3.1
Transient codes	SIMMER-III, SIM-ADS DYNAMOSS
Data basis nuclear	ENDF/B-VI, JEF 2.2, JEFF 3.0, JEFF 3.1, JENDL 3.3
Data basis thermal-hydraulics (EOS) etc.	RRC-KI: Flow Vision EOS FZK: SIMMER-III EOS
Results of benchmarking activity in this CRP and lessons learned	The results of the benchmark underline that for systems like MOSART the choosing of nuclear data must be done very carefully. It was demonstrated the significant difference between JEF 2.2 and all other cases even JEFF 3.1. The reasons for this difference were investigated at BME by considering originally all data from JEFF 3.1 and then replacing data for particular nuclides by those from JEF 2.2. This result underlines the importance of using new evaluated data (which are assumed here to be more accurate) for the mentioned non-heavy nuclides in the molten salt case. The results show that the parameters are favourable for reactor safety, mainly due to the strong density and fuel Doppler effect. The results are in principal agreement with respect to the major reactivity effects. 560-group deterministic and Monte-Carlo k_{eff} results are in excellent agreement (provided that the same nuclear data are employed) giving a higher confidence to the results. The influence of different nuclear data options on the k-eff values is quite strong. Comparison of different data sets revealed a strong contribution from data differences for Cm isotopes and light (^{9}Be, ^{19}F) elements, the latter being present in large quantities in the carrier salt. Major kinetics parameters computed by different participants agree reasonably well taking into account data and modelling differences. Major contributions to β-eff come from ^{241}Pu (ca. 60%), Pu^{239} (ca. 17%), ^{245}Cm (ca. 9%) and ^{247}Cm (ca. 4%).
Status of methods, tools and data used and further needs for development	Further specification of thermal hydraulics characteristics of core and reflectors may be received by use of two-temperature model of a porous body. Also it will be necessary to take into account reactor vessel protection required, by e.g. 30 cm width iron blocks with (1% of fuel salt) installed to reduce the damage flux arriving at surface of the 5cm reactor vessel wall made of Ni based alloy Hastelloy NM. The further acceleration of neutronics module of SIMMER coupled with the thermal hydraulic part as applied to MOSART design. The simulation of the space-time dependence of the individual neutron precursor families has high importance. Preliminary evaluations of the effect of delayed precursor movement at steady-state show a relatively high reduction of the effective delayed neutron fraction (by ca. 40 to 50%). This effect (as well as the temperature distribution in the core) strongly depends upon the velocity profile that in its turn depends at upon the distribution plate design and may vary strongly during the transient. Additional effort should be paid to confirm the computed effect
Long term general needs for theoretical and experimental work	A full safety analysis of MOSART has not been performed because it would require a much more comprehensive design than is currently available. While a substantial R&D effort would be required to commercialize MOSART, there are no unresolved killing issues in the needed technology. The major technical uncertainties in the conceptual design are in the area of tritium confinement, fuel salt processing and behavior of some fission products.

13.7. Domain-VII: Gas cooled hybride (ADS) reactor with fertile-free fuel

A 400 MW(th) helium cooled ADS was proposed by CEA. The actinides (Pu, Np, Am and Cm) bearing CERCER fuel (Pu enrichment 36.4wt%) has an MgO matrix, with a fuel/matrix ratio of approximately 34%. Helium pressure is 60 bar, pressure drop 0.5 bar, inlet and outlet gas temperature 200 and 350°C, respectively. The CRP participants analyzed this benchmark exercise with the help of various Monte-Carlo (TRIPOLI4, MCNP4C, OCTOPUS (MCNP4C3+FISPACT), MCNPX.2.5.0 and deterministic codes (ERANOS2.0, DANTSYS+C4P), using the JEF2.2, JEFF3.1, JENDL3.3, ENDF/B-VI nuclear data libraries. In the first stages of the analysis, large discrepancies were observed between the participants' results (in particular those obtained with ERANOS2.0) with regard to the sub-criticality level. These discrepancies were explained by the overlapping effect of the magnesia and oxygen resonances that requires a fine-group treatment for both nuclides. Since JEFF3.1 is the only library used by ERANOS2.0 to include both nuclides in fine groups, the benchmark participants concluded that ERANOS2.0 analyses of cores containing large amounts of MgO and MAs must use JEFF3.1 and fine-group treatment for magnesia, oxygen and all MAs. With this provision, beginning-of-life sub-criticality results converged to the value of k_{eff}=0.98. The agreement between the participants' results concerning the safety relevant static parameters is satisfactory: β_{eff} are in the range 173 to 179 pcm, except for the MCNP value calculated using JEF2.2 (144 pcm). The spread of the reactivity insertion due to depressurization (60 to 1 bar) is calculated as 239-289 pcm. The spread in the calculated Doppler reactivity effect is larger, with 40 to 94 pcm for a fuel temperature change from 993 to 180°C. The results obtained for the burnup reactivity loss show a large discrepancy between the ERANOS2.0 results (1965 pcm using JEFF3.1) and the other participants' results that are in the range 2737-2847 pcm. The reason was identified in the different ERANOS2.0 ^{242}mAm branching ratio. Results obtained for the transmutation rates are in satisfactory agreement, with total (including U and Pu) values in the range of -41 to -43 kg/TWh thermal. Key parameters and key data and results of gas cooled hybride (ADS) reactor with fertile-free fuel are shown in Table 7.

TABLE 7. KEY PARAMETERS AND KEY DATA AND RESULTS OF GAS COOLED HYBRIDE (ADS) REACTOR WITH FERTILE-FREE FUEL

Key Parameter	Key Data and Results
Reactor analyzed	Gas cooled ADS
Transmutation potential	The ADS system is He-cooled, with fertile-free fuel and shows the maximum possible TRU burning potential, in the range from 42 to 43 kg/TWh (th), almost all burned TRU's being MAs.
Fuel masses and configurations, inventories	23.4 kg/MW(th), that is relatively large compared to the values for LBE-cooled systems (7.5 or 9 kg/MW(th) depending on the inert matrix type). Pu/MA (with Np in the MA part): 36/64 Fuel/Matrix (Volume Fractions): 34/66
Safety coefficients and kinetic data (Doppler, structure, coolant, β_{eff})	Doppler constant: in the range from -20 to -40 pcm Core void effect: ca. 250 pcm (as pressure drops from 60 to 1 bar) Core structure removal effect is not evaluated, but should be appreciably higher than the core void effect β_{eff}: in the range from 170 to 180 pcm.
Transients analyzed	No transient codes available from participating institutions
Results of transient analyses	None
Key transient phenomena and key safety parameters	Though the safety is not investigated, loss of He pressure and voiding can be considered as the main safety case.

Key Parameter	Key Data and Results
Feedback mechanisms	The main stabilizing effect comes through the sub-criticality as the Doppler plays no role. The high reactivity worth of structure may lead to a dramatic reactivity increase in case of loss of coolant and subsequent clad and fuel failure and relocation. The impact of potential fuel relocation is difficult to predict without performing computer simulations. Until the clad is failed, reactivity variations are small compared to the sub-criticality level Doppler plays no role as in other fertile-free systems, the coolant void worth is much smaller compared to HLM-cooled fertile-free systems, other reactivity effects (related to structure) are assumed to be similar to other fertile-free systems.
Typical timescales of transients	Very fast power response (in μs to ms scale) to beam variations. Longer time scales (of the order of 10 s) are typical for other initiators from reactor side.
Control systems	Proton beam controls the power
Static neutronic codes	ERANOS(CEA), deterministic OCTOPUS (MCNP4-FISPACT) (NRG), Monte-Carlo MCNP4C (CEA) , Monte-Carlo MCNPX (SCK) , Monte-Carlo TRIPOLI (CEA), Monte-Carlo C4P-ZMIX-DANTSYS-TRAIN(FZK), deterministic
Transient codes	None
Data basis nuclear	JEF 2.2 JEFF 3.1 ENDF/B-VI.8 JENDL 3.3
Data basis thermal-hydraulics (EOS) etc.	CEA
Results of benchmarking activity in this CRP and lessons learned	— The uncertainties (in criticality, coolant/structure reactivity effects and burnup reactivity loss) due to nuclear data remain relatively high: deviations with respect to particular isotopes (^{242}Am, ^{242m}Am, ^{242}Cm, ^{242}Pu) due to different branching ratios, mainly due to the branching ratios for ^{241}Am>^{242}Am/^{242m}Am (8-9% for ^{241}Am>^{242m}Am for non-CEA: coming from JEFF 3.1/EAF; 15% for CEA) — The branching ratios also influence the reactivity loss per cycle: ca. 2800 pcm after 1450 EFPD for non-CEA vs. ca. 1900 pcm for CEA. This reactivity loss is lower (500 to 700 pcm per year) than one for considered LBE-cooled systems (ca. 1500 pcm per year) due to higher relative (per unit power) fuel inventory. — Using of fine-group (more than 100) data is important in case of employing the ERANOS code system for systems with MgO.
Status of methods, tools and data and further needs for development	— The available codes are at sufficiently high level in general to investigate the key phenomena — Additional efforts should be paid to perform transient analyses, for that purpose additional codes and dabases should be used, these codes may need benchmarking and/or extension for gas-cooled reactor application.

Key Parameter	Key Data and Results
General needs for theoretical and experimental work	1) Nuclear data for MAs are still associated with high uncertainties; 2) ADS designs optimisation may improve their safety and burnup performance, in particular a higher unit power could be conisdered. Development and benchmarking of transient codes.

13.8. Domain-VIII: Fission-fusion hybride system

The fusion-fission system benchmarks are based on ASIPP and AGH Univ. of Science and Technology proposals (FDS-I and Tandem Mirror Concept, respectively). The Tandem Mirror Concept is of the 500 MW(th) class with a subcritical k_{eff} of 0.84 with MA loaded blankets. The static neutronic analyses have been performed with MCNP5. FDS-I is a sub-critical system (k_{eff}=0.946) in which 14.1 MeV neutrons produced by a 150 MW(th) DT-plasma are driving a blanket loaded with actinides and fission products. The actinide fuel is carbide particle fuel cooled by lithium-tritium eutectic. The neutron static benchmark calculations were performed with the help of the ASIPP in-house VisualBUS multifunctional neutronics analysis code system (containing both SN and Monte Carlo modules) and multi-group cross sections based on HENDL. Due to the expansion of the coolant with temperature, the temperature reactivity coefficient is negative, which is a determining factor for the transient behaviour of the system. No severe accident occurs for protected transients. The following unprotected transients were analyzed: Plasma Overpower (UPOP), Transient Overpower (UTOP), Loss Of Flow (ULOF), Loss Of Coolant (ULOC), Loss Of Heat Sink (LOHS), and Collapse Accident (CA). For the UPOP transient, a rapid increase of the neutron source is assumed by increasing the fusion power by a factor of 3 in 4 s, with coolant inlet parameters kept constant. The power in the blanket increases by almost a factor 2.5, but the negative reactivity feedback (about 1080 pcm) stabilizes the outlet temperature at less than 800°C, and thus no melting of fuel particles or structures is occurring. An instantaneous (0.01 s) reactivity insertion of 1000 pcm into the blanket (UTOP) results in a 15% increase of its power and 40 K fuel and coolant temperature increase. For the ULOF, the coolant flow rate (reduced with 6 s half-time) stabilizes at natural convection level of about 10% of the operational value, while fusion power and coolant inlet temperature are kept constant. The results indicate that the remaining natural convection of the coolant provides 30 s grace time before melting of fuel particles and structural materials would start. For the very severe transient ULOC it is assumed that coolant is prevented from reaching the blanket, while the plasma power is kept constant. This transient leads to the melting of the plasma first wall within 70 s. As for the CA, sub-criticality is maintained if the number of collapsed blanket modules does not exceed 3. For the 500 MW(th) Tandem Mirror Concept (k_{eff}=0.84), the analysis of the worst credible accident scenario (collapse of the Tandem Mirror System) shows that the system remains sub-critical. Key parameters and key data and results of fission/fusion hybride system are shown in Table 8.

TABLE 8. KEY PARAMETERS AND KEY DATA AND RESULTS OF FISSION-FUSION HYBRIDE SYSTEM

Key Parameter	Key Data and Results
Reactors analyzed	Fission-Fusion Hybride
Transmutation potential	The analysis of Fission-Fusion Hybrid systems in the present benchmark has demonstrated its transmutation potential. Toroidal configuration (Tokamak) The actinide composition consists of: Pu and MA (^{237}Np, ^{241}Am, ^{243}Am, ^{244}Cm) where the Pu-to-MA mass ratio (in the option of 3D model) is 3 9010 kg: 4702 kg or 89.24%: 10.76%. After one year of operation, while the system power dropped from 13.8 to 4.4 GW 4 485 kg of Pu and 356 kg of MA have been transmuted. In

Key Parameter	Key Data and Results
	addition Long Lived Fission Products (LLFP) have been incinerated too, namely : 112 kg of ^{135}Cs, 71 kg of ^{129}I and 331 kg of ^{99}Tc Cylindrical configuration (Mirror). It has been shown that in that sense some nuclides are effectively destroyed (fissioned), namely ^{239}Pu ^{240}Pu, ^{241}Pu. As a result, the fissioning of all Pu isotopes has reached 42 kg/TWh. For comparison, the net incineration rate of ^{243}Am is high too, but mostly as a result of its transmutation into ^{244}Cm. Optimization of the transmutation process requires further studies.
Fuel masses and configurations, inventories	The actinide inventories are large: Cylindrical configurations (Mirror) The inventory can be in the range 10 mg, depending on the assumed FW load and k_{eff}. Toroidal configurations (Tokamak) These devices are characterized by very large FW areas, thus the inventories must be greater, e.g. in this study amount to 41-53 mg depending on the selected model.
Safety coefficients and kinetic data (Doppler, structure, coolant, β_{eff})	Toroidal configurations (Tokamak) Tokamak (BOC), k_{eff}=0.97 Doppler Void pcm/K pcm/% T=700 K 1.2 413 The Doppler coefficient values can be negative for other actinide compositions whereas the void one is also negative for fuel in the form of actinide carbide particles suspended in the LiPb eutectic coolant (its expansion results in effective fuel 'dilution'). β_{eff}=285 pcm (fundamental mode)
Transients analyzed	— Toroidal configuration (Tokamak) — Unprotected Plasma Over Power UPOP — Unprotected Loss Of Flow ULOF — Unprotected Transient Over Power UTOP — Collapse Accident — Cylindrical configuration (Mirror) — Collapse Accident
Result of transients	In view of the danger of superprompt criticality, the most demanding would be the collapse of the system. Toroidal configuration (Tokamak): The performed calculations have shown that melting of one module of the blanket increases the k_{eff} only slightly to the value of 0.977, whereas the collapse of 3 modules leads to 0.994. Thus, the number of collapsed blankets must not exceed 3, if the supercriticality has to be avoided. Cylindrical configuration (Mirror) : In this case a total collapse of the system is less dramatic, drawing behind an increase in the k_{eff} from 0.84 to 0.96. Toroidal configuration (Tokamak): Unprotected loss of flow ULOF with the assumptions of a pump failure with a flow-halving time of 6 s. Natural convection flow equal to 10% of the nominal one. Results: The power drop from 7.2 GW to 4.8 GW. The k_{eff} decrease from 0.94 to 0.91 and reactivity decreased about 3 960 pcm. The maximum coolant temperature (1 920 K) is still less than the melting point of fuel particles material (~2 773 K). The construction material (steel) would not melt within 30 s.

Key Parameter	Key Data and Results
Key transient phenomena and key safety parameters	All fusion-driven systems are distinct by very large cavity surrounded by the blanket containing actinides. This makes consideration of the system collapse particularly justified.
Feedback mechanisms	Toroidal configuration (Tokamak): Unprotected Plasma Over Power UPOP with the assumptions: A ramp increase in the neutron source strength within 4s from 100 to 300%. Results: After 5 s from the ramp start the reactor power increased by 144% (from 7.2 GW to 17.6 GW) while simultaneously the reactivity decreased by about 1080 pcm. The coolant temperature achieved maximum at 1050 K that does not bring any risk of blanket melt. Unprotected Transient Over Power UTOP with the assumptions: A ramp reactivity insertion of 1000 pcm during 0.01 s. Then, constant. Results: The observed increase in power after the reactivity insertion was about 15%. The associated increase in the LiPb coolant temperature was only 40 K at maximum. Toroidal configuration (Tokamak) : In all the above cases the fraction of fuel particle in coolant decreases with the increase in temperature, which results in the nuclear power and the k_{eff} decrease. So the reactivity feedback is negative during the course of ULOF, UPOP and UTOP.
Typical timescales of transients	Time scale of system transients for LiPb eutectic used as a coolant is similar to that in case of LBE. Thus, for the loss of flow (ULOF) it is about half a minute whereas several seconds in the remaining cases The source overpower event (UPOP) is hardly probable, whereas the threat of ULOF and transients over power UTOP similar to that of HLM-cooled systems.
Control systems	Active countermeasures: In fusion systems the plasma burn in case of emergency can be off very fast e.g. by injection of heavier ions increasing the energy losses from plasma. On the other hand the plasma disruptions are very undesirable as the deposition of plasma energy in short pulse in its surrounding materials rises the temperature of the surface leading e.g. to its evaporation.
Static neutronic codes	Code System VisualBUS consisted of 3 codes: MCAM (Monte-Carlo Automatic Modeling Code), SNAM (SN Automatic Modeling Code), and RCAM (Radiation Coupled Automatic Modeling Code) MCNP5
Transient codes	Neutronics-Thermohydraulics Coupling code NTC2D
Data basis nuclear	Nuclear database HENDL (Hybrid Evaluated Nuclear Data Library) Standard MCNP nuclear data e.g. ENDF/B-6
Data basis thermal-hydraulics (EOS) etc.	In connection with thermal-hydraulic data base the used method is based on generalized Van-der-Waals equation with the most reliable experiment data of liquid phase density and vapor pressure to obtain critical parameters. Then the EOS parameters are determined from the characteristic of the critical point and vapor thermodynamic states which are represented by using MRK equation. Next, internal energy and enthalpy of vapor and liquid are calculated with the evaluated EOS. The speed of sound in liquid materials, which is required to calculate their compressibility, is also estimated.
Results of benchmarking activity in this CRP and lessons	The major finding is the confirmation of fission-fusion hybrid transmutation potential and its satisfying level of operational safety. At the same time the analyzed devices have been far from being optimum

Key Parameter	Key Data and Results
learned	(composition of actinides: Pu vector, MA and their ratio, neutron spectrum, system size etc.
Status of methods, tools and data used and further needs for development	At the present state of research on fission-fusion hybrid methods seem sufficient but a wide-range integral code development might be indicated simulation the whole reactor concept. Nevertheless, the accuracy of performed calculations is not sufficient for other reasons, first of all because of homogenization of system geometry that has been made in the calculations up to now. This signifies that further studies are needed and a continuation of the subject in a next CRP is very desirable.
Long term general needs for theoretical and experimental work	The forecasted above improvement of calculations will require investment of great effort in the detailed description of systems in question.

13.9. Overall conclusions

In 2003 the IAEA has initiated a Coordinated Research Project (CRP) on Studies of Advanced Reactor Technology Options for Effective Incineration of Radioactive Waste. The CRP concentrated on the assessment of the dynamic behaviour of various transmutation systems. The major results obtained in the study are been reported here. The reactor systems comprised critical reactors, subcritical accelerator driven systems with heavy liquid metal and gas cooling, critical molten salt systems and hybride fusion/fission systems. For all reactor systems, fertile and a fertile-free fuel options were investigated.

The transmutation systems with a high minor actinide load generally show deteriorated safety parameters. Benchmarking of tools and data is therefore mandatory. The major effort of the CRP consisted in the benchmarking of steady state core configurations and performing transient simulations. In afirst step, a general assessment and comparison of the dynamics properties of these systems was performed on the basis of the relevant safety coefficients that were determined for the individual systems. In a second step, transient analyses were performed, which reflected the generic behaviour of the various reactors types. In addition, but to a lesser extent, performance issues, e.g. the transmutation potential, burnup behaviour, and decay heat of minor actinide bearing fuels were also investigated.

Detailed conclusions and comparative assessments based on the results obtained for each transmutation system considered are given in Chapter 13. In the following, the most salient general conclusions are summarized one more time.

The results of the CRP show that for steady state analyses the neutronic tools are advanced enough to provide good agreement for all the transmutation systems investigated. This holds for both mechanistic SN and Monte Carlo codes. Larger spreading of results is generally caused by the different nuclear data libraries used. These deviations may not only be caused by the minor actinide data, but also by data of other constituents, e.g. the treatment of the fuel matrix material in inert fuels and the fission products.

Transient calculations were performed for all the transmutation systems, with one exception, the gas cooled ADS. Very different code systems were employed, ranging from point-kinetics to space-time kinetics methods. By the same token, the analyses were based on various levels of sophistication as far as the thermal-hydraulic modeling is concerned. The benchmarking shows that there is no single code able to cover all the time scales of the transients considered for the various transmutation systems. The very detailed codes have difficulties in their running times, e.g. for long-lasting loss of heat sink

transients, while the less detailed codes naturally neglect important phenomena. The need for an intermediate class of codes becomes obvious.

Inclusion of severe transients for each of the considered transmutation systems leading to core disruption was not within the scope of this CRP. Hence, with one exception (ADS with fertile-free fuel), the benchmarking has exclusively been performed in the range of transients without core disruption. However, inclusion of such severe transients might be of interest for a future CRP.

In summarizing, the comparison of the dynamic behaviour of the different transmutation systems performed within the framework of the CRP, has allowed identifying the intrinsic transient behaviour and time-scales of the various systems, as well as the dominating feedback effects. For fertile systems the prompt Doppler feedback is the important balancing effect. In non-fertile systems this part is taken over e.g. by the subcriticality or the thermal structural expansion. Noteworthy is also the slow and sluggish dynamic behaviour of the molten salt systems, compared to the other systems investigated. When looking at the comparative assessment of the various transmutation systems performed within the framework of this CRP, it is important to keep in mind that, while there is a large knowledge base for the critical fast reactors, much less is known for the other innovative systems, e.g. the fission-fusion hybrid systems. Nevertheless the characteristic transients, phenomena and time scales can be identified for all the transmutation systems considered.

The CRP results confirmed the transmutation capability of the various systems, as well as some fuel cycle related issues. Last but not least, a material data base was developed within the framework of the CRP, providing valuable input for other projects.

APPENDIX I. THERMO PHYSICAL DATA USED IN CALCULATIONS FOR PFBR ACCIDENT ANALYSIS IN THE PRE-DISASSEMBLY PHASE*

TABLE AI.1. THERMO PHYSICAL DATA USED IN CALCULATIONS FOR PFBR ACCIDENT ANALYSIS IN THE PRE-DISASSEMBLY PHASE

Property	Fuel	Steel	Sodium
Specific heat ($J\ g^{-1}C^{-1}$)	0.325	0.570	1.286
Thermal expansion coefficient C^{-1}	0.112×10^{-4}	0.200×10^{-4}	0.95×10^{-4}
Melting point (C)	2750	1427	
Boiling point (C)			889
Heat of fusion ($J\ g^{-1}$)	280	270	
Heat of vapourization ($J\ g^{-1}$)			4000
Thermal conductivity ($W\ cm^{-1}\ C^{-1}$)	0.022	0.196	0.68

* The same thermo physical properties were used for the analysis of FBR-MA

APPENDIX II. MINOR ACTINIDES BEARING FAST REACTOR FUEL

The fabrication of minor actinide fuels requires automation and heavy shielding, which goes beyond the current state of the art for MOX fuel fabrication. The latter is highly automated, but operator intervention is possible, and needed either for repairs or for adjustments. For minor actinides, dust free processes are preferred. In one of these, developed at the JRC/ITU, conventional laboratories or glovebox facilities can be used to fabricate, via a sol gel process, precursor materials, such as $(Zr,Y)O_2$, $(Zr,Pu)O_2$ or PuO_2, in the form of highly porous beads with diameters between 40 and 150 μm. At the JRC/ITU, these are then introduced into a special installation for handling minor actinides (the so called MALAB), where they are infiltrated with an americium nitrate solution, prepared by dissolution of the oxide in nitric acid. (Eventually in an industrial scenario, the Am or minor actinide solution would come directly from the reprocessing unit). The infiltrated beads are calcined to convert the actinide nitrate to oxide. The Am content can be controlled by the Am concentration in the infiltrant solution, and one repeats the infiltration/calcinations cycle several times. The principle of the process has been demonstrated, but as with any process, scaling up to an industrial scale will require significant effort to ensure that complete uniformity is obtained in the actinide content. Present studies show that a single phased actinide compound is obtained. Finally, the infiltrated beads are mixed with the Mo matrix in the volume fraction required and compacted into pellets, which are then sintered at high temperature to give the final product. Sintering conditions should be chosen (Ar/H_2) so that the minor actinides remain in the reduced valence III state to ensure there is no oxygen loss from the ceramic to the Mo at high temperatures.

The irradiation of CER, CERCER and CERMET fuels is being initiated now in the Phénix fast reactor and the HFR-Petten material testing reactor, within the FUTURIX and HELIOS irradiation programs, respectively. In principle, thorium based fuels can also be manufactured in a similar route, whereby ThO_2 or even $(Th,Pu)O_2$, beads are produced in conventional facilities, before being infiltrated with the minor actinides. Implementation of the thorium cycle based on breeding of ^{233}U, will need extensive shielding in the fabrication facilities, particularly to eliminate the hard γ emanating from the daughter products of ^{232}U, which is always present. Again, this goes beyond the standards achieved in MOX fabrication plants today.

Fuel reprocessing

Two types of processes can be applied to the separation of long lived radionuclides: hydro-chemical ('wet') and pyro-chemical ('dry') processes. Both have advantages and disadvantages and should be applied in a complementary way.

Aqueous reprocessing

The PUREX process is the industrial hydro-chemical reprocessing technique to separate U and Pu from spent fuel and is based on the dissolution of the fuel in nitric acid. For the separation of minor actinides the process should be modified/extended using also hydro-chemical extraction techniques. Extensive research is presently done in this field, e.g. to co-extract neptunium in a modified PUREX process and to separate americium and curium in the so-called extended PUREX process in which additional extraction steps follow the base process [7]. This extension must include the separation of higher actinides (Am, Cm) from the fission product lanthanides (strong neutron poisons). This separation is an extremely challenging task due to very similar chemical properties of these elements.

An alternative to the PUREX approach could be the UREX process developed in the US and the four-group separation process proposed by JAERI in Japan, both of course far from being developed to an industrial level. In the UREX process uranium, technetium and iodine are extracted and the transuranic elements and other fission products directed to the liquid waste stream. The uranium is sufficiently pure that it could be classified as a low-level waste. The transuranics are not separated from each other, and thus, the UREX process has certainly advantages from an economic and proliferation resistance point of view.

In principle the so-called THOREX process, developed in the US and in Germany for reprocessing of Th fuels, is similar to the PUREX process. A direct utilization of existing industrial facilities like the ones in La Hague or Sellafield is however not possible, because, due to the bad extraction behaviour of Th, a salting-out agent is required. Also the separation from U is not possible as for Pu with a simple valency change, it can only be achieved through the difference in distribution factors between aqueous and organic phase. The problem of the non-extractable decay product ^{231}Pa (3.28×10^4 years half-life) also needs to be solved; a selective Pa adsorption as proposed in the THOREX scheme needs to be further developed.

Pyro-reprocessing

Alternatives to hydro-chemical processes are the pyro-chemical ones in which refining is carried out in the absence of water in molten salt. In nuclear technology, they are often based on electrorefining or on extraction from the molten salt phase into liquid metal. Even if a few large-scale treatments are under investigation at INL Idaho in the US or in Dimitrovgrad, Russia, those processes are certainly not available for reprocessing at an industrial level, yet.

Pyro-chemistry could be preferred in particular for advanced oxide fuels (mixed transuranium, inert matrix or composite), metal fuels, and also nitride fuels.

The major advantages of the pyro-chemical approach to reprocess advanced fuels, in comparison to hydro-chemical techniques, are a higher compactness of equipment and the possibility to form an integrated system between irradiation and reprocessing facility, thus reducing considerably transport of nuclear materials [5].

In addition, the radiation stability of the salt in the pyro-chemical process as compared to the organic solvent in the hydro-chemical process offers an important advantage when dealing with highly active spent minor actinide fuel. Shorter cooling times reduce storage cost. One of the major objectives defined by the GEN-IV roadmap for the fuel cycle of future reactor systems is the grouped management of actinides. Recently, it could be shown on an experimental level that a grouped recovery of actinides with an efficient separation from the lanthanide fission products is possible with molten salt electrorefining [6].

A general advantage of reprocessing and a closed fuel cycle is its environmentally smaller impact in comparison to that of a once-through cycle. This is mainly due to the reduced mining and milling [8]. The pyro-reprocessing could make the closed fuel cycle even cleaner. The feasibility to include minor actinides in the separation scheme is at present studied in the European projects PYROREP and EUROPART. In the frame of these projects, reprocessing of EBR-II type metallic alloy fuel with 2% of Am and 5% of lanthanides ($U_{60}Pu_{20}$-$Zr_{10}Am_2Nd_{3.5}Y_{0.5}Ce_{0.5}Gd_{0.5}$) is being carried out by electrorefining at JRC/ITU. An excellent grouped separation of actinides from lanthanides (An/Ln mass ratio = 2 400) had been obtained.

Almost nothing is known concerning the handling of Th-based materials in pyro-reprocessing, with perhaps the exception of molten salt reactors, where some research was carried out already in the early 60 s. For solid Th-fuelled reactors, however, molten salt technologies for reprocessing require a completely new R&D program. A number of problems specifically related to the Th fuel based cycle need to be solved including:

— Fuel dissolution in molten salt;
— Conversion processes of ThO_2 if metallic concepts have to be applied;
— ^{232}U behaviour also in view of subsequent fuel fabrication;
— ^{231}Pa problem; this can possibly be transferred to the waste treatment part of the process;
— Fuel fabrication after reprocessing.

APPENDIX III. MOSART FUEL MATERIAL COMPOSITIONS

Table III.1. START-UP MATERIAL COMPOSITION IN FINITE Na,Li,Be/F CRITICAL CORE WITH 20 cm GRAPHITE REFLECTOR (in 10^{-24} cm^{-3})

Li-6	2.1500E-07
Li-7	4.3010E-03
Na-23	1.7740E-02
Be-9	8.0300E-03
F-19	3.8560E-02
Np-237	8.6755E-06
Pu-238	4.2892E-06
Pu-239	5.9333E-05
Pu-240	2.8732E-05
Pu-241	1.8271E-05
Pu-242	1.0652E-05
Am-241	7.4230E-07
Am-242m	1.5043E-08
Am-243	3.1523E-06
Cm-242	7.9628E-11
Cm-243	9.0333E-09
Cm-244	1.0626E-06
Cm-245	1.4036E-07
Cm-246	1.1921E-08
Cm-247	1.9376E-10

Table III.2. MASS PROPORTION AT EQUILIBRIUM IN FININTE Na,Li,Be/F CRITICAL CORE WITH 20 cm GRAPHITE REFLECTOR *IN 10^{-24} cm^{-3})

Li-6	3.856E-06
Li-7	4.301E-03
Na-23	1.774E-02
Be-9	8.030E-03
F-19	3.856E-02
Np-237	5.713E-06
Np-239	4.407E-11
U-234	3.993E-07
U-235	3.378E-07
U-236	2.522E-07
U-237	1.617E-09
U-238	2.172E-09
Pu-236	4.843E-12
Pu-238	2.088E-05
Pu-239	4.111E-05
Pu-240	7.585E-05
Pu-241	3.322E-05
Pu-242	4.954E-05
Pu-244	1.049E-11
Am-241	3.728E-06
Am-242m	1.266E-07
Am-243	1.789E-05
Cm-242	7.802E-07
Cm-243	1.359E-07
Cm-244	2.849E-05
Cm-245	1.286E-05
Cm-246	9.889E-06
Cm-247	3.473E-06
Cm-248	1.202E-06
Bk-249	2.336E-07
Cf-249	2.878E-07
Cf-250	3.215E-07
Cf-251	2.169E-07
Zr-93	1.121E-06
Nd-143	1.252E-06
Nd-145	8.960E-07
Nd-147	3.608E-08
Pm-147	3.011E-07
Sm-149	2.055E-07
Sm-150	2.402E-07
Sm-151	1.554E-07
Sm-152	1.736E-07
Eu-153	1.966E-07
Eu-154	9.447E-08
Eu-155	8.558E-08
Gd-157	2.378E-08
B-10*	5.282E-07

* effective fission product (simulates FP that aren't included in fuel composition)

TABLE III.3. MCNP INPUT FOR BENCHMARK, EQUILIBRIUM STATE.

```
1 0 -1 : 2 : 5 imp: n=0

2 0 3 4 -2 -5 imp: n=0
3 2 0.0903 4 -2 -3 8 imp: n=1 $ graphite reflector above active core
4 2 0.0903 7 -2 -8 1 imp: n=1 $ radial graphite reflector
5 2 0.0903 1 -6 -7 imp: n=1 $ bottom graphite reflector
6 1 6.89471E-02 8 -4 -5 imp: n=1 $ fuel salt
7 1 6.89471E-02 6 -7 -8 imp: n=1 $ fuel salt

1 pz 0.
2 cz 190.
3 kz 437.749 9 -1
4 cz 50.
5 pz 500.
6 pz 20.
7 cz 170.
8 kz 416.667 9 -1

m1 3006.60c 3.85580E-06
 3007.60c 4.30097E-03
 4009.60c 8.02973E-03
 9019.60c 3.85601E-02
 11023.60c 1.77402E-02
 92234.80c 3.99343E-07
 92235.16c 3.37828E-07
 92236.80c 2.52237E-07
 92237.80c 1.61715E-09
 92238.16c 2.17177E-09
 93237.80c 5.71277E-06
 93239.80c 4.40702E-11
 94236.80c 4.84313E-12
 94238.80c 2.08777E-05
 94239.16c 4.11116E-05
 94240.80c 7.58531E-05
 94241.80c 3.32192E-05
 94242.80c 4.95412E-05
 94244.80c 1.04879E-11
 95241.80c 3.72822E-06
 95242.81c 1.26588E-07
 95243.80c 1.78890E-05
 96242.80c 7.80210E-07
 96243.80c 1.35892E-07
 96244.80c 2.84853E-05
 96245.80c 1.28594E-05
 96246.80c 9.88873E-06
 96247.80c 3.47349E-06
 96248.80c 1.20175E-06
 97249.60c 2.33557E-07
 98249.60c 2.87834E-07
 98250.60c 3.21539E-07
 98251.60c 2.16943E-07
 40093.50c 1.12081E-06
 60143.50c 1.25167E-06
 60145.50c 8.96013E-07
```

```
 60147.50c 3.60844E-08
 61147.50c 3.01070E-07
 62149.50c 2.05489E-07
 62150.50c 2.40242E-07
 62151.50c 1.55362E-07
 62152.50c 1.73614E-07
 63153.50c 1.96612E-07
 63154.50c 9.44731E-08
 63155.50c 8.55847E-08
 64157.50c 2.37773E-08
 5010.50c 5.28239E-07
c Graphite (950 K)
m2 6012.50c 1.0
mt2 grph.18t
print
tmp1 j j 8.186E-08 8.186E-08
 8.186E-08 7.755E-08 7.755E-08
kcode 4000 1. 50 1050
ksrc 0. 0. 180.
```

REFERENCE TO APPENDIX III

[1] IGNATIEV, V. et al., Integrated Study of Molten Na,Li,Be/F Salts for LWR Waste Burning in Accelerator Driven and Critical Systems, paper presented in GLOBAL 2005, Tsukuba, Japan, 9-13 October 2005.

APPENDIX IV. FUEL SALT PROPERTIES

The operating conditions of a liquid fuel in MOSART require fulfillment of the following physical and technological conditions:

- Elements constituting the fuel diluents should not absorb neutrons to anywhere near considerable extent.
- The melting temperature of the fuel salt composition should not be too high (<500-550°C) at sufficient concentrations of fissile and fertile materials.
- A low vapor pressure at operating temperatures.
- Chemical stability at operating temperatures and radiation resistance.
- The absence of explosive exothermal reactions upon contact with water, air and other substances in the reactor.
- Compatibility with constructional materials and the moderator.
- Transport properties of the fuel salt composition should ensure sufficiently efficient removal of the generated heat at operating temperatures.
- Possibility for the relatively simple extraction from the fuel salt composition of fission products absorbing neutrons in the core.

Several options exist, including salts containing 7Li, Be, Na, Rb, and Zr fluorides. New ternary Na,Li,Be/F solvent system was selected for MOSART concept. It is important that for molten Na,Li,Be/F system, was found quite wide range with minimal of LiF (17-15 mole%) and of BeF2 (27-25mole%) content in the ternary composition, which provide fuel salt able to get PuF3 solubility of 2 and 3 mole%, respectively, at 6 000°C, to keep adequate melting point (<500°C) and very low vapour pressure, to have good nuclear properties, low activation, suitable transport properties, to be well compatible with the materials in the system (<750°C) and moderately expensive (about 25$ per kg).

Below are listed the main physical properties of molten 15LiF-27BeF_2-58NaF (mole %) mixture to be used within CRP in the MOSART design calculation. Composition selected for fuel circuit corresponds to ternary eutectic with liquidus temperature 479±2°C.

1. Solubility of (TRUF3 +AnF3), mole %

Original technique of local γ-spectrometry developed by VNIITF, provide reliable determination of equilibrium in system melt-solid state and measurement of PuF_3 concentration in the 58NaF-15LiF-27BeF_2 (mole %) melt with relative error less than 9%. The effect of NdF_3 in diminishing the solubility of PuF_3 in molten Na,Li,Be/F mixture was experimentally determined. Presence of EuF_2 up to 0.3 mole % in solvent did not affect PuF_3 solubility in molten NaF- LiF-BeF_2 mixture.

$$\ln P = -0,5936 \cdot \frac{10^4}{T} + 7,49$$

2. Density, g/cm^3

Density of molten 58NaF-15LiF-27BeF_2 (mole%) mixture has been measured at KI by hydrostatic weighing method in temperature range 482-770°C. The mistake of measurement is estimated as 0.9%.

$\rho = 2.163 \pm 0.0023 - (4.06 \pm 0.29)10^{-4}(t\,[°C] - 601.4)$

3. Thermal conductivity, W/(m•K)

Thermal conductivity of molten Na,Li,Be/F system has been measured at KI by monotonous heating technique in temperatures range 500-7 500°C. Total dispersion of measurements is determined by accuracy of calibration and estimated as 15%.

$\lambda = 0.838 + 0.0009\ [t\ (°C) - 610.3]$

4. Viscosity (cP)

Viscosity of molten Na,Li,Be/F mixtures have been measured at KI by method of attenuation torsional oscillations of the cylinder with melt under study in a temperature range from freezing up to 8 000°C. Accuracy of measurement is 4-6% (dispersion).

$\log\eta = (-0.9942 \pm 0.0025) + (1603.2 \pm 2.0)/T\ [K]$

5. Heat capacity (Cp ≠ f (T))

Heat capacity for temperature range from 700 to 1000 K was evaluated by IHTE basing on data molten for binary systems and individual components.

$Cp = 2090\ J\ k\tilde{g}^{-1}\cdot K^{-1}$

6. Vapor pressure (Pa)

Vapor pressure was evaluated at FZK by ideal mixture method.

Boiling temperature of the most volatile component of the fuel salt BeF_2 is 1448 K at the pressure level of 1 bar.

$\ln p = 18.920 - 1.469*10^{-4}\ T(K) - 25283/T + 0.9819\ \ln(T)$

REFERENCE TO APPENDIX IV

[1] IGNATIEV, V., et al., Integrated Study of Molten Na,Li,Be/F Salts for LWR Waste Burning in Accelerator Driven and Critical Systems, paper presented in GLOBAL 2005, Tsukuba, Japan, 9-13 October (2005).

APPENDIX V. MOSART FISSION PRODUCTS REMOVAL AND TRU RECYCLING

Methods and cycle times for fission products removal and TRU recycling are given in Table 3.1. For Na,Li,Be/F MOSART concept there are two main tasks of fuel salt cleanup, including (1) multiple recycling of actinides with minimum losses to waste stream and (2) removal of soluble fission products (FP's), first of all lanthanides. Fig. 3.1. shows preliminary conceptual flow sheet for MOSART fission products cleanup unit. As can see, at the initial stage 'noble' metals and zirconium are extracted into liquid metal (cadmium, zinc, bismuth). Then actinides are extracted into liquid bismuth. At the final stage of process all actinides and admitted amount of fission products are re-extracted into purified salt in order to return actinides into the core without any delay.

TABLE V.1. METHODS AND CYCLE TIMES FOR FISSION PRODUCTS REMOVAL AND TRU RECYCLING

Component	Removal time	Removal operation
Kr, Xe	50 sec	Sparging with He
Zn,Ga,Ge,As,Se,Nb,Mo,Ru,Rh,Pd,Ag,Tc, Cd,In,Sn,Sb,Te	2.4 hr	Plating out on surfaces To off gas system
Zr	300efpd	Reductive extraction Oxide precipitation Electrodeposition Distillation
Ni, Fe, Cr		
Np, Pu, Am, Cm		
Y, La, Ce, Pr, Nd, Pm, Gd, Tb, Dy, Ho, Er, Sm, Eu		
Sr, Ba, Rb, Cs	>30 yr	
Li, Be, Na		Salt discard

Reductive extraction is now the most feasible method for TRU recycling. The efficiency of the process can be rather high, as far as it is limited only by diffusion processes and can be easily intensified by mixing of molten salt and liquid metal in extractors. Important advantage of this method is the simplicity to move liquids between apparatus.

On intermediate stage between extraction and re-extraction of actinides, salt solvent is purified from lanthanides. To manage it the salt is heated up to 800-8 500°C, then the salt is saturated by cerium trifluoride. After salt cooling down to 5 000°C, the main part of lanthanides accumulated in the salt cocrystallized together with cerium trifluoride and precipitates. About 10% of initial amount of lanthanides (mainly cerium) remains in dissolved in salt.

Then, purified solvent goes for actinides re-extraction with subsequent reintroduction to fuel circuit. Precipitate of lanthanides with salt residues is directed to distillation facility for vacuum evaporation of salt constituents. Lanthanides (possibly with some amount of salt constituents, mainly, sodium fluoride) after salt distillation are directed to the wastes.

REFERENCE TO APPENDIX V

[1] IGNATIEV, V., et al., Integrated Study of Molten Na,Li,Be/F Salts for LWR Waste Burning in Accelerator Driven and Critical Systems, paper presented in GLOBAL 2005, Tsukuba, Japan, 9-13 October 2005.

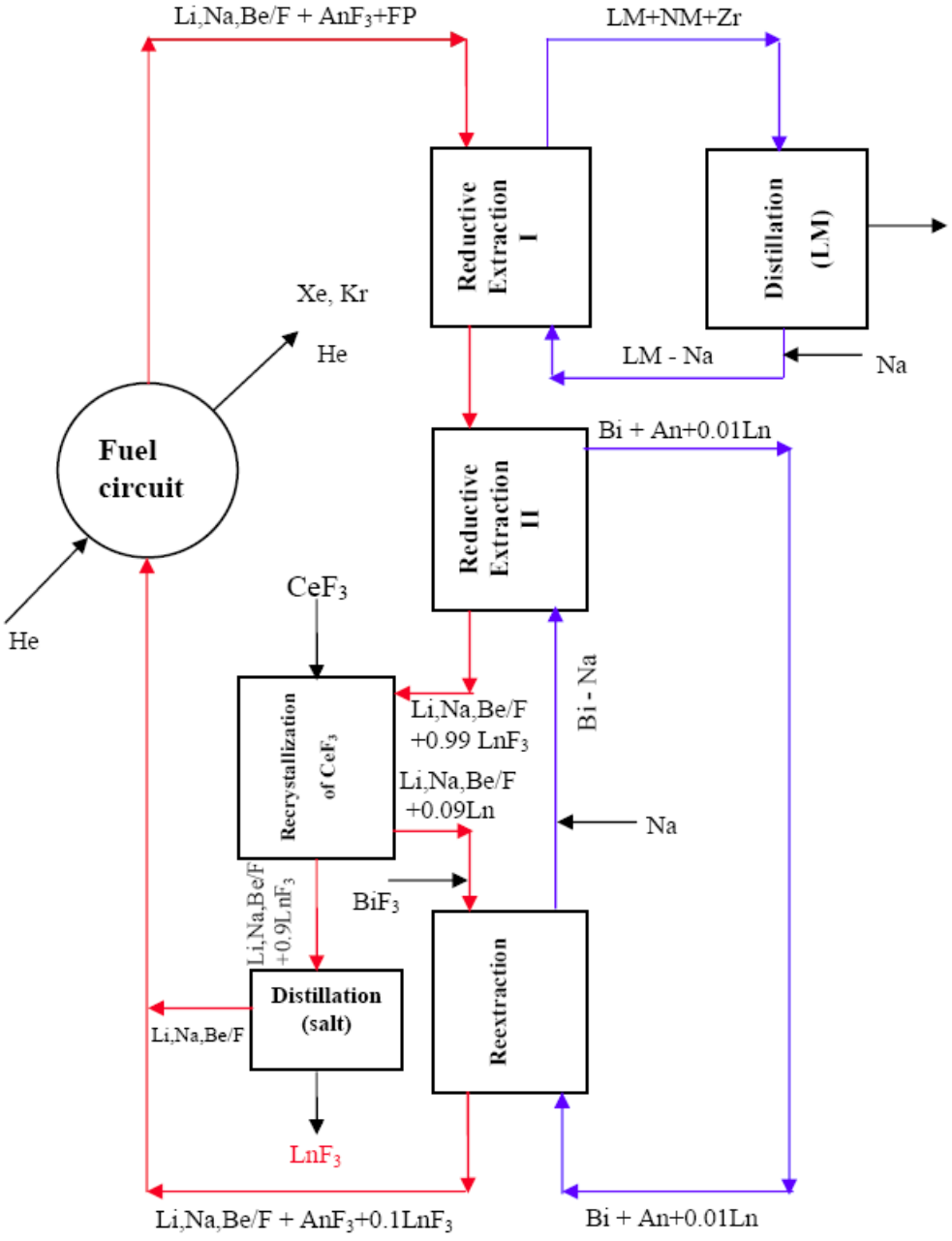

FIG. III.1. Conceptual scheme of MOSART fuel salt cleanup.

APPENDIX VI. POSSIBLE FRONT-ENDS OF MOSART FUEL CYCLE

Because the MOSART fuel feed loadings are generally based on the molten fluoride salt basis, in some cases with short enough cooling time, the advanced pyrochemical fluoride-based technologies have a great chance to be used as the initial front-end process. For all that, the front-end technology based on the industrialized hydrometallurgical PUREX process supplemented by advanced hydrometallurgical partitioning processes and by subsequent conversion of nitride solutions into fluorides could be taken into account as well.

1. Front-end based on the PUREX process

Hydrometallurgical separation technologies, which are also known as the aqueous separation technologies are the only techniques currently used on industrial scale. It refers predominantly to the PUREX process, which is universally employed in the spent fuel reprocessing industry. PUREX process is a wet chemical extraction process, based on the use of tributyl phosphate (TBP). TBP, the extraction solvent containing phosphorus, displays the property of extracting actinide cations in oxidation states IV and VI, in the form of a neutral complex, from an acidic aqueous medium. Unlike this, the actinide cations with odd oxidation stages are not significantly extracted, at least in the high acidity conditions prevailing during reprocessing operations.

The basic principle of the PUREX process comes out from the chemical attributes of uranium and plutonium, whose stable oxidation stages in nitric medium are VI and IV, respectively. Based of this, uranium and plutonium are co-extracted by TBP and thus separated from the bulk of the fission products and minor actinides, which remain in the aqueous phase. Uranium and plutonium are recovered with an industrial yield close to 99.9%. Among the minor actinides, neptunium, whose stable oxidation stage is V, is slightly extractable by TBP.

However, if neptunium is oxidized to the oxidation stage VI, then the extractability of Np(VI) by TBP is good, approaching that of U(VI) and Pu(IV). Therefore for neptunium recovery, the Improved PUREX process has been developed and used. After the co-extraction of Np with U and Pu, neptunium can be selectively separated from these elements by butyraldehydes. Americium and curium, which are stable in oxidation stage III, are not extracted by TBP and remain in the aqueous phase. They accordingly follow the path of the fission products and, in the commercial PUREX process; they are currently managed like the latter by conditioning in a glass matrix. The improved PUREX process is able to separate sufficiently also iodine and technetium.

The main advanced hydrometallurgical processes, which are under the development at present, are in the first instance focused to the trivalent actinide/lanthanide separation. The most important processes, designated for the actinide/lanthanide separation from the high active raffinate coming out from the Improved PUREX process, are DIAMEX, SANEX and SESAME. The DIAMEX process, suitable for americium, curium and lanthanides co-extraction, is based on the use of malonamide extractants at high acidity conditions (3-4 molar HNO_3.). The SANEX process is focused to the americium and curium co-extraction from trivalent lanthanides. The SANEX technology is based on the extraction by polydendate nitrogen ligands (BTP) or dithiophosphinic acids synergistic mixtures at lower acidity (0.5 to 1 molar HNO_3).

The SESAME process can be used for selective Am/Cm separation. The SESAME process is based on the specific property of americium, which is able to exist in nitric medium in the unstable oxidation stages IV and VI, unlike of curium, which remains in oxidation stage III. Selective extraction of Am(VI) is provided by TBP. These advanced hydrometallurgical processes are under development mainly in European countries, so far in laboratory conditions [15].

TABLE VI.1. PUREX (IMPROVED PUREX) PROCESS

Chemical element	Recovered yield (%)
U	99.9
Pu	99.9
Np	95 - 99
Tc	~99
I	99.9
Am, Cm	individually inseparable (in high active raffinate stream together with most of fission products)

TABLE VI.2. ADVANCED HYDROMETALLURGICAL METHODS (DIAMEX, SANEX)

Chemical element	Achieved separation efficiency (%)
Am	99.9*
Cm	99.9*
Cs	99.9

*less than 2% of Ln(III) contamination.

Also some non-European countries are active in the development of these processes. Among these, in the first place, Japanese DIDPA process based on extraction by di-isodecylphosporic acid (DIDPA) and TRUEX process, developed originally in the USA, based on the extraction by di-isobutyl-phenyl-octylcarbamoylmethylphosphine oxide (CMPO) should be taken into consideration [1, 2]. The possible scheme of fuel cycle dedicated to MOSART is shown in Fig. VI.1. Separation efficiencies of selected spent fuel components by using hydrometallurgical processes are listed in Tables A.VI.1 and A.VI.2.

2. Front-end based on pyrochemical fluoride-based processes

The fluoride-based separation processes seems to be very suitable for the processing of transuranium fuel for MOSART. The main advantage of these processes should be the property to convert the oxide form of the spent LWR fuel into the fluorides, which constitute the chemical basis of MOSART fuel. The leading role among the fluoride technologies dedicated to the fuel cycle front-end of the MOSART should play the fluoride volatility method (FVM). The FVM, which was originally designed for FBR fuel reprocessing, was studied mainly in U.S., Russia, France, Czech Republic, Belgium and Japan. The process of oxide spent fuel fluorination was realized either in a fluidized bed reactor (U.S., France, Belgium and Japan) or in a flame fluorinator (Russia and Czech Republic). All volatilization studies have confirmed high efficiency of uranium recovery. However, the efficiencies of individual minor actinides recovery have not been verified yet.

The process is proposed for the use within the MSR fuel cycle by the NRI. R&D in the field of FVM has been concentrated to the development and verification of experimental semi-pilot technology for PWR spent fuel reprocessing, which may result in a product the form and composition of which might be applicable as a starting material for the production of liquid fluoride fuel for MOSART. The FVM is based on the direct fluorination of spent fuel with fluorine gas in a fluorination reactor, where the volatile fluorides (represented mainly by UF_6, partially NpF_6) are separated from the non-volatile ones (e.g. PuF_4, AmF_3, CmF_3, fluorides of majority of fission products), and on the subsequent purification

of the volatile components by using technological operations of condensation, rectification and sorption. Consequently, the objective is a separation of a maximum fraction of uranium component from plutonium, minor actinides and fission products. The anticipated efficiencies of selected spent fuel components by using of FVM are described in Table VI.3.

As evident from the description of the process, the FVM can convert the oxide form of LWR spent fuel into fluorides and separate the main parts of uranium and plutonium and neptunium, but the separation of trivalent actinides (Am, Cm) from the majority of fission products (represented mainly by trivalent lanthanides) is impossible. Therefore the front-end technology based on the FVM has to be supplemented by additional pyrochemical separation technology for the final separation of transplutonium actinides. The suitable technologies proposed for the final fuel processing are either the molten-salt electrochemical processes or the molten-salt/liquid metal extraction processes. Possible scheme of fuel cycle dedicated to MOSART based on pyrochemical front-end technologies is shown in Fig. VI.2.

Table VI.3. ACHIEVED SEPARATION EFFICIENCIES OF SELECTED SPENT FUEL COMPONENT BY USING OF FLUORIDE VOLATILITY METHOD

Chemical elements	Achieved separation efficiency (%)
U	95 – 99.5
Pu	~98 – 99.5
Np	~60 - 70
Nb, Ru	~95 – 99
Am,Cm	individually inseparable (in non-volatile fluoride stream)
FP forming solid fluorides	individually inseparable (in non-volatile fluoride stream)

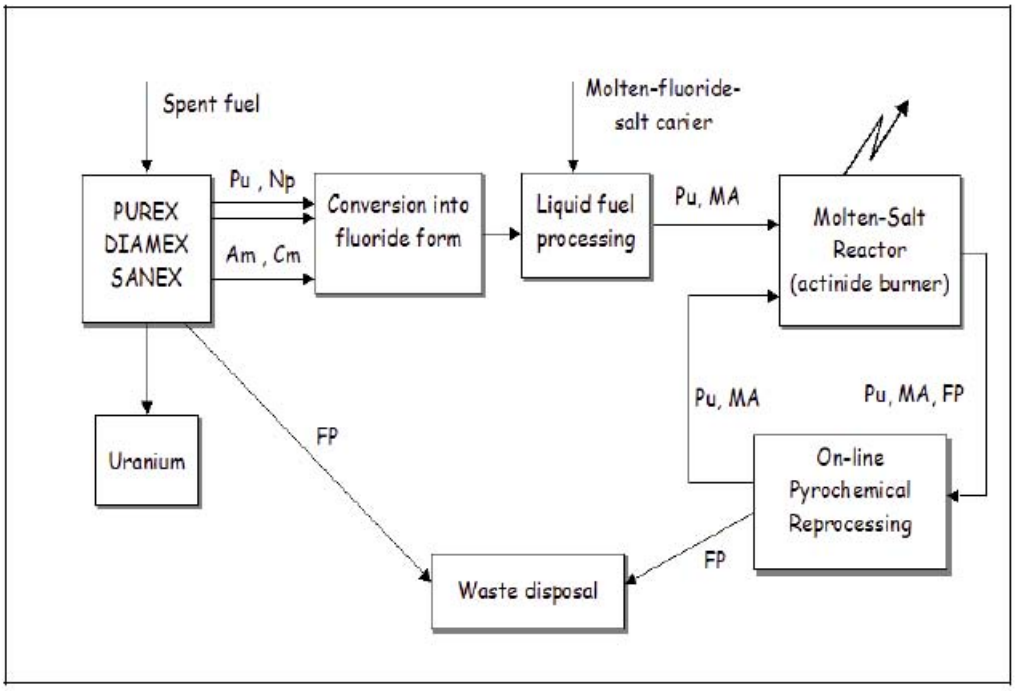

FIG. VI.1. Possible front-end of MOSART fuel cycle based on hydrometallurgical technology.

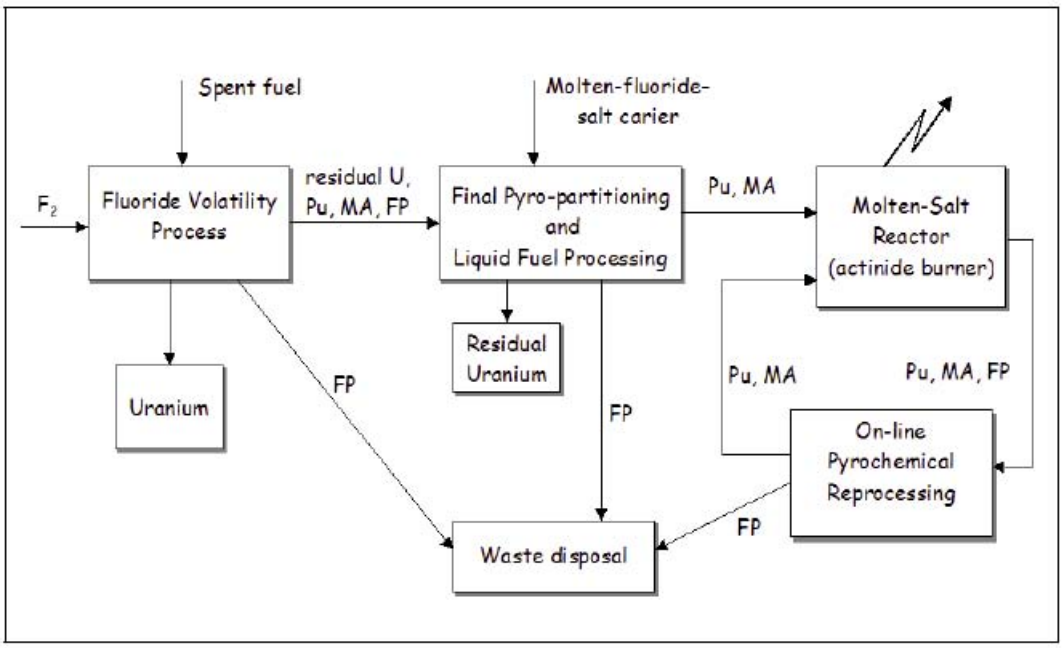

FIG. VI.2. Possible front-end of MOSART fuel cycle based on pyrochemical technology.

REFERENCES TO APPENDIX VI

[1] UHLÍŘ J., P. SOUČEK, G. MODOLO, E. WALLE, R. NANNICINI, EC/EURATOM report of the FP5 project MOST, FIKWT-CT-2001-00096, 08/2003 MOST-D7F.

[2] PYROCHEMICAL SEPARATIONS IN NUCLEAR APPLICATIONS — A Status Report, OECD-NEA No. 5427, OECD (2004).

APPENDIX VII. FAST SIMPLE EVALUATION OF ACTINIDE EQUILIBRIUM COMPOSITION IN TRANSMUTATION SYSTEMS

The knowledge of equilibrium state is important since the system unavoidably approaches to it in the course of transmutation process, and a prediction of the system properties (e.g. reactivity coefficients) is essential. The respective lengthy calculations following the fuel evolution during incineration, can be radically shortened when a guess of asymptotic composition is made, thus being a starting point of transmutation evaluations. The walk in the phase space lies in adapting actinide concentrations that to balance all the production and destruction processes of each actinide at its desired/or resulted/external supply or removal (Fig.A.VII.1.) [1], while keeping the criticality of the system. The savings in computation expense are due to: 1) the initial composition a much closer to the asymptotic one than e.g. the spent fuel to be incinerated, thus 2) the walk towards the equilibrium is short, besides 3) it does not require time evolution calculations. It should be noted that the balance of nuclear processes (reactions and decays) alone is not possible for all actinides without external supply since some of them, being raw materials for production of other ones, cannot be generated from the latter. Literally, the condition of uninterrupted flow of materials can be realized solely in molten salt systems, where a constant reprocessing of fluid fuel is carried out, yet a channel-type systems (e.g. like CANDU), where the refueling is done on-line, the assumption of continuous material flow is acceptable.

The above approach is simplified, nevertheless its accuracy seems sufficient, as seen in the Fig. VII.1., where the equilibrium actinide compositions in transmutation systems are compared [1, 2].

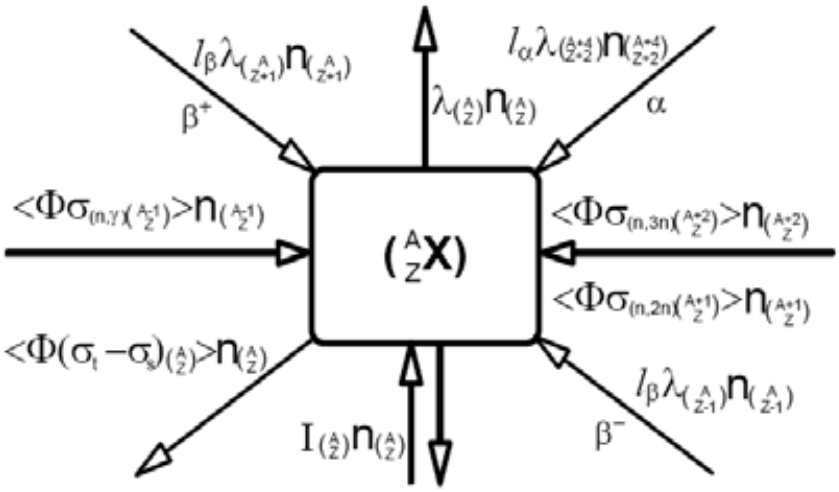

FIG. VII.1. Model of the transmutation balance of the nuclide.

where:

$(^{A}_{Z})$	=	nuclide index
$n_{(^{A}_{Z})}$	=	number of atoms of this nuclide in the system
Φ	=	neutron flux
$< >$	=	integration over neutron energy system volume
$<\Phi\sigma_{(^{A}_{Z})}>$	=	reaction rate /per atom/ of cross-section σ
λ	=	decay constant
l_α, l_β	=	branching ratios of the respective decays
$\sigma_t - \sigma_s$	=	transmutation cross-section
$I_{(^{A}_{Z})} n_{(^{A}_{Z})}$	=	rate of supply or removal of the nuclide $(^{A}_{Z})$

The balance ${}^{j}n'_{(A_Z)}$ /due to zero/of the nuclide ${}^{A}_{Z}X$ in j-th iteration step towards the asymptotic composition is obtained:

$$
\begin{aligned}
{}^{j}P_{(A_Z)} &= \lambda_{(A+4\,Z+2)}\gamma_{\alpha}\,{}^{j}n_{(A+4\,Z+2)} + \lambda_{(A\,Z-1)}\gamma_{\beta}\,{}^{j}n_{(A\,Z-1)} + \left[\langle\Phi\sigma_{(n,\gamma)(A-1\,Z)}\rangle\,{}^{j}n_{(A-1\,Z)} + \right. \\
&\left. \langle\Phi\sigma_{(n,2n)(A+1\,Z)}\rangle\,{}^{j}n_{(A+1\,Z)} + \langle\Phi\sigma_{(n,3n)(A+2\,Z)}\rangle\,{}^{j}n_{(A+2\,Z)}\right]{}^{j}N \qquad (1)\\
{}^{j}D_{(A_Z)} &= \lambda_{(A_Z)}\,{}^{j}n_{(A_Z)} + \langle\Phi(\sigma_t - \sigma_s)_{(A_Z)}\rangle\,{}^{j}n_{(A_Z)}\,{}^{j}N - I_{(A_Z)}\,{}^{j}n_{(A_Z)} \qquad (2)\\
{}^{j}n'_{(A_Z)} &= {}^{j}P_{(A_Z)} - {}^{j}D_{(A_Z)} \qquad (3)
\end{aligned}
$$

The number of neutrons ${}^{j}N$ in the system, determined by the assumed energy release W and mean fission energy Q_f is (l designates walk over A and Z of all actinides):

$${}^{j}N = W/\left(\sum_{l}\langle\Phi\sigma_{f(A_Z)}Q_f\rangle\,{}^{j}n_{(A_Z)}\right) \qquad (4)$$

All components of expressions (1-4) are known either from nuclear data, or from transport calculations, whereas the amount of nuclide ${}^{A}_{Z}X$ in the consecutive, j+1 step is:

$${}^{j+1}n_{(A_Z)} = \left[1 + \frac{{}^{j}P_{(A_Z)} - {}^{j}D_{(A_Z)}}{\max\left({}^{j}P_{(A_Z)}, {}^{j}D_{(A_Z)}\right)}c\right]{}^{j}n_{(A_Z)} \qquad (5)$$

where, e.g. c = 0.2.

The present approach, though assuming a number of simplifications/confinement to most important nuclides and reactions, no fission product evolutions, integral reaction rates instead of local ones, etc./is a fast way of sufficiently reliable estimation of the actinide composition in the given circumstances.

REFERENCES TO APPENDIX VII

[1] TACZANOWSKI, S., Selected Properties of Asymmetrically Coupled Subcritical Systems for Transmutations, IAEA Tech. Com. Meeting, Madrid, Sept. 1997, IAEA TC-903.3, pp. 403-428, (1999).

[2] TACZANOWSKI, S., Transmutations of Long Lived Radioactive Nuclides of the Spent Nuclear Fuel, Summer School of Nuclear Energy, Warsaw, Rep. IEA-71/A, p.197 (2001)/in Polish/.

ABBREVIATIONS

AMSTER	Actinides Molten Salt TransmutER
BOL	Beginning-of-Life
CER	Ceramic fuel
CERCER	Ceramic-Ceramic fuel
CERMET	Ceramic-Metallic uel
CR	Conversion Ratio
ECS	Emergency Cooling System
GEN-IV	Generation-IV
LFR	Lead-Cooled Fast Reactor
LLFP	Long lived Fission Products
LWR	Light Water Reactor
LMFBR	Liquid Metal Fast Breeder Reactor
MA	Minor Actinides
MCB	Monte Carlo Continuous Burnup code
MOSART	MOlten Salt Advanced Reactor Transmuter
MOX	Mixed Oxide
MSBR	Molten Salt Breeder Reactor
MSRE	Molten Salt Reactor Experiment
P/D	Pitch-to-Diameter Ratio
PFBR	Prototype Fast Breeder Reactor
PUREX	Plutonium Uranium Recovery by Extraction
SFR	Sodium-Cooled Fast Reactor
SVRE	Sodium Void Reactivity Effect
TRU	Transuranium Elements
UOX	Uranium Oxide
UREX	Uranium Extraction

CONTRIBUTORS TO DRAFTING AND REVIEW

Afonichkin, V.	Institute of High Temperature Electrochemisty, Russian Federation
Arien, B.	Belgian Nuclear Research Centre, Belgium
Bai, Y.	Chinese Academy of Sciences, Hefei, China
Boccaccini, M.	Forschungszentrum Karlsruhe, Germany
Carlsson, J.	Joint Research Centre of the European Commission, Netherlands
Chabert, C.	Commissariat à l'Energie Atomique, Cadarache, France
Chebeskov, A.N	Institute of Physics and Power Engineering, Russian Federation
Chen, M.	Chinese Academy of Sciences, Hefei, China
Chen, X.-N.	Forschungszentrum Karlsruhe, Germany
Da Cruz, D.F.	Nuclear Research and Consultancy Group, Netherlands
Dekusar, V.M	Institute of Physics and Power Engineering, Russian Federation
Devan, K.	Indira Gandhi Centre for Atomic Research, India
Dulla, S.	Politecnico di Torino, Italy
Feynberg, O.	Kurchatov Institute, Russian Federation
Glatz, J.-P.	Institute for Transuranium Elements, Germany
Gopalakrishnan, V.	Indira Gandhi Centre for Atomic Research, India
Haeck, W.	Belgian Nuclear Research Centre, Belgium
Harish, R.	Indira Gandhi Centre for Atomic Research, India
Heusdains, S.	Belgian Nuclear Research Centre, Belgium
Ignatiev, V.	Kurchatov Institute, Russian Federation
Jiang, J.	Chinese Academy of Sciences, Hefei, China
Kophazi, J.	Budapest University of Technology and Economics, Hungary
Li, J.	Chinese Academy of Sciences, Hefei, China
Malambu, E.	Belgian Nuclear Research Centre, Belgium
Maschek, W.	Forschungszentrum Karlsruhe, Germany
Merzlyakov, A.	Kurchatov Institute, Russian Federation
Mohanakrishnan, P.	Indira Gandhi Centre for Atomic Research, India
Morita, K.	Kyushu University, Japan
Pandikumar, G.	Indira Gandhi Centre for Atomic Research, India
Panov, A.	Snezinsk Physics Technical Institute, Russian Federation
Peneliau, Y.	Commissariat à l'Energie Atomique, Cadarache, France
Plisson-Rieunier, D.	Commissariat à l'Energie Atomique, Cadarache, France
Ravetto, P.	Politecnico di Torino, Italy
Rimpault, G.	Commissariat à l'Energie Atomique, Cadarache, France
Rineiski, A.	Forschungszentrum Karlsruhe, Germany
Schikorr, W.M.	Forschungszentrum Karlsruhe, Germany

Smirnov, V.	Kurchatov Institute, Russian Federation
Sobolev, V.	Belgian Nuclear Research Centre, Belgium
Somers, J.	Joint Research Centre of the European Commission, Netherlands
Srivenkatesan, R.	Bhabha Atomic Research Centre, India
Stanculescu, A.	International Atomic Energy Agency
Subbotin, V.	Snezinsk Physics Technical Institute, Russian Federation
Surenkov, A.	Kurchatov Institute, Russian Federation
Suzuki, T.	Forschungszentrum Karlsruhe, Germany
Szieberth, M.	Budapest University of Technology and Economics, Hungary
Taczanowski, S.	AGH University of Science and Technology, Poland
Tommasi, J.	Commissariat à l'Energie Atomique, Cadarache, France
Tretiakov, I.	Kurchatov Institute, Russian Federation
Tuček, K.	Joint Research Centre of the European Commission, Netherlands
Uhlir, J.	Nuclear Research Institute Řež plc, Czech Republic
Vidović, D.	Joint Research Center of the European Commissio, Netherlands
Wider, H.	Joint Research Centre of the European Commission, Netherlands
Wang, S.	Forschungszentrum Karlsruhe, Germany
Wu, Y.	Chinese Academy of Sciences, Hefei, China
Zakirov, R.	Snezinsk Physics Technical Institute, Russian Federation
Zeng, Q.	Chinese Academy of Sciences, Hefei, China
Zheng, S.	Chinese Academy of Sciences, Hefei, China